Effect of the Deformation History on the Recrystallisation Kinetics of Al-1%Mg Alloy

by

ELI SAUL PUCHI CABRERA, B.Met.

A thesis submitted for the degree of Doctor of Philosophy in the Department of Metallurgy, University of Sheffield.

February 1983.

This work is dedicated to my beloved Susana.

...Everyone who has done any kind of Creative work has experienced, in a greater or less degree, the state of mind in which, after long labour, truth or beauty appears, or seems to appear, in a sudden glory. It may be only about some small matter, or it may be about the universe. The experience is, at the moment, very convincing; doubt may come later, but at the time there is utter certainty....

Bertrand Russell, 1946

CONTENTS

SUMMARY

The literature concerning the industrial hot rolling of commercial aluminium alloys and the structural modifications that take place throughout the operations of such processes has been reviewed. Particular attention has been given to the static restoration processes that occur during the time intervals between deformations of non-heat treatable commercial alloys. Experimental and predictive methods of analysis of strain and temperature distributions developed during deformation under plane strain compression conditions have also been surveyed. Single and multiple deformation tests were performed on specimens of commercial-purity aluminium, Al-1%Mg and Al-1%Mg-1%Mn alloy using a plane strain compression testing machine operated by computer-controlled servohydraulic systems, with furnaces and quenching facilities. Basic stress-strain data derived from such tests in the range 300-500°C and 1-100 s^{-1} were used in conjunction with the appropriate model to describe previous deformation history, in the simulation of hot rolling operations carried out on these materials both on laboratory and industrial scales. However, such a model required knowledge of the functional dependence of the time to a fixed recrystallised fraction and the recrystallised grain size, on variables such as: strain, strain rate, temperature and initial grain size, which was achieved by means of restoration and recrystallisation experiments after one deformation. Also, restoration studies carried out after two deformations allowed the investigation of the effect of the presence of recrystallisation between the first two deformations on the kinetics of recrystallisation and the recrystallisation-restoration relationship during the interpass interval between second and third

deformations. Recrystallisation of the individual fractions with different accumulated strains seems to take place independently of each other. Reasonable agreement has been obtained between the computer predicted load trend and the one found experimentally during the industrial hot rolling of commercial-purity aluminium and Al-1%Mg alloy.

CHAPTER I

1. Industrial Hot Rolling of Aluminium Alloys

1.1 Casting Processes

The vast majority of the feedstock of aluminium and its alloys provided for rolling operations is produced by semi-continuous direct chill (DC) casting. However, it was not until World War II that this process was developed and, as with other metals, the early production of aluminium was characterized by the use of small piece weights, traditionally obtained by the process referred to as "chill casting". Although such a process is still employed for the production of pure-grades of aluminium rolling blocks, its use is very limited [1].

Chill-casting processes involve pouring metal from a ladle down one edge of a trunnion-mounted cast iron or copper mould tilted to near horizontal at the start of the pour and gradually brought to the vertical position. Topping-up of the casting is essential since solidification shrinkage may give rise to the formation of a deep central pipe. Many quality problems such as risks of oxide entrainment, the possibility of internal unsoundness due to incomplete feeding of the interior during topping-up and variation in cooling rate, are associated with this practice. Such drawbacks make this process unsuitable to the production of rolling slabs approaching the size now used in modern aluminium plants. Nevertheless, the process presents some advantages as far as the production of commercial-purity aluminium rolling blocks for deep-drawing applications is concerned. Such "pure"

grades of aluminium [2] contain iron and silicon as principal impurities, and during solidification some of these elements give rise to intermetallic phases, the particles of which form an interdendritic network such as that shown in Figure 1. The shape of this network depends on the grain structure, being different in columnar or in local "feather" grains from that in the more equiaxed grains produced by melt inoculation with grain-refining additives such as 4-6 Ti titanium alloy or 5Ti-1B titanium-boron master alloy. Either the secondary dendrite arm spacing or the interdendritic cell size (in equiaxed structures) can be closely correlated to the solidification rate. In the chill-casting process where a slow solidification takes place, the cells are large (100-120 μm) and the intermetallic particles are large and spiky as compared with those obtained with faster solidification rates where the cells are smaller (20-40 μm) and the intermetallics are also smaller and more rounded. Such comparison is shown in Figure 2. The coarse intermetallics from the cast structure tend to improve the final grain and also are associated with low recrystallisation temperatures during the softening anneal after cold working. If the grain size is not fine, or if the grains, though fine, are in groups with common orientations, formed components may show "orange peeling" or parabolic markings perpendicular to the direction of metal flow [3,4]. As well, and more important, a slow solidification rate reduces the level of solute supersaturation that could cause precipitation of the residual elements during the final annealing on high-angle boundaries and restrict the preferential growth of cubic grains. Therefore, a high-temperature homogenisation would no longer be required in order to obtain the low earing associated with such cubic textures.

The development of the DC casting process constituted a major factor in the shaping of the modern aluminium industry. Casting of

good-quality blocks of virtually unlimited cross-section and length was made possible by the advent of this process. The whole scale of rolling operations was increased by increasing the size of the rolling blocks cast and the number of billets poured at one time. The DC casting process is shown diagrammatically in Figure 3. The liquid metal is subjected to primary cooling by conduction of heat through the wall of the water-cooled mould and to secondary cooling through direct application of water to the solid shell as it emerges from the mould cavity. Due to the rapid solidification at the water-cooled mould wall, the structure of the cast in this area will consist of a thin zone of fine-celled metal. At some point above the base of the mould the shell shrinks away from the mould wall leaving an air gap. Extraction of heat through the mould wall is greatly reduced by the air gap and this may lead to partial remelting of the shell before the secondary cooling can take effect. In this zone of reduced cooling rate, the structure is a coarse cellular one. Its thickness depends on the length of time that the air gap is effective, that is to say, on the level of metal in the mould and the casting speed. If the mould is deep and the metal level in it high, then the air gap will extend over a greater length of the mould and the risk of surface defects through local collapse or liquation of the shell may be expected to increase.

The finer cell and intermetallic structure of DC blocks has made a large contribution to the ease of rolling and better treatment response of age-hardenable alloys. The interdendritic cell network formed by the intermetallic particles becomes greatly elongated in rolling and if the original network is coarse owing to slow solidification, then the final anodized product will show a regular structural pattern which is readily visible to the eye and may be obtrusive. Local variations in the number, size, shape and distributions of Fe-Si intermetallics, such

as can arise from large feather grains or mixed grain size in the rolling block, can also give rise to banding or streaking of the final product. Also, a fine cell size in strong alloys can promote quicker and more complete solution heat-treatment by shortening diffusion distances and reducing the particle size of the phases to be dissolved.

1.2 Hot Rolling Operations

The cast ingots either rectangular or round in cross-section obtained from the casting methods described above constitute the starting material for almost all working operations [5]. This stock is converted into final forms such as plate, sections, bars, tubes or forged components as well as into intermediate products like slab, forging stock, or tube blooms, through hot working operations such as rolling, extrusion or forging. Finishing operations may be carried out with or without intermediate thermal treatments by further forming operations such as rolling, drawing and pressing either at room temperature or elevated temperature. This route of production accounts for the largest proportion of commercial tonnage of wrought aluminium alloys. However, there has been considerable incentive to bypass the hot line by continuously casting a strip of reroll gauge that can be directly coiled and later cold strip rolled, or, alternatively, a thicker strip which can be passed hot through a limited number of roll-stands in-line and then coiled for cold strip rolling [2].

In general, much of the improvement of product quality in recent years has been achieved by ingot improvements, especially those deriving from better techniques for liquid metal, degassing, the introduction of metal filtration, and the achievement of better ingot structures [6]. Rolling of the initial ingot to products such as plate, sheet and strip, bar, rod and sections, constitutes a very important

operation among all the initial forming processes used to break-down the as-cast structure of the stock. As in many other forming processes, during rolling a strain gradient is set up from surface to centre of the rolled material. This may be explained by the complementary effects of the compressive roll force and the shear stresses within the stock. It has been shown [7,8,9] that the magnitude of this strain gradient is reduced by increasing the reduction per pass and/or increasing the ratio roll radius/product thickness, since deformation would be substantially uniform through the thickness of the material. Also, during a pass the strain rate rises rapidly to a maximum on entry and falls to zero at exit [10]. At the same time, the surface chills quickly by conduction to the rolls, whereas the centre temperature increases due to the deformation heat. Therefore, even if the strain were uniform there would be a greater increase in the stored energy through most of the pass for the surface than for the centre of the slab. Since after exit the temperature gradients are eliminated by conduction within the working piece, static recrystallisation would be favoured at the surface and the final structure will vary from a recrystallized surface with central sub-grain zones to a through-thickness unrecrystallised structure with sub-grains of varying perfection within deformed as-cast grains. Despite the high hot-rolling temperatures used in the industrial practice, fully recrystallised structures are rarely obtained at the customary hot mill gauges of 5-10 mm. Whether recrystallisation of the hot rolled products occurs or not depends critically on the rolling conditions, particularly on the finishing temperature and rate of cooling after rolling [10].

1.2.1 Plate, Sheet and Strip Production

Figure 4 is a diagram of the basic process route for the production of plate [6]. Usually,aluminium alloy plate is defined as a hot-rolled flat product greater than 6 mm thick and whose maximum sizes available may vary according to the different standards of production in every country. Plate is produced in a wide range of non-heat-treatable and heat-treatable alloys with applications that range from general engineering to electrical, shipbuilding, cryogenics and aircraft industry uses. Prior to rolling, many of the alloys used in plate manufacture require homogenisation. As stated above, ingot structures usually consist of a cored dendritic matrix in which mainly insoluble iron-bearing constitutes as well as silicon-rich inclusions and also copper-bearing particles, arising from non-equilibrium micro-segregation during solidification outline the cell boundaries.

Homogenisation [11] is one of the most important metallurgical processes controlling properties and characteristics such as grain size, earing, mechanical properties, response to etching, anodizing, partial annealing, or solution heat treatment. This process contributes to the solution and reprecipitation of solute elements and soluble phases such as Mg_2Si, $MgZn_2$ and $CuAl_2$, precipitation of supersaturated transition elements such as Cr and Mn as well as Zr-bearing compounds which would tend to precipitate during the treatment in fine particle sizes and characteristic distributions, and also it would enhance the spheroidization of insoluble phases such as $FeAl_3$ and α- and β-AlFeSi, therefore optimizing the subsequent behaviour of the material during hot and cold working. Additionally, the elevated temperature treatment provides stress relief of ingots of those complex alloys which possess high residual stresses after DC casting and which are susceptible to spontaneous stress cracking. Figure 5 shows the

effect of the homogenisation treatment on the structure of as-cast Al-0.1%Cu-1.2%Mn [2].

The number and nature of the second phase particles present in the microstructure of any particular alloy may be extremely complex depending on its composition. As an example, Table I shows the phases formed in Aluminium-Magnesium alloys depending on their content of Magnesium and other elements such as Si, Fe, Mn, Cr, Cu and Zn. The precipitation of the transition elements into compounds of very fine size can affect the recrystallisation behaviour during the hot rolling sequence and produce either completely or partially unrecrystallised grain structures or dislocation sub-structures. Preheating temperatures of ingots range between 475°C and 540°C depending on their composition and initial dimensions [13]. Most plate alloys require homogenisation-preheating cycles controlled to within narrow temperature limits and therefore furnaces are normally designed to be controlled within ±10°C. Overheated ingots as well as ingots with temperatures below the required range are prone to edge cracking therefore affecting the yield and restricting the shape of the rolled product. Most plate is rolled on wide, 4-high reversing mills, many of which serve as the initial breaking-down facility for the production of hot rolled strip [6]. Figure 6 shows a typical hot rolling mill layout capable of producing up to 1500 rolled tonnes/week. Usually, ingots are fed by overhead crane to soaking pits which are aligned adjacent to the mill entry table. The hot metal is charged on to the line from the pits by over-head crane and is conveyed to the mill by driven table rollers. Normally, the beginning of a rolling plan is marked by a nominal sizing pass to give a reference thickness for a defined cross-rolling sequence. By means of a driven, split roller table the ingot is then rotated through 90° and crossed-rolled to the required width dimension.

Depending on the plate size, the ingot may either continue to be crossed-rolled to final thickness or be returned to its original axis and rolled to final thickness. Shearing of the part-rolled product into a number of pieces may occur at an intermediate stage of the process which would allow greater rolling control on wide thin plate where a number of final plates are to be cut from each multiple. In those lines where intermediate break-down mills between the principal mill and the finishing tandem stands for strip are available, the part-rolled sheared multiples may be reheated before further rolling. This would offer gains in productivity by allowing the use of larger ingots and additionally could be employed to enhance the properties of some heat-treatable alloys [6]. Two basic requirements prevail in the design for plate rolling: firstly, to ensure that the mill has adequate power to achieve the heavy penetrating reductions applied which may be as high as 52% during the late stages of the roughing process where the thickness of the ingot may be about 80 mm. The second requirement is the ability to roll material up to maximum widths with good shape control and transverse gauge uniformity. Ingots of initial widths of 1100 mm may increase up to 2100 mm at the end of the finishing stage.

It is evident that any rolling schedule will strongly depend on the particular alloy being worked since the resistance that the material imposes to the deformation applied depends on the alloy content as well as on the conditions of temperature and strain rate of the operation. The production of hot-mill coil [11] requires casting of ingots to a width which minimizes the need for cross-rolling. Several factors govern the maximum weight per unit width of coil that could be produced, e.g.

(a) Dimensions which can be handled on the casting plant.

(b) Dimensions of the pre-heating furnaces.

(c) Number and spacing of the hot rolling units.

(d) Capacity of the terminal equipment.

The fundamental limiting factor to ingot size appears to be the rate of heat extraction in DC casting. The width of the hot rolled coil is limited by the number of multiples of the cold-finished width required for further processing and by the mill equipment. Depending upon the tonnage of material to be processed, hot lines for rolling aluminium and its alloys may be divided into three main types:

(a) large-tonnage mills

(b) medium-tonnage mills

(c) small-tonnage mills.

Depending on whether the mill has to serve the dual purpose of sheet coil and plate production, large-tonnage mills will adopt different break-down mill sizes and mills up to 5000 mm wide are available for this purpose. Finishing mills for sheet coil only may be limited to a width from 1500 to 2500 mm. Among other factors, the type of alloy and gauge to be rolled will determine the use of 3- or 5-stand tandem mills for hot finishing. Figure 7 is a schematic layout of an up-dated version of a hot rolling line capable of producing about 176,800 tonnes per year of hot coil. In such cases production is no longer limited by the capacity of the rolling line, instead it is limited by the capacity of the plant's preheat furnaces [14].

1.2.2 Rod and Bar Production

Production of rods by means of rolling techniques has been closely

allied to the introduction of aluminium for electrical conductors, first for overhead use and later for insulated cables [15]. Failure in an overhead transmission line could be associated with sagging during service or excessive tension during installation or softening due to heating after accidental short circuits [16]. Also, a feeder cable may undergo gross yielding during conduit pulling or may completely fail by breaking. Failure in house wiring may arise from contact-heating due to stress relaxation or by repeated bending during installation. Therefore, the highest possible tensile strength in the finished wire is demanded, minimum strengths ranging from 159 to 193 N/mm^2 depending on diameter, as well as resistance to steady state creep necessary for smaller transmission-line sagging or creep of magnet wire in electrical machines, resistance to stress relaxation necessary for contact stability, high low cycle fatigue resistance to withstand repeated bending during fabrication and installation and temperature stability required for performance at service temperature or higher temperatures during short times. Since electrical resistivity and mechanical strength are interrelated properties, any of the mechanisms chosen to increase the mechanical properties of the material will invariably increase the resistivity and therefore the first approach for the selection of the production route would be to seek maximum strengthening with minimum increase in resistivity [16].

Rod rolling is almost dominated by the production of the electrical-purity aluminium which normally is of 99.5% purity but with special control of those impurities which greatly affect the electric conductivity. As far as this material is concerned, the conductivity of the finished rod and the resulting wire depend on the preheating conditions. Satisfactory levels of conductivity (62 to 64% IACS) are achieved by preheating in conveyor furnaces where the rolling

temperature is reached in about two hours or more. For this reason, rapid methods of heating have not been used. In general, the rolling temperatures would be determined by a compromise between the decrease in hot strength and the onset of hot shortness [15]. Mechanical strength on the other hand, is achieved by controlling the cooling conditions during rolling and thus producing a considerable degree of cold working in the hot-rolled rod. Lower finishing temperatures are obtained by means of adequate lubricants and also by spray cooling the section before entry into the finishing train.

A wide range of alloys that includes both heat-treatable and non-heat-treatable is also rolled to rod. Some of them call for special production techniques especially as far as the power requirements of the process are concerned [15]. In this case, maximum strength with minimum loss of conductivity is achieved by means of subgrain strengthening together with a fine dispersion of non-deformable precipitates. A well formed sub-structure could be established during the hot rolling operations that usually are carried out in the range 400-450°C and the stabilization of such sub-structure would be achieved by means of precipitation of fine, closely spaced (< 2 µm) particles. This mechanism as well as the presence of alloying elements in solid solution will largely contribute to improve both fatigue and creep resistance [16].

Figure 8 is a representative layout of a semi-continuous rod mill where wire bars of 100 mm squared section and 2600 mm long, weighing about 68 kg can be processed.

Such bars are preheated in three forced air circulating electric furnaces each rated at 620 KW and are transferred to a roller approach table to enter the roughing train. The first seven passes are carried out in a 3-high, 530 mm roughing mill driven by a 375 KW ac motor. The

section is then conveyed into a 2-stand 405 mm intermediate mill driven by a 560 KW ac motor where five passes are imparted. Finally the finishing train comprises seven stands, arranged with the rolls alternately horizontal and vertical. The first three rolls are 380 mm diameter and the last four 275 mm diameter, all of them driven by 110 KW dc variable speed motors. On the outgoing side a selector pipe delivers the rod to one of three coilers, from which the coil is discharged to the coiling conveyor. The finishing speed is about 18 m/sec and up to 9.5 and 12.7 mm diameter rod in electrical-purity aluminium and aluminium alloy may be obtained.

CHAPTER II

2. Hot Working Characteristics of Aluminium Alloys

2.1 Introduction

The high temperature deformation (deformation at temperatures >0.6 Tm where Tm represents the absolute melting temperature in kelvin) carried out at relatively high strain rates (10^{-1} to 10^{3} s^{-1}) is usually termed as "hot deformation" and the capability of a metal or alloy to be deformed under such conditions is known as "hot workability" [17]. Most of the industrial rolling operations of aluminium and its alloys that take place during the early stages of the breakdown of as-cast ingots as well as during the finishing tandem-mill operations, are carried out under conditions of hot deformation. Therefore, the response of such alloys in terms of both the strength that they impose to the deformation process as well as the final microstructures achieved are intimately related to the structural changes that occur both during deformation and in the periods between deformations. In contrast to cold forming operations, hot deformation processes are characterised by the fact that simultaneously with the deformation imposed, dynamic restoration processes take place which allow large strains to be achieved with little or not strain hardening. Further and more significant structural modifications take place due to the static softening processes that occur during the time between passes in multi-pass industrial hot forming operations in which the total strain is applied in increments at decreasing temperatures.

The kinetics of such static restoration processes is strongly dependent upon the deformation conditions (deformation temperature, strain applied and rate of straining), chemical composition and on the intrinsic microstructural features of the particular alloy (grain size, distribution of secondary phases, etc) which in turn, are determined by casting conditions and homogenisation treatment. The occurrence of recrystallisation in the periods between deformations of hot rolling operations of aluminium alloys, particularly non-heat-treatable and work-hardening type alloys of the Al-Mn, Al-Mg and Al-Mg-Mn alloy series, has a profound effect on the properties of the final sheet [18,19]. Such alloys are extensively used in applications where some type of forming operation is involved and therefore control of the grain size, earing and other forms of directionality is required. Fine recrystallised grain sizes are important to prevent unsightly "orange-peel" effects and to ensure no loss in formability due to coarse grain. Control of this parameter is exerted through both the distribution of second-phase particles and the deformation conditions throughout the rolling operation. Earing, on the other hand, is controlled by balancing the predominant texture components that occur as a result of recrystallisation (the cube texture, 90° earing) and deformation (the deformation texture, 45° earing). As mentioned before, such a balance is strongly dependent on composition, casting conditions and homogenisation as well as on the structural changes that occur during hot rolling since recrystallisation could produce a shift towards 90° earing by introducing cube texture at an intermediate stage of the process and hence modifying the subsequent pattern of texture changes [18,20]. However, simple aluminium alloys have a strong tendency to recover rather than to recrystallise and therefore close control of the parameters that constitute the rolling schedule e.g. ingot dimensions,

reheating temperature, as-cast grain size, mill dimensions, initial rolling temperature, reduction per pass, delay time between passes, cooling conditions between passes, etc. has to be achieved. If finishing temperatures on the hot line are low enough, it is very likely that the final product will retain a recovered sub-structure instead of recrystallising. Nevertheless, the deformation history will influence the formation of such sub-structure and thus, both work-hardening behaviour and earing of the fully annealed sheet will be affected, possibly due to the alteration in the nucleation rate of new grains arising from differences in either the total strain energy stored in the material or the way in which it is stored in the cold-rolled sheet [18]. It has been found that the amount of 45° earing in annealed commercial-purity aluminium increases as the sub-grain size in hot mill coil decreases [18]. Lack of control of the processing variables during hot rolling of aluminium alloys could also lead to coarse recrystallised grain sizes which in turn, could give rise to longitudinal defects such as "ribbing". If such grains are elongated in subsequent rolling operations it is possible that on annealing areas with either a significantly different texture or grain size from neighbouring areas could be produced.

Variations in the surface grain structure and grain size produced by hot working can also result in streaking-type defects if the material is subjected to subsequent surface treatments, either chemical or anodic [18]. As far as the high-strength plate aluminium alloys are concerned, where the main need is a high level of mechanical properties, control of the microstructural features is achieved by ensuring a fine grain size of the as-cast ingot and the application of correct homogenisation treatments, thus reducing the tendency towards hot cracking during rolling. Improvement of the directional tensile

properties as well as fatigue and fracture properties in general has been achieved by pre-forging ingots before hot rolling and also by increasing mill power,such that heavy penetrating reductions capable of transforming the as-cast structure could be applied [18,21]. However, a considerable effort has been directed towards the improvement of the combinations of thermal and deformation processes that could give rise to interactive microstructural features and would enhance final plate properties. In summary, optimisation of the industrial hot rolling processes can only be achieved by means of a clear understanding of the functional relationships that exist between the kinetics of static recovery and recrystallisation, and the processing parameters already mentioned. Also, a precise knowledge of the effect of partially recrystallised structures upon further softening processes, particularly in relation to the occurrence of recrystallisation, and the role of such recrystallised fractions on the distribution of strain during subsequent deformation is required. The picture could be further complicated by the interaction between the restoration processes and the precipitation of secondary phases since both processes exert a mutual influence upon each other [22].

2.2 Flow Stress Dependence on Deformation Conditions

It has long been established that for both pure metals and simple alloys the flow stress increases with increasing strain rate and decreasing temperature [23]. Figures 9, 10 and 11 demonstrate this particular feature for commercial-purity aluminium deformed under conditions of plane strain compression [24]. Similar results have been obtained in torsion [25-31], tension [32-35], compression [36-43] and extrusion [44-47]. As far as Al and Al-alloys are concerned, the exact form of the equation that relates flow stress to strain, strain rate

and temperature has not yet been determined. However, there is general agreement in that the temperature component should be in the Arrhenius form, such as:

$$\dot{\varepsilon} = f(\sigma) \exp[- \frac{Qdef}{RT}] \qquad .....(2.1)$$

where $\dot{\varepsilon}$ represents the strain rate, σ the flow stress, T the absolute temperature, R the universal gas constant and Qdef an experimental activation energy that has been correlated to the deformation mechanism that operates at high temperatures and which is found not to be significantly temperature dependent within the range of hot working temperatures.

Several investigations [36,38,48-52] have suggested that at low stresses ($\sigma < 20$ N/mm^2), the stress function of equation (2.1) can be expressed as a power law:

$$f(\sigma) = A_1 \sigma^n \qquad .....(2.2)$$

where "A_1" is a material constant that depends on composition [23] and "n" is a temperature-independent constant. Application of such power relationship to data above 20 N/mm^2 results in a change of "n" with temperature [53]. Data at high values of stress ($\sigma > 20$ N/mm^2) are best described by an exponential relationship [37,42] such as:

$$f(\sigma) = A_2 \exp(\beta\sigma) \qquad .....(2.3)$$

where again "A_2" and "β" are material constants dependent on composition and independent of temperature.The similarities existing between the steady-state conditions of creep and those achieved during hot deformation led [53] to the development of a more general equation:

$$f(\sigma) = A_3 [\sinh (\alpha\sigma)]^{n1} \qquad .....(2.4)$$

Such a relationship covers a wider range of stresses since at low values of stress ($\alpha\sigma < 0.8$) it reduces to equation (2.2) and at high stresses ($\alpha\sigma > 1.2$) to equation (2.3). A_3, α and n^1 are found to be related by means of the equation:

$$\alpha = \frac{\beta}{n^1} \qquad .....(2.5)$$

Assuming that $n^1 \simeq n$, both constants α and n^1 are determined from data at high and low stresses. The determination of the activation energy for deformation can be carried out by introducing equation (2.2) and (2.3) into equation (2.1):

$$\dot{\varepsilon} = A_1 \sigma^n \exp(-Qdef/RT) \qquad .....(2.6a)$$

and

$$\dot{\varepsilon} = A_2 \exp(\beta\sigma) \exp(-Qdef/RT) \qquad .....(2.6b)$$

Clearly, the stress function chosen will be the one that best fits the experimental data. Introducing equation (2.4) into equation (2.1) and re-arranging gives a temperature-compensated strain rate parameter:

$$\dot{\varepsilon} \exp(Qdef/RT) = A_3 [\sinh(\alpha\sigma)]^{n^1} \qquad .....(2.7a)$$

or

$$Z = A_3 [\sinh(\alpha\sigma)]^{n^1} \qquad .....(2.7b)$$

where "Z" is usually known as Zener-Hollomon parameter [54]. The experimental activation energies determined by means of equation (2.6b) [42] and equation (2.7a) [24,31,43,55] agree on a value of about 156 kJ/mol which is very close to similar activation energies reported for both creep [23,43] (138-156 kJ/mol) and self-diffusion [23] (138 kJ/mol). Figure 12 illustrates the relationship between Z and σ

assuming that equation (2.4) is upheld. It has therefore been suggested [23,43] that diffusion-controlled recovery processes, such as the motion of jogged screw dislocations or the climb of edge dislocations aided by cross-slip [56] are the rate-controlling dynamic softening process during the hot deformation of aluminium. Tests carried out on commercial-purity aluminium, commercial 17S duraluminium and aluminium-4% copper alloy [57] in the range of strain rates from 10^{-4} to 10^{3} s^{-1}, showed that although the exponential relationship of equation (2.3) is valid over a wide range of temperatures, a remarkable increase in the strain rate sensitivity takes place at strain rates of about 100 s^{-1} in the range of hot working temperatures, Figure 13. Here, it is observed that the strain rate sensitivity both at low and high strain rates, although 3 to 15 times different in magnitude, increases with increasing temperature up to about 150°C and that above 250°C it remains almost constant, whereas for the alloys above 250°C the strain rate sensitivity increased monotonically with the increase of temperature. However, tests in which the strain rate was changed about 2.3 times from both low (2×10^{-4} s^{-1}) and high (2.5×10^{2} s^{-1}) initial strain rates showed that in the range of temperatures concerning hot working practice, the parameter $\Delta\sigma/\Delta \log \dot{\varepsilon}$ determined from the stress-strain curves obtained during the strain rate change, was temperature-independent for pure aluminium while for the alloys this parameter was found to increase with increasing temperature at high initial strain rates and decrease with increasing temperature at low strain rates. Similar experiments carried out on Al-1.1%Mg alloy [58] showed similar results and also it was found that the exponential relationship applied to the stress-strain rate data obtained from tests performed at constant strain rate, was somewhat distorted at strain rates lower than 10 s^{-1} because of the presence of lumps in otherwise

smooth curves, Figure 14. It was suggested that such humps were caused by the interactions between mobile dislocations and magnesium atoms.

More recent work carried out on superpurity aluminium, commercial-purity aluminium, aluminium-1%magnesium and aluminium-1%magnesium-1%manganese alloys [24] in the range of 300 to 500°C and different constant strain rates varying from 1 to 100 s^{-1}, has shown that the power relationship of equation (2.2) can be used to describe the strain rate sensitivity of flow stresses below 20 N/mm^2 and that above this level the exponential relationship can be applied. However, neither of the two relationships yielded an obvious straight-line plot over the whole strain rate range. Figures 15-17 show this fact for commercial-purity aluminium. A change in the strain rate sensitivity was also reported above a strain rate of 20 s^{-1} at all temperatures, even though the materials had achieved steady-state at the highest testing temperature. Such a change in the strain rate sensitivity was taken to imply a change in the rate-controlling dynamic softening process. It was suggested that at high strain rates ($\dot{\varepsilon} > 20\ s^{-1}$), dislocation glide would be slower than the commonly proposed mechanisms of dislocation climb and motion of jogged screw dislocations and therefore it would constitute the rate-controlling mechanism. This was based firstly on the fact that both climb-controlled as well as viscous glide-controlled creep are processes associated with a power-law of the type given in equation (2.2) with "n" in the range 4-6 and 3-3.6 respectively depending on the operating mechanism, and secondly, that the "n" values found when such law is applied to the data for commercial-purity aluminium both at low stresses ($\sigma < 20\ N/mm^2$) and at high strain rates, are well within such ranges. For the alloys the exponent found was slightly higher but this was attributed to the effect of solute atoms on the friction stress.

In general the activation energy for deformation has been reported to remain constant in single phase alloys even though the strength level for a given deformation is significantly increased with the alloy content [10]. Figure 18 shows the effect of copper and magnesium additions on the maximum flow stress of super-purity aluminium in the range of 250-550°C. Such increase, taken in the context of a constant value of the activation energy, would imply an increase of the flow stress sensitivity to strain rate. Most values of β (equation (2.3)) reported for commercial-purity aluminium [31,38,43,53,55] are in the range 0.16-0.19 mm^2/N whereas for the alloys [31,55] the range reported is about 0.06-0.11 mm^2/N with a slight trend to higher β values (lower strain rate sensitivity) for the materials with higher alloy content (Al-4%Cu-1%Mg-1%Si-1%Mn alloy [31]). The above investigations also reported values of α and n^1 (equation (2.4)) for commercial-purity aluminium ranging between 0.04-0.09 mm^2/N and 3.7-4.8 respectively, whereas for the alloys 0.01-0.03 mm^2/N for α and 3.2-5.3 for n^1. The activation energy for deformation was also found to remain constant at about 155 ± 25 kJ/mol independently of composition.

The relationships expressed by equations (2.2)-(2.4) restrict the application of data to conditions of strain equivalent to those under which the flow stress was obtained [17]. Therefore, there have been numerous attempts to fit simple algebraic functions to the stress-strain curves obtained at constant temperature and strain rate. A successful equation should be a general relationship capable of describing the stress-strain behaviour of any particular alloy at any temperature and strain rate within the hot working range. Equations such as:

$$\sigma = k\varepsilon^{m} \qquad .....(2.8a)$$

$$\sigma = \sigma_0 + k\,\varepsilon^m \qquad .....(2.8b)$$

$$\sigma = A(B + \varepsilon)^m \qquad .....(2.8c)$$

where K, σ_0, A, B and m are constants dependent on temperature and strain rate, have been used to try to fit aluminium data [37]. It was concluded that equation (2.8a) provided the best fit. Nevertheless, its applicability is limited to strains less than those where a steady-state of stress is achieved as deduced from the shape of the stress-strain curves [17]. Equations such as

$$\sigma = A-(A-B)\exp(-C\varepsilon) \qquad .....(2.9a)$$

$$\sigma = \sigma_0 + B[1-\exp(-C\varepsilon)]^m \qquad .....(2.9b)$$

$$\sigma = A[1-\exp(-C\varepsilon^{mn})]^{1/n} \qquad .....(2.9c)$$

have been found to be more appropriate to fit data at higher strains since they lead to a steady-state stress at high strains [37,59-61]. Despite the fact that relationships such as those expressed by equations (2.8) and (2.9) are in themselves quite limited, numerous advantages could be gained by combining them with equations (2.6)-(2.7) in such a way that both flow stress and work done for any strain, strain rate and temperature can be subsequently used in computational procedures to calculate working forces in hot working operations, since it is improbable to find the experimental data for the exact deformation conditions of interest. For example, equation (2.9b) reduces to:

$$\sigma = \sigma_0 + (BC^m)\varepsilon^m \qquad .....(2.10a)$$

at low strains and to:

$$\sigma_{ss} = \sigma_0 + B \qquad .....(2.10b)$$

at high strains. "σ_{ss}" represents the stress to steady-state. Therefore, if "σ_o" and "σ_{ss}" are both expressed as a function of the strain rate and temperature by means of the exponential law of equation (2.6b) as:

$$\sigma_o = \frac{1}{\beta_o} \ln[Z/(A_2)_o] \qquad .....(2.11a)$$

and

$$\sigma_{ss} = \frac{1}{\beta_{ss}} \ln[Z/(A_2)_{ss}] \qquad .....(2.11b)$$

then the constant "B" of equation (2.10b) can be readily determined:

$$B = \sigma_{ss} - \sigma_o \qquad .....(2.11c)$$

Also, from the stress-strain data obtained at low strains and constant temperature and strain rate, the constants "C" and "m" can be determined and the final constitutive equation written as:

$$\sigma = \frac{\ln[Z/(A_2)_o]}{\beta_o} + \left[\frac{\ln[Z/(B_o)_{ss}]}{\beta_{ss}} - \frac{\ln[Z/(A_2)_o]}{\beta_o}\right] [\,1 - \exp(-C\varepsilon)]^m \qquad .....(2.12)$$

Alternative equations have also been proposed [62-66] but it is also quite important to point out that in order to apply derived flow stress data, the earlier thermomechanical history of the material has to be considered [17]. Calculation of flow stresses in most metal working theories is carried out by assuming that under hot-working conditions a metal behaves as an ideal plastic solid, i.e. a material insensitive to strain rate and to changes in temperature during the forming operations [67-69]. Therefore, a mean stress of the material is obtained by integrating the area under the stress-strain curve defined for the

given conditions of strain rate and temperature over the strain of interest. This procedure neglects any effect that the strain rate profile in the working process may have on the flow stress [17]. A possible variation of the strain rate through the roll gap for plane-strain conditions has already been indicated [70]. Also, very steep temperature gradients can exist during the rolling of steel [71-74] and aluminium [75-77]. Combining these factors, large variations of the Zener-Hollomon parameter could be possible within the deformation zone resulting in a variation in structure and flow stress [75]. Extrusion experiments carried out with multiple-hole dies of differing reduction ratios on a series of aluminium alloys [46] concluded that application of the Zener-Hollomon relationship was not possible and that a correction factor, function of the die geometry had to be used. The reason for such correction was connected to the fact that the "Z" parameter was traditionally calculated as an average value based upon a mean strain rate and temperature. Recent plane strain compression experiments carried out on Al-1%Mg-1%Mn alloy [24] and under conditions of varying strain rate have shown that both schedules with a rolling-type strain rate profile and schedules at a mean constant strain rate produced no noticeable difference on both sub-structure and tensile properties at room temperature. It was, therefore, concluded that tests at constant strain rate could be used to simulate rolling deformations provided that the time average strain rates were the same. Similar experiments carried out on ferritic st ainless steel [78] gave similar results for the simulation of both rolling- and extrusion-type strain rate profiles and moreover it was concluded that under conditions of varying strain rates this particular alloy followed an equation of state which enabled the form of the stress-strain curve and the mean flow stress for strain rate histories of hot working operations to be

predicted accurately from data obtained at constant strain rate. This seems not to be the case for commercial-purity aluminium, although aluminium-1%magnesium has shown a similar behaviour to the ferritic stainless steel [79]. On the other hand, temperature profiles developed in the work piece which will significantly affect the structural evolution of the material can be more accurately calculated. Mathematical models based on the well known finite-difference approach to solve Fouries partial differential equation for heat conduction, have been proved to be successful both during laboratory hot rolling of plates [71,73-77] and hot extrusion of cylindrical billets [80]. Nevertheless, it should be pointed out that the simplifying assumptions generally required to develop such methods could lead to errors in the distribution of temperature of the work piece during industrial processing, e.g. breakdown passes of industrial hot rolling operations where the nature of deformation is not clearly defined and plane-strain conditions are not upheld.

2.3 Restoration Mechanisms Associated to Hot Working of Aluminium Alloys

Multi-pass industrial forming operations carried out under hot deformation conditions entail softening mechanisms both during and after deformation by means of which the dislocation density of the material is reduced and its ductility is restored allowing very large strains to be applied without increasing the strength of the alloy as the deformation proceeds. Such mechanisms have been termed "dynamic" and "static" respectively [23, 81] depending on whether they take place concurrently under the stress applied or not.

2.3.1 Dynamic Recovery

During deformation the dislocation density of the material increases from about 10^{10}-10^{11} m^{-2} in annealed polycrystalline samples to 10^{14}-10^{15} m^{-2} in the steady-state region [81]. Although the movement of individual dislocations occurs in response to long range internal stress fields, their motion is opposed by various short range barriers which are overcome by thermal activation. Aluminium [82], with a high stacking fault energy (0.2 J/m^2) as compared with copper (0.07 J/m^2) and silver (0.02 J/m^2), facilitates the recombination of the partial dislocations enabling cross slip of the extended screw dislocations. This mechanism, as well as climb and unpinning of attractive junctions, which are also thermally activated processes, control the rate of annihilation of dislocations and eventually will allow the attainment of a dynamic equilibrium with the generation rate. By the time that such a balance is achieved, the dislocations have re-arranged themselves into subgrains whose perfection, dimensions and misorientation depend upon the strain rate and the deformation temperature [23,81]. Since the dislocation density is kept constant, the rate of work hardening is diminished to negligible levels and the flow stress of the alloy will just be determined by the Zener-Hollomon parameter. In practice, the flow stress may change due to the operation of other mechanisms such as adiabatic heating, precipitate coarsening and modification of "hard" and "soft" textures. It has been demonstrated [83] that a uniform distribution of dislocations capable of motion will form "clusters" whose wavelength will be proportional to the mean dislocation density. If it is assumed that the stress level at a dislocation wall is entirely due to the nearest-neighbour dislocation and that dislocations at adjacent walls do not have any influence upon them, it would be expected that a higher density of sub-boundaries

which results in a smaller equilibrium sub-grain size, would arise at higher stresses. Experimentally, it has been found [10,23,24,81,84] that the mean sub-grain size increases with increasing temperature for deformations at constant strain rate, or with decreasing strain rate at constant temperature as shown in Figure 19. This could be explained in terms of the decrease in the generation rate with decreasing strain rate and the increase in the annihilation rate with both increasing temperature and decreasing strain rate. Many workers [10,23,45,46,81, 85] agree in expressing the subgrain size as a function of the Zener-Hollomon parameter with an equation such as:

$$d^{-1} = a + b \log Z \qquad .....(2.13)$$

where "a" and "b" represent empirical constants determined by the experimental conditions. Also, the strain interval required to achieve steady-state deformation has been found to be dependent on the deformation conditions [81] (deformation temperature and strain rate). It is believed that as the temperature decreases or the strain rate increases the number of recovery events per unit strain is reduced. In general, it has been found [81,85,86] that increases in the alloy content can both reduce climb through the binding energies that tie vacancies to solute atoms and promote the extension of dislocations into partials separated by a ribbon of stacking fault. This would make climb and cross-slip more difficult and would preclude the recovery processes, favouring static recrystallisation during the time interval between deformations. Therefore, it would be expected that the sub-structures produced in the heavily alloyed materials would tend to be more ragged than in less alloyed materials, with sub-boundaries less well formed and a higher dislocation density inside the sub-grains. During the steady-state deformation, the mean misorientation between subgrains

remains constant in the range 1-4° [10]. Several mechanisms have been proposed to account for this fact as well as why subgrains remain equiaxed even at large strains, whereas the grains deform in conformity of the external shape of the work piece. Repeated unravelling and subsequent reformation of sub-boundaries at locations which keep their average spacing and dislocation density constant has been put forward as a viable mechanism [87]. It has been termed "repoligonisation" by analogy with recrystallisation. A dynamic equilibrium subgrain size could also be maintained solely by sub-boundary migration [88]. According to this mechanism the driving force is the stress acting on the wall dislocations, possibly assisted by the "pressure" build-up inside the subgrains by the concentrations of like edge dislocations "piled-up" behind the sub-boundary awaiting climb [23]. In this way, sub-boundaries of opposite signs will migrate in opposite directions and therefore, collisions with other boundaries of opposite signs will result in a reduction of the dislocation density and an increase in the mean subgrain size. Hardening produced by the continuous replacement of sub-boundaries by a fine slip process will lead to a dynamic equilibrium with the subgrain size independent of strain even at extremely large deformations.

Recent investigations [83,89] carried out on commercial-purity aluminium and on aluminium-2%magnesium alloy, deformed in multi-pass rolling operations, have reported the observation of the "fragmenting" and migration of the sub-boundaries established by the previous pass to form new subgrains of a size characterised by the strain rate and temperature conditions of the new pass, Figure 20. The boundaries of the sub-divisions were observed to be weak and tended to migrate in the direction of larger dislocation densities. This led these workers to propose that unpinning of dislocations occurs due to the action of a "pile-up" on a weakly formed sub-boundary and that such dislocations

then glide to interact with other dislocations and form a new boundary as shown in Figure 21. Such a view was supported by electron beam heating experiments by means of which a carbon film was deposited on a foil. This carbon film developed stresses that generated dislocation activity on the sub-structure already present. Although this experiment was conducted at room temperature it was suggested that such a mechanism could also operate at high temperatures.

2.3.2 Flow Stress and Sub-Grain Size Relationship

Both the steady-state flow stress and the yield stress and hardness measured at room temperature have been correlated to the subgrain size obtained after deformation at elevated temperatures [10,23-26,81, 84,89,90]. The most general relationship between subgrain size and flow stress at high temperatures is expressed as:

$$\sigma_{ss} = \sigma_o + Kd^{-m} \qquad .....(2.14)$$

where σ_o, K, and m are constants. Several investigations carried out on aluminium and aluminium alloys under both creep and hot working conditions [23,91-95] found negligible values for "σ_o", increasing values of "K" with increasing alloy content and a mean value of 1.5 for "m". Another set of experiments [81,87,96-98] carried out on commercial purity Al deformed to a variety of strains from 0.7 to 3.7 within the steady state regime, found that the best correlation was given by the equation:

$$\sigma_{ss} = K_f d^{-1} \qquad .....(2.15)$$

where "K_f" represents an empirical constant. Equation (2.15) would seem to suggest that the developed stress is uniquely related to subboundary density 3/d as already proposed [90]. However, it is not

clear whether the sub-boundaries are the principal source of the stress set up by the developed structure (internal stress) or the relationship arises through a link with the dislocation density within the subgrains [23,81]. The room temperature flow stress has been correlated to the presence of high-temperature sub-boundaries by means of a modified Hall-Petch relationship [90]:

$$\sigma_{RT} = \sigma_o + K_1(d)d^{-\frac{1}{2}} \qquad .....(2.16)$$

Here, "σ_o" represents the friction stress and $K_1(d)$ the sub-boundary strength parameter which is found to be dependent on both the misorientation between sub-grains and the redundant dislocations within them. Thus, $K_1(d)$ has been expressed as:

$$K_1(d) = K_2 d^{-p} \qquad .....(2.17)$$

where "K_2" represents an empirical constant. By substituting equation (2.17) into (2.16), a general relationship would be obtained:

$$\sigma_{RT} = \sigma_o + K_2 d^{-p} d^{-\frac{1}{2}} \qquad .....(2.18)$$

For commercial-purity aluminium, a value of "p" between 0.5-1.25 has been reported [32,91,93,99] whereas for aluminium-magnesium a value of $p \simeq 0$ seems to fit the data [91,100].

The friction stress also represents the strength of a single crystal and its value has been reported to increase with alloy content [91]. In general, it is expected that the strengthening at room temperature due to the high-temperature sub-grains is less than that produced by an equal density of grain boundaries [90].

2.3.3 Effect of Inherited Sub-Structures on Sub-Grain Formation

During steady-state deformation if the temperature is lowered or the strain rate increased, the existing sub-structure has larger sub-grains with less dense boundaries than the equilibrium one [81,100]. Since after deformation long dislocation link lengths are established, the flow stress is lower than the expected steady state value but gradually approaches it [100-106]. Generally, the structure is altered as dislocations accommodate themselves in the existing sub-boundaries and new sub-grains are created within the old ones. Thus, the average spacing between sub-grains decreases to the equilibrium value determined by the new conditions of temperature and/or strain rate. Provided that recrystallisation or failure does not intervene, the final equilibrium sub-structure will depend just on the deformation conditions regardless of the initial sub-structure [81,100,103,107-110]. In hot working operations carried out at decreasing temperatures and increasing strain rates, a series of deformations separated by stress-free intervals are applied, most of which are not sufficiently large to achieve the steady-state condition. The final sub-structure at the end of a given pass is more recovered and less strong than recrystallised metal deformed isothermally at the same strain rate and to the same cummulative strain [91,98,111]. Torsion tests on super-purity aluminium [98] conducted at a mean strain rate of 2.3 s^{-1} and decreasing temperatures from 600-400°C in which a series of deformations were applied each of $\varepsilon \simeq 0.8$, separated by 30 sec. intervals, resulted in a final flow stress that was lower than the flow stress developed during continuous isothermal tests, Figure 22. The difference between the flow stress during isothermal and non-isothermal tests seemed to increase as the temperature was decreased but it was also observed that by increasing the delay time between deformations and hence allowing

more static recovery to take place, such a difference was reduced. Therefore, deformation at declining temperature or rising strain rate enhances the formation of a sub-structure in the material which is softer than would be expected if the total deformation had occurred at the final pass conditions. Similarly, a stronger sub-structure relative to the final pass conditions can be obtained by deforming in a series of passes at increasing temperatures or decreasing strain rates. In this case, a finer and denser sub-structure is inherited by each succeeding deformation (100,110). Industrially, these sort of schedules are not common but a rising temperature could result from adiabatic heating if both strain-rate and strain were high and the intervals short.

2.3.4 Dynamic Recrystallisation

It has been suggested [45,112,113] that under certain deformation conditions some aluminium alloys may dynamically recrystallise. However, the analysis of the available evidence would tend to indicate that such a process would not occur by the classical mechanism of nucleation and growth concurrently to the deformation applied, but rather as a consequence of a very advanced form of recovery. Metallographic observations [112] carried out on specimens of Al-Mg and Al-Zn alloys deformed by 50% reduction in axisymetric compression at temperatures about 0.9 Tm and quenched to room temperature, revealed significant recrystallisation, particularly in areas adjacent to the as-compressed grain boundaries of the alloys with higher alloy content, e.g. Al-5% Mg. Electron microscope examination of such areas showed a fairly high density of dislocations suggesting that the recrystallised grains were formed dynamically. Since such phenomenon was not observed in similar experiments carried out on super-purity aluminium, it was

proposed that the alloying additions had reduced the stacking fault energy of the material, thus hindering the recovery process and enhancing high-density dislocation structures within the sub-grains and therefore promoting dynamic recrystallisation. A comparison of the microstructures obtained is shown in Figure 23. In order to assess the reduction in stacking fault energy, sheets of the various alloys were heavily cold-rolled and the technique described by Dillamore et al [114] used. The reduction in the intensity ratio was taken to imply that additions of both magnesium and zinc in solid solution produced a significant decrease in the stacking fault energy of aluminium. These results, however, seem somewhat inconclusive. First of all, the fact that small equiaxed grains appeared at original grain boundaries after deformation, does not necessarily indicate the presence of dynamic recrystallisation since such places would be preferred sites for nucleation of statically recrystallised grains after deformation. Besides, no systematic comparison of dynamically and statically recrystallised grains was carried out and therefore a positive identification was not achieved. Secondly, although there is no reason to deny the possibility of the occurrence of dynamic recrystallisation as a classical nucleation and growth process if indeed the stacking fault energy of the material has been reduced, the method employed to assess such a reduction, strictly should not be applied to high stacking fault energy materials such as aluminium.

More recent work [113] carried out on a commercial Al-5%Mg-0.8Mn alloy deformed in extrusion at about 450°C, an extrusion ratio of 40:1 (ε eq $\simeq$ 3.7), and a ram speed of 14 mm/sec., has revealed a duplex microstructure developed during deformation. Metallographic observations carried out towards the die exit on specimens quenched immediately after deformation, showed the presence of elongated grains

aligned in the deformation direction with small equiaxed grains at the original grain boundaries. Electron microscopy investigation of these areas revealed the existence of very small grains ($\sim$ 1.5 μm) with very high misorientations across their boundaries ($\sim$ 45°), as observed in Figure 24. Such small and equiaxed grains were found to be associated mainly with original grain boundaries and second-phase particles and were identified as dynamically recrystallised grains since further observation showed the existence of an extensive dislocation newtwork within them, consisting of tangled high density areas and extensive pinned dislocations. Such observations were taken as a positive proof of the occurrence of dynamic recrystallisation since the sweeping of a high-angle boundary during static recystallisation would have removed such dislocations. Also, the possibility of dislocation generation during quenching because of differences in thermal contraction of particle-matrix interface was ruled out since calculations based on Dew-Jones' model [115] for punching of dislocation loops, gave dislocation densities orders of magnitude lower than those observed.

Such a duplex deformation mechanism was not found during the extrusion of the superpure-based Al-5%Mg alloy [116] and therefore, it was concluded that dynamic recrystallisation did not occur as a consequence of a reduction in the stacking fault energy of the alloy but due to the formation of precipitates and second phase particles owing to the solute addition as well as a smaller initial grain size in the commercial alloy. It was put forward that second-phase particles could have increased the dislocation density and therefore high misorientation in subgrains affected by both second-phase particles and grain boundaries could have developed, leading to recrystallisation nucleation.

Before analysing the evidence so far presented, it is worth considering some microstructural features associated with dynamic

recrystallisation as it has been observed in metals where its occurrence has already been demonstrated. In such cases, a dislocation sub-structure developes in the initial stage of deformation which is rather poorly recovered. The subgrains are relatively smaller and have more tangled walls than those formed in metals which undergo a high degree of recovery [81]. At strain rates characteristic of hot working conditions, a fine tangled cellular structure is developed throughout all the grains and with increasing strain, some tangles build up to high misorientations, giving rise to nuclei throughout each grain. it is likely to have a higher density of nuclei near grain boundaries because the strain is higher in such places as a result of accommodation of plastic anisotropy. As soon as steady-state deformation is achieved, new small equiaxed grains have replaced the original grains, remaining constant in size and equiaxed shape [81]. Since dynamic recrystallisation involves deformation of the new recrystallised grains during their growth, it is possible, (depending on the stress applied), that enough strain is accumulated in such grains, to achieve the critical strain to produce recrystallisation and, therefore, initiating a new cycle of recrystallisation before the previous one has been completed. Hence, depending upon the strain rate in tests at constant temperature, dynamic recrystallisation can occur periodically or continuously [23]. At low strain rates, the strain required to achieve a certain recrystallised fraction εx is much less than the critical strain to initiate dynamic recrystallisation, εc. Thus, once recrystallisation starts, it is completed long before the regions which first recrystallised can work harden and nucleate a second time. This behaviour is reflected on the stress-strain curve of the material as cycles of stress of decreasing period. At high strain rates, εx is much greater than εc and therefore before recrystallisation is

complete, the regions which first recrystallised reach the critical strain for a second nucleation. Since more than one cycle of recrystallisation may be taking place in the metal at the same time in which each one is at a different stage of the recrystallisation process, the result is an equilibrium distribution of regions having different strains between zero and ε_c, giving rise to a constant average flow stress. In any case, dynamic recrystallisation involves extensive migration of grain boundaries and is therefore quite distinct from the dynamic recovery process in which grain boundary migration is restricted [23].

The experimental evidence of the development of duplex microstructures during deformation of certain aluminium alloys has in common mainly two features: firstly, the small equiaxed grains were observed to be associated with original grain boundaries and second-phase particles and secondly, no such grains were present in specimens of superpure-base material after deformation under the same conditions. Since second phase particles of as-cast alloys preferably locate at grain boundaries [2], it is feasible to propose that the nucleation of such equiaxed grains is highly dependent on their presence, which would explain the lack of recrystallisation of the superpure-based materials. Whenever dynamic recrystallisation (understood in the classical sense) has been observed to occur at grain boundaries, the mechanism involved was "strain-induced boundary migration" or bulge nucleation [61,117-118], a process that requires the pinning of local regions of the boundaries at their periphery and also, tangled subgrains rather than sharp [119]. Moreover, dynamic recrystallisation as such, implies the growth throughout the matrix of the nucleated grains and the continuous replacement of the grain structure during deformation. Neither grain-boundary bulging nor growth of the nucleated grains and consumption of

the original as-cast structure through massive migration of high-angle boundaries were reported. Therefore, it may be concluded that although recrystallisation is taking place concurrently with the strain applied, it cannot be considered as dynamic recrystallisation such as it is defined in the usual sense.

The presence of new small equiaxed grains at the original grain boundaries, however, could be explained in terms of the operation of recovery to a very significant degree in areas where pinning of the dislocations produced during deformation is promoted by the presence of second-phase particles and precipitates, enhancing the re-arrangement of the sub-structures in more stable configurations with higher lattice misorientation across their boundaries. Therefore nucleation of recystallisation could occur when the dislocation networks within a subgrain assume the character of high-angle boundaries, promoting its "rotation" with respect to its neighbours, although the conditions for boundary migration have not been fulfilled. The occurrence of recrystallisation without migration of high-angle boundaries throughout the structure, a process observed mainly during annealing after cold deformation of super-saturated or meta-stable alloys, has been termed "continuous recrystallisation" or "recrystallisation in situ"[120-122]. According to this mechanism, if the existing mobile high-angle boundaries are held by preferential precipitation or second-phase particles, and/or that no substructural re-arrangement to form such boundaries can occur, then annealing out of defects would be controlled by the coarsening of such particles as a result of which defect regions, and the angles between them may increase. The process is illustrated in Figure 25 and may be described quite well by subgrain coalescence or Y-node motion. As soon as a particle located at a dislocation node dissolves, these dislocations can migrate much more easily than those

still pinned by particles and a subgrain boundary can anneal out, which occurs as soon as the particles at other nodes have dissolved [122].

Further evidence of the occurrence of recrystallisation without migration of high angle boundaries during high temperature deformation, has been given by Lombry et al [126] who also observed the formation of new small equiaxed grains during hot torsion experiments carried out on an Fe-Cr ferritic steel. Transmission electron microscopy investigations of such specimens revealed the existence of subgrains of sizes between 2-10 μm. An example of such microstructure is shown in Figure 26 where it is clearly observed that the small equiaxed grains situated at the original grain boundaries are indeed groups of subgrains that have coalesced among themselves and have increased their misorientation or rotated with respect to the deformed matrix through the re-arrangement of the dislocations generated during the deformation. Therefore, it would be feasible to propose that as far as high stacking fault energy materials are concerned, duplex deformation structures are achieved through the operation of both dynamic recovery and dynamic recrystallisation though not understood in the classical sense which involves migration of high angle boundaries but rather as a "continuous", "in-situ" or "rotation" recrystallisation mechanism.

2 3.5 Static Recovery

After deformation, static restoration processes take place and modify the deformed structures and therefore the flow stress of the material. Such processes can be divided into two groups [81]: (a) those which involve the annihilation of dislocations in individual events and (b) those in which dislocations are eliminated in large numbers as a result of the motion of high angle boundaries, e.g. recrystallisation. Static recrystallisation has also been termed as "discontinuous

recrystallisation" [122] in order to differentiate it from those processes that also involve the elimination of large numbers of dislocations without motion of high-angle grain boundaries through the deformed matrix and that are controlled by particle growth. Static recovery starts with the annihilation of redundant dislocations and the re-arrangement of dislocations in cell walls [100]. Subgrain growth occurs by weaker walls decomposing and then dislocations forming other arrays which in certain cases could lead to the build-up of misorientation in certain walls that can nucleate recrystallisation. Static recovery is rather a slow process and it is slowed further by self-reduction of its driving force [100]. The main experimental variables that affect the recovery rate are temperature, strain, strain rate and composition [81]. In general it has been observed that decreasing the deformation temperature the rate of recovery is decreased. The same effect is observed by increasing the time between passes in multi-pass deformation processes, indicating that the stored energy or driving force is progressively diminished. Also, it has been observed that increases in strain and strain rate lead to increases in the recovery rate which can be attributed to the increase in dislocation density and therefore in driving force. In general, metals with a high stacking fault energy have a higher rate of recovery than metals with low stacking fault energies, which could be attributed to the decrease in worked dislocation density that is associated with stacking fault energy increase [81]. As pointed out earlier, the addition of solutes hinders dislocation interactions by hindering the recombination of partial dislocations and climb. Therefore, it would be expected that the addition of alloying elements should reduce the recovery rate and promote static recrystallisation.

2.3.6 Static Recrystallisation

Static recrystallisation after hot working like classical recrystallisation during annealing after cold working, are processes that take place by the nucleation and growth of new grains in the statically recovered microstructures [10]. However, differences arise due to the much lower dislocation density of the hot deformed materials as a consequence of the dynamic restoration processes. In general it would be expected that nucleation takes place preferentially in regions where there is a high degree of deformation and/or local misorientation [190]. At small strains there is usually more deformation at grain edges and/or grain corners than is the case for grain interiors. Therefore, grain boundaries and their triple points are likely to be of special significance as the locations of recrystallisation nuclei in metals which have been slightly deformed. However, as the deformation increases its general distribution becomes more homogeneous and consequently recrystallisation nuclei can be found in grain interiors as well, especially at the intersection of deformation transition bands [114].

Also, the particle-matrix interfaces at dispersed second-phase particles provide sites for nucleation provided that the interparticle spacing is sufficient to allow for the successful development of a viable nucleus in the matrix phase [119]. Recrystallisation in aluminium after hot deformation has been observed to develop from both original grain boundaries and grain interiors [10,39,98,111]. It would be expected that if grain boundaries were favoured as nucleation sites, the recrystallisation kinetics would also be strongly dependent on the initial grain size. Nucleation from subgrains within original grains would appear to be favoured in materials of large initial grain size [10]. The various mechanisms which have been proposed to account for the formation of recrystallisation nuclei have already been reviewed

[127-129]. In general it is agreed that any mechanism proposed should fulfill several conditions that can be summarized by saying that a viable nucleus must be a relatively large region having an orientation similar to the same region in the deformed state but being at least partially surrounded by a high misorientation, relative to its immediate surrounds, all within a wider region of general high local misorientation. This general description is encompassed within models such as: strain induced boundary migration, polygonization and subgrain coalescence. Such models describe possible ways in which a subgrain, existing in the deformed state, can develop selectively until it becomes a viable recrystallisation nucleus. The distinction between them being in the specific way in which this selective development occurs [119] The nucleation stage is followed by the growth or migration of the high-angle boundaries which surround the new expanding grains throughout the deformed structure. The rate of migration of such boundaries is generally considered to be the simple product of the driving force and boundary mobility [130]:

$$G = Mp \qquad .....(2.19)$$

The mobility "M" is an intrinsic property of the boundary which is related to the structure but is independent of the size or nature of the driving force [131]. Among all the factors which alter the mobility, differences in orientation of the lattices of the two grains on either side of a migrating boundary have been found to be of significant importance [132,133]. Several investigations carried out on aluminium specimens concluded that migration into regions of orientation similar to that of the growing grain or into regions possessing its twin orientation were exceptionally slow [132]. Moreover, "insular grains" or regions of deformed material, completely surrounded by

recrystallised regions of a single orientation which had grown by the advancement of boundaries from nuclei situated elsewhere, have also been reported [133].

Most investigators agree in the use of the Avrami equation to describe the isothermal kinetics of recrystallisation:

$$Xv = 1 - \exp(-Bt^n) \qquad .....(2.20)$$

where "Xv" is the volume fraction recrystallised, "t" is time and "B" and "n" are constants. Values of "n" are most commonly in the range 1 to 2 but its exact value is sure to vary with the experimental material and circumstances [8,6]. A low value of "n" implies one- or two-dimensional recrystallisation, i.e. new grains growing in the form of rods or platelets. A complete analysis of the different nucleation mechanisms for different "n" values has been given by Christian [134] and is shown in Table II. Equation (2.20) can be more usefully expressed in terms of the time to obtain a fixed recrystallised fraction such as 0.5

$$Xv = 1 - \exp[-0.693(t/t_{0.5})^n] \qquad .....(2.21)$$

The value of "n" for zone-refined polycrystalline aluminium with or without small additions of copper, cold deformed by 40%, have been reported [135] to be about 2. This value agrees very well with the value reported for ferritic steel [136]. Since recrystallisation is a thermally activated process, the time to obtain a given percentage transformation can be expressed in terms of an Arrhenius-type equation:

$$\frac{1}{t_{0.5}} = W' \exp(-Q_{rex}/RT) \qquad .....(2.22)$$

or

$$t_{0.5} = W_{0.5} \exp(Q_{rex}/RT) \qquad .....(2.23)$$

"Q_{rex}" is the experimental activation energy for recrystallisation. T and R have their usual meaning. Also, $t_{0.5}$ has been found to be a function of the Zener-Hollomon parameter, strain applied and the initial grain size of the alloy [10]:

$$t_{0.5} = A\ do^{a}\ \varepsilon^{b}\ Z^{c} \qquad .....(2.24)$$

Experiments carried out on carbon-manganese [137], titanium [73] and niobium-steels [74] have found that for deformations less than the critical strain to produce dynamic recrystallisation, $t_{0.5}$ depends just on "do" and "ε":

$$t_{0.5} \alpha\ do^{a}\ \varepsilon^{b}$$

where $a \simeq 2$ and $b \simeq -4$. For deformations greater than the critical strain:

$$t_{0.5} \simeq Z^{c}$$

where "c" has been found to be about -0.60. Torsion experiments carried out on 304 stainless steel [138] have found that $t_{0.5}$ can be expressed as:

$$t_{0.5} \alpha\ do^{2}\ \varepsilon^{-4}\ Z^{-0.375}$$

From equation (2.24) it could be stated that:

$$\frac{1}{A} = \frac{1}{Ao} \exp(-Q_{rex}/RT) \qquad .....(2.25a)$$

or

$$A = Ao \exp(Q_{rex}/RT) \qquad .....(2.25b)$$

and by substituting equation (2.25b) into (2.24), we obtain a general equation that expresses the time for 50% recrystallisation as a function of the deformation parameters:

$$t_{0\,5} = Ao\ do^{a}\ \varepsilon^{b}\ Z^{c}\ \exp(Q_{rex}/RT) \qquad .....(2.26)$$

If the activation energy for recrystallisation "Q_{rex}" is known as well as the activation energy for deformation "Q_{def}", the dependence of "$t_{0.5}$" on "Z" can be readily found by defining an apparent activation energy "Q_{app}". Thus, from equation (2.26):

$$t_{0.5} = A\ do^{a}\ \varepsilon^{b}\ \dot{\varepsilon}^{c}\ \exp(C\ Q_{def}/RT)\exp(Q_{rex}/RT)$$

or

$$t_{0.5} = A\ do^{a}\ \varepsilon^{b}\ \dot{\varepsilon}^{c}\ \exp[(CQ_{def} + Q_{rex})/RT]$$

and, if $CQ_{def} + Q_{rex} = Q_{app}$ then:

$$t_{0.5} = Ado^{a}\varepsilon^{b}\ \dot{\varepsilon}^{c}\ \exp\ (Q_{app}/RT) \qquad .. ..(2.27)$$

"Q_{app}" can be determined from recrystallisation experiments carried out at different temperatures and constant strain rates and so can be the constant "C". However, if the determination of the activation energy for recrystallisation is to be carried out, tests at constant "Z" rather than constant strain rate have to be used since such a value will only be obtained if prior deformation conditions lead to equivalent driving forces, as stated in equation (2.26).

In multi-pass industrial forming operations such as rolling, isothermal conditions are never achieved and the material cools in between deformations at different rates depending on the particular product [10]. In order to carry out studies on the recrystallisation behaviour at decaying temperatures on a ferritic steel, Whittaker [139]

defined a temperature-compensated time parameter "W". Thus from equation (2.23) it can be generalised that for isothermal conditions:

$$W_{0.5} = t_{0.5} \exp (- Q_{rex}/RT) \qquad .....(2.28)$$

and for non-isothermal conditions:

$$W = \Sigma [\delta t_i \exp (- Q_{rex}/RT_i)] \qquad .....(2.29)$$

where the cooling curve is considered in terms of time increments (δt_i) at successively lower values of temperature T_i. If sufficiently small intervals of time are considered:

$$W = \int_0^t \exp [- \frac{Q_{rex}}{RT(t)}] dt \qquad .....(2.30)$$

where T(t) represents the variation of temperature with time through a determined cooling rate. If such a cooling rate is known as well as the values of the activation energies for both deformation and recrystallisation, and also the functional dependence of "$t_{0.5}$" on the deformation parameters, then by substituting "t" in equation (2.21) for "W" in equation (2.30) and using equation (2.28) to determine "$W_{0.5}$", it is possible to compute the recrystallised fraction that is likely to be obtained after a cooling period in between deformations. Furthermore, if information concerning the variation of the flow stress with strain, strain rate and temperature is available, then a mean flow stress "$\bar{\sigma}$" could be calculated from the integration of the stress-strain curves for a number of fractions of material with different accumulated strains:

$$\bar{\sigma} = \frac{f_1}{(\varepsilon p)_1} \int_{\varepsilon_1}^{\varepsilon_1 + (\varepsilon p)_1} \sigma d\varepsilon + \frac{f_2}{(\varepsilon p)_2} \int_{\varepsilon_2}^{\varepsilon_2 + (\varepsilon p)_2} \sigma d\varepsilon + \cdots\cdots + \frac{f_n}{(\varepsilon p)_n} \int_{\varepsilon_n}^{\varepsilon_n + (\varepsilon p)_n} \sigma d\varepsilon$$

$$f_1 + f_2 + \ldots + f_n = 1 \qquad .....(2.31)$$

where f_1, f_2, ..., f_n are fractions of the material which have accumulated strains ε_1, ε_2, ..., ε_n in previous history and that are deformed by amounts $(\varepsilon p)_1$, $(\varepsilon p)_2$, ... , $(\varepsilon p)_n$ during the pass under consideration. Such a value of stress could then be used in hot rolling theories [140-142] to calculate the loads and torques required to deform the material throughout a particular schedule. Although simplifying assumptions have to be made, especially those concerning the distribution of strain among fractions with different accumulated strains and the interaction of such fractions during recrystallisation, it is quite feasible to use such a model as a means of simulation of complex industrial processes carried out under conditions of decaying temperature.

Factors which influence the driving force for recrystallisation would also be expected to influence the recrystallised grain size [10]. Therefore, a relation such as:

$$d_{rex} = B\, do^{n}\, \varepsilon^{m}\, Z^{p} \qquad .....(2.32)$$

could also be proposed. In steels it has been found that for deformations lower than the critical strain $n \simeq 0.67$, $m \simeq -1$ and $p \simeq 0$, whereas for strains greater than ε_c, $n \simeq 0$, $m \simeq 0$ and $p \simeq -0.1$ [73,74,137]. For 304 stainless steel it has been found that $n \simeq 0.5$, $m \simeq -0.75$ and $p \simeq -0.15$ [138]

2.3.6.1 Single and Multiple Deformation Testing

The recrystallisation kinetics after hot deformation is usually followed by means of single isothermal deformation tests, annealing at the deformation temperature and quenching after different delay times. Following this method Cotner [26] was able to determine the time for 50% recrystallisation of aluminium specimens deformed in torsion, with

different initial strains and at different temperatures. His results are shown in Table III. According to the reported data:

$$t_{0.5} \alpha \ \varepsilon^{-1}$$

for super-purity aluminium and:

$$t_{0.5} \alpha \ \varepsilon^{-\frac{1}{2}}$$

for aluminium - 1% magnesium alloy. Since all these experiments were conducted at a constant surface shear-strain rate of 3.93 s^{-1} ($\dot{\varepsilon}_{eq}$ = 4.54 s^{-1}), the activation energies reported are apparent and not true activation energies for recrystallisation. The effect of strain reported in this investigation, at levels well into steady state is quite surprising since the rate of recrystallisation, once the balance between work hardening and dynamic recovery has been achieved, should be independent of the subsequent strain applied. It has been suggested [10] that such results could arise from the increase in grain boundary area/vol. or an increase in maximum misorientation between subgrains with increasing strain as well as adiabatic heating effects due to the strain rate employed [143]. As far as the recrystallised grain sizes are concerned, no quantitative information was given and it was just reported that the recrystallised grain sizes were larger than the starting grain sizes (ranging between 15-30 μm) in all cases.

Recrystallisation studies have also been carried out by means of multiple-pass deformation tests. Using this technique Evans and Dustan [39] investigated the kinetics of recrystallisation of commercial purity aluminium deformed under conditions of plane-strain compression at different temperatures and strain rates. Figures 27a and b show examples of such deformation schedules and Figures 28a, b and c summarise their results based on the definition of a restoration index from

the stress-strain curves obtained from the experiments. These researchers found that after initial applied strains of 0.37 at strain rates of 8.1 s^{-1}, the apparent activation energy for recrystallisation was about 65 kJ/mol. Also it was reported that 60-70% restoration of the second stress-strain curve with respect to the curve for the first deformation, was due only to recovery, the degree of restoration increasing with decreasing values of Z. An unusual yield phenomenon occurring during the multiple-compression testing of pure and alloyed aluminium under hot working conditions, has recently been reported [24] Figure 29 represents a typical example of the apparent hardening found after different delay periods in between deformations in two-deformation schedules, with commercial-purity aluminium performed at 400°C and at a strain rate of 11.5 s^{-1}. Such a hardening was reported to be present at strain rates greater than 1 s^{-1} and was not found to be dependent upon alloying content, ageing time or temperature. Varying the amount of strain imparted in the first deformation showed no particular trend in the magnitude of the hardening peak after the initial strain reached about 0.3. No effect of the tool-specimen geometry could be observed either. Prior heat treatment however, was observed to have an effect in that the hardening peak could also be present at the beginning of the first deformation as well as the second. In order to explain this phenomenon it was proposed that on unloading the mobile dislocation density is reduced by the alteration of the distribution of dislocation link lengths by the dislocation line tensions. On reloading, the reduced number of mobile dislocations have to move faster to match the required strain rate. The production of mobile dislocations on reloading could be either by unlocking of the stable arrays formed during the unloading or, if those arrays are too stable, by the creation of new mobile dislocations. During this

investigation it was also observed that tests in which the two uniform strain rate deformations were separated by an interval of much lower strain rate, that is to say, conditions of reduced load rather than complete unloading, no hardening peak was present, Figure 30. Such observation is in complete agreement with the change in the mobile dislocation density during rate changes reported for commercial purity aluminium [144]. In torsion tests carried out between 400-500°C in which the strain rate was changed by two orders of magnitude, it was concluded that an excess of mobile dislocations was produced during a downward strain rate change. Therefore, it would be reasonable to assume that whereas complete unloading would produce a decrease in the mobile dislocation density due to the static restoration processes, a decrease in the strain rate would produce an excess of mobile dislocations that on reloading will not have to move faster to achieve the initial strain rate.

Recrystallisation studies have also been conducted by means of rolling experiments [19]. This technique has the inherent disadvantage of the lack of control of the deformation parameters as far as the quantitative information of the effect of individual variables is concerned. Nevertheless, it could provide very useful qualitative information as well as a basis for comparison with the theoretical models developed from more controlled forms of testing. Using this technique, Blade [19] carried out rolling of wedge-shape ingots at various temperatures in a single pass so as to produce a rolled slab which had undergone reductions, varying between 40% and 60% and that could be quenched after predetermined delay times. Specimens of super-purity aluminium were observed to recrystallise during the first 20-30 seconds after exit from the mill and that after this time the rate of recrystallisation decreased rapidly possibly due to the cooling of the

slab. It was also reported that at all temperatures, the specimens with more accumulated strain recrystallised first, although the effect was somewhat confused at the lowest entry temperature, Figure 31. It is also observed that, by changing the entry temperature by 100°C, no significant effect on the time to get a fixed recrystallised fraction is produced which suggests a relatively low value of the apparent activation energy. Recrystallisation in partially recrystallised specimens was reported to develop mainly near the surface. The same technique was also used to study the effects of additions of Cu, Si, Fe, Mn, Mg and Zn at various levels up to 1% on the recrystallisation of hot-rolled super-purity aluminium as well as commercial-purity aluminium. Such results are shown in Figure 32. It is clearly observed that both Fe and Mn when added to super-purity aluminium have a pronounced effect on the kinetics of recrystallisation, whereas copper was noticed to have very little effect. Mg and Zn on the other hand, were observed to increase the recrystallisation kinetics. The effect of Si was somewhat uncertain. In general, the effects of alloying additions to the commercial-purity-base were reported to be very similar to those observed for super-purity aluminium with the exception that recrystallisation was far less easy to achieve possibly due to the presence of Fe. A very interesting result from these experiments and also experiments conducted on Al-1.2%Mn was that the kinetics of recrystallisation of commercial-purity aluminium as well as the alloy mentioned was not affected by the presence of fine precipitates but was rather dependent upon the solid-solution composition.

CHAPTER III

3. Strain and Temperature Distribution Under Plane Strain Compression Conditions

3.1 Introduction

The plane strain compression test has been extensively used as a method of obtaining information about the stress-strain behaviour of metals both at low and elevated temperatures [145,146]. Its development stems from the fact that many working operations, e.g. strip and plate rolling, and forging of long thin slabs, nearly satisfy the condition of plane strain and also from the difficulty of simulating such processes with other testing techniques, e.g. torsion, tension and axisymetric compression. Although it has the advantage of being rapidly carried out with the minimum specimen preparation, the punch loads observed do not quite represent the real plane strain yield stress of the metal since they are significantly dependent upon test geometry and frictional conditions. At low temperatures, for example, it was found [145] that if the ratio tool width to initial specimen thickness W/ho was lower than 2, the punch loads became strongly dependent on such ratio, whereas if W/ho was greater than 4, then the effect of friction could no longer be considered negligible. Therefore the test is often conducted in a series of steps with re-lubrication between stages. Assuming that metals behave as rigid-plastic materials, accurate correction parameters have been obtained from slip line field theory, which allows the required yield stress to be determined from the

established punch loads and W/ho values [28,147,148]. Moreover, since during testing at low temperatures the flow stress is not significantly dependent on the strain rate, the punch velocity is unimportant.

At elevated temperatures, however, the flow stress is highly strain rate sensitive and both the punch temperature and velocity become very important. Therefore, it is necessary to maintain the specimen and punch at a constant temperature (isothermal tests) and to impose a punch velocity which ensures a constant true macroscopic strain rate during the test. Also, in order to be able to determine the stress-strain curve from the observed punch loads and displacements, it is necessary to know the adequate correction parameters, since they will not be the same as those for the low temperature curves.Similarly, since incremental loading and relubrication is not practicable at high temperatures, large strains would have to be achieved without interruption and therefore the ratio W/ho will be taken out of the recommended range. Many of these shortcomings have already been overcome, for example, by means of logarithmic-shaped cams which would allow deformation of the specimens at constant strain rate [28,49], the use of graphite-based lubricants suitable to the range of testing temperatures of aluminium [24,49,146] and also the use of empirical corrections capable of compensating for geometry, friction and spread effects [24,146]. However, since the important influence of strain, strain rate and temperature on the recrystallisation kinetics of aluminium alloys has already been established, it becomes apparent that in order to simulate industrial hot deformation processes and predict microstructural evolution throughout their complex shedules by means of plane strain compression, knowledge of the strain distriubtion in the specimen and the temperature distribution in both specimen and punch are necessary. If such information were available, plane strain

compression tests carried out under hot working conditions would allow the correlation of the recrystallised fractions and recrystallised grain sizes experimentally obtained to the exact conditions of strain, strain rate and temperature developed during the test.

3.2 Distribution of Strain

The determination of the exact nature of the deformation under conditions of plane strain compression requires the establishment of the vector velocity field from which both strain rates and stresses could also be calculated. Slip-line field theory provides a powerful technique for solving such a problem in terms of deformation and local stress distribution as well as overall forces, but it has two important deficiencies: individual solutions are time-consuming and detailed material properties cannot be included directly in the theoretical solutions [68]. Also, it is possible to operate entirely on algebraic and trigonometric equations representing stress and velocity continuity and boundary conditions. Upperbound procedures can be used in which the stress boundary conditions need not be met, or more precise solutions can be obtained using the virtual work principle or variational techniques. Such methods are capable of giving very detailed information, in matrix form, about the strain rate, strain and stress distributions [68]. They are not limited by the restrictive assumptions of slip-line field theory and with suitable modifications and approximations can include the dependence of the flow stress of the material on strain rate, strain and temperature. They could also be extended to axisymetric and other geometrical shapes.

Visio-plasticity techniques in which the experimental measurement of metal flow with the subsequent calculation of strain, strain rate

and stress distributions are combined, have been applied to solve problems in plane strain or axial symmetry [24,146,149]. Such methods are based on the observation of the metal flow by sectioning the sample on a plane containing the direction of major deformation. The surfaces should be ground flat and polished on both sides of the cut. A regular grid of circles or squares is scribed to one of the faces and the distortion of the grid is observed with a microscope or on an enlarged photograph after a small increment of deformation has been applied to the specimen. The displacement and hence the velocity of each element of the grid can thus be assessed. However, if such grids are deformed in a finite step rather than by incremental strains, careful consideration of the accuracy of the solution should be taken especially when dealing with problems such as plane strain compression, where a non-uniform deformation is involved.

Beynon [24], using the grid technique was able to evaluate the distribution of strain under conditions of plane strain compression, after imparting nominal reductions of 25 and 50% to specimens initially 10 mm thick and also reductions of 25% to specimens of initial thickness of 5 mm. These thicknesses and strains were chosen in such a way that the final dimensions of the heaviest deformed specimen could be achieved with the smallest reduction initially applied. The effect of mean strain was obtained by means of the equation:

$$\bar{e} = \frac{2}{3}\left[e_1^2 - e_3\, e_1 + e_3^2 + 2e_{31}^2\right]^{\frac{1}{2}} \qquad .....(3.1)$$

which derives from the more general quadratic invariant of infinitesimal deviator strains generally used in plasticity theory [150]. e_1 and e_3 represent the tensile strains in the directions 1 and 3 respectively and are determined by the change in magnitude of the vectors that represent the initial grid edges, as illustrated in Figure 33. e_{31}, on

the other hand, represents the shear strain or rotation of such vectors and is taken as the change in angle between them. The co-ordinates of the different points of the deformed grid could be given either in terms of the change in displacement with respect to the co-ordinates of the undeformed grid, in which case it is called the "material displacement gradient approach" [151]:

$$dx_i = [\frac{\partial u_i}{\partial X_j} + \delta_{ij}]\, dX_j \qquad .....(3.2)$$

or, in terms of the change of displacement with respect to the co-ordinates of the deformed grid and the co-ordinates of the undeformed grid, also termed as "spatial displacement gradient approach":

$$dx_j = \frac{dX_j}{[\delta_{ij} - \frac{\partial u_i}{\partial x_j}]} \qquad .....(3.3)$$

where "δ_{ij}" represents the Kronecker delta. If though, it is assumed that during deformation all the points of the grid travel along a straight line, then the magnitude of the final vectors of the grid is readily obtained by applying Pythagoras' theorem. Figures 34a, b and c illustrate the distribution of strain obtained for the grids mentioned above in terms of the initial goemetry. The development of a cross-like pattern of high strain is clearly observed which resembles the simple cross patterns developed from the slip-line field theory but with the important difference that, in the present case, such bands are of a finite width possibly due to the strain-hardening and strain rate sensitivity effects on the flow stress, which are not considered in the theory. It could also be seen that as the strain applied increases, the tendency to form two, rather than one, crosses at the centre adjacent to the tool faces is quite apparent. However, if the initial specimen thickness is reduced, the strain distribution is observed to

be much more uniform, since tne diagonal bands of high deformation terminate at the spots of high localised strain, leaving the centre portion at about the same strain. Figures 35a, b and c show the strain distributions obtained but in terms of the final specimen geometry. Thus, the same features described above tend to be more significant, especially those related to the development of the high strain bands and also the variation of the strain over very small distances along the gauge length of the specimen. Figure 35c gives a clear picture of the region of relatively uniform strain in the centre of the specimen and the areas of rapid changes in strain, confined to the sides, and therefore it is concluded that the specimen of greater tool width/initial thickness ratio will provide a more uniform strain in the material. Figure 36 is a comparative picture of the strain distributions obtained by folding the information for each grid into one quadrant, all expressed in terms of the original geometry, and also the strain distribution obtained by subtraction of the pattern shown in Figure 36d to that of Figure 36c, which can be compared directly to the distribution of Figure 36b, since both patterns represent overall reductions of 25% . The striking similarity of these two pictures led Beynon to the important conclusion that previous strain history (such as that embodied in quadrant (a)) does not affect the strain distribution which a specific geometry will be subject to on deformation.

Further work, carried out under the consideration that during deformation, the points of the grid will travel along a rectangular hyperbola rather than a straight line, has produced results which differ by less than 5% from those previously reported [152]. In general, the visio-plasticity method provides very detailed information and is extremely valuable for the determination of the strain distributions directly from the experiment, that is to say, it is accurately

deductive but it is not predictive. Therefore, theoretical approaches have been devised to solve different problems other than plane strain compression, but whose principles are equally applicable. Upper-bound solutions further developed to solve rather complex problems and also to describe axisymmetric deformation has been facilitated [153] by the introduction of the concept of "unit deformation regions". Thus, the specimen is divided into suitable rectangular regions and each of these is then sub-divided into rigid triangles or other shapes. It is also assumed that the metal is non-hardening, rigid-plastic, obeys Von Mises yield criterion and that the flow stress follows the Levy-Mises stress-strain rate relationship. The application of the limit theorem which states that the rate at which work is done by the applied tractions is not larger than the internal rate of energy dissipation, $\dot{E}$, derived from any admissible velocity field, can be expressed for plane strain conditions as:

$$\dot{E} = \sqrt{2}\ K \int_V [\dot{e}_1^2 + \dot{e}_3^2 + \tfrac{1}{2}\dot{e}_{13}^2]^{\frac{1}{2}}\, dV + 2K \int_S f\, \dot{s}\, ds \qquad .....(3.4)$$

where "K" denotes the yield shear stress, "f" the shear or frictional resistance on the discontinuity surface divided by the plane-strain compressive yield stress 2K of the material ($\tau/2K$) and "$\dot{s}$" represents the rate of relative slip of the surface. Thus, the problem reduces to finding a pattern of internal velocity discontinuities that is compatible with the imposed velocity conditions and gives as low an energy dissipation as possible [68].

Finite-element analysis, although well established in advanced design of elastically-deforming structures, has only recently been applied to general deformation processes, among which is plane-strain compression. It is widely thought that for general studies concerning metal working problems, this method will supersede both slip-line field

and upper-bounds techniques, since it is much more versatile and allows the prediction of strain, strain rate, temperature and stress distributions of deformation problems whose degree of complexities is just limited by the size of the computer available [68]. Essentially, in the finite element analysis, a structural part is divided into segments, called elements, superimposed on a co-ordinate grid system. The co-ordinate points of elements corners are identified and their values are arranged according to a prescribed formula into a so-called [B] matrix for each element. Another array of numbers called a [D] matrix is set up from the elastic properties of the material and specified set of multiplications and divisions then transforms the [B] and [D] matrices into [K] or stiffness matrices. These [K] matrices are assembled into a master stiffness matrix for the entire part. Specific elements within the matrix are combined with certain of the applied loads to reveal the displacements (and thus strains) imposed by the loads. These strains, as in conventional analysis, then indicate stresses [153].

In plastic deformation [154], however, the forces are considered in terms of the uniform stresses acting on the faces of the elements, not as discrete forces at the nodes, and only incremental deformations are relevant. The forces are divided into two categories, body forces "F" and surface tractions "T", and are also related to the displacements "U" through a stiffness matrix:

$$[\Delta F] + [\Delta T] = [K][\Delta U] \qquad \ldots\ (3.5)$$

implying that increments in displacement are caused by increments in forces. In these cases the stiffness matrix can no longer be found from the co-ordinates [B] and the elastic constants [D] but it can be determined by an application of the principle of virtual work. There-

fore a hypothetical change $\delta(\Delta u_i)$ in the increment of displacement Δu_i is proposed, and the work done by the external forces F_i and T_i is equated to the work done by internal shearing to complete this change in deformation. For an element of original area So, and original volume Vo, this is expressed as:

$$\int_s \frac{T_i}{S_o}\ \delta(\Delta u_i)ds + \int_v \frac{F_i}{V_o}\delta(\Delta u_i)dv = \int_v s_{ij}\ \delta(\Delta\varepsilon_{ij})dv \qquad .....(3.6)$$

where the integrations are carried over the entire new surface and volume respectively, and $\Delta\varepsilon_{ij}$ and ΔS_{ij} representing the incremental linear strain and incremental linear stress. A similar equation can be set up for the virtual work required to produce a further hypothetical change in the increment of deformation, starting with the material that has undergone the major increment of deformation Δu_i, and then a new equation for the incremental work related to the deformation itself can be obtained by subtracting from this equation the first expression for the virtual work before the deformation:

$$\delta[\ \int_v (S_{ij}\ \Delta n_{ij} + \tfrac{1}{2} t_{ij}\ \Delta\varepsilon_{ij})dv] =$$

$$= \delta[\ \int_v \frac{\Delta F_i\ \Delta u_i}{V_o}\ dv + \int_s \frac{\Delta T_i}{S_o}\ \Delta u_i ds] \qquad .....(3.7)$$

where Δn_{ij} and t_{ij} represent the non-linear term of the new incremental strain and the stress measured in the deformed and rotated system. In order to solve this equation it is necessary to find a set of continuous weighting functions α_{ij} such that, for any one of the discrete elements, the displacement $\Delta u_j(x,y)$ under conditions of plane strain, forms part of a continuous displacement field. This allows both a stiffness matrix $[K_G]$ linking the displacement with the force and a stiffness matrix $[K_C]$ that depends on the constitutive relation used and therefore on the material properties, to be determined:

$$[K_G][\Delta U] + [K_C][\Delta U] = [K_G + K_C][\Delta U]$$
$$= [K][\Delta U] = [\Delta F] + [\Delta T] \qquad .....(3.8)$$

Since the force increments $[\Delta F]$ and $[\Delta T]$ are known and the stiffness matrices $[K_G]$ and $[K_C]$ are established from the nodal co-ordinates and the stress-strain rate increment relationship, the nodal displacement $[\Delta U]$ can be readily calculated. Lee and Kobayashi [155] used an improved finite-element representation to carry out a detailed study of cold plane-strain and axisymetric flat punch indentation into a specimen of finite dimensions in which the development of the plastic zone, the load-displacement relationship and stress and strain distributions during continued loading were investigated with variations in friction and specimen dimensions. Unloading and residual stresses were also considered. For plane-strain indentation the punch width was 2w, the specimen width, 2W and the specimen height, h ; W/w = 2.7 for all cases and the depths of the specimens were h/w = 0.6, 1.0, 1.7 and 2.5. The effect of friction at the punch-specimen interface was examined also by using a smooth punch and a rough punch (complete sticking). The material properties used for the computation were: Young's modulus $E \simeq 69 \times 10^3$ N/mm^2, Poisson's ratio $\nu = 0.33$, initial yield stress $Y \simeq 90$ N/mm^2 and the slope of the effective stress and plastic strain curve $H' \simeq 138$ N/mm^2. These values approximated the room temperature stress-strain curve for commercially pure aluminium. Some results concerning the distribution of strain obtained for conditions of both plane-strain and axisymetric compression are shown in Figure 37. These contours reflect the manner in which the plastic zone is developed during deformation and reveal the existing differences between the two deformation modes for the same punch displacements. Distribution of stresses during deformation and residual stresses after unloading were also obtained,

and although no experimental counterpart to this theoretical approach was carried out in order to assess the accuracy of the solutions, it was concluded that the finite-element method was a very efficient method for the study of elastoplastic problems since it removes many restrictions imposed by other methods and offers a possibility of obtaining information that the other methods could not provide.

Madnaik et al [156] have also carried out an analysis of the problem of cold plane-strain compression of rectangular blocks by means of the finite element method, assuming sticking friction conditions at the interface of tool and specimen. The computational procedure was applied to the plane-strain compression of three rectangular blocks of commercial-purity aluminium of h/w = 0.5, 1.0 and 2.0. Similar elastic constants, as above, were used and it was also considered that the stress-strain relationship in the plastic regime could be expressed as:

$$\bar{\sigma} \simeq 100 + 182.4(\bar{\varepsilon})^{0.35} \quad (N/mm^2)$$

Results of the variation of average dimensionless pressure (-Pav/Y) with reduction, for the different values of h/w, were reported to be in agreement with the values obtained by upper bound solutions and the slab method. Also, information on the distribution of stresses and strains could be derived, though again no comparison with either experimental results or results of any other theoretical model were presented.

Evans [148] has also used the finite element method, but to analyse the plane-strain compression test for hot metals by introducing a series of correction parameters to account for the strain rate sensitivity of the flow stress, thus allowing the determination of flow stresses from punch-displacement curves in the absence or presence of frictional forces. Since during hot working metals are strained by

very large amounts, the elastic strains could be neglected and a visco-plastic description of the material behaviour would be appropriate. The relationship used to correlate the values of stress and strain rate was:

$$\dot{\varepsilon} = A\,[\mathrm{Sinh}\,(\alpha\bar{\sigma})]^{n}$$

Thus, finite element computations were carried out for various values of h/w in the range 1 to 2. Punch velocities were chosen and updated to ensure a constant macroscopic strain rate and the resulting punch load-displacement curves were then calculated from nodal reactions. Runs were carried out for slipping friction (μ = 0) conditions and full sticking friction between the punch and the specimen. Neither distributions of strain and stress nor comparison with work carried out by other researchers was reported.

3.3 Distribution of Temperature

In order to predict the changing temperature distributions that occur in specimens deformed under conditions of plane strain compression, Foster [74] developed a two-dimensional finite difference computer programme, based on the formulation of Fourier's differential equation for heat conduction within the specimen and its solution by methods of numerical analysis. The problem is somewhat more complicated than the determination of the temperatures distribution during air cooling since heat conduction from the specimen to the tools, heat flow within the testing tools, changing geometry of the specimen during deformation and temperature rise in the specimen due to the deformation have to be taken into account. Figure 38 shows the representation of both tool and specimen by means of an array of elements of small finite depth "L". The relative positioning of the elements in both tool and

specimen are clearly shown, as well as the number of specimen elements beneath the tool. During deformation the elements in the specimen shoulder remain unchanged while the geometries of the elements initially in the deformation zone are changed as shown in Figure 39. The elements completely within the deformation zone remain rectangular in shape while the deformed elements outside the deformation zone become rhomboidal, ensuring that the area of the elements remains equal. Before and after deformation, heat is considered to flow in the specimen thickness direction and along the specimen length for all the specimen elements, as illustrated in Figure 40. Considering the element of the Nth row and Mth column, the amount of heat flowing in the Y direction is given by:

$$Q1 = \frac{(T_{N,M} - T_{N+1,M})K\ AZ(M+1)\ L\ \delta t}{V(1,M)}$$

and

$$Q3 = \frac{(T_{N-1,M} - T_{N,M})K\ AZ(M+1)\ L\ \delta t}{V(1,M)} \qquad .....(3.9)$$

where "T" represents the temperature of the node, "K" the thermal conductivity and "δt" the interval time over which the heat flow calculation is carried out. However, in the X direction the heat flow is given by:

$$Q4 = \frac{(T1 - T_{N,M})K\ B(1,\ M+1)\ L\ \delta t}{XA(M)}$$

and

$$Q2 = \frac{(T2 - T_{N,M-1})K\ B(1,M)\ L\ \delta t}{XA(M-1)}$$

.....(3.10)

where T1 and T2 also represent temperatures obtained by linear interpolation between $T_{N,M+1}$ and $T_{N+1,M+1}$, and $T_{N,M}$ and $T_{N+1,M}$ respectively. Therefore, the net flow into the N,M element is given by:

$$\Sigma Q = -Q1 - Q2 + Q3 + Q4 \qquad .....(3.11)$$

and the new temperature for this element at the end of the interval is given by:

$$T^{*}_{N,M} = T_{N,M} + \frac{\Sigma Q}{V\rho S} \qquad .....(3.12)$$

where "V" represents the volume of the element, "ρ" density and "S" specific heat of the material.

As far as the surface elements are concerned, the total heat lost from the element surface in the X and Y directions during the time interval δt can be expressed as:

$$Q5 = Ho\ AQ\ (1,M)\ L\ \delta t\ 10^{3} \qquad .....(3.13)$$

where "Ho" represents the heat transfer coefficient for the test furnace cooling, which is calculated using the surface temperatures at the start of the interval. For surface elements of the specimen outside the deformation zone during deformation, Q5 is included in the net heat flow and the new element temperature is given by equation (3.12). The surface temperatures for the deformed columns of elements outside the deformation zone are calculated assuming a parabolic temperature distribution in the Y direction and are given by:

$$Ts^{*} = T^{*}_{W,M} + \frac{Ho\ 10^{3}}{2WK} V(1,M) \cos\phi \left[\frac{W^{3}-(W-1)^{3}}{3} - W^{2}\right] \qquad .....(3.14)$$

where "W" represents the number of elements in the half specimen thickness. The model of heat conduction between the specimen and tool assumes that the rate of heat transfer per unit area between the

specimen and tool is proportional to the difference in their surface temperatures, i.e.:

$$H = C(Ts - As) \qquad .....(3.15)$$

"Ts" and "As" represent the surface temperatures of the specimen and tool face respectively, and "C" is a constant. By considering that the mean temperature T_1^* of the surface element at the end of the interval lies at a distance Dx/2 from the surface, where "Dx" represents the distance penetrated by the temperature gradient during deformation and is given by:

$$Dx = \sqrt{\frac{6K\ \delta t}{\rho S}} \qquad .....(3.16)$$

Then, the surface temperature of the specimen elements may be expressed as:

$$Ts^* = T1^* - \frac{H_1\ D3}{2WK}\left[2W - \frac{Dx}{2D2}\right]\left[\frac{Dx}{2D2}\right] \qquad .....(3.17)$$

where "H_1" represents the heat transfer coefficient at the end of the interval. Although the value of "δt" acceptable for both the specimen and tool will be determined by the smallest specimen and tool element dimensions respectively, the smaller of these two values will be used as the time interval over which the heat flow calculations are carried out. Thus, with increasing strain the time intervals must decrease and the distance penetrated by the temperature gradient in the tool, in each interval, may become much less than the tool element thickness. Therefore, in order to estimate accurately the surface temperature of the tool element it is assumed that the origin of the temperature gradient in the tool is at the innermost edge of the rotational row of elements. Hence, it can be shown that:

$$A_S^* = A_1^* + \frac{(F10)\ D4\ H1\ 10^3}{2(NR+1)\ K_1} \qquad .....(3.18)$$

where:

$$F10 = (NR+1)^2 - \left[\frac{(NR+1)^3 - NR^3}{3}\right]$$

The temperature rise in the specimen due to deformation was determined from calculations of the work done per unit volume for each interval during a deformation from the relevant stress-strain curve. However, it was assumed that the distribution of strain throughout the deformation zone was uniform and therefore the increase in temperature did not vary along this region. The temperature rise in the interval is given by:

$$\Delta T = \frac{\Delta Q \Big/ \begin{matrix}\text{Volume of material in} \\ \text{the deformation zone}\end{matrix}}{S\rho}$$

or

$$\Delta T = \frac{\bar{\sigma}\ \Delta\varepsilon\ 10^6}{S\rho} \qquad \text{.....(3.19)}$$

ΔQ = the work done over the interval

$\bar{\sigma}$ = the mean stress in N/mm^2 over the strain interval $\Delta\varepsilon$

ΔT = temperature rise on each element temperature and surface temperature in the deformation zone in °C

therefore, in general for each element in the deformation zone:

$$T'_{N,M} = T_{N,M} + \Delta T \qquad \text{.....(3.20)}$$

In order to evaluate the accuracy of the predictions made by the computer programme, Foster also carried out experiments on Al-0.5Mn-0.5Mg alloy (among other materials), at approximately 290°C at 2 different strain rates: 15 and 30 s^{-1}, and with three different initial thicknesses for each: 4, 6 and 10 mm. Effects of deformational heat generation in the thermocouple beads were avoided by

limiting the maximum strain applied so that the deformation produced in the thermocouple was relatively small. Thus, the computer model was used to predict the temperature-strain curves obtained for this material but relying on stress-strain data obtained from similar tests in which implanted thermocouples were not employed. Figures 41a and b show the results obtained from which it can be observed that a very good agreement between the measured and computed curves is achieved if a value of "C" (equation 3.15) of 150 $Kw/m^2°C$ is used in the calculations. The comparisons take into account the final thermocouple positions, although the model predicted that the temperature gradients established across the deformation zone during deformation were very small, presumably due to the relatively high strain rates used in these tests.

CHAPTER IV

4. Experimental Techniques

4.1 Introduction

The present investigation has mainly been focused to the study of the effect of the deformation history on the kinetics of recrystallisation of a commercial, non-heat treatable Al-1%Mg alloy under conditions of hot deformation. Particular attention has been paid to the recrystallisation mechanism that a partially recrystallised structure would adopt after being deformed and maintained at elevated temperatures. However, in order to accomplish this research work, a study aimed at the determination of the effect of the deformation parameters: strain, strain rate and temperature, and initial grain size on the time to obtain a fixed amount of recrystallisation, usually 50%, and on the recrystallised grain size achieved once recrystallisation has been completed, was also undertaken. All these experiments were carried out on a plane strain compression testing equipment and the results derived from restoration curves and direct metallographic observation of specimens quenched after different delay times at the deformation temperature, once deformation had been completed. Electron microscopy investigations were also carried out to characterize the large intermetallic particles and to determine whether precipitation had taken place after various cycles of deformation and annealing at the deformation temperature. Both isothermal and non-isothermal tests were carried out in order to establish and evaluate constitutive equations

that would allow determination of the flow stress value of the material at any particular strain, strain rate and temperature, and thus all this information together could be used in computational procedures that take into account microstructural changes occurring in multiple-pass hot deformation processes. Also, further investigations on the hardening peak already reported to appear during the multiple deformation of commercial-aluminium alloys [24] were carried out, especially concerning those factors related to the compensation of the equipment and to the temperature of the deformation tools.

4.2 Experimental Alloys and Specimen Preparation

The metals used in the present investigation were mainly two aluminium alloys: Al-1%Mg and Al-1%Mg-1%Mn, although some experiments were carried out on commercial-purity aluminium. The quantometer analyses for these materials are presented in Table 4. The two alloys are typical of simple, commercial, non-heat-treatable wrought alloys. Both started as the same base alloy, Al-1%Mg from which melt half was DC cast. Manganese was added to the remainder of the melt to give Al-1%Mg-1%Mn. The alloys were homogenised at temperatures ranging between 550°C-560°C for 16 hours and rolled direct from homogenisation to plate $\sim$ 10 mm thick, finishing at temperatures between 250-300°C, whereas the commercial-purity material was hot rolled without previous heat treatment. Since the rolled surfaces of the plates supplied were reasonably good, as far as flatness and lack of holes and scratches were concerned, further treatment before machining was not required. Specimens for plane strain compression tests were cut from these plates in such a way that the rolling direction was kept parallel to the long edge of the sample. This, in turn, implied that the tools made contact perpendicular to the rolling direction. Before testing, all the specimens

were annealed in a muffle furnace with an air atmosphere for one hour at 525°C and allowed to cool in air. Special care was taken to identify the faces of the specimens that made contact with the top and bottom tool respectively.

As well as plate, the Al-1%Mg alloy was also available as slab obtained from DC casting, of about 26 mm thickness. Specimens for rolling were machined from this stock and, as before, the long edges of the samples were parallel to the pouring direction. These specimens were annealed at 550°C in air atmosphere for 16 hours and furnace cooled. After reheating at 400°C for 1 hour, the samples were rolled in three passes to plate about 10 mm thickness and quenched. Specimens for plane strain compression were machined from these plates as already described and annealed at 525°C in air atmosphere for one hour and air cooled. Figure 42 shows the standard dimensions of the specimens used both in plane strain compression and rolling. In order to determine the centre temperature of the specimens in those experiments that required it, a 1.5 mm diameter (Pyrotenax) chromel-alumel thermocouple was inserted at the centre of the specimens. Plane strain compression tests carried out to provide information about the flow stress dependence on the deformation parameters were always performed in duplicate with and without an implanted thermocouple, in order to avoid the normal response of the alloy to the deformation imposed to be altered by the presence of a thermocouple.

4.3 Plane Strain Compression Testing

4.3.1 The Electro-Hydraulic Testing Equipment

The plane strain compression tests were performed on an electron-

ically controlled, hydraulically driven testing machine, also capable of carrying out controlled tension, axisymetric compression and fatigue tests, although for the present purpose it was adapted for compression tests only. Figure 43 is a view of the machine without furnaces or quenching apparatus which allows the load cell on the base of the machine, the tools in the testing position and the specimen carriage drive system to be displayed.

The bed of the machine is a 150 mm thick cadmium-plated steel plate supported at each corner by four shock absorbers. Its cross-head is also supported by four 125 mm diameter threaded columns, and it can be raised or lowered depending on the testing temperature, and locked in position on each column once it has been positioned correctly for testing. Three independent servo-hydraulic, oil-based actuators have been fitted to the machine. The main actuator, also called the ram, is a down strocking piston housed in the cross-head as shown in Figure 44. This actuator can attain a maximum speed of 1000 mm/sec under a full load of $\pm$ 450 KN, with a maximum stroke of 100 mm. In order to perform plane strain compression tests, appropriate tools are attached to the ram and the load cell respectively. These tools were machined from a 13%Cr hot die steel (H21 alloy) whose chemical composition is given in Table 5. Their use was limited to a maximum test temperature of 520°C. Surface grinding after every 100 tests was necessary to ensure a satisfactory performance. Figure 45a shows the relevant dimensions of the plane strain compression tools and the testing arrangement.

The investigation of the microstructural evolution in multiple-pass deformation testing requires that the individual deformations of the specimen terminate at specified strains. Since the hydraulic system is not capable of stopping the ram instantly, a wedge is driven by a

second actuator, horizontally positioned and also housed in the cross-head. It is designed such that a square block fixed to the main ram will strike the top surface of the wedge at some part of its stroke, thus preventing further downward movement. This actuator has a capacity of 10 KN and the wedge has a horizontal to vertical movement ratio of 10:1 with a maximum horizontal stroke of 150 mm, which is equivalent to an upward and downward movement of the ram of 15 mm. The wedge is also used as a safety device, since it lies just below the position of the ram block at the end of the deformation. This will prevent the top tool from over-shooting during testing whenever the resistance of the specimen is not high enough to do it.

The third actuator is a hydraulic motor which drives an endless chain around four sprockets fastened to the track frame. Its maximum stroke is $\pm$ 2.5 revolutions which produces approximately a 400 mm forward and backwards movement of the chain. The specimen handling equipment, also known as the trolley, is connected to the chain by a replaceable metal pin, which is designed to shear whenever the trolley is impeded from moving freely. Thus, the specimen handling equipment can be driven to and from the testing, quenching and finishing positions.

The position of the three actuators is monitored and controlled by a displacement transducer accurate to approximately 0.3%. In order to reduce noise and vibration, a single relatively small power pack of 11 KW capacity is used. This unit is provided with two accumulators of 18 and 9 lts. capacities, which enable the machine to meet the requirements of load and velocity. The larger accumulator contains oil at 21 N/mm^2 pressure and drives the three actuators of the system. The smaller serves as a temporary storage for oil as it rushes out of the larger accumulator at a high rate while the actuators are working, and therefore, prevents a build-up of back pressure in the exhaust pipe.

4.3.2 Description of the Trolley or Conveyor

The trolley is mounted on four wheels which run along rails; its movement is transmitted through a steel pin which connects it to the chain driven by the third actuator. Thus, provided that abnormalities during the testing sequence do not arise, the trolley or conveyor moves from the starting/finishing position at one end of the rail to the testing position at the other end, quenching being carried out in an intermediate position. In the starting/finishing position the specimen can be turned manually towards either the reheating furnace before or after the test, or to the annealing furnace after the test, especially used to control the cooling rate of the specimen during the simulation of slow cooling rate processes such as coiling. The specimen is held in position by two pins in slots cut in two long cantilever arms made from 25%Cr, 20%Ni stainless steel (Immaculate 5). The arrangement is such that the sideways extension undergone by the specimen is accommodated while keeping the sample in the same position, which prevents different areas of the specimen being deformed in each deformation in a multiple pass deformation schedule. Also, the system is capable of maintaining the specimen in contact with the tools just for the period of time over which deformation takes place. This is particularly important for non-isothermal tests where the specimen and tools are at different temperatures and also for isothermal tests since a difference in temperature between the tools and the test furnace has been reported [79], which depending upon the conditions of strain rate present during the deformation, may cause cooling of the specimen. Therefore, the design used helps to reduce the transfer of heat to a minimum. Heat lost by conduction along the length of the arms is reduced by means of a series of holes drilled along their length, but without weakening them mechanically, Figure 46.

4.3.3 Ancillary Equipment

In order to allow non-isothermal tests by means of which simulation of the industrial hot processes could be carried out, as well as isothermal tests required for the investigation of more basic phenomena three furnaces have been incorporated to the machine, as shown in Figure 44. both the preheating and annealing furnaces are mounted to run along tracks at 45° (in the horizontal plane) to the specimen carriage track. The specimen is inserted in either of these two furnaces by pushing them forward to enclose the specimen once the cantilever arms have been swung into position. The testing furnace surrounds the tools and the tests are carried out inside this furnace. All three furnaces have external dimensions of 370 mm x 370 mm x 320 mm (high), with front apertures of 126 mm x 38 mm for inserting the specimen. Both the preheating and testing furnaces have four 18 mm diameter silicon carbide heating elements running from the back to the front with about 88 mm of refractory insulation around all walls. Both furnaces are capable of use up to 1300°C although the maximum test furnace temperature is limited by the maximum operating temperature of the tool alloy. The test furnace has a 100 mm x 25 mm aperture in the top and bottom through which the testing tools are positioned. To reduce heat losses around the tools they are packed with insulating material. The bases of the tools are water cooled to protect the rest of the structure from overheating, particularly the load cell. The annealing furnace, on the other hand, has a 300 mm x 200 mm x 100 mm muffle with 19 gauge nichrome heating element wound round it for operation at lower temperatures. The temperature of all three furnaces is maintained within $\pm$ 2°C of their setting by means of individual proportional temperature controllers, and it is displayed on a common digital temperature indicator through a rotatory switch.

Simulation of hot rolling processes can be carried out by setting the preheating furnace at the billet reheating temperature and the test furnace at a lower temperature in such a way that the cooling rate of the specimen can be controlled to simulate the rolling temperature changes during and between passes. The annealing furnace can be used to simulate a different cooling rate such as the slower cooling of coil following hot-strip rolling. The structure developed either during the high temperature deformation or after an annealing period subsequent to the deformation, can be retained to room temperature by means of a quenching unit available on the machine. The quenching rig, essentially consists of 2 flat water spraying jackets positioned either side of the specimen and parallel to it, and it is situated between the test furnace and the specimen carriage track. Water is pumped through the inter-connected jackets from a 25 lts. circulating reservoir below the spray unit. Once the specimen is moved to the quenching position, a signal from the computer then activates a sliding door which drops vertically closing the front and back openings of the unit, and operates a microswitch to start the quench. After the required quenching time the pump is switched off and the conveyor moved back to its finishing position.

4.3.4 Computer Control Facility

A PDP 11/10 computer incorporated to the equipment, is used to program the three actuators. Communication between the computer and the machine is established by means of a number of digital to analog (D/A) and analog to digital (A/D) converters. The equipment has available a standard electronic control unit which amplifies the difference and feeds it to the servovalve controlling the actuator in order to close the servo-loop. Therefore, the actuator keeps moving as long as there

is a difference between the command and the actual position. Also, a velocity compensation electronic circuit is provided to enable the ram to attain the command velocity instantly, which otherwise would be impeded by the hydraulics of the machine. If this compensation device is properly calibrated, the displacement can be made to match the command almost exactly. Since control of the ram velocity is achieved by varying it in steps, a four-range ramp generator has been incorporated. This unit provides four velocity ranges: 0-500, 0-50, 0-5 and 0-0.5 mm/sec, and therefore allows better control. During a test the velocity range is selected according to the specified test velocity. Within each range the smallest step possible is 1/2000 of the range's maximum velocity, i.e. 0.25, 0.025, 0.0025 and 0.00025 mm/sec, respectively. The maximum ram velocity that allows feed-back control is 500 mm/sec, which is imposed by the response of the hydraulic system. Above this limit, the velocity can either be kept constant at the machine maximum of 1000 mm/sec, or varied in a manner determined by the inertia of the hydraulic of the machine. During testing, as the tools come into contact with the specimen, the load on the ram rises sharply within a few miliseconds, producing a slight extension of the machine frame. In order to correct this situation, a load/elongation compensation device has also been incorporated which makes the machine effectively infinitely stiff. However, since the servo-system is not capable of responding to the change in ram speed in such a short time, an undesired fluctuation in strain rate at the start of the deformation is always produced. This effect is partially overcome by starting the ram at a velocity V2, higher than that required for deformation, V1 (20%-50% higher); in general, it is very difficult to remove completely. Vibration effects on the machine, particularly those produced at ram speeds above 300 mm/sec ($\dot{\varepsilon}_{eq} \simeq 35\ s^{-1}$ for standard specimens 10

mm thick), are overcome by means of an accelerometer fitted inside the hollow base of the lower tool. Its output is connected through a compensating circuit to a strain gauge bridge of the load cell. The accelerometer measures the magnitude of the oscillations in the load readings and the compensating circuit adds or subtracts from the load readings an amount in proportion to this magnitude.

4.3.5 Types of Tests

The computer has been programmed to perform five types of test:

TYPE 1: During the execution of this test, the ram is commanded to move at maximum velocity: 1000 mm/sec until a stop signal is given at some preselected position. Due to the inertia of the hydraulic system the ram moves up to 6.50 mm beyond this position. During this time the strain rate increases very rapidly to a maximum and then decreases to zero. Both the amount of deformation and the maximum strain rate can be controlled by varying the position at which the stop signal is given. The strain rate profile developed during this test allows simulation of rolling operations where the strain rate rises sharply on entry and decreases gradually to zero on exit of the roll gap.

TYPE 2: This test is similar to the Type 1, but it is carried within the feed-back control region ($V1 < 500$ mm/sec) of the machine. In this case the velocity of the ram is decreased linearly with time during the deformation to become zero at the required strain, specified by the ram position at the end of the deformation.

TYPE 3: In this case the velocity of the ram is controlled to give a uniform strain rate throughout the deformation.

TYPE 4: This particular test allows almost any strain rate profile of deformation to be obtained (within the limitations imposed by the response of the servo-hydraulic system and the memory space in the computer), by defining the individual strain rate values at given intervals of strain.

TYPE 5: This test enables different types of deformation in the individual "passes" to be imparted, as long as test Type 1 is not used in the combination.

In all five types of test, up to five deformations may be applied and the strain rate in all deformations need not be the same.

4.3.6 Data Handling

The built-in computer of the equipment is also programmed to collect the results of the tests and to present them in a variety of ways. Load and displacement are converted to stress, strain and strain rate, and the millivolt output from a thermocouple, if recorded, can also be converted into temperature in degrees celsius. Data are collected at a rate specified by an adjustable frequency clock provided with the machine.

4.3.6.1 Calculation of Stress

The flow stress of the material can be obtained from the recorded values of load and from the initial dimensions of the specimen. The load during a test is monitored by a temperature compensated load cell which has an accuracy of 0.2% and is situated below the lower tool. Thus, the average pressure exerted by the tools can be expressed as:

$$\bar{p} = \frac{L}{A} \qquad .....(4.1)$$

where "L" represents the load applied and "A" the contact area between tool and specimen (initially about 750 mm^2 for a standard specimen). However, pure plane strain conditions are rarely achieved and, in practice, some spread along the tools always occurs which makes "A" vary throughout the test. This departure from ideal plane strain conditions can be allowed for by using the following relation [146]:

$$\frac{b}{bo} = 1 + C - C\,(\frac{h}{ho})^{\frac{1}{2}} \qquad .....(4.2)$$

where, "bo" and "ho" are the initial values of breadth and thickness, "b" and "h" the instantaneous dimensions and "C" the spread coefficient. The instantaneous specimen thickness "h" can be determined at any stage of the deformation from the ram displacement. The value of the spread coefficient used in the present investigation was C = 0.280, which has already been reported for the spread correction of aluminium and aluminium alloys in the temperature range of 300°C-500°C [24]. Thus, by using equations (4.1) and (4.2), the tool-specimen contact area and the average pressure could be determined throughout the deformation. However, equation (4.1) assumes that the coefficient of friction between specimen and tools is zero which, in practice, is not the case. The frictional conditions that may be present over the tool-specimen contact area can be divided into three categories: sliding, partially sticking and sticking friction. The predominance of any of these conditions can be assessed by means of Figure 47, which shows the plane strain compression of a plate with tools of width "W". The equilibrium equation of the element shown in this figure can be expressed as:

$$\frac{dp}{dX} = -\frac{2\tau xy}{h} \qquad .....(4.3)$$

If the shearing stress is related to the normal pressure by Coulomb's law of sliding friction, then: $\tau_{xy} = \mu p$, where "μ" represents the friction coefficient. The solution of this differential equation allows the determination of the compressive stress"p":

$$p = (2K)\exp\left[\frac{2\mu}{h}\left(\frac{W}{2} - X\right)\right] \qquad .....(4.4)$$

where "X" represents the distance over which sticking friction conditions are prevalent and can be evaluated from equation (4.4) considering that at the transition point between sliding and sticking friction, $\mu p = K$. Thus, it is obtained that:

$$X = \frac{W}{2} - \frac{h}{2\mu}\ln\frac{1}{2\mu} \qquad .....(4.5)$$

If $X \leqslant 0$, sliding friction operates over the entire tool surface and the average pressure exerted by the tools can be expressed as:

$$\bar{p} = \frac{2}{W}\int_{0}^{W/2} p\,dx$$

or

$$\frac{\bar{p}}{2K} = \left(\frac{h}{\mu W}\right)\exp\left[\frac{\mu W}{h} - 1\right] \qquad .....(4.6)$$

If $X \geqslant W/2$, sticking friction is present over the whole of the tool-specimen contact area, and it can be shown that:

$$\frac{\bar{p}}{2K} = 1 + \frac{W}{4h} \qquad .....(4.7)$$

If $0 < X < W/2$, there will be sticking friction down the centre of the tools in a band 2x wide. In this case:

$$\frac{\bar{p}}{2K} = \left(\frac{1}{\mu W}\right)\left(\frac{1}{2\mu} - 1\right) + \frac{\left(\frac{W}{2} - Zo\right)}{\mu W} + \frac{\left(\frac{W}{2} - Zo\right)^2}{h/W} \qquad .....(4.8)$$

Any of equations (4.6), (4.7) or (4.8) that applies depending on the friction conditions, will yield a value of 2K that can be used to find the equivalent uniaxial yield stress "Y" by means of Von Mises' criterion:

$$2K = \frac{2}{\sqrt{3}} Y$$

or

$$Y = \sqrt{3}\, K \qquad .....(4.9)$$

Since this conversion is strictly applicable to pure plane strain conditions only, a correction factor has been introduced [146] which takes account of the departure from plane strain conditions observed in practice. Therefore, the equivalent uniaxial yield stress is given by:

$$Y = \frac{2K}{f} \qquad .....(4.10)$$

where:

$$f = \frac{1}{b} \left[\frac{2}{\sqrt{3}} (b - W) + W\right] \qquad .....(4.11)$$

4.3.6.2 Calculation of Strain

The equivalent uniaxial strain can be obtained from the strain in plane strain compression by using the conversion factor f (equation 4.11). Thus, the equivalent strain is given by:

$$\varepsilon = f \ln \left(\frac{ho}{h}\right) \qquad .....(4.12)$$

4.3.6.3 Calculation of Strain Rate

Since the strain rate may change during a test, it must be determined over a reasonably small interval of strain, to preserve the

character of the overall strain rate profile. This is done over strain intervals of about 0.05:

$$\dot{\varepsilon} = \frac{\Delta\varepsilon}{\Delta t} \qquad .....(4.13)$$

The time interval "Δt" can be derived from the known frequency of data collection.

4.3.6.4 Calculation of Average Stress and Strain Rate.Area Under the Stress-Strain Curve

The strain energy per unit volume in the deformed material can be calculated from the area under the stress-strain curve derived from the test. In the present case it is calculated by taking the product of the strain difference between two consecutive data and the arithmetic mean of the stress, and summing these values over the appropriate strain interval. The average stress between a selected minimum strain, EMIN, and the point of calculation, is obtained by dividing the strain energy over this interval by the strain differential. The average strain rate over the same interval is calculated by dividing the strain differential by the time elapsed. The average stress is essential for comparing test results with stress values in the material during rolling. Also it can be used to calculate the rise in temperature that occurs during deformation. The average strain rate describes the strain rate-strain profile and can also be compared with the one obtained in a similar pass in rolling. Both values of average stress and strain rate are tabulated on the teletype printout for strain intervals of 0.10 and they are referred to as "Energy Table".

4.3.6.5 Origin, Temperature and Geometry Corrections

The initial part of the stress-strain curve derived from the

deformation of lubricated specimens, is characterised by a shallow increase of stress with strain, due to the squeezing out of the lubricant from between the specimen and tools, and it is not related to the deformation of the specimen itself. Therefore, an origin correction becomes necessary such that the ram displacement readings are adjusted by a constant amount until the specimen thickness derived from the maximum ram displacement readings equal the measured final specimen thickness [74]. This correction must be made before performing the calculations for stress, strain, etc.

The temperature correction [74] arises from the fact that the specimen temperature changes during deformation. Therefore, a hypothetical isothermal stress-strain curve, determined at a constant strain rate, can be calculated assuming that an equation of state (such as equation 2.6b) is upheld. Thus, the stress at a given strain, ε, corrected for temperature and strain rate can be expressed as:

$$\sigma_2 = \sigma_1 - \frac{1}{\beta} \ln \{\frac{\dot{\varepsilon}_1}{\dot{\varepsilon}_2} \exp[\frac{Qdef}{R} (\frac{1}{T_1} - \frac{1}{T_2})]\} \qquad .....(4.14)$$

σ_1, $\dot{\varepsilon}_1$ and T_1 represent the actual values of stress, strain rate and temperature, whereas $\dot{\varepsilon}_2$ and T_2 represent the values of strain rate and temperature at which the correction is to be carried out.

Finally, it has been shown that tests performed using specimens of differing initial thickness may give rise to different stress-strain curves, even after applying the respective spread, friction and temperature corrections [24]. This geometry effect is believed to be related to the fundamental nature of the deformation process. It could be corrected by incorporating the empirical correction equation developed by Beynon [24] into the correction programmes:

$$\sigma = \sigma_0 + (\sigma_1 - \sigma_0)(1 - \frac{Bho}{\varepsilon W}) \qquad .....(4.15)$$

where "σ" and "σ_1" represent the corrected and instantaneous flow stress, "σ_0" the flow stress at which the stress-strain curve departs from the initially linear portion, "ho" the initial specimen thickness, "B" a constant of the material and "W" tool width. This equation enables the alignment of the stress-strain curves towards that of the smallest initial thickness, since, as already shown, grid analysis work showed that thinner specimens present a more uniform deformation pattern. The $(\sigma_1 - \sigma_0)$ term ensures that the correction only operates upon flow stresses greater than "σ_0" and the strain "ε" is included to reduce the influence of the equation at high strains. The stress-strain curves obtained in the present investigation were not corrected for geometry.

4.4 Preliminary Temperature Measurements on the Tools

A difference in temperature between the test furnace and the tools of the plane strain compression testing equipment, constitutes a serious drawback especially for testing aluminium alloys, since the experimental temperature range generally lies between 300°C-500°C. If the tools' temperature is lower than both the preheating and test furnace temperatures, and therefore lower than the initial specimen temperature, cooling of the specimen during deformation will take place unless the conditions of strain rate are such that the deformational heat is enough to compensate for the heat lost to the tools. Although corrections can be made to modify the stress level of the stress-strain curves to the initial specimen temperature, in multiple-pass deformation tests, the sample would be annealed at a higher temperature than that at which deformation took place. Therefore, the microstructural evolution that occurs in between deformations would not correspond to an isothermal schedule of deformation and annealing. Although, most of

the multi-pass industrial hot working operations are carried out under conditions of decaying temperature in between passes, a situation more similar to the present state of the equipment, it would not be possible to carry out experiments that could provide us with more basic information of the restoration processes that take place during and after deformation at elevated temperatures.

In order to overcome this situation, several attempts were made to bring the temperature of the tools to that of the test furnace. The fundamental reason that gives rise to this difference in temperature between the test furnace and tools is thought to be due to the conduction of heat from the tools to the cooling jackets that operate on the machine and which impede the transfer of heat from the test furnace to the rest of the structure. The situation is further complicated by the fact that a "chimney effect" is established within the test furnace in which cool air comes into the chamber through the clearance between the bottom tool and the furnace, despite the fact that the space is filled up with Al_2O_3- SiO_2 wool of insulating material. For this reason the temperature of the bottom tool is always lower than the temperature of the top tool, and the difference between the average temperature and the test furnace temperature has been found to decrease as the test furnace temperature is increased above 500°C, possibly due to the more pronounced radiation effects. Figure 48 shows the variation of the difference in temperature between the top, bottom and average temperatures with the test furnace temperature.

To solve this problem, it was first thought that the heat transfer could be decreased by reducing the mass of the tools in such a way that the path of heat conduction would be altered, but without causing mechanical weaknesses that could lead to fracture of the tools. Therefore, a pair of tools of 10 mm width were used for this purpose. One

of them was drilled as illustrated in Figure 49 and measurements of the tools temperature were carried out, first with the drilled tool situated at the top and then at the bottom. These measurements included both the individual tools' temperature taken on the face and on the front side, and also included the mean temperature when the tools were brought together with a thermocouple in between them. In this case, a small load of 1 kN was applied in order to bring the tools into contact and to avoid deformation of the thermocouple. Unfortunately this attempt did not turn out to be successful and on the contrary it made worse the situation of the bottom tool, since a bigger surface area was now available which enhanced lost heat by convection processes. Hence, a different approach had to be considered in order that the effect could be satisfactorily corrected.

4.5 Subsequent Modifications to the Tools

A second attempt made to improve the temperature of the tools consisted in drilling them along the breadth to allow a 600 watt cartridge heater to be set across the tool as shown in Figure 50. The heater was connected to a variac initially graduated in the range 0-240 watts. Therefore, different amounts of heat could be generated and different temperatures on the faces of the tools could be achieved which was demonstrated by the subsequent measurements carried out. It was found that in the mentioned range of power supply the temperature of both tools could be brought to that of the test furnace and therefore it was decided to perform the same modification to the tools of 15 mm width, the ones used throughout the present investigation. In order to accomplish this, a softening annealing was first given to the tools by heating at 880°C for 2 hours and furnace cooling. After drilling, the tools had to be hardened again by heating at 1140°C for

1 hour, oil quenching and tempering at 570°C for 2 hours. The tools were then sand blasted and their faces re-machined before setting them back into the equipment. Since both cartridge heaters are connected to independent variacs, the power supply that brings the tool temperature to that of the test furnace, had to be determined separately for each tool in the range 300°C-500°C.

4.6 Determination of the Heat Transfer Coefficient of the Specimen

The finite difference computer programme already mentioned in Section 3.3, which is used to calculate the temperature distribution of the specimens deformed under conditions of plane strain compression and which allows the temperature correction of the stress-strain curves to be performed, requires knowledge of both the heat transfer coefficient during deformation and also during the interpass periods in the test furnace either before further deformation or before quenching. Multiple-pass deformation schedules carried out at an early stage of the research project, before modifying the deformation tools, gave rise to drops in specimen temperature during deformation, the magnitude of which increased as the thickness of the specimen was reduced. Since both static recovery and recrystallisation are processes strongly dependent upon the deformation temperature, the determination of the mean specimen temperature as well as its distribution throughout the gauge length becomes quite necessary. Restoration results obtained from multiple deformation tests in which the times between passes are smaller than the times required for the specimen to achieve its initial temperature due to the conduction of heat from the undeformed parts, and also experimental studies of the distribution of the recrystallised fraction can be much easier to interpret in terms of both its mean temperature and its distribution during deformation. Therefore, it is

necessary to determine the equation that gives the rate of heating per unit area of the specimen as a function of the test furnace temperature and specimen surface temperature. This equation would also facilitate simulation of hot rolling operations in terms of the mean rolling temperatures, since accurate calculations of the times required for the specimen to achieve a certain temperature at which deformation should take place, could be carried out. If such non-isothermal schedules, however, involve air cooling periods before or after deformation, the mean specimen temperature and its distribution along the thickness would depend upon the rate of cooling per unit area in air, and therefore an equation that describes this parameter as a function of the specimen surface temperature is also required.

It has already been established (Section 3.3) that the heat transfer coefficient during deformation can be expressed as:

$$H = C(Ts - As)$$

and that the heat transfer constant, C = 150 $kJ/m^2 s^{\circ}c$ for aluminium alloys [74]. Unfortunately, the heat transfer coefficient during either heating or cooling in the test furnace as well as during air cooling cannot be expressed with a similar simple equation. Instead, it is given by an equation that includes both convection and radiation terms:

$$H = b(Ts - To) + C(Ts^4 - To^4) \qquad .....(4.16)$$

Thus, "H" represents the amount of heat gained or lost per unit area per unit time in $kJ/m^2 s$; "Ts" and "To", the surface specimen temperature and the temperature of the medium in which heating or cooling is taking place, in Kelvin; "b" and "C" are constants determined from the experimental data derived from the temperature-time curves obtained in such experiments.

If it is assumed that after a certain time of tests furnace heating or cooling, or air cooling from the furnace, steady state conditions are achieved, that is to say, the heating or cooling rate is identical at every point within the specimen the temperature gradient across the specimen thickness can then be described by means of a parabolic equation [71]:

$$Ts = Tx + \frac{S\rho\dot{T}}{2k}(a^2 - x^2) \qquad .....(4.17)$$

where "Ts" represents the surface temperature at the centre of the top or bottom face; "Tx" the temperature at a distance "X" from the centre of the plate; "2a", the thickness of the plate; "$\dot{T}$" the uniform cooling rate of the plate and "S", "ρ" and "k" the specific heat, density and thermal conductivity of the material. Equation (4.17) also considers that the heat lost or gained by the specimen is essentially one-dimensional and symmetrical about the mid-thickness plane of the specimen. Therefore, the rate of change of the plate heat content can be expressed as:

$$\frac{dQ}{dt} = mS\frac{dT}{dt} = mS\dot{T} \qquad .....(4.18)$$

where "m" is the mass and "v" the volume of the specimen. Since it has been assumed that the heat change occurs only through the thickness, the heat transfer coefficient can be expressed as:

$$H = \frac{dQ}{dt} \text{ / unit area} \qquad \text{(a)}$$

or .....(4.19)

$$H = \frac{V\rho S\dot{T}}{2A} \qquad \text{(b)}$$

where "A" represents the surface area losing heat. However, the specimen volume is given by:

$$V = 2aA \qquad .....(4.20)$$

and therefore:

$$H = \rho S a \dot{T} \qquad .....(4.21)$$

If the temperature-time curve resulting from the particular experiment is obtained by means of an implanted thermocouple situated at the centre of the specimen, equation (4.17) can be written as:

$$Ts = To + \frac{S\rho\dot{T}a^2}{2k} \qquad .....(4.22)$$

In the present investigation, $\dot{T}$ was evaluated by adjusting a third degree polynomial to the temperature values as a function of time:

$$T = A + Bt + Ct^2 + Dt^3$$

and taking its derivative:

$$\dot{T} = \frac{dT}{dt} = B + 2Ct + 3Dt^2 \qquad .....(4.23)$$

Thus, by means of equations (4.21) and (4.22) both "H" and "Ts" may be calculated and "b" and "c" obtained by applying the least squares method to equation (4.16), as explained in Appendix II.

4.6.1 Test Furnace Heating Experiments

The first stage in the determination of an equation of "H" that could describe the heating or cooling of the specimen in the test furnace, as a function of both test furnace and specimen surface temperatures, consisted of heating up undeformed and unlubricated specimens in the cantilever arms of the trolly. For this purpose the test furnace was set at three different temperatures: 300, 400 and 500°C. Once the furnace temperature was stable both the specimen and

cantilever arms that initially were at room temperature, were transferred inside the furnace chamber. The centre temperature of the specimen was plotted continuously using the graph plotter incorporated in the equipment. Changes in the test furnace temperature were also observed in order to determine the period over which the furnace regained its initial temperature.

4.6.2 Test Furnace Cooling Experiments

Cooling experiments were also performed using undeformed standard, lubricated and unlubricated specimens. These were preheated at an initial temperature of 580°C and transferred to the test furnace, set at room temperature. As in the previous case, both the changes in test furnace and specimen centre temperatures were simultaneously recorded as a function of time.

4.6.3 Air Cooling Experiments

The determination of equation (4.16) for air cooling was carried out from results of cooling experiments of undeformed specimens with and without lubricant, both starting from an initial temperature of 580°C. This allowed the assessment of the effect of the graphite compound upon the emissivity of the material during air cooling.

4.7 Metallographic Techniques

4.7.1 Optical Metallography

After deformation, some of the specimens were maintained in the test furnace for different periods of time, so that the recrystallised fraction could be determined. If periods long enough were allowed, the

recrystallised grain size could also be measured. These specimens were sectioned longitudinally, perpendicular to the direction in which the tools made contact with the specimen. Strips 1 cm wide were obtained from which the deformed part was removed, cleaned in hydrochloric acid and mounted in a slow resin. A hole was drilled into the plastic so that a stainless steel screw could be inserted to make electrical contact with the sample. All the mounted specimens were ground down through a series of successively finer silicon carbide papers, polished on diamond wheels to 1/4 μm and electropolished with a solution of 95% ethyl alcohol and 5% perchloric acid at 0°C using fast stirring. The electropolishing was carried out with a stainless steel cathode and a potential of 27 Volts. In no circumstances was the solution allowed to rise much above 0°C, since this led to pitting of the surface. In order to develop the microstructure, the samples were anodized using a solution of 46 ml tetrafluoroboric acid (HBF_4), 7 g boric acid and 970 ml water. With the specimens as anode and using a stainless steel cathode, a potential of 20 Volts was applied with a maximum current density of 0.2 A/cm^2. The time to obtain satisfactory anodizing was found to be dependent upon the degree of recrystallisation of the sample. A fully recrystallised specimen would take a longer time than a deformed one, which would mean that the stored energy of the material plays a very important role in the formation of the corrugated oxide film. After anodizing, the specimens were examined on an optical microscope using polarized light.

As well as the microstructural features already mentioned, the distribution of intermetallic particles after different schedules of deformation and annealing was also determined. In this case, after mechanical polishing the samples were immersed in a solution of 10% H_3PO_4 (85%) and water for 1 min. Although a general pattern of the

distribution of the intermetallics could be observed, the technique had to be complemented by the use of a scanning electron microscope for the identification of such phases. Macroetching was also carried out on the deformed and partially recrystallised specimens in order to have an overall view of the distribution of the recrystallised fraction after different holding periods. For this purpose, a solution of 60% HCl (conc.), 30% HNO_3 (conc.), 5% HF (48%) and 5% water was used. Neither the etchant nor the specimen should be allowed to heat up during etching.

4.7.2 Quantitative Optical Metallography

4.7.2.1 Grain Size Determination

The recrystallised grain size was measured as mean linear intercept, L. However, since such grains were observed to have an aspect ratio different to 1 even after long annealing periods at the temperature of deformation, the measurements had to be carried out both in the transversal and longitudinal directions, so that the grain size could be expressed as [157]:

$$\bar{d} = (\bar{L}_T \cdot \bar{L}_L)^{\frac{1}{2}} \qquad .....(4.24)$$

rather than being characterised by other parameters such as three-dimensional grain size or maximum grain diameter, which are readily obtained from mean linear intercept measurements but applicable only to equiaxed grain structures. The grain size in the gauge length of the specimen was measured along parallel lines 1 mm apart over the entire section of the specimen that finished under the tools after the deformation was completed. This ensured a sufficiently large number of grains to allow a valid statistical measurement. Also, a large number

of grains were measured on the shoulder of the specimen in order to determine the initial grain size of the material.

4.7.2.2 Determination of the Recrystallised Fraction

Point counting was used to determine the different amounts of recrystallisation present after annealing in the test furnace. As for the grain size determinations, the recrystallised fractions were evaluated along 16 parallel lines separated by 1 mm from each other. Unfortunately no microscope equipped with a travelling stage linked to a counting unit could be used since the specimen had to be examined under crossed polarizers. Instead, a graduated eyepiece previously calibrated with an objective micrometer (1 mm divided into 100 parts) was employed. Calibration of this eyepiece was carried out at all magnifications that it was used. Given the number of measurements performed, the relative error of the recrystallised fraction (provided that it lays between 0.1 and 0.9) was estimated to be about $\pm$ 5%. The individual measurements of the recrystallised fraction required to cover the length of the imaginary lines were based on the observation of 21 grains which correspond to the number of points of scale on the eyepiece. Once the measurement was completed the specimen was displaced in such a way that a new set of grains could now be observed, until the whole line was covered. The specimen was then moved 1 mm perpendicularly to this line and a new set of measurements was thus started. Since the co-ordinates of every local measurement could be easily determined, a recrystallisation map was drawn that could, at least, give a qualitative picture of the distribution of the recrystallised grains and its development throughout the gauge section of the specimen. The specimen was considered to be symmetrical about its centre line and therefore it

was divided into four quadrants. Symmetrical measurements of the fractions were found by linear interpolation between the points determined experimentally and their arithmetic average was then considered. The patterns thus obtained could readily be compared with those already shown of strain distribution as well as with similar patterns of temperature distribution developed in the latter sections of Chapter V. Finally, it is worth noting that the magnifications used in all these measurements were chosen in such a way that every grain observed fell upon a single point of the eyepiece scale, which otherwise would have hindered the evaluation of the errors involved.

4.7.3 Electron Metallography

4.7.3.1 Scanning Electron Microscopy

In order to complement the determination of the relative amount, size and distribution of the second phase intermetallics present in the commercial Al-1%Mg alloy, a Phillips PSEM 500 Scanning Electron Microscope (S.E.M.) with a "Link" x-ray energy dispersive analysis system was used. Such a system provides rapid simultaneous analysis of elements of atomic number higher than sodium, which enabled the identification of the chemical elements present in such particles. As for their optical examination, the samples were immersed in a solution of 10% H_3PO_4 and water previous to the observation.

4.7.3.2 Transmission Electron Microscopy

Transmission electron microscopy was used to investigate the possibility of precipitation in the Al-1%Mg alloy as a result of the deformation and annealing cycles to which some of the samples were

subjected and that could alter their recrystallisation characteristics, especially in multiple-pass deformation tests where long interpass times were involved. Slices about 2.0 mm thick, parallel to the plane for optical observations, were cut from the deformed and annealed specimens and discs 3 mm diameter were spark machined from them. These discs were ground to about 0.3 mm and thinned using a solution fo 10% perchloric acid and 90% ethanol at room temperature, 24 Volts and a constant intensity current of 0.105-0.110 amps for approximately 100 sec. The foils were examined in a Phillips EM 301 microscope at 100 KV for general observation of the microstructure or in a Phillips STEM 400 microscope with micro-analysis facilities, whenever information of the chemical composition of the particles present was required.

4.8 Rolling of the As-Cast Alloy

It was mentioned in section (4.2) that specimens for plane strain compression were also obtained from DC cast Al-1%Mg alloy, homogenised and rolled to plate of about 10 mm thickness. The rolling operations were carried out on a 50 ton (498 KN) capacity, 2-high reversible, Hille 50 rolling mill. The work rolls (of 139.7 mm diameter) are driven, through a number of gears, by a 20 H.P. (14.9 KW) motor. The gearing arrangement allows the roll speed to be varied continuously between 2 and 63 r.p.m., the roll speed setting being indicated on a graduated scale between 0 and 10. The roll gap setting can be changed using a screwdown mechanism which can be operated either manually, or electrically through a clutch system (at a speed of 50 mm/min.). This setting is indicated on a scale graduated in 0.2 mm increments which can be set to an accuracy of $\pm$ 0.05 mm. The mill is fully instrumented to measure and record rolling load and roll speed. In the present investigation the angular roll speed was set at 28 r.p.m. ($\sim$ 205

mm/sec.) and the slabs rolled from a reheating temperature of 400°C. Three passes of 35, 27 and 19% reduction were applied with 15 sec. between them. This deformation sequence proved to produce a material that after annealing has a recrystallised grain size of about 60 µm and a distribution of second-phase intermetallics similar to the material supplied as plate [76].

CHAPTER V

5. Experimental Restults and Discussion

5.1 Stress-Strain Relationships for Al-1%Mg Alloy and Commercial-Purity Aluminium

5.1.1 Isothermal Tests on Al-1%Mg Alloy

Simulation of industrial hot rolling operations, especially as far as predictions of rolling loads and torques are concerned, requires a description of the flow stress of the material as a function of strain, strain rate and temperature. In order to determine appropriate relationships, single deformation experiments were carried out on specimens of Al-1%Mg alloy at three different temperatures: 300, 400 and 500°C and six different strain rates: 1, 5, 10, 20, 50 and 100 s^{-1}, where equivalent strains up to about 1.00 were achieved. Such testing conditions covered most of the range of temperature, strain and strain rate found during the industrial hot rolling of commercial aluminium alloys and therefore, the flow stress data derivable from these experiments, in conjunction with the appropriate models capable of describing the deformation history of the material, could be used to predict accurately the strength of the material during a sequence of deformations applied at decaying temperatures and with different roll speeds. Figures 51-53 show the stress-strain curves obtained from such experiments and Table 6 summarizes the flow stress data at different values of strain, as well as the measured and computed temperatures developed during the test. The stress-strain curves display the usual behaviour found for both pure metals and commercial alloys when deformed at

elevated temperatures, namely that the flow stress increases with increasing strain rate at constant temperature and decreases with increasing temperature at constant strain rate. The curves are characterised by the presence of a strain-hardening interval followed by the achievement of a steady state region at higher strains. The strain-hardening part is more readily appreciated at the lower temperatures (300°C and 400°C) and strain rate (1 s^{-1}), since at higher temperatures the steady-state region is achieved very quickly (at strains less than 0.15) and at higher strain rates the presence of small "humps" alters the smooth increase in flow stress with strain normally expected. Such "humps" on the stress-strain curves have already been reported to appear during testing of commercial-aluminium alloys under conditions of plane-strain compression [24,77] and it is believed that they are related to the interaction of the mobile dislocations with more stable substructures inherited from previous deformation history and that have not been removed with the initial heat treatment applied to the material (Section 2.3.6.1). Also, it is clearly observed especially at 300 and 400°C, that the strain interval over which such hardening occurs increases as the strain rate is increased from 5 s^{-1} to 20 s^{-1}. Although at this strain rate the specimen temperature has increased about 35°C at 300°C and 23°C at 400°C, due to deformational heat as the strain applied reaches about 1.00, the stress level remains fairly constant and therefore, the strain interval to steady state can be easily determined. At 50 s^{-1}, however, the specimen temperature increases about 42°C at 300°C and 28°C at 400°C and the stress level keeps on dropping as the strain applied increases, which makes it difficult to determine the interval over which the hardening takes place. An interesting feature observed is that at strain rates of about 100 s^{-1} (achieved by means of type-1

tests) the stress level does not show any appreciable reduction as a consequence of the increase in temperature of the specimen which at the end of the deformation may reach about 46°C when deformed at 300°C. Even more, the stress level of these particular stress-strain curves is observed to increase slightly with strain as the deformation temperature increases.

The mathematical formulation of the stress-strain curves of Figures 51-53 has been carried out by assuming an ideal behaviour of the material, that is to say, that a small strain-hardening interval exists which depends upon the deformation conditions and which is followed by the attainment at higher strains of a steady-state of stress uniquely related to the Zener-Hollomon parameter. Equation (2.9b) in Section 2.2 could be readily used for such a purpose since at small strains it reduces to Ludwik's equation [158]:

$$\sigma = \sigma o + K\epsilon^{m} \qquad .....(5.1)$$

which represents the equation of the stress-strain curve of a strain-hardening material, and at higher strains it reduces to a steady-state level of stress in which the stress is no longer dependent upon the strain applied. Therefore, if σo, σss, K and m could be expressed as either functions of the deformation conditions or constants characteristic of the material, the flow stress could also be easily computed at any strain, strain rate and temperature at which it were required. However, Ludwik's equation has proved to be a difficult equation to fit to stress-strain data of commercial-purity aluminium at high temperatures and strain rates [37]. In the present investigation, it was also found that such a relationship is unsuitable to describe the stress-strain behaviour at small strains mainly because of the difficulty in determining the "σo" values from the curves. If it is assumed that

"σo" corresponds to the flow stress at any particular arbitrarily chosen strain, the log (σ - σo) vs. log ε plots could lead to unrealistic variations of both the strain-hardening exponent "m" and the strength coefficient "K" with the deformation parameters, which hinders the task of formulating a general equation that could be used to describe such data. Therefore, equation (2.9b) was simplified to:

$$\sigma = \sigma ss\ [1 - \exp(-C\varepsilon)]^{m} \qquad .....(5.2)$$

This equation equally predicts the attainment of a steady-state of stress at large strains but reduces to the much simpler power equation:

$$\sigma = K\ \varepsilon^{m} \qquad .....(5.3)$$

at small strains, which has already proved to be adequate for the description of stress-strain data of commercial purity aluminium in the strain-hardening region [37]. At small strains, equation (5.2) reduces to:

$$\sigma = \sigma ss\ [1 - (1 - C\varepsilon)]^{m}$$

or

$$\sigma = \sigma ss\ C^{m}\ \varepsilon^{m}$$

therefore, if $K = \sigma ss\ C^{m}$ then:

$$\sigma = K\ \varepsilon^{m} \quad \text{and} \quad C = \left(\frac{K}{\sigma ss}\right)^{\frac{1}{m}} \qquad .....(5.4)$$

Thus, the first step followed to establish all the parameters of equation (5.2) was to find an appropriate equation of state capable of describing the flow stress data at some particular values of strain as a function of the deformation temperature and the strain rate. The exponential law (equation (2.6b)) was found to fit the data best as is shown in Figures 54-59, where the flow stress at values of 0.05, 0.20,

0.40, 0.60, 0.80 and 1.00 of strain were plotted against the Zener-Hollomon parameter assuming a value of 156 kJ/mol for the activation energy for deformation. In general, it can be observed that within the experimental scatter, the exponential law can be used to correlate the values of stress with the Zener-Hollomon parameter, particularly at strain rates between 1 and 20 s^{-1}, since at higher strain rates there seems to be a shift of the points towards lines of the same slope (same β values) situated on the right of the general curve, indicating a possible increase in the activation energy for deformation. Although the temperature dependence of such a deviation is somewhat unclear, the shift seems to become less apparent at higher values of strain. The data at 0.05 strain includes results obtained from axisymmetric compression tests of a different investigation [58] in which much higher strain rates were achieved. It is quite noticeable that most of these data fall within the scatter bands of the results of the present research work, with the exception of those carried out at 300 and 350°C, mostly at very high strain rates. In this case, a shift also exists but towards a parallel line situated to the left of the general curve. This deviation cannot be explained in terms of the increase in the specimen temperature due to the deformation since at a strain of 0.05 the amount of work done per unit volume of material is rather small. Therefore, it would seem that at temperatures lower than 350°C, the activation energy for deformation decreases from a value of 156 kJ/mol to about 142 kJ/mol, independently of the strain rate, and which still is within the range of activation energies reported for the hot deformation of commercial aluminium alloys. In general, the β values are observed to decrease as the strain applied increases. Ideally, it should be expected that once steady-state has been achieved at all

temperatures and strain rates, the changes in flow stress due to changes in temperature at constant strain rate or changes in strain rate at constant temperature, would be independent of strain. Since that is not the case for the present investigation, a further assumption had to be made, that the stress level during the steady-state corresponds to the maximum flow stress achieved during the test:

$$\sigma ss = \sigma_{max}$$

This assumption does not seem unreasonable, since different mechanisms, other than dynamic recovery, could operate after the steady-state has been attained, and modify the resulting flow stress [81]. Table 6 also contains the data corresponding to the maximum values of the flow stress and Figure 60 shows their representation in terms of the Zener-Hollomon parameter. Therefore, the stress to steady-state can be expressed as:

$$\sigma ss = 8.20 \ln \left[\frac{Z}{1.4565 \times 10^9}\right] (N/mm^2) \qquad .....(5.5)$$

The variation observed of β with strain, once steady-state has been achieved could be explained in terms of adiabatic heating or deterioration of the lubricant film, thereby increasing the friction between the tools and the specimen, which would tend to increase the stress level as the deformation proceeds. In order to determine both "C" and "m" in equation (5.2), two tests were chosen both at a strain rate of 1 s^{-1} and carried out at 300 and 400°C. Table 7 summarizes the stress-strain data of these tests and Figure 61 shows the results obtained. The strain hardening exponent "m" does not present any systematic variation with temperature whereas the strength coefficient "K" does, as predicted by equation (5.4). At 300°C it was found that the flow stress, in the strain-hardening interval could be well

expressed as:

$$\sigma = 112.8\ \varepsilon^{0.1}$$

and at 400°C:

$$\sigma = 69.02\ \varepsilon^{0.1}$$

Therefore, a strain-hardening exponent of 0.1 would seem to be appropriate to use in equation (5.2). The constant "C" can also be evaluated if any equation that expresses the flow stress as a function of the deformation conditions, at any value of strain is available. For example, the flow stress at a strain of 0.05 can be expressed as:

$$\sigma_{0.05} = 7.02 \ln \left(\frac{Z}{5.5807 \times 10^{8}}\right) (N/mm^2) \qquad .....(5.6)$$

However,

$$\sigma_{0.05} = \sigma ss\ [1 - \exp(-0.05\ C)]^{0.1}$$

That is to say,

$$C = 20 \ln \left[\frac{1}{1 - (\sigma_{0.05}/\sigma ss)^{10}}\right] \qquad .....(5.7)$$

Thus, equations (5.5)-(5.7) can be used to describe the flow stress data within the range of strain, strain rate and temperature used in the present investigation, especially those obtained between strain rates of 1 and 20 s^{-1} since no account of the deviations previously reported has been considered.

5.1.1 Non-isothermal Tests on Al-1%Mg Alloy

In order to verify the validity of these flow stress equations, double deformation non-isothermal tests were carried out on as-cast

specimens of Al-1%Mg alloy, reheated at 483°C and allowed to cool in the test furnace for about 10 seconds before the first deformation. Both test furnace and deformation tools were initially at 20°C and, as for the isothermal test, strains of about 1.00 were reached at strain rates of 5, 10, 20 and 50 s^{-1}. Tables 8-11 give details of such tests and Figures 62-65 show the corresponding stress-strain curves obtained as well as the flow stress values predicted from Figures 55-60. In all cases, it can be observed that the values of flow stress obtained from non-isothermal tests are somewhat underestimated when computed with the equations developed from isothermal tests, particularly at strain rates higher than 20 s^{-1}, which may be due partially to the fact that such equations were determined from data obtained at strain rates between 1 and 20 s^{-1}, and also that the non-isothermal tests were carried out with as-cast and homogenised specimens, with a different thermo-mechanical history from the specimens used in the isothermal tests. In general, there is not enough evidence to believe that flow stress data of tests carried out under non-isothermal conditions could not be predicted by means of equations obtained from isothermal tests. If the flow stress of non-isothermal tests is plotted as a function of the Zener-Hollomon parameter, according to the exponential law (equation (2.6b)). it is found that, regardless of the strain at which the stress is measured, it is uniquely related to the mean temperature of the specimen and to the strain rate. Figure 66a shows the results obtained, and from which the flow stress can be expressed as:

$$\sigma_{(\text{non-isothermal})} = 9.59 \ln \left[\frac{Z}{2.9398 \times 10^9}\right] \quad \ldots\ldots(5.8)$$

The mean temperature of the specimen, as in the isothermal tests, was calculated by means of the two-dimensional computer programme already described (Section 3.3) and the strain rate used was the mean

strain rate developed over the interval of strain in consideration. Figures 64 and 65 also indicate the presence of a hardening peak in the stress-strain curve of the as-cast material as the strain rate applied increases, which is reflected on the log Z vs σ plot as a deviation towards higher values of stress than those corresponding to the particular Z values. This situation is then corrected as the deformation proceeds and the stress values are observed to return to those predicted by equation (5.8). In general, these results would seem to indicate that the hardening produced by the continuous drop in temperature of the specimen would supersede the hardening caused by the increment in strain during deformation at constant temperature and strain rate, which is not surprising as it can be seen from Figures 51-53 that the change in stress due to changes in strain are very small in comparison to the changes in stress brought about by changes in temperature or strain rate. Figure 66b contains the flow stress data of the second deformation applied after a period of 15 seconds, once the first deformation had been completed. As for the first deformation, the application of the exponential law to this set of data yields also a straight line (illustrated as a broken line in Figure 66b) particularly below a stress level of 100 N/mm^2, above which there seems to be a deviation towards much higher values of flow stress than those predicted by both equations of state. This deviation is very likely to be due to frictional effects which appear to have a noticeable influence upon the flow stress, especially after a strain of 0.4-0.5 in the second deformation has been achieved, causing the stress-strain curves to bend upwards beyond this point, as observed in Figures 62-65.

It is very unlikely that such deviations are due to errors in the determination of the mean temperature of the specimen, since differences up to about 100°C would be required to account for their

presence. Also, it is quite important to point out that in the region where friction has a negligible effect on the stress, the flow stress values appear to be much lower than the flow stress predicted by the equation that represents the variation of "σ" with "Z" for the first deformation. This phenomenon could partially be interpreted in terms of the occurrence of recovery during the interval between deformations, which may take place as a consequence of the small changes in the mean temperature of the specimen as reported in Tables 8-11. Thus, it can be observed that the maximum drop in temperature that takes place is of 26°C which occurs during tests carried out at strain rates of 50 s^{-1}, whereas in tests performed at 5 s^{-1} even a slight increase in temperature during the interpass period has been produced. A lower flow stress in the second deformation could also be interpreted in terms of the inheritance of a coarser sub-structure from the first deformation, a phenomenon already reported to occur during non-isothermal testing of commercial aluminium alloys [25,77]. Therefore, it is concluded that, in general, the theoretical prediction of the flow stress during multiple pass deformation operations carried out under conditions of decaying temperatures should always overestimate the actual flow stress of the material, particularly in those Z intervals where an "equilibrium" sub-structure has not been achieved, unless enough strain is accumulated during the passes to promote the occurrence of static recrystallisation between deformations, which would avoid the inheritance of any sub-structure from previous passes.

5.1.3 Stress-Strain Relationships for Commercial-Purity Aluminium

Similar equations to those developed for Al-1%Mg alloy were obtained for commercial-purity aluminium, using the data provided by

the stress-strain curves shown in Figures 9-11. Table 12 summarizes the values of stress, strain rate and temperature obtained at different strains and Figures 67-71 illustrate their graphical representation, also in terms of the exponential relationship. In general, it is quite noticeable that the plane strain compression data tend to develop three different lines at different temperatures as soon as the strain rate of the test reaches 20 s^{-1}, independently of the deformation temperature. These results have also been confirmed by tests performed under conditions of axisymmetric compression [57], carried out on commercial-purity aluminium up to strain rates of about 1000 s^{-1}, Figure 67. However, in this particular investigation, it was found that the change towards higher strain rate sensitivities occurred at strain rates of about 100 s^{-1}, also independently of temperature. A different set of data also obtained from axisymmetric compression of commercial-purity aluminium specimens [37] was observed to follow the exponential law over the range of Z values under consideration without appreciable deviation of the points. Beynon [24] has explained the change in strain rate sensitivity as a result of a change in the deformation mechanism, from dislocation climb and movement of jogged screw dislocations to dislocation glide control at strain rates higher than 20 s^{-1}. However, it seems rather peculiar that such a change is not temperature-dependent and that just appears at a fixed strain rate: 20 s^{-1} in the case of plane strain compression and 100 s^{-1} in the case of one of the axisymmetric set of data, whereas for the other set the phenomenon was not present at all. Therefore, doubts still remain concerning the reasons for the occurrence of such a change in strain rate sensitivity and no particular explanation is offered in order to account for this phenomenon.

As for the Al-1%Mg alloy, the application of equation (5.2) requires of the description of "$\sigma_{0.05}$" and "σss" both as a function of Z. From the plane strain compression data it is obtained that:

$$\sigma_{0.05} = 2.50 \ln\left[\frac{Z}{2.6289 \times 10^{8}}\right] \ (N/mm^2)$$

and that,

$$\sigma ss = 5.59 \ln\left[\frac{Z}{9.8095 \times 10^{9}}\right] \ (N/mm^2) \qquad .....(5.9)$$

These equations, however, are adequate for the prediction of flow stress data at strain rates lower than 20 s^{-1} since the deviation towards higher strain rate sensitivities has not been taken into account. Hocketts' equations [37], on the other hand:

$$\sigma_{0.05} = 3.11 \ln\left[\frac{Z}{2.8327 \times 10^{7}}\right] \ (N/mm^2)$$

and

$$\sigma ss = 5.73 \ln\left[\frac{Z}{5.7963 \times 10^{8}}\right] \ (N/mm^2) \qquad .....(5.10)$$

can be applied in the range of strain rates 0.14-216 s^{-1}. The nominal difference between the flow stresses predicted by these two sets of data may arise from differences in their chemical composition. The value of the strain hardening exponent was determined from two of tests carried out under plane strain conditions, at 300°C and 400°C respectively, both performed at a mean strain rate 10 s^{-1}. Such conditions ensured that the adiabatic heating generated during deformation compensated for the cooling effect caused by the deformation tools and therefore that the flow stress values were least affected by the changes in specimen temperature. Table 13 contains the stress-strain data of such tests and Figure 72 illustrates the application of equation (5.3). Thus a value of the strain hardening exponent of about 0.17 is obtained,

which is somewhat higher than previously found for Al-1%Mg alloy, although it compares well with the one also reported for commercial purity aluminium of 0.18 [37] in the range 20-400°C. A higher value of "n" for commercial-purity aluminium than for Al-1%Mg alloy would be reflected on the stress-strain curves as an increase in the interval of strain required to achieve conditions of steady-state, under the same conditions of temperature and strain rate. Thus, a general expression for the flow stress as a function of strain, strain rate and temperature can be written as:

$$\sigma = \sigma ss\ [1 - \exp(-C\varepsilon)]^{0.17} \qquad .....(5.11)$$

where "C" is given by:

$$C = 20\ \ln\left[\frac{1}{1 - (\sigma_{0.05}/\sigma ss)^{5.88}}\right] \qquad .....(5.12)$$

and both $\sigma_{0.05}$ and σss are obtained from either equation (5.9) or (5.10). As already explained for Al-1%Mg alloy, it is expected that the above equations would overestimate the value of the flow stress of the material under multiple-pass, non-isothermal conditions, unless recrystallisation takes place during the time between deformations.

5.2 Further Investigations of the Effect of Machine Variables on the Reloading Hardening of Commercial Aluminium Alloys

5.2.1 Al-1%Mg - 1%Mn Alloy

Since restoration experiments were carried out by means of multiple-pass deformation tests, it was decided to perform a series of experiments on Al-1%Mg-1%Mn alloy and commercial purity aluminium to determine the extent of the influence of several machine variables upon

the hardening observed in multiple deformation tests. Such variables included the amount of compensation used to automatically account for the extension of the machine frame during testing, approach velocity, displacement loop gain and temperature of the deformation tools. Although it is believed that such a reloading hardening is a material property inherent to commercial-aluminium alloys, it was considered important to determine the way in which the appearance of the phenomenon could be altered by the change of certain features intrinsic to the testing equipment. The first step in this particular investigation was to perform a series of two-deformation tests using different values of compensation, under the same conditions of approach velocity, loop gain and temperature of the specimen. Tests carried out on steels have shown that the use of different amounts of compensation could give rise, in multipass deformation schedules, to a hardening phenomenon similar to the one observed during testing of aluminium specimens [159, 160]. Figure 73 illustrates this effect where it can be seen that interruption and reloading under conditions of 100% compensation produces an apparent hardening of the material, whereas the use of 0% compensation shows that on reloading, the stress-strain curve is a smooth continuation of the first curve, at least in the region before the peak stress is achieved and therefore, where dynamic recovery is the only restoration mechanism in operation. Figure 74 shows the results of similar experiments carried out on specimens of Al-1%Mg-1%Mn alloy at 400°C and using a strain rate of 10 s^{-1}, and Figure 75 illustrates similar results obtained at 460°C. As it has already been explained, the load/elongation compensation device has been incorporated to the machine with the purpose of making it infinitely stiff in the sense that if the right amount of compensation is applied, even loading of the machine to its full capacity would not give rise to

variations in the displacement readings which would ensure that the elastic extension of the machine is not included in the total deformation of the specimen. In this case, the displacement reading is the one at the surface of the specimen and therefore, as the load rises causing the extension of the machine frame, the load/elongation compensation electronics sends out a signal for the ram to move faster and account for this extension. Since the servo-system is not capable of responding as soon as such a signal is sent, the strain rate decreases during the first part of the deformation, which is then followed by another period of increasing strain rate. Under normal conditions this situation is partially corrected by the use of an approach velocity (a velocity with which the ram starts the test) higher than the actual velocity that gives the right strain rate during the deformation. If no compensation at all is used, as depicted in Figures 74a and 75a, the strain rate in the specimen decreases and, although the sharp fluctuations present at the beginning of each deformation have virtually disappeared, the hardening observed on reloading is still present after a short interruption. At 460°C, however, the peak shape is seen to be different and also the peak strain interval is observed to be somewhat shorter than at 400°C. The rise in stress at the end of the second deformation is most likely to be due to friction effects since at higher temperatures the lubricant degrades more quickly. The use of more compensation than required, as shown in Figure 75c, produces an increase in the strain rate of the specimen at the beginning of both deformations, which tends to increase slightly the hardening effect, but that could be corrected by means of an appropriate equation of state. It is also important to point out that some of the specimens, although tested under the right conditions of load compensation, presented a similar hardening at the beginning of

the first deformation. Both this hardening effect, as well as the one observed at the beginning of the second deformation, appear to increase as the deformation temperature increases, Figures 74b and 75b. This observation agrees with a number of previous findings [24] obtained from tests carried out on the same alloy, although it has not been possible to confirm it for either Al-1%Mg alloy or super-purity and commercial-purity aluminium. Therefore, an apparent temperature-effect on such a hardening phenomenon may be present for Al-1%Mg-1%Mn alloy, which would emphasize its entirely structural nature. However, no systematic investigation was carried out to verify this particular point.

The approach velocity used to correct the fluctuations in strain rate present at the beginning of any deformation is never higher than 20% of the initial deformation velocity. This range has been established by trial and error from a number of tests carried out up to a temperature of 500°C [146]. In order to investigate the effect of this parameter on the appearance of the hardening phenomenon, several tests were performed in which the approach velocity was changed, both with 0% and 100% compensation. However, no significant effect of this parameter on either the magnitude or shape of the reloading hardening could be determined. A different aspect also investigated was that concerning the value of the displacement loop gain set to the standard electronic control unit available on the machine. This control unit is used to amplify the feedback signal from the transducer, compare it with the command signal, amplify the difference and feed it to the servovalve controlling the particular actuator in order to close the servoloop. Thus, all the actuators keep on moving as long as there is a difference between the command signal and the actual position. In general, it is expected that too high values of the displacement loop gain would

produce excessive scatter in the strain rate values, whereas too low values could increase the lag existing between the command signal and the actual displacement of the ram. However, double deformation tests carried out with different values of loop gain did not show any significant effect of this variable upon the stress-strain behaviour of this alloy.

The final variable investigated concerning the state of the equipment was that related to the temperature of the deformation tools. As it was explained in Chapter IV, a difference in temperature between the tools and the test furnace was detected, which was corrected by the use of a pair of cartridge heaters capable of raising the temperature of the tools to that of the furnace. Figure 76 shows a comparison of the stress-strain curves obtained with and without use of such heaters, carried out under the normal conditions of load compensation, approach velocity and displacement loop gain. As it can be observed, the effect of equalizing the temperature of the tools to that of the test furnace is to increase slightly the magnitude of the hardening peak both during the first and second deformation, although such a difference is well within the experimental reproducibility of each test.

Thus, in general it can be stated that although some changes in the parameters that characterise the hardening effect observed in some commercial aluminium alloys are made, there is no evidence that such a phenomenon is a result of any machine effect and, on the contrary, more evidence has been made available to confirm its structural nature.

5.2.2 Commercial-Purity Aluminium

A number of tests were carried out on specimens of commercial-purity aluminium in which the third and fourth deformations were inter-

rupted just after the maximum in the hardening peak. Figure 77 illustrates one of these tests where it can be observed that after reloading the specimen, following a short interval of 1.0 sec., a hardening peak was again produced but at the same level as that of the previous deformation. This result implies that the hardening is not a cumulative effect and therefore that the production of mobile dislocations on reloading is carried out by unlocking of the stable arrays formed during the unloading. However, if the interruption occurs beyond the strain over which the maximum stress is produced, then it is observed that the peak stress increases although the absolute magnitude of the hardening ($\Delta\sigma$) is kept constant. This can be better appreciated in Figures 78 and 79 which show a five deformation schedule on both commercial-purity aluminium and Al-1%Mg-1%Mn alloy, carried out under the same deformation conditions. In the case of commercial-purity aluminium it is not clear whether this is due to the fact that at 400°C the strain interval over which steady-state is achieved is much higher than for the alloy, which is not very surprising since it has been previously shown that commercial-purity aluminium work hardens at a faster rate than Al-1%Mg alloy, and therefore, is also likely to work harden faster than Al-1%Mg-1%Mn alloy. If steady-state has not been achieved, then it is expected that the peak stress also increases because of the higher rate of dislocation multiplication than of annihilation events per unit of strain. However, as observed, for example in Figure 74b, the strain hardening interval of the stress-strain curve obtained for Al-1%Mg-1%Mn alloy under the same conditions is very small and between 0.05 and 1.3 strain, the flow stress is maintained almost constant. Nevertheless, if a first interruption is applied once steady-state has been achieved followed by further interruptions before the stress reaches the steady-state level, it can be

observed that the peak stress increases, implying that a certain cumulative effect has taken place and, therefore, that creation of new mobile dislocations has occurred. However, a feature that this explanation does not encompass is the fact that the magnitude of the hardening ($\Delta\sigma$) does not change after every interruption, since the density of mobile dislocations is somewhat higher than the existing before the previous interruption. Finally, another important observation that can be made from both Figures 78 and 79 is that the strain interval over which the hardening occurs (εp), increases with the number of deformations applied. This is an entirely reproducible result that suggests a strain-history effect on the reloading hardening, contrary to previous findings and that also points towards a structural nature of this unusual yield phenomenon.

5.3 Restoration and Recrystallisation Results After One Deformation

As has already been explained (section 2.3.6), both the time required to develop a fixed recrystallised fraction during annealing after deformation either under isothermal or non-isothermal conditions, and the grain size achieved once recrystallisation has been completed, depend upon the deformation conditions, cooling rate (in non-isothermal processes) and the initial grain size of the material, provided that precipitation of secondary phases does not take place in such intervals. Since one of the principal aims of the present investigation was to determine such relationships, a number of isothermal experiments were carried out on specimens of Al-1%Mg alloy, in which the recrystallisation kinetics was followed by means of both restoration of the flow stress of the material determined by a second deformation subsequent to an annealing period, and the use of quantitative optical metallography

in order to correlate the fraction restored with the fraction recrystallised present at the end of such a period. Thus, the effect of variables such as strain, strain-rate, temperature and initial grain size were quantified so that general equations to predict both the time to obtain 50% restoration and the recrystallised grain size, could be developed for use in a computational procedure suitable to study microstructural evolution during hot rolling operations both on a laboratory and an industrial scale.

5.3.1 Effect of Strain on the Recrystallisation Kinetics

In order to determine the influence of the amount of strain applied on the recrystallisation kinetics, double deformation tests were performed at a nominal temperature of 400°C and a mean strain rate 1 s^{-1}. Tests carried out under such conditions ensured the absence of any hardening effect on reloading, as already explained in Section 5.2. After imparting initial strains of 0.15, 0.33, 0.67 and 1.00, a whole range of interpass times were allowed before applying a second deformation, from which the stress-strain curve was also determined. Figure 80 shows the mean stress-strain curve obtained for the first pass of the two deformation schedules carried out under the present conditions. This curve has been used for comparison with the stress-strain curve obtained in the second pass of the same schedule in order to allow the calculation of a "restoration index" used to evaluate the degree of restoration of the second curve with respect to the first one. Figures 81-84 show the set of stress-strain curves obtained after the initial strain has been imparted and different times between deformations allowed. Table 14 gives details corresponding to such tests. In every case the curves obtained during the second deformation were traced by

adjusting the stress level of the first stress-strain curve to the stress level of the mean curve previously drawn. For these particular sorts of schedules the restoration index was defined as:

$$R_1 = \frac{(\sigma_{max})_1^{EXT} - (\sigma_0)_2}{[(\sigma_{max})_1^{EXT} - (\sigma_0)_2^{\infty}]} \times 100 \qquad .....(5.13)$$

Figure 85 gives a graphical illustration of the parameters involved: $(\sigma_{max})_1^{EXT}$ represents the value of flow stress of the first mean curve extrapolated to a value of 0.05 of strain in the second deformation, $(\sigma_0)_2$ represents the flow stress of the second curve also measured at 0.05 strain, and $(\sigma_0)_2^{\infty}$ represents also the flow stress of the second curve but measured after a sufficiently long interpass time has been allowed and therefore, when no more softening occurs with increasing annealing time between deformations. The features observed in Figures 81-84 are characteristic of the results obtained from similar restoration experiments reported elsewhere [39]. The stress level of the second stress-strain curve decreases due to the operation of static restoration processes. The rate of decrease is observed to be strongly dependent upon the initial strain applied to the material, Table 14. In the present case, however, a peculiar feature has also been found: the stress level of the stress-strain curve obtained once recrystallisation had been completed was consistently observed to be lower than the initial flow stress of the annealed metal. This could lead to restoration values higher than 100% if the more commonly found definitions of R_1 are used. The restoration index such as defined in equation (5.13) allows the normalisation of the values obtained, and therefore a direct comparison can be carried out in order to assess the strain effect on the kinetics of the phenomenon. Table 14 also contains details of the restoration indexes which are graphically represented in Figure 86a as

a function of the interpass time, for the different initial strains applied. The picture shown is as expected, namely that restoration processes and hence recrystallisation during the rest period, occurs more rapidly as the initial strain is increased, presumably due to the consequent increase of stored energy in the material. An interesting point to be noticed in these curves is the linear variation of the restoration coefficient with log (time) if relatively small strain ($\varepsilon \approx$ 0.33 or less) are applied in the first pass. Such a degree of softening is believed to be associated with recovery, although as it will be shown later, a very small recrystallised fraction has been observed to be present mainly along the high strain bands of the specimen deformed by 0.33 strain and annealed 1000 seconds at the deformation temperature. As the strain applied increases the restoration due to static recovery decreases in relation to the occurrence of recrystallisation, which may be interpreted in terms of the stored energy to initiate the nucleation of strain-free regions and their migration throughout the deformed matrix. However, if the strain applied in the first pass increases, the degree of restoration associated with those tests where the interpass time is less than 10 seconds, is also observed to increase. This somewhat unclear phenomenon is believed to be related to the difference in temperature between the tools and the test furnace that existed at the time that the present series of experiments were performed. Figure 87 illustrates the patterns of temperature distribution developed in a standard specimen deformed under the initial conditions of the testing equipment. Such distributions have been obtained assuming a mean temperature for both tools and, therefore, they have been considered to be symmetrical about the centre of the specimen. As the deformation takes place, the mean temperature of the specimen decreases from the reheating temperature of 400°C to about

380°C once a strain of 1.00 has been achieved. These changes in temperature modify the flow stress value of the second deformation giving rise to a spurious degree of recovery in the annealing period between deformations. Therefore, a temperature effect as well as a strain effect are believed to be involved in the present set of results and, which is particularly important if the interpass time is small (< 10 sec), since longer intervals allow the initial temperature of the specimen to be regained because of the heat flux from the undeformed shoulders of the sample as well as from the test furnace. Final specimen geometry is also important since thinner specimens will heat back to temperature quicker than thicker samples, despite their lower final temperature.

In general, it has been found that the restoration coefficients are accurate to a degree of about $\pm$ 5% of the reported values. Friction effects are particularly significant in their calculation since the stress-strain curves in the second pass can be severely affected by high friction conditions brought about by the deterioration of the lubricant film during the interpass periods. This was observed to occur randomly without apparent reason during the performance of such tests and, therefore, some of them were not included in Figure 86a, in spite of a reduction in the number of experimental points through which the curves were traced. Table 14 also gives details of tests in which high friction conditions were determined.

As shown later in the present section, the maximum degree of restoration associated to recovery effects was found to be about 30%. This allowed a recovery-correction of the data of Figure 86a to be carried out, as shown in Figure 86b, which represents the restoration values solely associated to the occurrence of recrystallisation. This plot was found to be particularly useful in the interpretation of restoration

results after two deformations with different time intervals between the first and second passes, and which will be the subject of section 5.4. The effect of equalizing the tool temperature to that of the test furnace is shown in Figure 88, which represents the results of tests carried out with the use of cartridge heaters in the tools. The corresponding data are summarized in Table 15. This figure clearly illustrates the fact that if the tool temperature is increased, the restoration kinetics is delayed, which is particularly noticeable after 60% restoration has been achieved. This phenomenon could be due either to the reduction in the driving force that a decrease of T implies, or a change in the general pattern of strain distribution brought about by a change in temperature distribution during deformation.

In order to determine the power dependence of the time to a fixed fraction restored on the strain applied, values of the time to 70% restoration were taken from Figure 86a and plotted on a logarithmic scale as a function of strain, as shown in Figure 89. However, such values have been corrected to a deformation temperature of 400°C, since as already explained, the lower temperature of the tools produces a decrease in the mean temperature of the specimen during the first deformation. The correction factors were obtained from the relation:

$$t_{50\%} \alpha \exp [54800/RT]$$

whose derivation is the subject of section 5.3.2. Thus, an exponent of about 2.7 seems to fit the data best and this is found to remain almost constant if the time to obtain any fraction other than 70% is chosen. Therefore:

$$t_{70\% \text{ Rest.}} \alpha \varepsilon^{-2.7}$$

which is somewhat lower than the power dependence found for steels [73,

74, 137, 138] but much higher than the previously reported values of pure and commercial aluminium alloys [26] (section 2.3.5.1). Figure 89, however, also illustrates that as the strain applied increases beyond 0.67, $t_{70\%\ Rest.}$ becomes constant (shown by the broken lines), indicating the existence of a critical value at which $t_{70\%\ Rest}$ eventually becomes independent of strain.

The fraction restored is not equivalent to the fraction recrystallised since restoration is accounted for by both recovery and recrystallisation, provided that no other process such as precipitation is involved. In order to determine the relationship between these two fractions a number of specimens were deformed by applying strains of 0.33 and 0.67, and quenched after different holding periods at the deformation temperature. Such specimens were sectioned and prepared metallographically in order to measure the fraction recrystallised present along the gauge section of the sample. Table 16 contains the results obtained from such measurements and Figure 90 illustrates their representation as a function of log (time). Figure 91 shows an Avrami-type plot of the same data which allows the determination of the Avrami exponent "n" (equation (2.20)) that governs the relationship. The recrystallisation data for the samples deformed by 0.67 strain give a value of "n" of about 2 which has been reported elsewhere for both aluminium and ferritic steel [135, 136]. This recrystallisation curve is observed to be smooth and to follow the classical sigmoidal pattern characteristic of any nucleation and growth process. A striking feature, however, is that an induction period is observed to be required for the nuclei to form before the stage of growing. This has been found before for polycrystalline aluminium [161] but is not always the case [135].

The recrystallisation data obtained from the samples deformed by

0.33 strain present a somewhat different type of curve in which the value of "n" appears to be about 1. As observed from Table 2, a change of the Avrami exponent from a value of 2 to 1 would imply a change in the nucleation mechanism from saturation at grain edges to saturation at grain boundaries. Nevertheless, it is believed that rather than a change in the nucleation mechanism, the change in "n" is entirely due to the heterogeneous nature of the strain distribution present under such conditions, as already illustrated in Figure 35a. In order to get a better understanding of this phenomenon, let us consider equation (2.21):

$$Xv = 1 - \exp\left[-0.693 \left(\frac{t}{t_{0.5}}\right)^n\right] \qquad .....(2.21)$$

a modified form of equation (2.20). It has already been established that,

$$t_{0.7} \alpha \varepsilon^{-2.7} \qquad .....(5.15a)$$

or,

$$t_F = A\varepsilon^{-2.7} \qquad .....(5.15b)$$

where "A" is a constant, different if either t_F restoration or t_F recrystallisation are being considered.

By replacing equation (5.15b) into equation (2.21) and allowing "n" a value of 2, it is obtained that:

$$Xv = 1 - \exp\left[-0.693\, \varepsilon^{5.4} \left(\frac{t}{A}\right)^2\right] \qquad .....(5.16)$$

This equation allows us to trace a whole series of curves expressing the recrystallised fraction "Xv" as a function of the parameter (t/A), when different initial strains are applied. Figure 92 shows the results obtained, from which it is clearly observed that whenever heterogeneit-

ies in the distribution of strain are present, recrystallisation will not occur according to equation (5.16) but rather as a process in which the material with a higher strain recrystallises first and the material less deformed recrystallises last, provided that the rest of the parameters that determine t_F (such as Z and do, encompassed in constant A) do not have a different and predominant distribution that could alter the whole picture. If the recrystallisation curve obtained after 0.67 strain (Figure 90) is superimposed on the corresponding one in Figure 92, it is observed that the experimental points match almost exactly the theoretical prediction, which indicates that although a distribution of strain is also present during deformation under these conditions, as shown in Figure 35b, it is much more homogeneous than the distribution obtained after a deformation by 0.33 strain. However, it is also observed that the experimental points of the recrystallisation curve obtained with the less deformed specimens spreads out between the curves corresponding to 0.67 and 0.15 strain, indicating that recrystallisation progresses slowly as nuclei form and grow in regions of different accumulated strain, until the whole deformed section is replaced by a new strain-free structure.

The effect of strain on the distribution of the recrystallised fraction is much better appreciated from macrographs of the gauge section of the specimens such as those shown in Figure 93, where the recrystallisation is observed to follow closely the pattern of strain distribution determined by the deformation imposed. As already explained, due to this heterogeneity in the strain distribution it was decided to carry out the recrystallisation measurements along the whole deformation zone and therefore, the values reported of recrystallised fraction and recrystallised grain size correspond to a mean value obtained along the complete section. Figure 94 shows the micro-

structures developed in specimens deformed by 0.33 strain after different annealing periods before quenching. Figure 95 shows some electron micrographs of a specimen annealed 1000 seconds after deformation in which no signs of recrystallisation could be revealed. A striking feature observed from Figure 94d is that even after a long annealing time, undeformed regions of the matrix are still present. This was confirmed by the use of transmission electron microscopy by means of which it could be determined that such regions were composed of subgrain bands surrounded by recrystallised grains. It is believed that such a phenomenon is in some way related to the previous observation of "insular regions of deformed material" surrounded by recrystallised zones of a single orientation, reported from experiments carried out on aluminium specimens [133], and which have been explained in terms of a similar orientation of the lattices of both the recrystallised and deformed grains, on either side of the migrating boundary [132,133], therefore making its advancement extremely slow. Figure 96, on the other hand, shows the microstructures revealed in specimens deformed by 0.67 strain and annealed for periods of 80, 100, 160 and 320 sec., when a very high degree of restoration has been achieved despite that recrystallisation has not been completed. In particular, Figures 96b and c illustrate that recrystallisation begins mainly at grain boundaries although some new grains are also observed to develop within the elongated structure. All these micrographs were taken at the centre of the deformation zone of every specimen.

Also, composite micrographs that could reveal the structure of the deformed sections were built up by assembling individual micrographs to be able to carry out quantitative measurements on them that could be compared with the theoretical predictions given by the recrystallisation equations. Figure 97 shows the results obtained, in which the

whole gauge section of the different specimens are presented, all of them with an initial strain applied of 0.67. Figure 97a shows the complete section of a specimen deformed and annealed for 60 seconds before quenching. The structure reveals clearly the deformation pattern developed in the specimen which resembles quite well the distributions obtained by means of visioplasticity techniques. Two crosses of high strain are observed to develop following a line just to the outside of the tool edges. It is expected that recrystallisation begins at the centre of such crosses and spreads out along the deformation bands, before any other part of the section is consumed. The developments of the first signs of recrystallisation are better illustrated in Figure 98 which shows the centre of the crosses obtained after deforming a specimen of Al-1%Mg-1%Mn alloy by 50% reduction and annealing for 300 seconds at the deformation temperature, 400°C. Figure 97b shows a large part of the section corresponding to a specimen annealed for 240 seconds. Recrystallisation signs are now quite evident since the high strain bands are now observed to have been consumed, whereas the centre of the specimen remains with a higher degree of deformation. A striking feature is that recrystallisation of the less deformed regions appears to require the formation of new nuclei since migration of the regions where it first took place into the less deformed zones does not seem to occur. After 320 seconds annealing, a high degree of recrystallisation has taken place and only the "dead zones" situated above and below the centre of the high strain crosses, remain unrecrystallised. After 480 seconds, the material appears to be fully recrystallised and the structure does not seem to be modified upon further annealing. The quantitative measurements carried out on the specimens also allowed the construction of patterns of recrystallised fraction as they developed upon annealing after deformation by 0.67 strain. Such patterns are

shown in Figure 99 and as for the temperature distribution results presented earlier, they are schematically drawn in a quarter of the specimen and considered to be symmetrical about its centre line.

The measurements of the recrystallised fraction obtained can also be correlated to the values of fraction restored found under similar conditions. Figure 100 illustrates the results of such a correlation, in which the striking feature appears to be that full restoration of the flow stress in double deformation tests can be achieved without full recrystallisation of the sample in the period between passes. This rather surprising result contrary to previous findings could be explained in terms of the concentration of the strain applied upon further deformation, in the softer recrystallised regions of a partially recrystallised structure. Therefore, if it is assumed that in a two deformation schedule the strain applied in the second pass will continue to be carried out along the high strain bands formed during the first deformation, until the change in geometry leads to further development of high strain crosses, then it would be expected that the fraction recrystallised present on such bands at the end of the interpass period, rather than the total fraction recrystallised on the gauge section, should determine the degree of restoration of the flow stress during the second deformation.

As well as the fraction recrystallised, the recrystallised grain size was measured in order to determine the relationship of this parameter with the strain applied. Figure 101 illustrates the results obtained which includes results of experiments performed with and without cartridge heaters in the deformation tools. The grain sizes obtained without the use of heaters have also been corrected to a deformation temperature of 400°C by means of the relationship:

$$d_{rex} \propto Z^{-0.136}$$

which will also be discussed in Section 5.3.2. As the strain applied increases, the recrystallised grain size decreases presumably due to the increase in the density of nuclei brought about by the increase in stored energy. In all cases, the final recrystallised grain size was found to be higher than the initial grain size, of about 90 μm. Figure 102 illustrates the final distribution of the recrystallised grains of some of the samples along the entire deformation section. A peculiar feature observed from these macrographs is that the grain structure of the transition zone between the deformation section and the undeformed shoulders appears to coarsen whenever deformation with cartridge heaters is carried out, whereas a fine grain structure is observed to remain after deformation under normal conditions. Figures 103 and 104 show the corresponding micrographs of such specimens, also taken at the centre of the deformed section of the samples. Since an appreciable difference in grain sizes is still present between samples deformed with and without heaters in the deformation tools, even after the appropriate corrections to account for the differences in temperature have been made, it is believed that a general change in the deformation pattern has taken place, which appears to increase the mean grain size, as measured along the whole gauge section of the specimens deformed with the use of cartridge heaters. Therefore, deformation under conditions of rather slight heating produces a levelling of the curve towards an independent value of "d_{rex}" with strain, although the critical strain appears to be somewhat higher than for $t_{0.5}$. A noticeable feature clearly visible from the micrographs of the recrystallised samples is that the recrystallised grains do not appear to be equiaxed but rather elongated with an aspect ratio different to 1. This phenomenon, very common in most commercial aluminium alloys is believed to be due to the retardation effect caused by the coarse

intermetallics of the alloy, which align themselves in the deformation direction, therefore hindering the growth of the recrystallised grains in the transversal direction.

The power dependence of the relationship between "d_{rex}" and strain can be deduced from Figure 105, which represents a log-log plot of the parameters involved. Thus, it has been found that for isothermal tests:

$$d_{rex} \propto \varepsilon^{-\frac{1}{3}} \qquad .....(5.17)$$

which is a much lower value than the one reported for steels [73,74, 137,138].

5.3.2 Effect of Temperature and Strain Rate on the Recrystallisation Kinetics

In order to investigate the effect of both temperature and strain rate upon the recrystallisation kinetics, Irrisari [76] carried out a number of restoration experiments on specimens of Al-1%Mg alloy. Complementary tests on specimens of the same batch were also part of the present research project. The effect of temperature was determined by performing double deformation tests at 500, 460, 420, 390 and 350°C at a strain rate 1 s^{-1}, imparting a strain of 0.67 in the first pass and with an alloy of initial grain size about 70 μm. Also tests at 460, 420 and 390°C and strain rates of 0.1 s^{-1} and 3.76 s^{-1} were carried out, which allowed us to determine both "Qapp" and the power dependence of $t_{0.5}$ upon Z. Figures 106 and 107 show the results obtained from these two batches of experiments and Tables 17 and 18 summarize the corresponding data. As expected, as the deformation temperature increases, the time to obtain a fixed fraction restored decreases which is entirely consistent with the thermally-activated nature of the

processes involved. However, the striking feature of Figure 106 is that within the temperature range of 500-390°C, t_F ($t_{0.5}$ in the present case) changes by less than an order of magnitude, whereas within the range 390-350°C, $t_{0.5}$ increases more than 50 times which indicates that below 390°C, a different process may be taking place and therefore recrystallisation is retarded. The values of $t_{0.5}$ from Figures 106 and 107 have been plotted against 1/T in Figure 108 using a semi-logarithmic scale according to equation (2.27):

$$t_{0.5} = A\, do^a \varepsilon^b \dot{\varepsilon}^c \exp(Q_{app}/RT) \qquad .....(2.27)$$

and a value of "Qapp" of about 55 kJ/mol has been obtained. This value is somewhat lower than others previously reported [26,39] for commercial aluminium alloys. Figure 108 however, highlights a remarkable surprising effect of strain rate upon the recrystallisation kinetics, much higher than the effect of temperature in the range covered by the present investigation. From the graph, it is apparent that:

$$t_{0.5} \alpha\ Z^{-1} \qquad .....(5.18)$$

which can be corroborated with the calculation of "Qrex" as stated in Section (2.3.6). This effect of strain rate could be interpreted in terms of the importance, not just of the number of dislocations generated in the material during deformation but also the manner in which such dislocations are arranged, since it is expected a higher degree of "disorder" in such arrays as the strain rate increases, during deformation at constant temperature.

The determination of the activation energy for recrystallisation can only be carried out from experiments in which the stored energy of the material input in the first pass is constant. This situation is

achieved when deformation at different temperatures is compensated by straining at different rates which would lead to equivalent initial conditions in terms of "Z". Thus, one more series of experiments was carried out, deforming at 510°C and 3.76 s^{-1} strain rate in such a way that initial equivalent structures in terms of the driving force in the material, could be achieved in the range 510-390°C. Figure 107b includes the results obtained from the tests carried out at 510°C, whereas Figure 109 illustrates the results of plotting $t_{0.5}$, after deformation at a constant value of Z, as a function of temperature. Thus, a value of Qrex ≃ 230 kJ/mol has been obtained which is somewhat higher than the activation energy for deformation, despite the fact that both are diffusion-controlled processes. The power dependence of $t_{0.5}$ on "Z" can now be re-calculated since:

$$C = \frac{Qapp - Qrex}{Qdef}$$

If substitution of such parameters is carried out, a value of C ≃ 1.1 is obtained in agreement with the proposition made above (expression (5.18).

The recrystallised grain size was also determined as a function "Z" by measuring the resulting value obtained after a prolonged annealing at the deformation temperature, following deformation by 0.67 strain at a strain rate of 1 s^{-1}. Figure 110 shows the results obtained from which it may be concluded that:

$$d_{rex} \propto Z^{-0.136} \qquad .....(5.19)$$

Table 19 summarizes the corresponding data and Figure 111 reveals the microstructure of the corresponding specimens. Thus, the recrystallised grain size appears to be slightly less dependent on Z than steels [73,74,137,138], which is rather surprising given the strong dependence of $t_{0.5}$ on that parameter.

5.3.3 Effect of Initial Grain Size on the Recrystallisation Kinetics

Irrisari [76], also carried out studies in order to determine the effect of grain size on the kinetics of recrystallisation, followed by means of restoration, on Al-1%Mg alloy deformed at 460°C, at a nominal strain rate of 1 s^{-1} and imparting a mean initial strain of 0.67. Different grain sizes were achieved by rolling of as-cast specimens from about 25 mm thickness to 10 mm, starting from different reheating temperatures. The as-cast material presented an initial grain size of about 112 μm. Specimens were machined from this stock and heat treated before reheating to testing temperature. Table 21 contains the results obtained from such tests and Figure 112 illustrates their graphical representation. Values of $t_{0.5}$ were taken from this graph and plotted as a function of "do" in a double logarithmic scale, shown in Figure 113 and from which it is obtained that:

$$t_{0.5} \alpha\ do^2 \qquad .....(5.20)$$

The strong influence of the initial grain size on the kinetics of recrystallisation, identical to results obtained for steels, indicates that grain boundaries play a very important role as nucleation sites, in comparison with places such as transition bands situated within the grains. Also, another important feature is that the as-cast specimens, in spite of having a different initial structure of coarse particles of intermetallics to that of the specimens obtained from rolling, gave results that follow well the relationship found, therefore, suggesting that such coarse intermetallics do not have any appreciable influence on the recrystallisation kinetics.

The recrystallised grain size was also determined as a function of the initial grain size, under the present deformation conditions. Table 20 summarizes the results obtained and Figure 114 shows the

relationship that exists between these two parameters. Thus, it was found that:

$$d_{rex} \alpha \; do^{1.3} \qquad .....(5.21)$$

which can be interpreted in terms of the decrease in the number of nuclei per unit volume of material as the initial grain size of the material increases, therefore confirming the importance of grain boundaries as nucleation sites. Figure 111 also includes the microstructures of the relevant specimens.

5.3.4 General Recrystallisation Equations

The relations determined for the dependence of both $t_{0.5}$ and d_{rex} on parameters such as strain, strain rate, temperature and initial grain size can, therefore, be used in the elaboration of general equations capable of predicting the recrystallised fraction present after deformation and annealing at constant temperature, as well as the grain size of the material transformed. However, as already explained in Section 2.3.6, such equations could also be used to predict microstructural evolution in processes carried out at decaying temperatures, such as hot rolling operations performed either at industrial or laboratory scale. Thus, by replacing the values of a, b, c and Qrex in equation (2.26) for those found in the present section, it is obtained that:

$$t_{0.5} = Ao \; do^{2} \varepsilon^{-2.7} Z^{-1.1} \exp(225000/RT)(sec) \qquad .....(5.22)$$

The constant "Ao" can be evaluated from the recrystallisation data of Figure 90 since all the parameters of equation (5.22) are readily known. Therefore, equation (5.22) can also be expressed as:

$$t_{0.5} = 4.7597 \times 10^{-8} do^{2} \varepsilon^{-2.7} Z^{-1.1} \exp(225000/RT)(sec) \quad ...(5.23)$$

which allows the recrystallised fraction to be calculated as a function of the period of isothermal annealing, according to equation (2.21).

$$Xv = 1 - \exp(-0.693\ (t/t_{0.5})^{2}) \quad .....(5.24)$$

Equations (5.23) and (5.24) can readily be used in combination with the strain and temperature distribution patterns already presented, in order to predict the distribution of recrystallised material along the gauge section of the specimens and therefore be compared either with the actual micrographs or the patterns of recrystallised fraction derived from the measurements performed, Figure 99. Since strain appears to be the most influential variable, as far as the determination of $t_{0.5}$ is concerned, and since relatively small variations of temperature have been reported up to deformations of about 0.67 strain, it is expected that the pattern of the distribution of recrystallisation should be influenced mostly by strain and strain rate, which is precisely the case for the present investigation. Equation (5.24) can also be modified to calculate the fraction recrystallised present in a specimen after a cooling period subsequent to deformation at elevated temperature:

$$Xv = 1 - \exp(-0.693\ (W/W_{0.5})^{2}) \quad .....(5.25)$$

where "W" is given by equation (2.30):

$$W = \sum_{i=1}^{n} \exp[-\frac{Q_{rex}}{RT_i(t)}]\ \delta t_i$$

as already explained in Section (2.3.6), and "$t_{0.5}$" given by equation (5.23). Also, a general equation that predicts the recrystallised grain size has been developed:

$$d_{rex} = 14.68\ do^{1.3}\ Z^{-0.136}\ \varepsilon^{-1/3}\ (\mu m) \qquad .....(5.26)$$

As for equation (5.23), the proportionality constant has been evaluated from the data reported in Section 5.3.1. It is also expected that the resulting pattern of grain size distribution should follow closely that of strain distribution, unless that growth of the recrystallised into the surrounding deformed regions takes place, which could considerably alter the general picture. However, as indicated in Figures 97c and 97d, the composite micrographs of recrystallised specimens show that a band of fine recrystallised grains run along the high deformation bands developed during deformation, and that the regions less severily strained have given rise to somewhat coarser recrystallised grains, which confirms that no migration of the recrystallised grains into the non-recrystallised areas has taken place. Figure 94d is a very clear example that shows the lack of migration of the recrystallised grains into the adjacent un-recrystallised area of smaller grain size. On the contrary, this micrograph highlights the early stages of the development of new recrystallised grains, mainly from grain boundaries and triple points within the deformed structure, corroborating that recrystallisation of regions of different accumulated strains is carried out independently of each other. Therefore, it can be concluded that equations (5.23) to (5.26) could be used to determine the fraction recrystallised and the recrystallised grain size after a single pass deformation and annealing either at constant temperature or cooling through a temperature gradient, since prediction of the microstructural evolution in multiple-pass deformation processes would require knowledge of the strain distribution within a partially recrystallised structure. This particular point constitutes the subject of the following section.

5.4 Restoration and Recrystallisation After Two Deformations

5.4.1 Introduction

Recrystallisation between deformations in multiple-pass operations carried out at elevated temperatures, arises due to the increase in the stored energy of the material such that the recrystallisation times become of the order of the interpass periods. Further deformation of this partially recrystallised structure gives rise to a distribution of strain between the recrystallised and un-recrystallised fractions. The former enters the pass with zero retained strain whereas the latter is considered to have the accumulated strains of previous passes. Therefore an "aggregate" of two fractions: a "hard" un-recrystallised and a "soft" recrystallised fraction are considered to be present before the subsequent deformation is carried out. This simplistic picture neglects recovery effects and considers recrystallisation as the only mechanism by means of which the strain applied can be removed. Since both fractions can be regarded as macroscopically homogeneous, the plastic properties of the "aggregate" could be described in terms of the properties of the individual constituents, provided that both the strain and stress distributions in every fraction, as well as the way in which such fractions interact between themselves during deformation have been determined. The simplest hypotheses that can be used to determine the stress-strain behaviour of such an "aggregate" are either to consider that the strain in each fraction is equally distributed, or that both fractions are subjected to equal stresses. If the first supposition is admitted, the average stress of the partially recrystallised structure for a given strain "ε_{pass}", will decrease linearly with the volume fraction of recrystallised material present:

$$\bar{\sigma} = f_\alpha \bar{\sigma}_\alpha + f_\beta \bar{\sigma}_\beta \qquad .....(5.27)$$

where $\bar{\sigma}$ represents the mean stress, f_α the fraction recrystallised, f_β the fraction un-recrystallised, $\bar{\sigma}_\alpha$ the mean flow stress determined at a strain "εpass" and $\bar{\sigma}_\beta$ the mean flow stress of the material with a total strain "ε_T" ($\varepsilon_T = \varepsilon$acc + εpass). However, since $f_\alpha + f_\beta = 1$, then:

$$\bar{\sigma} = \bar{\sigma}_\beta - f_\alpha (\bar{\sigma}_\beta - \bar{\sigma}_\alpha) \qquad .....(5.28)$$

On the other hand, if the second hypothesis is assumed, then the average strain in the alloy at a given stress is given by:

$$\bar{\varepsilon} = f_\alpha \varepsilon_\alpha + f_\beta \varepsilon_\beta \qquad .....(5.29a)$$

or

$$\bar{\varepsilon} = \varepsilon_\beta - f_\alpha (\varepsilon_\beta - \varepsilon_\alpha) \qquad .....(5.29b)$$

where ε_α and ε_β represent the accumulated strains in the recrystallised and un-recrystallised fractions. In order to investigate the way in which the strain applied to a two-phase alloy is distributed between the phases, Clarebrough [162] and Clarebrough and Perger [163], studied the recrystallisation behaviour of both silver-magnesium alloys and duplex brasses after cold deformation, in which different amounts of the hard β phase were present. The results of such investigations indicated that if $0.40 < f_\beta < 0.70$ for silver-magnesium alloys or $0.35 < f_\alpha < 0.70$ for duplex brasses, the hypothesis of equal distribution of strains between the "soft" and "hard" phases was acceptable. However, it was also found that if $f_\beta < 0.40$ (Ag-Mg) or $f_\beta < 0.35$ (Cu-Zu), the strain accumulated in the "hard" phase was less than the accumulated in the "soft" matrix. In both cases it was assumed that for f_β values between 0.7 and 1.0, the hypothesis of equal strains should still apply since the deformation in this range is governed by the "hard" β matrix.

However, this point was not experimentally confirmed. It was also proposed that these results could be applied generally to duplex alloys in which both phases are plastic, but which differ in flow stress and work-hardening characteristics.

Recent computational procedures [163] developed to predict the evolution of microstructure during hot rolling operations, have assumed the equal strain hypothesis as a model valid to deal with the recrystallised and non-recrystallised fractions of a deforming partially-recrystallised structure. Where comparison could be made, the predictions obtained for low C-Mn steel were in agreement with practical observations.

5.4.2 Restoration and Recrystallisation Results

The validity of the hypothesis of equal strain distribution between the recrystallised and deformed fractions of a partially-recrystallised structure under current deformation, was also investigated by means of restoration results of three-deformation schedules performed on specimens of Al-1%Mg, at a nominal temperature of 400°C and a mean strain rate of 1 s^{-1}. After an initial deformation of 0.67 strain, interpass times of 1.7, 100, 320 sec. and 16 hours were allowed and subsequently, a second deformation of 0.33 was imparted after which a whole range of time intervals were permitted before a third pass of 0.33 strain was applied. This deformation sequence allowed a certain fraction recrystallised to be present before the second deformation, equivalent to a two-phase alloy with different proportions of "hard" and "soft" phases. As for the restoration experiments carried out in two-deformation schedules, a mean curve was traced from the stress-strain curves of the second deformation and the curves of the third deformation were drawn by adjusting the stress level of the stress-strain curves of the second deformation to the mean curve already

mentioned. Figure 115 shows the mean curves obtained for the second deformation after annealing periods of 1.7 and 320 sec. respectively. In three-deformation schedules the restoration index was defined as:

$$R_2 = \frac{(\sigma_{max})_2^{EXT} - (\sigma_o)_3}{(\sigma_{max})_2^{EXT} - (\sigma_o)_3^{\infty}} \times 100 \qquad .....(5.30)$$

where again $(\sigma_{max})_2^{EXT}$ represents the flow stress value of the second curve extrapolated to 0.05 strain in the third stress-strain curve, $(\sigma_o)_3$ represents the flow stress value of the third curve measured at 0.05 strain, and $(\sigma_o)_3^{\infty}$ represents the flow stress value of the third pass but measured after a holding period where no more softening occurs with increasing interpass time. The different values are also represented in Figure 116. All the set of stress-strain curves obtained in the third pass after different annealing periods between the second and third deformations have been allowed, are shown in Figure 117, determined for interpass times between the first and second deformations of 1.7, 100, 320 sec. and 16 hrs. respectively. Table 22 summarizes the complete set of data. The values of the restoration index "R_2" are illustrated in Figure 118a as a function of the interpass time between the second and third deformations, "t_2". All the deformation conditions are shown on the graph. The striking feature of Figure 118a is the fact that as the interpass time between the first and second deformation increases, thereby increasing the recrystallised fraction present in such an interval, the restoration kinetics after further deformation is strongly retarded. The key to the explanation of the results obtained being the distribution of the recrystallised grains during the occurrence of recrystallisation after the first deformation and also the way in which the strain applied is distributed between the different fractions during the second deformation. As observed in Figures 93d-e, recrystallisation after one deformation by

an initial strain of 0.67 takes place along the high strain bands developed in the specimen, through which deformation is carried out. Therefore, on reloading it is expected that the restoration of the flow stress will be strongly dependent on the fraction recrystallised present along such bands, since the material situated outside such places will not initially be involved in the deformation process. This point is clearly shown in Figure 100 where it can be observed that the presence of a small recrystallised fraction such as 30% can account for up to 90% restoration of the flow stress, whereas recrystallisation of the remaining 70% will hardly increase the fraction restored. The way in which the strain applied during the second pass is distributed between the different fractions is also dependent upon the fraction recrystallised present along such bands since it has already been mentioned that more strain can be accumulated in the softer fraction depending on the proportion in which the different fractions occur.

As for the restoration results, after one deformation, spurious recovery effects are expected to be present, particularly for interpass times less than 10 sec., in which the mean temperature of the specimen is observed to be lower than the mean deformation temperature of the schedule. After 16 hrs. annealing between the first and second deformations, the recovery effects can be clearly determined, particularly conspicuous because of the higher degree of restoration achieved without the occurrence of recrystallisation, as compared with the results obtained after one deformation. However, this anomalous behaviour is not surprising since relubrication of such specimens was carried out at room temperature and therefore improved friction conditions are expected to give rise to marginally higher restoration values. Thus, in order to have a better understanding of the restoration processes involved, it was decided to correct such values

in terms of the degree of restoration achieved by the operation of recovery. Figure 118b shows the results obtained, in which as for Figure 86b, the restoration coefficient is considered to be dependent just on the fraction recrystallised present at the end of the particular time interval. If an annealing period of 1.7 sec. is allowed between the first and second deformations, no recrystallised fraction would be present before the second pass. Therefore, it is expected that after a subsequent deformation of 0.33, the material would have a stored energy equivalent to the acquired after a single deformation by a strain of 1.00, since in the first pass a strain of 0.67 was imparted. Hence, it is also expected that the restoration behaviour under these conditions should be similar to the restoration observed in Figure 86b of the specimens deformed by a strain of 1.00. Figure 119a shows a comparison between these two curves (A and A'), where it can be observed that within the experimental scatter of the curves, and below restoration values of about 65%, their behaviour is very similar. However, above this restoration level curve "A" is observed to be slightly shifted towards higher time intervals in order to achieve similar degrees of restoration. Figure 120a illustrates a schematic representation of the temperature distribution in the present case, which compares well with the distribution shown in Figure 87d. The recrystallised grain size obtained after a prolonged annealing at temperature before the third pass, was found to be about 148 μm which also compares very well with the value of 151 μm obtained after annealing following a deformation by a strain of 1.00. Figure 121 compares the microstructures of a specimen annealed 105 sec. after the second deformation with that of a specimen fully recrystallised. Recrystallisation is observed to occur randomly throughout the deformed matrix. Since curves "A" and "D" in Figure 118b represent the extreme

conditions of the restoration behaviour after two deformations, they could serve as a basis to give a qualitative explanation of curves "B" and "C", which represent intermediate stages in the range of time intervals between the first two passes.

If a time interval of 100 sec. is allowed before the second deformation, a recrystallised fraction of about 0.10 would be present, mainly distributed along the high strain bands developed during the first deformation, as shown in Figures 93d and 99b. If a subsequent deformation by 0.33 strain is applied to the specimen, it would be expected that most of the strain were concentrated on such bands and therefore, that restoration of the flow stress were dependent upon the extent of recrystallisation in these places.

In order to understand better the present set of results, let us consider Figure 119b which represents the relationship that exists between the fraction restored and the fraction recrystallised, assuming that restoration is only dependent upon the extent of recrystallisation. Since an interpass time of 100 sec. between the first and second deformations gives rise to a recrystallised fraction of 0.1, situated along the most active regions of the specimen, as far as the deformation process is concerned, it should be expected that after a second deformation and subsequent annealing, the relationship between these two fractions (R and Xv) were represented by a different curve, such as it is illustrated in Figure 119c. Thus, it can be shown that recrystallisation of the material situated outside the deformation bands will lead to about 82% restoration of the flow stress and that 100% restoration will be achieved after recrystallisation of the small fraction that first recrystallised during the initial time interval takes place. Therefore, the R vs. Xv curve should follow the initial path "ABC" in Figure 119b which represents the recrystallisation of the

material outside the current deformation bands, then followed by the segment "OA", leading to full restoration when recrystallisation has been completed. A similar interpretation of these results can be given in terms of the restoration-time curves of Figures 86b and 118b. It has already been mentioned that an interpass time of 100 sec. will allow a recrystallised fraction of 0.1 to be present before the second deformation is applied. According to curve "B" in Figure 86b, such a fraction would give rise to 18% restoration of the flow stress and therefore further deformation by 0.33 strain would lead to the development of two different fractions with different accumulated strains and different initial grain sizes: (a) a fraction of 0.1 of the material with an initial grain size of 183 μm and an accumulated strain of 0.33, and a fraction of 0.9 of the material with an initial grain size of 90 μm and an accumulated strain of 1.00. This last fraction is expected to restore following the path IMJ of curve "A" in Figure 118b.

This is observed in curve B' in Figure 119a which corresponds to the theoretical prediction of curve "B" (Figures 118b and 119a). After the path IMJ has been covered, it is expected that some time elapses until the remaining fraction with less accumulated strain and bigger initial grain size starts restoring according to the segment KL of curve "D" in Figure 118b. If curves B and B' are compared it is observed that the predicted plateau JK occurs at a higher restoration level than the experimentally found, and also that the restoration of the fraction with less accumulated strain takes place at a shorter time. However, it is also important to point out that a number of simplyfying assumptions have been made, particularly as far as the distribution of strain upon further deformation is concerned. For example, it has been assumed that on reloading, deformation of the specimen will be carried out along the high strain bands that previously recrystallised, which

may not be the case in the present situation since it is possible that during the second deformation a new strain pattern is established in which just part of the new shear bands coincide with the previous recrystallised zones, giving rise to a different restoration-recrystallisation relationship. Therefore, despite the fact that an accurate quantitative prediction of the restoration behaviour cannot be made due to the uncertainties in the redistribution of strain inherent to the deformation mode, it can be stated that qualitatively the model of the independent recrystallisation of the different fractions seems to be followed, at least in this particular example.

Figure 122 shows the microstructures present after different annealing times subsequent to the second deformation have been allowed. After 122 sec. very few signs of recrystallisation are present which accounts for the low degree of restoration achieved. After 640 sec. however, recrystallisation is clearly observed to occur, both by nucleation of new grains and also extensive migration into the surrounding areas. A very important feature observed from Figure 122c is that despite the increase in the recrystallised fraction present after 2560 sec. annealing, the degree of restoration experimentally found has hardly changed, which confirms the fact that further restoration will take place when the remaining fraction with a smaller accumulated strain, and also situated on the current high strain bands of the specimen, begins to recrystallize, which is observed to occur after about 5000 sec. annealing. The recrystallised grain size achieved after long annealing periods was found to be about 170 μm. Figure 122d shows a picture of the fully recrystallised structure.

If an interpass time of 320 sec. is allowed between the first two deformations, a fraction recrystallised of about 0.70 is expected to be present along most of the gauge length of the specimen, as shown in

Figures 93f and 99d. Therefore, a further deformation by 0.33 strain would also give rise to the presence of two different fractions: firstly a fraction of about 0.70 of the material with an accumulated strain of 0.33 and an initial grain size of 183 μm and secondly, a fraction of 0.30 of the material with an accumulated strain of 1.00 and an initial grain size of 90 μm. This last fraction, however, is situated in the least favourable places as far as the deformation process is concerned, and therefore, despite the fact that recrystallisation will occur faster in such places because of the higher accumulated strain and smaller grain size, the degree of restoration achieved will be quite limited. As observed in Figure 119b, the R vs. Xv curve for this particular case should start along the segment "BC", giving rise to full restoration of the flow stress, following the path OAB of the same curve. This is also illustrated in Figure 119c where now three different curves representing the different restoration recrystallisation relationships can be compared, depending on the degree of recrystallisation that took place before the second pass was applied. As for the previous case, the restoration-time behaviour can also be predicted from Figure 118b. Thus, after further annealing following the second deformation by 0.33 strain, it is expected that the fraction with less accumulated strain should restore following the path MJ of curve "A" in Figure 118b. After this period, a plateau should be reached until the remaining fraction starts recrystallising following the segment KLN of curve "D" of Figure 118b. All these stages are schematically shown in curve C' of Figure 119a, which is observed to be well behind the corresponding one found experimentally (curve "C" of the same Figure). As for the previous set of results, the model of different fractions with different accumulated strains recrystallising independently of each other seems to provide a

reasonable qualitative explanation of the restoration behaviour experimentally observed, although a quantitative prediction cannot be made, possibly for similar reasons to the ones previously mentioned. It is also important to point out that strain distribution effects cannot account for such a discrepancy since there is a net shift of the experimental curve with respect to the theoretical prediction towards shorter times to achieve any restored fraction. If the strain applied were not equally distributed between the fractions of different accumulated strain, it would be expected that the different portions of curve "C" in Figure 119a which represent the recrystallisation of the two existing fractions were shifted in opposite directions since more strain would have been accumulated in the softer fraction and less strain in the harder one, as previously found by Clarebrough [162] and Clarebrough and Perger [163]. The pattern of temperature distribution obtained after the second deformation is much the same as the one obtained after a first interruption of 100 sec. Such a pattern is shown in Figure 120b. The microstructural evolution after different annealing times can be observed in Figure 123. After 220 sec., mainly a deformed structure is present with very few signs of recrystallisation visible principally at grain boundaries. After 640 and 2560 sec., however, extensive nucleation and migration of the recrystallised grains is observed which leads to a final recrystallised grain size of about 208 μm, as shown in Figure 123d. Finally, Figure 118b also illustrates the predicted curve under the present deformation conditions, assuming a material of homogeneous initial grain size of 183 μm, which compares very well within the experimental scatter with the actual curve observed, after the proper recovery correction has been applied.

5.5 Simulation of Experimental and Industrial Rolling Operations

5.5.1 Introduction

The stress-strain relationships developed in Section 5.1 and the recrystallisation equations of Section 5.3 can be used to predict both the structural evolution that takes place throughout deformation processes carried out at elevated temperatures and the load, torques and power requirements that such processes need as a consequence of the strength inherent to the material involved in the operation. By means of a computational procedure that combines a finite difference model to describe temperature changes in plate rolling [71] and a structural evolution model that predicts the changes produced by the recrystallisation and grain growth kinetics as functions of the variations in deformation conditions which was developed for C-Mn steels [164], Leduc [73] carried out simulation of hot rolling operations of both mild and titanium-bearing steels. This procedure also included the development of averaging methods to calculate the fraction recrystallised present and the mean grain size of either a partially or a fully recrystallised structure, which can be used both for load calculations and also for comparison with actual metallographic measurements. In order to simulate both industrial and experimental rolling schedules of commercial aluminium alloys several modifications to this computational procedure were carried out and some simplifying assumptions were made particularly in relation to the recrystallisation of structures composed of fractions with different accumulated strains, as well as grain growth after recrystallisation. The present section encompasses the description and discussion of the results obtained from rolling experiments carried out on Al-1%Mg alloy and also experimental

schedules reported in the literature [84] carried out on commercial-purity aluminium, as well as actual industrial operations carried out on both materials.

5.5.2 Laboratory Rolling Schedules

5.5.2.1 Aluminium-1% Magnesium Alloy

As explained in Chapter 4, specimens for plane strain compression were obtained from plates resulting from hot rolling of as-cast and homogenised slabs of initial thickness of about 25 mm. Table 23 contains the data corresponding to one of these schedules which includes details of pass geometry reductions, time between passes and rolling loads experimentally determined. Such a table also describes the relevant characteristics of the rolling mill and slab dimensions. Figure 124 shows the corresponding microstructures of the starting materials and Figure 125a illustrates a strain-time diagram of the deformation sequence. Figure 125b, on the other hand, shows a comparison between the computer predicted and experimental rolling loads. Figure 126 shows the evolution of the centre, mean and surface temperatures of the slab during the rolling schedule. The computer programme calculates loads and torques by means of Sims' theory. The flow stress values required for these calculations are given by the flow stress equations derived in the first section of the present chapter for Al-1%Mg alloy, taking into account the microstructural evolution that takes place during the operation. As observed from Figure 125b, the prediction of the rolling loads for this particular schedule is in agreement, within the uncertainties involved in the calculation of the flow stress, with the load values experimentally

found. As far as the microstructural evolution is concerned, the programme predicts the presence of 2% of recrystallised material at the surface of the slab before the third pass is given and also a fully deformed structure at the time of quenching. Figure 127 shows the microstructures of four different slabs deformed under similar conditions and quenched. All the micrographs were taken at the mid-section between the centre and surface of the specimens. Particularly noticeable is the appearance of sub-grain bands within the deformed grains of the as-cast structure and where recrystallisation signs are not visible as yet.

5.5.2.2 Commercial-Purity Aluminium

Table 24 contains data of four experimental rolling schedules carried out on commercial-purity aluminium (99.78% purity) reported in the literature [84]. However, since no information concerning the mill size was available, a roll radius of 125 mm was assumed. Also, the initial grain size of the material was considered to be about 110 μm. Figure 128 shows the strain-time history for these particular schedules in which the reductions per pass did not vary from one schedule to another and the only difference consisted in the time intervals between passes. Figures 129-132 show the temperature-time plots predicted by the computer programme and Figures 133 and 134 illustrate the comparison between the predicted and experimental rolling loads for all the schedules. In this particular case, it is found that in spite of the satisfactory agreement between the predicted centre temperatures of the specimens and the actual measurements, there is a remarkable disagreement in the load values, which becomes worse as the interpass time increases. The general trend is to overestimate the experimental

values with the exception of the calculation of the first rolling load. These discrepancies could be explained in terms of the assumption made in the structural model that the restoration of the flow stress is solely dependent upon the extent of recrystallisation, without taking into consideration the effect of static recovery. Dunstan and Evans [39] have found that up to 70% restoration of the flow stress of commercial-purity aluminium could be accounted for by the occurrence of static recovery and that such a degree of softening increased as Z decreased. Since the computer programme does not predict the occurrence of recrystallisation throughout the schedules, it is expected that the values of flow stress used in the calculation of loads are much higher than the actual flow stresses of the material, giving rise to an over-estimation of the loads. Another phenomenon that could also explain this discrepancy is the inheritance of a recovered sub-structure from one pass to another, since the application of a series of passes at decreasing temperatures and increasing strain rates, in which the strain applied in every pass is not sufficient to achieve steady-state conditions, is expected to favour a final sub-structure more recovered and therefore less strong than the sub-structures obtained during isothermal deformation. Thus, if recrystallisation does not take place to the extent of eliminating the sub-structures formed in previous passes, it is expected that the flow stress used to predict rolling loads (derived from isothermal experiments) appears to be higher than the actual flow stress of the material. Experimentally, it was reported that some recrystallisation had taken place after the first pass, which indicates that the recrystallisation kinetics for this particular material is somewhat different from the one used in the present model.

5.5.3 Industrial Rolling Schedules

5.5.3.1 Aluminium-1% Magnesium Alloy

Simulation of industrial hot rolling operations for Al-1%Mg alloy ingots was also carried out, particularly of those concerning roughing operations in which ingots initially 283 mm thick were transformed to plate 5.5 mm thick, in a reversible rolling mill. The relevant data concerning these particular schedules is contained in Table 25. This includes details of ingot and roll dimensions, geometry reduction per pass, experimental loads, initial entry temperature and roll speed. Figure 135 shows the strain-time history for the first schedule and Figure 136 illustrates the temperature evolution of the ingot throughout the rolling operation. Particularly noticeable in this figure is the increase of the centre temperature of the specimen during the first passes of the process. Since the original computer programme considered homogenous deformation through the ingot thickness, such thermal conditions would favour recrystallisation at the centre of the work piece rather than at the surface, as is experimentally observed, despite the Z effect introduced by the chilling caused by the rolls. Therefore, a crude attempt was made to introduce a deformation pattern through the thickness of the slab by means of which the strain changes according to a parabolic function from centre to surface and whose distribution becomes more homogenous as the ingot thickness is reduced (Appendix 1).

This arbitrary pattern would, therefore, enhance the conditions of accumulating more stored energy at the surface of the slab and would define a clear recrystallisation pattern through its thickness. It is also important to point out that this simplistic approach was adopted

in view of the immense difficulties implied in the development of a more refined technique to predict strain distribution during hot rolling operations, and which was beyond the scope of the present investigation. Thus, Figure 137 shows the prediction of the recrystallisation pattern that is likely to be obtained during this particular operation. As expected and in accordance to the industrial practice, the surface of the slab begins to recrystallise quicker than the centre due to the increase in stored energy brought about by the increase in the strain applied and the lower deformation temperature caused by the chilling effect of the rolls. This pattern, however, is altered by the occurrence of subsequent recrystallisation cycles. Figure 138 illustrates the prediction of the rolling loads obtained with the use of the same equations employed in the simulation of the laboratory schedule of a similar alloy (laboratory schedule "A"), and they are compared with the actual loads reported in the operation. The correction of the rolling loads carried out in the first three passes arises due to the contribution of inhomogeneous deformation to the rolling load. The solution to Siebel's "elementary homogeneous differential equation" [165] or the horizontal equilibrium equation of a section of the deformation zone in strip rolling:

$$\frac{d(\sigma_x\, y)}{d\phi} = p\,(R \sin\phi \pm \mu R \cos\phi) \qquad .....(5.31)$$

has been based upon certain assumptions, of which the most important are:

(a) homogeneous compression in the roll gap,

(b) material infinitely wide, and

(c) sliding friction conditions along the contact surface.

The theories developed by Siebel [165], Von Karman [166], Celikov [167] Galeji [168], Orowan-Pasque [169], Bland and Ford [170] and Ekelund

[171], have all assumed homogeneous compression, implying that parallel sides of a parallelepiped remain parallel after deformation, or that vertical and horizontal direct stresses and shear stresses remain constant through the slab thickness. However, under high friction conditions such as found during hot rolling operations, this is not true since high shear stresses develop at the surface, which gradually decrease towards the centre and cause the parallel elements to bend. By studying this phenomenon, Orowan [172] developed a graphical solution which has been improved by Sims [173] by elaborating the sticking case to give a solution today known as the Sims-Cook-McCrum method, and which is used in the present model to calculate loads and torques. This theory, however, does not give correct results when the arc of contact is short compared with the mean thickness of the material, due to the influence of the free ends outside the roll gap, and therefore, the load values derived are not much better than the other theories.

In order to account for this effect, Green and Wallace [174] assumed that a rigid triangular zone exists under the arc of contact, such as is shown in Figure 139. These workers also considered that all deformation took place along the sides of the triangle through shear strains and, therefore, the forces that arose from these zones were in equilibrium with the roll pressure and the frictional stresses at the arc of contact. Thus the rolling load per unit width can be expressed as

$$\frac{P}{W} = \frac{\sigma_s L}{2} \left[\frac{hm}{L} + \frac{L}{hm}\right] \qquad .....(5.32)$$

where "σs" represent the flow stress of the material, "L" the length of projected arc of contact, $L = \sqrt{R\Delta h}$, and "hm" the mean thickness of the slab, $hm = (h_1 + h_2)/2$. Slip lines fields have also been reported by

Alexander [175], and Lugovskij [176] has transformed a slip-line field solution from compression between plates to the rolling case, reaching the expression:

$$\frac{P}{W} = \sigma_s \, L \, [1.25 \, (\frac{L}{hm} + Ln \, \frac{hm}{L}) - 0.25] \qquad .....(5.33)$$

Results from Sandmark [177] and Ruddle [178] obtained fom experiments on steels, at temperatures between 900-1100°C, concluded that if the ratio L/hm was less 1.0 and the width to height quotient, δ = Wi/hi was greater than 4.0, the effect of inhomogeneous deformation had to be taken into account by using either equation (5.32) or (5.33). Both equations give similar results, except that equation (5.32) cannot be used for L/hm ratios less than 0.5. Figure 138 illustrates that the load values predicted by the computer programme are about 30% lower than the experimentally found but also that the trend is quite similar, which is rather encouraging since it demonstrates that the use of appropriate stress-strain relationships characteristic of the same material under processing may give rise to the prediction of values which would compare very well with the experimental results. Table 25 also contains data of a second industrial schedule carried out on Al-1%Mg alloy whose strain-time history, temperature evolution, and predicted microstructural evolution and rolling loads are shown in Figures 140-143. In this particular schedule, the ingot was reported to enter into the rolling mill at a temperature of 511°C, finishing at about 438°C, whereas the previous one was reported to enter at 528°C and finish at 453°C. These temperatures were considered to be surface temperature readings, given the conditions under which they were taken. The important fact is the noticeable change in the recrystallisation pattern brought about the relatively small changes in temperature and rolls speed, since the dimensions of both ingots and both mills are

exactly the same. Recrystallisation is also predicted to start before the third pass is applied, and the fraction recrystallised present at the surface is marginally higher than the one present at the centre. From this point onwards, however, the recrystallisation pattern is drastically changed, becoming more regular towards the end of the schedule. The rolling loads are also observed to be somewhat higher than those of the previous schedule, and that the prediction of the load values again follows quite closely the trend of the experimental ones. The absolute values are again observed to be about 30% lower.

5.5.3.2 Commercial-Purity Aluminium

Table 26 gives details of two industrial schedules carried out on commercial-purity aluminium (Al 99.2% purity), using a mill of the same characteristics of the previous two schedules but ingots of rather higher initial thickness and width. In both schedules the spread coefficient has been simplistically assumed to be given by:

$$S = \frac{\ell n\ (Wf/Wo)}{\ell n\ (ho/hf)} \qquad .....(5.34)$$

and that it remained constant during the first six passes, since during the last five deformations the width was kept constant to a value of 990 mm. The strain-time history of schedule No.3, as well as the predicted temperature and recrystallisation pattern evolution, and rolling loads are shown in Figures 144-147. The entry temperature to the rolling mill was reported to be about 533°C and the finishing temperature 420°C. The computer programme predicts a somewhat lower finishing temperature, which may give rise to somewhat higher values of stress at the end of the schedule. The recrystallisation evolution predicted in Figure 146 shows the characteristic trend observed previously. Recrystallisation begins before the fourth pass is applied,

with a higher fraction present at the surface than at the centre. The rolling loads on the other hand appear to be consistently lower than the experimental values, with the trend of approaching the actual measurements towards the end of the schedule. As mentioned above, this may be due to the lower temperature predicted by the model.

A very important observation is the fact that these load values have been calculated with the same equations used to predict the rolling loads of the experimental schedules "B-E" in (5.5.1.2). Such equations gave an overestimation of the experimental loads, whereas in the present case, the opposite is observed. Similar graphics for schedule No.4 are presented in Figures 148-151. In this particular case the entry temperature was reported to be about 482°C and the finishing temperature of 400°C, a lower drop in temperature despite similar conditions of pass reductions. The computer programme has also predicted a slightly lower final temperature than the experimentally observed. The differences in temperature-time history for both schedules give rise to strikingly different recrystallisation patterns, particularly from the sixth pass to the end of the schedule. It has long been recognized that the occurrence of recrystallisation during the interpass periods of such schedules has a profound effect upon the properties of the final products of these commercial, non-heat treatable aluminium alloys, particularly as far as texture and surface quality of the material are concerned. Therefore, computer modelling constitutes a powerful technique of monitoring microstructural evolution during hot rolling, aimed at the determination of the optimum processing routes, by means of comparing such patterns of evolution of recrystallised fraction throughout the thickness of the slab with the final properties achieved. In so far as the prediction of the rolling loads for this schedule is concerned, again an underestimation of the

experimental values is observed, but also with the noticeable fact that the trend can be closely followed, indicating that the stress-strain equations used for this purpose correspond to a somewhat softer commercial-purity aluminium than the one being rolled.

Finally, three more industrial schedules of hot rolling of commercial-purity aluminium, all from different mills, were simulated with the computer model. Tables 27-29 summarize the data of these industrial operations. Schedule No.5 is a 18 passes rolling programme that comprises both breakdown as well as tandem mill stages. Figure 152 shows the strain-time history for this schedule and Figures 153-155 illustrate the temperature evolution, the predictions of the fraction recrystallised present before pass and the comparison between torque data supplied for this operation and the corresponding predicted torques. Unfortunately, no temperature information other than the reheating temperature of 480°C were available. Therefore, several assumptions had to be made as far as the time between reheating and rolling and also the time between roughing and finishing were concerned. These were arbitrarily chosen to be 190 sec. and 160 sec. respectively. Under these conditions, the predicted mean entry temperature to the roughing mill was of 473°C, and the entry temperature to the finishing stands was of 382°C. The spread coefficient was calculated by means of equation (5.34) and it was assumed to remain constant throughout the schedule. The initial as-cast grain size was also considered to be about 110 μm. As for previous schedules, the structural calculations made by the computer model predict a higher recrystallised fraction at the surface of the slab than in the middle, and also that recrystallisation will start between the seventh and eighth passes. Metallographic observations carried out for this particular schedule have always suggested the presence of a higher

recrystallised fraction at the surface than at the centre and that recrystallisation begins at rather late stages (certainly not as early as the 4th and 5th passes). As far as the prediction of torques is concerned, the theoretical values are well out of comparison with the experimental measurements. Only isolated values are well predicted and not even the trend can be followed. On this particular point, however, it is quite important to point out that the experimental torque values were not measured since strain gauging for such a purpose had not been installed on the mill and, on the contrary, they constitute indirect assessments derived from computation from mill amperage readings. It is, therefore, concluded that the validity of the present computer model cannot be evaluated from such comparisons and that actual experimental measurements, as in previous cases, would be required for such a purpose. Figures 152 and 156 show the strain-time histories of two more schedules carried out in somewhat purer commercial aluminium (alloy 1050), in which similar assumptions to the previous schedule were made. The time between reheating and rolling was considered to be 150 sec., and the initial grain size and the spread coefficient were assumed to be the same as before. Figures 157 and 160 show their respective temperature-time curves and Figures 158 and 161, the structural evolution predicted throughout the schedules. Figures 159 and 162 compare the results of the predicted rolling torques with the indirect assessments of torques of the data supplied. Consistently, it has been found that the theoretical values are much lower, but bearing in mind that the data provided do not correspond to actual measurements, it is not surprising to find such discrepancies, since the comparison of the theoretical values predicted by the model with actual experimental measurements has shown that at least there is a close agreement in the trend followed. Also it is important to point out

that in the present case not correction of the torque values to take into account inhomogeneous deformation has been carried out, despite the low ratio L/hm for the first passes, particularly of schedules No.5 and 6, reported in Tables 26 and 27 respectively.

CHAPTER VI

Conclusions and Suggestions for Further Work

Conclusions

(1) Basic stress-strain data have been derived for aluminium-1% magnesium alloy in the range 300°C-500°C. The use of an exponential relationship of the form:

$$Z = A_1 \exp(\beta\sigma)$$

where Z represents the Zener-Hollomon parameter and that can be expressed as:

$$Z = \dot{\varepsilon} \exp(Qdef/RT)$$

to describe the strain rate sensitivity of the flow stress has been shown to apply, confirming previous findings which indicate the preponderance of dislocation climb and movement of jogged screw dislocations as the rate controlling processes. However, at strain rates higher than 20 s^{-1} there seems to be a slight increase in the activation energy for deformation "Qdef", normally found to be about 156 kJ/mol, and which becomes less noticeable as the strain applied increases. In general the β values are observed to decrease with increasing strain.

(II) A general equation has been derived to compute the flow stress of the material as a function of strain, strain rate and temperature. This equation can be expressed as:

$$\sigma = \sigma ss \, [1 - \exp(-C\varepsilon)]^{0.1} \; (N/mm^2)$$

where:

$$C = 20 \ln \left[\frac{1}{1 - (\sigma_{0.05}/\sigma ss)^{10}}\right]$$

$$\sigma ss = 8.20 \ln \left[\frac{Z}{1.4565 \times 10^9}\right] (N/mm^2)$$

and

$$\sigma_{0.05} = 7.02 \ln \left[\frac{Z}{5.5807 \times 10^8}\right] (N/mm^2)$$

"Z" again represents the Zener-Hollomon parameter.

(III) Flow stress data for commercial-purity aluminium obtained from previous work have been used to derive similar equations to the ones developed for the alloy. These equations can be expressed as:

$$\sigma = \sigma ss \, [1 - \exp(-C\varepsilon)]^{0.17}$$

$$C = 20 \ln \left[\frac{1}{1 - (\sigma_{0.05}/\sigma ss)^{5.88}}\right]$$

$$\sigma ss = 2.50 \ln \left[\frac{Z}{2.6289 \times 10^8}\right] (N/mm^2)$$

$$\sigma_{0.05} = 5.59 \ln \left[\frac{Z}{9.8095 \times 10^9}\right] (N/mm^2)$$

which can readily be used in computational procedures aimed at the determination of loads, torques or power requirements of hot working operations carried out on these materials.

(IV) Previous work carried out on pure and alloyed aluminium reported the presence of a hardening phenomenon in multiple-pass deformation tests carried out at elevated temperatures and strain rates greater than 1 s^{-1}. This reloading hardening was found to be independent of alloying content, ageing time, temperature and prior strain. Experiments performed on specimens of Al-1%Mg-1%Mn alloy have demonstrated that in general, machine variables such as: (a) electronic compensation of the machine frame extension, (b) approach velocity, (c) displacement loop gain and (d) tool temperature, although they produce some changes in the parameters that characterize such a hardening phenomenon, yet they do not determine its presence. However, contrary to previous findings both a temperature and a strain effect have been observed which would confirm the entirely structural nature of this phenomenon.

(V) Recrystallisation studies carried out on specimens of Al-1%Mg alloy by means of both optical metallography and restoration of the flow stress during a second deformation subsequent to an annealing period at the deformation temperature, allowed the determination of the functional dependence of both the time for 50% restoration and the recrystallised grain size upon variables such as: strain applied, rate of straining, deformation temperature and initial grain size of the material. Thus, the temperature-compensated time for 50% recrystallisation can be expressed as:

$$W_{0.5} = 7.4921 \times 10^{-7} Z^{-1.1} do^{2} \varepsilon^{-2.7} \exp\left(-\frac{225000}{RT}\right) \quad (sec)$$

$$Z = \dot{\varepsilon} \exp\left(\frac{156000}{RT}\right)$$

and $$d_{rex} = 14.68\ Z^{-0.136} do^{1.3}\ \varepsilon^{-0.33} \quad (\mu m)$$

whereas for commercial-purity aluminium:

$$W_{0.5} = 7.1385 \times 10^{-7} \varepsilon^{-2.7} Z^{-1.1} do^{2} \exp\left(-\frac{225000}{RT}\right) \quad (sec)$$

These equations can be used to calculate the fraction recrystallised present during the interpass intervals of multiple-pass deformation operations carried out at elevated temperatures, by means of the equation:

$$X_v = 1 - \exp\left[-0.639\ (W/W_{0.5})^2\right]$$

where

$$W = t \exp\left(-\frac{225000}{RT}\right)$$

which in turn would allow the calculation of the mean flow stress of the material during deformation subsequent to the interpass period. Strain rate has been found to have a remarkable influence on the recrystallisation kinetics as compared with ferrous materials, which points out the importance of the way in which dislocations arrange themselves during deformation, as well as their density.

(VI) Restoration and recrystallisation experiments carried out after two deformations allowed the assessment of the influence of the presence of different recrystallised fractions after a first deformation on the kinetics of recrystallisation after two deformations. Qualitatively, the recrystallisation of fractions of material with different accumulated strains can be

treated separately and therefore recrystallisation of such fractions would require the individual formation of nuclei, since growth of the material that first recrystallised into the remaining unrecrystallised fractions does not seem to occur. However, fully quantitative predictions to confirm this model could not be made mainly because of the heterogeneity in strain imposed by the deformation mode which enhances the recrystallisation of the high strain bands developed during the first deformation which do not tend to coincide with the new strain pattern established after a second deformation.

(VII) In general, it has been observed that up to 30% restoration can be accounted for by the operation of static recovery, and that full restoration does not require the achievement of full recrystallisation, which points out the fact that restoration of the flow stress is solely dependent upon the static processes that occur along the high strain bands developed during deformation under plane strain compression conditions.

(VIII) Simulation of both laboratory and industrial multiple-pass hot rolling operations has been carried out, taking into account the microstructural evolution that occurs in the material during its processing. Reasonable agreement has been obtained, particularly in the computer prediction of the load trend during industrial rolling of both commercial-purity aluminium and aluminium-1%Magnesium, which constitutes a very important step towards the development of a general structural model based on deformation parameters that would allow monitoring of loads, torques and power requirements of such schedules.

Prediction of the recrystallisation cycles that take place during these operations would also allow the correlation of the schedule characteristics with the final properties of the product, particularly in relation to the application of further forming operations. However, results of simulation of rolling schedules carried out on commercial-purity aluminium on a laboratory scale indicate that either recovery effects or inheritance of the sub-structures created in previous passes, which are not considered in the model, may give rise to huge discrepancies between the computed and experimental rolling loads.

Suggestions for Further Work

(I) Since a clear determination of dependence of both the hardening parameter defined as $\Delta\sigma/\sigma_1$ and the strain interval εp over which the hardening is observed has not been established, more experiments are required, carried out particularly in the higher temperature interval of the range of testing temperatures of commercial-aluminium alloys.

(II) More experiments are also required to investigate the apparent change in activation energy for deformation observed during testing at strain rates greater than 20 s^{-1}. Particular attention must be given to both friction and spread effects under these testing conditions due to the strong influence of both parameters on the flow stress.

(III) Studies of grain growth kinetics should be carried out in commercial aluminium alloys, in order to be included in the general computational model so that more accurate predictions of final grain sizes can be made.

(IV) It has been assumed that the model to describe the effect of the deformation history on the recrystallisation kinetics under isothermal conditions is also applicable at decaying temperatures. Therefore, a thorough investigation should be carried out in order to determine the validity of this assumption, particularly in relation to the effect of inherited substructures on the kinetics of recrystallisation.

(V) Multiple-pass isothermal rolling tests should be carried out in order to study the effect of the fraction recrystallised in previous time intervals on subsequent recrystallisation of the material, since adequate ratios of the length of projected arc of contact to the mean slab thickness would give rise to a more homogeneous deformation than plane-strain compression.

ACKNOWLEDGEMENTS

I would like to express my sincere thanks to Dr. C. M. Sellars for his help, guidance and patience during the course of this research work and also for his constant support, encouragement and understanding.

I also would like to thank "La Facultad de Ingenieria de la Universidad Central de Venezuela" and "El Consejo de Desarrollo Cientifico y Humanistico" for their financial support.

The Department of Metallurgy of the University of Sheffield is also to be thanked for the use I have made of its facilities and the collaboration I found in its technical staff.

Thanks are also gratefully due to all my friends, colleagues, research students and academic staff for all their friendship and encouragement shown during my stay in this department. In particular, I would like to thank Dr. J. J. Urcola, Dr. J. H. Beynon, Dr. A. M. Irisarri, Dr. R. Versaci, Dr. S. R. Foster, Mr. F. C. Castro, Mr. R. Colas, Mr. F. Al-Jouni, Mr. R. Ghomashi, Miss N. Diniz, Mr. R. Barbosa, Mr. C. Janampa and Mr. L. Fernandez for their help and interest.

I am also very grateful to Professor Gonzalo Castro Farinas and Dr. K. Ishizaki for their continuous encouragement and advice in the completion of this work.

Also, I would like to thank all my family for all the moral support they have given me throughout this period, in particular my wife, Susana, for her love and patience.

Finally, I would like to thank Mrs. Linda Whitaker for the magnificent typing of this thesis.

God bless you all...

APPENDIX I

Description of the Changes made to the Computer Programme Used in the Simulation of Hot Rolling Operations

The present appendix contains a complete listing of the modified version of the computer programme used in the simulation studies of hot rolling of Ti-bearing steels, since a detailed line by line explanation has already been given by Leduc [73]. The programme was run on an ICL-1906 S computer with "virtual memory". A typical set of data is also given with the corresponding running commands.

(I) Line 13 to 26 of the original programme define some logical variables used in ulterior decision making. Lines 21 to 34 of the present programme contain such variables but include a new one: "Distr", which is the control variable if a strain distribution through the thickness of the slab is under consideration.

(II) Line 38 of the original programme indicated the reading of the oxide thickness used in the calculations of air cooling heat losses. Line 52 of the new version also indicates the reading of the coefficients "c" and "b" of the air cooling heat transfer coefficient equation:

$$H = b(T - To) + c(Ts^4 - To^4) \qquad .....(4.16)$$

(III) Lines 150-152 and 251-253 of the new version are equivalent to lines 116-118 and 228-230, and express the thermal properties of the material (specific heat, density and thermal conductivity) as a function of temperature.

(IV) Line 290 of the new programme calculates the heat transfer coefficient as a function of the constants b, and c input in line 38.

(V) Line 547 of the new version replaces the value of the activation energy for recrystallisation to 225600 J/mol.

(VI) Line 553 calculates the distance from the centre of the slab according to:

$$\text{Dist (N)} = (N - 0.5) \times D22$$

where "N" is the row number and "D22" is the elemental height of the elements. This equation is then used to establish a distribution of strain through the thickness of the material by means of:

$$\varepsilon = \varepsilon(NP)\ [1 + 1.76\ (\frac{\text{Dist (N)}}{\text{thick(NP)}})^2\ (\frac{\text{thick(NP)}}{\text{Rad (NP)}})^{\frac{1}{2}}]$$

where "ε(NP)" represents the nominal strain applied during the pass, "thick (NP)" the final thickness after the pass and "Rad (NP)" the roll radius. However, it is important to point out that this is an empirical equation that gives rise to a parabolic variation of the strain through the thickness of the slab which reduces as the thickness decreases.

(VII) Lines 591-593 calculate the time for 50% recrystallisation according to equation:

$$t_{0.5} = 7.4921 \times 10^{-7} \times do^2 Z^{-1.07} \varepsilon^{-2.7} \exp\ (\frac{225600}{RT})$$

(VIII) Lines 1206, 1236, 1302, 1342 and 1410 calculate the recrystallised grain size given by the equation:

$$d_{rex} = 14.68\ Z^{-0.136} do^{1.3}\ \varepsilon^{-0.33}$$

(IX) Lines 1329-1330 constitute one of the most significant modifications to the original programme. During an interpass time and whenever there is a recrystallised fraction present, the original programme considers that the development of new recrystallised material will be provided by both the previous recrystallised fraction as well as the unrecrystallised one (line 1239). The modified version considers that the new recrystallised fraction present after an air cooling period is provided just by the unrecrystallised material and then is added up to the recrystallised fraction present at the end of the former period. The result constitutes the total recrystallised fraction present at the end of the current air cooling period.

(X) Lines 1346-1347 calculate the temperature-compensated time for 50% recrystallisation.

(XI) Lines 1360-1372 calculate the amount of material that has been rejected because of the consideration only of the fractions greater than 0.5%. Once this amount has been calculated, it is added to the fraction that first recrystallised. If there is no recrystallised fraction present (greater than 0.5%), it is added back to the unrecrystallised fraction.

(XII) Lines 1545-1565 and 1572-1592 calculate the flow stress of the material as a function of strain, strain rate and temperature according to equations (5.5)-(5.7).

A typical set of data is given below, and which corresponds to the Industrial Schedule No.7

```
RUN BIN BIN-AL-MAG,ROUTE STG,*LPO=UTIN1 (MULTIPLE,APPEND,LIMIT
20000), *LP1=TAB-UTIN,TL 2000
1
UTI-1
.T..F..F..F..F..T..T..T.
0.000001 0.000000000035435 0.0162
0.7 0.23 32.5 1 1 80 3 3 7 110.0
2.0
525.0
0.278 0.301 0.310 0.375 0.420 0.483 0.567
4.43 4.88 5.07 6.45 7.51 9.16 11.76
1.625 1.625 1.625 1.625 1.625 1.625 1.625
157.1 164.61 172.67 181.51 191.78 204.64 222.78 253.85
0.812 0.812 0.812 0.812 0.812 0.812 0.812
0.0 0.0 0.0 0.0 0.0 0.0 0.0 0.0
0.0 0.0 0.0 0.0 0.0 0.0 0.0 0.0
0.0 0.0 0.0 0.0 0.0 0.0 0.0 0.0
****
```

The running command for this particular file would be:

RJ Industrial, data, JD(JT 5000)

```
 1:       SHORT LIST
 2:       PROGRAM (ENDA)
 3:       COMPRESS INTEGER AND LOGICAL
 4:       INPUT 1=CR0
 5:       OUTPUT 2=LP0
 6:       OUTPUT 3=LP1
 7:       OUTPUT 4=LP2
 8:       TRACE 1
 9:       END
10:       MASTER DATAENTRY
11:C
12:C      INPUT OF DATA FOR A MAXIMUM OF 20 PASSES OF A 20*20 SLAB MATRIX
13:C
14:C       LOGICAL VARIABLES THAT DEFINE WHETHER OR NOT   A UNIFORM
15:C       ORIGINAL TEMPERATURE IS INPUT, AN ACTUAL READING OF
16:C       TEMPERATURE RISES, LOAD OR TORQUES WILL BE USED FOR
17:C       TEMPERATURE RISE CALCULATIONS, THE WHOLE TEMPERATURE
18:C       MATRIX IS TO BE PRINTED, A GRAPH OF CALCULATED TEMPERA-
19:C       TURES WILL BE REQUIRED, STRUCTURAL CALCULATIONS
20:C       ARE NEEDED AND STRAIN DISTRIBUTION IS CONSIDERED
21:C
22:       LOGICAL UNTEMP,TRISE,LOADS,TORQS,MATPRINT,IFPLOT,STRUCT,DISTR
23:       DIMENSION A(60,20),T(61,22),STL(60),G(60),Z(83),SPEED(20),U(20),
24:      1          P(20),D(20),IR(20),I(63),IAC(42),RTO(20),TRO(20),B(20)
25:      2          ,RLO(20),DSRY(999),W(999),R(999,20),RST(20),F(999,21)
26:      3          ,STIME(21),IW(21),SWC(21),WC(21),WCH(21)
27:       DIMENSION PRAVTE(20),OXSUTE(20),OXLSUTE(20)
28:       COMMON/CONDIT/T2,T1,ZP(20),STIME
29:       COMMON/WORK/E(20),E1(20)
30:       COMMON/STRENGTH/S0,B1,B5,EP,C5,THICKN(21),RAD(20)
31:       COMMON /LINK1/D0,D3,SL,UL,NWR0,NUMINT,STRUCT
32:       COMMON/TEMP/RMEANT(20),N0A(20),YDIF,NP,Y,SPRT(20),W2(20)
33:       COMMON/STORE/S(100,8,20),SS(100,8,20)
34:       COMMON/LINK2/R1,S1,VNC,WNR,RAVTEM(20),DEFTEM(20)
35:       COMMON/PRIOUT/DIST(20)
36:C
37:       READ (1,5000) NUMDATA
38:       DO 1500 JJ=1,NUMDATA
39:C
40:C       SPECIMEN IDENTIFICATION
41:C
42:       READ (1,5020) SPECIMEN
43:       WRITE (2,6080) SPECIMEN
44:C
45:C
46:C
47:       READ (1,5010) UNTEMP,TRISE,LOADS,TORQS,MATPRINT,IFPLOT,STRUCT,
48:      1DISTR
49:C
50:       IF (IFPLOT) WRITE (3,9030) SPECIMEN
51:       IF (STRUCT) WRITE (4,9030) SPECIMEN
52:C
53:C       OXIDE THICKNESS,COEFFICIENTS "C" AND "B" OF THE HEAT TRANSFER EQUATION
54:       READ (1,5000) OXTH,CHTC,BHTC
55:C
56:C       INPUT OF SPECIMEN THICKNESS AND BREADTH (M), HEAT
```

```
57:C      TRANSFER COEFFICIENT DURING ROLLING, PRINTING
58:C      FREQUENCIES DURING AIR COOLING AND ROLLING,ROLL
59:C      TEMPERATURE, NUMBER OF ROWS, COLUMNS AND PASSES
60:C      AND INITIAL GRAIN SIZE
61:C
62:       READ (1,5000) WIDTH,THICKN(1),C1,KPAC,KPR,RTEMP,NWR,NVC,NPA,GS
63:C
64:C      TIMIN=TIME INTERVAL FOR STRUCTURE CALCULATIONS (SECONDS)
65:       IF (STRUCT) READ (1,5000) TIMIN
66:C
67:       NPA22=NPA*2+2
68:       NPA1=NPA+1
69:       NWR1=NWR+1
70:       NVC1=NVC+1
71:       NVC2=NVC+2
72:       WNR=FLOAT(NWR)
73:       VNC=FLOAT(NVC)
74:C
75:       IF (UNTEMP) GO TO 10
76:       CALL FTEMPDIST(A,T,STL,U,DTIG,Z1,NVC,NWR,NWR1,NVC1,RTEMP,GS)
77:       GO TO 35
78:C
79:    10 READ (1,5000) STEMP
80:       WRITE (2,6000) RTEMP,STEMP
81:C
82:C       INPUT OF REDUCTION, PERCENT OF SPREAD, PERIPHERICAL ROLL
83:C       SPEED, TIME AND ROLL RADIUS(M) FOR EACH PASS, TIMES(SEC)
84:C       TO START AND DURATION OF WATER COOLING AND WATER COOLING
85:C       HEAT TRANSFER COEFFICIENTS
86:C
87:    35 READ(1,5000) (P(JP),JP=1,NPA),(D(JP),JP=1,NPA),(SPEED(JP),JP=1,NPA
88:      1),(STIME(JP),JP=1,NPA1),(RAD(JP),JP=1,NPA),(SWC(JP),JP=1,NPA1),
89:      2(WC(JP),JP=1,NPA1),(WCH(JP),JP=1,NPA1)
90:       WRITE(2,6010) (P(JP),JP=1,NPA)
91:       WRITE(2,6012) (D(JP),JP=1,NPA)
92:       WRITE(2,6014) (SPEED(JP),JP=1,NPA)
93:       WRITE(2,6016)(STIME(JP),JP=1,NPA1)
94:       WRITE(2,6017) (RAD(JP),JP=1,NPA)
95:       WRITE(2,6018) (SWC(JP),JP=1,NPA1)
96:       WRITE (2,6022) (WC(JP),JP=1,NPA1)
97:       WRITE(2,6024) (WCH(JP),JP=1,NPA1)
98:C
99:       IF (TRISE) CALL DEFHEAT(TRO,NPA)
100:      IF (LOADS) CALL DEFHEAT(RLO,NPA)
101:      IF (TORQS) CALL DEFHEAT(RTO,NPA)
102:      C1=C1*1000.
103:C
104:C      CALCULATION AND PRINTING OF THE DIMENSIONS OF THE ELEMENTS
105:C
106:      D2=THICKN(1)/(2.*WNR)
107:      D1=WIDTH/(2.*VNC)
108:   40 WRITE (2,6020)D1,D2,NWR,NVC,NPA,C1
109:C
110:      MMT=INT(1+NVC/1.732)
111:      NR=NWR
112:      RN=FLOAT(NR)
```

```
113:C      ORIGINAL CONDITIONS IN THE STRUCTURAL CALCULATIONS
114:       SS(1,1,1)=100.
115:       SS(1,4,1)=GS
116:       SS(1,5,1)=0.
117:       DO 20 N=1,NWR
118:       S(1,1,N)=100.
119:       S(1,4,N)=GS
120:       S(1,5,N)=0.
121:       NOA(N)=1
122:               STL(N)=STEMP
123:               DO 20 M=1,NVC
124:               A(N,M)=STEMP
125:    20 CONTINUE
126:C
127:       DO 30 M=1,NVC
128:               U(M)=STEMP
129:    30 CONTINUE
130:C
131:       Z1=STEMP
132:       DTIG=0
133:C
134:       DO 50 JP=2,NPA1
135:               THICKN(JP)=THICKN(JP-1)*(1-P(JP-1))
136:    50 CONTINUE
137:C
138:       DO 55 JP=1,NPA
139:               E(JP)=1.155*ALOG(THICKN(JP)/THICKN(JP+1))
140:               E1(JP)=E(JP)*SPEED(JP)
141:               E1(JP)=E1(JP)/SQRT(RAD(JP)*(THICKN(JP)-THICKN(JP+1)))
142:           IF(E1(JP).GE.10) WRITE (2,6026) JP
143:    55 CONTINUE
144:C
145:       WRITE(2,6030) (THICKN(JP),JP=1,NPA1  )
146:       WRITE(2,6090) (E(JP),JP=1,NPA)
147:       WRITE(2,6100) (E1(JP),JP=1,NPA)
148:C
149:C      THERMAL PROPERTIES OF THE SPECIMEN AT THE INITIAL TEMPERATURE
150:C
151:       S1=890.58+0.46*STEMP
152:       R1=2706.63-0.21*STEMP
153:       COND=167.15+0.12*STEMP-2.75E-4*(STEMP**2)+1.72E-7*(STEMP**3)
154:       CONSTFAC=R1*S1*D1*(WNR-0.75)/(4*COND*WNR**2)
155:       CONST=2.*D1*WNR
156:       CONSTFAC1=S1*R1*(3.*WNR-0.75)/(216.*COND*WNR**3)
157:       Z(4*NPA1-3)=CONSTFAC*(THICKN(NPA1))**2/(CONST+THICKN(NPA1))
158:       Z(4*NPA1-2)=Z(4*NPA1-3)
159:       Z(4*NPA1-1)=Z(4*NPA1-2)
160:C
161:C      CALCULATION OF THE CONTACT AND ROLLING STABLE TIMES
162:       DO 60 JP=1,NPA
163:               B(JP)=1-(THICKN(JP)-THICKN(JP+1))/(2.*RAD(JP))
164:               B(JP)=RAD(JP)*ATAN(SQRT(1-B(JP)**2)/B(JP))/SPEED(JP)
165:               Z(4*JP-3)=CONSTFAC*THICKN(JP)**2/(CONST+THICKN(JP))
166:       Z(4*JP-2)=Z(4*JP-3)
167:       Z(4*JP-1)=Z(4*JP-2)
168:               Z(4*JP)=CONSTFAC1*THICKN(JP+1)**2
```

```
169:              IR(JP)=0.99999+ B(JP)/Z(4*JP)
170:      Z(4*JP)=B(JP)/IR(JP)
171:              IF (IR(JP).GT.999) GO TO 1500
172:              IF (IR(JP).GE.3) GO TO 60
173:            IF (NWR.GT.10) GO TO 60
174:              IF (.NOT.UNTEMP) GO TO 1500
175:              NWR=2*NWR
176:              WNR=FLOAT(NWR)
177:              NWR1=NWR+1
178:              D2=0.5*D2
179:              GO TO 40
180:    60 CONTINUE
181:C
182:      WRITE (2,6040) (B(JP),JP=1,NPA)
183:      WRITE(2,6045) (IR(JP),JP=1,NPA)
184:      IF (STRUCT) WRITE (4,9040) NWR
185:C
186:C      CALCULATION OF STABLE TIMES DURING AIR AND WATER COOLING
187:      IF (WC(1).EQ.0.) GO TO 65
188:      IAC(1)=0.99999+ SWC(1)/Z(1)
189:      Z(1)=SWC(1)/IAC(1)
190:      I(1)=IAC(1)
191:      IW(1)=0.99999+ WC(1)/Z(2)
192:      Z(2)=WC(1)/IW(1)
193:      I(2)=I(1)+IW(1)
194:      IAC(2)=0.99999 +(STIME(1)-SWC(1)-WC(1))/Z(3)
195:      IF (IAC(2).EQ.0) GO TO 63
196:      Z(3)=(STIME(1)-SWC(1)-WC(1))/IAC(2)
197:    63 I(3)=I(2)+IAC(2)
198:      GO TO 67
199:    65 IAC(1)=0.99999+  STIME(1)/Z(1)
200:      Z(1)=STIME(1)/IAC(1)
201:      Z(2)=Z(1)
202:      Z(3)=Z(2)
203:      I(1)=IAC(1)
204:      I(2)=I(1)
205:      I(3)=I(2)
206:C
207:    67 DO 70 JP=2,NPA1
208:      IF (WC(JP).EQ.0.) GO TO 69
209:      IAC(2*JP-1)=0.99999+ (SWC(JP)-STIME(JP-1)-B(JP-1))/Z(4*JP-3)
210:      IAC(2*JP)=0.99999+ (STIME(JP)-SWC(JP)-WC(JP))/Z(4*JP-1)
211:      IW(JP)=0.99999+ WC(JP)/Z(4*JP-2)
212:      Z(4*JP-3)=(SWC(JP)-STIME(JP-1)-B(JP-1))/IAC(2*JP-1)
213:      Z(4*JP-2)=WC(JP)/IW(JP)
214:      IF (IAC(2*JP).EQ.0) GO TO 68
215:      Z(4*JP-1)=(STIME(JP)-SWC(JP)-WC(JP))/IAC(2*JP)
216:    68 I(3*JP-2)=I(3*JP-3)+IAC(2*JP-1)+IR(JP-1)
217:      I(3*JP-1)=I(3*JP-2)+IW(JP)
218:      I(3*JP)=I(3*JP-1)+IAC(2*JP)
219:      GO TO 70
220:    69 IAC(2*JP-1)=(STIME(JP)-STIME(JP-1)-B(JP-1))/Z(4*JP-3)+  0.99999
221:      Z(4*JP-3)=(STIME(JP)-STIME(JP-1)-B(JP-1))/IAC(2*JP-1)
222:      Z(4*JP-2)=Z(4*JP-3)
223:      Z(4*JP-1)=Z(4*JP-2)
224:      I(3*JP-2)=I(3*JP-3)+IAC(2*JP-1)+IR(JP-1)
```

```
225:       I(3*JP-1)=I(3*JP-2)
226:       I(3*JP)=I(3*JP-1)
227:    70 CONTINUE
228:       WRITE (2,6050) (IAC(JP),JP=1,NPA22)
229:C
230:       NP=0
231:       IU=0
232:       JP=1
233:       Y=0
234:       IPF=1
235:       IPS=1
236:       DZ=Z(1)
237:       KPS=KPAC
238:       RD=RAD(1)
239:C      ************************************************
240:C
241:C            ATENTION THIS IS THE START OF THE OVERALL LOOP
242:C
243:C      ****************************************************************
244:   100 IF (IU.EQ.I(3*JP-2)) DZ=Z(4*JP-2)
245:       IF (IU.EQ.I(3*JP-1)) DZ=Z(4*JP-1)
246:       IF (IU.EQ.I(3*JP)) DZ=Z(4*JP)
247:       Y=Y+DZ
248:       IU=IU+1
249:C
250:C      CALCULATION OF THE THERMAL PROPERTIES AT SLAB MEAN TEMPERATURE
251:C
252:       COND=167.15+0.12*Z1-2.75E-4*(Z1**2)+1.72E-7*(Z1**3)
253:       R1=2706.63-0.21*Z1
254:       S1=890.58+0.46*Z1
255:C
256:       D11=1000.*D1
257:       D22=1000.*D2
258:       CONS1=S1*R1*D1*D2
259:       CONS2=D22*(WNR-0.25)/(2.*WNR*COND)
260:       CONS3=D11*(NVC-0.25)/(2.*NVC*COND)
261:       Z1=0
262:C
263:C      HEAT FLOW BETWEEN THE SLAB ELEMENTS
264:C
265:       INFINPASS=I(3*JP)+IR(JP)
266:C
267:C      CALCULATION OF THE HEAT TRANSFER WITHIN THE SLAB
268:C
269:       DO 230 M=1,NVC
270:          DO 220 N=1,NWR
271:             Q=0
272:             IF (M.EQ.1) GO TO 110
273:             Q=D2*COND*DZ*(A(N,M-1)-A(N,M))/D1
274:             IF (M.EQ.NVC) GO TO 120
275:   110       Q=Q-D2*COND*DZ*(A(N,M)-A(N,M+1))/D1
276:             GO TO 150
277:   120 G(N)=CHTC*((STL(N)+273)**4)+BHTC*STL(N)-(18*BHTC)
278:   140       Q=Q-G(N)*D22*DZ
279:   150       IF (N.EQ.1) GO TO 160
280:             Q=Q+D1*COND*DZ*(A(N-1,M)-A(N,M))/D2
```

```
281:              IF (N.EQ.NWR) GO TO 170
282:  160         Q=Q-D1*COND*DZ*(A(N,M)-A(N+1,M))/D2
283:              GO TO 210
284:  170 IF (IU.LE.I(3*JP-2)) GO TO 180
285:       IF (IU.LE.I(3*JP-1)) GO TO 195
286:       IF (IU.LE.I(3*JP)) GO TO 180
287:       CALL EHEATBETWEENSLABROLL (M,A5,COND8,DZ,V1,V8,S8,R8,NRRX,RD,
288:      1     D1,WNR,D2,COND,S1,R1,NVC1,KPS,IPF,NVC,B3,D3,B2,C,Q,R,DSRY,W,
289:      2          RST,U,T,F,A,NWR,VNC,MATPRINT)
290:              GO TO 230
291:  180 H=CHTC*((U(M)+273)**4)+BHTC*U(M)-BHTC*18
292:       GO TO 200
293:  195 H=WCH(JP)
294:  200           Q=Q-H*DZ*D11
295:  210           T(N,M)=A(N,M)+Q/CONS1
296:  220      CONTINUE
297:           U(M)=T(NWR,M)-H*CONS2
298:  230 CONTINUE
299:C
300:       DO 240 N=1,NWR
301:              STL(N)=T(N,NVC)-G(N)*CONS3
302:  240 CONTINUE
303:C
304:       IF (IU.GT.I(3*JP).AND.IU.LE.INFINPASS) GO TO 241
305:       YDIF=Y-Y1
306:       IF(IPS.EQ.KPS4.AND.STRUCT.AND.NP.NE.0)GOTO243
307:       IF ((YDIF.GE.TIMIN.OR.IU.EQ.I(3*JP)).AND.STRUCT.AND.NP.NE.0)
308:      1            GO TO 243
309:       IPS=IPS+1
310:       GO TO 246
311:C
312:C      CALCULATION OF AVERAGE DEFORMATION TEMPERATURE (EVERY THIRD ROW)
313:C
314:  241 DO 242 N=1,NR
315:       NN=3*N-1
316:       DEFTEM(N)=(A(NN,MMT)+T(NN,MMT))/2.
317:  242 CONTINUE
318:       GO TO 246
319:C
320:  243 T5=T5+YDIF
321:       DL=0
322:       DT=0
323:       WRITE (2,6130) Y,T5
324:       WRITE (2,6133)
325:       DO 244 N=1,NWR
326:       PRAVTE(N)=RAVTEM(N)
327:       RAVTEM(N)=T(N,MMT)
328:       RMEANT(N)=(PRAVTE(N)+RAVTEM(N))/2.
329:       OO=E(NP)
330:C
331:C       THE SUBROUTINE THAT CALCULATES STRUCTURAL CHANGES DURING
332:C       AIR COOLING IS CALLED HERE
333:C
334:       CALL TEMPCOMPTIME(NP,N,OO,DEFTEM,T5)
335:       JQ1=NOA(N)
336:       SUM=0
```

```
337:       DO 249 I1=1,JQ1
338:       IF (S(I1,5,N).NE.0) GO TO 249
339:       SUM=SUM+S(I1,1,N)
340:   249 CONTINUE
341:C
342:C       CALCULATION OF THE AVERAGE STRUCTURE
343:C
344:       DO 244 I1=1,JQ1
345:       IF (SUM.GT.99.9999) GO TO 247
346:       XI=1
347:       IF (I1.EQ.1.) GO TO 248
348:       XI=(S(I1,1,N)+S(I1-1,1,N))/100.
349:   248 X=S(I1,1,N)/100.
350:       CONST=EXP(0.866*S(I1,5,N))
351:       IF (S(I1,5,N).EQ.0) GO TO 245
352:       DL=DL+X/(S(I1,2,N)*CONST)
353:       DT=DT+X*CONST/S(I1,2,N)
354:       GO TO 244
355:   245 CONTINUE
356:       IF(S(I1,3,N).EQ.0) GO TO 244
357:           DL=DL+(X**(2./3.)*XI**(1./3.))/S(I1,3,N)
358:       DT=DT+(X**(2./3.)*XI**(1./3.))/S(I1,3,N)
359:       GO TO 244
360:   247 DL=DL+S(I1,1,N)/(100.*S(I1,4,N))
361:       DT=DT+S(I1,1,N)/(100.*S(I1,4,N))
362:   244 CONTINUE
363:C
364:C       CALCULATION AND PRINTING OF THE AVERAGE GRAIN SIZE
365:C
366:       AVGS=RN/SQRT(DL*DT)
367:       WRITE (2,6134) AVGS
368:C
369:       Y1=Y
370:       IF (KPS4.GT.4E6) KPS4=4E6
371:       KPS4=2*KPS4
372:       IPS=1
373:C
374:C       CALCULATION OF THE MEAN SLAB TEMPERATURE
375:C
376:   246 DO 250 M=1,NVC
377:           DO 250 N=1,NWR
378:               A(N,M)=T(N,M)
379:               Z1=Z1+T(N,M)
380:   250 CONTINUE
381:       Z1=Z1/(VNC*WNR)
382:C
383:       IF (IU.NE.I(3*JP).OR.JP .EQ.NPA1)  GO TO 260
384:C      STORE THE MEAN ROW AND SLAB TEMPERATURES AT THE START OF THE PASS
385:       DO 257 N=1,NR
386:            SPRT(N)=T(N,MMT)
387:   257 CONTINUE
388:       Z0=Z1
389:C
390:       CALL CINCREASENUMELMTS (T,G,NVC,NWR,STL,Z,DZ,D2,KPR,NRRX,KPS,A
391:      1,U,JP,NWR1,D22,WNR,NP,IR,NWR0)
392:       GO TO 280
```

```
393:C
394:C      DECISION IF IT IS TIME TO PRINT
395:C
396:  260 IF (JP.EQ.1) GO TO 270
397:       EPP=STIME(JP-1)+B(JP-1)
398:       EPP10=EPP+10*DZ
399:       IF (Y.GT.EPP.AND.EPP10.GT.Y) GO TO 280
400:  270 IF (IPF.EQ.KPS) GO TO 280
401:       IF (IU.EQ.I(3*NPA1)) GO TO 280
402:       IF (IU.EQ.INFINPASS.OR.IU.EQ.I(3*JP-1).OR.IU.EQ.I(3*JP-2)) GOTO280
403:       IPF=IPF+1
404:       GO TO 320
405:C
406:C      NEXT BLOCK PRINTS MATRIX TEMPERATURES
407:C
408:  280 TRTI=Y+DTIG
409:       WRITE (2,6060) Y,TRTI,D22,Z1,DZ
410:       IF(.NOT.MATPRINT) GO TO 311
411:       DO 290 M=1,NVC
412:              DO 290 N=1,NWR
413:              T(N,M)=A(N,M)
414:              T(NWR1,M)=U(M)
415:              T(N,NVC1)=STL(N)
416:  290 CONTINUE
417:C
418:       DO 300 N=1,NWR
419:              T(N,NVC2)=(N-0.5)*D22
420:  300 CONTINUE
421:C
422:       T(NWR1,NVC2)=0
423:       T(NWR1,NVC1)=STL(NWR)+U(NVC)-A(NWR,NVC)
424:C
425:       DO 310 N=1,NWR1
426:              IF (NVC.GT.13) GO TO 305
427:       WRITE (2,6070) (T(N,M),M=1,NVC2)
428:       GO TO 310
429:  305 WRITE (2,6070) (T(N,M),M=1,NVC2,2)
430:  310 CONTINUE
431:  311 IF (.NOT.IFPLOT) GO TO 315
432:C
433:C      CALCULATION OF THE AVERAGE TEMPERATURE IN THE SURFACE ROW
434:C
435:       TSURF=0
436:       NVNV=NVC2-2
437:       NAL=1
438:       DO 3850 ML=1,NVNV
439:       TSURF=TSURF+U(ML)
440: 3850 CONTINUE
441:       TSURF=TSURF/VNC
442:C
443:C      CENTRE, SLAB MEAN, SURFACE TEMPERATURES AND TIME ARE STORED
444:C      IN A FILE FOR POSTERIOR PLOTTING
445:       WRITE (3,9000) T(1,1),Z1,TSURF,TRTI
446:C
447:       IF (Y.GT.EPP.AND.EPP10.GT.Y) GO TO 315
448:       KPS=2*KPS
```

```
 315 IPF=1
C
 320 IF (IU.EQ.I(3*NPA1)) GO TO 3210
     IF (IU.LT.I(3*JP)) GO TO 100
     IF (IU.EQ.I(3*JP)) GO TO 330
C
C         IF NONE OF THE PREVIOUS IS TRUE  IT SHOULD BE DURING A PASS
C
     CALL BCHANGED2 (IU,INFINPASS,B0,B2,B3,B4,THICKN,RD,NWR,C1,C
    1         ,T,A,U,STL,Z9,Z1,NVC,D2,SPEED,JP,NOA)
     IF (IU.NE.INFINPASS) GO TO 100
     CALL DDECREASENUMELMTS (NWR,NVC,A,T,G,STL,D,D1,D2,KPAC,KPS,Z
    1       ,JP,DZ,WNR,NWR1,D22)
     KPS4=4*KPS
     RD=RAD(JP)
     IF(.NOT.STRUCT) GO TO 100
C
C         AVERAGE STRUCTURE CALCULATION
C
     IF (NP.EQ.1) N0=1
     IF(NP.EQ.1) GO TO 329
3210 N1=0
     DO 327 N=1,NR
     N1=N1+N0A(N)
 327 CONTINUE
     IF (N1.GT.50) N1=50
     DO 328 J=1,8
     DO 328 I1=1,N1
     SS(I1,J,1)=0.
 328 CONTINUE
C
     N0=0
     DO 326 N=1,NR
             NN=N+1
             JQ1=N0A(N)
C
             DO 326 I1=1,JQ1
C
          N0=N0+1
               JQ3=N0
             DO 321 J=1,JQ3
     IF (SS(J,1,1).EQ.0) GO TO 321
             F2=ABS(SS(J,5,1)-S(I1,5,N))
          IF (F2.GE.0.0001) GO TO 321
          N0=N0-1
        GO TO 326
 321        CONTINUE
C
          SS(N0,1,1)=S(I1,1,N)
          P0=S(I1,4,N)*S(I1,1,N)
          P1=S(I1,1,N)
          SS(N0,5,1)=S(I1,5,N)
          K1=I1+1
          IF(K1.GT.JQ1) GO TO 323
          DO 322 I2=K1,JQ1
          F2=ABS(S(I1,5,N)-S(I2,5,N))
```

```
505:             IF (F2.GE.0.0001) GO TO 322
506:             SS(NO,1,1)=SS(NO,1,1)+S(I2,1,N)
507:             PO=PO+S(I2,1,N)*S(I2,4,N)
508:             P1=P1+S(I2,1,N)
509:  322        CONTINUE
510:C
511:  323          IF(NN.GT.NR) GO TO 325
512:C
513:               DO 324 M=NN,NR
514:               JQ2=NOA(M)
515:C
516:               DO 324 II=1,JQ2
517:               F2=ABS(S(II,5,N)-S(II,5,M))
518:               IF (F2.GE.0.0001) GO TO 324
519:               SS(NO,1,1)=SS(NO,1,1)+S(II,1,M)
520:             PO=PO+S(II,1,M)*S(II,4,M)
521:             P1=P1+S(II,1,M)
522:  324          CONTINUE
523:C
524:  325          SS(NO,1,1)=SS(NO,1,1)/RN
525:      IF (P1.EQ.0) GOTO 326
526:            SS(NO,4,1)=PO/P1
527:  326 CONTINUE
528:C
529:C      PRINTING OF THE AVERAGE STRUCTURE
530:       WRITE(2,6125)
531:       DO 3276 II=1,NO
532:       WRITE (2,6127) (SS(II,1,1),SS(II,5,1),SS(II,4,1))
533: 3276 CONTINUE
534:C
535:       IF (IU.EQ.I(3*NPA1)) GO TO 350
536:  329 ZZ1=(Z1+Z0)/2.
537:C
538:C      CALL THE SUBROUTINE TO CALCULATE LOAD AND TORQUE IN THE PASS
539:       CALL LOAD (1,ZZ1,SS,NO,NP,M)
540:C
541:C     STRUCTURE CONDITIONS AFTER PASS
542:C
543:       YDIF=B(NP)/2.
544:       OO=E(NP)
545:       T5=0.
546:       DO 336 N=1,NWR
547:               DEFTEM(N)=(A(N,MMT)+SPRT(N))/2.
548:               W2(N)=YDIF*EXP(-226000/(8.31*(DEFTEM(N)+273)))
549:               JQ1=NOA(N)
550:       NO=0
551:               DO 334 II=1,JQ1
552:       NO=NO+1
553:               SS(NO,8,1)=0.
554:       DIST(N)=(N-0.5)*D22
555:C
556:C      STRAIN DISTRIBUTION ACROSS THE SLAB THICKNESS
557:C
558:       IF (DISTR) GO TO 3310
559:       EO=E(NP)
560:       GO TO 3311
```

```
561: 3310 E0=(DIST(N)/(1000.0*THICKN(NP)))**2
562:      E0=1.76*E0*(THICKN(NP)/RAD(NP))**0.5
563:      E0=E(NP)*(1+E0)
564: 3311 E0=E0+S(II,5,N)
565:      ZP(N)=E1(NP)*EXP(156000/(8.31*(DEFTEM(N)+273)))
566:      IF (S(II,1,N).EQ.100.0.AND.S(II,5,N).EQ.0.) GO TO 331
567:      IF (S(II,5,N).NE.0.) GO TO 331
568:      X=S(II,1,N)/100.
569:      XI=(S(II,1,N)+S(II+1,1,N))/100.
570:      GS=S(II,3,N)
571:      GO TO 333
572:  331         GS=S(II,4,N)
573:C*
574:  333       SS(NO,1,N)=S(II,1,N)
575:            SS(NO,2,N)=GS
576:            SS(NO,3,N)=GS
577:            SS(NO,4,N)=GS
578:            SS(NO,5,N)=E0
579:            SS(NO,6,N)=0.
580:            SS(NO,7,N)=0.
581:C*
582:  334 CONTINUE
583:      NOA(N)=NO
584:      DO 335 J=1,8
585:      DO 335 IK=1,NO
586:      S(IK,J,N)=SS(IK,J,N)
587:C
588:C      CALCULATION OF THE RECRYSTALLISATION TIME
589:C
590:  335 CONTINUE
591:      DO 4000 IK=1,NO
592:      T1=E1(NP)*EXP(156000/(8.31*(DEFTEM(N)+273)))
593:      T1=7.4921E-7*(S(IK,4,N)**2)*(T1**(-1.07))*(S(IK,5,N)**(-2.7))
594:      T1=T1*EXP(225600/(8.31*(DEFTEM(N)+273)))
595:      S(IK,6,N)=T1
596: 4000 CONTINUE
597:  336 CONTINUE
598:C
599:      WRITE (2,6136)
600:      WRITE(2,6135) NP
601:      WRITE(2,6137)
602:      DO 337 N=1,NWR
603:      NO=NOA(N)
604:C
605:C      PRINTING OF DISTANCES FROM THE CENTRE, PERCENT OF
606:C      MATERIAL, GRAIN SIZE, STRAIN, RECRYSTALLISATION TIME
607:C      AND TEMPERATURE OF DEFORMATION
608:C
609:      DO 337 IK=1,NO
610:      WRITE(2,6140) (DIST(N),S(IK,1,N),S(IK,4,N),S(IK,5,N),S(IK,6,N),
611:     1   DEFTEM(N))
612:  337 CONTINUE
613:      WRITE (2,6136)
614:C
615:      DO 338 N=1,NWR
616:      RAVTEM(N)=T(N,MMT)
```

```
  338 CONTINUE
      Y1=Y
      GO TO 100
C
C
  330 CALL ADEFINEROLLCOND (DSRY,W,R,RST,F,NVC,RD,SPEED,D2,D1,R1,S1,
     1 NWR,TRO,RTO,RLO,H1,IR,THICKN,DZ,B0,B2,B3,B4,NRRX,A5,S8,COND8
     2          ,R8,Z9,V8,WNR,VNC,TRISE,LOADS,TORQS,RTEMP,Z1,C,C1,P,JP)
C
      SL=0.
C
      GO TO 100
C
C
  350 IF (IFPLOT) WRITE(3,9010)
      IF (STRUCT) WRITE(4,9010)
 1500 CONTINUE
      IF (IFPLOT) WRITE(3,9020)
      IF (STRUCT) WRITE (4,9020)
       STOP
C
C
 5000 FORMAT (170G0.0)
 5005 FORMAT (I1)
 5010 FORMAT (8L3)
 5020 FORMAT(A6)
C
 6000 FORMAT (1H ,20X,'ROLL TEMPERATURE=',F4.0,35X,'INITIAL TEMPERATURE
     1=',F6.0)
 6010 FORMAT (1H ,10X,'REDUCTIONS:',/,5X,20F7.4)
 6020 FORMAT  (9X,'D1=',F7.5,2X,'D2=',F7.5,2X,'NUMBER OF ROWS=',I2,2X,
     1'NUMBER OF COLUMNS=',I2,5X,'NUMBER OF PASSES=',I2,30X,'H.T.C. DURI
     2NG ROLLING=',F10.1)
 6030 FORMAT (1H ,10X,'THICKNESS: (M)',/,5X,21F6.3)
 6040 FORMAT (1H ,10X,'CONTACT TIME:',1X,12F8.5)
 6045 FORMAT (1H ,6X,'ROUND UP QUOTIENT:',1218)
 6050 FORMAT (1H ,5X,'AIR COOLING ROUND UP QUOTIENTS:',/,5X,4415)
 6080 FORMAT(1H1,52X,'****',1X,A6,1X,'****')
 6012 FORMAT (1H ,10X,'SPREAD: (%) ',/,5X,20F5.2)
 6014 FORMAT (1H ,10X,'SPEEDS:(M/SEC) ',/,5X,20F7.3)
 6016 FORMAT (1H ,10X,'TIME FOR START OF PASSES: ',/,5X,21F7.2)
 6017 FORMAT (1H ,10X,'ROLL RADIOUS: (M)',/,5X,20F8.5)
 6018 FORMAT (1H ,10X,'WATER COOLING START:',/,5X,21F7.2)
 6022 FORMAT (1H ,10X,'WATER COOLING PERIOD:',/,5X,21F6.2)
 6024 FORMAT (1H ,10X,'WATER COOLING HEAT TRANSFER COEFF:',/,5X,21F9.2)
 6026 FORMAT (1H ,35X,'STRESS STRAIN EQUATIONS ON PASS',I13,'OUT OF
     1RANGE')
 6015 FORMAT (1H ,10X,'**** MATERIAL: COMMERCIAL PURITY ALUMINIUM ****')
 6025 FORMAT (1H ,10X,'**** MATERIAL:  ALUMINIUM - MAGNESIUM ****')
 6060 FORMAT (1H0,5X,'TIME=',F9.5,5X,'TRUE TIME=',F9.5,5X,'D2=',F8.5,5X,
     1'MEAN TEMP.=',F10.4,5X,'TIME INCREMENT=',F10.7)
 6070 FORMAT (1H ,15F8.2)
 6090 FORMAT (1H ,10X,'STRAIN:',/,5X,20F6.2)
 6100 FORMAT (1H ,10X,'STRAIN RATE (1/SEC):',/,5X,20F7.2)
 6125 FORMAT (1H ,50X,'*AVERAGE  STRUCTURE*',/,10X,'% OF MATERIAL',
     1 25X,'STRAIN',25X,'GRAIN SIZE')
```

```
673: 6127 FORMAT (1H ,10X,1F9.5,26X,1F9.5,25X,1F9.5)
674: 6130 FORMAT (1H ,22X,'STRUCTURE AT ',1F6.2,1X,'SEC',35X,
675:     1  'COOLING TIME ',1F6.2,1X,'SEC')
676: 6133 FORMAT (1H ,1X,'DISTANCE',6X,'TEMPERATURE',6X,'% OF MATERIAL',6X,
677:     1  'STRAIN',6X,'REX. G.S.',6X,'ACTUAL G.S.',6X,'MEAN G.S.')
678: 6134 FORMAT (1H ,10X,'AVERAGE GRAIN SIZE ',1F7.1)
679: 6135 FORMAT (1H ,'*',42X,'STRUCTURE AFTER PASS',1X,I2,53X,'*')
680: 6136 FORMAT (1H ,120('*'))
681: 6137 FORMAT (1H ,10X,'DISTANCE',10X,'% OF MATERIAL',10X,
682:     1  'GRAIN SIZE',10X,'STRAIN',10X,'REX. TIME',10X,'DEF.TEMP.')
683: 6140 FORMAT (1H ,'*',10X,1F7.2,13X,1F6.2,16X,
684:     1  1F6.2,9X,1F9.3,7X,1F12.5,12X,1F7.2,4X,'*')
685:C
686: 9000 FORMAT (1X,3(F7.2,1X),F10.5)
687: 9010 FORMAT (1X,'END')
688: 9020 FORMAT (1X,'****')
689: 9030 FORMAT (1X,A6)
690: 9040 FORMAT (1H ,I3)
691:      END
692:C
693:      SUBROUTINE DEFHEAT (C,NPA)
694:C
695:C      THIS SUBROUTINE INPUTS AN ACTUAL TEMPERATURE RISE OR ROLLING
696:C      LOADS OR TORQUES FOR TEMPERATURE RISE CALCULATIONS WHEN THE
697:C      STRUCTURE IS NOT BEING CALCULATED
698:C
699:            DIMENSION C(20)
700:            READ (1,5001) (C(JP),JP=1,NPA)
701:            WRITE (2,6001) (C(JP),JP=1,NPA)
702:      RETURN
703:C
704: 5001 FORMAT (10G0.0)
705: 6001 FORMAT (1H ,10X,'VARIABLE FOR TEMPERATURE RISE CALCULATION:',10(F9
706:     1.1,1X))
707:C
708:      END
709:C
710:      SUBROUTINE FTEMPDIST(A,T,STL,U,DTIG,Z1,NVC,NWR,NWR1,NVC1,RTEMP,GS)
711:C
712:C
713:C      THIS SUBROUTINE ALLOWS THE INPUT OF A STARTING TEMPERATURE
714:C      DISTRIBUTION; EACH ROW IS CONSIDERED IN TURN, WHEN THE LAST
715:C      ROW HAS BEEN INPUT THEN THE BOTTOM SURFACE TEMPERATURES ARE
716:C      READ, WHEN THIS HAS BEEN DONE THE SIDE SURFACE TEMPERATURES ARE
717:C      INPUT. READING AND PRINTING OF THE MEAN TEMPERATURE, GRAIN
718:C      SIZE AND CURRENT TIME IS ALSO DONE
719:C
720:C
721:            DIMENSION A(60,20),T(61,22),STL(60),U(20)
722:            READ (1,5002) DTIG,Z1,GS
723:            READ (1,5002) ((A(N,M),M=1,NVC),N=1,NWR),((U(M),M=1,NVC),
724:     1      STL(N),N=1,NWR)
725:            T(NWR1,NVC1)=0
726:C
727:            DO 10 M=1,NVC
728:               T(NWR1,M)=U(M)
```

```
729:                  DO 10 N=1,NWR
730:                  T(N,M)=A(N,M)
731:    10          CONTINUE
732:C
733:                DO 20 N=1,NWR
734:                  T(N,NVC1)=STL(N)
735:    20          CONTINUE
736:C
737:                WRITE (2,6002) DTIG,Z1,RTEMP
738:C
739:                DO 40 N=1,NWR1
740:                  IF (NVC.GT.14) GO TO 30
741:                  WRITE (2,6011) (T(N,M),M=1,NVC1)
742:                  GO TO 40
743:    30            WRITE (2,6011) (T(N,M),M=1,NVC1,2)
744:    40          CONTINUE
745:       RETURN
746:C
747: 5002 FORMAT (20G0.0)
748:C
749: 6002 FORMAT (1H ,'TIME OF DIST.=',F8.5,1X,'MEAN TEMP.=',F7.2,1X,
750:      1'ROLL TEMP.=',F2.0)
751: 6011 FORMAT (1H ,15F8.2)
752:C
753:       END
754:C
755:       SUBROUTINE CINCREASENUMELMTS (T,G,NVC,NWR,STL,Z,DZ,D2,KPR,NRRX,
756:      1            KPS,A,U,JP,NWR1,D22,WNR,NP,IR,NWRO)
757:C
758:C       SUBROUTINE TO INCREASE THE NUMBER OF ELEMENTS BY A FACTOR
759:C       OF 3, THE ELEMENT THICKNESS IS REDUCED ACORDINGLY AND
760:C       THE NEW ELEMENTS TEMPERATURES EXTRAPOLATED
761:C
762:       DIMENSION  T(61,22),G(60),Z(83),A(60,20),U(20),STL(60),IR(20)
763:C
764:       C13=1./3.
765:       C23=2./3.
766:       C43=4./3.
767:       C16=1./6.
768:       C56=5./6.
769:C
770:       DO 10 M=1,NVC
771:               DO 10 N=1,NWR
772:               T(3*N-1,M)=A(N,M)
773:    10 CONTINUE
774:C
775:       DO 20 M=1,NVC
776:               T4=2.*A(2,M)-A(1,M)-A(3,M)
777:            IF (T4.EQ.0.) GO TO 15
778:               T5=A(3,M)+3.*A(1,M)-4.*A(2,M)
779:               T(1,M)=A(1,M)+(T5**2)/(8.*T4)-T4/2.*(T5/(2.*T4)-C13)**2
780:               T(3,M)=A(1,M)+(T5**2)/(8.*T4)-T4/2.*(T5/(2.*T4)+C13)**2
781:            GO TO 20
782:    15 T(1,M)=(A(1,M)-A(2,M))/3.+A(1,M)
783:                  T(3,M)=2.*(A(1,M)-A(2,M))/3.+A(2,M)
784:    20 CONTINUE
```

```
785:C
786:       NWRO=NWR-1
787:       DO 30 M=1,NVC
788:           DO 30 N=2,NWRO
789:           T4=2.*A(N,M)-A(N-1,M)-A(N+1,M)
790:        IF (T4.EQ.0.) GO TO 25
791:           T5=A(N+1,M)+3.*A(N-1,M)-4.*A(N,M)
792:           T(3*N-2,M)=A(N-1,M)+(T5**2)/(8.*T4)-T4/2.*(T5/(2.*T4)+C23)**2
793:           T(3*N,M)=A(N-1,M)+(T5**2)/(8.*T4)-T4/2.*(T5/(2.*T4)+C43)**2
794:        GO TO 30
795:   25         T(3*N-2,M)=(A(N-1,M)-A(N,M))/3.+A(N,M)
796:              T(3*N,M)=2.*(A(N-1,M)-A(N,M))/3.+A(N,M)
797:   30 CONTINUE
798:C
799:       DO 40 M=1,NVC
800:           T4=2.*A(NWR-1,M)-A(NWR-2,M)-A(NWR,M)
801:           T5=A(NWR,M)+3.*A(NWR-2,M)-A(NWR-1,M)*4.
802:           T6=A(NWR-2,M)+(T5**2)/(8.*T4)-T4/8.*(T5/T4+3.)**2
803:C
804:           T4=2.*A(NWR,M)-T6-U(M)
805:           T5=U(M)+3.*T6-4.*A(NWR,M)
806:C
807:           T(3*NWR-2,M)=T6+(T5**2)/(8.*T4)-2.*T4*(T5/(4.*T4)+C16)**2
808:           T(3*NWR,M)=T6+(T5**2)/(8.*T4)-2.*T4*(T5/(4.*T4)+C56)**2
809:   40 CONTINUE
810:C
811:C
812:C
813:       DO 50 N=1,NWR
814:           G(3*N-1)=STL(N)
815:   50 CONTINUE
816:C
817:       T4=2.*STL(2)-STL(1)-STL(3)
818:       IF(T4.EQ.0.) GO TO 52
819:       T5=STL(3)+3.*STL(1)-4.*STL(2)
820:       G(1)=STL(1)+(T5**2)/(8.*T4)-T4/2*(T5/(2.*T4)-C13)**2
821:       G(3)=STL(1)+(T5**2)/(8.*T4)-T4/2*(T5/(2.*T4)+C13)**2
822:       GO TO 54
823:   52 G(1)=(STL(1)-STL(2))/3.+STL(1)
824:       G(3)=2.*(STL(1)-STL(2))/3.+STL(2)
825:C
826:   54 DO 60 N=2,NWRO
827:           T4=2.*STL(N)-STL(N-1)-STL(N+1)
828:        IF (T4.EQ.0.) GO TO 55
829:           T5=STL(N+1)+3.*STL(N-1)-4.*STL(N)
830:C
831:           G(3*N-2)=STL(N-1)+(T5**2)/(8.*T4)-T4/2.*(T5/(2.*T4)+C23)**2
832:           G(3*N)=STL(N-1)+(T5**2)/(8.*T4)-T4/2.*(T5/(2.*T4)+C43)**2
833:        GO TO 60
834:   55           G(3*N-2)=(STL(N-1)-STL(N))/3.+STL(N)
835:            G(3*N)=2.*(STL(N-1)-STL(N))/3.+STL(N)
836:   60 CONTINUE
837:C
838:       T4=2.*STL(NWR-1)-STL(NWR-2)-STL(NWR)
839:       T5=STL(NWR)+3.*STL(NWR-2)-4.*STL(NWR-1)
840:       T6=STL(NWR-2)+(T5**2)/(8.*T4)-T4/8.*(T5/T4+3.)**2
```

```
841:C
842:       T4=STL(NWR)-T6+A(NWR,NVC)-U(NVC)
843:       T5=3.*T6-A(NWR,NVC)+U(NVC)-3.*STL(NWR)
844:       G(3*NWR-2)=T6+(T5**2)/(8.*T4)-2.*T4*(T5/(4.*T4)+C16)**2
845:       G(3*NWR)=T6+(T5**2)/(8.*T4)-2.*T4*(T5/(4.*T4)+C56)**2
846:C
847:       NWR=3*NWR
848:       NWR0=NWR-1
849:       WNR=FLOAT(NWR)
850:       D2=D2/3.
851:       NWR1=NWR+1
852:       D22=1000.*D2
853:       NRRX=IR(JP)
854:       KPS=KPR
855:       DZ=Z(4*JP)
856:C
857:       DO 70 M=1,NVC
858:           DO 70 N=1,NWR
859:       A(N,M)=T(N,M)
860:    70 CONTINUE
861:C
862:       DO 80 N=1,NWR
863:           STL(N)=G(N)
864:    80 CONTINUE
865:C
866:       NP=JP
867:C
868:       RETURN
869:       END
870:C
871:       SUBROUTINE ADEFINEROLLCOND (DSRY,W,R,RST,F,NVC,RD,SPEED,D2,D1,
872:      1 R1,S1,NWR,TRO,RTO,RLO,H1,IR,THICKN,DZ,B1,B2,B3,B4,NRRX,A5,S8,
873:      1 COND8,R8,Z9,V8,WNR,VNC,TRISE,LOAD,TORQS,RTEMP,Z1,C,C1,P,JP)
874:C
875:C       DEFINE ROLLING CONDITIONS AT THE BEGINNING OF THE PASS
876:C
877:       DIMENSION DSRY(999),W(999),R(999,20),RST(20),F(999,21),SPEED(20),
878:      1                TRO(20),IR(20),RTO(20),RLO(20),THICKN(21),P(20)
879:       COMMON/LINK1/D0,D3,SL,UL,NWR0,NUMINT,STRUCT
880:       COMMON/WORK/E(20),E1(20)
881:C
882:       LOGICAL TRISE,LOAD,TORQS,STRUCT
883:       NAMELIST/CHECKING/CONTLENGTH,STRAIN,STRENGTH,Z9NL
884:C
885:       DO 10 IRCB=1,NVC
886:              DO 10 IRRA=1,NRRX
887:              R(IRRA,IRCB)=RTEMP
888:              RST(IRCB)=RTEMP
889:    10 CONTINUE
890:C
891:C       THERMAL PROPERTIES AND DIMENSIONS OF THE ROLL ELEMENTS
892:C
893:       Z3=RTEMP
894:       S8=527.184
895:       COND8=46.4424
896:       R8=7790
```

```
      A5=1.4*SQRT(DZ*2.*1.E-08*COND8/(S8*R8))
      V8=A5*D1
      DSRY(1)=RD-SQRT(RD**2-2.E+04*A5*RD)
      W(1)=SQRT((RD**2 +(RD-DSRY(1))**2)/2.)
      DS1=DSRY(1)
C
      DO 20 IRRA=2,NRRX
            DSRY(IRRA)=RD-SQRT((RD-DSRY(IRRA-1))**2-A5*2.E+04*RD)
            W(IRRA)=SQRT(((RD-DSRY(IRRA))**2+(RD-DSRY(IRRA-1))**2)
     1/2.)
   20 CONTINUE
C
      B4=SPEED(JP)*DZ/RD
      B1=1.-(THICKN(JP)-THICKN(JP+1))/(2.*RD)
      TE=SQRT(1.-B1*B1)
      B1=ATAN(TE/B1)
      B2=B1-B4/2.
      D0=D2
      D2=(RD*(1-COS(B2))+THICKN(JP+1)/2.)/WNR
C
      C=C1
C
      B3=B1-B4
      D3=(RD*(1.-COS(B3))+THICKN(JP+1)/2.)/WNR
C
C     CALCULATION OF THE TEMPERATURE RISE FOR EACH INTERVAL (Z9)
      IF (TRISE) GO TO 30
      IF (LOAD) GO TO 40
      IF (TORQS) GO TO 50
      IF (STRUCT) GO TO 25
      WRITE(2,7020) Z9
   25 RETURN
   30 Z9=TRO(JP)/IR(JP)
      WRITE(2,7020) Z9
      RETURN
C
C     STRENGTH IS ESTIMATED FROM ALEXANDER'S FORMULAE P=WKL(PI/2+L/H1+H2)
C
   40 CONTLENGTH=SQRT(RD*(THICKN(JP)-THICKN(JP+1)))
      STRENGTH=0.833*RLO(JP)/(VNC*D1*CONTLENGTH*(1.57+CONTLENGTH/(THICKN
     1(JP)+THICKN(JP+1))))
      STRAIN=1.155*ALOG(1/(1-P(JP)))
      Z9=STRENGTH*STRAIN/(R1*S1*IR(JP))
      Z9NL=Z9
      WRITE (2,CHECKING)
C
      WRITE(2,7020) Z9
      RETURN
   50 Z9=RTO(JP)/(2.*D1*VNC*R1*S1*IR(JP)*SQRT(THICKN(JP)*THICKN(JP+1
     1)))
      WRITE (2,7020) Z9
      RETURN
C
 7020 FORMAT (1H ,40X,'TEMP.RAISE DURING INTERVAL:',3X,F6.2)
C
      END
```

```
953:C
954:       SUBROUTINE GADDTEMPRISE (A,U,STL,Z9,Z1,NVC,NWR,SPEED,B0,B3,
955:      1  JP,NOA,RD,T)
956:C
957:C       SUBROUTINE TO ADD THE TEMPERATURE RISE AT EACH INTERVAL DURING
958:C       THE PASS AND IT IS ACCESED AT THE END OF EACH INTERVAL DURING
959:C       THE ROLL CONTACT PERIOD
960:C
961:       DIMENSION T(61,22),A(60,20),NOA(20),U(20),STL(60),SPEED(20)
962:       COMMON/LINK1/D0,D3,SL,UL,NWR0,NUMINT,STRUCT
963:       COMMON/STORE/S(100,8,20),SS(100,8,20)
964:       COMMON/WORK/E(20),E1(20)
965:       COMMON/STRENGTH/S0,B1,B2,EP,C,THICKN(21),RAD(20)
966:       COMMON/LINK2/R1,S1,VNC,WNR,RAVTEM(20),DEFTEM(20)
967:C      EXTERNAL ASINH
968:       LOGICAL STRUCT
969:       IF (STRUCT) GO TO 40
970:C
971:       DO 10 M=1,NVC
972:           DO 10 N=1,NWR
973:           A(N,M)=A(N,M)+Z9
974:   10 CONTINUE
975:C
976:       DO 20 M=1,NVC
977:           U(M)=U(M)+Z9
978:   20 CONTINUE
979:C
980:       DO 30 N=1,NWR
981:           STL(N)=STL(N)+Z9
982:   30 CONTINUE
983:C
984:       Z1=Z1+Z9
985:C
986:       GO TO 80
987:C       TEMPERATURE RISE IS CALCULATED INDIVIDUALLY FOR EACH INTERVAL
988:C       BY NUMERICAL INTEGRATION OF THE STRESS-STRAIN CURVE FOR THE
989:C       AVERAGE TEMPERATURE AND STRAIN RATE OF THE INTERVAL
990:   40 EINC=1.155*ALOG(D0/D3)
991:      E1INC=EINC*SPEED(JP)/(RD*(B0-B3))
992:      NUMINT=10
993:      UL=SL+EINC
994:      Z1=0.
995:C
996:      DO 70 N=2,NWR0,3
997:      NN=N/3+1
998:              NO=NOA(NN)
999:              AREAT=0.
1000:            S0=DEFTEM(NN)
1001:            C=E1INC
1002:C
1003:              DO 50 I=1,NO
1004:              CALL SIMPINT(I,STR,3,AREA,S,NN,JP)
1005:              AREAT=AREAT+S(I,1,NN)*AREA/100.
1006:  50          CONTINUE
1007:C
1008:              AREAT=AREAT*1.E+3
```

```
1009:                Z9=AREAT/(R1*S1)
1010:                STL(N)=STL(N)+Z9
1011:C
1012:                DO 60 M=1,NVC
1013:                A(N,M)=A(N,M)+Z9
1014:              A(N-1,M)=A(N-1,M)+Z9
1015:              A(N+1,M)=A(N+1,M)+Z9
1016:              Z1=Z1+A(N,M)+A(N-1,M)+A(N+1,M)
1017:   60           CONTINUE
1018:C
1019:                IF (N.LT.NWR0) GO TO 70
1020:C
1021:                DO 65 M=1,NVC
1022:                U(M)=U(M)+Z9
1023:   65       CONTINUE
1024:   70 CONTINUE
1025:      SL=UL
1026:      Z1=Z1/(VNC*WNR)
1027:   80 DO 90 M=1,NVC
1028:      DO 90 N=1,NWR
1029:      T(N,M)=A(N,M)
1030:   90 CONTINUE
1031:      RETURN
1032:      END
1033:C
1034:      SUBROUTINE EHEATBETWEENSLABROLL(M,A5,COND8,DZ,V1,V8,S8,R8,NRRX
1035:     1  ,RD,D1,WNR,D2,COND,S1,R1,NVC1,KPS,IPF,NVC,B3,D3,B2,C,Q,R,
1036:     2  DSRY,W,RST,U,T,F,A,NWR,VNC,MATPRINT)
1037:C
1038:C          CALCULATION OF HEAT TRANSFER BETWEEN SLAB AND ROLL
1039:C          AND ROLL TEMPERATURE DISTRIBUTION
1040:C
1041:      DIMENSION R(999,20),DSRY(999),W(999),RST(20),T(61,22),F(999,21),
1042:     1         A(60,20),U(20)
1043:      LOGICAL MATPRINT
1044:C
1045:C
1046:      IRCB=M
1047:      CONST=A5*COND8*DZ/D1
1048:      CONST1=D1*COND8*DZ*1.E-04
1049:      QUOT=V8*S8*R8
1050:      NRRX1=NRRX+1
1051:      RNRX=FLOAT(NRRX)
1052:C
1053:C               BACKWARDS DO LOOP JD IS A DUMMY COUNTER
1054:C
1055:      DO 50 JD=1,NRRX
1056:                IRRA=NRRX1-JD
1057:                HRJ=0
1058:                IF (IRCB.EQ.1) GO TO 10
1059:                HRJ=(R(IRRA,IRCB-1)-R(IRRA,IRCB))*CONST
1060:                IF (IRCB.EQ.NVC)GO TO 20
1061:   10           HRJ=HRJ-(R(IRRA,IRCB)-R(IRRA,IRCB+1))*CONST
1062:   20           IF (IRRA.EQ.1) GO TO 30
1063:                HRJ=HRJ+(R(IRRA-1,IRCB)-R(IRRA,IRCB))*CONST1*(RD-DSRY(IRR
1064:     1          A-1))/(RD*(W(IRRA-1)-W(IRRA)))
```

```
1065:                IF (IRRA.EQ.NRRX) GO TO 40
1066:                HRJ=HRJ-(R(IRRA,IRCB)-R(IRRA+1,IRCB))*CONST1*(RD-DSRY(IRR
1067:     1          A))/(RD*(W(IRRA)-W(IRRA+1)))
1068:                GO TO 40
1069:    30          HRJ=HRJ-(R(IRRA,IRCB)-R(IRRA+1,IRCB))*CONST1*(RD-DSRY(IRR
1070:     1          A))/(RD*(W(IRRA)-W(IRRA+1)))
1071:                D4=(2.*WNR*D2/3.-SQRT(0.4444*(WNR*D2)**2-8.*WNR*COND*DZ/(3
1072:     1          .*S1*R1)))/D2
1073:C
1074:C       HEAT FLOW BETWEEN SLAB AND ROLL
1075:C
1076:                D5=RD**2-2*RD*CONST1/QUOT
1077:                A1=Q/(D1*D2*S1*R1)-HRJ/QUOT
1078:                A2=C*DZ/10.*(1./(D2*R1*S1*COS(B2))+D1*1.E-04/QUOT)
1079:                A3=C/2.*(D3*D4*(WNR-D4/4.)/(WNR*COND*COS(B3))+(RD**2-D5)
1080:     1          /(RD*COND8))
1081:                A3=C*(A(NWR,M)-R(1,IRCB)+A1-A2*(U(M)-RST(IRCB)))/
1082:     1          (9.*A2+A3+1)
1083:                A1=C*(U(M)-RST(IRCB))
1084:                A2=(A1+9.*A3)/10.
1085:C
1086:                T(NWR,M)=A(NWR,M)+Q/(D1*D2*S1*R1)-A2*DZ/(D2*S1*R1*COS(B2))
1087:                U(M)=T(NWR,M)-A3*D3*D4*(WNR-D4/4.)/(2.*WNR*COND*COS(B3))
1088:                F(1,IRCB)=R(1,IRCB)+(HRJ+A2*D1*1.E-04*DZ)/QUOT
1089:                RST(IRCB)=F(1,IRCB)+A3*(RD**2-D5)/(2.*RD*COND8)
1090:                IF (M.EQ.NVC) GO TO 60
1091:                GO TO 110
1092:    40          F(IRRA,IRCB)=R(IRRA,IRCB)+HRJ/QUOT
1093:    50 CONTINUE
1094:C
1095:    60 Z3=0
1096:C
1097:       DO 70 IRCB=1,NVC
1098:              DO 70 IRRA=1,NRRX
1099:              R(IRRA,IRCB)=F(IRRA,IRCB)
1100:              Z3=Z3+R(IRRA,IRCB)
1101:    70 CONTINUE
1102:C
1103:       Z3=Z3/(RNRX*VNC)
1104:       IF (IPF.NE.KPS) GO TO 110
1105:C
1106:C       PRINTING OF ROLL TEMPERATURES AND DISTANCES
1107:C       FROM THE CENTRE  OF THE ROLL
1108:       DO 80 IRCB=1,NVC
1109:              DO 80 IRRA=1,NRRX
1110:              F(1,IRCB)=RST(IRCB)
1111:              F(IRRA+1,IRCB)=R(IRRA,IRCB)
1112:              F(IRRA+1,NVC+1)=W(IRRA)*1000.
1113:    80 CONTINUE
1114:C
1115:       F(1,NVC1)=RD*1000.
1116:C
1117:       WRITE(2,6004) Z3
1118:       IF (.NOT.MATPRINT) GO TO 110
1119:C
1120:       DO 100 IRRA=1,NRRX1
```

```
1121:              IF (NVC.GT.13)GO TO 90
1122:              WRITE (2,6013) (F(IRRA,IRCB),IRCB=1,NVC1)
1123:              GO TO 100
1124:   90         WRITE (2,6013) (F(IRRA,IRCB),IRCB=1,NVC1,2)
1125:  100 CONTINUE
1126:C
1127:  110 RETURN
1128:C
1129: 6004 FORMAT (1HO,10X,'MEAN ROLL TEMP=',2X,F6.2)
1130: 6013 FORMAT (1H ,15F8.2)
1131:C
1132:      END
1133:C
1134:      SUBROUTINE BCHANGED2 (IU,INFINPASS,BO,B2,B3,B4,THICKN,RD,NWR,C1,C
1135:     1                      ,T,A,U,STL,Z9,Z1,NVC,D2,SPEED,JP,NOA)
1136:C
1137:C      SUBROUTINE TO DECREASE ELEMENTAL THICKNESS AFTER EACH
1138:C      INTERVAL DURING THE PASS
1139:C
1140:      DIMENSION THICKN(21),NOA(20),A(60,20),U(20),STL(60),SPEED(20)
1141:      DIMENSION T(61,22)
1142:      COMMON/LINK1/DO,D3,SL,UL,NWRO,NUMINT,STRUCT
1143:      COMMON/STORE/S(100,8,20),SS(100,8,20)
1144:      COMMON/WORK/E(20),E1(20)
1145:      COMMON/LINK2/R1,S1,VNC,WNR,RAVTEM(20),DEFTEM(20)
1146:      IF (IU.EQ.INFINPASS) GO TO 10
1147:      CALL GADDTEMPRISE (A,U,STL,Z9,Z1,NVC,NWR,SPEED,BO,B3,JP,NOA,RD,T)
1148:      BO=B3
1149:      B2=B2-B4
1150:      B3=B3-B4
1151:      DO=D3
1152:      D2=(THICKN(JP+1)/2.+(1.-COS(B2))*RD)/WNR
1153:      D3=(THICKN(JP+1)/2.+(1.-COS(B3))*RD)/WNR
1154:      RETURN
1155:   10 B2=B2-B4/2.
1156:      D2=(THICKN(JP+1)/2.+(1.-COS(B2))*RD)/WNR
1157:      D3=D2
1158:      CALL GADDTEMPRISE (A,U,STL,Z9,Z1,NVC,NWR,SPEED,BO,B3,JP,NOA,RD,T)
1159:      C=C1
1160:      RETURN
1161:      END
1162:C
1163:      SUBROUTINE DDECREASENUMELMTS (NWR,NVC,A,T,G,STL,D,D1,D2,KPAC,
1164:     1           KPS,Z,JP,DZ,WNR,NWR1,D22)
1165:C
1166:C      DECREASES THE NUMBER OF ELEMENTS BY A FACTOR OF 3 AND
1167:C      INCREASES THE ELEMENTAL THICKNESS AT THE END OF THE PASS
1168:C
1169:      DIMENSION A(60,20),T(61,22),G(60),STL(60),D(20),Z(83)
1170:      NWR=NWR/3
1171:      WNR=FLOAT(NWR)
1172:      NWR1=NWR+1
1173:C
1174:      DO 10 M=1,NVC
1175:             DO 10 N=1,NWR
1176:             A(N,M)=(T(3*N-2,M)+T(3*N-1,M)+T(3*N,M))/3.
```

```
1177:                T(N,M)=A(N,M)
1178:    10 CONTINUE
1179:C
1180:       DO 20 N=1,NVC
1181:                G(N)=(STL(3*N-2)+STL(3*N-1)+STL(3*N))/3.
1182:                STL(N)=G(N)
1183:    20 CONTINUE
1184:C
1185:       D2=D2*3.
1186:       D22=1000.*D2
1187:       D1=D1*(1+D(JP)/100.)
1188:       KPS=KPAC
1189:       JP=JP+1
1190:C
1191:       DZ=Z(4*JP-3)
1192:C
1193:       RETURN
1194:C
1195:C
1196:       END
1197:       SUBROUTINE EQUIAXGRAINS (NP,D,I,E0,K,N0,T,T0)
1198:C
1199:C       CALCULATES GRAIN GROWTH AFTER COMPLETE RECRYSTALLISATION
1200:C
1201:       COMMON /STORE/A(100,8,20),B(100,8,20)
1202:       COMMON/CONDIT/T2,T1,Z(20)
1203:       COMMON/WORK/E(20),E1(20)
1204:C
1205:       D=1.
1206:       Z(K)=E1(NP)*EXP(156000/(8.31*(T+273)))
1207:       D1=14.68*Z(K)**(-0.136)*A(I,4,K)**1.3*E0**(-0.33)
1208:     6 B(N0,7,1)=(T2-T1)*EXP((225600/8.31)*(1/(T+273)-1/(T0+273)))
1209:       D2=D1
1210:         B(N0,1,1)=A(I,1,K)
1211:       IF (B(N0,1,1).LT.0.5) GO TO 30
1212:       B(N0,2,1)=A(I,4,K)
1213:       B(N0,3,1)=D1
1214:       B(N0,4,1)=D2
1215:       B(N0,5,1)=0
1216:       B(N0,6,1)=T1
1217:       B(N0,8,1)=T
1218:       GO TO 40
1219:    30 N0=N0-1
1220:    40 RETURN
1221:       END
1222:       SUBROUTINE MIXEDSTRUCT (NP,I,D,E0,K,N0,T)
1223:C
1224:C       THIS SUBROUTINE IS ACCESED WHENEVER A RECRYSTALLISED FRACTION
1225:C       APPEARS FOR THE FIRST TIME AND CALCULATES THE RECRYSTALLISED
1226:C       FRACTION AFTER A COOLING PERIOD
1227:C
1228:       COMMON /STORE/A(100,8,20),B(100,8,20)
1229:       COMMON/CONDIT/T2,T1,Z(20)
1230:       COMMON/WORK/E(20),E1(20)
1231:       B(N0,1,1)=A(I,1,K)*(1-EXP(-0.693*(T2/T1)**2))
1232:       D=1
```

```
1233:       Z(K)=E1(NP)*EXP(156000/(8.31*(T+273)))
1234:       IF (B(NO,1,1).LT.0.5) GO TO 10
1235:       B(NO,2,1)=A(I,4,K)
1236:       EC=500
1237:     5 D1=14.68*(Z(K)**(-0.136))*(A(I,4,K)**1.3)*(E0**(-0.33))
1238:     6 B(NO,3,1)=D1
1239:       B(NO,4,1)=D1
1240:       B(NO,5,1)=0
1241:       B(NO,6,1)=T1
1242:       B(NO,7,1)=0.
1243:       B(NO,8,1)=0.
1244:       GO TO 20
1245:    10 NO=NO-1
1246:    20 NO=NO+1
1247:       B(NO,1,1)=A(I,1,K)-A(I,1,K)*(1-EXP(-0.693*(T2/T1)**2))
1248:       IF (B(NO,1,1).LT.0.5) GO TO 30
1249:       B(NO,2,1)=A(I,4,K)
1250:       B(NO,3,1)=A(I,4,K)
1251:       B(NO,4,1)=A(I,4,K)
1252:       B(NO,5,1)=E0
1253:       B(NO,6,1)=T1
1254:       B(NO,7,1)=0.
1255:       B(NO,8,1)=0.
1256:       GO TO 40
1257:    30 NO=NO-1
1258:    40 RETURN
1259:       END
1260:       SUBROUTINE TEMPCOMPTIME (NP,K,OO,DEFTEM,T5)
1261:C
1262:C       CALCULATES STRUCTURAL CHANGES DURING AIR COOLING
1263:C
1264:       DIMENSION DEFTEM(20)
1265:       COMMON/STRENGTH/THICKN(21)
1266:       COMMON /STORE/ A(100,8,20),B(100,8,20)
1267:       COMMON/TEMP/RMEANT(20),NOA(20),W5,N,T1,SPRT(20),W2(20)
1268:       COMMON/CONDIT/T2,T1,ZP(20),STIME(21)
1269:       COMMON/WORK/E(20),E1(20)
1270:       COMMON/PRIOUT/DIST(20)
1271:       JQ1=NOA(K)
1272:       T=RMEANT(K)
1273:       TO=DEFTEM(K)
1274:       Z=ZP(K)
1275:       D=1.
1276:       T2=W5
1277:       W2(K)=W2(K)+T2*EXP(-225600/(8.31*(T+273)))
1278:       NO=0
1279:C
1280:       DO 170 I=1,JQ1
1281:       NO=NO+1
1282:       T1=A(I,6,K)
1283:C       CALCULATION OF THE ZENER-HOLLOMON PARAMETER
1284:       Z=E1(NP)*EXP(156000/(8.31*(T+273)))
1285:C
1286:       T2=W2(K)*EXP(225600/(8.31*(TO+273)))
1287:       TGG=A(I,8,K)
1288:             IF (T1.GT.T2) GO TO 80
```

```
1289:       IF (A(I,4,K).GT.A(I,3,K)) GO TO 120
1290:            IF (A(I,5,K).NE.0.) GO TO 167
1291:       DO 166 J=1,8
1292:  166 B(NO,J,1)=A(I,J,K)
1293:       GO TO 170
1294:  167 IF (I.EQ.1) GO TO 35
1295:       IF (A(I,6,K).NE.A(I-1,6,K)) GO TO 75
1296:            B(NO,1,1)=A(I,1,K)+A(I-1,1,K)
1297:            B(NO,2,1)=A(I,2,K)
1298:            B(NO,3,1)=A(I-1,3,K)
1299:       GO TO 40
1300:   35 B(NO,1,1)=A(I,1,K)
1301:       B(NO,2,1)=A(I,2,K)
1302:C       CALCULATION OF RECRYSTALLISED GRAIN SIZE
1303:       D1 =14.68*(Z**(-0.136))*(A(I,4,K)**1.3)*(A(I,5,K)**(-0.33))
1304:       B(NO,3,1)=D1
1305:C
1306:   40 B(NO,8,1)=T
1307:       TGG=T
1308:       T2=(T2-T1)*EXP((225600/8.31)*(1/(T+273)-1/(T0+273)))
1309:       B(NO,7,1)=T2
1310:       D2=B(NO,3,1)
1311:            B(NO,4,1)=D2
1312:            B(NO,5,1)=0.
1313:            B(NO,6,1)=A(I,6,K)
1314:       IF (NO.EQ.1) GO TO 170
1315:            DO 70 J=1,8
1316:               B(NO-1,J,1)=B(NO,J,1)
1317:        B(NO,J,1)=0.
1318:   70       CONTINUE
1319:       NO=NO-1
1320:            GO TO 170
1321:   75 CALL EQUIAXGRAINS (NP,A(I,2,K),I,A(I,5,K),K,NO,T,T0)
1322:       GO TO 170
1323:   80       IF (A(I,5,K).NE.0.0) GO TO 169
1324:       DO 168 J=1,8
1325:  168 B(NO,J,1)=A(I,J,K)
1326:       GO TO 170
1327:  169 IF (NO.EQ.1.) GO TO 100
1328:       IF (A(I,6,K).EQ.A(I-1,6,K).AND.A(I,5,K).EQ.A(I-1,5,K))GO TO100
1329:            IF (A(I,6,K).NE.A(I-1,6,K)) GO TO 100
1330:          B(NO,1,1)=A(I,1,K)*(1-EXP(-0.693*(T2/T1)**2))
1331:            B(NO-1,1,1)=B(NO,1,1)+A(I-1,1,K)
1332:       B(NO,1,1)=A(I,1,K)-B(NO,1,1)
1333:            DO 90 J=2,8
1334:            B(NO-1,J,1)=A(I-1,J,K)
1335:            B(NO,J,1)=A(I,J,K)
1336:   90       CONTINUE
1337:       GO TO 170
1338:  100 CALL MIXEDSTRUCT(NP,I,A(I,2,K),A(I,5,K),K,NO,T)
1339:            GO TO 170
1340:  120       IF (A(I,5,K).EQ.0.) GO TO 130
1341:C
1342:C       CALCULATION OF RECRYSTALLISED GRAIN SIZE
1343:       D1=14.68*(Z**(-0.136))*(A(I,4,K)**1.3)*(A(I,5,K)**(-0.33))
1344:            GO TO 140
```

```
1345:  130      D1=A(I,3,K)
1346:  140 CONTINUE
1347:      T2=W5*EXP(-225600/(8.31*(T+273)))
1348:      T2=T2*EXP(225600/(8.31*(T+273)))+A(I,7,K)
1349:      D2=D1
1350:C
1351:           B(NO,4,1)=D2
1352:          B(NO,1,1)=A(I,1,K)
1353:          B(NO,2,1)=A(I,2,K)
1354:          B(NO,3,1)=D1
1355:          B(NO,5,1)=0.
1356:          B(NO,6,1)=A(I,6,K)
1357:          B(NO,7,1)=T2
1358:             B(NO,8,1)=A(I,8,K)
1359:  170 CONTINUE
1360:C
1361:      SUMM=0.
1362:      DO 999 I=1,NO
1363:      SUMM=SUMM+B(I,1,1)
1364:  999 CONTINUE
1365:      AMI=0.
1366:      DO 998 I=1,NO
1367:      IF (B(I,5,1).NE.0.) GO TO 998
1368:      B(I,1,1)=B(I,1,1)+(100.-SUMM)
1369:      AMI=1.
1370:      SUMM=100.
1371:  998 CONTINUE
1372:      IF (AMI.EQ.1.) GO TO 1268
1373:      B(NO,1,1)=B(NO,1,1)+(100.-SUMM)
1374:C
1375: 1268 DO 175 J=1,8
1376:           DO 175 I=1,NO
1377:           A(I,J,K)=B(I,J,1)
1378:  175 CONTINUE
1379:C
1380:      DL=0
1381:      DT=0
1382:      SUM=0
1383:      AVGS=0
1384:      DO 176 I=1,NO
1385:      IF (B(I,5,1).NE.0.) GO TO 176
1386:        SUM=SUM+B(I,1,1)
1387:  176 CONTINUE
1388:      DO 180 I=1,NO
1389:      IF (SUM.GT.99.9999) GO TO 178
1390:      XI=1
1391:      IF (I.EQ.1) GO TO 179
1392:      XI=(B(I,1,1)+B(I-1,1,1))/100.
1393:  179 X=B(I,1,1)/100.
1394:      CONST=EXP(0.866*B(I,5,1))
1395:      IF (B(I,5,1).EQ.0.) GO TO 177
1396:      DL=DL+X/(B(I,2,1)*CONST)
1397:      DT=DT+X*CONST/B(I,2,1)
1398:      GO TO 180
1399:  177 DL=DL+(X**(2./3.)*XI**(1./3.))/B(I,3,1)
1400:      DT=DT+(X**(2./3.)*XI**(1./3.))/B(I,3,1)
```

```
1401:       GO TO 180
1402:   178 DL=DL+B(I,1,1)/(100.*B(I,4,1))
1403:       DT=DT+B(I,1,1)/(100.*B(I,4,1))
1404:   180 CONTINUE
1405:       NOA(K)=NO
1406:       DO 4001 I=1,NO
1407:       IF (T1.GT.T2.OR.A(I,5,K).EQ.0.) GO TO 4001
1408:C
1409:C       CALCULATION OF THE RECRYSTALLISED GRAIN SIZE
1410:       A(I,3,K)=E1(NP)*EXP(156000/(8.31*(T+273)))
1411:       A(I,3,K)=14.68*(A(I,3,K)**(-0.136))*(A(I,5,K)**(-0.33))
1412:       A(I,3,K)=A(I,3,K)*(A(I,4,K)**1.3)
1413: 4001 CONTINUE
1414:       DO 182 I=1,NO
1415:       AVGS=AVGS+A(I,1,K)*A(I,4,K)/100
1416:   182 CONTINUE
1417:       DO 181 I=1,NO
1418:C
1419:C       PRINTING OF DISTANCE FROM THE CENTRE, ROW MEAN TEMPERATURE
1420:C       PERCENT OF MATERIAL, RECRYSTALLISED GRAIN SIZE, ACTUAL GRAIN
1421:C       SIZE AND AVERAGE GRAIN SIZE
1422:C
1423:       WRITE(2,7000) (DIST(K),T,A(I,1,K),A(I,5,K),A(I,3,K),
1424:      1    A(I,4,K),AVGS)
1425:   181 CONTINUE
1426:       WRITE(4,7030) K,T,AVGS,TI
1427:       RETURN
1428:C
1429: 7000 FORMAT (1H ,1F9.2,8X,1F7.2,11X,1F6.2,9X,
1430:      1  1F5.3,8X,1F7.2,9X,1F7.2,8X,1F7.2,8X,F6.2)
1431: 7030 FORMAT (1H ,I3,3(2X,F10.2))
1432:C
1433:       END
1434:C
1435:       SUBROUTINE LOAD (K,T,A,NO,N)
1436:C
1437:C       CALCULATES LOAD AND TORQUE IN THE PASS FROM SIMS THEORY
1438:C
1439:       DIMENSION A(100,8,20)
1440:       COMMON/WORK/E(20),E1(20)
1441:       COMMON/STRENGTH/SO,B1,B2,EP,C,H(21),R(20)
1442:       COMMON/LINK1/DO,D3,SL,UL,NWRO,NUMINT,STRUCT
1443:       SO=T
1444:       C=E1(N)
1445:C
1446:             STRTOR=0.
1447:             STRLOAD=0.
1448:       DO 10 I=1,NO
1449:C
1450:C      THE SUBROUTINE FOR NUMERICAL INTEGRATION IS CALLED HERE
1451:C
1452:             CALL SIMPINT (I,STR,1,AREA,A,1,N)
1453:           STRTOR=STRTOR+A(I,1,K)*STR/100.
1454:             CALL SIMPINT(I,STR,2,AREA,A,1,N)
1455:             STRLOAD=STRLOAD+A(I,1,K)*STR/100.
1456:    10 CONTINUE
```

```
1457:C
1458:       ALPHA=1-(H(N)-H(N+1))/(2.*R(N))
1459:       ALPHA=ATAN (SQRT(1-ALPHA**2)/ALPHA)
1460:       TETHA=(ATAN(ALPHA*((R(N)/H(N+1))**(0.5)))-0.785*ALOG (H(N)/
1461:      1       H(N+1))*((R(N)/H(N+1))**(-0.5)))/2.
1462:       TETHA=((R(N)/H(N+1))**(-0.5))*SIN(TETHA)/COS(TETHA)
1463:       HN=H(N+1)+2.*R(N)*(1-COS(TETHA))
1464:       QP=SQRT(H(N+1)/(4*(H(N)-H(N+1))))*(3.14159*ATAN(((H(N)-H(N+1))/
1465:      1  H(N+1))**0.5)-((R(N)/H(N+1))**0.5)*ALOG(HN**2/(H(N)*H(N+1))))
1466:      2      -0.785
1467:C
1468:C       CALCULATION AND PRINTING OF LOAD AND TORQUE OF THE PASS
1469:       FLOAD=STRLOAD*SQRT(R(N)*(H(N)-H(N+1)))*QP
1470:       TORQUE=2.*R(N)*R(N)*STRTOR*(ALPHA/2.-TETHA)
1471:       TNL=T
1472:       NAMELIST/NL1/QP,SO,B1,EP,AO,C,STRLOAD,STRTOR,ALPHA,TETHA,HN,TNL
1473:       WRITE (2,NL1)
1474:       WRITE (2,8000) FLOAD,TORQUE
1475:       RETURN
1476: 8000 FORMAT (1H ,'LOAD(KN/M):',1F16.4,10X,'TORQUE(KN-M/M):',1F16.4)
1477:       END
1478:C
1479:       SUBROUTINE SIMPINT (I,STR,L,AREA,A,K,N)
1480:C
1481:C       NUMERICAL INTEGRATION BY SIMPSOM METHOD
1482:C
1483:       DIMENSION A(100,8,K)
1484:       COMMON/WORK/E(20),E1(20)
1485:       COMMON/STRENGTH/SO,B1,B2,EP,C,H(21),R(20)
1486:       COMMON/LINK1/DO,D3,SL,UL,NWRO,NUMINT,STRUCT
1487:       EXTERNAL FUNCT
1488:       IF (L.EQ.2) GO TO 10
1489:       IF (L.EQ.3) GO TO 25
1490:       SL=0.
1491:       UL =E(N)
1492:       GO TO 20
1493:    10 UL=0.
1494:       SL=1-(H(N)-H(N+1))/(2.*R(N))
1495:       SL=ATAN (SQRT(1-SL**2)/SL)
1496:    20 FA=FUNCT(SL,L,N,I,A,1)
1497:       FB=FUNCT(UL,L,N,I,A,1)
1498:       NUMINT=ABS ((UL-SL)/0.02)
1499:       KK=MOD(NUMINT,2)
1500:       NUMINT=NUMINT+KK
1501:       GO TO 27
1502:    25 FA=FUNC1(SL,I,A,K)
1503:       FB=FUNC1(UL,I,A,K)
1504:    27 DELTA=(UL-SL)/NUMINT
1505:       M1=NUMINT-1
1506:       M2=NUMINT-2
1507:C
1508:       FODD=0.
1509:       DO 30 J=1,M1,2
1510:            VALUE=J*DELTA
1511:            F=FUNCT(VALUE,L,N,I,A,K)
1512:            FODD=FODD+F
```

```
1513:   30 CONTINUE
1514:C
1515:      FEVEN=0.
1516:      DO 40 J=2,M2,2
1517:            VALUE=J*DELTA
1518:            F=FUNCT(VALUE,L,N,I,A,K)
1519:            FEVEN=FEVEN+F
1520:   40 CONTINUE
1521:C
1522:C      CALCULATION OF THE STRESS
1523:C
1524:      AREA=DELTA*(FA+FB+4*FODD+2.*FEVEN)/3.
1525:      STR=AREA/(UL-SL)
1526:      RETURN
1527:      END
1528:C
1529:C
1530:C      FUNCTION THAT DISTINGUISH BETWEEN THE VALUES OF THE MEAN
1531:C      FLOW STRESS USED FOR LOAD AND TORQUE CALCULATIONS
1532:      FUNCTION FUNCT(VALUE,L,N,I,A,K)
1533:      DIMENSION A(100,8,K)
1534:      COMMON/STRENGTH/S0,B1,B2,EP,C,H(21),R(20)
1535:      EXTERNAL FUNC1,FUNC2
1536:      IF (L.EQ.1.OR.L.EQ.3) FUNCT=FUNC1(VALUE,I,A,K)
1537:      IF (L.EQ.2) FUNCT=FUNC2(VALUE,N,I,A,K)
1538:      RETURN
1539:      END
1540:C
1541:      FUNCTION FUNC1(VALUE,I,A,K)
1542:C      DEFINE THE STRESS AS A FUNCTION OF THE ACCUMULATED STRAIN FOR
1543:C      TORQUE AND TEMPERATURE RISE CALCULATIONS
1544:      DIMENSION A(100,8,K)
1545:      COMMON/STRENGTH/S0,B1,B2,EP,C,H(21),R(20)
1546:      ZENER=C*EXP(156000/(8.31*(S0+273)))
1547:      IF (ZENER.LE.1.4565E9) ZENER=1.4565E9
1548:      SIGMA005=16.16*ALOG10(ABS(ZENER/5.5807E8))
1549:      SIGMASS=18.88*ALOG10(ABS(ZENER/1.4565E9))
1550:      STRAIN=ABS(VALUE+A(I,5,K))
1551:      IF (SIGMASS.LE.0) GOTO 8
1552:      IF (SIGMA005.GE.SIGMASS) GOTO 9
1553:      C0=20*ALOG(1/(1-(SIGMA005/SIGMASS)**10))
1554:      SIGMA=SIGMASS*(1-EXP(-C0*(STRAIN)))**0.1
1555:      FUN=1155*SIGMA
1556:      FUNC1=FUN
1557:      GOTO 10
1558:    8 SIGMA=SIGMA005
1559:      FUN=1155*SIGMA
1560:      FUNC1=FUN
1561:      GOTO 10
1562:    9 SIGMA=SIGMASS*(1-EXP(-76.57*STRAIN))**0.1
1563:      FUN=1155*SIGMA
1564:      FUNC1=FUN
1565:   10 RETURN
1566:      END
1567:C
1568:      FUNCTION FUNC2(VALUE,N,I,A,K)
```

```
1569:C      DEFINE THE STRESS LEVEL FOR LOAD CALCULATIONS
1570:       DIMENSION A(100,8,K)
1571:       COMMON/STRENGTH/SO,B1,B2,EP,C,H(21),R(20)
1572:       VAL=ABS(1.155*ALOG(H(N)/(H(N+1)+2.*R(N)*(1-COS(VALUE)))))
1573:       ZENER=C*EXP(156000/(8.31*(SO+273)))
1574:       IF (ZENER.LE.1.4565E9) ZENER=1.4565E9
1575:       SIGMA005=16.16*ALOG10(ABS(ZENER/5.5807E8))
1576:       SIGMASS=18.88*ALOG10(ABS(ZENER/1.4565E9))
1577:       STRAIN=ABS(VAL+A(1,5,K))
1578:       IF (SIGMASS.LE.0) GOTO 8
1579:       IF (SIGMA005.GE.SIGMASS) GOTO 9
1580:       CO=20*ALOG(1/(1-(SIGMA005/SIGMASS)**10))
1581:       SIGMA=SIGMASS*(1-EXP(-CO*(STRAIN)))**0.1
1582:       FUN=1155*SIGMA
1583:       FUNC2=FUN
1584:       GOTO 10
1585:     8 SIGMA=SIGMA005
1586:       FUN=SIGMA*1155
1587:       FUNC2=FUN
1588:        GOTO 10
1589:     9 SIGMA=SIGMASS*(1-EXP(-76.57*STRAIN))**0.1
1590:       FUN=1155*SIGMA
1591:       FUNC2=FUN
1592:    10 RETURN
1593:       END
1594:       FINISH
```

APPENDIX II

Determination of the Surface Heat Transfer Coefficient

The computational model used in the determination of the temperature distribution of the specimens tested under plane strain compression conditions, required the calculation of the constants "b" and "c" of the equation that rules the surface heat transfer from the test furnace to the deformed specimen during the intervals between deformations. As has already been pointed out, the difference in temperature between the test furnace and tools gave rise to a decrease in the mean specimen temperature during deformation. Therefore, during an interpass period there will be an increase in the mean temperature due to both conduction from the undeformed shoulders and convection and radiation from the test furnace. The last two processes are included in the equation:

$$H = b(Ts - To) + c(Ts^4 - To^4) \qquad .....(4.16)$$

whose terms have already been described in Section 4.6. Therefore, in order to determine "b" and "c" in equation (4.16) a series of experiments was carried out in which standard lubricated specimens were transferred from room temperature to the test furnace at different temperatures and the centre temperature of the specimen recorded as a function of time. The temperature-time curves obtained were used in the calculation of "H" and "Ts" according to:

$$H = \rho sa \dot{T} \qquad .....(4.21)$$

and

$$Ts = To + \frac{s\rho\dot{T}a^2}{2k} \qquad .....(4.22)$$

respectively. All the terms of both equations have also been defined in Section 4.6. The present appendix describes the mathematical procedure used in the determination of constants "b" and "c" of equation (4.16), which has been carried out assuming that "To" remains constant throughout the experiment, which is not absolutely true, since a slight decrease in the furnace temperature was observed as soon as the specimen was transferred, but that gradually levelled up to its initial value. Thus, the standard "method of least squares" [179] was applied and the regression curve between "H" and "Ts" traced.

The difference between any value of "H" as determined from equation (4.21), which can be considered an experimental value and that given by equation (4.16), a predicted one, can be defined as:

$$e_i = H - [b(Ts-To) - c(Ts^4-To^4)] \qquad .....(A-1)$$

the least squares estimates of "b" and "c" are obtained by choosing the values which minimize the sum of squares of these differences given by:

$$s = \sum_{i=1}^{n} \{H_i - b[(Ts)_i - To] - c[(Ts)_i^4 - To^4]\}^2 \qquad .....(A-2)$$

The minimisation of s is carried out by calculating $\partial s/\partial b$ and $\partial s/\partial c$, setting both these partial derivatives equal to zero, and solving the two simultaneous equations to obtain the least squares estimates of "b" and "c".

Thus, by setting

$$(Ts)_i - To = T_i$$

and

$$(Ts)_i^4 - To^4 = T_i'$$

then:

$$e_i^2 = (H_i - bT_i - cT_i')^2$$

and:

$$s = \Sigma\,(H_i - bT_i - cT_i')^2$$

However,

$$\frac{\partial s}{\partial b} = \Sigma\ 2(H_i - bT_i\ cT_i')(-T_i) = 0$$

which results in:

$$\Sigma H_i T_i - b\Sigma T_i^2 - c\Sigma T_i' T_i = 0 \qquad .....(A\text{-}3)$$

Similarly:

$$\frac{\partial s}{\partial b} = \Sigma 2(H_i - bT_i - cT_i')(-T_i') = 0$$

giving that:

$$\Sigma H_i T_i' - b\Sigma T_i T_i' - c\Sigma (T_i')^2 = 0 \qquad .....(A\text{-}4)$$

Equations (A-3) and (A-4) can be re-arranged as:

$$b\Sigma T_i^2 + c\Sigma T_i' T_i = \Sigma H_i T_i$$

$$b\Sigma T_i T_i' + c\Sigma (T_i')^2 = \Sigma H_i T_i'$$

Setting $\Delta = \begin{vmatrix} \Sigma T_i^2 & \Sigma T_i' T_i \\ \Sigma T_i T_i' & \Sigma (T_i')^2 \end{vmatrix} = (\Sigma T_i^2)(\Sigma (T_i')^2) - (\Sigma T_i T_i')^2$

which leads to:

$$\Delta = \Sigma((Ts)_i - To)\ \Sigma((Ts)_i^4 - To^4)^2 - \Sigma((Ts)_i - T_o)((Ts)_i^4 - To^4)^2$$

Therefore, b and c can be readily obtained:

$$b = \frac{\Sigma(H_i T_i)\ \Sigma(T_i')^2 - \Sigma(H_i T_i')\ \Sigma(T_i T_i')}{\Delta}$$

and

$$c = \frac{\Sigma(T_i)^2\ \Sigma(H_i T_i') - \Sigma(T_i T_i')\ \Sigma(H_i T_i)}{\Delta}$$

Figure 163 constitutes an example of the use of these equations in the determination of "b" and "c" during heating of a standard specimen at 495°C. This Figure also includes the resulting equation for "H".

However, it is important to point out that similar experiments were carried out at different temperatures and that slightly different values of "b" and "c" were obtained, presumably due to the inherent experimental uncertainties. Therefore, the final equation used to describe the surface heat transfer coefficient was found to be:

$$-H(J/m^2s) = 10.255\ (Ts-To) + 4.8244 \times 10^{-8}(Ts^4-To^4) \qquad .....(A-5)$$

This equation can be used to re-calculate the temperature vs. time curve of a specimen heated up from room temperature to any other temperature inside the test furnace. Figure 164 shows a comparison between the experimental and the computer predicted curves of the specimen heated up to 495°C. The close agreement found indicates that equation (A-5) can be used satisfactorily in the calculation of the temperature changes that occur in the specimen after deformation, particularly important in multiple-pass deformation sequences with short time intervals between deformations.

This procedure was also applied in the determination of the equations of "H" that rule the air cooling process of both lubricated and non-lubricated standard plane strain compression specimens. Thus, it was found that for non-lubricated specimens the air cooling of a specimen can be described by:

$$-H(J/m^2s) = 15.381\ (T-To) + 1.8212 \times 10^{-8}\ (Ts^4-To^4) \qquad .....(A-6)$$

whereas that for lubricated ones:

$$-H(J/m^2s) = 16.066\ (T-To) + 3.6103 \times 10^{-8}\ (Ts^4-To^4) \qquad .....(A-7)$$

The use of equations (A-6) and (A-7) can be observed in Figure 165 in which the experimental cooling curves obtained in both cases are compared with their respective computer predictions.

At this stage it is also important to mention that constant "c" in equation (4.16) also represents the product of the emmissivity of the material and the Stefan-Boltzman coefficient (5.67×10^{-8} J/m^2s):

$$c = 5.67 \times 10^{-8} \varepsilon$$

It is, therefore, observed that for non-lubricated specimens $\varepsilon \simeq 0.32$ and that for lubricated specimens $\varepsilon \simeq 0.64$, indicating that the radiation term can be increased by a factor of two because of the presence of a graphite film on the surface of the specimen. Although the reasons to account for this phenomenon are somewhat unclear, it is believed that the apparent increase in emmissivity arises because of the increase in surface roughness of the specimen, which has also been reported to increase the emmissivity of chromium-plated steels [74].

REFERENCES

1. R.S. Clegg and C.M. Jackson, Met.Tech., 1975, 3, 120-129.
2. E.F. Emley, Internat. Met. Rev., 1976, 6, 75-115.
3. C.M. Jackson and E.H. Welch, Sheet Metal Ind., 1975, 52, 34-.
4. E. Buschmann, Z. Metallkunde, 1968, 59, 372-.
5. A.J. Bryant, Met.Tech., 1975, 1, 21-32.
6. P. Band and J.G. Harris, Met.Tech., 1975, 7-8, 287-293.
7. J.M. Alexander, Proc. Inst. Mech. Eng., 1955, 109, 1021-1028.
8. F.A.A. Crane and J.M. Alexander, J.Inst. Metals, 1968, 96, 289-.
9. H. Ford and J.M. Alexander, J. Inst. Metals, 1963-64, 92, 397-.
10. C.M. Sellars, "Aluminium Transformation Technology and Applications", A.S.M., Metals Park, Ohio, 1980, 405-440.
11. L.J. Cartmell, F. King and G. Salt, Met. Tech., 1975, 7-8, 313-317.
12. L.F. Mondolfo, "Aluminium Alloys. Structure and Properties", Butterworths, London-Boston, 1976.
13. J.C. Blade, "Private Communication", Alcan International Ltd., Banbury, 1980.
14. Interview, "Rogerstone Hot-Line Upgraded to Modern Aluminium-Rolling Standards", Metals and Mat., 1981, 9, 34-38.
15. A.J. Swain, Met. Tech., 1975, 7-8, 378-381.
16. R. Iricibar, C. Pampillo and H. Chia, "Aluminium Transformation Technology and Applications", A.S.M., Metals Park Ohio, 1980, 241-303.
17. C.M. Sellars and W.J. Mc. G. Tegart, International Met. Rev., 1972, 17, (158), 1-24.

18. J.C. Blade, A.J. Bryant and A.T. Thomas, Metals Tech., 1976, 8, 380-389.

19. J.C. Blade, Metal Sci., 1979, 3-4, 206-210.

20. R.T. Thorley and G.E.G. Tucker, J. Inst. Metals, 1961-62, 90, 374-.

21. R.E. Zinkham, Trans. AIME, 1969, 245, 1519-1525.

22. E. Hornbogen and H. Kreye, "Textures in Research and Practice", (ed. J. Grewen and G. Wasserman), Springer, Hamburg, 1969, 274.

23. J.J. Jonas, C.M. Sellars and W.J. Mc.G. Tegart, Met. Rev., 1969, 14, (130), 1-23.

24. J.H. Beynon, Ph.D. Thesis, University of Sheffield, 1979.

25. M.M. Farag, Ph.D. Thesis, University of Sheffield, 1964.

26. J.R. Cotner, Ph.D. Thesis, University of Sheffield, 1966.

27. H.P. Stuwe, Z. Metallkunde, 1965, 56, 633-642.

28. J.M. Alexander, J. Mech. Phys. Solids, 1955, 3, 323-.

29. D. Hardwick and W.J. McG. Tegart, Mem. Sci. Rev. Met., 1961, 58, 869-880.

30. S.J. Patterson, Ph.D. Thesis, University of London, 1981.

31. M.A. Zaidi, Ph.D. Thesis, University of London, 1980.

32. C.J. Ball, Philosophical Magazine, 2, 1957, 1011-1017.

33. R.P. Carreker Jr. and W.B. Hibbard Jr., Trans. AIME, 209, 1957, 1157-1163.

34. J.G. Morris, Mat. Sci and Engineering, 13, 1974, 101-108.

35. J.G. Morris and B.J. Roopchard, ibid., 17, 1975, 77-80.

36. R.R. Arnold and R.J. Parker, J. Inst. Metals, 1959-60, 88, 255-259.

37. J.E. Hockett, Trans. Met. Soc. AIME, 1967, 239, 969-976.

38. J.F. Alder and V.A. Phillips, J.Inst. Metals, 1954-55, 83, 80-86

39. R.W. Evans and G.R. Dunstan, J. Inst. Metals, 99, 1971, 4-14.

40. J.L. Chiddister and L.E. Malvern, Exp. Mech., 8, 1968, 1-9.

41. M. Motomura, S. Shimamura and T. Nishimura, J. Japan Inst. Light Metals, 26, 1976, 432-440.

42. S.K. Samanta, J. Mech. Phys. Solids, 19, 1971, 117-135, and Int. J. Mech. Sci., 11, 1969, 433-453.

43. W.A. Wong and J.J. Jonas, Trans. Met. Soc. AIME, 242, 1968, 2271-2280.

44. M.M. Farag and C.M. Sellars, J. Inst. Metals, 101, 1973, 137-145.

45. D. Raybould and T. Sheppard, ibid, 65-72.

46. A.F. Castle and T. Sheppard, Metals Tech., 1976, 3, 454-464.

47. M.M. Farag and C.M. Sellars, Metals Tech., 1975, 2, 220-228.

48. J.E. Hockett, Proc. Amer. Soc. Test. Mat., 1959, 59, 1309-1319.

49. J.A. Bailey and A.R.E. Singer, J. Inst. Metals, 1963-64, 92, 404-408.

50. J.J. Jonas, H.J. McQueen and W.A. Wong, "Deformation Under Hot Working Conditions", (ed. P. Moore), special report No. 108, 1968, London (Iron and Steel Inst.), 49-59.

51. H. Ormerod and W.J. Mc.G. Tegart, J. Inst. Metals, 1960-61, 89, 94-96.

52. D.S. Fields and W.A. Backofen, Proc. Amer. Soc. Test. Mat., 1957, 57, 1259-.

53. C.M. Sellars and W.J. Mc.G. Tegart, Mem. Sci. Rev. Met., 63, 1966, 731-746.

54. C. Zener and J. Hollomon, J. App. Phys., 1944, 15, 22-32.

55. J.A. Bailey, S.L. Haas and M.K. Sah, Int. J. Mech. Sci., 14, 1972, 735-754.

56. P.R. Swann, "Electron Microscopy and Strength of Metals", Interscience, 1963.

57. K. Tanaka and T. Nojima, Proc. 19th Japan Congress on Materials Research, 1976, 48-52.

58. K. Tanaka and T. Nojima, Proc. 20th Japan Congress on Materials Research, 1977, 89-93.

59. E. Voce, J. Inst. Metals, 1948, 74, 536, 760-771; Engineer, 1953, 195, 53-; Metallurgia, 1953, 51, 219-.

60. J.P. Sah, G.J. Richardson and C.M. Sellars, J. Australian Inst. Metals, 1969, 14, 292-297.

61. G. Glover, Ph.D. Thesis, University of Sheffield, 1969.

62. S.K. Samanta, "Deformation under Hot Working Conditions", (ed. P. Moore), special report No. 108, 1968, London (Iron and Steel Inst.), 122-130.

63. R.A.C. Slater, W. Johnson and S.Y. Aku, International J. Mech. Sci., 1968, 10, 169-.

64. J.H. Hollomon and J.D. Lubahn, Phys. Rev., 1946, 70, 755-.

65. J.D. Lubahn, J. Appl. Mech., 1947, 14, A229.

66. N. Perrone, ibid., 1966, 33, 210-.

67. G.E. Dieter, "Mechanical Metallurgy", 1976, New York and London (McGraw-Hill).

68. G.W. Rowe, "Principles of Industrial Metal Working Processes", 1977, London (E. Arnold).

69. W. Johnson and P.B. Mellor, "Engineering Plasticity", 1978, New York and London (Van Nostrand).

70. G.C. Cornfield and R.H. Johnson, J.I.S.I., 1973, 211, 567-573.

71. R.A. Harding, Ph.D. Thesis, University of Sheffield, 1976.

72. R.E. Hughes, M.Met. Thesis, University of Sheffield, 1973.

73. L.A. Leduc, Ph.D. Thesis, University of Sheffield, 1980.

74. S.R. Foster, Ph.D. Thesis, University of Sheffield, 1982.

75. T. Sheppard and S. Wright, Metals Tech., 1980, 7, 274-281.

76. A.M. Irrisari, "Private Communication", University of Sheffield, 1982.

77. F. Castro, M.Met. Thesis, University of Sheffield, 1982.

78. J.P. Sah, and C.M. Sellars, "Hot Working and Forming Processes", Ed. C.M. Sellars and G.J. Davies, Metals Soc., London, 1980, 62-.

79. J.J. Urcola, "Private Communication", University of Sheffield, 1979.

80. C.M. Sellars and J.A. Whiteman, Metals Tech., 1981, 1, 10-21.

81. H.J. McQueen and J.J. Jonas, "Recovery and Recrystallisation During High Temperature Deformation", Treatise on Materials Science and Technology, Vol.6, 404-493, 1975, New York, Academic Press.

82. J.W. Martin and R.D. Doherty, "Stability of Microstructure in Metallic Systems", 1980, Cambridge University Press, (ed. R.W. Cahn).

83. D.L. Holt, J. Appl. Phys., 1970, 41, 3197-3201.

84. T. Sheppard and M.A. Zaidi, Metals Tech., 1982, 2, 52-59.

85. J.G. Byrne, "Recovery, Recrystallisation and Grain Growth", 1965, Macmillan, New York.

86. R.W. Cahn, "Physical Metallurgy", (ed. R.W. Cahn), 925-987, Wiley, New York.

87. H.J. McQueen, W.A. Wong and J.J. Jonas, Can. J. Phys., 1967, 45, 1225-1235.

88. S.F. Exell and D.H. Warrington, Phil. Mag., 1972, (8), 26, 1121-1136.

89. M.A. Zaidi and T. Sheppard, Metal Sci., 1982, 5, 229-238.

90. D.J. Abson and J.J. Jonas, Metal Sci. J., 1970, Vol.4, 24-28.

91. J. Cotner and W.J. Mc.G. Tegart, J. Inst. Metals, 1969, Vol.97, 73-79.

92. J.P. Airey, Ph.D. Thesis, University of Sheffield, 1964.

93. W.A. Wong, Ph.D. Thesis, McGill University, 1967.

94. I.S. Servi, J.T. Norton and N.J. Grant, Trans. Amer. Inst. Min. Met. Eng., 1952, 194, 965-.

95. D. McLean and M.H. Farmer, J. Inst. Metals, 1956-57, 87, 41-; D. McLean, ibid, 1952-53, 81, 287-.

96. H.J. McQueen and J.E. Hockett, Met. Trans., 1970, 1, 2997-3004.

97. W.A. Wood and W.A. Rachinger, J. Inst. Metals, 1949, 76, 237-253.

98. M.M. Farag, C.M. Sellars and W.J. Mc.G. Tegart, "Deformation Under Hot Working Conditions, (ed. P. Moore), Special Report No. 108, 1968, London (Iron and Steel Inst.), 60-67.

99. O. Kosik, D.J. Abson and J.J. Jonas, J.I.S.I., 1971, 209, 624-671.

100. H.J. McQueen, "Thermomechanical Processing of Aluminium Alloys", Proc. of a Symposium sponsored by the TMS-AIME Heat Treatment Committee at the TMS fall meeting in St. Louis, Missouri, October, 1978.

101. D. Kuhlman-Wilsdorf, "Work Hardening", (eds. J.P. Hirth and J. Weertman), 1968, 97-132, Gordon and Breach, New York.

102. O.D. Sherby, R.H. Klundt and A.K. Miller, Met. Trans., A, 1977, Vol. 8A, 843-850.

103. J.P.A. Immarigeon and J.J. Jonas, Acta. Met., 1971, Vol.19, 1053-1061.

104. V.K. Lindroos and H.M. Miekk-Oja, Phil. Mag.,1967, Vol.16, 593-610.

105. V.K. Lindroos and H.M. Miekk-Oja, ibid, 1968, Vol.17, 119-133.

106. D.R. Barraclough, Ph.D. Thesis, University of Sheffield, 1974.

107. J.E. Bird, A.K. Mukherjee and J.E. Dorn, "Quantitative Relation Between Properties and Microstructure", (eds. D.G. Brandon and A. Roser), 255-342.

108. J.J. Jonas and H.J. McQueen, Trans. Soc. Mfr. Eng., 1973, 2, 209-233.

109. H.J. McQueen, Met. Trans. A., 1977, Vol.8A, 807-824.

110. A.H. Cottrell and R.J. Stokes, Proc. Roy. Soc., (London), 1955, Vol. A233, 17-34.

111. T.B. Vaughan, "Deformation Under Hot Working Conditions", (ed. P. Moore), Special Report No.108, 1968, London (Iron and Steel Inst.), 68-77.

112. K.J. Gardner and R. Grimes, Metal Sci., 1979, 3-4, 216-222.

113. T. Sheppard and M.G. Tutcher, Metal Sci., 1980, 12, 579-589.

114. I.L. Dillamore, R.E. Smallman and W.T. Roberts, Phil. Mag., 1964, 9, 517-.

115. D. Dew-Jones, Acta. Met., 1960, 8, 816-.

116. T. Sheppard, M.G. Tutcher and H.M. Flower, Metal Sci., 1979, 8, 473-481.

117. G.J. Richardson, C.M. Sellars and W.J. Mc.G. Tegart, Acta. Met., 1966, 14, 1225-1236.

118. P. Tardy and S.S. Iskander, J. Mat. Sci., 1969, 4, 353-.

119. P. Cotterill and P.R. Mould, "Recrystallisation and Grain Growth in Metals", 1976, Surrey University Press, London p.341.

120. V. Koster and E. Hornbogen, Z. Matallk., 1968, 59, 792-.

121. H. Ahlborn, E. Hornbogen and V. Koster, J. Mat. Sci., 1969, 4, 944-.

122. F. Haessner,"Systematic Survey and Fundamental Problems of Recrystallisation" and "Recrystallisation of Metallic Materials", 1970, (ed. F. Haessner), Stuttgart, 159-194.

123. A.J. McEvily Jr., J.B. Clark, E.C. Utley and W.E. Herrnstein III Trans. Met. Soc. AIME, 1963, 227, 1093-.

124. A. Abel and R.K. Ham, Acta. Met., 1966, 14, 1495-.

125. R.K. Ham, Can. Met. Quart., 1966, 5, 161-.

126. R. Lombry, C. Rossard and B.J. Thomas, "Contribution a L'etude des Mecanismes de Deformation et D'adoucissement Dynamique des aciers Fe-Cr Ferritiques dans les Conditions du Formage a Chaud", October 1979, IRSID.

127. R.W. Cahn, "Recrystallisation, Grain Growth and Textures", 1966, (ed. H. Margolin), American Society for Metals, Cleveland, Ohio and "Recrystallisation of Metallic Materials", 1970, (ed. F. Haessner), Stuttgart, p.43.

128. R.D. Doherty, Metal Sci. J., 1974, 8, 132-.

129. R.D. Doherty and R.W. Cahn, J. Less-Common Metals, 1972, 28, 279-.

130. D. Turnbull, Trans. Met. Soc. AIME, 1951, 19, 661-.

131. K. Lucke, Z. Metallk., 1961, 52, 1-.

132. P. Lacombe and A. Berghezan, Metauz Sa Corrosion, 1949, 25, 1-.

133. T.J. Tiedema, W. May and W.J. Burgers, Acta. Cristallogr., 1949, 2, 151-154.

134. J.W. Christian, "Phase Transformation", (ed. R.W. Cahn), Wiley, New York, 525.

135. R.A. Vandermeer and P. Gordon, "Recovery and Recrystallisation of Metals", 1963, Interscience Publ., New York, p.211.

136. G. Glover and C.M. Sellars, Met. Trans. 1972, 3, 2271-2280.

137. C.M. Sellars, "The Physical Metallurgy of Hot Working", Sheffield International Conference on Hot Working and Forming Processes, 1980, Metals Soc., London.

138. D.R. Barraclough and C.M. Sellars, Metal Sci., 1979, 3-4, 257-267.

139. H.J. Whittaker, Ph.D. Thesis, University of Sheffield, 1973.

140. R.B. Sims, Proc. Inst. Mech. Eng., 1954, 168, 191-200.

141. A. Helmi and J.M. Alexander, J.I.S.I., 1969, 207, 1219-1231.

142. S. Ekelund, "The Analysis of Factors Influencing Rolling Pressure and Power Consumption in the Hot Rolling of Steel", 1933, 93, 8-14.

143. R. Sandstrom and R. Lagneborg, Acta. Met., 1975, 23, 481-488.

144. C. Perdix and F. Montheillet, Proc. 5th Int. Conf. 'Strength of Metals and Alloys', Aachen, Germany, 1979, 571-576.

145. A.B. Watts and H. Ford, Proc. Inst. Mech. Eng., 1955, 169, 1141-.

146. C.M. Sellars, J.P. Sah, J.H. Beynon and S.R. Foster, "Plane Strain Compression Testing at Elevated Temperatures", 1976, Report on research work supported by Science Research Council Grant No. B/RG/1481.

147. J.F.W. Bishop, J. Mech. Phys. Solids, 1958, 6, 132-.

148. R.W. Evans, "Numerical Methods in Industrial Forming Processes", Ed. J.F.T. Pittman, Pineridge Press, Swansea, U.K., 1982.

149. E.G. Thomsen, C.T. Yang and S. Kobayashi, "Mechanics of Plastic Deformation in Metal Processing", Macmillan, 1965.

150. N.P. Suh and A.L. Turner, "Elements of the Mechanical Behaviour of Solids", McGraw-Hill book company, 1975.

151. S.C. Hunter, Mechanics of Continuous Media", Ellis Horwood Ltd. Publisher, England, 1976.

152. J.H. Beynon, Private Communication, University of Sheffield, 1982.

153. W.C. Paulsen, Machine Des., 1971. 9, 46-52.

154. J.L. Gordon and A.S. Weinstein, Proc. 2nd N. Amer. Metalworking Res. Conf., Madison, 1974, pp.194-208.

155. C.H. Lee and S. Kobayashi, Int. J. Mech. Sci., 1970, Vol.12, 349-370.

156. S.D. Madnaik, S.K. Maiti and R.C. Chaturvedi, "Numerical Methods in Industrial Forming Processes", Ed. J.F.T. Pittman, Pineridge Press, Swansea, U.K., 155-163.

157. C.M. Sellars, "Quantitative Metallography", University of Sheffield, 1980.

158. P. Ludwik, "Elemente der Technologischen Mechanik", J. Springer, Berlin, 1909.

159. D. Lieversey, Private Communication, University of Sheffield, 1980.

160. R. Colas, Private Communication, University of Sheffield, 1981.

161. W.A. Anderson and R.F. Mehl, Trans. Met. Soc. AIME, 1945, 161, 140-.

162. L.M. Clarebrough, Aust. J. Sci. Res., 1950, A, Vol.3, 72-90.

163. L.M. Clarebrough and G.R. Perger, Aust. J. Sci. Res., 1952, A, Vol.1, 114-119.

164. C.M. Sellars and J.A. Whiteman, Met. Sci., 1979, 13, 187-194.

165. E. Siebel, "Die Formgebung im Bildsamen Zustand", Verlag Stahleisen, Dusseldorf, 1932.

166. T. Von Karman, Z. Angew. Math. Mech., 1925, 5, 138-141.

167. A.I. Celikov, Metallurg., 1945, 6, 61-76.

168. S. Galeji, Metallurgie Giess Techn., 1953, 3, 263-273.

169. First Report on the Rolling Mill Research Sub-Committee, Spec. Rep. No. 34, Iron and Steel Institute, London, 1964.

170. D.R. Bland and H. Ford, Proc. Inst. Mech. Engnrs., 1948, 159, 144-153.

171. S. Ekelund, Steel, 1933, 93, Nos. 8-14.

172. E. Orowan, Proc. Inst. Mech. Engnrs., 1943, 150, 140-167.

173. R. Sims, Proc. Inst. Mech. Engnrs., 1954, 168, 191-200.

174. J.W. Green and J.F. Wallace, J. Mech. Eng. Sci., 1962, 4, 132-142.

175. J.M. Alexander and H. Ford, "Progress in Applied Mechanics", Macmillan, New York, 1963, 191-203.

176. Z. Zamyslovsky and V. Crha, Hutnicle listy, 1966, 21, 23-29.

177. P.A. Sandmark, Scand. J. Metallurgy, 1972, 1, 313-318.

178. I. Ruddle, Private Communication to C.M. Sellars, Pittsburg, U.S.A., 1982.

179. C. Chatfield, "Statistics for Technology", Chapman and Hall, London, 1978, 166-199.

TABLE 1 : Phases Formed in Aluminium-Magnesium Alloys (after Mondolfo [12])

Mg	Mg < 2% in solid solution	Mg > 2% Mg_5Al_8	Si > 0.05% Mg_2Si	Cu > 0.2% $CuMg_4Al_6$			
Si	Fe < 0.3% Mg_2Si	Fe > 0.3%, Mg < 2% Fe_2SiAl_8	Fe > 0.3%, Mg ≪ 2%, Mn or Cr > 0.1% $(FeMn)_3Si_2Al_{15}$ or $(CrFe)_4Si_4Al_{13}$				
Fe	Si < 0.3% Mg > 2% $FeAl_3$	Si > 0.3% Mg < 2% Fe_2SiAl_8	Si > 0.3% Mg ≪ 2% Mn > 0.1% $(FeMn)_3Si_2Al_{15}$	Si < 0.3% Mg > 2% Mn > Fe $(FeMn)Al_6$	Si > 0.3% Mg ≪ 2% Cr > 0.1% $(CrFe)_4Si_4Al_{13}$	Si < 0.3% Mg > 2% Cr > 0.1% $(CrFe)Al_7$	Si < 0.2% Fe > 0.3% Cu > 1% Cu_2FeAl_7
Mn	Si < Mg $(FeMn)Al_6$	Si > 2Mg $(FeMn)_3Si_2Al_{15}$					
Cr	Si < Mg $(CrFe)Al_7$	Si > 2Mg $(CrFe)_4Si_4Al_{13}$					
Cu	Fe < Cu $CuMg_4Al_6$	Fe > Cu, Mg < 2% Cu_2FeAl_7					
Zn	Zn < 2% in solid solution	Zn > 2% Mg_3ZnAl_2					

TABLE 2: (After Christian [134])

Value of n in kinetic law $\zeta = 1 - \exp(-kt^n)$

(a) Polymorphic changes, discontinuous precipitation, eutectoidal reactions, interface controlled growth, etc.

CONDITIONS	n
Increasing nucleation rate	>4
Constant nucleation rate	4
Decreasing nucleation rate	3-4
Zero nucleation rate (saturation of point sites)	3
Grain edge nucleation after saturation	2
Grain boundary nucleation after saturation	1

(b) Diffusion controlled growth (early stages of reaction only)

CONDITIONS	n
All shapes growing from small dimensions, increasing nucleation rate	$>2\frac{1}{2}$
All shapes growing from small dimensions, constant nucleation rate	$2\frac{1}{2}$
All shapes growing from small dimensions, decreasing nucleation rate	$1\frac{1}{2}$-$2\frac{1}{2}$
All shapes growing from small dimensions, zero nucleation rate	$1\frac{1}{2}$
Growth of particles of appreciable initial volume	1-$1\frac{1}{2}$
Needles and plates of finite long dimensions, small in comparison with their separations	1
Thickening of long cylinders (needles) e.g. after complete edge impingement	1
Thickening of very large plates, e.g. after complete edge impingement	$\frac{1}{2}$
Segregation to dislocations (very early stage only)	$\frac{2}{3}$

TABLE 3 : Recrystallisation Times in Seconds at Different Deformation Conditions (after Cotner [26])

Material	Eq. Strain	Q_{app}(kJ/mol)	400°C	450°C	500°C	550°C	600°C	
S.P. Al	0.73	112.1	1200	---	78	---	7	Equivalent Strain Rate: $4.54\ s^{-1}$
S.P. Al	2.34	---	720	---	---	---	---	
S.P. Al	4.50	---	175	---	---	---	---	
Al-$\frac{1}{3}$%Mg	0.73	117.5	416	---	26	---	2.2	
Al-1%Mg	0.73	123.8	410	---	22	---	---	
Al-1%Mg	4.50	---	175	---	---	---	---	
Al-2%Mg	0.73	153.5	390	42	7	---	---	
Al-5%Mg	0.73	168.5	380	22.6	7	---	---	

TABLE 4 : Quantometer Analyses of the Experimental Metals

Material	% wt. Composition													Remarks
	Al	Cu	Pb	B	Si	Mn	Ti	Sn	Zn	Ni	Fe	Cr	Mg	
Al-1%Mg (plate)	bal.	0.16	<0.01	0.002	0.10	<0.02	<0.05	<0.01	<0.05	<0.02	0.40	<0.02	0.95	supplied as plate ∿ 10 mm thick. DC cast, homogenized 16 hours at 550°C-560°C, rolled from homogenisation to finish at 250°C-300°C, annealed before the tests 1 hour at 525°C.
Al-1%Mg (slab)	bal.	0.16	---	0.001	0.12	0.005	0.013	---	0.02	---	0.47	---	1.00	supplied as cast slab ∿ 26 mm thick.
Al-1%Mg-1%Mg (plate)	bal.	0.24	---	0.14	---	1,00	---	---	---	---	0.48	---	1.08	supplied as plate ∿ 10 mm thick. Treatment as Al-1%Mg (plate).
Commercial-purity Al (plate)	bal.	0.02	---	0.002	0.06	0.02	---	---	---	---	0.17	---	0.02	supplied as plate ∿ 10 mm thick. DC cast and hot rolled to plate without homogenisation treatment.

TABLE 5 : Chemical Analysis of the Hot Die Steel used in the Construction of the Plane Strain Compression Tools

Element	% wt.
W	8.25 - 9.25
Cr	3.00 - 3.50
C	0.30 - 0.35
Si	0.40 - 0.50
Mn	0.20 - 0.35
P	0.030 max
S	0.025 max
V	0.40 - 0.50
Fe	bal.

TABLE 6 : Stress-Strain Data for Aluminium-1% Magnesium Alloy

Specimen No.	$\sigma_{0.05}$ (N/mm^2)	T_{centre} (^oC)	T_{mean} (^oC)	$\ln Z_{0.05}$	$\sigma_{0.1}$	T_{centre} (^oC)	T_{mean} (^oC)	$\ln Z_{0.1}$
ESP-166	30.16	500.7	500.4	24.35	30.32	500.1	500.8	24.16
ESP-168	39.74	503.0	500.6	26.08	39.58	503.0	501.2	25.94
ESP-170	45.30	504.0	500.9	26.79	44.34	504.8	501.6	26.65
ESP-172	55.32	496.5	501.3	27.44	55.93	503.6	502.2	27.00
ESP-174	61.44	504.2	500.3	28.37	66.27	496.5	502.0	28.09
ESP-176	62.20	503.0	502.3	28.87	69.74	510.1	502.2	28.84
ESP-178	51.68	399.2	400.8	28.09	55.03	400.4	401.4	27.73
ESP-327	66.61	390.9	401.2	29.76	66.61	392.1	402.2	29.50
ESP-320	73.89	392.1	401.9	30.45	72.70	392.7	402.9	30.06
ESP-332	77.71	394.5	401.2	30.63	78.67	398.0	403.1	30.96
ESP-334	86.20	392.7	403.5	31.43	88.20	400.4	404.5	32.19
ESP-336	93.58	398.0	401.2	32.44	103.69	398.6	403.4	32.41
ESP-349	84.11	302.6	301.3	32.58	90.10	303.8	302.4	33.11
ESP-350	90.09	297.2	301.4	34.49	92.52	298.4	303.0	34.15
ESP-353	100.14	300.2	301.5	35.32	75.83	301.4	303.4	34.85
ESP-355	107.74	298.4	301.6	36.15	111.99	297.2	304.2	35.46
ESP-359	119.86	293.0	301.5	36.55	127.46	---	306.6	35.89
ESP-357	119.74	304.4	301.8	37.09	131.52	305.0	304.42	37.22

.....(continued)

TABLE 6 (...continued)

Specimen No.	$\sigma_{0.2}$ (N/mm^2)	T_{centre} (^oC)	T_{mean} (^oC)	ln $Z_{0.2}$	$\sigma_{0.4}$ (N/mm^2)	T_{centre} (^oC)	T_{mean} (^oC)	ln$Z_{0.4}$
ESP-166	30.98	500.1	501.5	24.60	30.16	498.9	502.5	24.57
ESP-168	39.95	503.0	502.5	25.77	40.76	504.2	504.6	25.55
ESP-170	43.49	504.8	502.9	26.61	42.60	506.0	505.4	26.53
ESP-172	51.55	506.0	504.0	27.23	50.00	504.8	506.9	27.01
ESP-174	66.46	508.9	505.4	28.05	61.71	497.1	509.0	28.20
ESP-176	72.01	508.9	504.7	29.00	69.15	504.2	509.5	28.98
ESP-178	57.25	399.2	402.7	28.15	53.47	399.8	404.6	28.07
ESP-327	68.89	395.1	404.2	29.28	69.53	398.0	408.0	28.97
ESP-320	71.43	395.7	405.0	29.81	73.19	402.2	409.7	30.03
ESP-332	76.93	402.2	405.7	31.05	75.88	406.9	410.2	30.95
ESP-334	88.22	399.8	406.5	31.72	85.56	408.1	412.4	31.32
ESP-336	105.60	401.0	407.0	32.42	105.17	409.9	414.2	32.29
ESP-349	94.77	305.6	304.5	33.19	97.85	305.6	308.0	32.90
ESP-350	97.69	304.4	306.0	34.24	101.04	310.4	311.8	33.51
ESP-353	103.48	307.4	306.8	34.79	106.97	311.6	313.5	34.42
ESP-355	110.13	302.0	308.0	35.79	110.41	311.6	315.3	35.10
ESP-359	130.63	---	309.6	36.31	126.86	---	318.7	35.82
ESP-357	133.06	310.4	308.9	36.91	133.14	322.4	318.3	36.65

.....(continued)

TABLE 6 (.....continued)

Specimen No.	$\sigma_{0.6}$ (N/mm^2)	T_{centre} (^oC)	T_{mean} (^oC)	ln $Z_{0.6}$	$\sigma_{0.8}$ (N/mm^2)	T_{centre} (^oC)	T_{mean} (^oC)	ln$Z_{0.8}$
ESP-166	29.08	498.3	503.2	24.42	29.12	497.7	503.6	24.07
ESP-168	37.99	504.8	506.4	25.65	37.49	504.8	507.9	25.60
ESP-170	41.06	506.5	507.6	26.18	39.61	507.7	509.7	26.27
ESP-172	47.84	506.0	509.8	26.77	45.64	507.1	512.4	27.46
ESP-174	58.26	502.4	512.9	27.98	55.51	497.7	513.9	28.25
ESP-176	71.57	511.2	514.3	28.95	70.56	512.4	519.0	28.95
ESP-178	57.86	400.4	406.1	28.01	57.70	400.4	407.0	27.68
ESP-327	68.24	401.6	411.4	28.65	67.35	403.4	414.3	28.54
ESP-320	72.35	405.1	413.7	29.62	70.77	407.5	417.2	29.73
ESP-332	77.16	411.1	414.9	30.68	74.05	413.4	419.3	30.67
ESP-334	82.61	412.8	417.3	31.24	80.12	417.0	422.8	31.12
ESP-336	103.61	415.2	421.4	32.18	101.64	422.9	428.4	32.10
ESP-349	98.39	307.4	310.5	32.41	98.74	307.4	312.2	32.56
ESP-350	101.18	315.2	316.8	33.84	101.29	319.4	321.2	33.00
ESP-353	106.65	314.6	319.8	34.40	105.74	319.4	325.6	33.90
ESP-355	110.07	320.0	322.1	34.74	109.07	326.0	328.7	34.39
ESP-359	121.78	---	327.3	35.21	119.57	---	334.9	34.98
ESP-357	130.89	330.8	327.8	36.30	128.27	335.6	336.9	36.02

TABLE 6 (.....continued)

Specimen No.	$\sigma_{1.0}$ (N/mm^2)	T_{centre} (^oC)	T_{mean} (^oC)	ln $Z_{1.0}$	σ_{ss} (N/mm^2)	T_{centre}(^oC)	T_{mean}(^oC)	lnZ_{ss}
ESP-166	26.55	497.7	503.9	25.22	30.98	---	501.5	24.60
ESP-168	35.93	504.8	509.2	27.70	39.95	---	502.5	25.77
ESP-170	38.95	508.9	511.4	26.35	44.34	---	501.6	26.65
ESP-172	43.62	507.7	514.6	27.47	55.93	---	502.2	27.00
ESP-174	54.01	506.0	519.1	27.98	69.25	---	505.4	28.05
ESP-176	72.24	503.6	523.6	28.90	79.00	---	507.9	28.85
ESP-178	56.90	399.8	407.7	27.47	58.44	---	405.4	27.90
ESP-327	65.47	405.1	416.6	28.92	69.53	---	408.0	28.97
ESP-320	64.13	407.5	419.9	29.99	74.50	---	411.6	29.84
ESP-332	72.23	417.0	423.1	29.57	78.67	---	403.1	30.96
ESP-334	78.11	422.9	427.5	30.73	89.00	---	406.5	31.72
ESP-336	101.78	427.6	435.4	31.96	107.00	---	410.6	32.37
ESP-349	98.06	308.0	313.4	32.87	99.62	---	311.4	31.79
ESP-350	99.98	322.4	324.6	33.11	103.28	---	314.2	33.66
ESP-353	100.03	323.0	330.2	33.54	108.48	---	316.6	34.27
ESP-355	106.74	332.0	334.8	34.65	112.00	---	304.2	35.46
ESP-359	116.78	---	341.7	34.41	130.63	---	309.7	36.31
ESP-357	126.54	337.4	345.7	35.7	133.14	---	318.3	36.65

TABLE 7 : Stress-Strain Data Used in the Determination of the Strain Hardening Exponent for Al-1%Mg Alloys

SPECIMEN: ESP-349 (Al-1%Mg alloy) Nominal strain rate: $1.09s^{-1}$ Nominal temperature: $300^{o}C$	
STRAIN	STRESS (N/mm^2)
0.026	77.01
0.030	79.25
0.036	80.88
0.045	82.75
0.050	84.11
0.054	83.76
0.062	85.93
0.075	87.16
0.080	88.23
0.087	88.69
0.094	88.87
0.097	89.95
0.106	90.10
0.110	90.31
0.112	90.58
0.124	91.24
0.128	91.17
0.135	91.92
0.141	92.38
0.147	92.85
0.153	92.75

SPECIMEN: ESP-178 (Al-1%Mg alloy) Nominal strain rate: $1.09s^{-1}$ Nominal temperature: $400^{o}C$	
STRAIN	STRESS (N/mm^2)
0.012	44.53
0.018	46.70
0.032	49.08
0.044	51.19
0.051	51.68
0.055	51.63
0.061	52.13
0.080	53.05
0.085	53.83
0.098	54.25
0.103	55.03

TABLE 8 : Stress-Strain Data Derived from Non-Isothermal Tests on Al-1%Mg Alloy.

(ESP-422)

ε	$\sigma(N/mm^2)$	$\dot{\varepsilon}(s^{-1})$	Computed Mean Temperature (^oC)	lnZ
0.10	55.50	5.04	446.62	27.70
0.20	60.30	5.03	434.74	28.14
0.30	64.00	5.04	423.99	28.55
0.40	67.50	5.04	414.05	28.94
0.50	71.00	5.02	405.10	29.30
0.60	74.50	5.05	395.80	29.69
0.70	78.00	5.04	386.96	30.06
0.80	81.00	5.04	378.32	30.44
0.90	84.50	5.02	370.10	30.80
1.00	88.00	5.04	361.89	31.19

2nd Deformation

1.10	74.50	4.99	376.26	30.52
1.20	86.00	5.03	351.84	31.66
1.30	96.50	5.01	334.88	32.49
1.40	109.00	5.02	319.58	33.29
1.50	123.00	5.07	308.45	33.91
1.60	140.50	5.08	298.48	34.47
1.70	160.00	5.07	291.28	34.89
1.80	182.00	5.04	284.71	35.28
1.90	200.00	5.02	279.04	35.62

TABLE 9 : Stress-Strain Data Derived from Non-Isothermal Tests on Al-1%Mg Alloy.

(ESP-423)

ε	$\sigma(N/mm^2)$	$\dot{\varepsilon}(s^{-1})$	Computed Mean Temperature (^oC)	lnZ
0.10	59.50	11.0	457.30	28.10
0.20	62.00	10.8	449.49	28.36
0.30	65.00	10.8	442.81	28.61
0.40	67.50	10.8	436.73	28.83
0.50	69.80	10.8	430.78	29.05
0.60	72.30	10.8	424.66	29.29
0.70	74.50	10.7	418.37	29.52
0.80	77.00	10.8	411.85	29.79
0.90	79.50	10.7	405.46	30.04
1.00	82.00	10.7	399.69	30.28

2nd Deformation

1.10	70.00	10.7	403.11	30.14
1.20	77.00	11.2	385.31	30.93
1.30	86.00	10.7	370.75	31.53
1.40	94.00	10.8	357.55	32.15
1.50	106.50	10.4	346.53	32.64
1.60	118.00	10.6	335.97	33.19
1.70	135.50	10.2	327.43	33.59
1.80	158.00	9.87	319.37	33.98
1.90	178.00	9.79	312.09	34.37

TABLE 10 : Stress-Strain Data Derived from Non-Isothermal Tests on Al-1%Mg Alloy.

(ESP-424)

ε	$\sigma(N/mm^2)$	$\dot{\varepsilon}(s^{-1})$	Computed Mean Temperature (^oC)	lnZ
0.10	66.80	18.1	462.54	28.42
0.20	67.30	19.6	458.74	28.63
0.30	68.00	20.1	454.51	28.80
0.40	69.00	20.1	451.00	28.93
0.50	70.50	20.3	447.59	29.06
0.60	72.00	20.6	443.70	29.22
0.70	73.30	20.6	439.75	29.36
0.80	74.60	20.6	435.58	29.52
0.90	75.60	20.7	431.24	29.69
1.00	77.10	20.9	426.63	29.87

2nd Deformation

1.10	73.00	19.0	419.29	30.06
1.20	77.00	20.0	407.15	30.60
1.30	82.00	19.7	395.52	31.06
1.40	87.50	20.0	386.43	31.46
1.50	94.00	19.7	377.34	31.85
1.60	103.50	19.9	368.22	32.27
1.70	114.50	19.6	360.35	32.62
1.80	127.50	19.3	352.51	32.97
1.90	143.00	18.6	345.25	33.29

TABLE 11 : Stress-Strain Data Derived from Non-Isothermal Tests on Al-1%Mg Alloy.

(ESP-425)

ε	$\sigma(N/mm^2)$	$\dot{\varepsilon}(s^{-1})$	Computed Mean Temperature (^oC)	lnZ
0.10	78.00	43.90	467.11	29.15
0.20	77.10	45.00	466.54	29.19
0.30	76.00	46.90	465.49	29.27
0.40	75.50	47.60	464.52	29.32
0.50	75.00	48.00	463.30	29.37
0.60	74.00	48.00	461.84	29.42
0.70	75.00	48.60	460.42	29.48
0.80	75.00	49.10	459.06	29.54
0.90	75.50	49.20	457.15	29.61
1.00	75.70	51.10	455.11	29.72

2nd Deformation

1.20	78.00	43.90	428.43	30.55
1.30	81.00	45.50	423.13	30.78
1.40	83.50	47.40	417.82	31.03
1.50	87.50	46.20	412.19	31.23
1.60	93.00	45.20	406.75	31.43
1.70	100.05	45.50	401.74	31.64
1.80	109.00	44.70	396.20	31.85
1.90	120.05	44.40	391.21	32.06
2.00	131.05	45.00	386.34	32.28

TABLE 12 : Stress-Strain Data for Commercial-Purity Aluminium

Specimen No.	$\sigma_{0.05}(N/mm^2)$	$\dot{\varepsilon}_{0.05}(s^{-1})$	T_{mean} (^oC)	ln $Z_{0.05}$	$\sigma_{0.2}(N/mm^2)$	$\dot{\varepsilon}_{0.2}(N/mm^2)$	T_{mean} (^oC)	ln Z
JB-192	12.59	1.2	490.5	24.77	14.60	1.3	486.03	24.99
JB-194	17.52	5.4	491.4	26.24	18.59	4.8	489.61	26.18
JB-191	19.69	11.0	494.2	26.87	20.42	11.0	493.32	26.89
JB-193	24.31	24.0	494.7	27.63	24.08	24.0	494.74	27.63
JB-195	28.48	54.0	495.6	28.41	30.76	51.0	496.23	28.34
JB-173	21.12	0.9	397.96	27.87	27.13	1.3	379.25	29.04
JB-182	26.18	6.0	394.00	29.94	31.81	6.0	391.84	30.03
JB-184	30.12	11.0	392.45	30.61	34.07	11.0	391.46	30.65
JB-183	34.13	22.0	394.80	31.20	39.74	18.0	395.30	30.98
JB-188	39.75	51.0	389.43	32.27	48.15	54.0	291.17	32.25
JB-238	42.76	90.0	404.92	32.19	51.56	99.0	407.79	32.17
JB-179	33.61	1.1	284.16	33.79	44.48	1.1	277.50	34.20
JB-181	38.24	5.0	287.94	35.08	48.95	7.0	286.09	35.52
JB-174	42.16	11.0	289.65	35.76	50.82	11.0	289.31	35.78
JB-180	45.93	24.0	290.17	36.51	56.47	24.0	291.44	36.44

.....(continued)

TABLE 12 (.....continued)

Specimen No.	$\sigma_{0.4}$(N/mm^2)	$\dot{\varepsilon}_{0.4}$(s^{-1})	T_{mean} (°C)	ln $Z_{0.4}$	σ_{ss}(N/mm^2)	$\dot{\varepsilon}_{ss}$(s^{-1})	T_{mean} (°C)	ln Z_{ss}
JB-192	15.00	1.1	482.4	24.95	15.00	1.2	471.3	25.37
JB-194	19.57	6.0	487.8	26.47	20.00	5.5	482.0	26.56
JB-191	20.57	11.0	492.5	26.92	21.50	11.4	489.5	27.05
JB-193	24.59	22.0	494.8	27.54	26.50	23.3	494.9	27.60
JB-195	30.54	57.0	497.2	28.42	35.05	45.9	500.8	28.09
JB-173	30.67	0.9	375.9	28.83	35.50	1.1	365.6	29.50
JB-182	34.67	6.0	389.9	30.11	39.5o	5.6	383.8	30.30
JB-184	37.76	9.0	391.2	30.46	41.30	11.2	390.3	30.71
JB-183	42.10	18.0	396.2	30.94	46.75	24.4	399.1	31.13
JB-188	50.78	57.0	393.7	32.20	58.00	48.3	401.9	31.69
JB-238	54.24	123.0	409.4	32.32	66.00	120.0	418.1	31.95
JB-179	52.96	1.1	274.8	34.36	67.30	1.1	267.7	34.81
JB-181	56.99	6.5	285.7	35.48	68.40	5.4	284.7	35.35
JB-174	57.74	12.0	290.2	35.82	69.00	11.0	293.5	35.54
JB-180	61.92	20.0	293.5	36.13	72.50	21.2	301.0	35.76

TABLE 13 : Stress-Strain Data Used in the Determination of the Strain Hardening Exponent for Commercial-Purity Aluminium.

Specimen : JB-184 (commercial-purity Al) Nominal strain rate: $10.33s^{-1}$ Nominal temperature: $391.2^{o}C$	
STRAIN	STRESS (N/mm^2)
0.020	17.84
0.033	19.50
0.044	20.31
0.053	21.12
0.067	21.62
0.078	22.42
0.088	22.38
0.100	23.45
0.111	24.24
0.121	24.47
0.135	25.24
0.143	25.48
0.156	25.70
0.168	25.92

Specimen : JB-174 (commercial-purity Al) Nominal strain rate: $11.67s^{-1}$ Nominal temperature: $290.2^{o}C$	
STRAIN	STRESS(N/mm^2)
0.010	31.29
0.022	36.09
0.032	39.17
0.044	40.81
0.055	42.16
0.067	43.21
0.078	43.69
0.089	44.46
0.101	45.50
0.112	45.98
0.124	46.45
0.135	47.20
0.147	47.39
0.158	48.42
0.170	49.16
0.181	49.91
0.193	50.36
0.204	50.82

TABLE 14 : Restoration After One Deformation.

Initial Strain : 0.15

Interpass Time (sec)	$(\sigma_o)_2$	% R_1	Date	Remarks		
1.7	60.00	0.00	30-05-80			
10	58.90	8.90	12-01-82			
20	58.00	16.18	02-06-80	high friction conditions		
40	57.80	17.80	04-06-80	"	$[\sigma_{max}]^{EXT}$: 60.00	
80	58.25	14.16	04-06-80			
160	55.50	36.41	10-06-80	"		
320	56.25	30.34	04-06-80			Δ = 12.36
640	56.25	30.34	04-06-80			
1280	56.00	32.36	04-06-80			
2560	55.40	37.22	04-06-80			
6310	54.50	44.50	19.01-82		$[\sigma_o]_2^{\infty}$: 47.64	
16000	48.50	93.04	11-06-80			
28800	52.75	-----	01-10-80	"		
57600	47.00	105.18	17-07-81	"		

.....(continued)

TABLE 14 (.....continued) : Restoration After One Deformation.

Initial Strain : 0.33

Interpass Time (sec)	$(\sigma_o)_2$	% R_1	Date	Remarks		
1.7	62.50	4.74	29-05-80			
10	60.80	15.50	12-01-82		$[\sigma_{max}]^{EXT}$: 63.25	
20	60.60	16.76	28-05-80			
40	60.60	16.76	12-01-82			
80	59.00	26.88	29-05-80			
100	60.00	20.56	28-05-80	high friction conditions		
320	56.60	42.06	28-05-80	"		Δ = 15.81
640	56.25	44.28	29-05-80	"		
1000	58.00	33.21	12-01-82		$[\sigma_o]_2^{\infty}$: 47.44	
2560	55.00	52.18	12-01-82			
3981	48.00	96.46	12-01-82			
6310	46.50	105.95	12-01-82			
8000	48.75	91.71	11-06-80			
10000	46.50	105.95	12-01-82			
57600	54.40	------	01-10-80	"		
64800	52.75	------	01-10-80	"		

.....(continued)

TABLE 14 (.....continued) : Restoration After One Deformation.

Initial Strain : 0.67

Interpass Time (sec)	$(\sigma_o)_2$	% R_1	Date	Remarks		
1.7	63.71	7.80	26-02-79 07-12-79	friction in some		
5	63.00	13.12	15-01-82	friction		
10	61.60	23.61	12-01-82			
26	62.75	14.99	14-09-78	friction	$[\sigma_{max}]^{EXT}$: 64.75	
50	62.00	20.61	15-09-78	friction		
75	60.50	31.86	15-09-78			
100	58.73	45.13	19-02-79	friction in some		Δ = 13.34
125	57.63	53.37	15-09-78			
160	54.00	80.58	19-02-79			
320	51.50	99.32	19-02-79 27-02-79			
640	52.38	92.73	21-02-79		$[\sigma_o]_2^{\infty}$: 51.41	
1280	52.17	94.30	07-12-79 21-05-80			
57600	51.50	99.33	03-10-80			
64800	49.50	114.32	03-10-80			

.....(continued)

TABLE 14 (.....continued) : Restoration After One Deformation.

Initial Strain : 1.00

Interpass Time (sec)	$(\sigma_o)_2$	% R_1	Date	Remarks		
1.7	65.50	1.94	04-06-80	high friction conditions		
5	58.75	54.39	18-01-82	"		
10	63.00	21.37	12-01-82		$[\sigma_{max}]_1^{EXT}$: 65.75	
20	65.00	5.82	04-06-80	"		
40	64.25	11.66	22-05-80	"		
50	55.75	77.70	13-01-82			
63	60.50	40.79	14-01-82	"		
80	57.50	64.10	10-06-80	"		Δ = 12.87
100	59.25	50.51	23-05-80	"		
120	58.75	54.39	12-01-82		$[\sigma_o]_2^{\infty}$: 52.88	
160	54.50	87.41	23-05-80			
250	54.75	85.47	12-01-82	"		
320	51.50	110.72	28-05-80			
640	50.25	120.44	10-06-80			
2560	51.25	112.67	10-06-80			
64800	52.75	101.01	17-12-81			

TABLE 15 : Restoration After One Deformation with Use of Cartridge Heaters.

Initial Strain Applied : 0.67

Interpass Time (sec)	$(\sigma_o)_2$ (N/mm^2)	% R_1
1.7	55.00	0
10	54.25	10
20	53.50	20
40	52.75	30
80	52.50	33.33
120	51.75	43.33
160	50.75	56.67
320	49.59	73.33
640	47.50	100
64800	47.50	100

$(\sigma_{max})^{EXT} = 55.00$; $(\sigma_o)_2^{\infty} = 47.50$

TABLE 16 : Recrystallisation After One Deformation

Initial Strain Applied : 0.33

Time (sec)	X_v	Log [ln $(\frac{1}{1-X_v})$]
10	0.0	---
20	0.0	---
40	0.0	---
80	0.0	---
100	0.0	---
320	0.12	-0.893
640	0.13	-0.856
1280	0.19	-0.676
2560	0.69	0.069
3980	0.78	0.180
6310	0.80	0.207
8000	0.82	0.234

.....(continued)

TABLE 16 (.....continued) : Recrystallisation After One Deformation

Initial Strain Applied : 0.67

Time (sec)	X_v	Log [ln $(\frac{1}{1-X_v})$]
1.7	0.00	---
5	0.00	---
10	0.00	---
26	0.00	---
40	0.01	-1.998
60	0.03	-1.560
80	0.06	-1.208
100	0.10	-0.977
120	0.18	-0.716
160	0.25	-0.541
240	0.59	-0.045
320	0.71	0.093
380	0.87	0.316
480	0.95	0.477
640	1.00	---
960	1.00	---
1280	1.00	---

TABLE 17 : Restoration After One Deformation

Initial Strain Applied : 0.67
Strain Rate : 1 s^{-1}
Temperature : 350°C

Interpass Time (sec)	$(\sigma_o)_2$ (N/mm^2)	% R_1
0	79.00	7.32
40	77.75	13.42
80	77.50	14.63
150	77.25	15.85
300	77.25	15.85
600	74.75	28.05
1800	75.00	26.83
3600	76.75	18.29
7200	67.25	64.63
14400	64.25	79.27
28800	62.25	89.02
57600	60.00	100
$[\sigma_{max}]_1^{EXT} = 80.50$; $[\sigma_o]_2^{\infty} = 60$		

.....(continued)

TABLE 17 (.....continued) : Restoration After One Deformation

Initial Strain Applied : 0.67

Strain Rate : 1 s^{-1}

Temperature : 390°C

Interpass Time (sec)	$(\sigma_o)_2$ (N/mm^2)	% R_1
10	51.00	23.46
31.6	50.13	32.10
56.1	49.50	38.27
80	47.88	54.32
100	45.25	80.25
251	43.25	100.00
1000	43.25	100.00
57600	44.25	90.12
$[\sigma_{max}]_1^{EXT} = 53.38$; $[\sigma_o]_2^{\infty} = 43.25$		

.....(continued)

TABLE 17 (.....continued) : Restoration After One Deformation

Initial Strain Applied : 0.67
Strain Rate : 1 s^{-1}
Temperature : 420°C

Interpass Time (sec)	$(\sigma_o)_2$ (N/mm^2)	% R_1
11.4	52.25	8.69
26.4	52.25	8.69
51.4	49.00	46.38
101.4	44.26	101.45
161.4	44.26	101.45
501.4	43.76	107.25
2200	45.25	89.86
$[\sigma_{max}]_1^{EXT} = 53.00$; $[\sigma_o]_2^{\infty} = 44.38$		

.....(continued)

TABLE 17 (.....continued) : Restoration After One Deformation

Initial Strain Applied : 0.67
Strain Rate : 1 s^{-1}
Temperature : 500°C

Interpass Time (sec)	$(\sigma_o)_2$ (N/mm^2)	% R_1
0	32.00	46.38
10	32.50	34.78
20	31.75	52.17
40	31.25	63.77
80	29.25	110.14
160	30.50	81.16
320	24.44	121.74
640	30.25	86.96

$[\sigma_{max}]_1^{EXT} = 34.00$; $[\sigma_o]_2^{\infty} = 29.69$

TABLE 18 : Restoration After One Deformation

Initial Strain Applied : 0.67
Strain Rate : 0.1 s^{-1}
Temperature : 420°C

Interpass Time (sec)	$(\sigma_o)_2$ (N/mm^2)	% R_1
28	38.13	0
154	38.13	0
239	37.13	24.63
364	37.38	18.47
714	35.63	61.58
1414	34.01	101.56
2014	35.13	73.89
5114	38.09	70.94
20000	34.13	98.52
$[\sigma_{max}]_1^{EXT} = 38.13$; $[\sigma_o]_2^{\infty} = 34.07$		

.....(continued)

TABLE 18 (.....continued) : Restoration After One Deformation

Initial Strain Applied : 0.67
Strain Rate : 0.1 s^{-1}
Temperature : 390°C

Interpass Time (sec)	$(\sigma_o)_2$ (N/mm^2)	% R_1
14	36.50	0.00
100	36.00	9.76
640	34.63	36.58
2000	32.74	73.27
8000	32.37	80.49
57600	31.38	100
$[\sigma_{max}]_1^{EXT} = 36.50$; $[\sigma_o]_2^{\infty} = 31.38$		

.....(continued)

TABLE 18 (.....continued) : Restoration After One Deformation

Initial Strain Applied : 0.67
Strain Rate : 3.76 s^{-1}
Temperature : 510°C

Interpass Time (sec)	$(\sigma_o)_2$ (N/mm^2)	% R_1
0	39.50	0.00
3	38.25	31.25
4	37.00	62.50
6	36.75	68.75
10	35.75	93.75
140	35.50	100.00
500	35.50	100.00

$[\sigma_{max}]_1^{EXT} = 39.50$; $[\sigma_o]_2^{\infty} = 35.50$

TABLE 19 : Recrystallised Grain Sizes

Initial Strain Applied : 0.67
Strain Rate : 1 s^{-1}
Initial Grain Size : 70 μm

$Z(s^{-1})$	$T(^{o}C)$	d_{rex} (μm)
1.30×10^{12}	400	70
1.33×10^{11}	460	116
3.52×10^{10}	500	162

TABLE 20 : Effect of Initial Grain Size on the Recrystallised Grain Size.

Initial Strain Applied : 0.67
Strain Rate : 1 s^{-1}
Temperature : $460^{o}C$

d_o (μm)	d_{rex} (μm)
54	85
69	116
92	165
112	222

TABLE 21 : Restoration After One Deformation

Initial Strain Applied : 0.67
Strain Rate : 1 s^{-1}
Temperature : 460°C
Initial Grain Size : 54.0 μm

Interpass Time (sec)	$(\sigma_o)_2$ (N/mm^2)	% R_1
10	39.25	26.37
20	38.75	35.16
40	38.50	39.56
80	35.25	96.70
160	35.00	101.10
320	34.50	109.89
57600	35.50	92.31

$[\sigma_{max}]_1^{EXT} = 40.75$; $[\sigma_o]_2^{\infty} = 35.06$

.....(continued)

TABLE 21 (.....continued) : Restoration After One Deformation

Initial Strain Applied : 0.67
Strain Rate : 1 s^{-1}
Temperature : 460°C
Initial Grain Size : 69.1 μm

Interpass Time (sec)	$(\sigma_o)_2$ (N/mm^2)	% R_1
10	40.25	0.00
20	39.50	16.67
40	37.00	72.22
80	37.50	61.11
160	36.00	94.44
320	35.25	111.11
57600	36.00	94.44

$[\sigma_{max}]_1^{EXT} = 40.25$; $[\sigma_o]_2^{\infty} = 35.75$

.....(continued)

TABLE 21 (.....continued) : Restoration After One Deformation

Initial Strain Applied : 0.67
Strain Rate : 1 s^{-1}
Temperature : 460°C
Initial Grain Size : 91.5 μm

Interpass Time (sec)	$(\sigma_o)_2$ (N/mm^2)	% R_1
10	40.68	10.53
20	39.90	36.84
40	39.42	52.63
80	39.11	63.16
160	38.00	100.00
320	37.68	110.53
57600	38.32	89.47
$[\sigma_{max}]_1^{EXT} = 41.00$; $[\sigma_o]_2^{\infty} = 38.00$		

.....(continued)

TABLE 21 (.....continued) : Restoration After One Deformation

Initial Strain Applied : 0.67
Strain Rate : 1 s^{-1}
Temperature : 460°C
Initial Grain Size : 112.2 μm
(as cast specimens)

Interpass Time (sec)	$(\sigma_o)_2$ (N/mm^2)	% R_1
10	42.75	0
20	41.55	15
40	41.15	20
80	38.75	50
160	38.35	55
320	36.75	75
57600	34.75	100

$[\sigma_{max}]_1^{EXT} = 42.75$; $[\sigma_o]_2^{\infty} = 34.75$

TABLE 22 : Restoration After Two Deformations

Initial Interruption Period : 1.7 sec.

Interpass Time (sec)	$[\sigma_o]_3$ (N/mm^2)	% R_2
1.7	66.00	3.03
5	62.25	25.76
10	62.25	25.76
40	62.25	25.76
80	59.50	42.42
100	55.75	65.15
160	53.75	77.27
320	52.00	87.88
640	50.25	98.48
57600	50.00	100
$[\sigma_{max}]_2^{EXT}$ = 66.50 N/mm^2 ; $[\sigma_o]_3^{\infty}$ = 50.00		

.....(continued)

TABLE 22 (.....continued) : Restoration After Two Deformations

Initial Interruption Period : 100 sec.

Interpass Time (sec)	$[\sigma_o]_3$ (N/mm^2)	% R_2
1.7	64.00	2.62
1.7	63.50	5.24
5	60.75	19.65
10	62.25	11.79
40	60.75	19.65
40	61.75	14.41
80	59.75	24.90
100	58.50	31.45
120	56.25	43.24
160	53.75	56.34
240	53.50	57.65
320	52.25	64.20
640	52.75	61.58
1000	52.50	62.89
2560	53.00	60.27
2560	52.25	64.20
5011	49.50	78.62
10000	45.25	100.89
20000	46.00	96.96
40000	45.00	102.20

$[\sigma_{max}]_2^{EXT}$ = 64.50 N/mm^2 ; $[\sigma_o]_3^{\infty}$ = 45.42 N/mm^2

Δ = 19.08

TABLE 22 (.....continued) : Restoration After Two Deformations

Initial Interruption Period : 320 sec.

Interpass Time (sec)	$[\sigma_o]_3$(N/mm^2)	% R_2
1.7	58.75	10.96
5	57.00	20.55
10	58.00	15.07
40	57.25	19.18
80	55.50	28.77
100	56.25	24.66
160	55.75	27.40
320	54.25	35.62
640	52.50	45.21
2560	52.00	47.95
5011	44.75	87.67
20000	42.50	100.00

$[\sigma_{max}]_2^{EXT}$ = 60.75 N/mm^2 ; $[\sigma_o]_3^{\infty}$ = 42.50 N/mm^2

TABLE 22 (.....continued) : Restoration After Two Deformations

Initial Interruption Period : 16 hrs.

Interpass Time (sec)	$[\sigma_o]_3$ (N/mm^2)	% R_2
1.7	59.75	12.5
5	58.50	21.4
10	58.00	25.0
20	57.00	32.1
40	56.50	35.7
80	56.50	35.7
160	56.50	35.7
320	57.00	32.1
640	56.25	37.5
1280	56.25	37.5
2560	56.25	37.5
5011	55.25	44.6
10000	52.75	62.5
20000	50.00	82.1
40000	47.50	100.0

$[\sigma_{max}]_2^{EXT} = 61.50$; $[\sigma_o]_3^{\infty} = 47.50$

TABLE 23: Experimental Rolling Schedule carried out on Al-1%Mg Alloy

Roll radius : 69.85 mm
Initial thickness : 24.15 mm
Initial slab temperature : 424°C
Initial length : 99.46 mm
Spread coefficient : 0.089

Material : Al-1%Mg Alloy
Initial width : 55.44 mm
Rolling speed : 212 mm/sec.
Initial grain size : 110 μm
Time between reheating and rolling : 27 sec.

THICKNESS AFTER PASS (mm)	WIDTH AFTER PASS (mm)	LENGTH AFTER PASS (mm)	TIME TO ROLL (sec)	X_v CENTRE BEFORE PASS	X_v SURFACE BEFORE PASS	EXPERIMENTAL LOAD (kN)	THEORETICAL LOAD (kN)	$\sqrt{R(h_o-h_f)}$ (mm)	h_m (mm)	m	n
16.01	57.48	144.7	27.17	0.00	0.00	102.3	104.84	23.84	20.08	1.187	----
11.70	59.16	192.1	40.07	0.00	0.00	97.67	97.57	17.35	13.86	1.252	----
10.14	60.56	216.9	53.37	0.00	0.02	69.70	63.67	10.44	10.92	0.956	1.00

TABLE 24: Experimental Rolling Schedules on Commercial-Purity Aluminium

Roll radius : 125 mm
Initial ingot thickness : 50 mm
Initial ingot temperature : ~ 538°C
Initial grain size : 110 μm
Time between reheating and rolling : ~ 16 sec.

Material : commercial-purity alminium
Slab width : 75 mm
Slab length : 200 mm
Spread coefficient : 0.133

(B)

THICKNESS AFTER PASS (mm)	WIDTH AFTER PASS (mm)	LENGTH AFTER PASS (mm)	TIME TO START PASSES (mm)	X_v CENTRE BEFORE PASS	X_v SURFACE BEFORE PASS	EXPERIMENTAL LOAD (kN)	PREDICTED LOAD (kN)	$\sqrt{R(h_o-h_f)}$	h_m (mm)	CENTRE TEMPERATURE (°C)	PREDICTED TEMPERATURE (°C)	$\bar{\sigma}$ (N/mm^2)
40	77.26	242.7	15.97	0.00	0.00	32.48	32.64	35.36	45	525	525	10.87
35	78.64	272.5	46.77	0.00	0.00	32.97	33.57	25.00	37.5	466	471	15.26
30	80.27	311.5	77.63	0.00	0.00	40.00	55.32	25.00	32.5	415	428	18.05
25	82.24	364.6	108.55	0.00	0.00	59.41	82.55	25.00	27.5	390	385	25.35

(C)

40	77.26	242.7	15.97	0.00	0.00	32.48	33.06	35.36	45	525	523	10.87
35	78.64	272.5	76.77	0.00	0.00	34.95	47.82	25.00	37.5	440	433	16.50
30	80.27	311.5	137.63	0.00	0.00	44.85	83.28	25.00	32.5	362	362	20.20
25	82.24	364.6	198.50	0.00	0.00	65.64	125.10	25.00	27.5	304	300	28.01

(D)

40	77.26	242.7	15.97	0.00	0.00	32.48	32.80	35.36	45	525	524	10.87
35	78.64	272.5	106.77	0.00	0.00	36.93	48.22	25.00	37.5	435	432	17.57
30	80.27	311.5	197.63	0.00	0.00	52.28	83.75	25.00	32.5	357	361	23.59
25	82.24	364.6	288.50	0.00	0.00	72.57	125.15	25.00	27.5	300	300	30.96

TABLE 24: (....continued)

(E)

40	77.26	242.7	15.97	0.00	0.00	32.48	33.07	35.36	45	525	523	10.87
35	78.64	272.5	136.77	0.00	0.00	39.41	51.93	25.00	37.5	431	423	18.60
30	80.27	311.5	257.63	0.00	0.00	59.70	89.38	25.00	32.5	338	348	26.94
25	82.24	364.6	378.55	0.00	0.00	80.00	133.27	25.00	27.5	295	285	34.13

TABLE 25: Industrial Schedule No. 1

Roll radius : 406 mm
Material : Al-1%Mg Alloy
Initial ingot thickness : 283 mm
Slab width : 845 mm
Slab length : 1710 mm
Initial entry temperature : 528°C

Roll speed : ∿ 52.3 rev/min.
Initial grain size : ∿ 110 μm

THICKNESS AFTER PASS (mm)	WIDTH AFTER PASS (mm)	LENGTH AFTER PASS (mm)	TIME TO ROLL (sec)	X_v CENTRE BEFORE PASS	X_v SURFACE BEFORE PASS	EXPERIMENTAL LOAD (kN)	THEORETICAL LOAD (kN)	THEORETICAL TORQUE (kN-M)	$\sqrt{R(h_o-h_f)}$ (mm)	h_m (mm)	m	n
238.2	845	2031.5	50.38	0.00	0.00	5115.6	3119.5	407.9	134.9	260.6	0.518	1.22
193.6	845	2499.9	59.46	0.00	0.00	5821.2	3442.0	456.1	134.6	215.9	0.623	1.11
148.7	845	3255.1	68.59	0.00	0.02	5703.6	3798.6	503.3	135.0	171.2	0.789	1.028
108.5	845	4462.0	79.75	0.36	0.74	5586.0	4020.8	500.6	127.8	128.6	0.994	1.000
83.6	845	5789.6	100.03	0.64	0.25	4880.4	3367.7	331.2	100.5	96.1	1.046	-----
54.5	845	8884.3	125.27	0.06	0.39	6232.8	4795.4	502.7	108.7	69.1	1.573	-----
28.6	845	16898.7	139.05	0.32	0.61	7408.8	5938.2	575.5	102.5	41.6	2.464	-----
13.9	845	34767.6	162.80	0.68	0.59	8232.0	6590.6	479.2	77.3	21.3	3.629	-----
5.5	845	88075.4	187.96	0.26	0.42	9996.0	9310.8	495.8	58.4	9.7	6.021	-----

TABLE 25: (...continued) Industrial Schedule No. 2

Roll radius : 406 mm
Material : Al-1%Mg Alloy
Initial ingot thickness : 283 mm
Slab width : 845 mm
Slab length : 1710 mm
Initial ingot temperature : 511°C

Roll speed : ∿ 56.1 rev./min.
Initial grain size : ∿ 110 μm

THICKNESS AFTER PASS (mm)	WIDTH AFTER PASS (mm)	LENGTH AFTER PASS (mm)	TIME TO ROLL (sec)	X_v CENTRE BEFORE PASS	X_v SURFACE BEFORE PASS	EXPERIMENTAL LOAD (kN)	THEORETICAL LOAD (kN)	THEORETICAL TORQUE (kN-M)	$\sqrt{R(h_o-h_f)}$ (mm)	h_m (mm)	m	n
239.1	845	2024.1	50.36	0.00	0.00	5380.2	3592.9	465.4	133.5	261.5	0.511	1.23
195.4	845	2476.4	59.47	0.00	0.00	6209.3	3834.5	503.7	133.2	217.3	0.613	1.12
152.1	845	3181.6	68.55	0.00	0.01	6036.8	4207.6	548.2	132.6	173.8	0.736	1.04
110.2	845	4391.2	76.65	0.15	0.19	6081.9	4649.3	590.7	130.4	131.2	0.994	1.00
85.1	845	5684.6	98.94	0.85	0.64	5324.3	3733.1	368.3	100.9	97.7	1.033	-----
53.5	845	90.43.5	123.13	0.00	0.20	6644.4	5552.9	603.8	113.3	69.3	1.635	-----
28.4	845	17002.0	132.83	0.20	0.80	7670.5	6255.7	596.7	100.9	41.0	2.461	-----
13.8	845	35164.2	155.67	0.81	0.71	8664.2	6817.7	496.3	77.0	21.1	3.649	-----
5.5	845	88225.6	179.03	0.27	0.31	9901.9	9458.6	499.1	58.0	9.7	5.979	-----

TABLE 26: Industrial Schedule No.3

Roll radius : 406 mm
Material : commercial-purity aluminium
Initial ingot thickness : 485 mm
Slab width : 960 mm
Slab length : 1710 mm
Initial entry temperature : 533°C

Roll speed : ∿ 50.88 rev./min.
Spread coefficient : 0.059
Initial grain size : 110 μm

THICKNESS AFTER PASS (mm)	WIDTH AFTER PASS (mm)	LENGTH AFTER PASS (mm)	TIME TO ROLL (sec)	X_v CENTRE BEFORE PASS	X_v SURFACE BEFORE PASS	EXPERIMENTAL LOAD (kN)	THEORETICAL LOAD (kN)	THEORETICAL TORQUE (kN-M)	$\sqrt{R}\,(h_o-h_f)$ (mm)	h_m (mm)	m	n
437.2	962.9	1891.3	50.40	0.00	0.00	2587.2	484.5	63.5	139.3	461.1	0.302	1.62
378.1	966.6	2178.2	66.42	0.00	0.00	3351.6	866.8	132.9	154.9	407.7	0.380	1.43
318.0	970.8	2578.9	75.50	0.00	0.00	3292.8	1043.5	161.2	156.2	348.1	0.449	1.31
261.4	975.1	3124.1	91.57	0.03	0.09	3234.0	1267.1	189.5	151.6	289.7	0.523	1.21
197.6	980.5	4108.5	100.73	0.08	0.17	3469.2	1680.5	265.1	160.9	229.5	0.701	1.07
137.4	986.5	5876.1	115.91	0.89	0.74	3528.0	2117.1	321.1	156.3	167.5	0.933	1.00
107.2	990.0	7500.7	137.35	0.00	0.19	2704.8	1642.2	177.9	110.7	122.3	0.905	1.00
57.0	990.0	14103.9	152.70	0.03	0.25	4233.6	3375.7	457.3	142.8	82.1	1.74	-----
29.6	990.0	27134.1	168.26	0.97	0.60	4410.0	3437.0	343.2	105.5	43.3	2.44	-----
14.5	990.0	55283.0	194.13	0.00	0.83	4998.0	4357.0	317.2	78.3	22.1	3.54	-----
5.4	990.0	147754.1	226.57	0.63	0.20	7467.6	7540.4	411.9	60.8	9.95	6.11	-----

TABLE 26: (....continued) Industrial Schedule No. 4

Roll radius : 406 mm
Material : commercial-purity aluminium
Initial ingot thickness : 485 mm
Slab width : 960 mm
Slab length : 1710 mm
Initial entry temperature : 482°C

Roll speed : ∿ 52.3 rev./min.
Spread coefficient : 0.059
Initial grain size : 110 μm

THICKNESS AFTER PASS (mm)	WIDTH AFTER PASS (mm)	LENGTH AFTER PASS (mm)	TIME TO ROLL (sec)	X_v CENTRE BEFORE PASS	X_v SURFACE BEFORE PASS	EXPERIMENTAL LOAD (kN)	THEORETICAL LOAD (kN)	THEORETICAL TORQUE (kN-M)	$\sqrt{R\ (h_o-h_f)}$ (mm)	h_m (mm)	m	n
438.2	962.8	1887.0	50.38	0.00	0.00	4233.6	1472.8	191.0	137.8	461.6	0.299	1.63
378.1	966.7	2178.2	70.42	0.00	0.00	5350.8	2045.3	316.2	156.2	408.2	0.383	1.43
317.8	970.8	2580.2	79.49	0.00	0.00	5468.4	2231.4	343.3	156.5	348.0	0.450	1.31
258.6	975.3	3156.4	94.57	0.00	0.03	5233.2	2459.3	376.0	155.0	288.2	0.538	1.20
198.2	980.5	4097.8	103.73	0.03	0.09	5115.6	2782.0	428.3	156.6	228.4	0.686	1.08
137.1	986.6	5884.2	125.95	0.97	0.89	5468.4	4432.2	801.4	157.5	167.7	0.939	1.00
108.1	990.0	7440.1	144.36	0.09	0.66	3939.6	2208.4	210.4	108.5	122.6	0.885	1.01
58.3	990.0	13795.3	160.70	0.18	0.29	5997.6	4234.8	511.6	142.2	83.2	1.709	-----
29.8	990.0	26963.8	190.16	0.76	0.90	6291.6	4421.5	401.7	107.6	44.1	2.440	-----
14.6	990.0	54941.6	214.00	0.24	0.20	6409.2	4903.7	321.1	78.6	22.2	3.541	-----
5.9	990.0	136078.7	251.60	0.77	0.86	8643.6	7320.4	354.4	59.4	10.3	5.767	-----

TABLE 27: Industrial Schedule No. 5

BDM Stage:

Mill dimensions : 905 x 1525 x 2900 mm, 4-high reversible mill.
Time between passes : 5 sec.
Material : commercial-purity aluminium.
Initial ingot thickness : 580 mm
Slab width : 1100 mm
Initial ingot temperature : 480°C
Roll speed : 50-65 r.p.m. randomly distributed by pass.

Tandem Mill Operations (3 stands)

Mill dimension each stand : 720 x 1500 x 2940 mm, 4-high.
Slab width : 1700 mm
Exit strip speeds (m/sec) : 1.42/2.84/4.16
Spread coefficient : 0.133

THICKNESS AFTER PASS (mm)	WIDTH AFTER PASS (mm)	LENGTH AFTER PASS (mm)	TIME TO ROLL (sec)	X_v CENTRE BEFORE PASS	X_v SURFACE BEFORE PASS	EXPERIMENTAL TORQUE (kN-M)	THEORETICAL TORQUE (kN-M)	THEORETICAL LOAD (kN)	$\sqrt{R\,(h_o-h_f)}$ (mm)	h_m (mm)	m	n
550	1107.8	3141.4	192.5	0.00	0.00	823.2	166.6	1556.6	116.5	565	0.206	1.98
570	1119.0	3353.8	198.7	0.00	0.00	940.8	306.4	2291.0	134.5	530	0.254	1.78
470	1131.2	3600.0	204.9	0.00	0.00	921.2	334.9	2317.0	134.5	490	0.274	1.71
430	1144.7	3888.5	211.2	0.00	0.00	715.4	325.2	2433.9	134.5	450	0.299	1.63
390	1159.6	4232.2	217.5	0.00	0.00	754.6	343.4	2570.0	134.5	410	0.328	1.55
350	1176.4	4648.6	224.0	0.00	0.00	872.2	364.0	2725.6	134.5	370	0.364	1.47
320	1190.5	5024.1	230.7	0.00	0.00	656.6	273.1	2359.3	116.5	335	0.401	1.39
280	1211.9	5640.5	237.4	0.00	0.01	627.2	409.4	3071.2	134.5	300	0.448	1.31
240	1237.0	6447.0	244.3	0.02	0.07	744.8	442.1	3323.1	134.5	260	0.517	1.22
200	1267.3	7551.5	251.3	0.08	0.20	744.8	482.2	3637.4	134.5	220	0.611	1.13
160	1305.5	9163.2	258.9	0.36	0.73	637.0	528.9	4025.1	134.5	180	0.747	1.05
120	1356.4	11759.1	267.0	0.54	0.00	627.2	614.0	4680.1	134.5	140	0.961	1.00
85	1420.1	15856.4	275.0	0.00	0.06	578.2	639.7	5225.5	125.8	102.5	1.227	----

TABLE 27: (....continued)

THICKNESS AFTER PASS (mm)	WIDTH AFTER PASS (mm)	LENGTH AFTER PASS (mm)	TIME TO ROLL (sec)	X_v CENTRE BEFORE PASS	X_v SURFACE BEFORE PASS	EXPERIMENTAL TORQUE (kN-M)	THEORETICAL TORQUE (kN-M)	THEORETICAL LOAD (kN)	$\sqrt{R(h_o-h_f)}$ (mm)	h_m (mm)	m	n
46	1540.9	27002.9	285.9	0.13	0.95	764.4	976.3	7761.7	132.8	65.5	2.027	----
22	1699.8	51182.5	298.7	0.87	0.41	764.4	929.1	9074.9	104.2	34.0	3.065	----
8.79	1920.4	113386.5	461.8	1.00	1.00	215.6	833.6	13320.9	68.96	15.39	4.48	----
4.39	2106.2	207003.6	463.9	0.00	0.00	431.2	456.2	12411.2	39.80	6.59	6.04	----
3.00	2215.6	287959.5	465.0	0.00	0.08	107.8	159.7	7452.8	22.37	3.69	6.06	----

TABLE 28: Industrial Schedule No. 6

Mill dimensions : 914 x 1524 x 3658 mm,
4-high reversible.
Material : commercial-purity aluminium.
Initial ingot thickness : 464.4 mm
Slab width : 1016.0 mm
Initial ingot temperature : 520°C
Roll speed : 1.68 m/sec.

Assumptions made:

Slab length : 3700 mm
Initial grain size : 110 μm
Spread coefficient : 0.133
Time between reheating and rolling : 150 sec.

THICKNESS AFTER PASS (mm)	WIDTH AFTER PASS (mm)	LENGTH AFTER PASS (mm)	TIME TO ROLL (sec)	X_v CENTRE BEFORE PASS	X_v SURFACE BEFORE PASS	EXPERIMENTAL TORQUE (kN-M)	THEORETICAL TORQUE (kN-M)	THEORETICAL LOAD (kN)	$\sqrt{R(h_o-h_f)}$ (mm)	h_m (mm)	m	n
455.9	1019.7	3787.4	151.1	0.00	0.00	1017.1	16.68	179.1	75.60	462.15	0.164	2.21
439.2	1024.7	3912.4	147.2	0.00	0.00	1356.2	39.50	339.7	87.38	447.55	0.195	2.04
406.4	1035.4	4184.5	163.4	0.00	0.00	732.3	96.45	792.7	122.46	422.80	0.290	1.66
355.6	1053.9	4698.1	169.7	0.00	0.00	908.6	202.1	1340.2	152.40	381.00	0.400	1.40
304.8	1075.8	5369.9	176.1	0.00	0.00	881.5	233.7	1551.4	152.40	330.20	0.462	1.29
254.0	1102.2	6289.6	182.7	0.00	0.00	813.7	273.1	1706.0	152.40	279.40	0.545	1.19
203.2	1135.4	7632.0	189.6	0.01	0.02	813.7	323.6	2161.2	152.40	228.60	0.667	1.09
152.4	1179.6	9794.1	196.8	0.12	0.29	867.9	395.2	2656.5	152.40	177.80	0.857	1.01
101.6	1245.0	13919.8	204.8	0.52	0.69	854.4	510.9	3470.5	152.40	127.00	1.200	----
68.6	1311.8	19571.7	213.9	0.35	0.05	637.4	413.7	3486.8	122.83	85.10	1.443	----
43.2	1395.1	29229.5	224.7	0.07	0.79	583.1	427.0	4137.7	107.76	55.90	1.928	----
27.4	1481.8	43318.4	238.4	0.69	0.19	420.4	350.3	4286.6	84.99	35.30	2.408	----

TABLE 29: Industrial Schedule No. 7

Mill dimensions : 812 x 2100 mm,
2-high reversible
Material : commercial-purity aluminium
Initial ingot thickness : 230 mm
Slab width : 700 mm
Initial ingot temperature : 525°C
Roll speed : 1.5-1.75 m/sec.

Assumptions made:

Slab length : 3700 mm
Initial grain size : 110 μm
Spread coefficient : 0.133
Time between reheating and rolling : 150 sec.

THICKNESS AFTER PASS (mm)	WIDTH AFTER PASS (mm)	LENGTH AFTER PASS (mm)	TIME TO ROLL (sec)	X_v CENTRE BEFORE PASS	X_v SURFACE BEFORE PASS	EXPERIMENTAL TORQUE (kN-M)	THEORETICAL TORQUE (kN-M)	THEORETICAL LOAD (kN)	$\sqrt{R(h_o-h_f)}$ (mm)	h_m (mm)	m	n
166	731.0	4908.9	157.1	0.00	0.00	529.2	244.7	1568.2	161.2	198.0	0.814	1.02
116	766.7	6697.8	164.6	0.00	0.00	450.8	243.3	1754.4	142.5	141.0	1.01	----
80	805.6	9243.6	172.7	0.12	0.37	352.8	214.9	1832.1	120.9	98.0	1.23	----
50	857.5	13893.6	181.5	0.88	0.63	532.8	238.9	2247.7	110.4	65.0	1.70	----
29	922.0	22280.1	191.8	0.00	0.34	284.2	241.2	2750.2	92.3	39.5	2.33	----
15	1006.4	39459.2	204.6	0.67	0.67	254.8	252.9	3546.3	75.4	22.0	3.43	----
6.5	1124.8	81474.8	222.8	0.35	0.61	235.2	298.6	5557.5	58.7	10.75	5.46	----

FIGURE 1: Cast 1200 alloy showing the interdendritic cell structure within the grains; microanodized and viewed in polarised light. ∿ 50 x.

(After Emley [2]).

FIGURE 2: Effect of solidification rate on as-cast structure of 1200 alloy: (a) interior of DC cast block (fast solidification), (b) interior of Isomet cast block (slow solidification). ∿ 100 x.

(After Emley [2]).

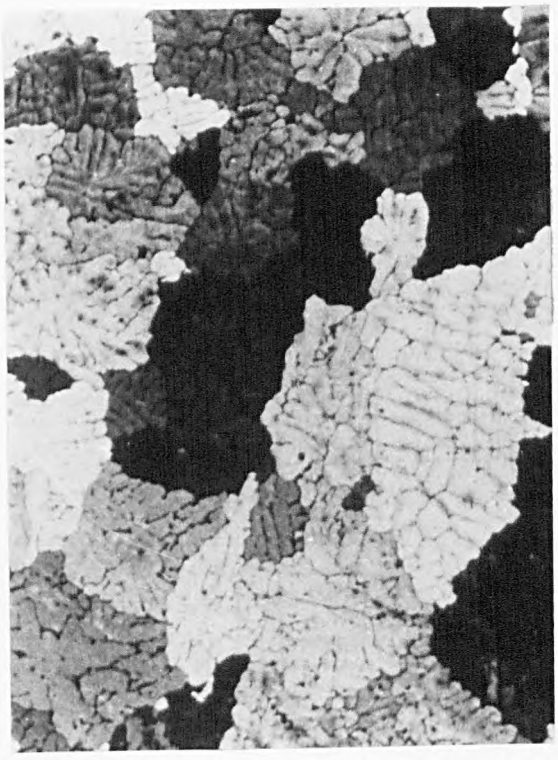

0,5 mm

(b)

0,1 mm

(a)

FIGURE 3: Schematic diagram of vertical DC casting as commonly practiced.

(After Emley [2]).

FIGURE 4: Basic production flow route for plate.

(After Band and Harris [6]).

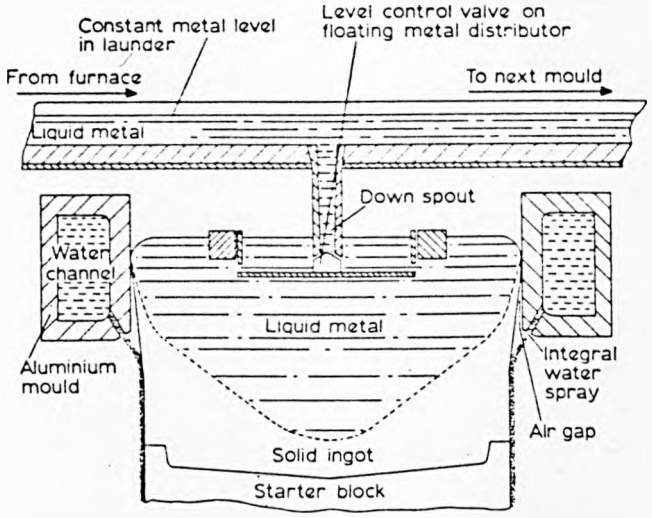
Constant metal level in launder
Level control valve on floating metal distributor
From furnace
To next mould
Liquid metal
Down spout
Water channel
Liquid metal
Aluminium mould
Integral water spray
Air gap
Solid ingot
Starter block

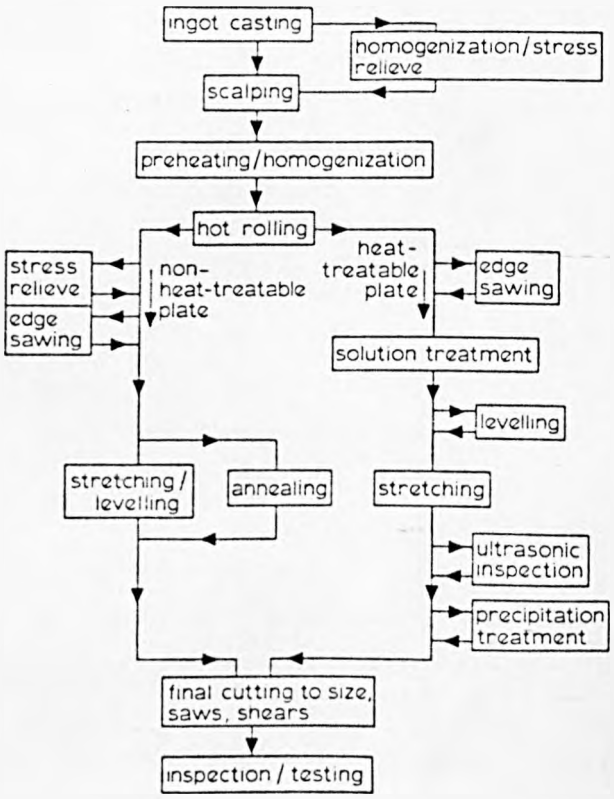
ingot casting
homogenization/stress relieve
scalping
preheating/homogenization
hot rolling
stress relieve
edge sawing
non-heat-treatable plate
heat-treatable plate
edge sawing
solution treatment
levelling
stretching/levelling
annealing
stretching
ultrasonic inspection
precipitation treatment
final cutting to size, saws, shears
inspection / testing

FIGURE 5: Effect of homogenisation treatment on structure of cast 3103 alloy: (a) as-cast, (b) homogenised for 16 hrs. at 600°C. ∿ 500 x.

(After Emley [2]).

FIGURE 6: Typical hot mill layout for production of plate.

(After Band and Harris [6]).

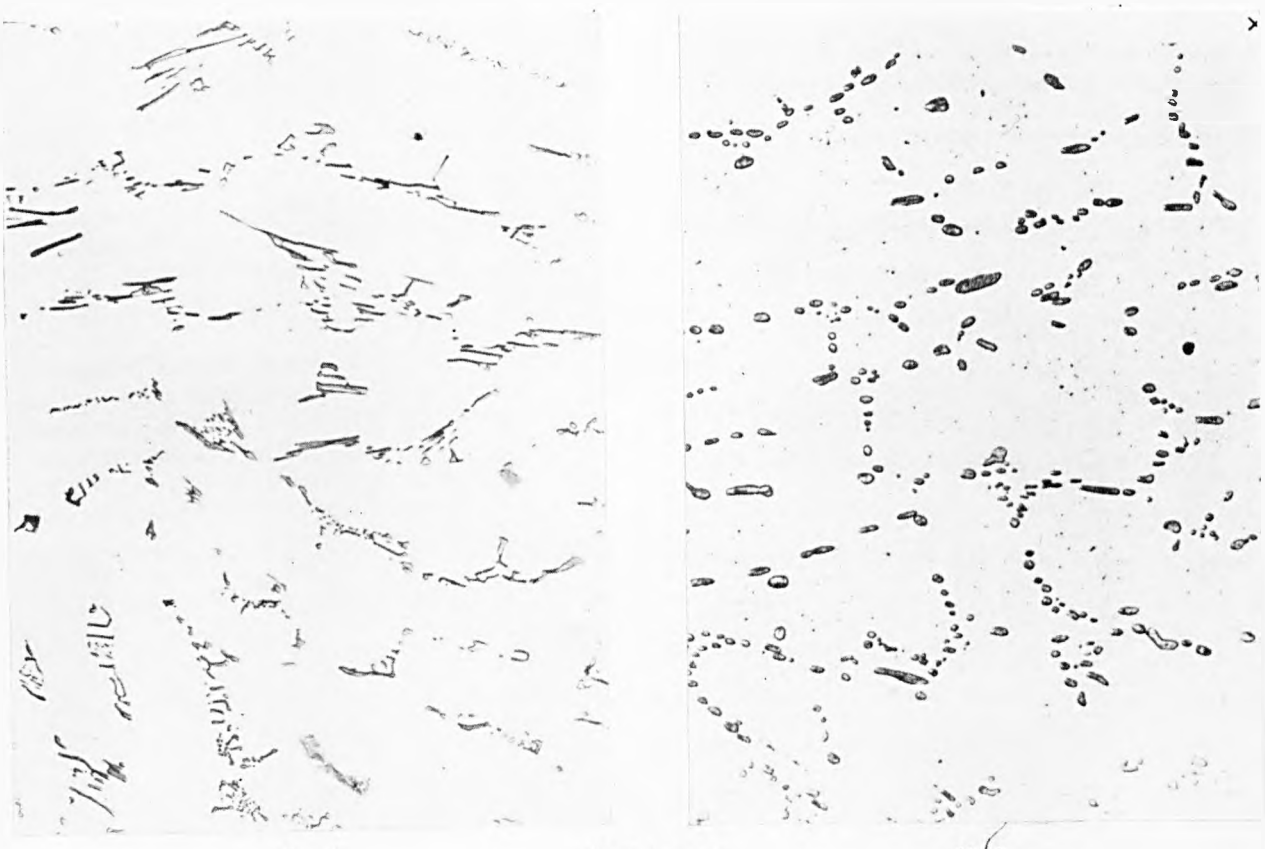
(a)
0,04 mm
(b)

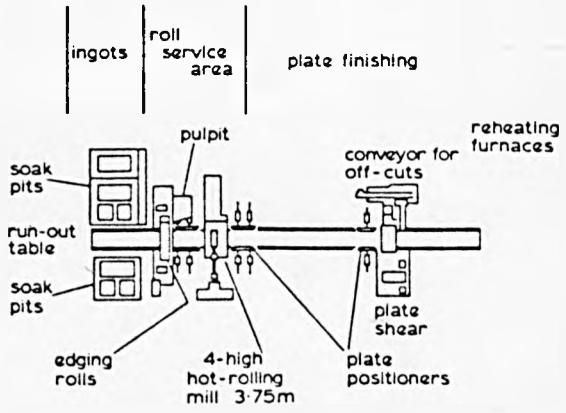
ingots
roll service area
plate finishing
pulpit
reheating furnaces
conveyor for off-cuts
soak pits
run-out table
soak pits
plate shear
edging rolls
4-high hot-rolling mill 3·75m
plate positioners

FIGURE 7: Hot rolling line at Rogerstone before removal of the 96 inch. two high mill.

(Interview [14]).

FIGURE 8: Schematic outline of semi-continuous rod mill at the Aluminium Wire and Cable Co. Ltd., Swansea.

(After Swain [15]).

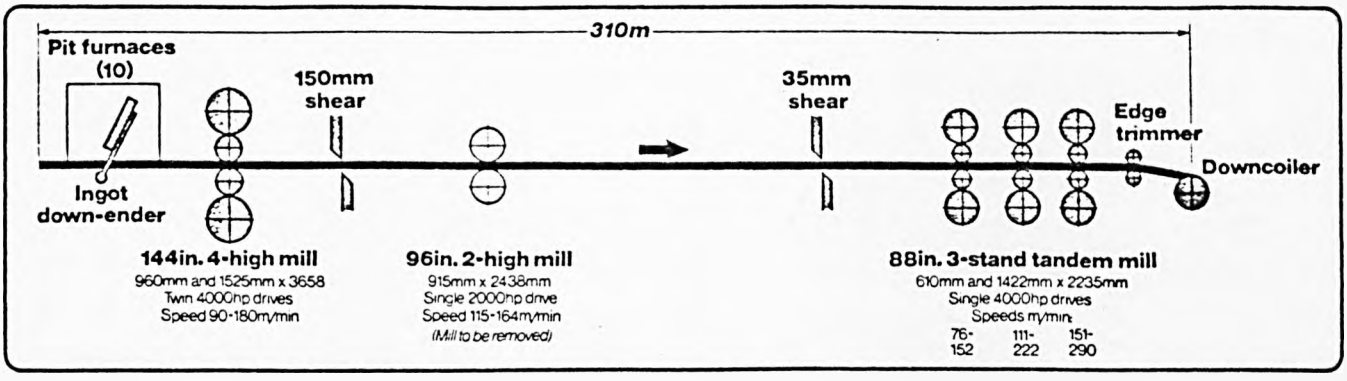
310m
Pit furnaces
(10)
150mm
shear
35mm
shear
Edge
trimmer
Downcoiler
Ingot
down-ender
144in. 4-high mill
960mm and 1525mm x 3658
Twin 4000hp drives
Speed 90-180m/min
96in. 2-high mill
915mm x 2438mm
Single 2000hp drive
Speed 115-164m/min
(Mill to be removed)
88in. 3-stand tandem mill
610mm and 1422mm x 2235mm
Single 4000hp drives
Speeds m/min:
76-152
111-222
151-290

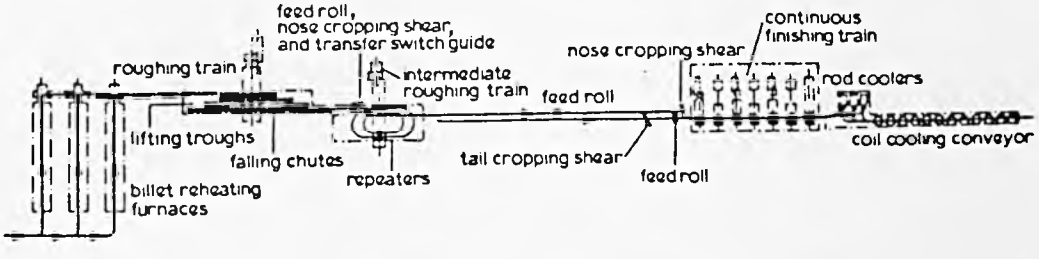
feed roll,
nose cropping shear,
and transfer switch guide
continuous
finishing train
nose cropping shear
roughing train
intermediate
roughing train
feed roll
rod coolers
lifting troughs
falling chutes
repeaters
tail cropping shear
feed roll
coil cooling conveyor
billet reheating
furnaces

FIGURE 9: Stress-strain curves for commercial-purity aluminium tested at 300°C.

(After Beynon [24]).

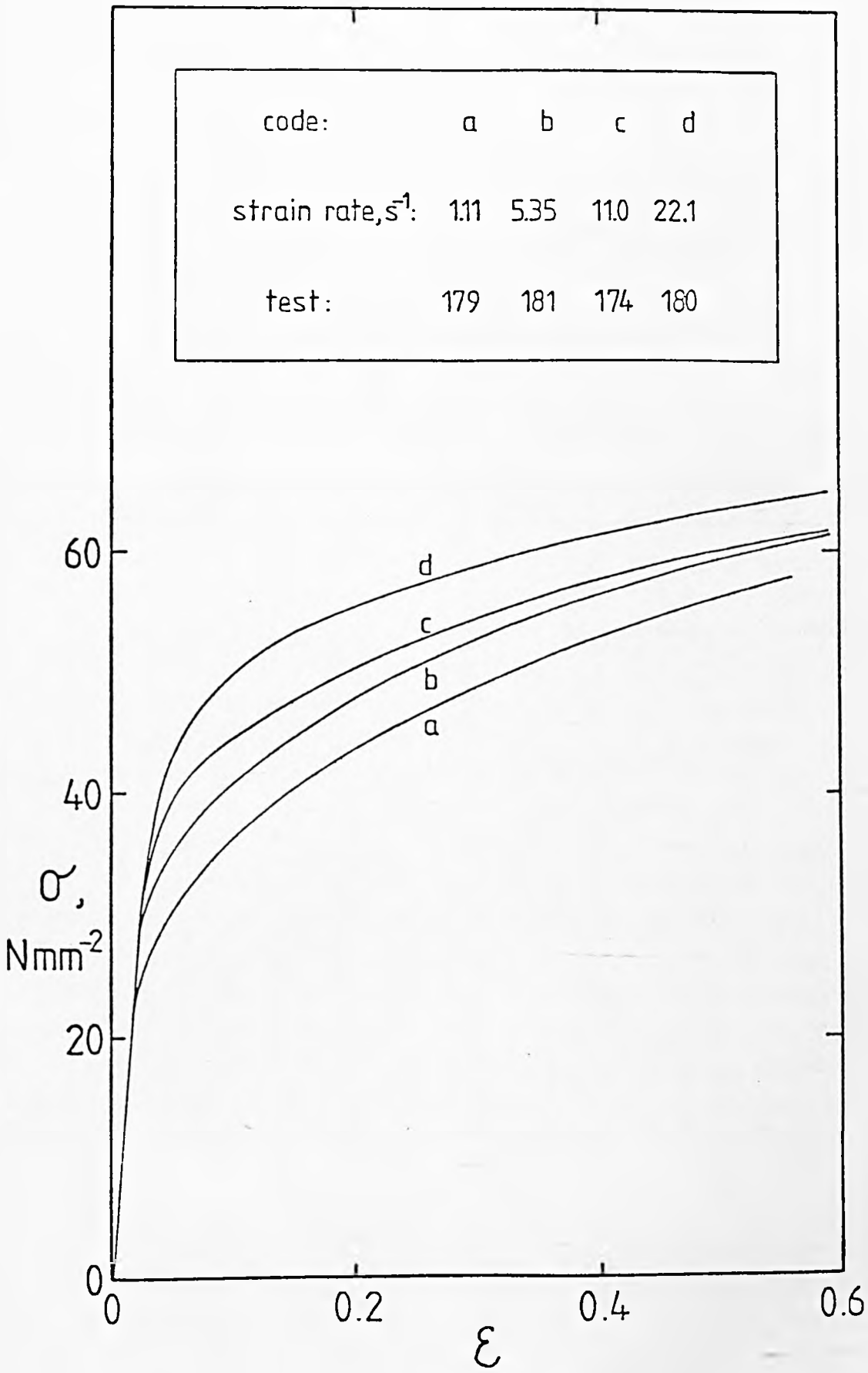
code: a b c d
strain rate, s⁻¹: 1.11 5.35 11.0 22.1
test: 179 181 174 180
d
c
b
a
60
40
20
0
σ, Nmm⁻²
0
0.2
0.4
0.6
ε

FIGURE 10: Stress-strain curves for commercial-purity aluminium tested at 400°C.

(After Beynon [24]).

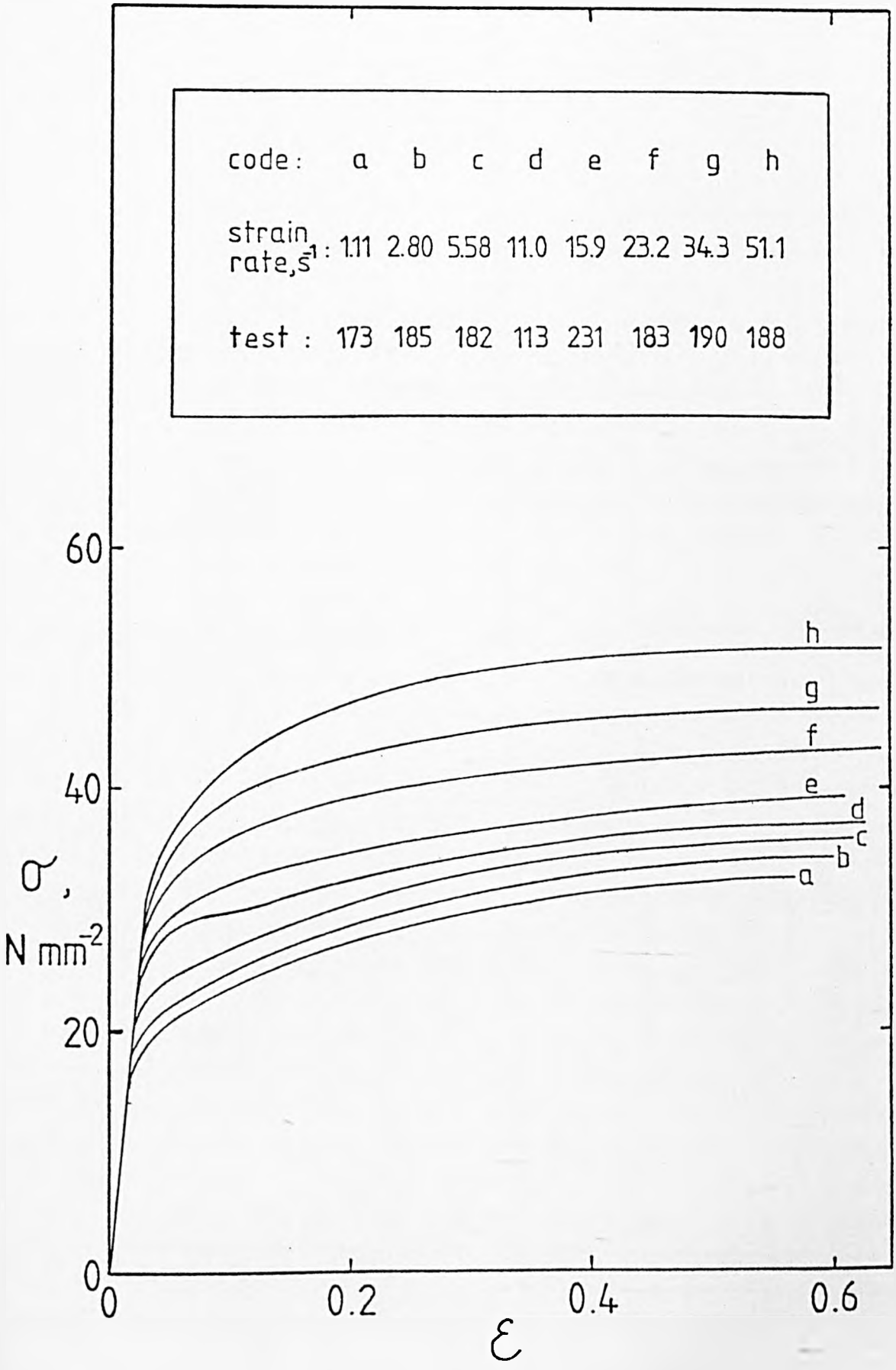
code: a b c d e f g h
strain rate, s⁻¹: 1.11 2.80 5.58 11.0 15.9 23.2 34.3 51.1
test: 173 185 182 113 231 183 190 188
60
40
20
0
σ, N mm⁻²
0
0.2
0.4
0.6
ε
h
g
f
e
d
c
b
a

FIGURE 11: Stress-strain curves for commercial-purity aluminium tested at 500°C.

(After Beynon [24]).

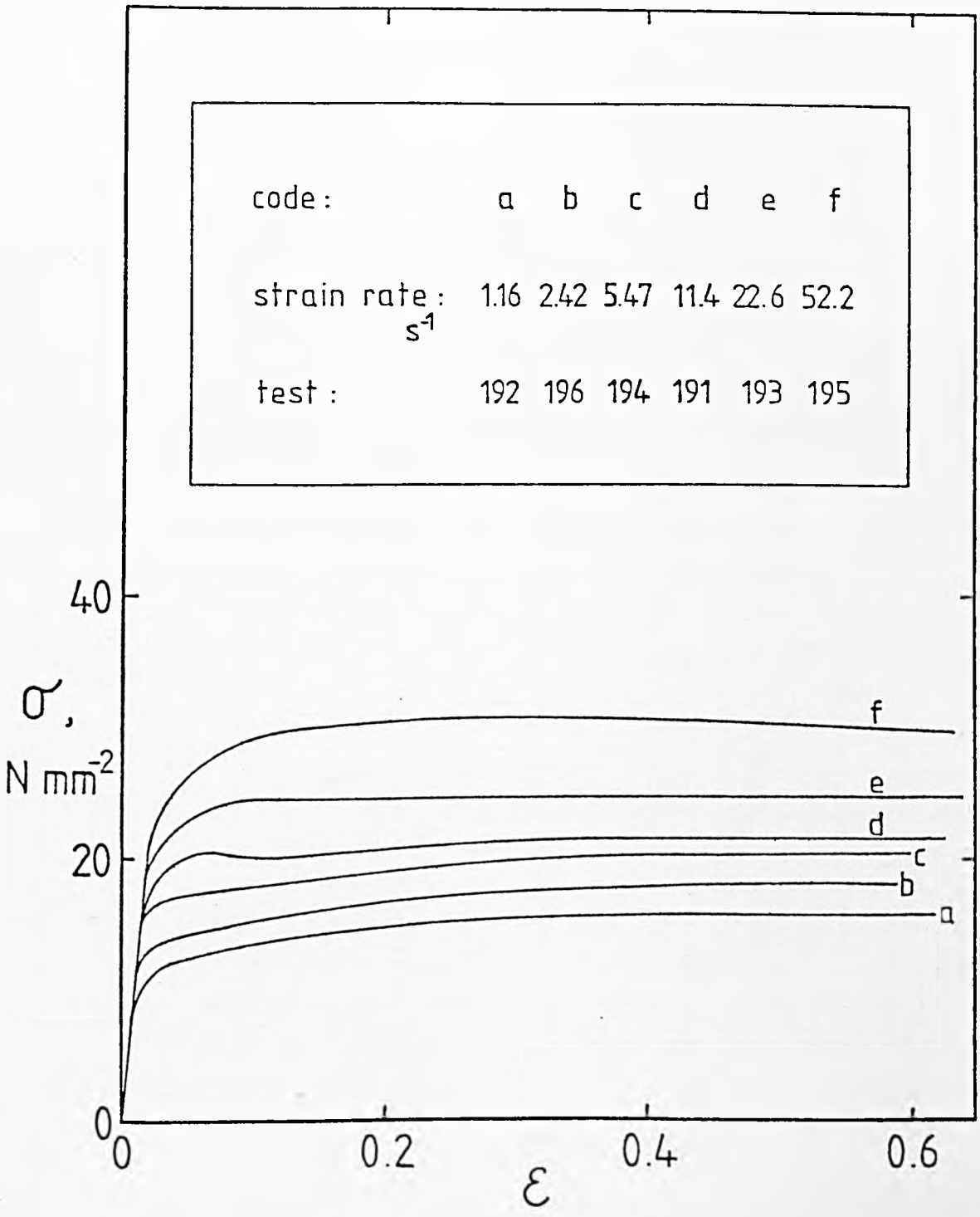
code : a b c d e f
strain rate : 1.16 2.42 5.47 11.4 22.6 52.2
s⁻¹
test : 192 196 194 191 193 195
40
20
0
σ,
N mm⁻²
0
0.2
0.4
0.6
ε
f
e
d
c
b
a

FIGURE 12: Linear relationship between log Z/A and log [Sinh ($\alpha\sigma$)] for aluminium.

(After Jonas et al [23]).

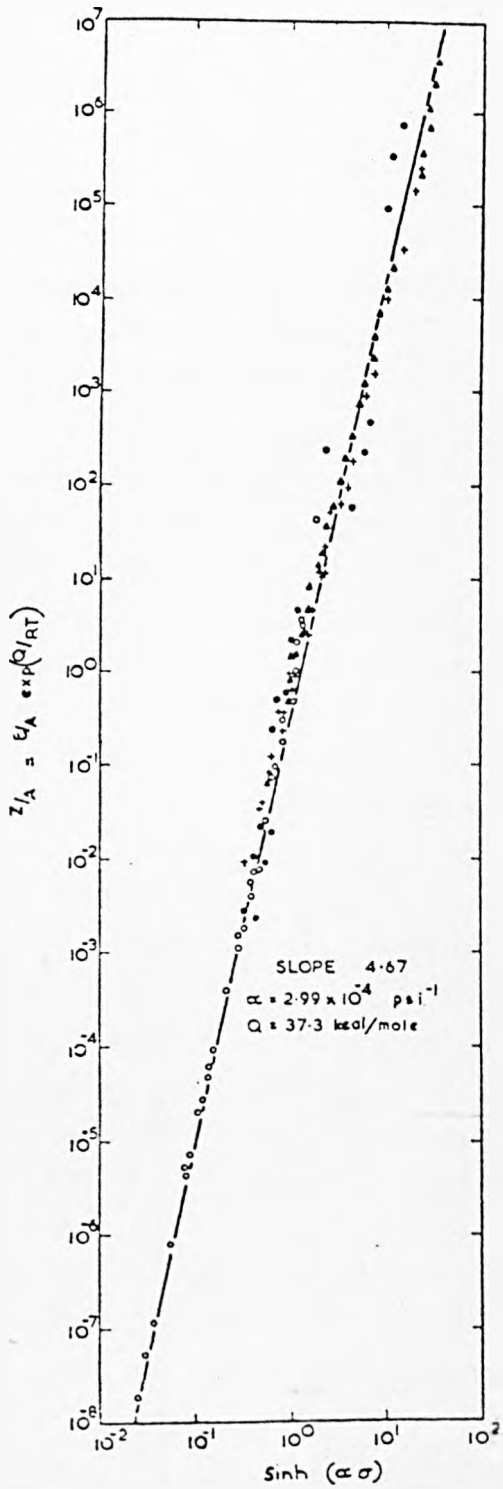
SLOPE 4·67
α = 2·99 x 10⁻⁴ psi⁻¹
Q = 37·3 kcal/mole
Z/A = ε/A exp(Q/RT)
Sinh (ασ)

FIGURE 13: Relation between the flow stress ($\sigma_{0.05}$) and log $\dot{\epsilon}$ for pure aluminium.

(After Tanaka and Nojima [57]).

FIGURE 14: Relation between the flow stress ($\sigma_{0.05}$) and log $\dot{\epsilon}$ for Al-Mg alloy.

(After Tanaka and Nojima [58]).

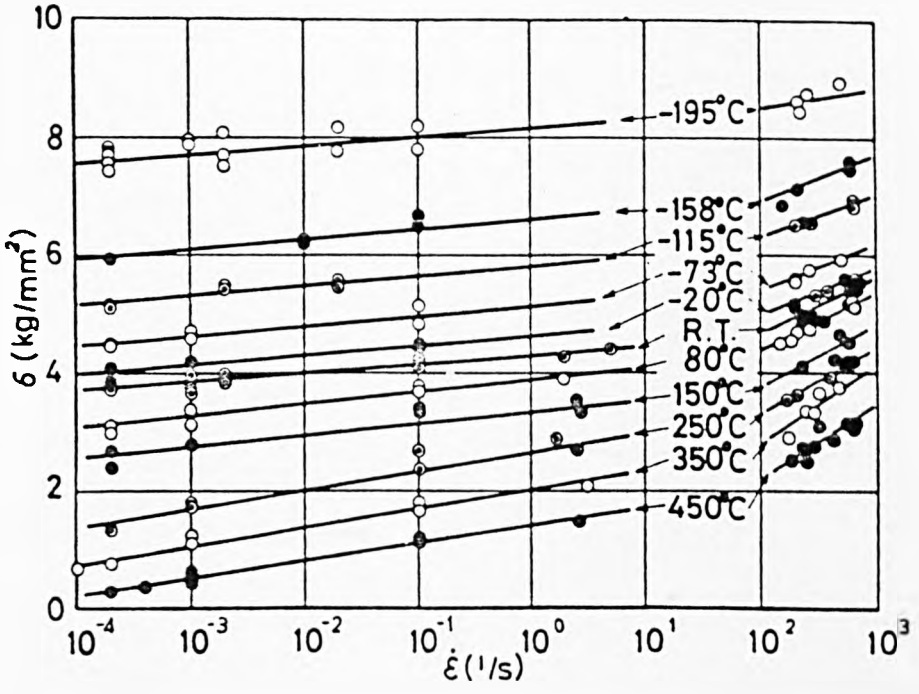
σ (kg/mm²)
10
8
6
4
2
0
-195°C
-158°C
-115°C
-73°C
-20°C
R.T.
80°C
150°C
250°C
350°C
450°C
10⁻⁴ 10⁻³ 10⁻² 10⁻¹ 10⁰ 10¹ 10² 10³
ε̇ (1/s)

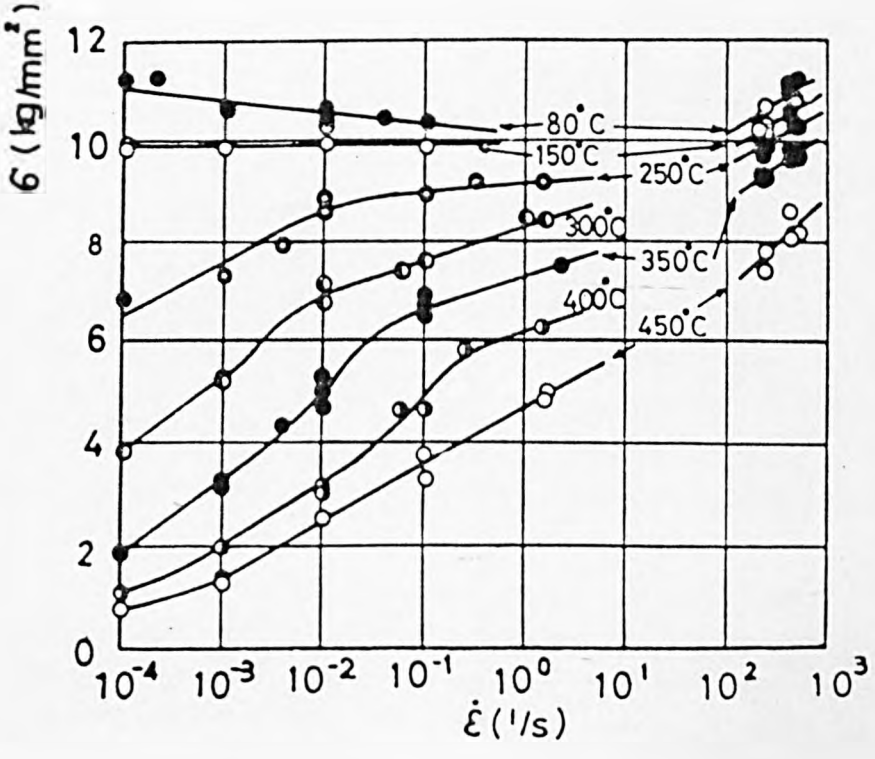
σ (kg/mm²)
12
10
8
6
4
2
0
80°C
150°C
250°C
300°C
350°C
400°C
450°C
10⁻⁴ 10⁻³ 10⁻² 10⁻¹ 10⁰ 10¹ 10² 10³
ε̇ (1/s)

FIGURE 15: Relation between log $\dot{\varepsilon}$ and σ for commercial-purity aluminium.

(After Beynon [24]).

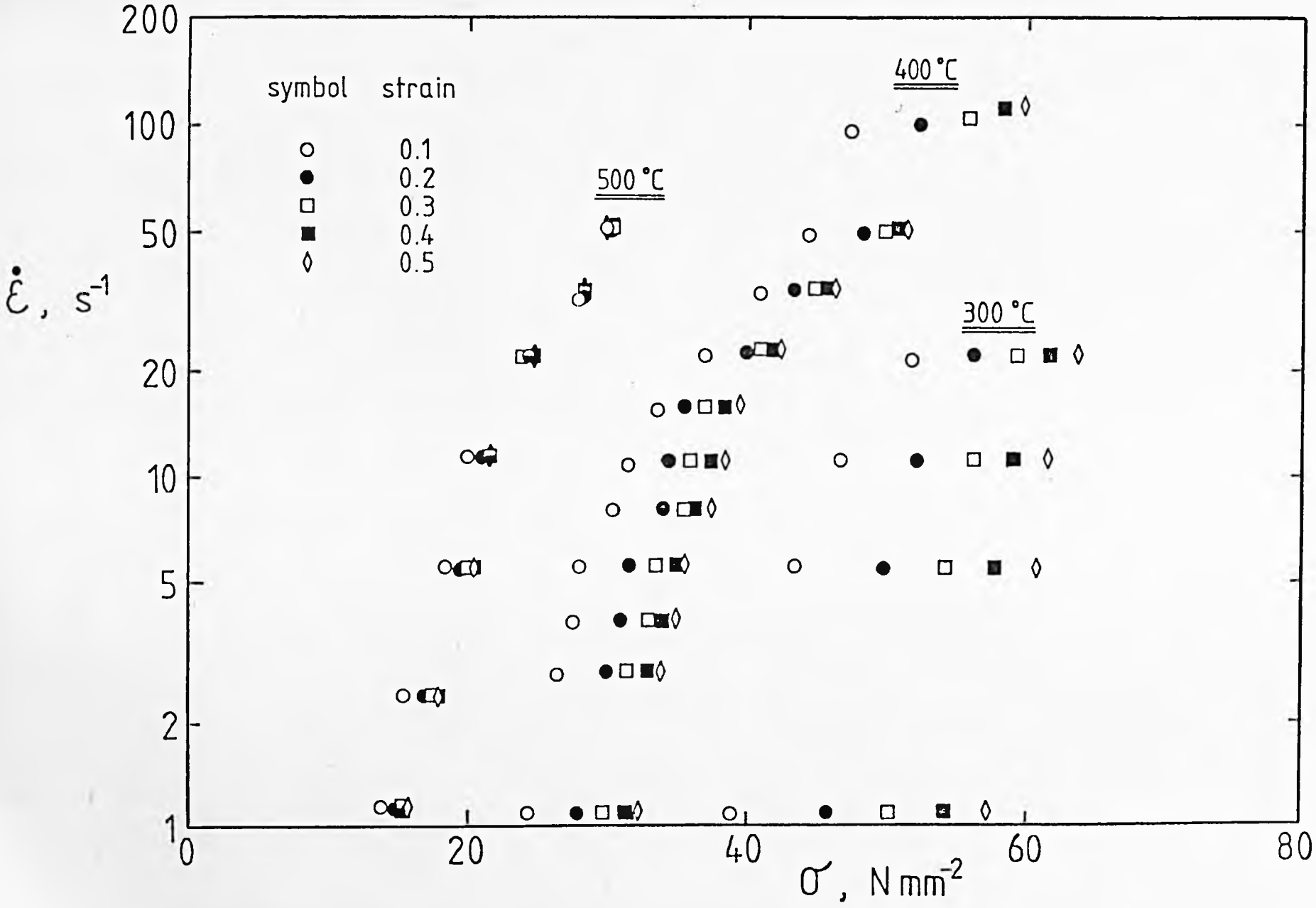
200
100
50
20
10
5
2
1
0
20
40
60
80
$\dot{\varepsilon}$, s^{-1}
σ, $N\,mm^{-2}$
symbol strain
0.1
0.2
0.3
0.4
0.5
400 °C
500 °C
300 °C

FIGURE 16: Relation between log $\dot{\varepsilon}$ and σ for commercial-purity aluminium.

(After Beynon [24]).

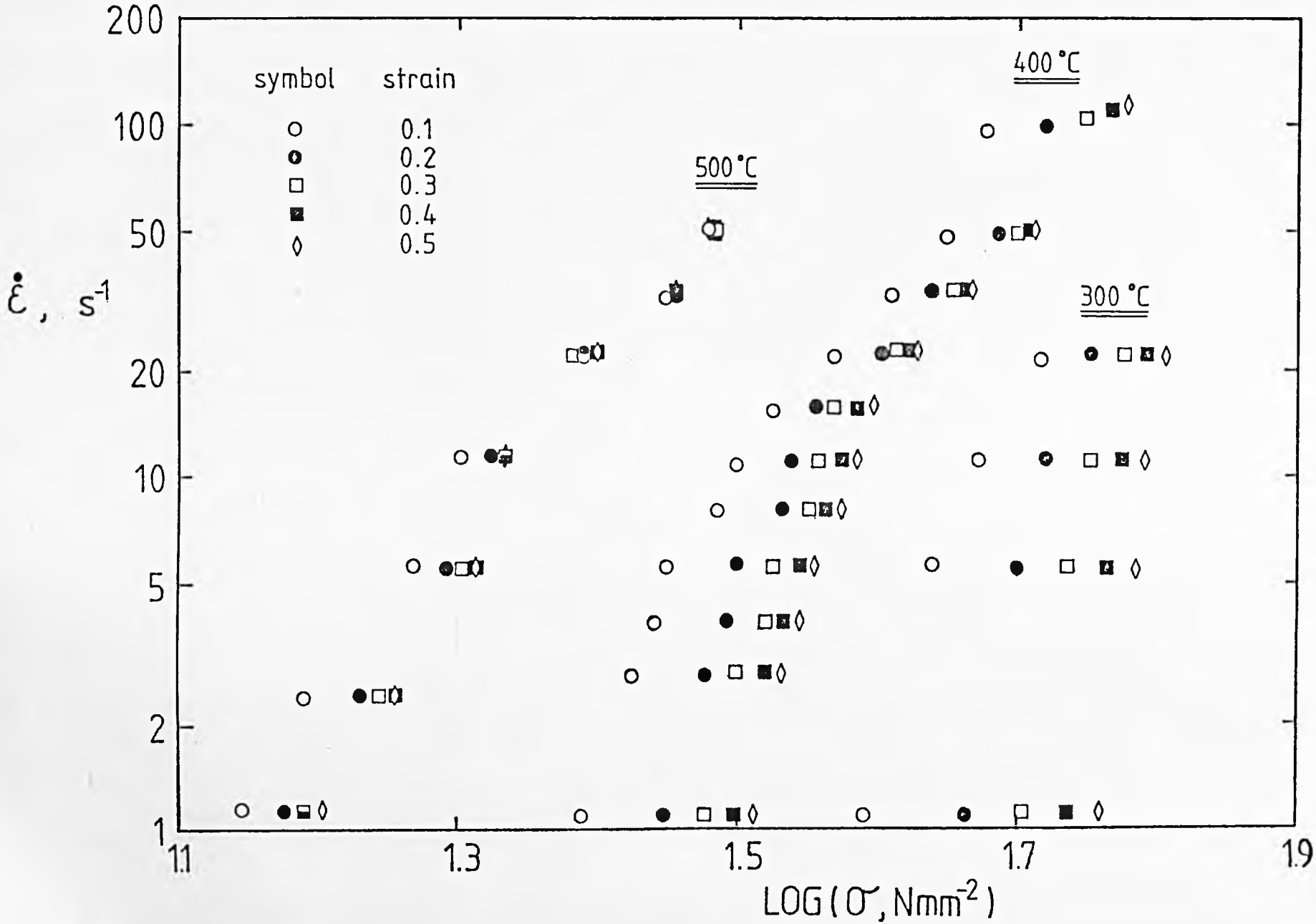
200
100
50
20
10
5
2
1
$\dot{\varepsilon}$, s^{-1}
symbol
strain
0.1
0.2
0.3
0.4
0.5
400 °C
500 °C
300 °C
1.1
1.3
1.5
1.7
1.9
LOG (σ, Nmm^{-2})

FIGURE 17: Relation between log $\dot{\epsilon}$ and log [Sinh ($\alpha\sigma$)] for commercial-purity aluminium using a value of 0.0432 mm^2/N for alfa.

(After Beynon [24]).

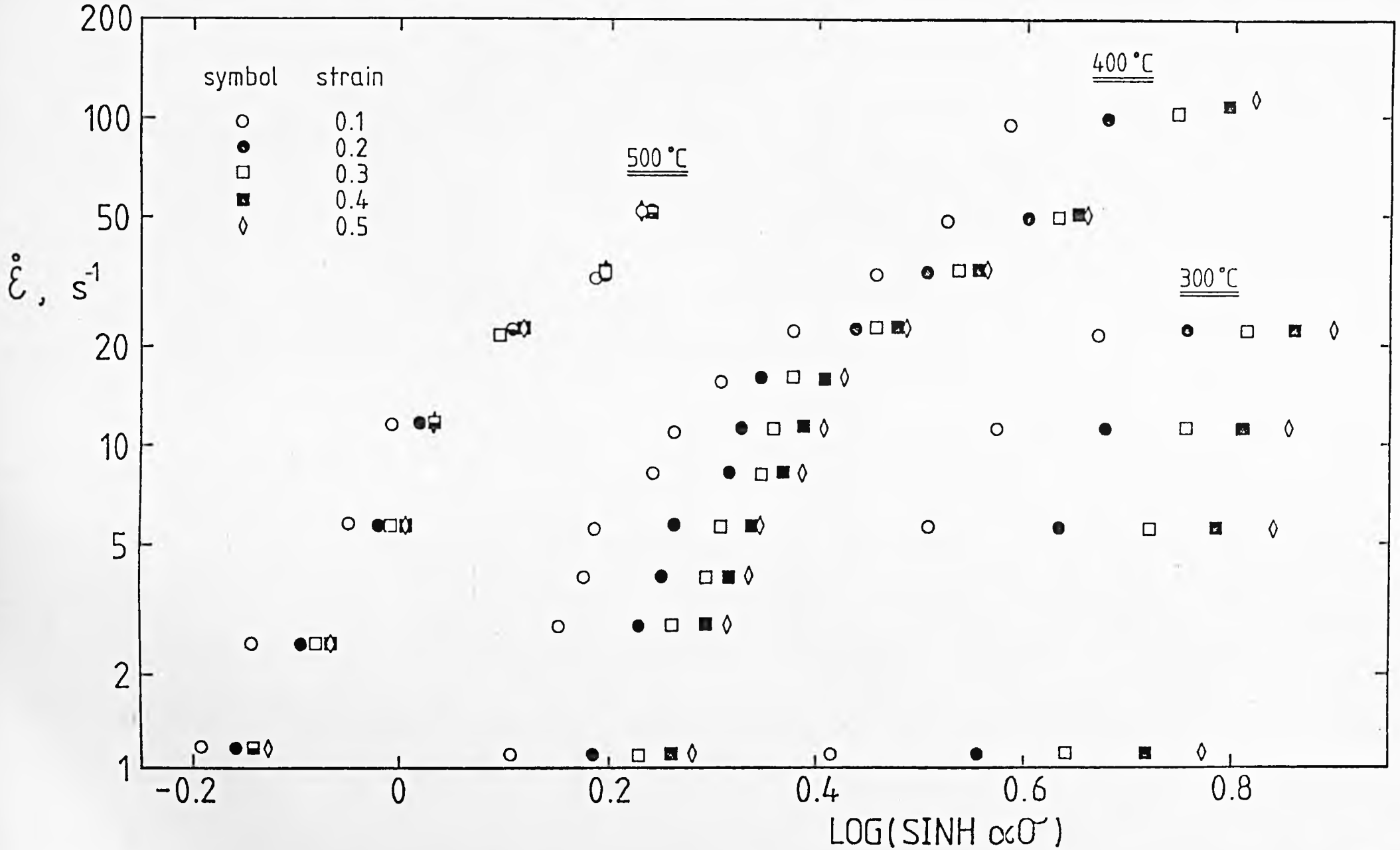
200
100
50
20
10
5
2
1
symbol
strain
0.1
0.2
0.3
0.4
0.5
400 °C
500 °C
300 °C
$\dot{\varepsilon}$, s^{-1}
-0.2
0
0.2
0.4
0.6
0.8
LOG(SINH ασ)

FIGURE 18: Effect of copper and magnesium in solid solution on the maximum flow stress in super-purity aluminium based alloys.

(After Sellars [10]).

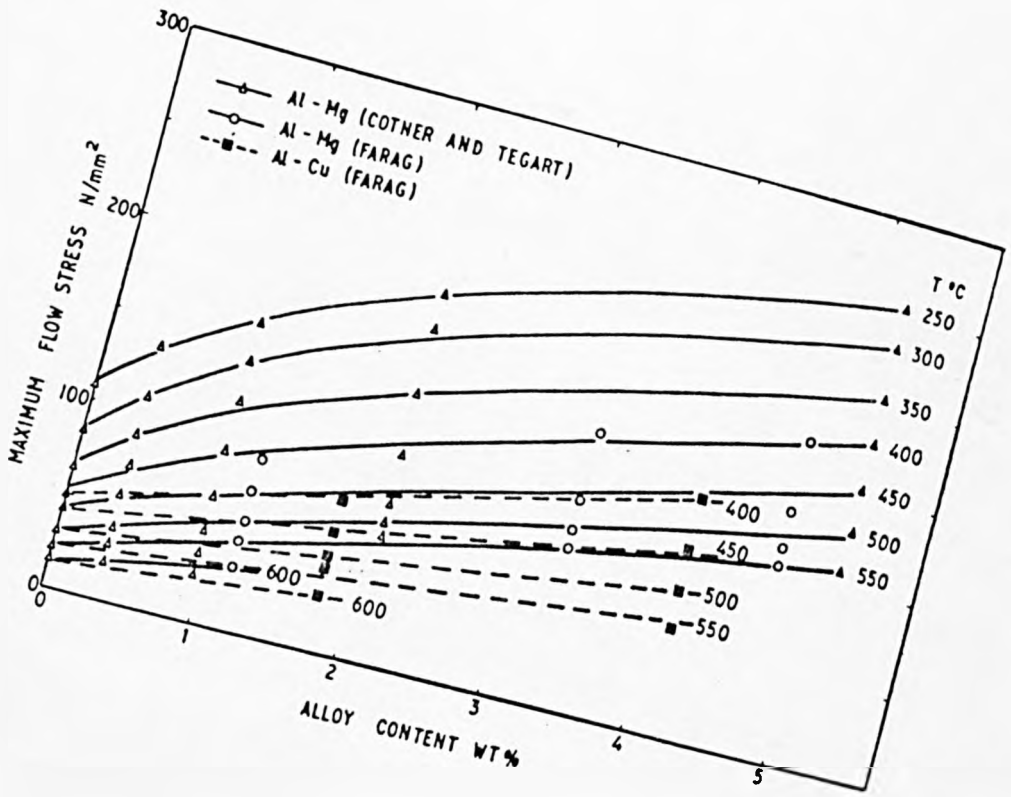
Al - Mg (COTHER AND TEGART)
Al - Mg (FARAG)
Al - Cu (FARAG)
MAXIMUM FLOW STRESS N/mm²
ALLOY CONTENT WT %
T °C
250
300
350
400
450
500
550
600
0
100
200
300
1
2
3
4
5

FIGURE 19: Thin foil micrographs of structures observed in commercial purity aluminium after deformation in plane strain compression.

Top, bottom, mid right and mid left - 1 sec. hold.

Centre - 10 sec. hold.

(After Sellars [10]).

FIGURE 20: Weakly formed sub-boundaries (arrowed) inside wall formed subgrains.

(After Zaidi and Sheppard [89]).

400°C 83 s^{-1}

300°C 11 s^{-1}

400°C 11 s^{-1}

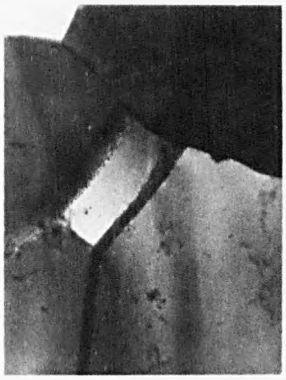

500°C 11 s^{-1}

5 µm

400°C 0·11 s^{-1}

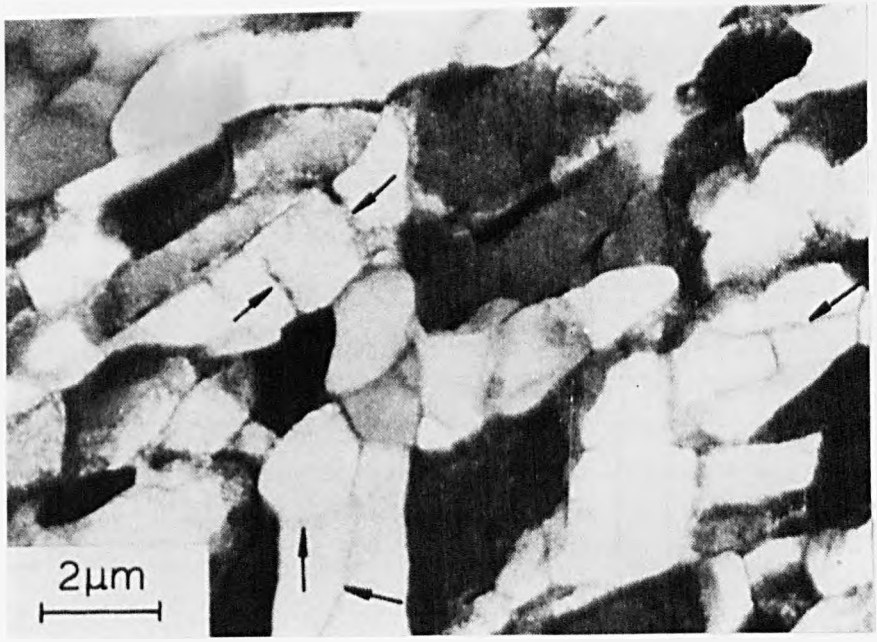

FIGURE 21: Desintegration of part of a subgrain boundary and formation of new boundary.

(After Zaidi and Sheppard [89]).

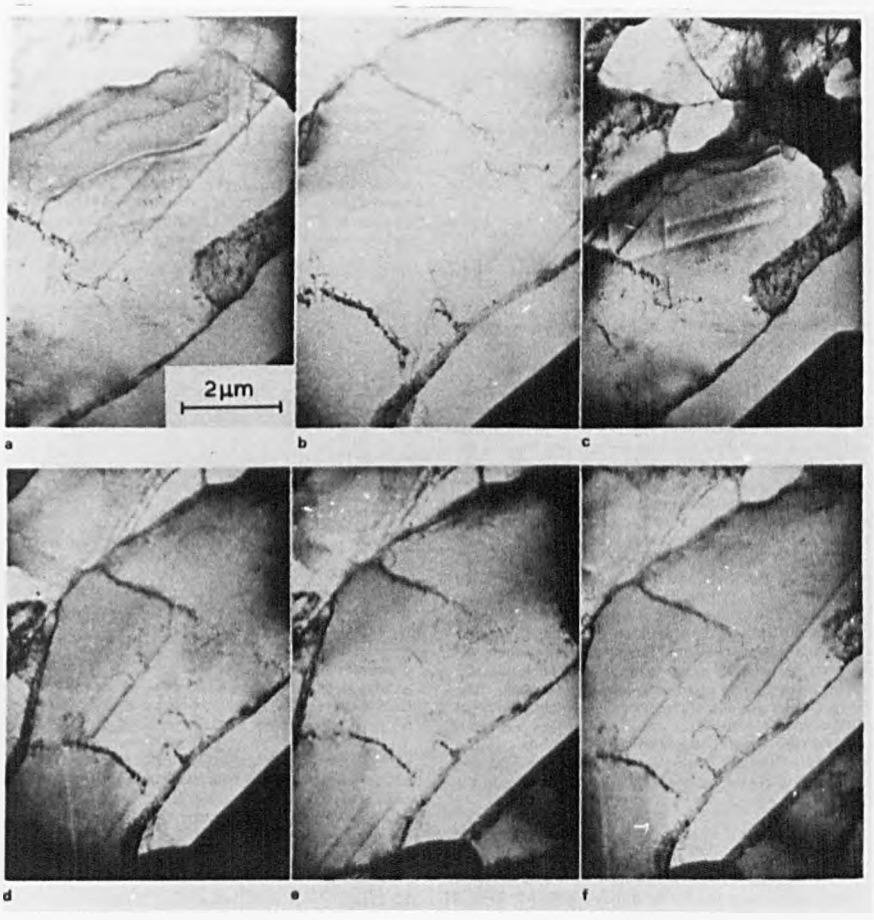
2μm
a
b
c
d
e
f

FIGURE 22: Temperature-time schedule of a series of torsion tests on superpurity aluminium conducted at a strain rate of 2.3 s^{-1}.

(After Farag et al [98]).

FIGURE 23: Microstructures of (a) 99.99%Al, (b) Al-1%Mg and (c) Al-5%Mg. Hot deformation by axisymmetric compression at 0.9 Tm. $\sim$ 75 x.

(After Gardner and Grimes [112]).

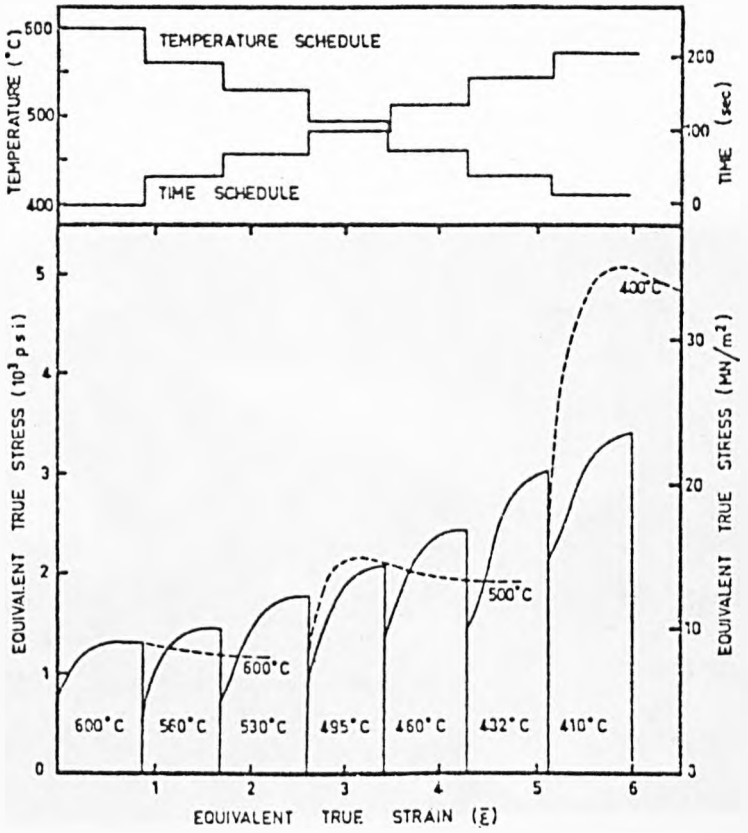
TEMPERATURE SCHEDULE
TIME SCHEDULE
TEMPERATURE (°C)
TIME (sec)
EQUIVALENT TRUE STRESS (10³ psi)
EQUIVALENT TRUE STRESS (MN/m²)
EQUIVALENT TRUE STRAIN ($\bar{\varepsilon}$)
600°C
560°C
530°C
495°C
460°C
432°C
410°C
600°C
500°C
400°C

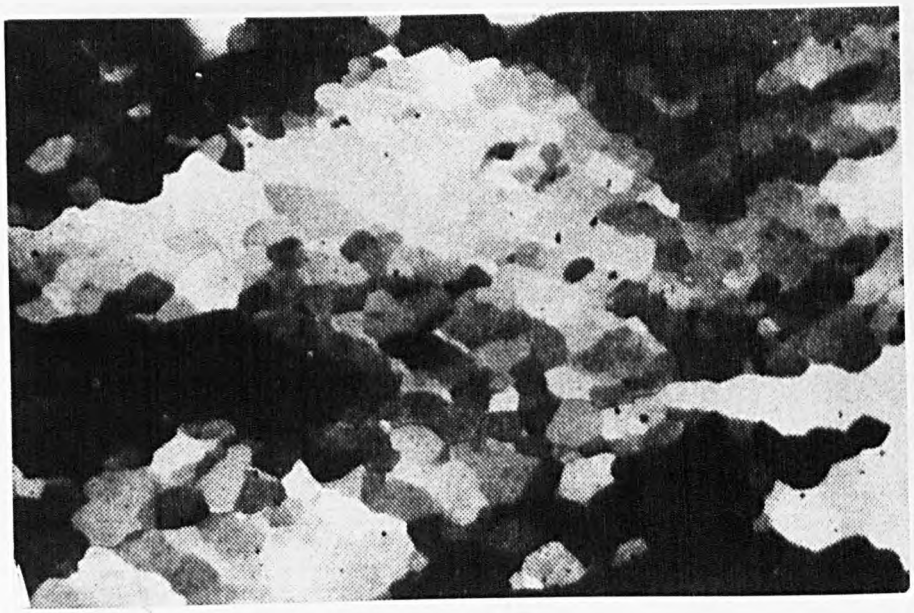

0,2 mm

(a)

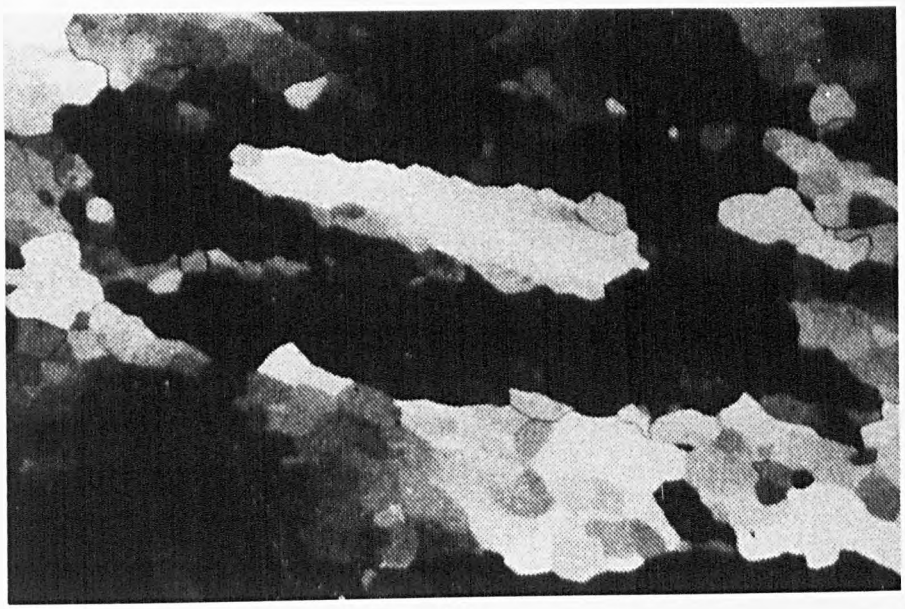

(b)

0,2mm

(c)

FIGURE 24: (a) dynamically recrystallised grain at a second-phase particle.

(b) and (c) SADP from (a).

(d) dislocation activity within recrystallised grain in (a).

(After Sheppard and Tutcher [113]).

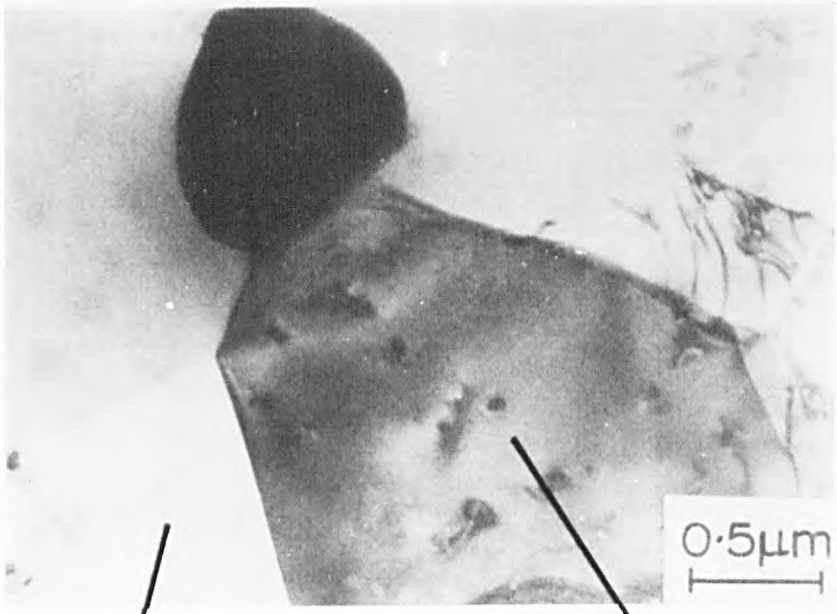

(a)

(b)

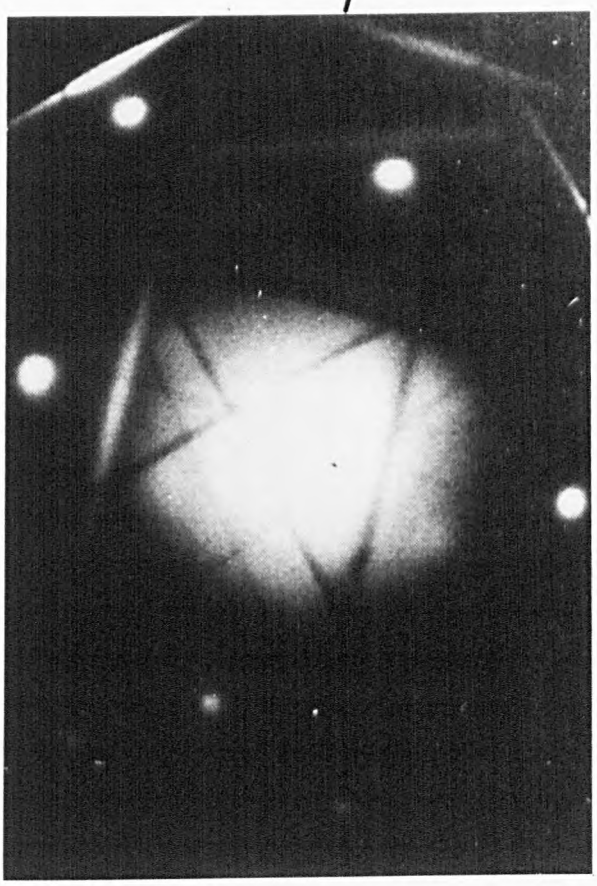

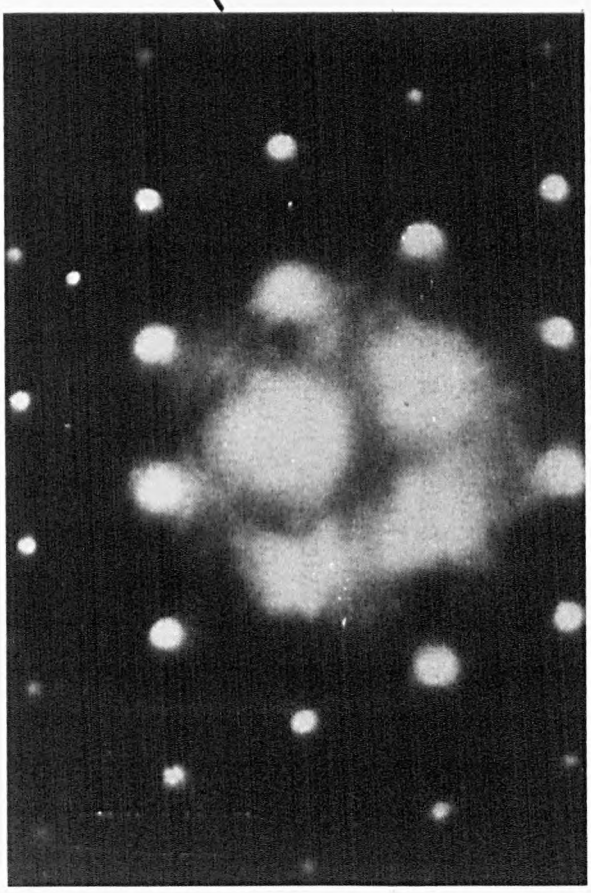

(c)

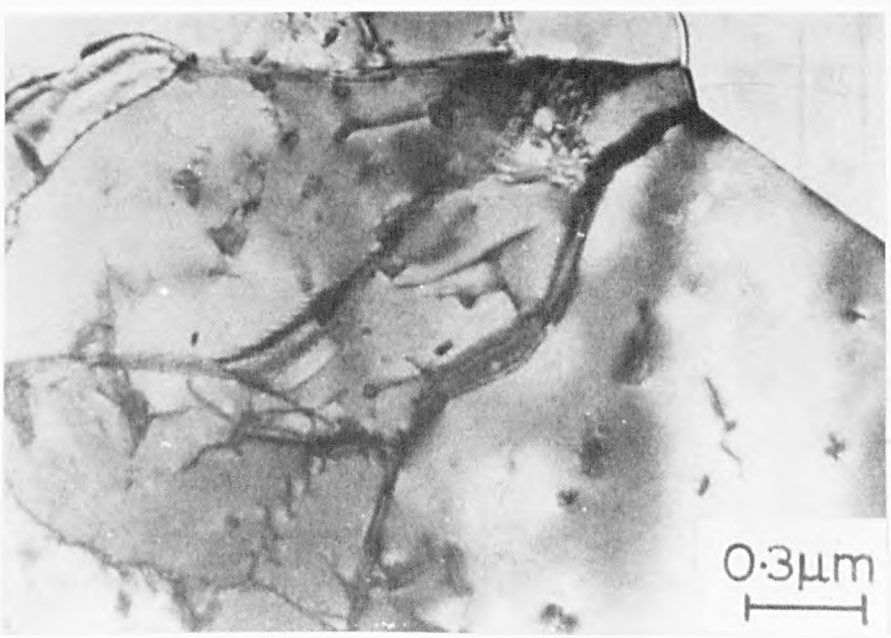

(d)

FIGURE 25: Schematic sketch of continuous recrystallisation.

(After Koster and Hornbogen [120]).

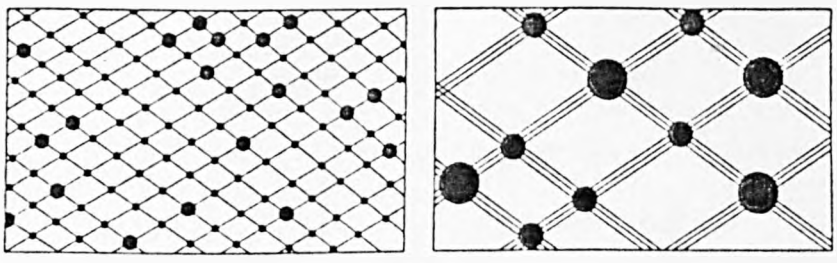

(a)

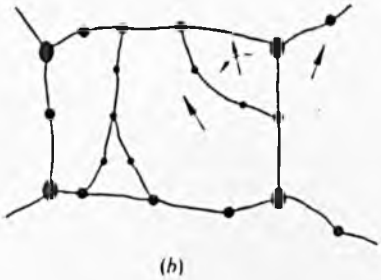

(b)

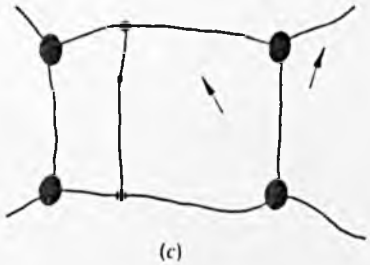

(c)

FIGURE 26: (a) Electron micrograph of an equiaxed grain of the steady-state regime.

(b) Misorientation among the different elements of the microstructure in (a).

(After Lombry et al [126]).

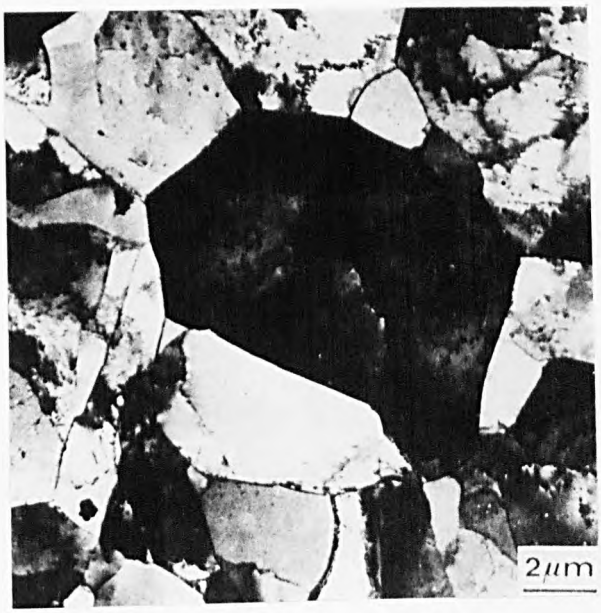

(a)

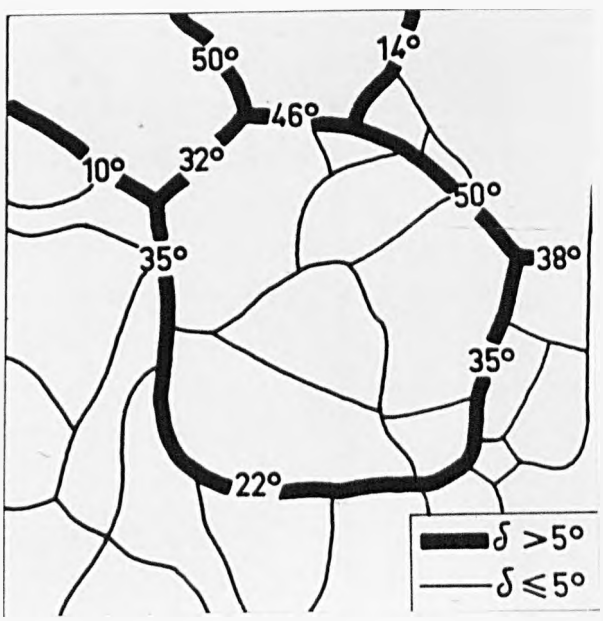

(b)

FIGURE 27: (a) Stress-strain curves for double deformation tests on commercial-purity Al at 410°C and 2.7 s^{-1}.

(b) At 330°C and 8.1 s^{-1}.

(After Evans and Dustan [39]).

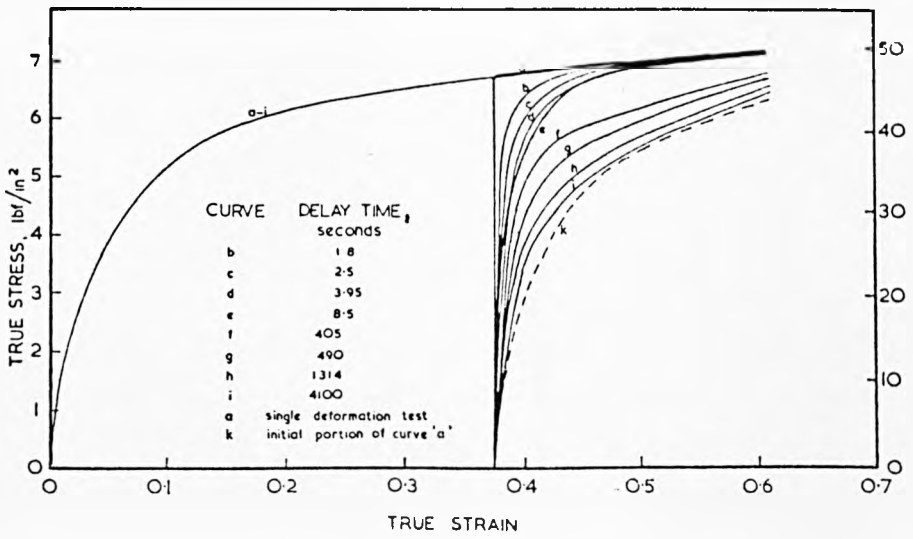
TRUE STRESS, lbf/in²
TRUE STRAIN
a–i
CURVE DELAY TIME, seconds
b 1·8
c 2·5
d 3·95
e 8·5
f 405
g 490
h 1314
i 4100
a single deformation test
k initial portion of curve 'a'

(a)

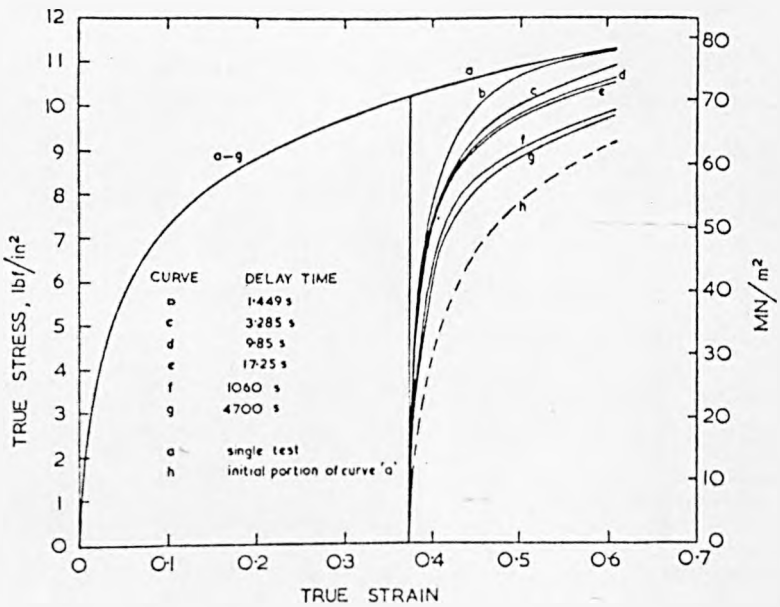
TRUE STRESS, lbf/in²
MN/m²
TRUE STRAIN
a–g
CURVE DELAY TIME
b 1·449 s
c 3·285 s
d 9·85 s
e 17·25 s
f 1060 s
g 4700 s
a single test
h initial portion of curve 'a'

(b)

FIGURE 28: (a) Variation of the restoration index R with delay time between deformations for commercial-purity Al.

(b) Variation of the volume fraction recyrstallised with delay time.

(c) Variation of restoration index R with the volume fraction recrystallised.

(After Evans and Dustan [39]).

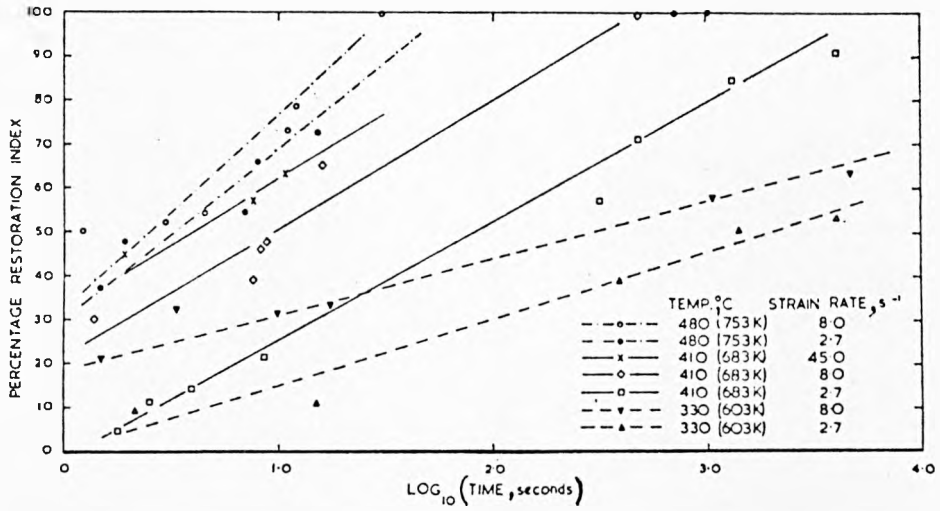
PERCENTAGE RESTORATION INDEX
LOG10 (TIME, seconds)
TEMP.,°C STRAIN RATE, s⁻¹
480 (753K) 8·0
480 (753K) 2·7
410 (683K) 45·0
410 (683K) 8·0
410 (683K) 2·7
330 (603K) 8·0
330 (603K) 2·7

(a)

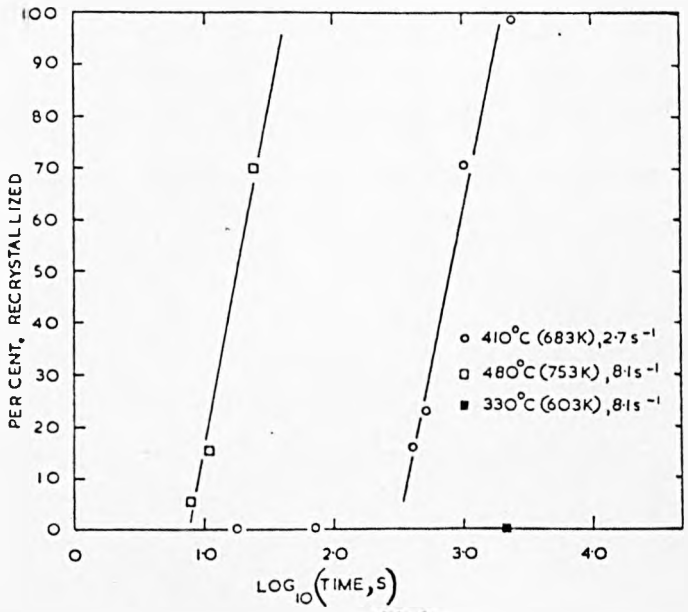
PER CENT. RECRYSTALLIZED
LOG10 (TIME, S)
410°C (683K), 2·7 s⁻¹
480°C (753K), 8·1 s⁻¹
330°C (603K), 8·1 s⁻¹

(b)

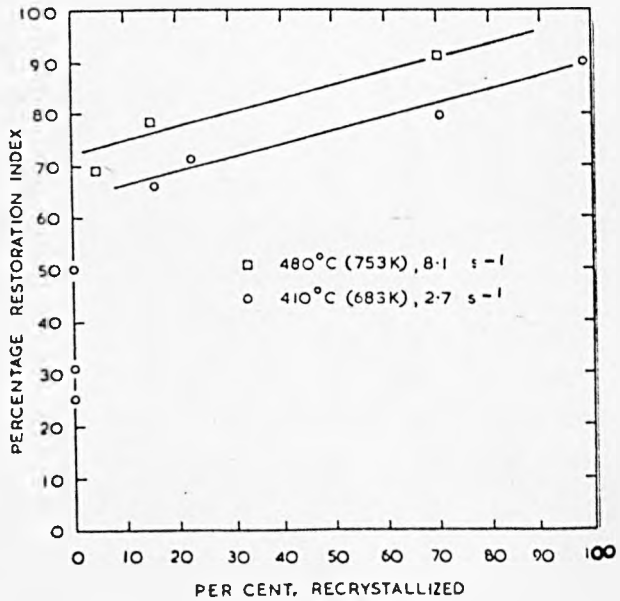
PERCENTAGE RESTORATION INDEX
PER CENT. RECRYSTALLIZED
480°C (753K), 8·1 s⁻¹
410°C (683K), 2·7 s⁻¹

(c)

FIGURE 29: Stress-strain curves for double deformation tests carried out on commercial-purity aluminium at 400°C and 11.5 s^{-1} with varying time intervals between deformations.

(After Beynon [24]).

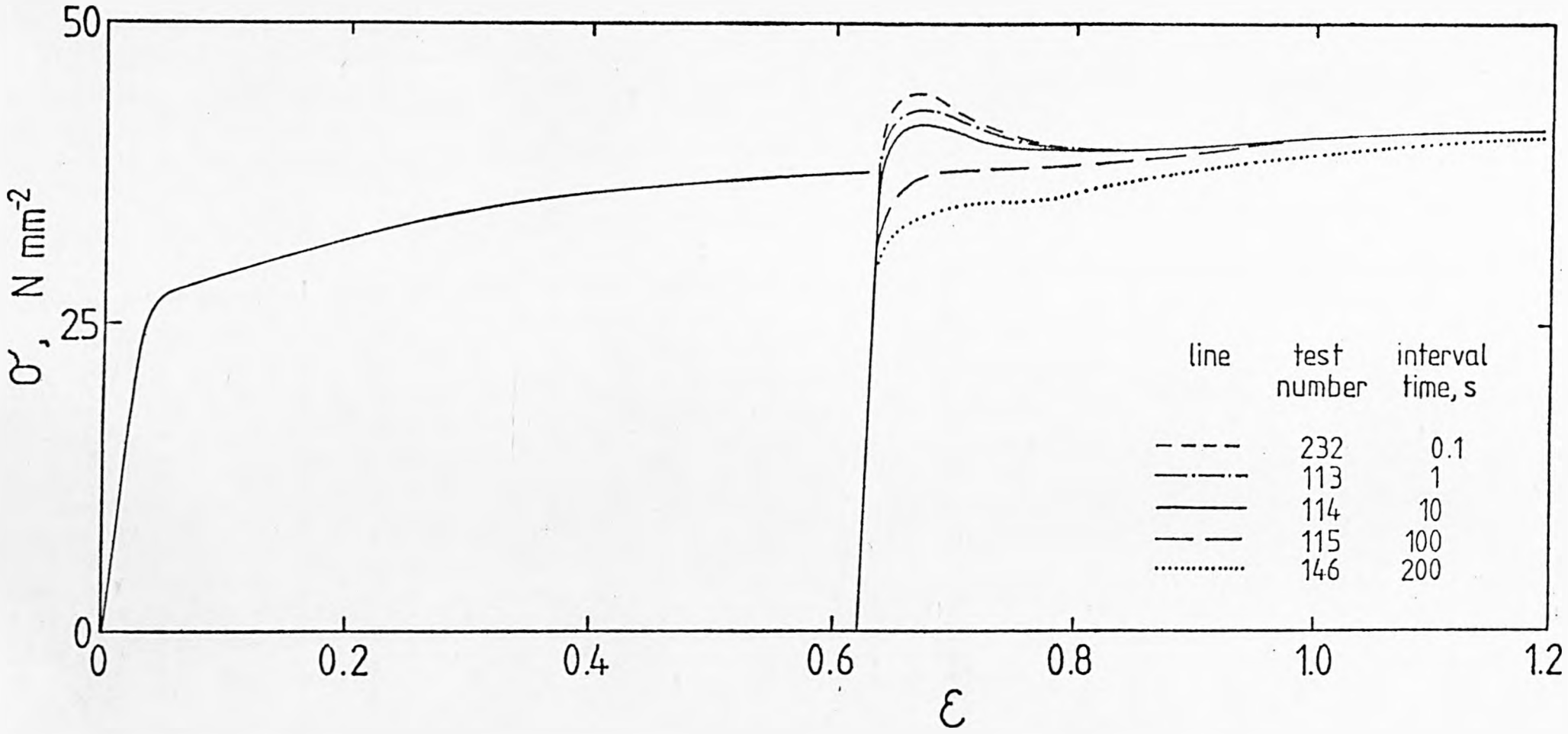
50
25
0
0
0.2
0.4
0.6
0.8
1.0
1.2
σ, N mm⁻²
ε
line
test number
interval time, s
232 0.1
113 1
114 10
115 100
146 200

FIGURE 30: Non-uniform strain rate test with commercial-purity aluminium at 400°C.

(After Beynon [24]).

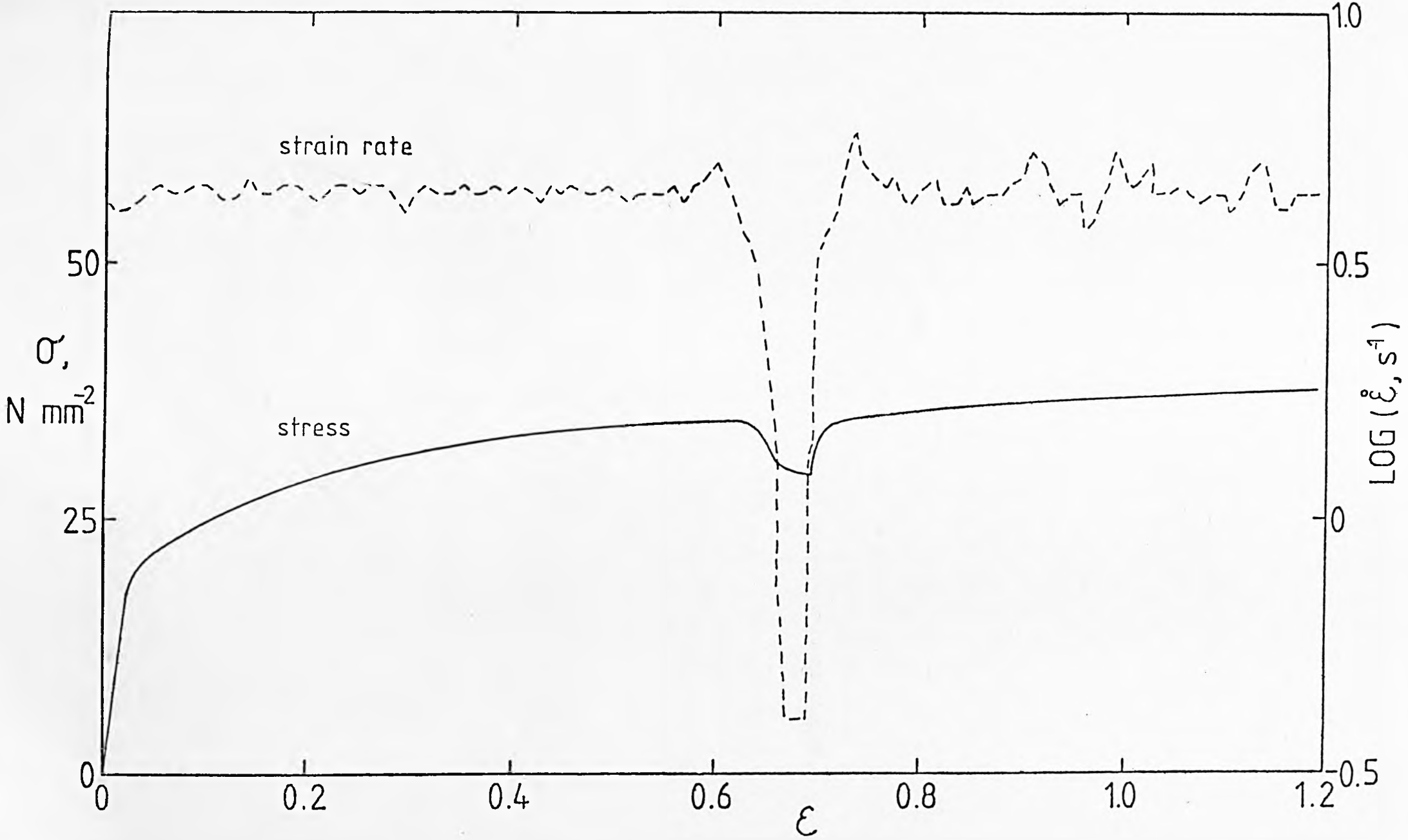
strain rate
stress
50
25
0
σ,
N mm⁻²
0
0.2
0.4
0.6
0.8
1.0
1.2
ε
1.0
0.5
0
-0.5
LOG (ε̇, s⁻¹)

FIGURE 31: Effect of delay time on recrystallisation of super-purity aluminium. Nominal entry temperatures: (a) 450°C (b) 500°C and (c) 550°C.

(After Blade [19]).

FIGURE 32: Effect of alloying additions on recrystallisation in hot rolling of super-purity aluminium.

(After Blade [19]).

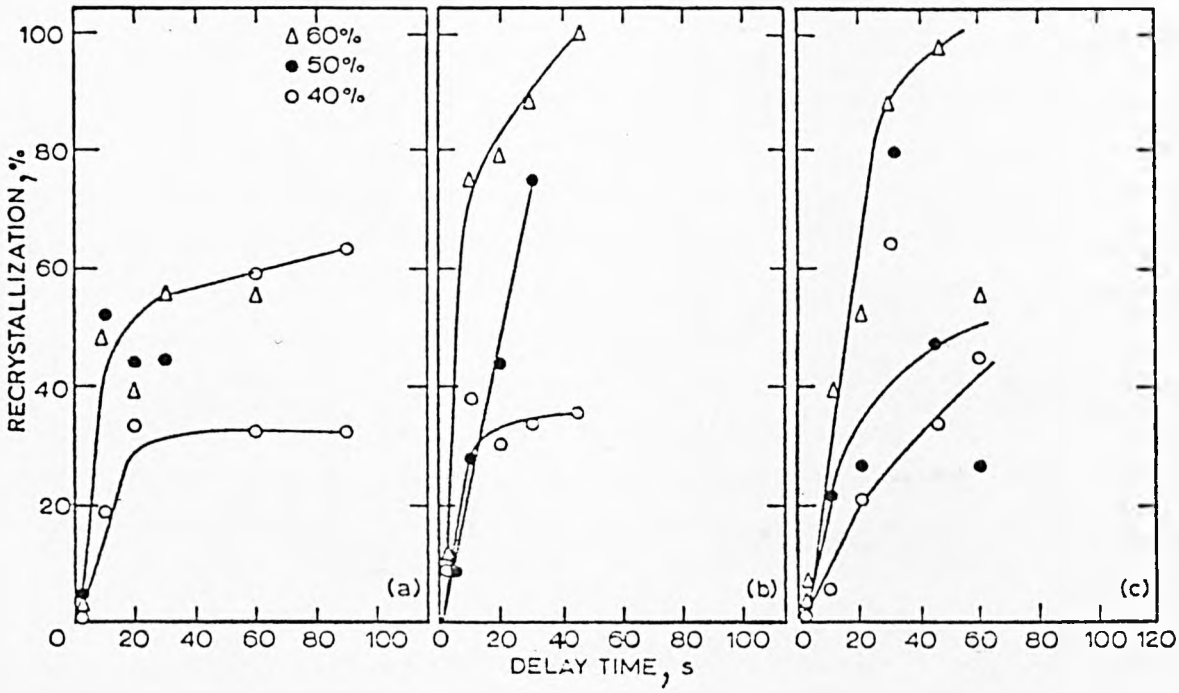
Δ 60%
● 50%
○ 40%
RECRYSTALLIZATION, %
DELAY TIME, s
(a)
(b)
(c)

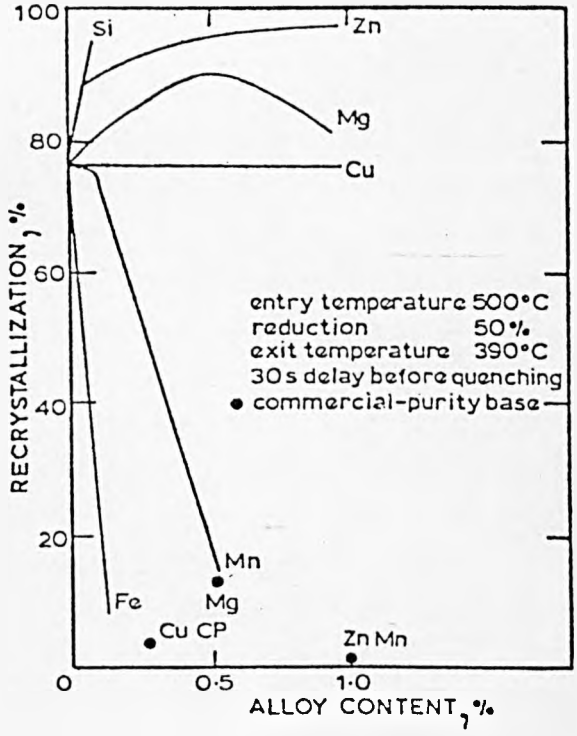
Si
Zn
Mg
Cu
Mn
Fe
Mg
Cu CP
Zn Mn
entry temperature 500°C
reduction 50%
exit temperature 390°C
30 s delay before quenching
● commercial-purity base
RECRYSTALLIZATION, %
ALLOY CONTENT, %

FIGURE 33: Deformation of an orthogonal grid scribed on a plane strain compression specimen.

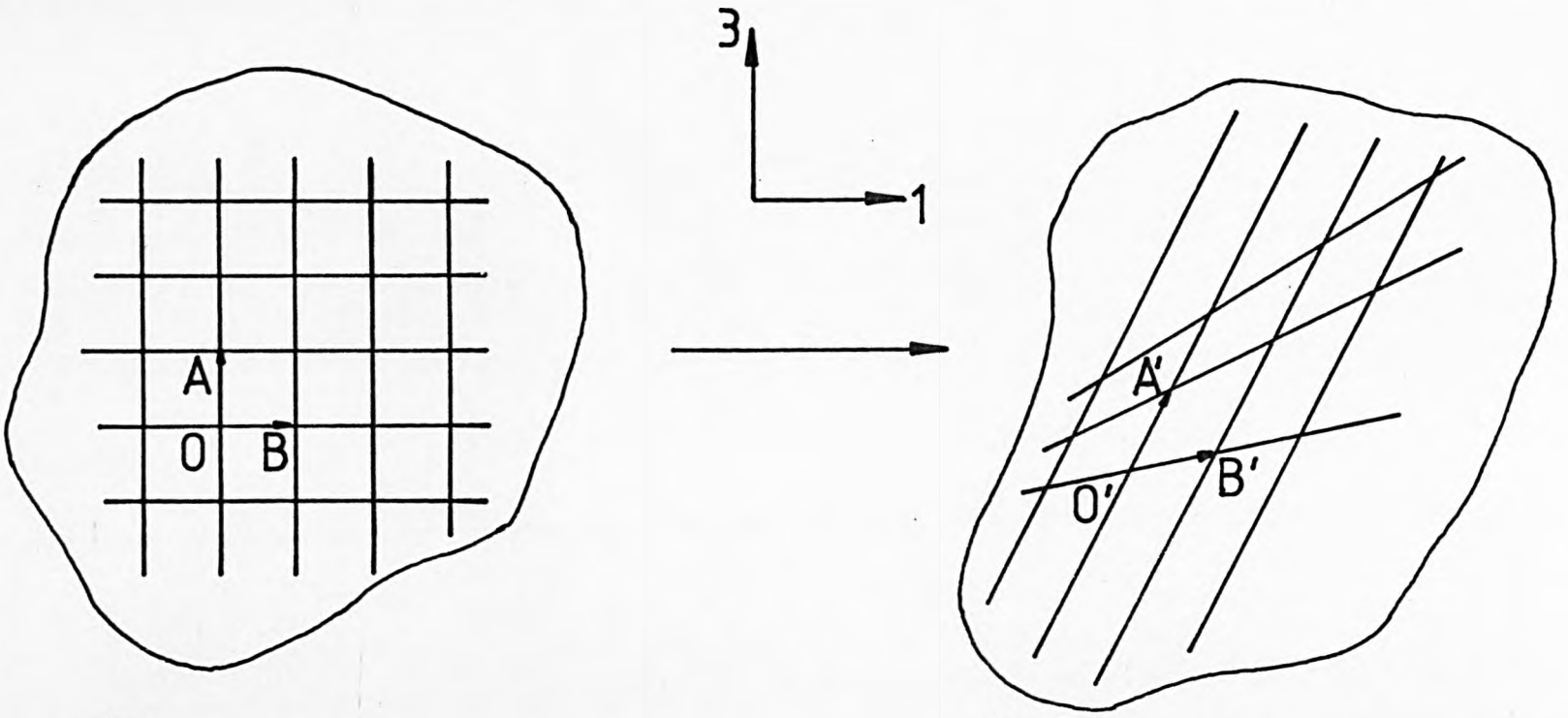

$\overrightarrow{OB} = [dX_1, 0, 0]$

$\overrightarrow{OA} = [0, 0, dY_3]$

$\overrightarrow{O'B'} = [dx_1, 0, dx_3]$

$\overrightarrow{O'A'} = [dy_1, 0, dy_3]$

$e_1 = \mathrm{Ln}(dx_1/dX_1)$; $e_3 = \mathrm{Ln}(dy_3/dY_3)$; $e_{13} = (\pi/2 - \theta)/2$

FIGURE 34: Mean strain distribution according to the initial geometry.

(a) ho = 10.12 mm. Nominal strain : 0.345.
(b) ho = 10.14 mm. Nominal strain : 0.783.
(c) ho = 7.05 mm. Nominal strain : 0.325.

(After Beynon [24]).

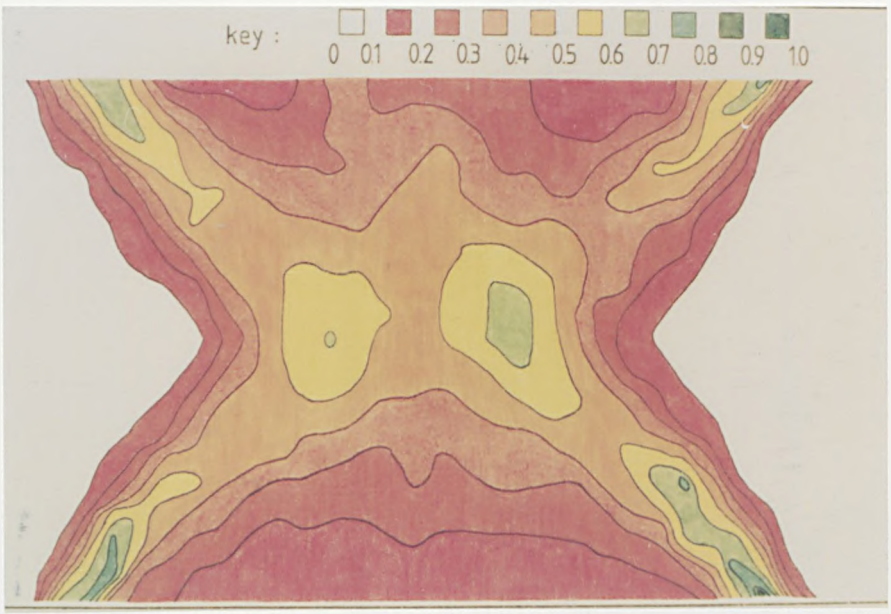
key :
0 0.1 0.2 0.3 0.4 0.5 0.6 0.7 0.8 0.9 1.0

(a)

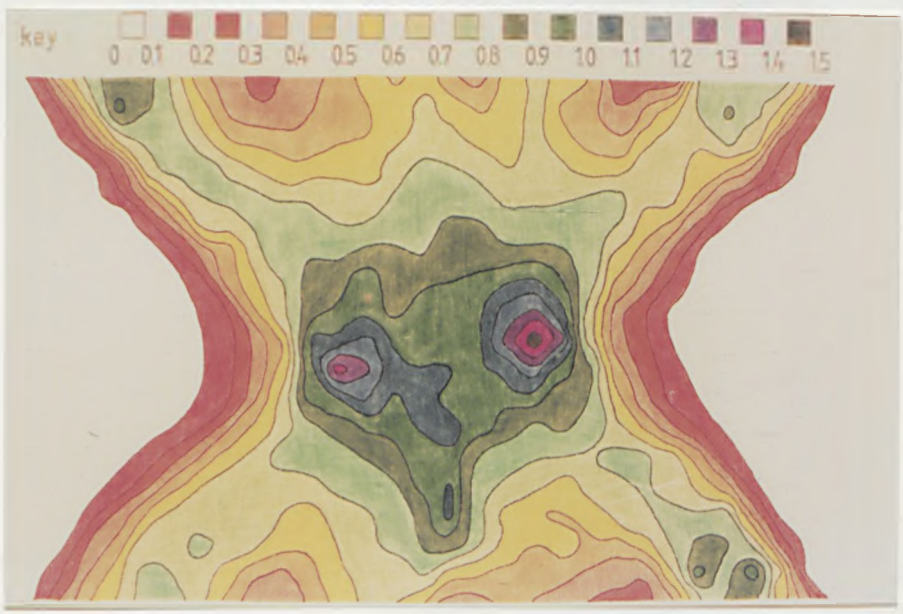
key
0 0.1 0.2 0.3 0.4 0.5 0.6 0.7 0.8 0.9 1.0 1.1 1.2 1.3 1.4 1.5

(b)

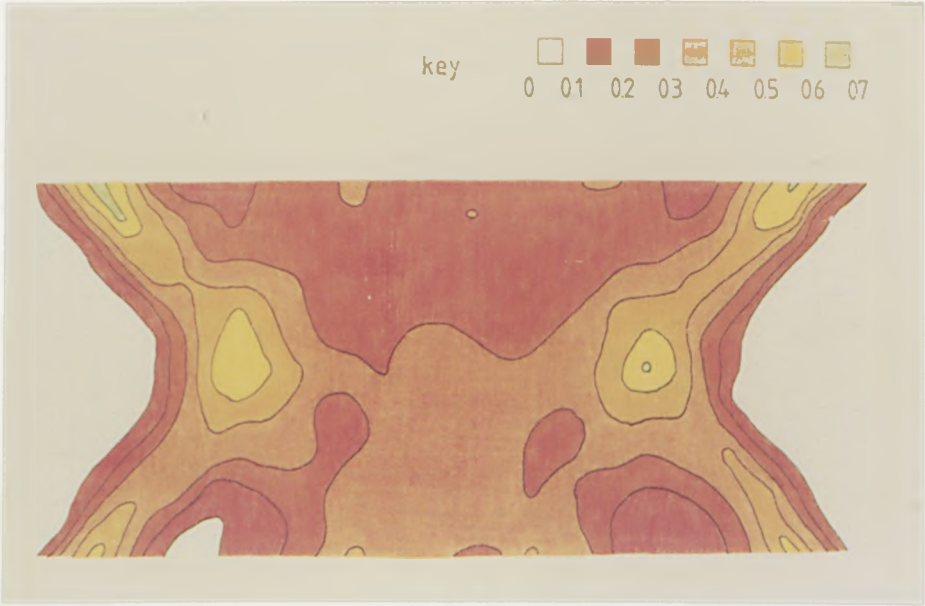

(c)

FIGURE 35: Mean strain distribution according to the final geometry.

(a) ho = 10.12 mm. Nominal strain : 0.345.
(b) ho = 10.14 mm. Nominal strain : 0.783.
(c) ho = 7.05 mm. Nominal strain : 0.345.

(After Beynon [24]).

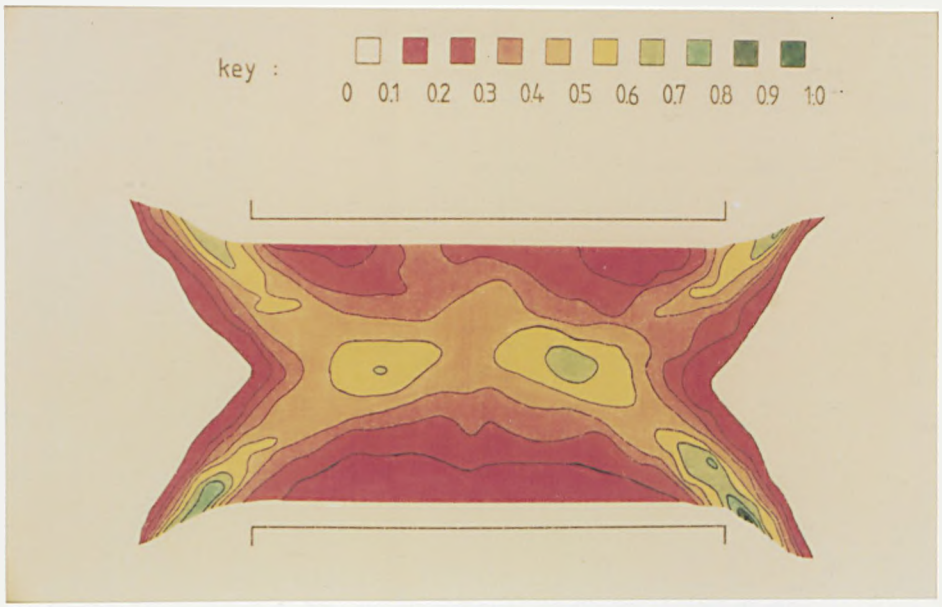
key :
0 0.1 0.2 0.3 0.4 0.5 0.6 0.7 0.8 0.9 1.0

(a)

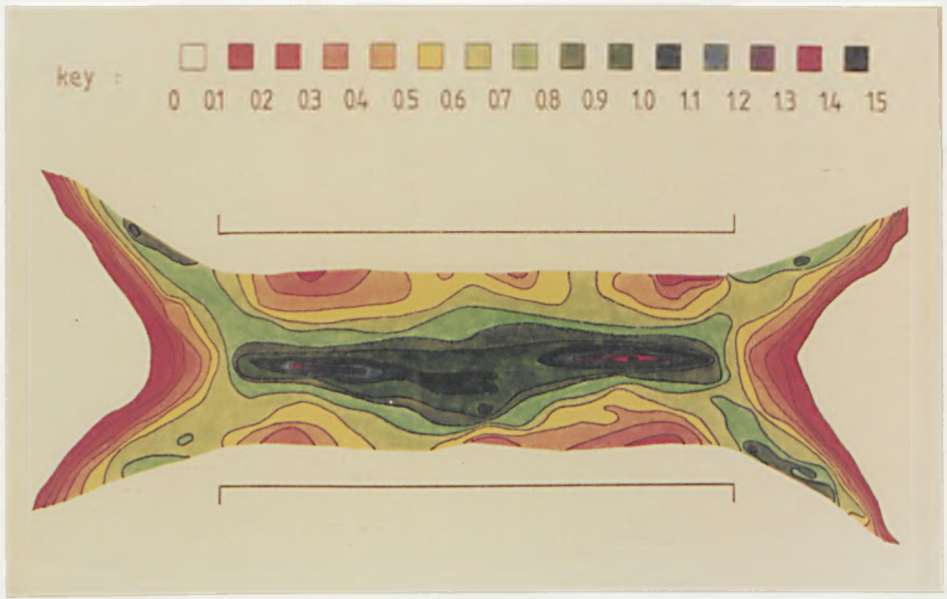
key :
0 01 02 03 04 05 06 07 08 09 10 11 12 13 14 15

(b)

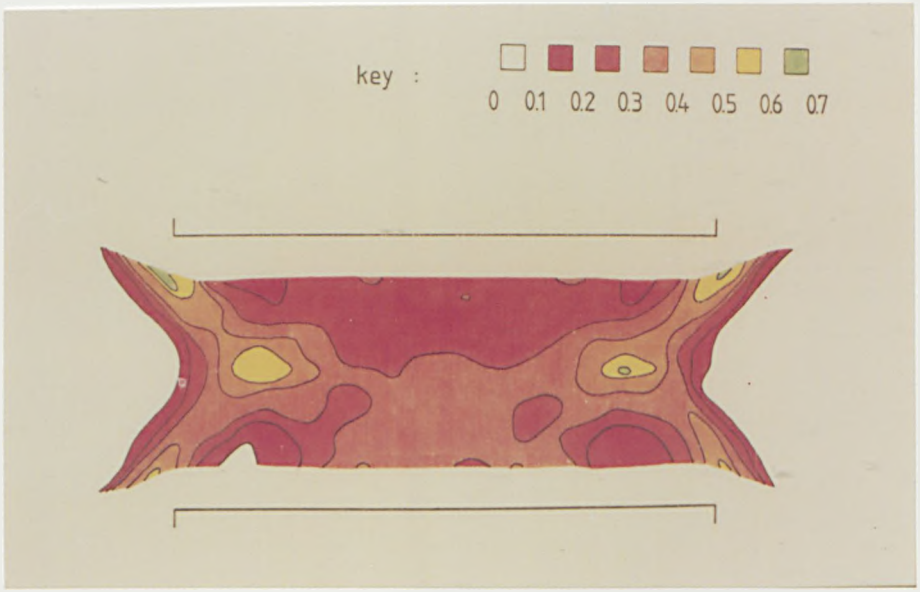
key :
0 0.1 0.2 0.3 0.4 0.5 0.6 0.7

(c)

FIGURE 36: Quadrant patterns of mean strain distribution according to the initial geometry:

(a) Figure 34b - Figure 34a.
(b) Figure 34c.
(c) Figure 34a.
(d) Figure 34b.

(After Beynon [24]).

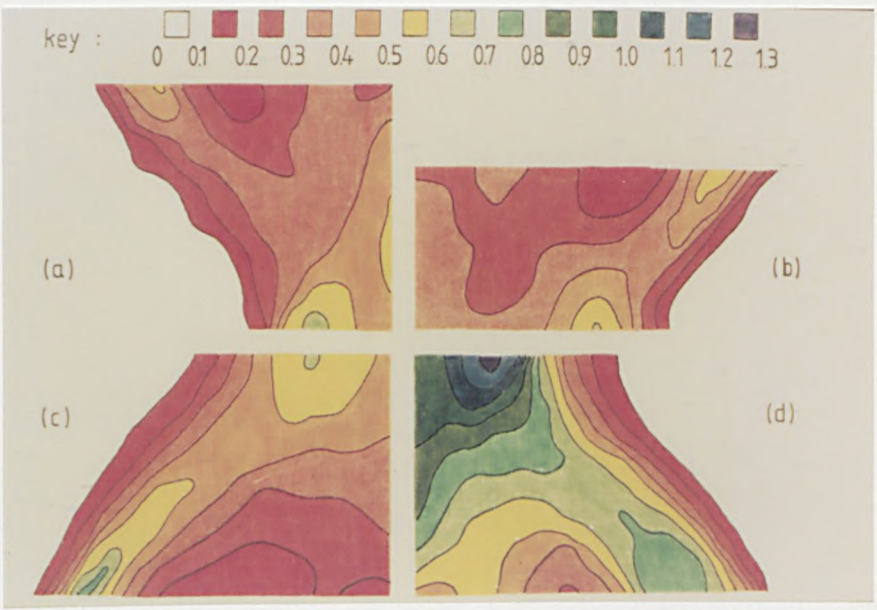
key :
0 0.1 0.2 0.3 0.4 0.5 0.6 0.7 0.8 0.9 1.0 1.1 1.2 1.3
(a)
(b)
(c)
(d)

FIGURE 37: Contours of constant effective strain at the punch displacement d/w = 0.15 for h/w = 1.7. Smooth punch.

(After Lee and Kobayashi [155]).

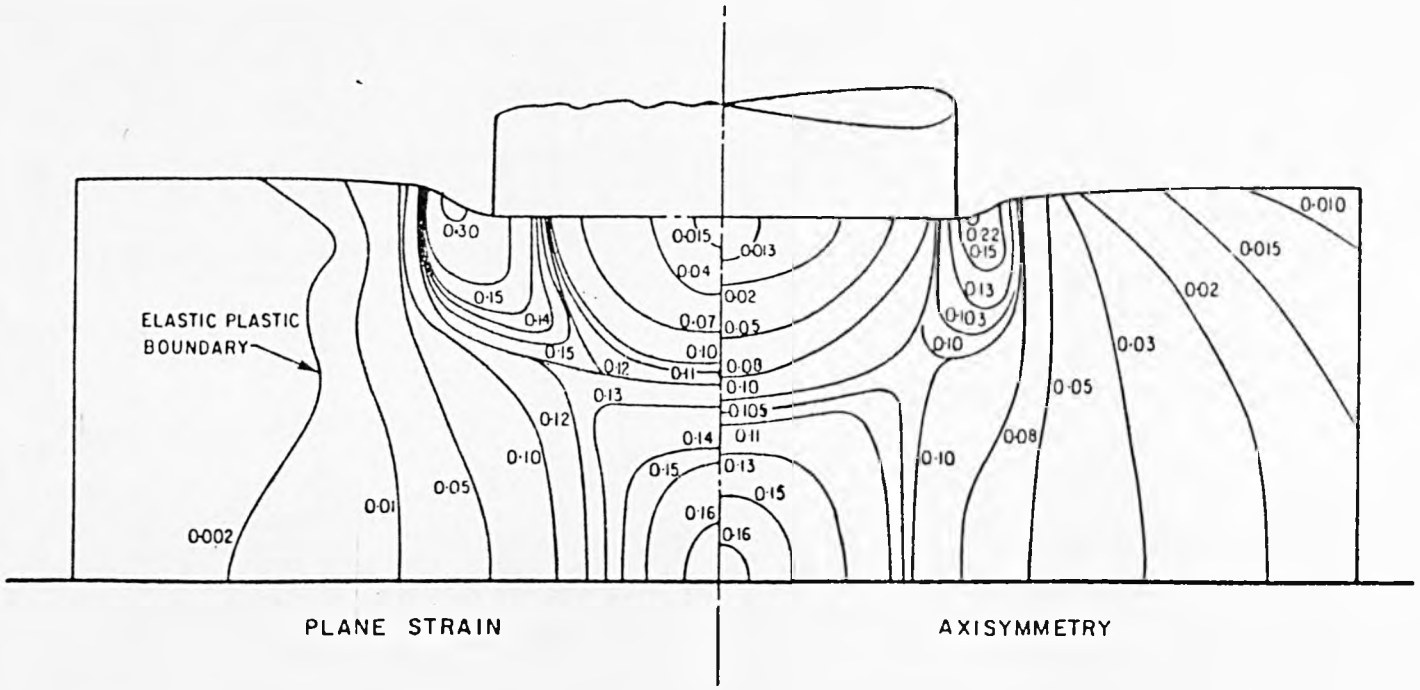
ELASTIC PLASTIC
BOUNDARY
0·30
0·15
0·14
0·15
0·12
0·11
0·13
0·12
0·10
0·05
0·01
0·002
0·015
0·013
0·04
0·02
0·07
0·05
0·10
0·08
0·10
0·105
0·14
0·11
0·15
0·13
0·15
0·16
0·16
0·22
0·15
0·13
0·10·3
0·10
0·10
0·08
0·05
0·03
0·02
0·015
0·010
PLANE STRAIN
AXISYMMETRY

FIGURE 38: Specimen and tool element arrangements before deformation under plane strain compression conditions.

(After Foster [74]).

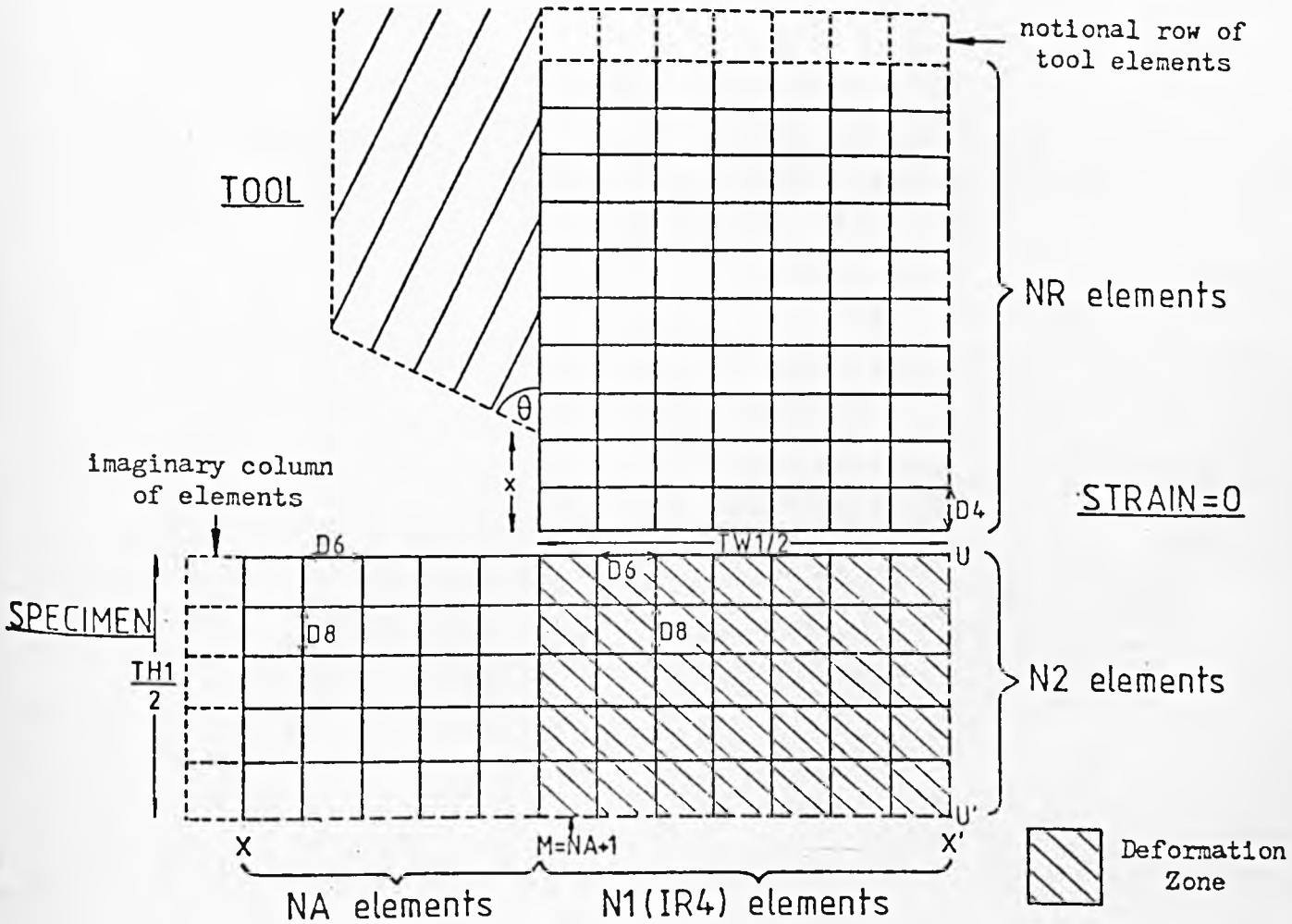
notional row of tool elements
TOOL
NR elements
θ
x
imaginary column of elements
D4
STRAIN=0
D6
TW1/2
U
D6
SPECIMEN
D8
D8
TH1/2
N2 elements
U'
X
M=NA+1
X'
Deformation Zone
NA elements
N1(IR4) elements

FIGURE 39: (a) and (b) specimen and tool arrangements during deformation. (c) Rhomboidal specimen element.

(After Foster [74]).

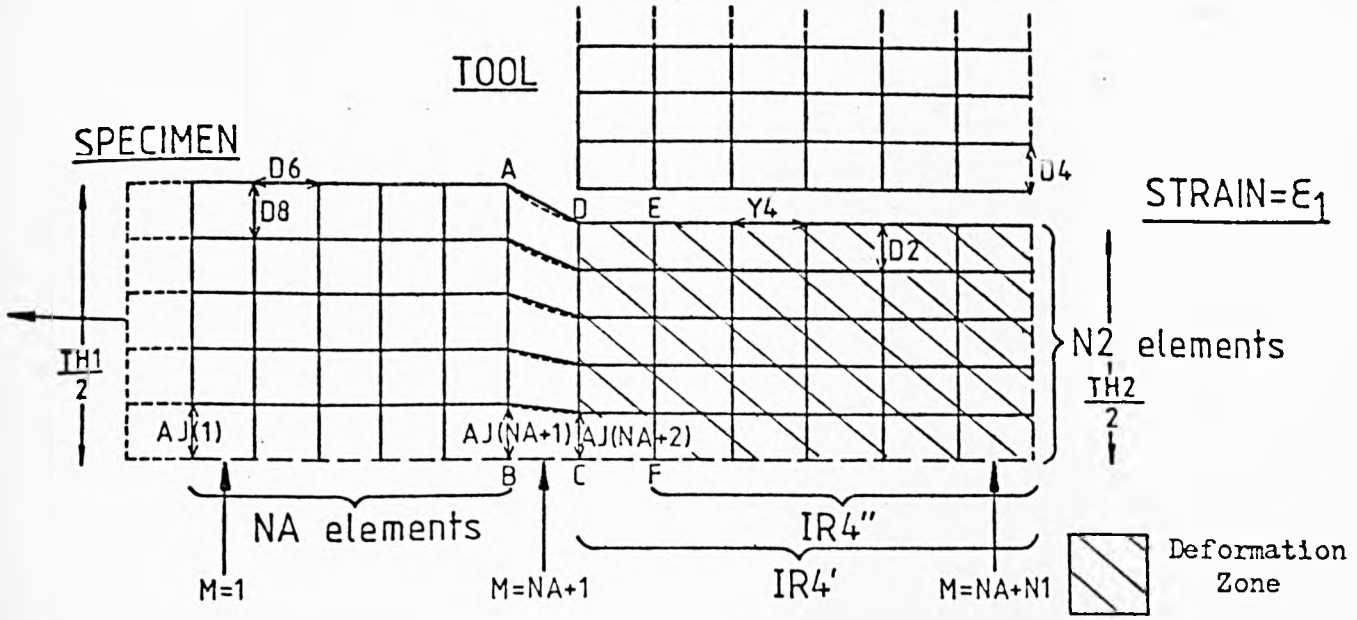
TOOL
SPECIMEN
D6
D8
A
D
E
Y4
D4
D2
STRAIN=ε1
TH1/2
N2 elements
TH2/2
AJ(1)
AJ(NA+1)
AJ(NA+2)
B
C
F
NA elements
IR4"
IR4'
M=1
M=NA+1
M=NA+N1
Deformation Zone

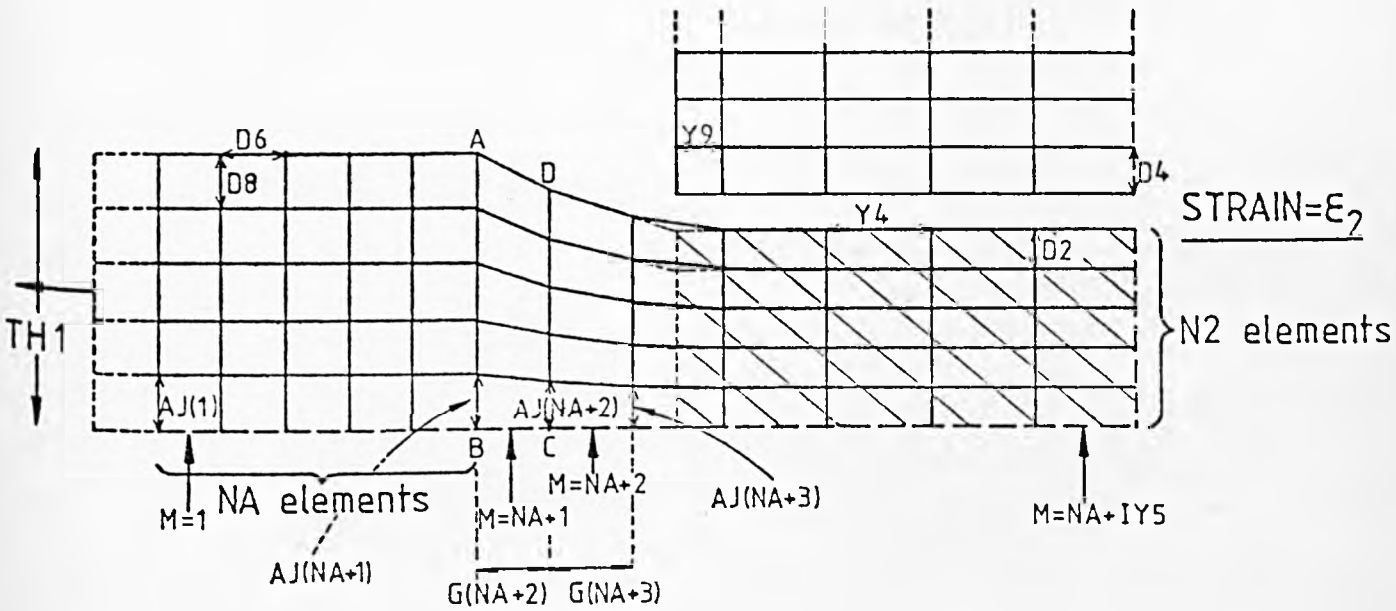
Y9
D6
D8
A
D
Y4
D4
D2
STRAIN=ε2
TH1
N2 elements
AJ(1)
AJ(NA+2)
B
C
M=NA+2
M=1
NA elements
M=NA+1
AJ(NA+3)
M=NA+IY5
AJ(NA+1)
G(NA+2)
G(NA+3)

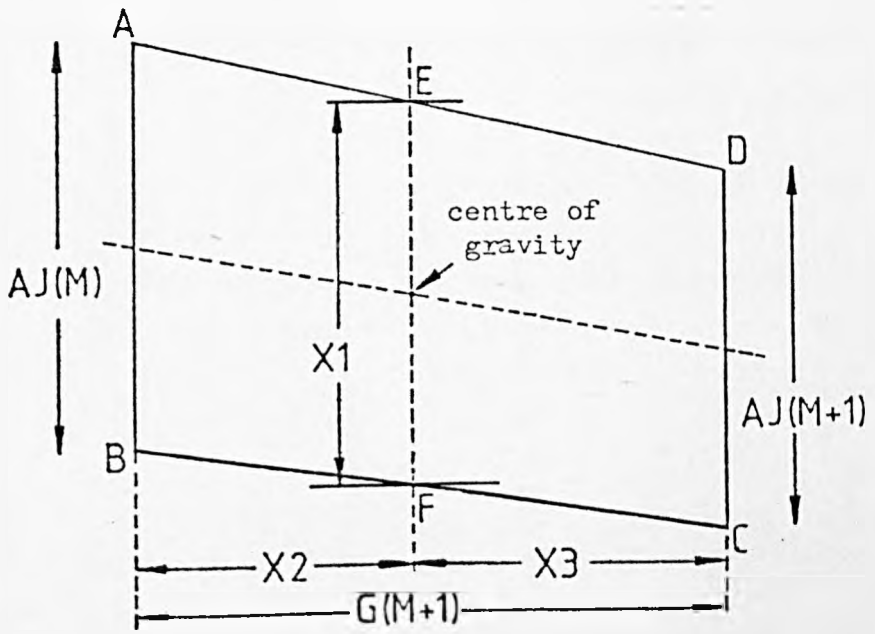
A
E
D
centre of gravity
AJ(M)
X1
AJ(M+1)
B
F
C
X2
X3
G(M+1)

FIGURE 40: Heat flow within the completely deformed specimen elements outside the deformation zone.

(After Foster [74]).

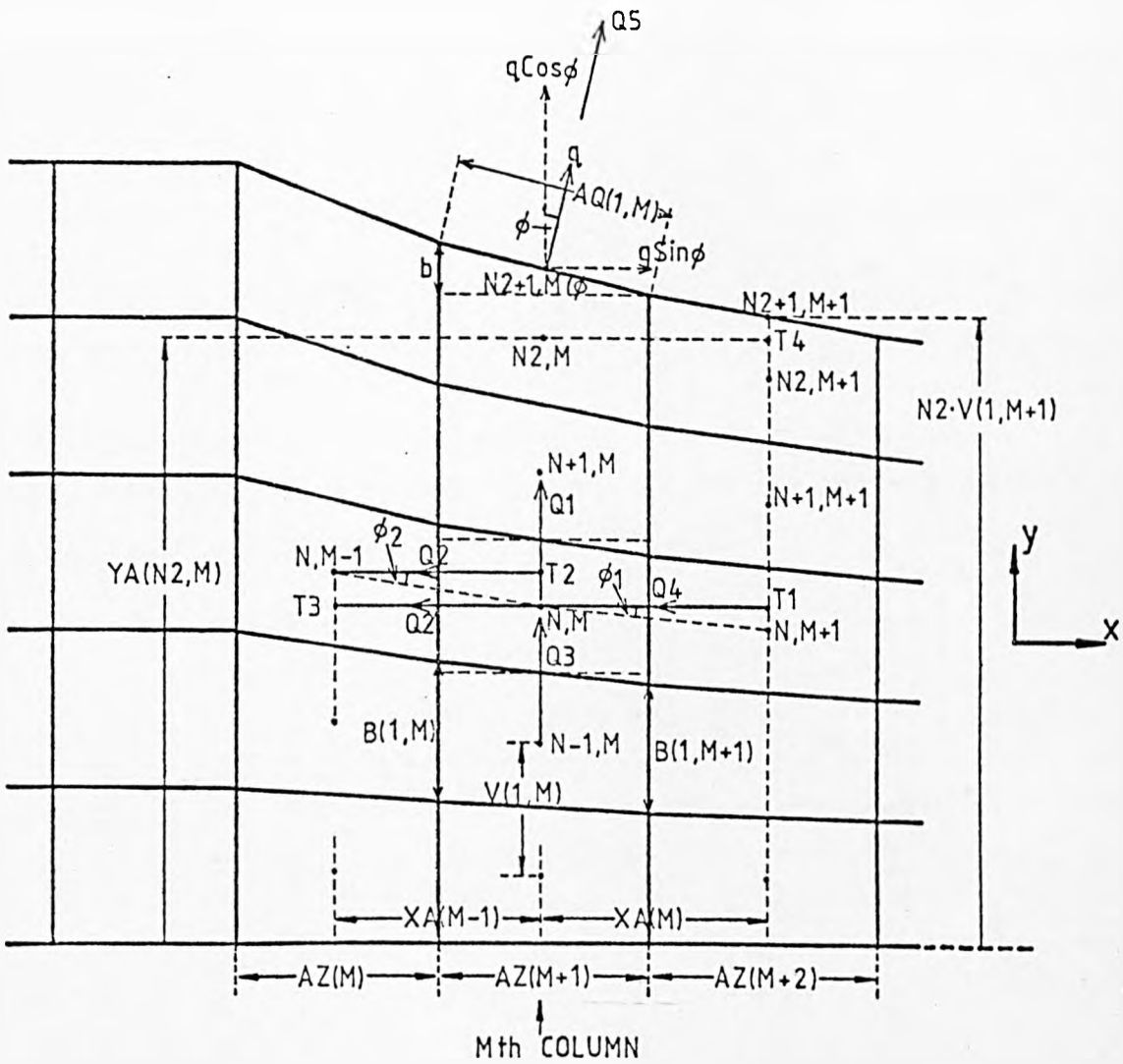
Q5
qCosϕ
q
AQ(1,M)
ϕ
gSinϕ
b
N2±1,M(ϕ
N2+1,M+1
T4
N2,M
N2,M+1
N2·V(1,M+1)
N+1,M
Q1
N+1,M+1
ϕ2
N,M-1
Q2
T2
ϕ1
Q4
T1
T3
Q2
N,M
N,M+1
Q3
YA(N2,M)
B(1,M)
N-1,M
B(1,M+1)
V(1,M)
y
x
XA(M-1)
XA(M)
AZ(M)
AZ(M+1)
AZ(M+2)
Mth COLUMN

FIGURE 41: (a) Comparison of measured and computed temperature-strain curves for plane strain compression tests on Al-0.5%Mg-0.5%Mn at 290°C and 15 s^{-1}.

(b) At 290°C and 30 s^{-1}.

(After Foster [74]).

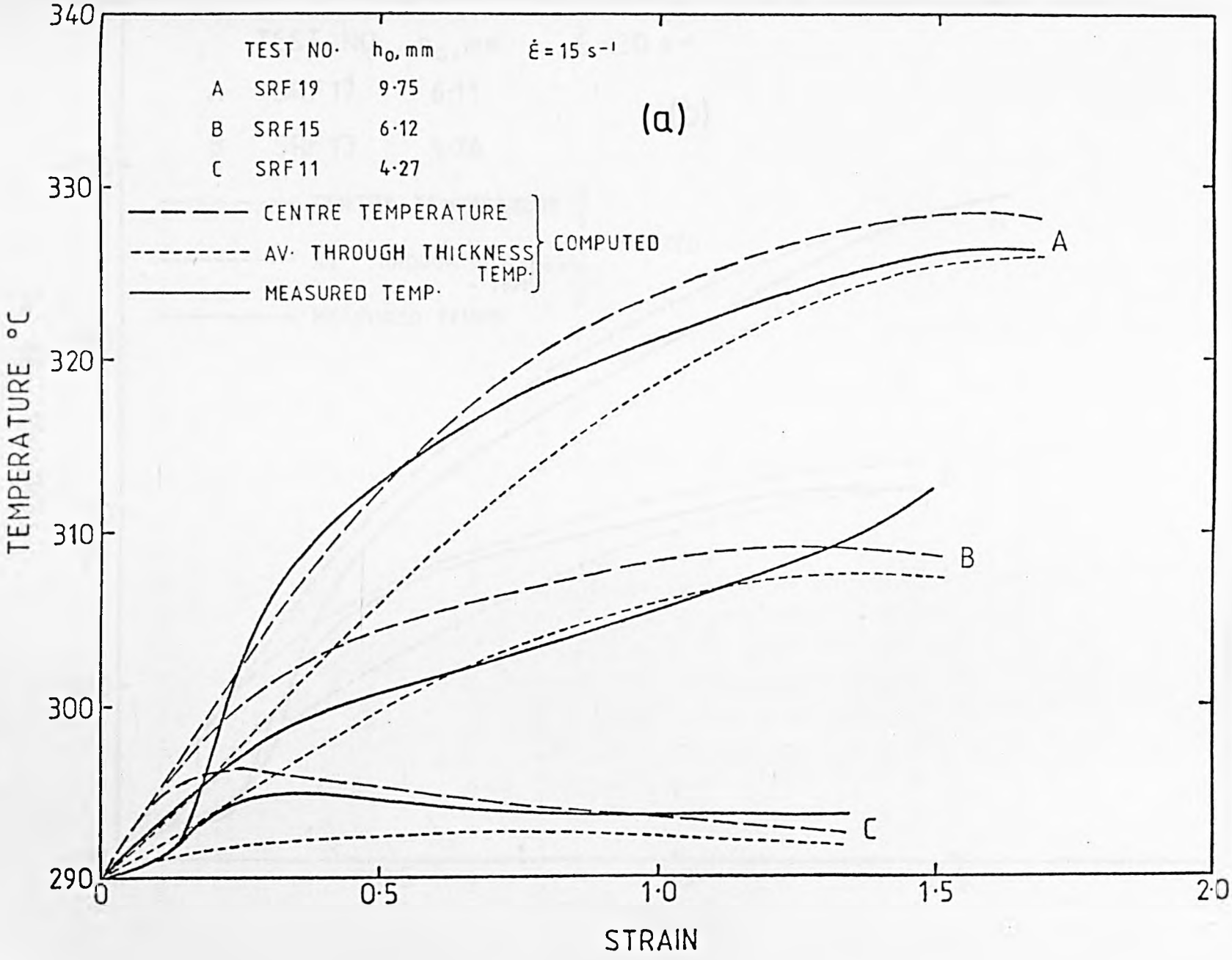
TEST NO· h_o, mm $\dot{\varepsilon} = 15\ s^{-1}$
A SRF 19 9·75
B SRF 15 6·12
C SRF 11 4·27
(a)
CENTRE TEMPERATURE
AV· THROUGH THICKNESS TEMP·
MEASURED TEMP·
COMPUTED
A
B
C
TEMPERATURE °C
340
330
320
310
300
290
0
0·5
1·0
1·5
2·0
STRAIN

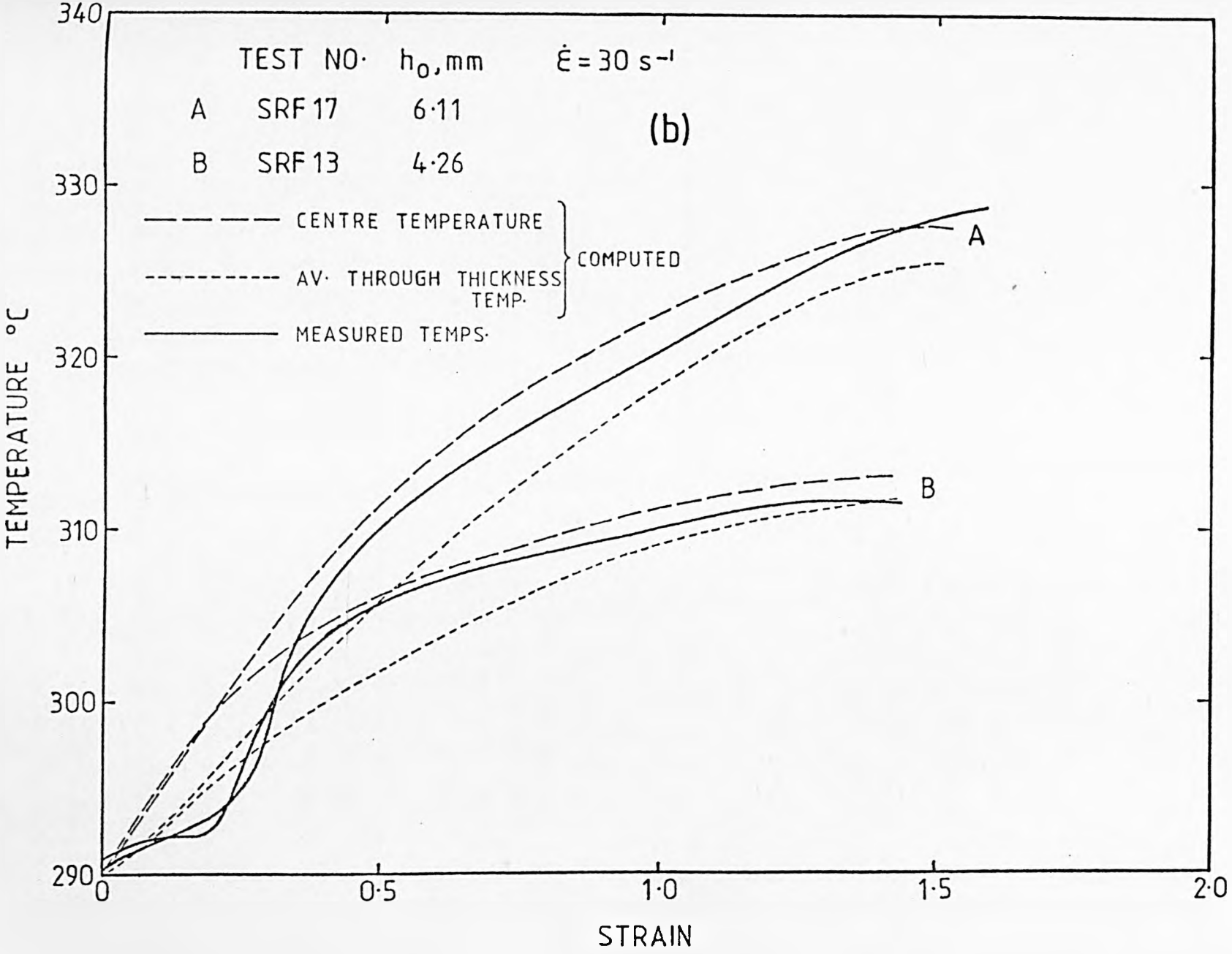
TEST NO· h₀,mm Ė = 30 s⁻¹
A SRF 17 6·11
B SRF 13 4·26
(b)
CENTRE TEMPERATURE
AV· THROUGH THICKNESS TEMP·
COMPUTED
MEASURED TEMPS·
A
B
TEMPERATURE °C
STRAIN
340
330
320
310
300
290
0
0·5
1·0
1·5
2·0

FIGURE 42: Standard dimensions of the specimens used for (a) plane strain compression and (b) rolling.

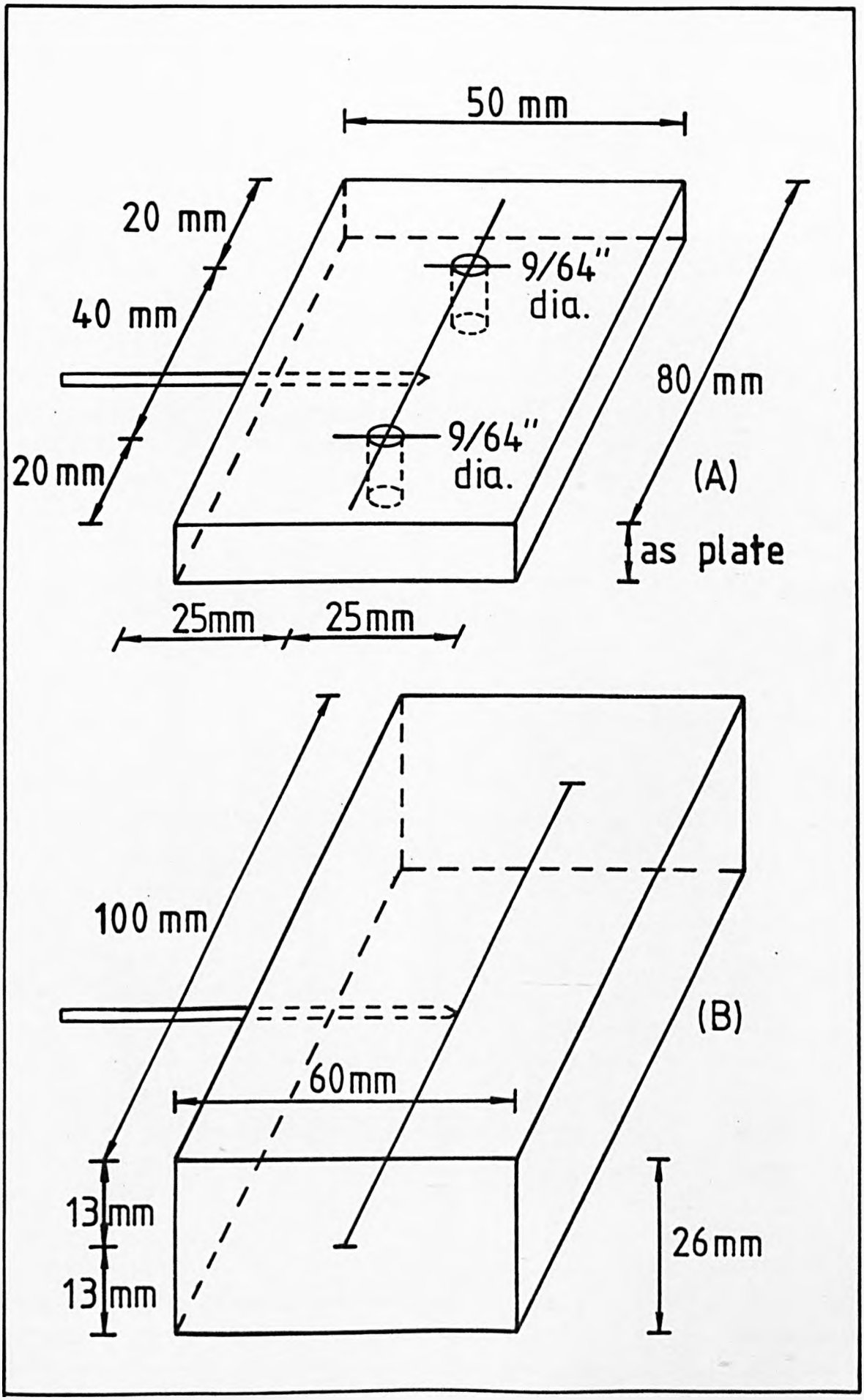
50 mm
20 mm
40 mm
20 mm
9/64" dia.
9/64" dia.
80 mm
(A)
as plate
25mm
25mm
100 mm
(B)
60mm
13 mm
13 mm
26mm

FIGURE 43: The electro-hydraulic machine without furnaces.

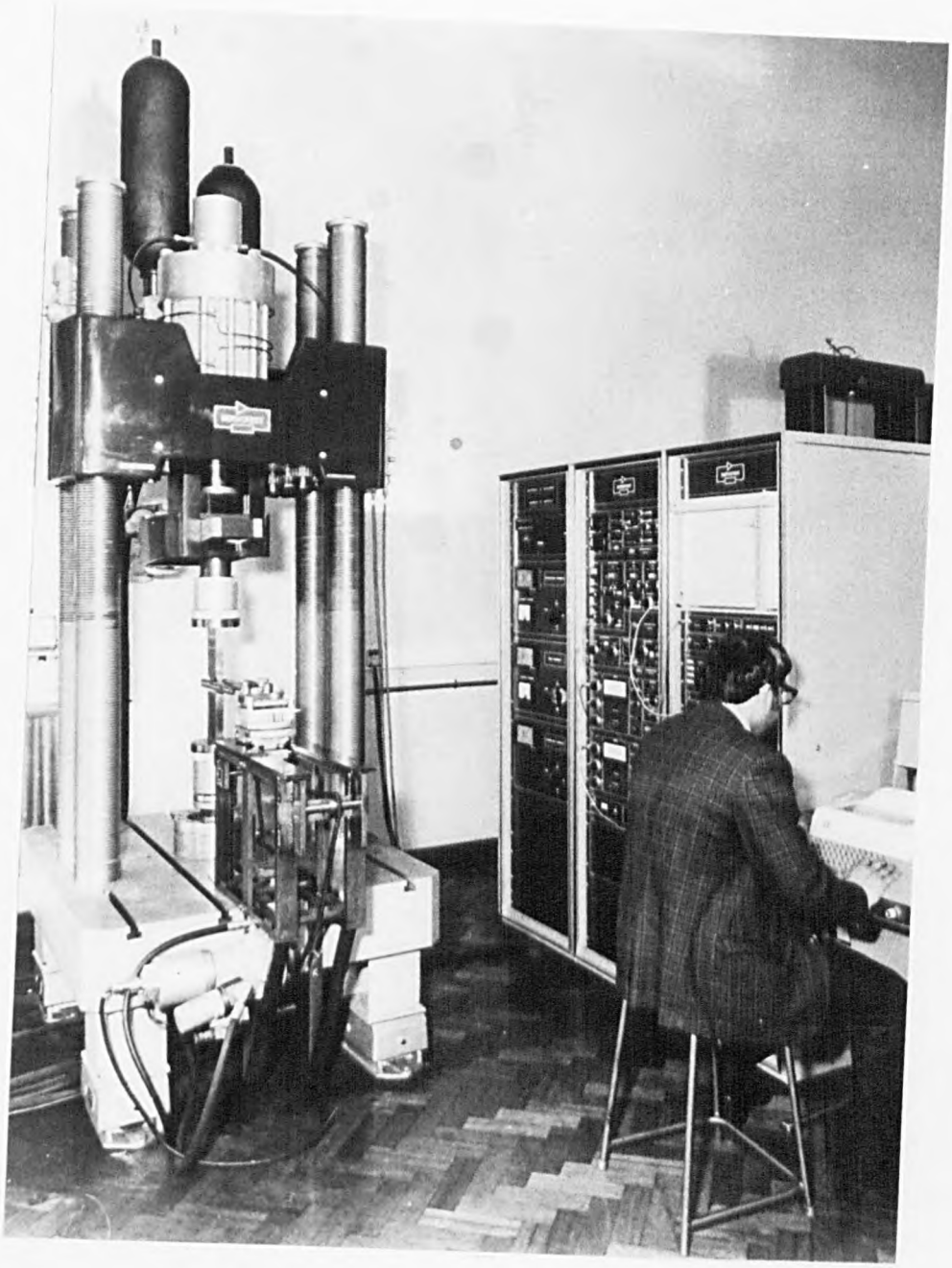

FIGURE 44: The electro-hydraulic machine with its full complement of furnaces and quenching rig.

A - the ram;
B - wedge;
C - conveyor;
O - quenching rig;
P - testing furnace;
Q - preheating furnace;
R - annealing furnace.

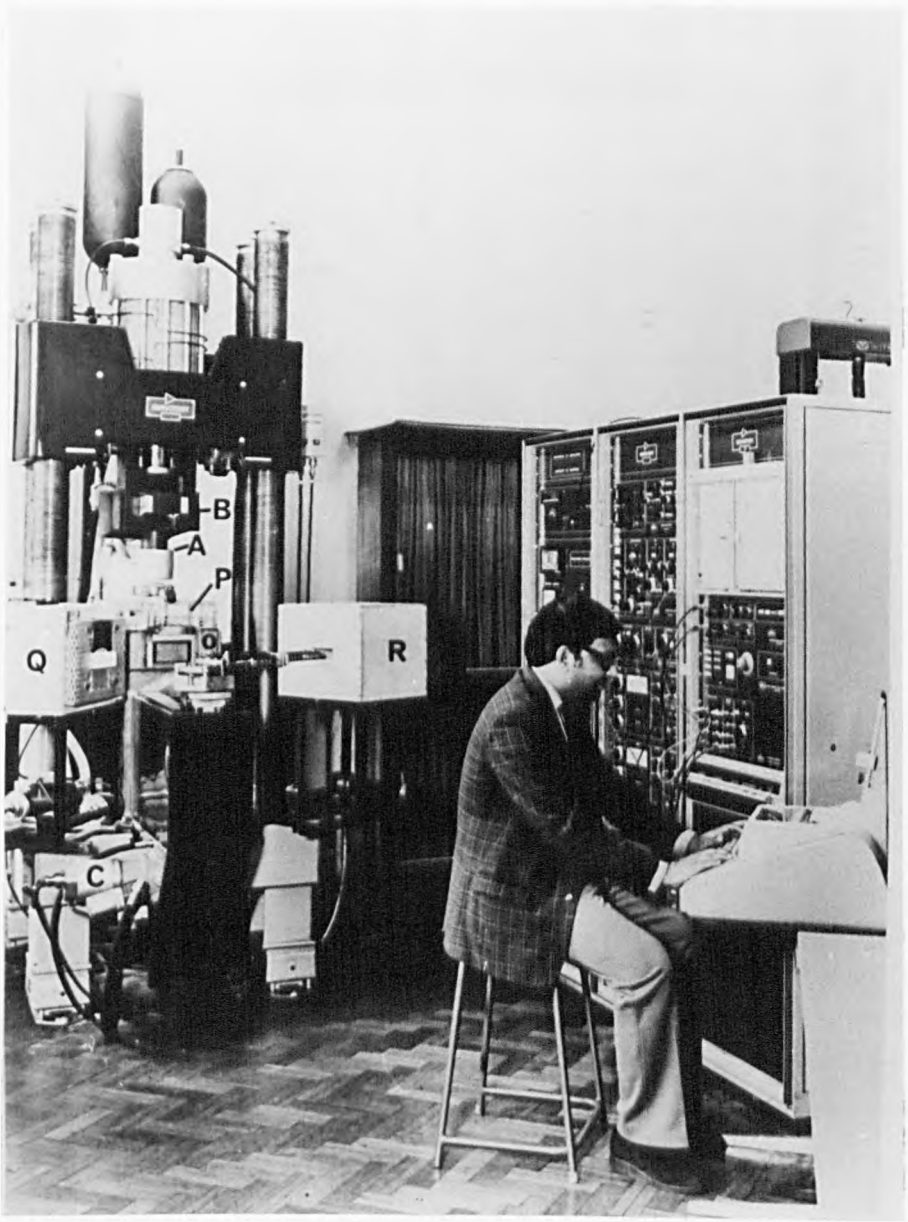
B
A
P
Q
R
C

FIGURE 45: (a) General arrangement of plane strain compression testing.

(b) Deformed specimen after testing.

(c) Mounted section for metallographic observation.

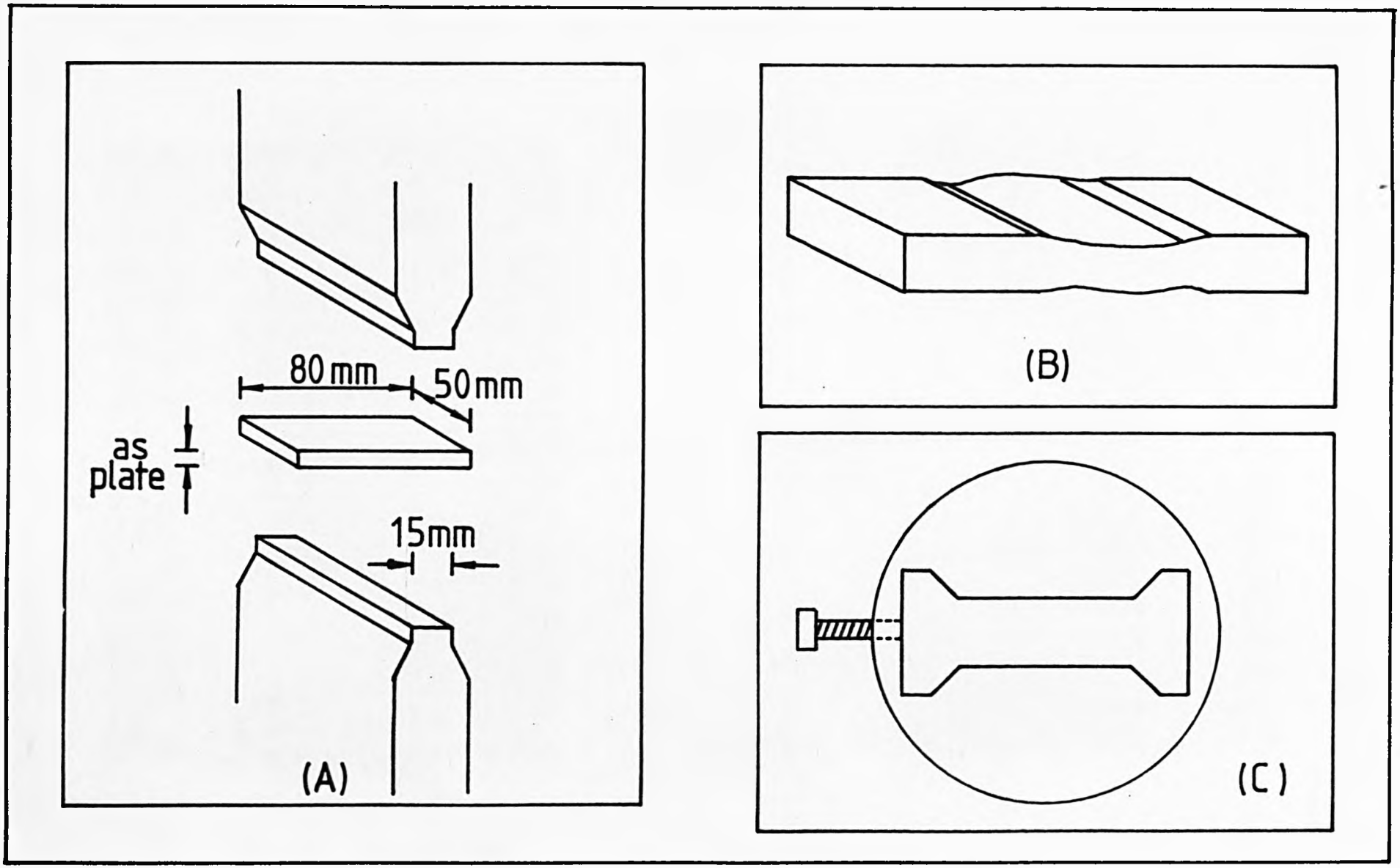
80 mm
50 mm
as plate
T
15mm
(A)
(B)
(C)

FIGURE 46: The specimen handling carriage; top and front views;

D - specimen;
E - cantilever arms, replaceable;
F - cantilever arm stock;
G - spring steel plate;
H - guiding arm;
I - bronze block for co-ordinated guiding arms motion;
J - upper aluminium block which swivels on;
K - lower aluminium block with ball-race wheels;
L - spring loaded positioning pin'
M - under plate, also with ball-race wheels;
N - heat shield;
O - quenching rig;
Q - preheating furnace with fire brick door.

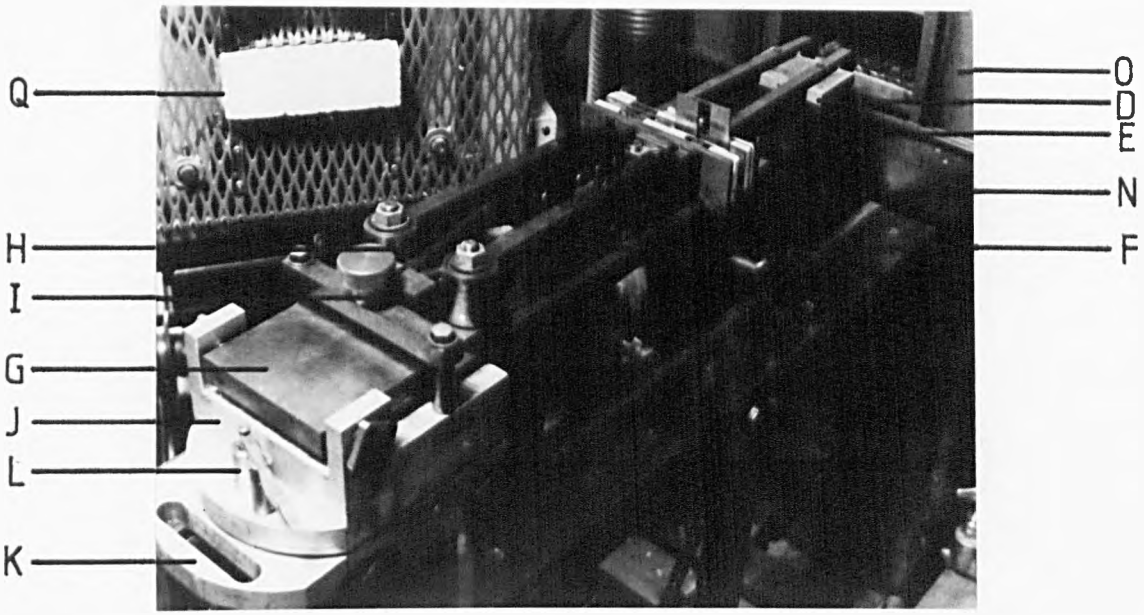
Q
H
I
G
J
L
K
O
D
E
N
F

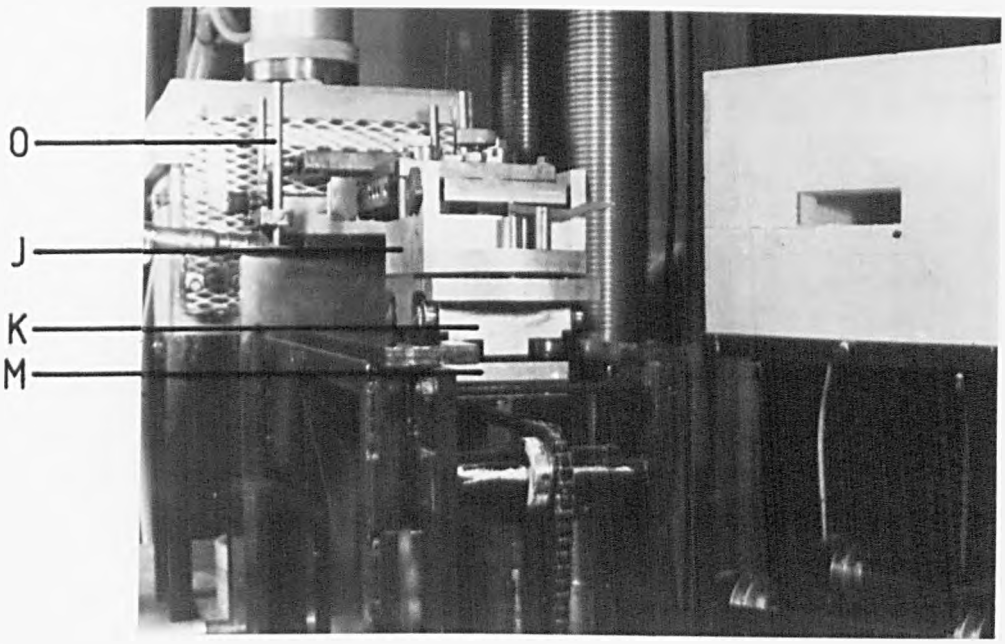
O
J
K
M

FIGURE 47: Plane strain compression of a plate with tools of width W.

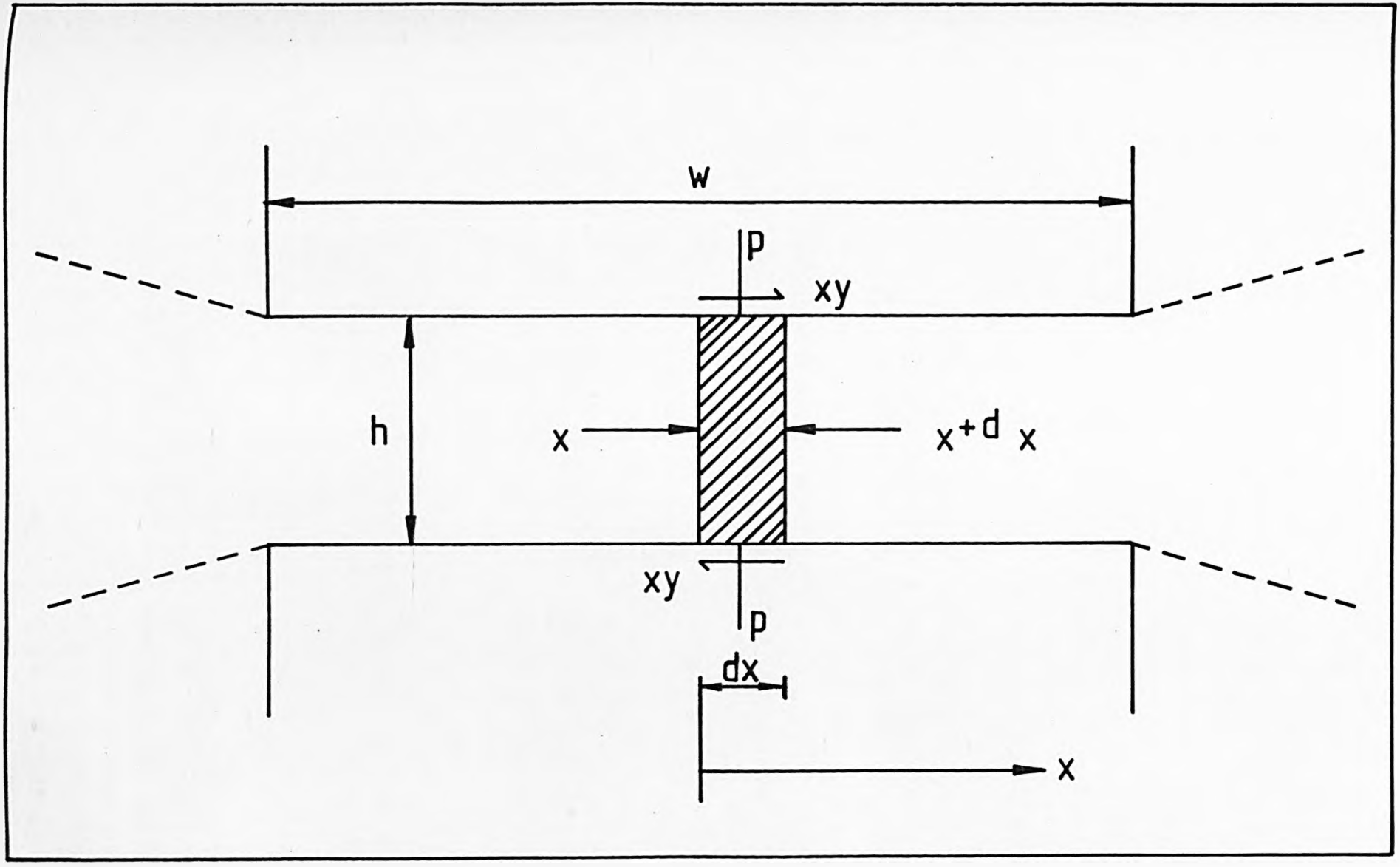
w
p
xy
h
x
x+d x
xy
p
dx
x

FIGURE 48: Plot of the differences between the top and bottom tool temperature as a function of test furnace temperature.

(After Foster [74]).

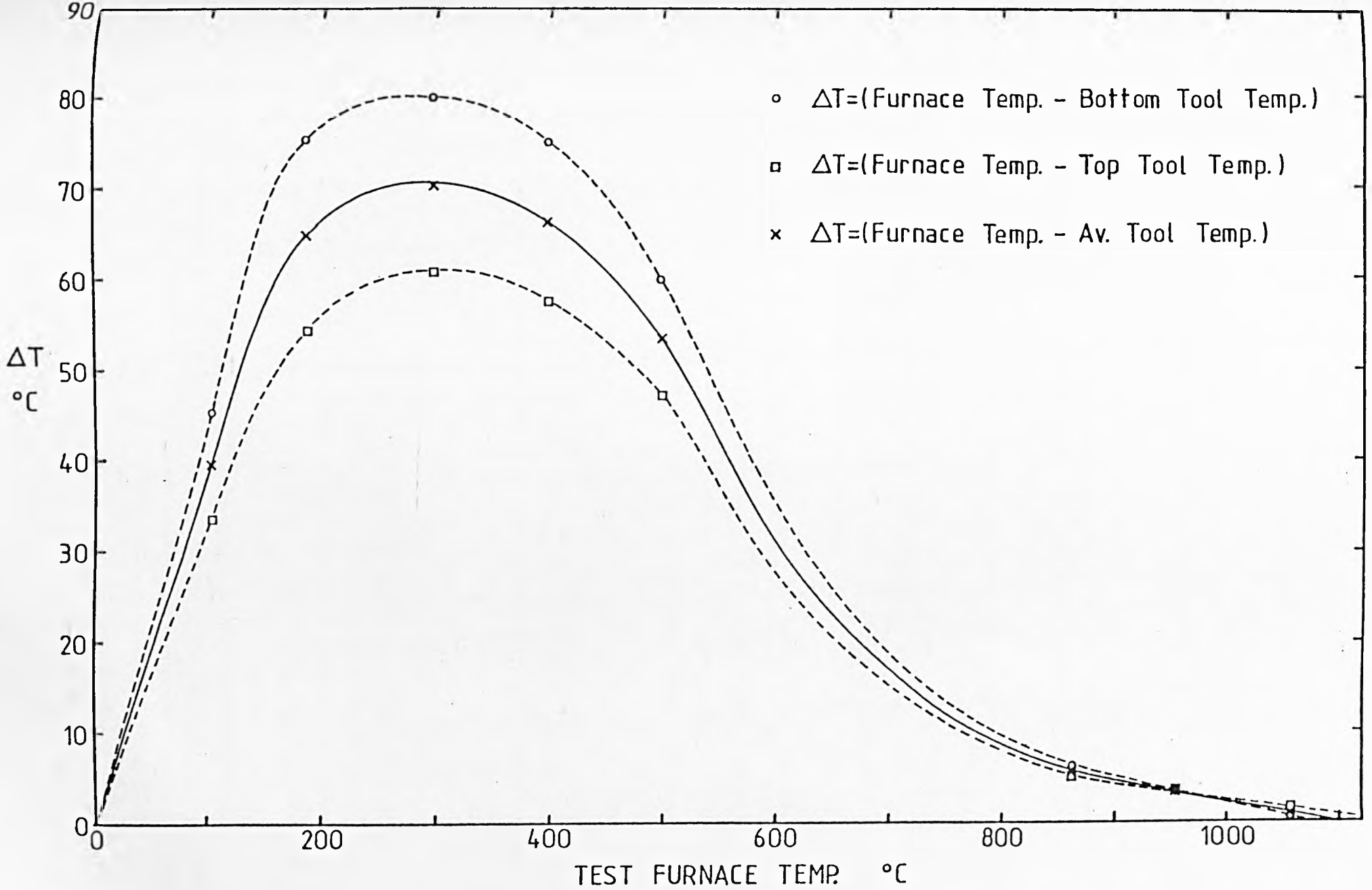
90
80
70
60
50
40
30
20
10
0
ΔT °C
0
200
400
600
800
1000
TEST FURNACE TEMP. °C
ΔT=(Furnace Temp. - Bottom Tool Temp.)
ΔT=(Furnace Temp. - Top Tool Temp.)
ΔT=(Furnace Temp. - Av. Tool Temp.)

FIGURE 49: Drilling of the initial pair of tools.

W = 10 mm.

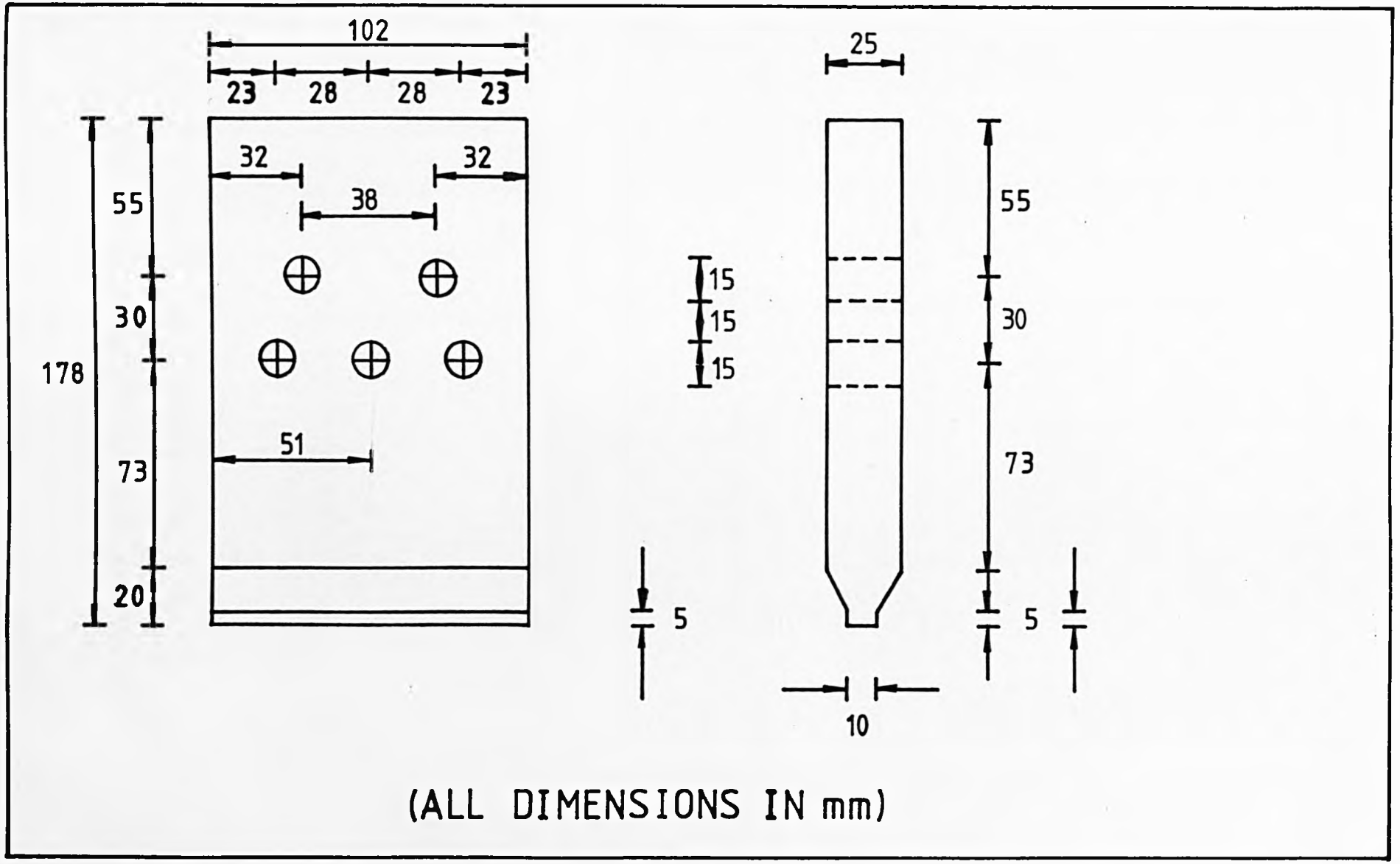

(ALL DIMENSIONS IN mm)

FIGURE 50: Preliminary use of a cartridge heater on a deformation tool.

W = 10 mm.

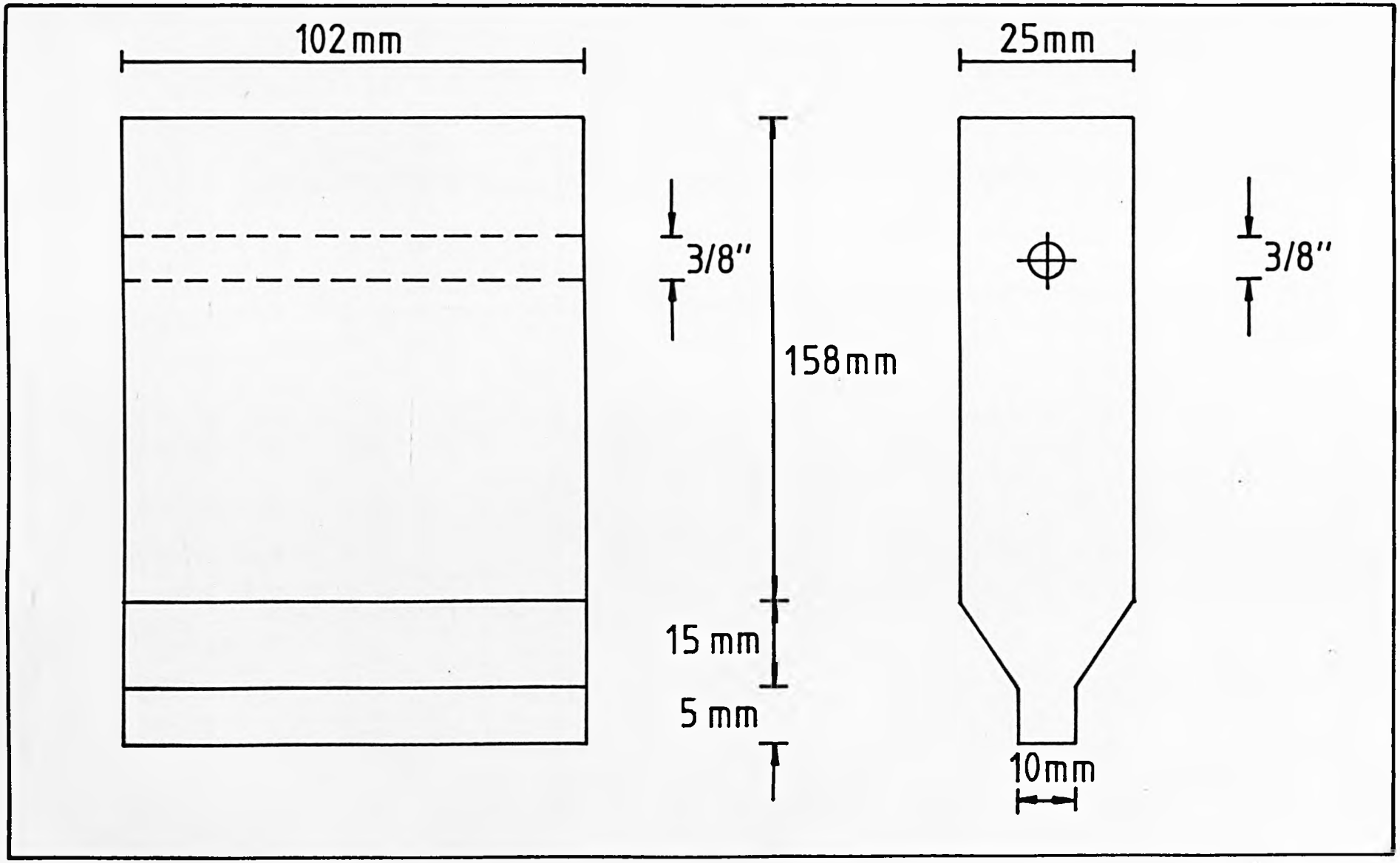
102 mm
25mm
3/8"
158mm
15 mm
5 mm
3/8"
10mm

FIGURE 51: Stress-strain curves for Al-1%Mg alloy at 300°C.

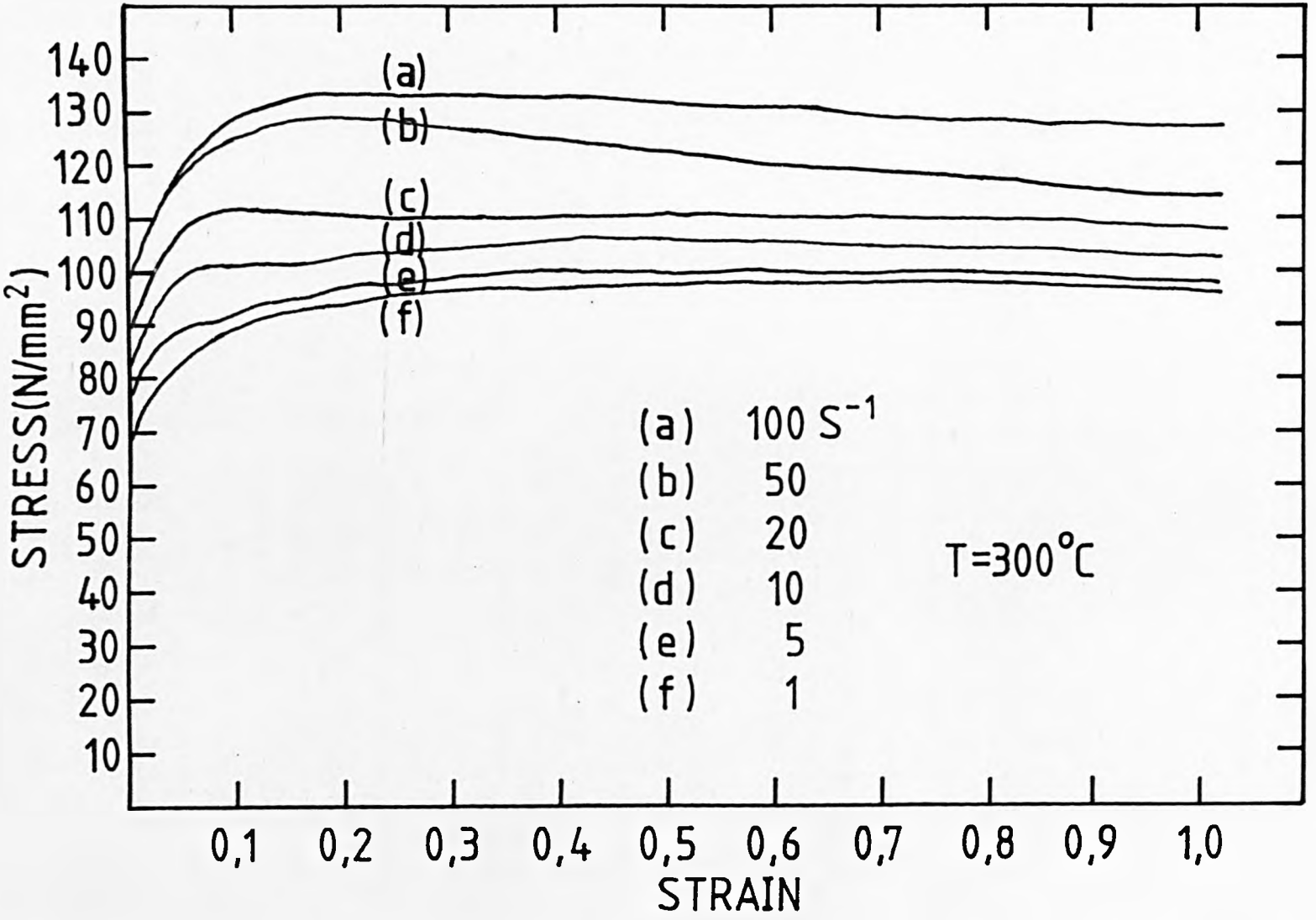
STRESS(N/mm²)
140
130
120
110
100
90
80
70
60
50
40
30
20
10
(a)
(b)
(c)
(d)
(e)
(f)
(a) 100 S⁻¹
(b) 50
(c) 20
(d) 10
(e) 5
(f) 1
T=300°C
0,1
0,2
0,3
0,4
0,5
0,6
0,7
0,8
0,9
1,0
STRAIN

FIGURE 52: Stress-strain curves for Al-1%Mg alloy at 400°C.

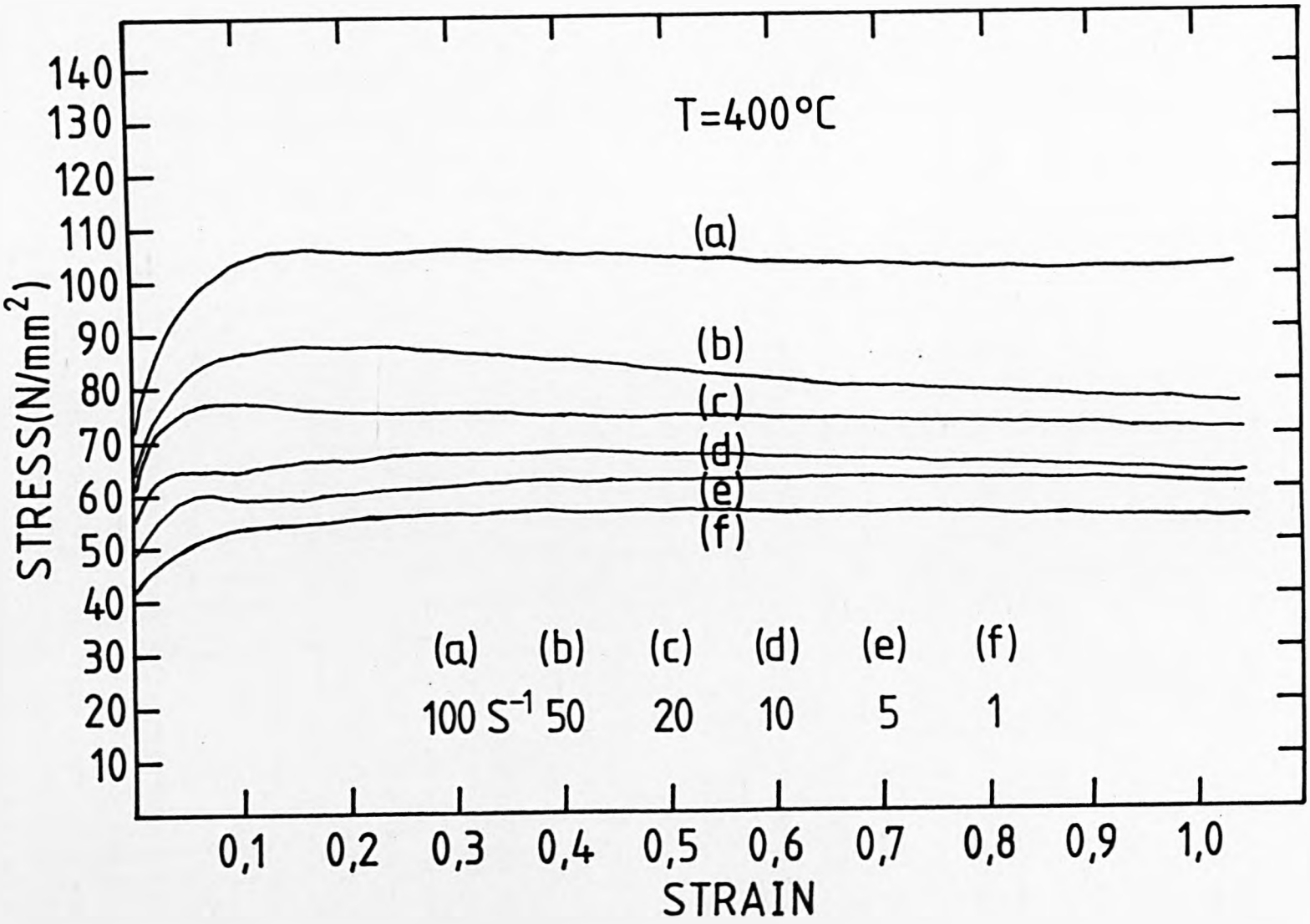
T=400°C
STRESS(N/mm²)
STRAIN
140
130
120
110
100
90
80
70
60
50
40
30
20
10
0,1
0,2
0,3
0,4
0,5
0,6
0,7
0,8
0,9
1,0
(a)
(b)
(c)
(d)
(e)
(f)
(a) (b) (c) (d) (e) (f)
100 S⁻¹ 50 20 10 5 1

FIGURE 53: Stress-strain curves for Al-1%Mg alloy at 500°C.

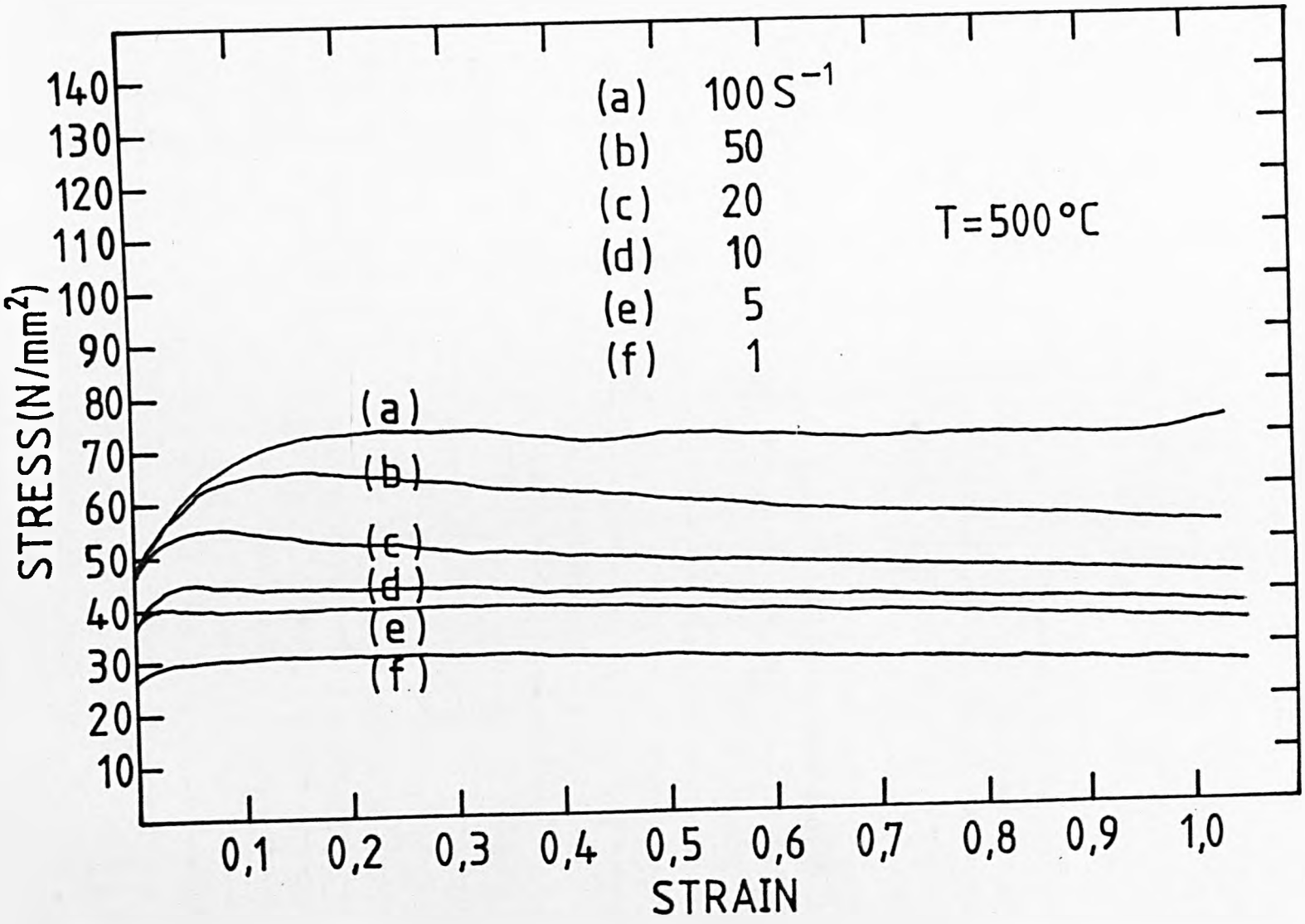
(a) 100 S⁻¹
(b) 50
(c) 20
(d) 10
(e) 5
(f) 1
T=500 °C
(a)
(b)
(c)
(d)
(e)
(f)
STRESS(N/mm²)
140
130
120
110
100
90
80
70
60
50
40
30
20
10
0,1
0,2
0,3
0,4
0,5
0,6
0,7
0,8
0,9
1,0
STRAIN

FIGURE 54: Relation between ln Z and σ at 0.05 strain for Al-1%Mg alloy.

Q_{def} = 156 kJ/mol.

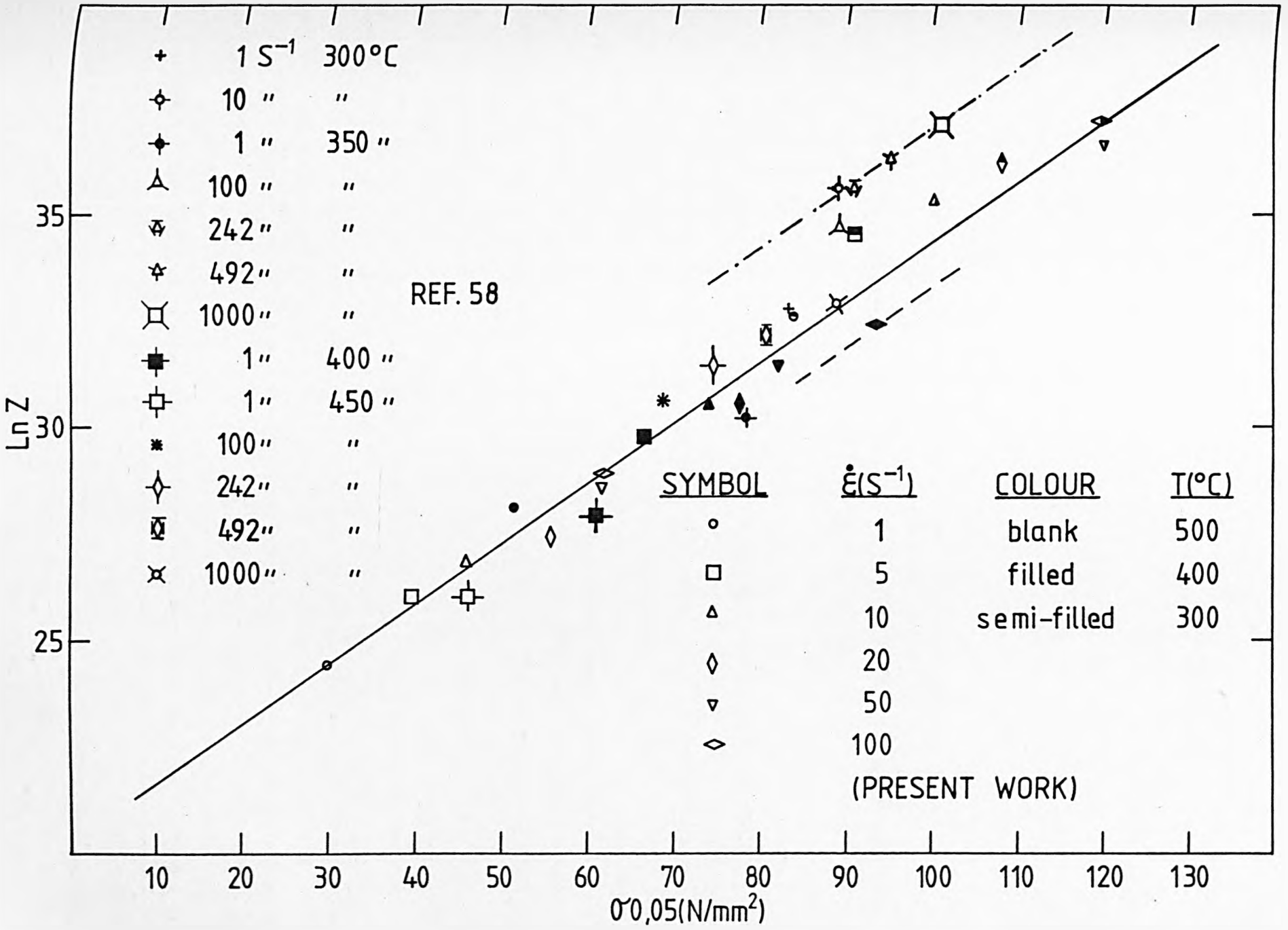
1 S⁻¹ 300°C
10 " "
1 " 350 "
100 " "
242 " "
492 " "
1000 " "
1 " 400 "
1 " 450 "
100 " "
242 " "
492 " "
1000 " "
REF. 58
SYMBOL
Ė(S⁻¹)
COLOUR
T(°C)
1
blank
500
5
filled
400
10
semi-filled
300
20
50
100
(PRESENT WORK)
Ln Z
35
30
25
10
20
30
40
50
60
70
80
90
100
110
120
130
σ 0,05(N/mm²)

FIGURE 55: Relation between ln Z and σ at 0.2 strain for Al-1%Mg alloy.

Q_{def} = 156 kJ/mol.

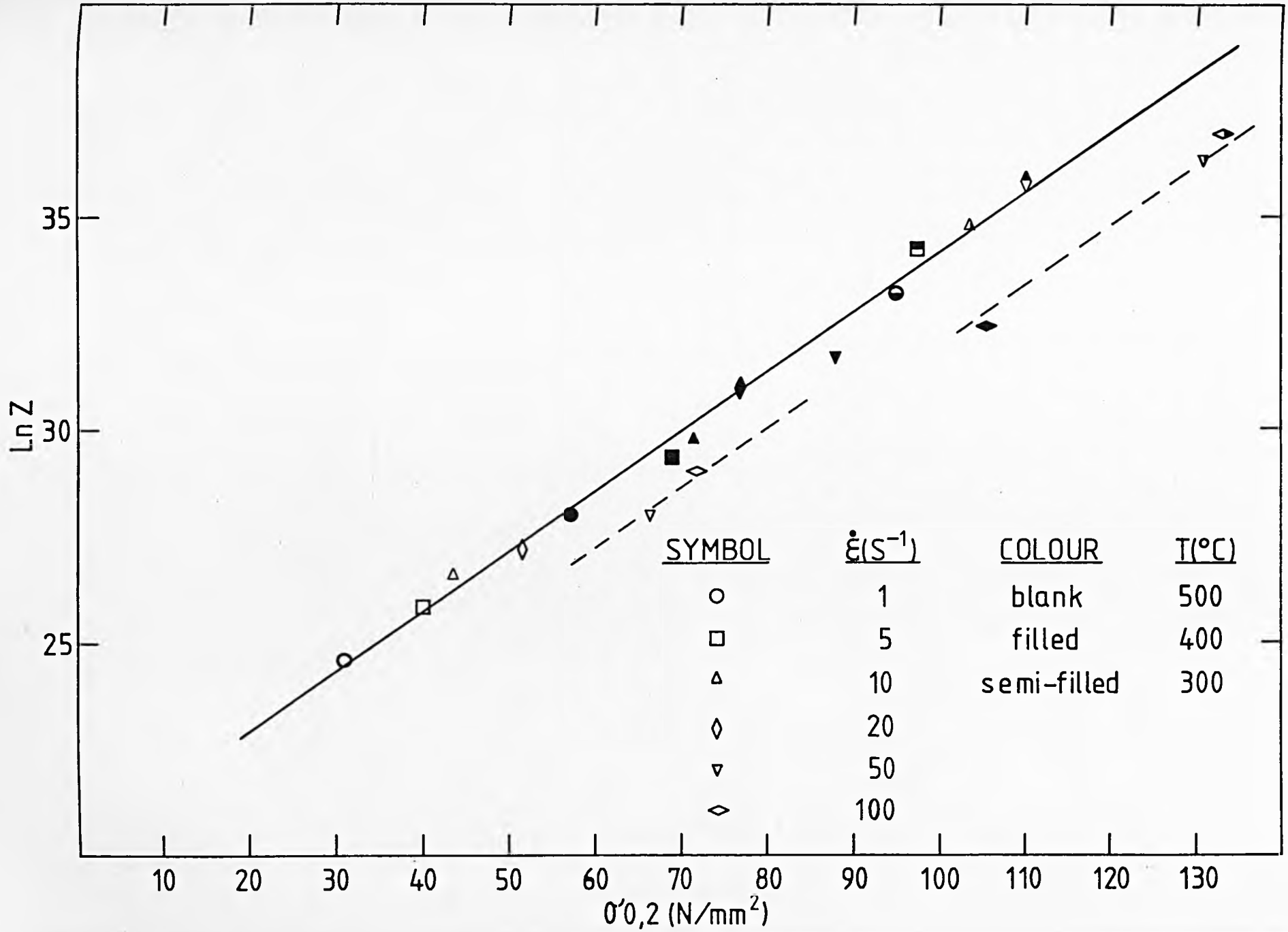
Ln Z
35
30
25
10
20
30
40
50
60
70
80
90
100
110
120
130
σ0,2 (N/mm²)
SYMBOL
ξ̇(S⁻¹)
COLOUR
T(°C)
1
blank
500
5
filled
400
10
semi-filled
300
20
50
100

FIGURE 56: Relation between ln Z and σ at 0.4 strain for Al-1%Mg alloy.

Q_{def} = 156 kJ/mol.

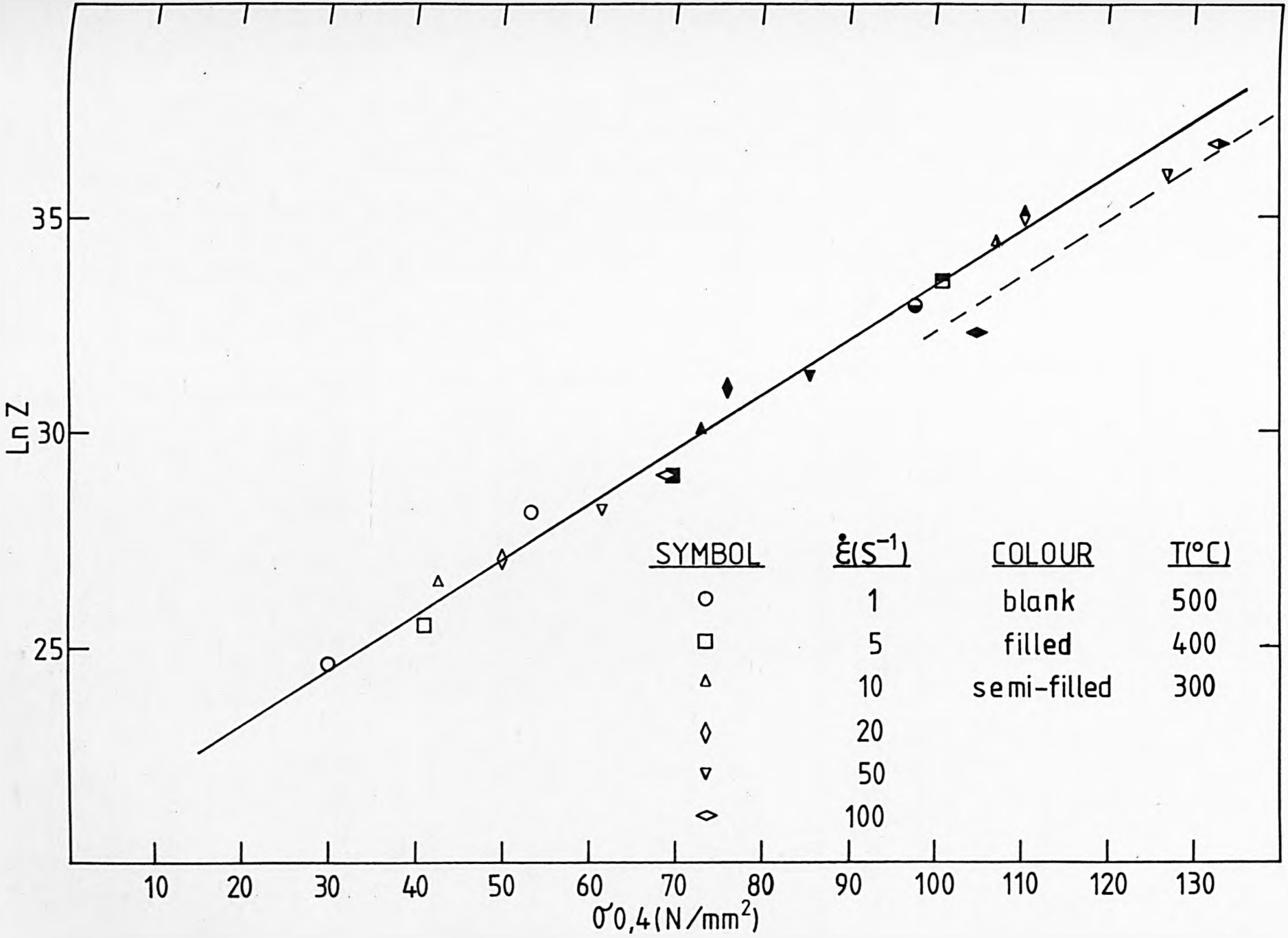
Ln Z
35
30
25
10
20
30
40
50
60
70
80
90
100
110
120
130
σ0,4 (N/mm²)
SYMBOL
Ė(S⁻¹)
COLOUR
T(°C)
1
blank
500
5
filled
400
10
semi-filled
300
20
50
100

FIGURE 57: Relation between ln Z and σ at 0.6 strain for Al-1%Mg alloy.

Q_{def} = 156 kJ/mol.

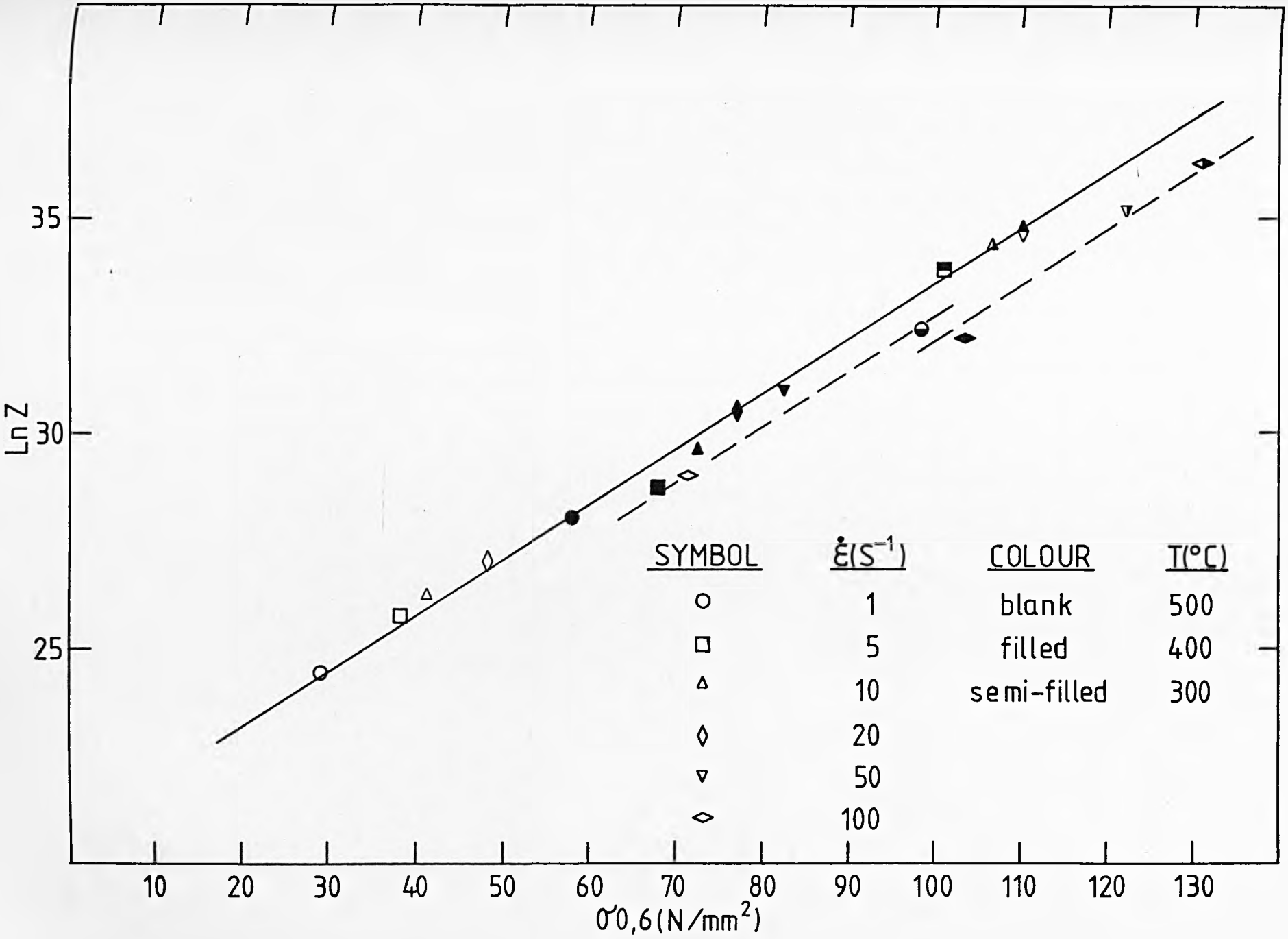
Ln Z
35
30
25
10
20
30
40
50
60
70
80
90
100
110
120
130
σ0,6 (N/mm²)
SYMBOL
Ė(S⁻¹)
COLOUR
T(°C)
1
blank
500
5
filled
400
10
semi-filled
300
20
50
100

FIGURE 58: Relation between ln Z and σ at 0.8 strain for Al-1%Mg alloy.

Q_{def} = 156 kJ/mol.

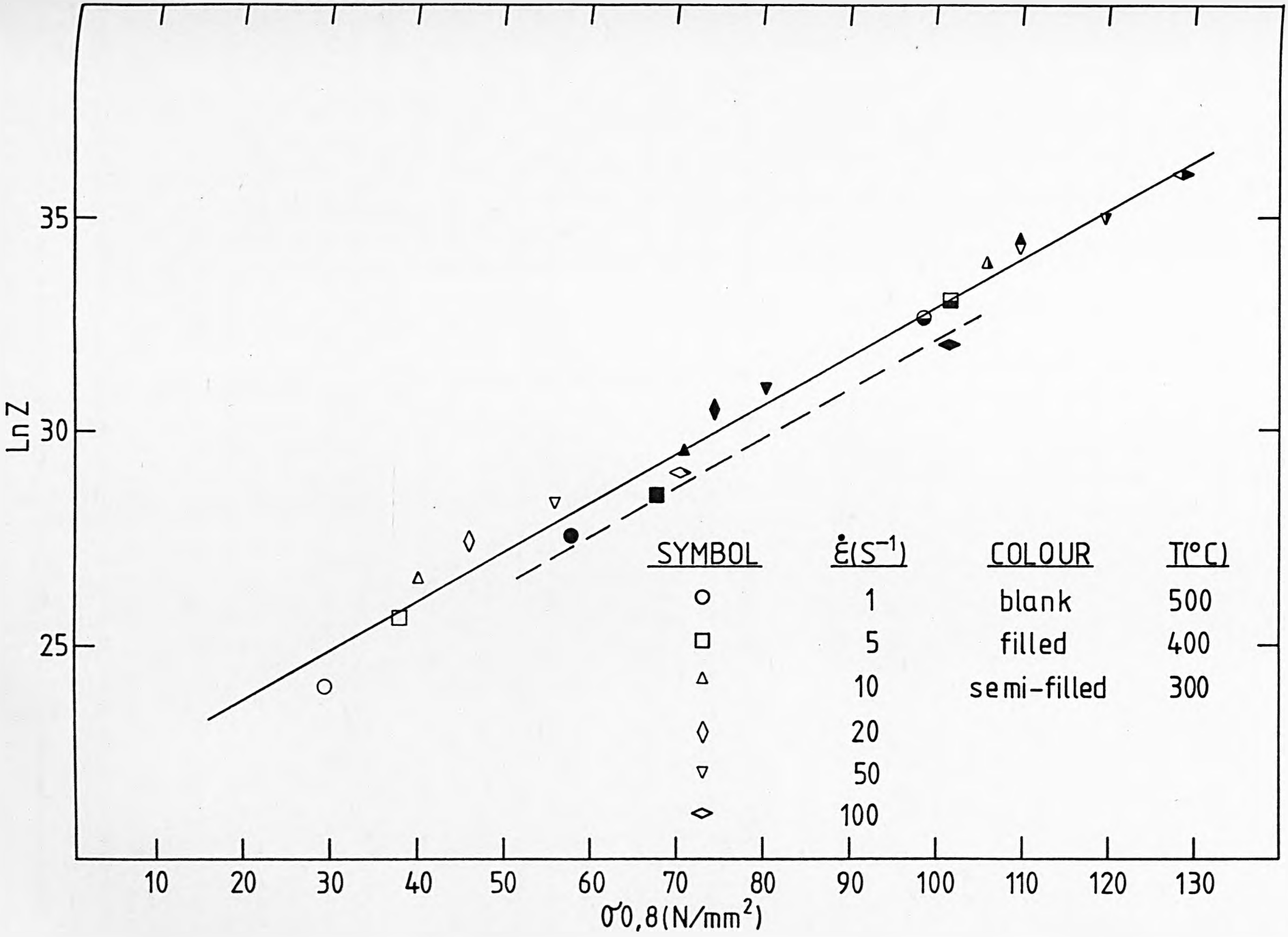
Ln Z
35
30
25
10
20
30
40
50
60
70
80
90
100
110
120
130
σ0,8 (N/mm²)
SYMBOL
Ė(S⁻¹)
COLOUR
T(°C)
1
blank
500
5
filled
400
10
semi-filled
300
20
50
100

FIGURE 59: Relation between ln Z and σ at 1.0 strain for Al-1%Mg alloy.

Q_{def} = 156 kJ/mol.

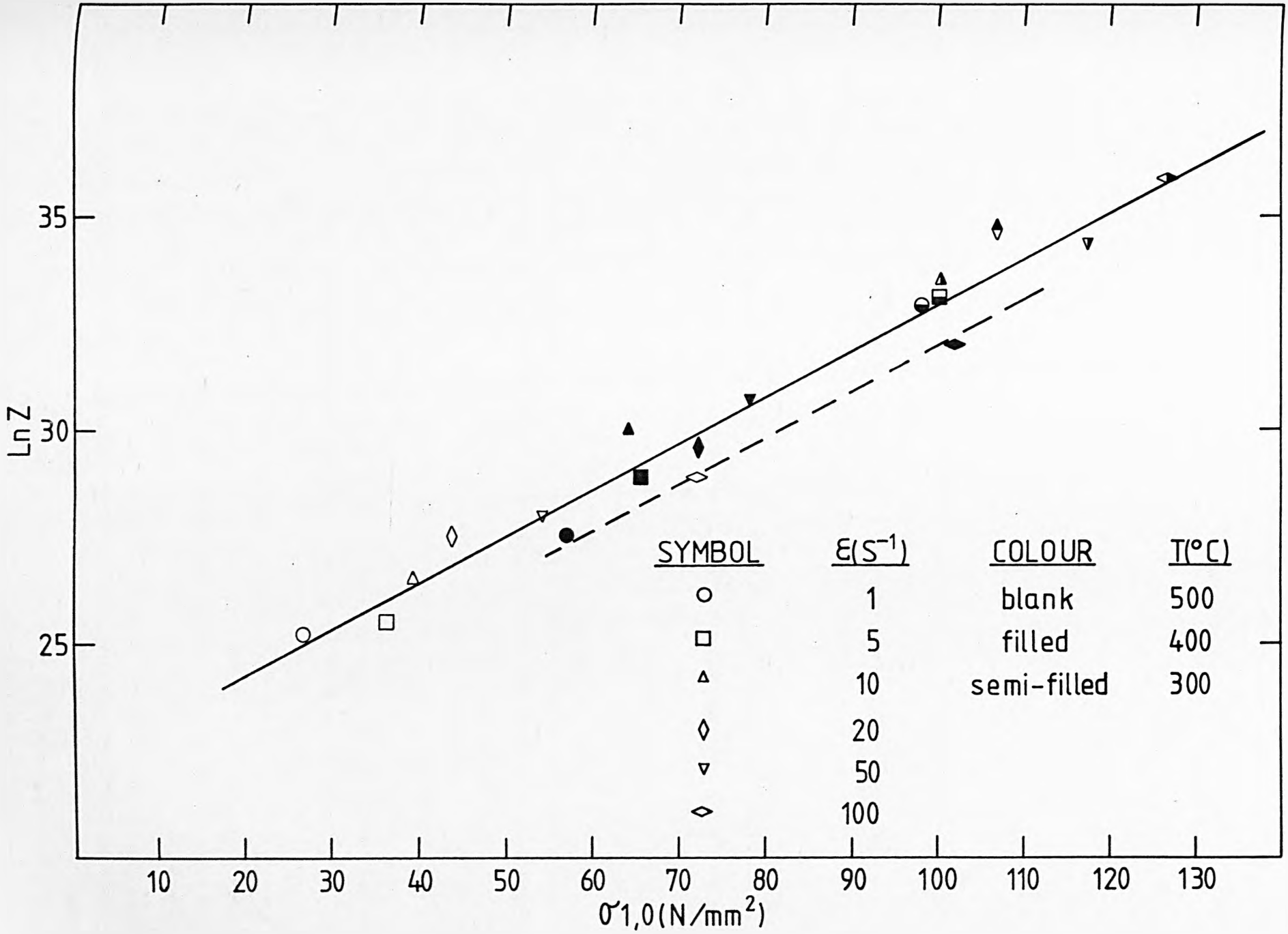
Ln Z
35
30
25
10
20
30
40
50
60
70
80
90
100
110
120
130
σ1,0 (N/mm²)
SYMBOL
ε(S⁻¹)
COLOUR
T(°C)
1
blank
500
5
filled
400
10
semi-filled
300
20
50
100

FIGURE 60: Relation between ln Z and σ of steady-state for Al-1%Mg alloy.

Q_{def} = 156 kJ/mol.

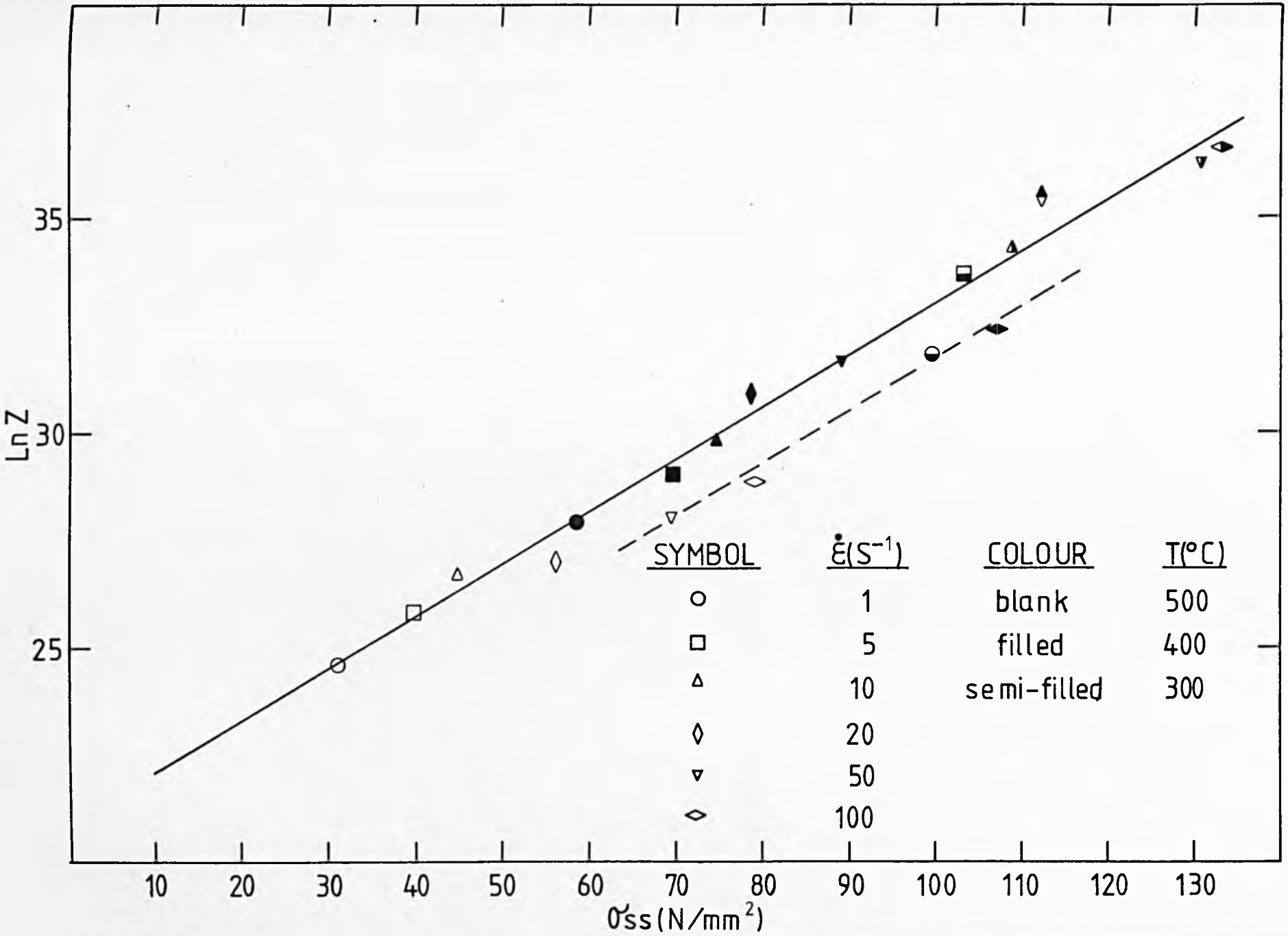
Ln Z
35
30
25
10
20
30
40
50
60
70
80
90
100
110
120
130
σss (N/mm²)
SYMBOL
Ė(S⁻¹)
COLOUR
T(°C)
1
blank
500
5
filled
400
10
semi-filled
300
20
50
100

FIGURE 61: Relation between log σ and log ε for Al-1%Mg alloy.

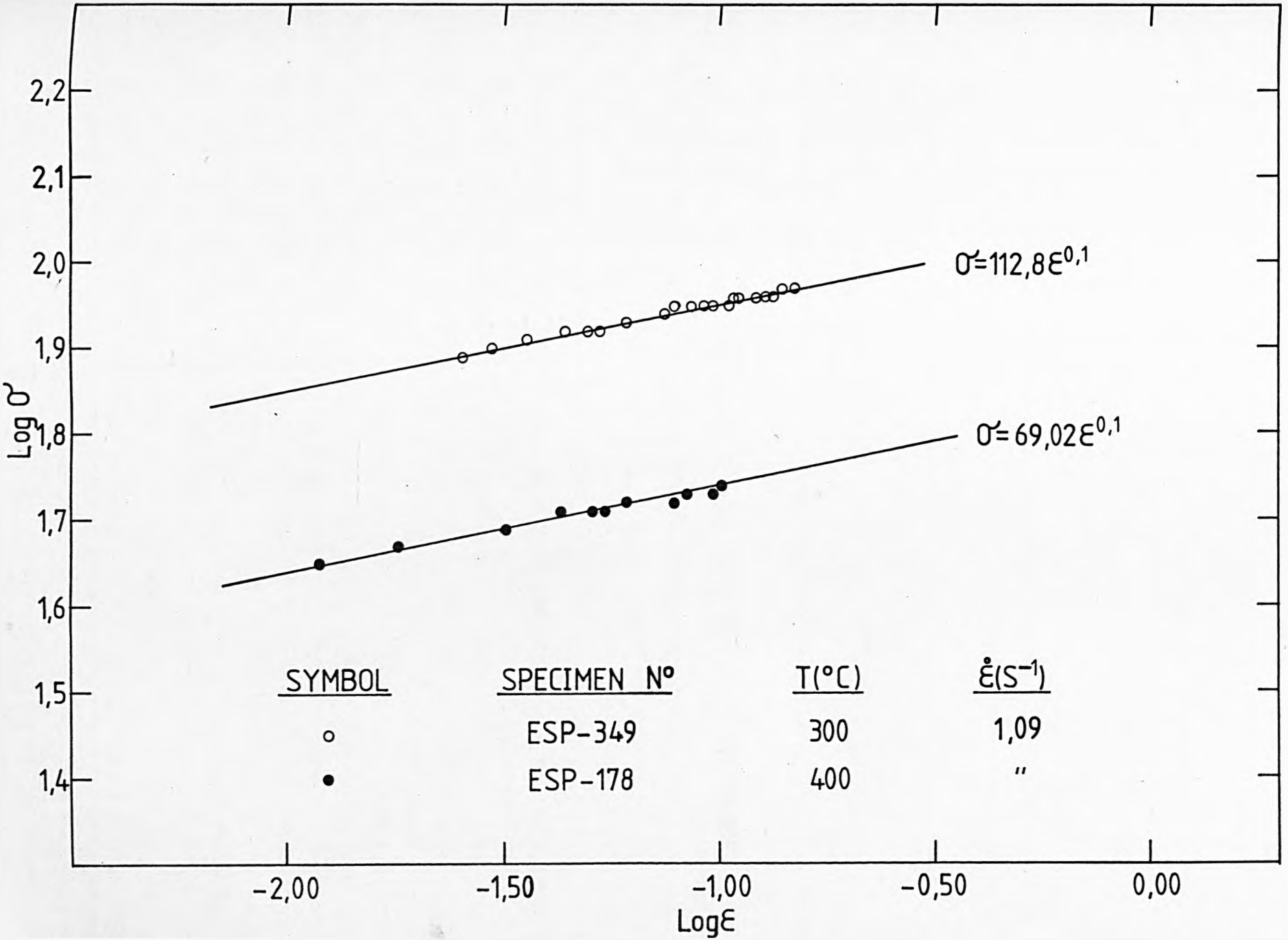
2,2
2,1
2,0
1,9
1,8
1,7
1,6
1,5
1,4
Log σ
σ=112,8ε^0,1
σ= 69,02ε^0,1
SYMBOL
SPECIMEN Nº
T(°C)
ε̇(S⁻¹)
ESP-349
300
1,09
ESP-178
400
"
-2,00
-1,50
-1,00
-0,50
0,00
Logε

FIGURE 62: Non-isothermal double deformation test on as-cast Al-1%Mg alloy. Reheating temperature: 483°C; tools temperature: 20°C; time interval before the first deformation: 10 sec; time interval between first and second deformation: 15 sec; mean strain rate: 5 s^{-1}.

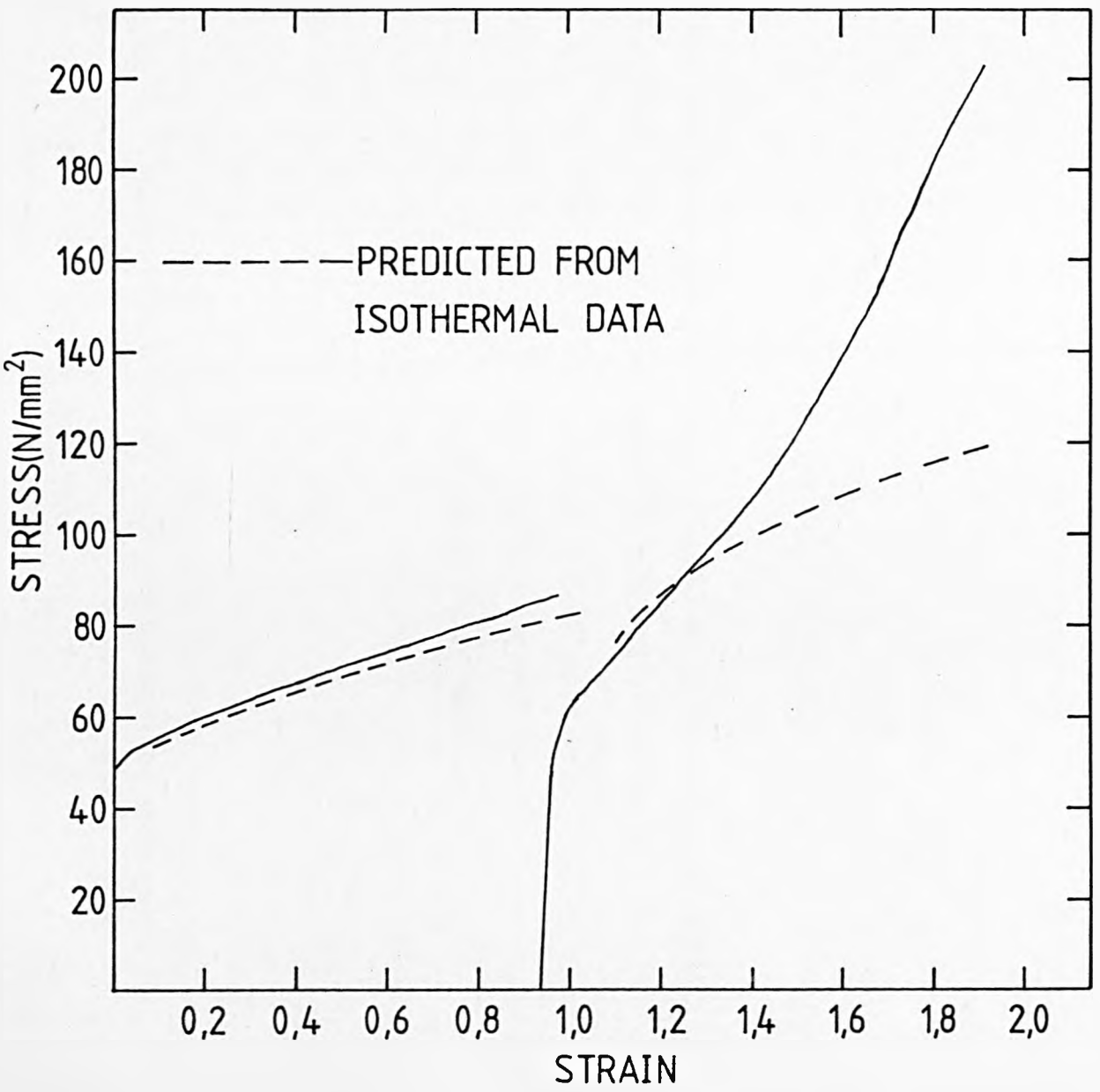
200
180
160
140
120
100
80
60
40
20
PREDICTED FROM
ISOTHERMAL DATA
STRESS(N/mm²)
0,2
0,4
0,6
0,8
1,0
1,2
1,4
1,6
1,8
2,0
STRAIN

FIGURE 63: Non-isothermal double deformation test on as-cast Al-1%Mg alloy. Reheating temperature: 483°C; tools temperature: 20°C; time interval before the first deformation: 10 sec; time interval between first and second deformation: 15 sec; mean strain rate: 10 s^{-1}.

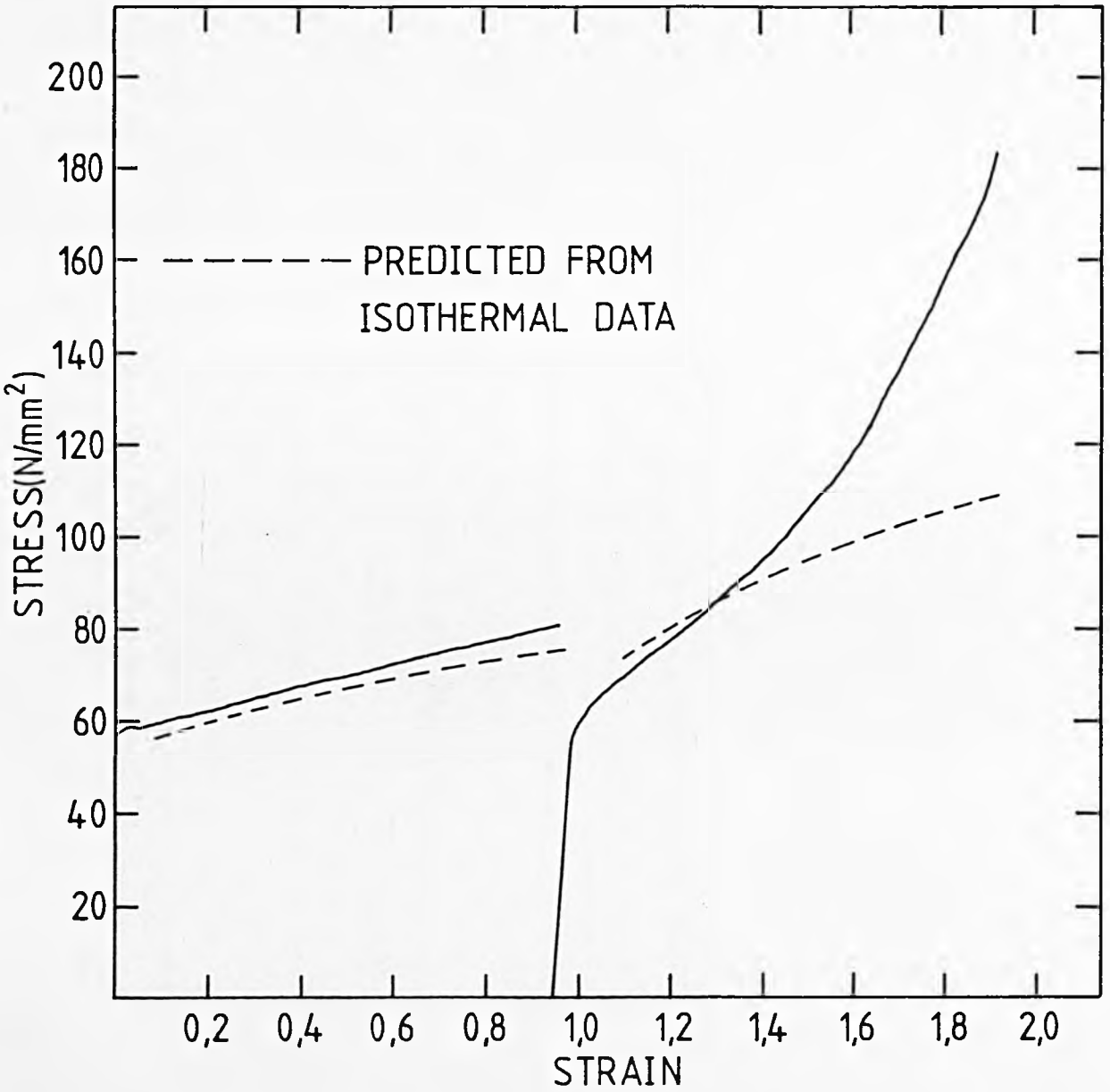
200
180
160
140
120
100
80
60
40
20
PREDICTED FROM
ISOTHERMAL DATA
STRESS(N/mm²)
0,2
0,4
0,6
0,8
1,0
1,2
1,4
1,6
1,8
2,0
STRAIN

FIGURE 64: Non-isothermal double deformation test on as-cast Al-1%Mg alloy. Reheating temperature: 483°C; tools temperature: 20°C; time interval before the first deformation: 10 sec; time interval between first and second deformation: 15 sec; mean strain rate: 20 s^{-1}.

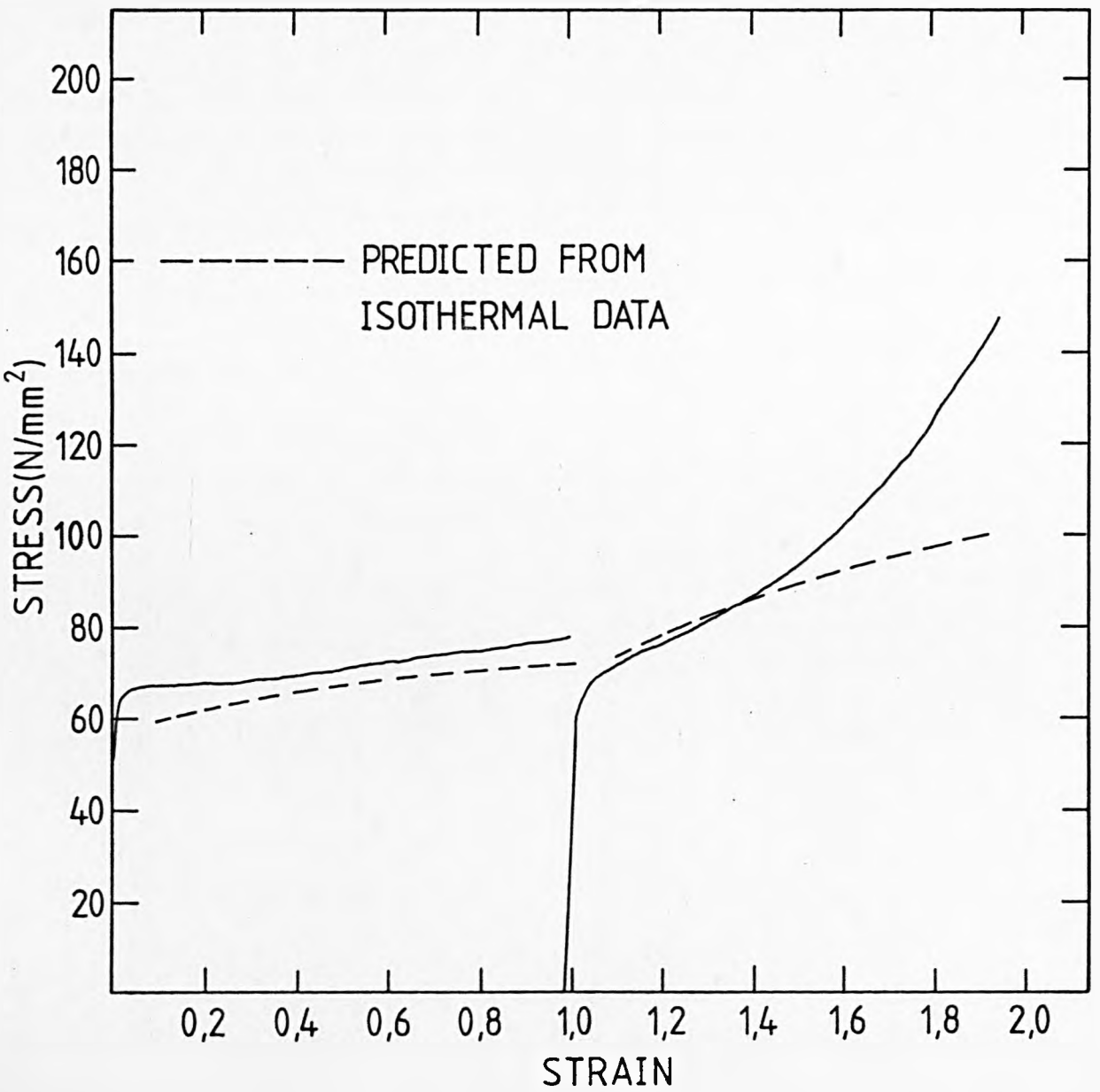
200
180
160
140
120
100
80
60
40
20
STRESS(N/mm²)
PREDICTED FROM
ISOTHERMAL DATA
0,2
0,4
0,6
0,8
1,0
1,2
1,4
1,6
1,8
2,0
STRAIN

FIGURE 65: Non-isothermal double deformation test on as-cast Al-1%Mg alloy. Reheating temperature: 483°C; tools temperature: 20°C; time interval before the first deformation: 10 sec; time interval between first and second deformation: 15 sec; mean strain rate: 50 s^{-1}.

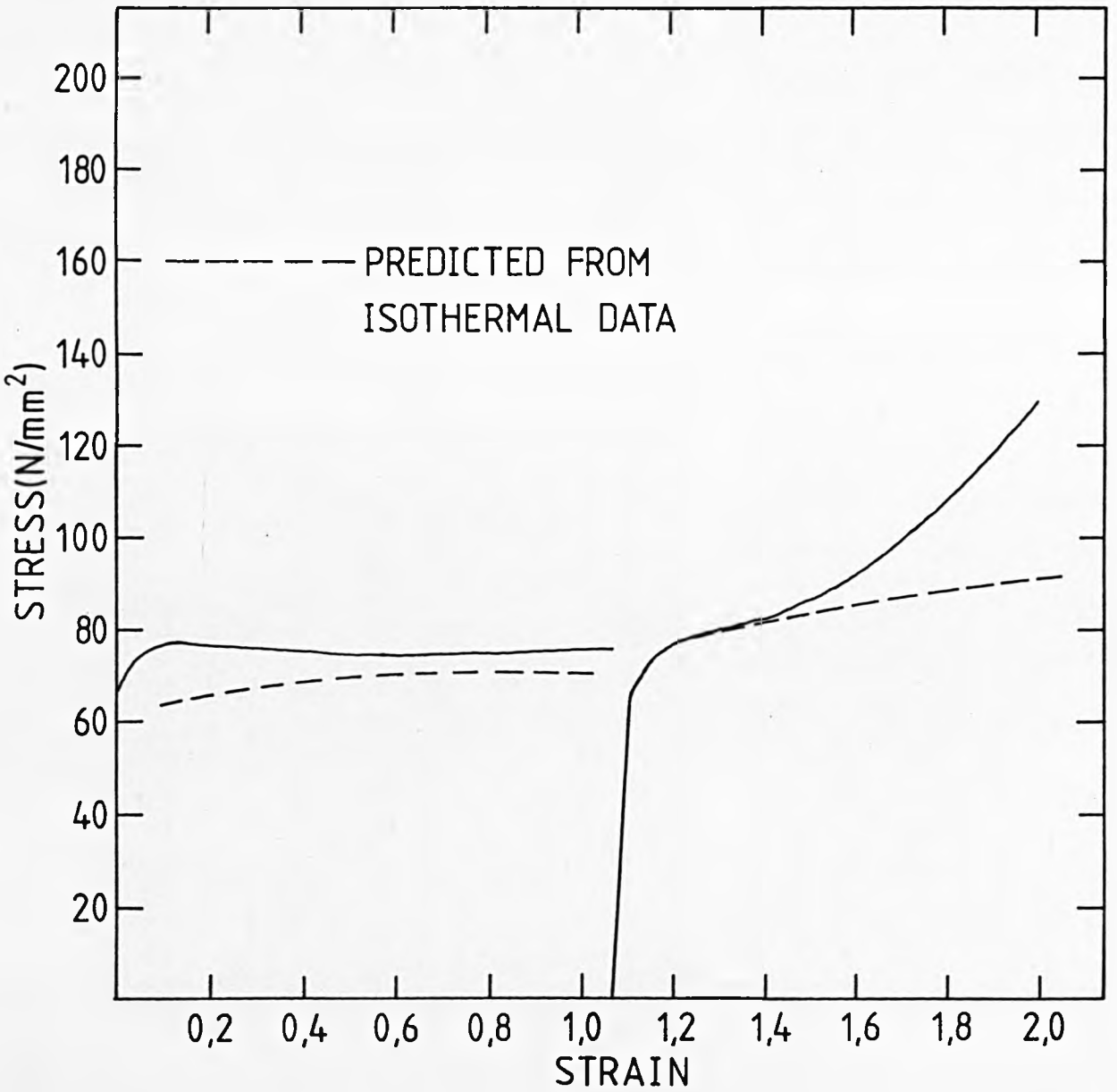
200
180
160
140
120
100
80
60
40
20
PREDICTED FROM
ISOTHERMAL DATA
STRESS(N/mm²)
0,2
0,4
0,6
0,8
1,0
1,2
1,4
1,6
1,8
2,0
STRAIN

FIGURE 66: Relation between ln Z and σ at different strains for non-isothermal double deformation tests on as-cast Al-1%Mg alloy.

(a) first deformation;
(b) second deformation.

Q_{def} = 156 kJ/mol.

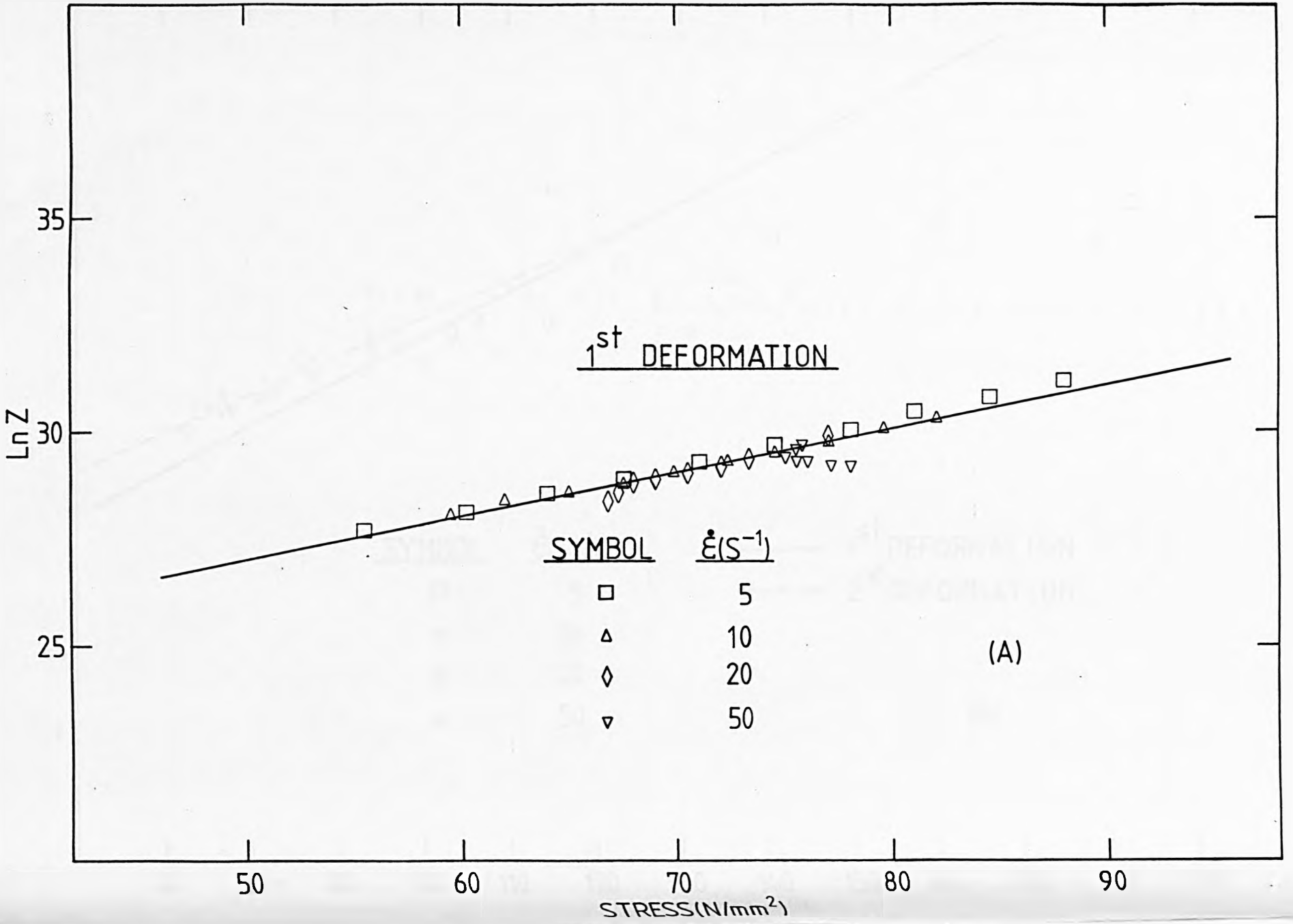
1st DEFORMATION
SYMBOL
$\dot{\varepsilon}(S^{-1})$
5
10
20
50
(A)
LnZ
35
30
25
50
60
70
80
90
STRESS(N/mm²)

FIGURE 67: Relation between ln Z and σ at 0.05 strain for commercial-purity aluminium.

Q_{def} = 156 kJ/mol.

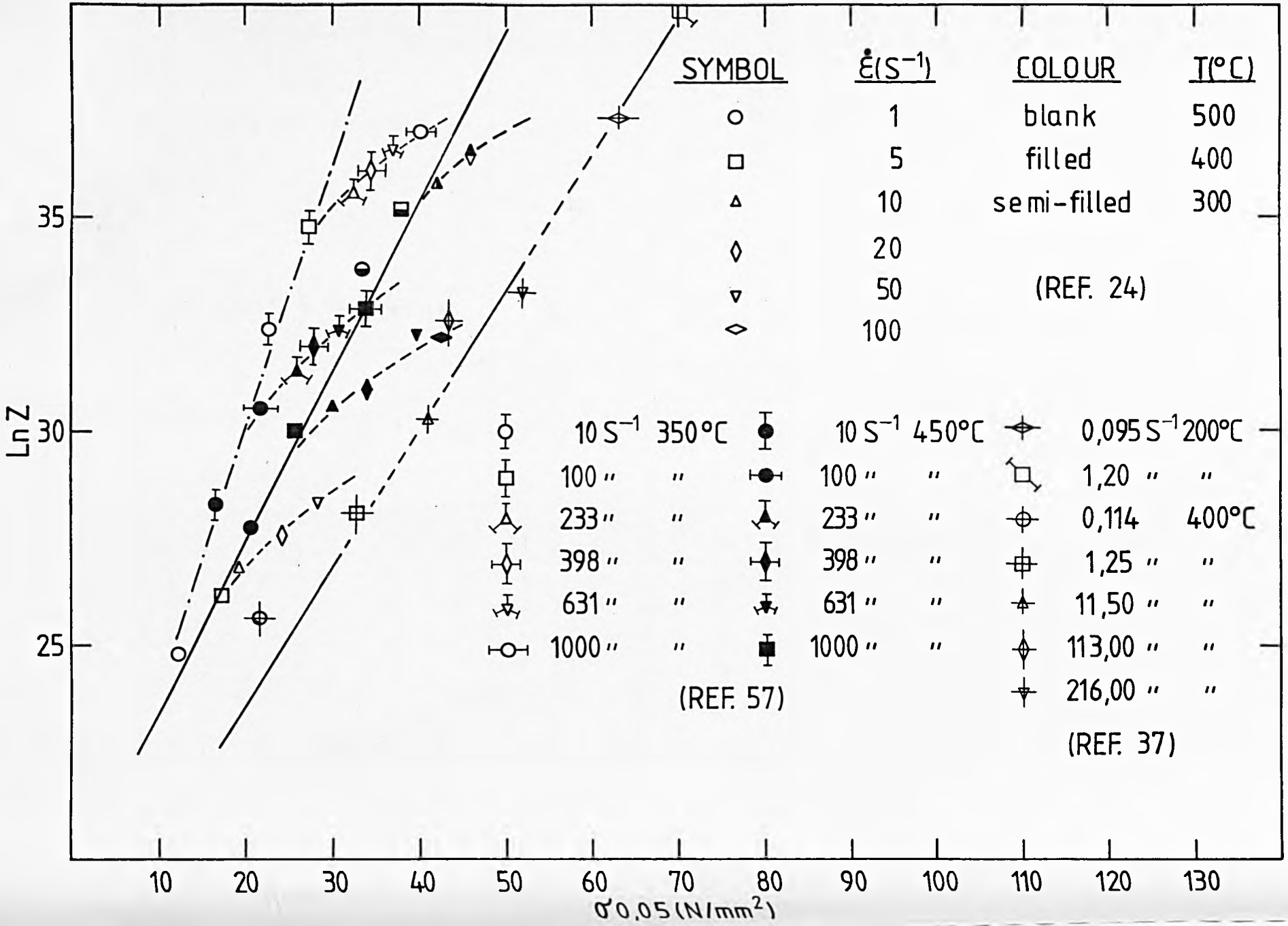
SYMBOL
$\dot{\varepsilon}(S^{-1})$
COLOUR
T(°C)
1
blank
500
5
filled
400
10
semi-filled
300
20
50
(REF. 24)
100
10 S⁻¹ 350°C
100 " "
233 " "
398 " "
631 " "
1000 " "
(REF. 57)
10 S⁻¹ 450°C
100 " "
233 " "
398 " "
631 " "
1000 " "
0,095 S⁻¹ 200°C
1,20 " "
0,114 400°C
1,25 " "
11,50 " "
113,00 " "
216,00 " "
(REF. 37)
Ln Z
35
30
25
10
20
30
40
50
60
70
80
90
100
110
120
130
$\sigma_{0,05}$ (N/mm²)

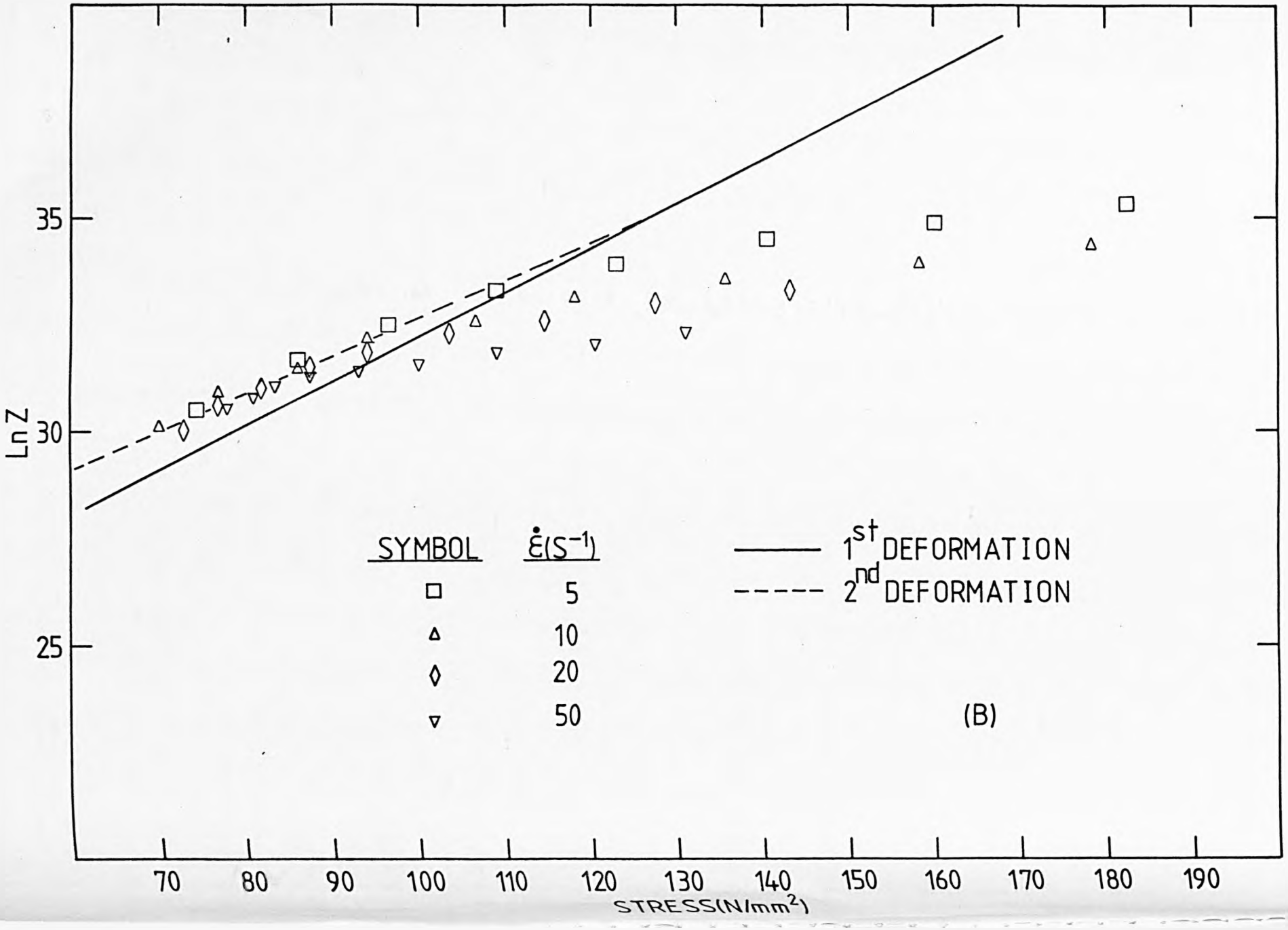
35
30
25
Ln Z
70
80
90
100
110
120
130
140
150
160
170
180
190
STRESS(N/mm²)
SYMBOL
Ė(S⁻¹)
5
10
20
50
1st DEFORMATION
2nd DEFORMATION
(B)

FIGURE 68: Relation between ln Z and σ at 0.2 strain for commercial-purity aluminium.

Q_{def} = 156 kJ/mol.

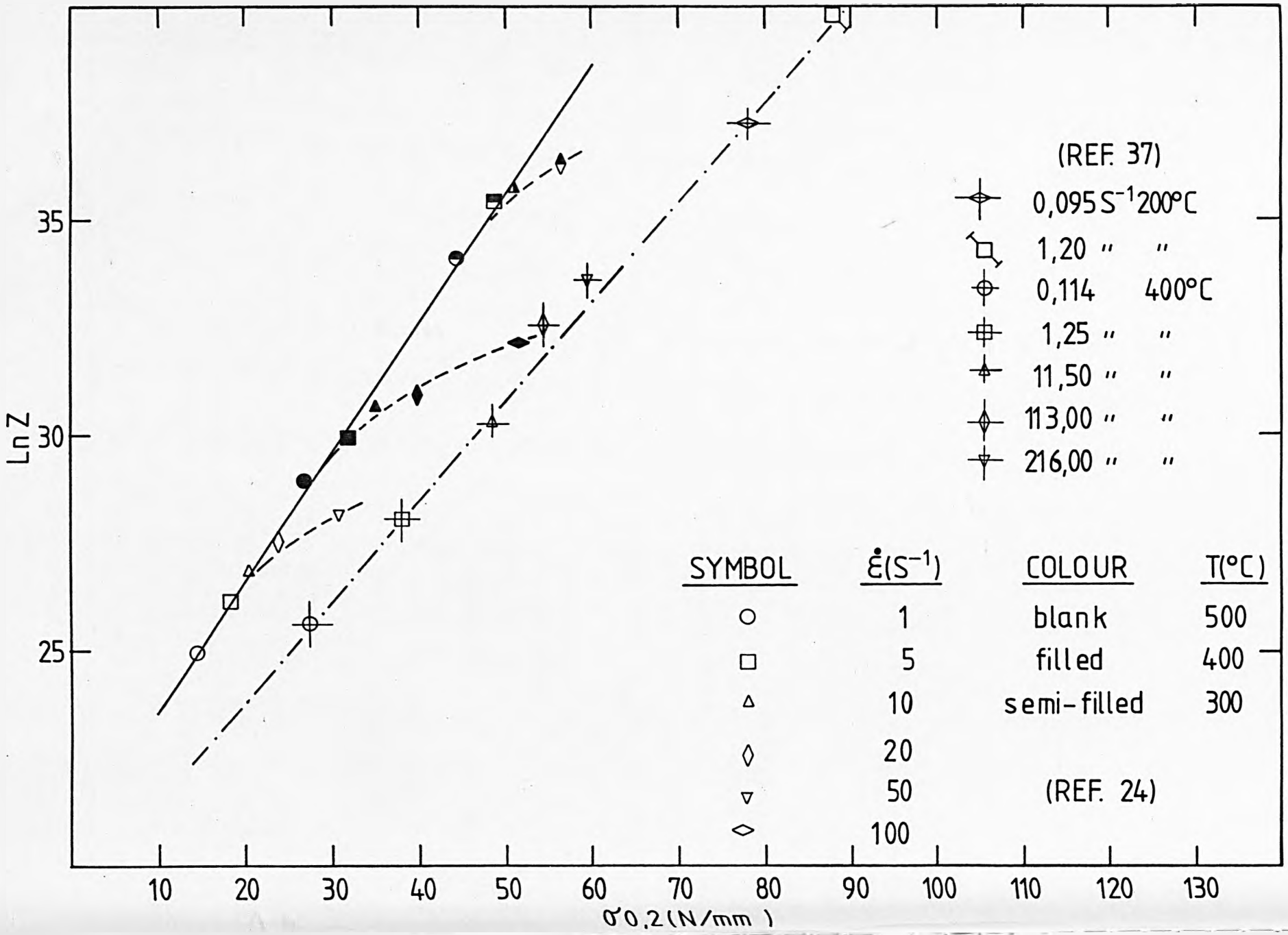
Ln Z
35
30
25
10
20
30
40
50
60
70
80
90
100
110
120
130
σ0,2 (N/mm)
(REF. 37)
0,095 S⁻¹ 200°C
1,20 " "
0,114 400°C
1,25 " "
11,50 " "
113,00 " "
216,00 " "
SYMBOL
Ė(S⁻¹)
COLOUR
T(°C)
1
blank
500
5
filled
400
10
semi-filled
300
20
50
(REF. 24)
100

FIGURE 69: Relation between ln Z and σ at 0.4 strain for commercial-purity aluminium.

Q_{def} = 156 kJ/mol.

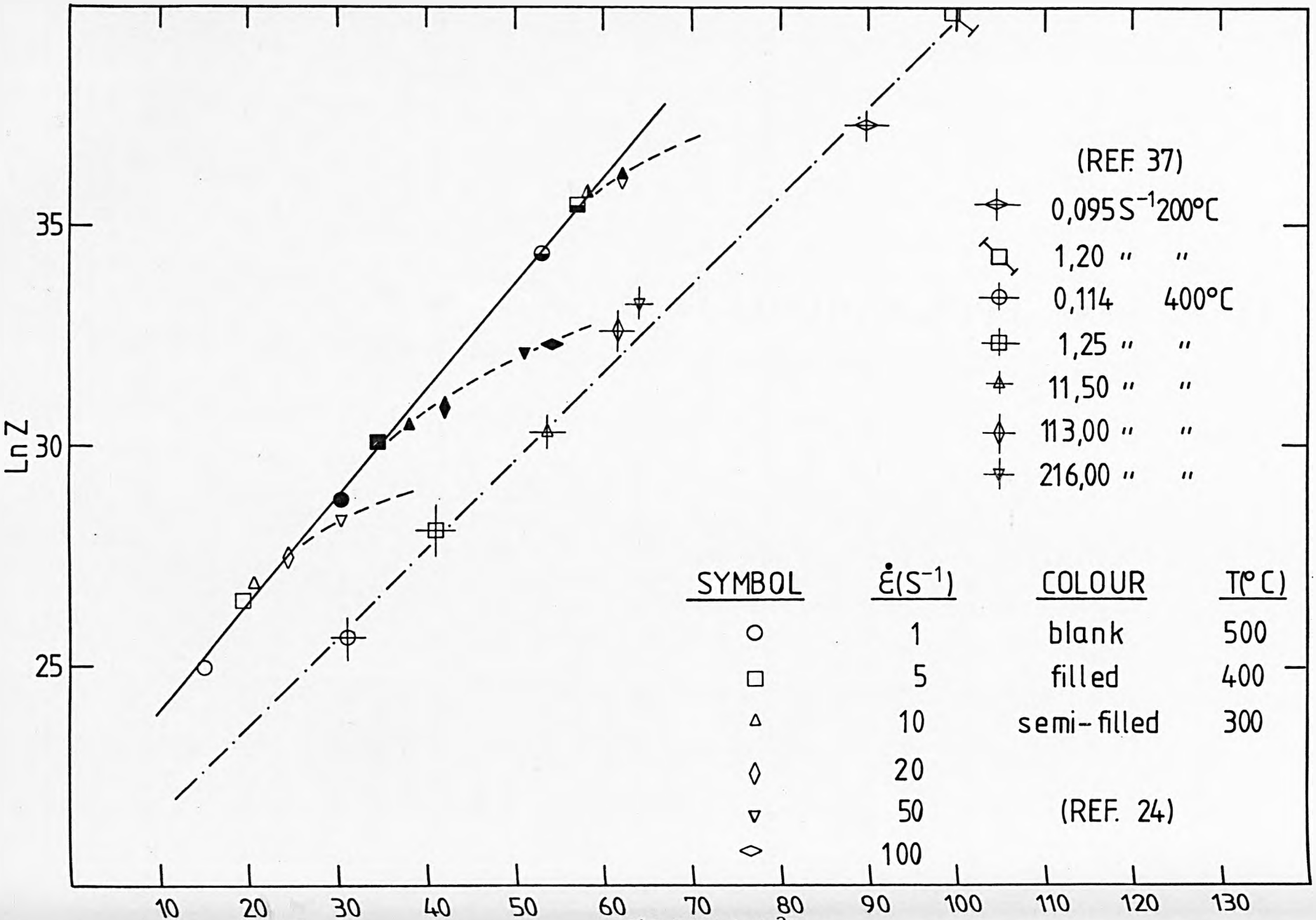
(REF. 37)
0,095 S⁻¹ 200°C
1,20 " "
0,114 400°C
1,25 " "
11,50 " "
113,00 " "
216,00 " "
SYMBOL
Ė(S⁻¹)
COLOUR
T(°C)
1
blank
500
5
filled
400
10
semi-filled
300
20
50
(REF. 24)
100
Ln Z
35
30
25
10
20
30
40
50
60
70
80
90
100
110
120
130
σ0,2 (N/mm²)

FIGURE 70: Relation between ln Z and σ at 0.55 strain for commercial-purity aluminium.

Q_{def} = 156 kJ/mol.

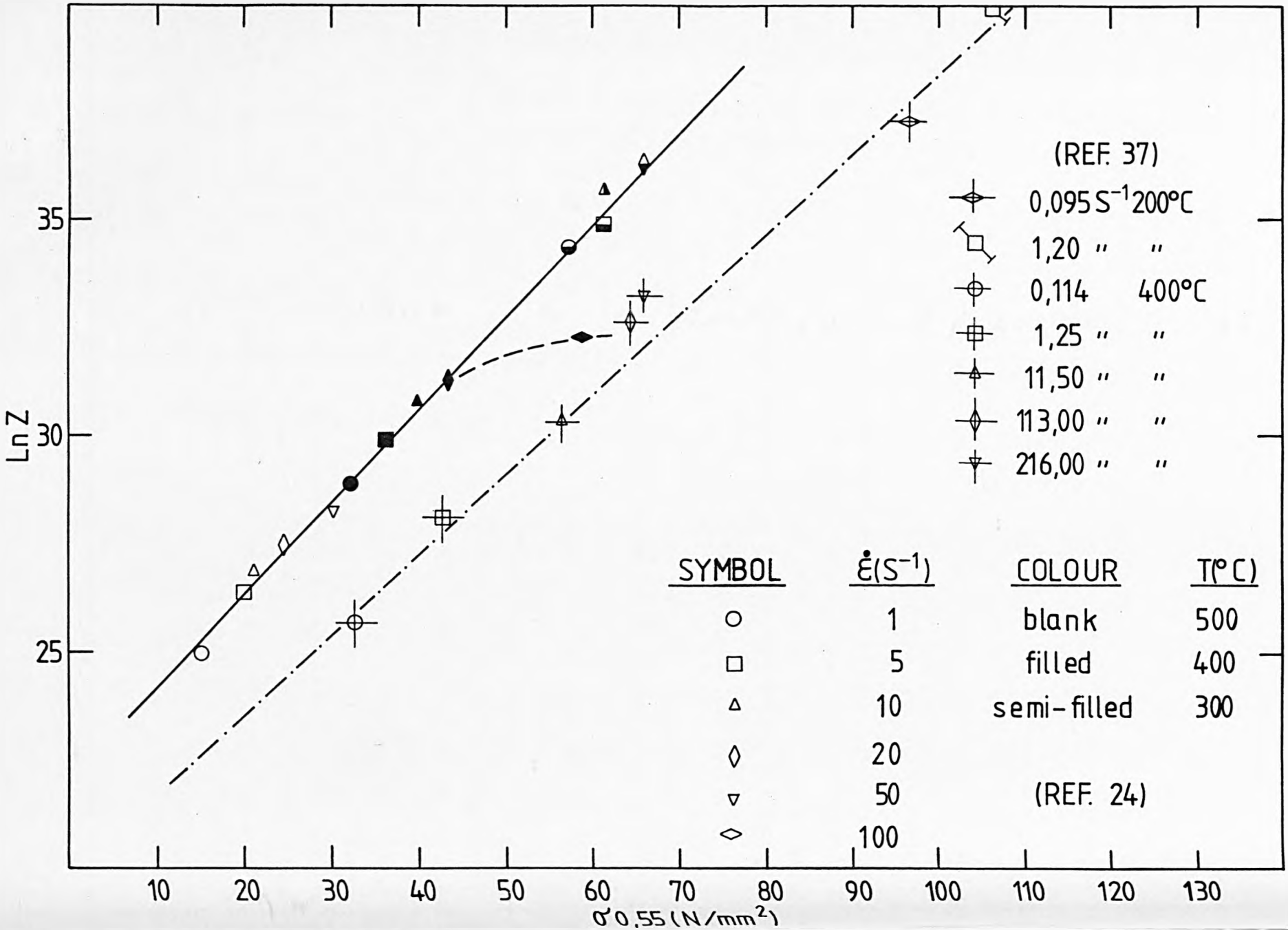
Ln Z
35
30
25
10
20
30
40
50
60
70
80
90
100
110
120
130
σ 0,55 (N/mm²)
(REF. 37)
0,095 S⁻¹ 200°C
1,20 " "
0,114 400°C
1,25 " "
11,50 " "
113,00 " "
216,00 " "
SYMBOL
Ė(S⁻¹)
COLOUR
T(°C)
1
blank
500
5
filled
400
10
semi-filled
300
20
50
100
(REF. 24)

FIGURE 71: Relation between ln Z and σ of steady-state for commercial purity aluminium.

Q_{def} = 156 kJ/mol.

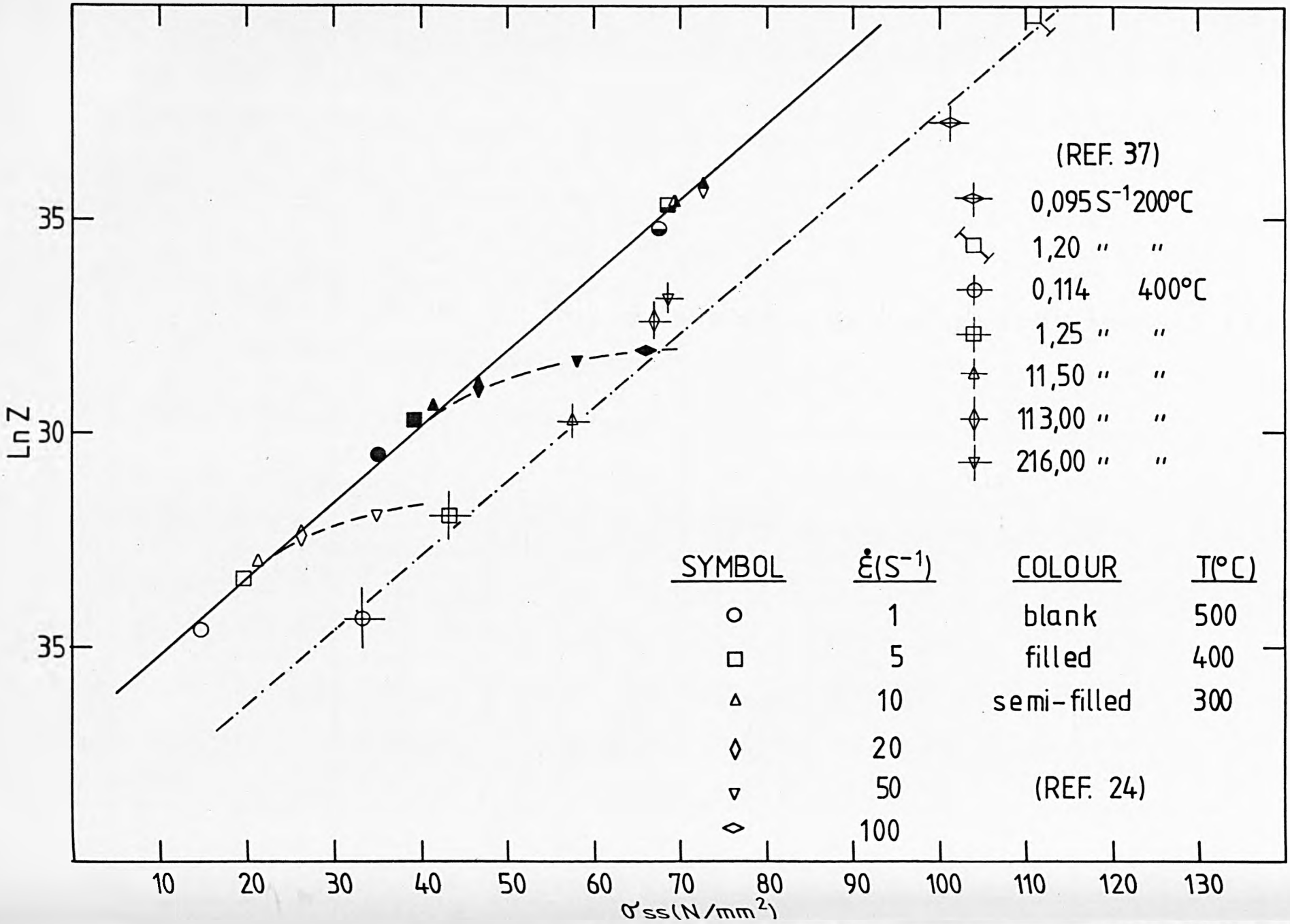
Ln Z
35
30
35
10
20
30
40
50
60
70
80
90
100
110
120
130
σss(N/mm²)
(REF. 37)
0,095 S⁻¹ 200°C
1,20 " "
0,114 400°C
1,25 " "
11,50 " "
113,00 " "
216,00 " "
SYMBOL
Ė(S⁻¹)
COLOUR
T(°C)
1
blank
500
5
filled
400
10
semi-filled
300
20
50
(REF. 24)
100

FIGURE 72: Relation between log σ and log ε for commercial-purity aluminium.

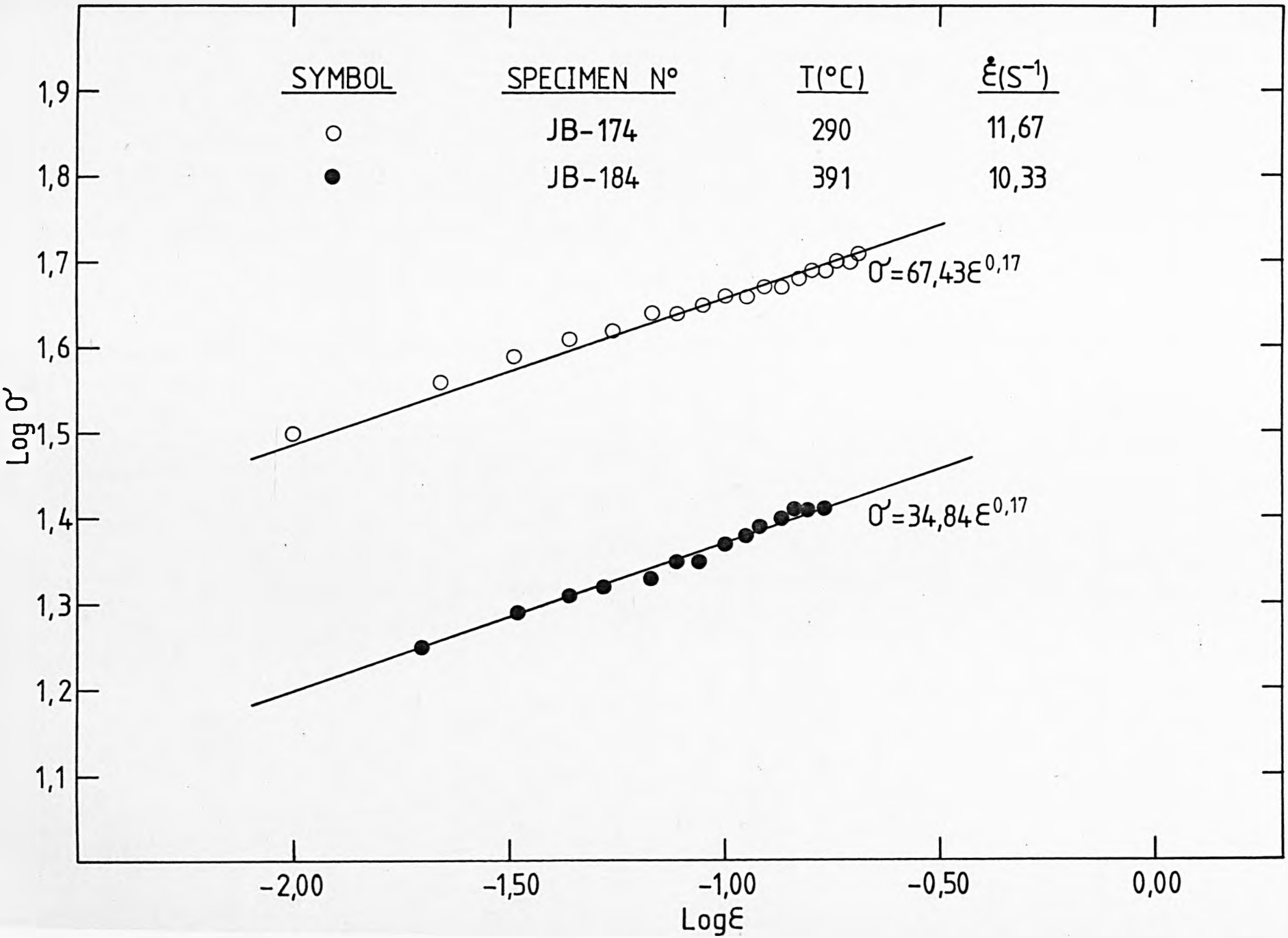
SYMBOL
SPECIMEN N°
T(°C)
$\dot{\varepsilon}(S^{-1})$
JB-174
290
11,67
JB-184
391
10,33
$\sigma = 67,43\varepsilon^{0,17}$
$\sigma = 34,84\varepsilon^{0,17}$
Log σ
Log ε
1,9
1,8
1,7
1,6
1,5
1,4
1,3
1,2
1,1
-2,00
-1,50
-1,00
-0,50
0,00

FIGURE 73: Double deformation tests on Ti-bearing steel under different conditions of load cell compensation and strain rate. Reheating temperature: 900°C; test temperature: 900°C; time interval between deformations: 0.5 sec.

(After Colas [160]).

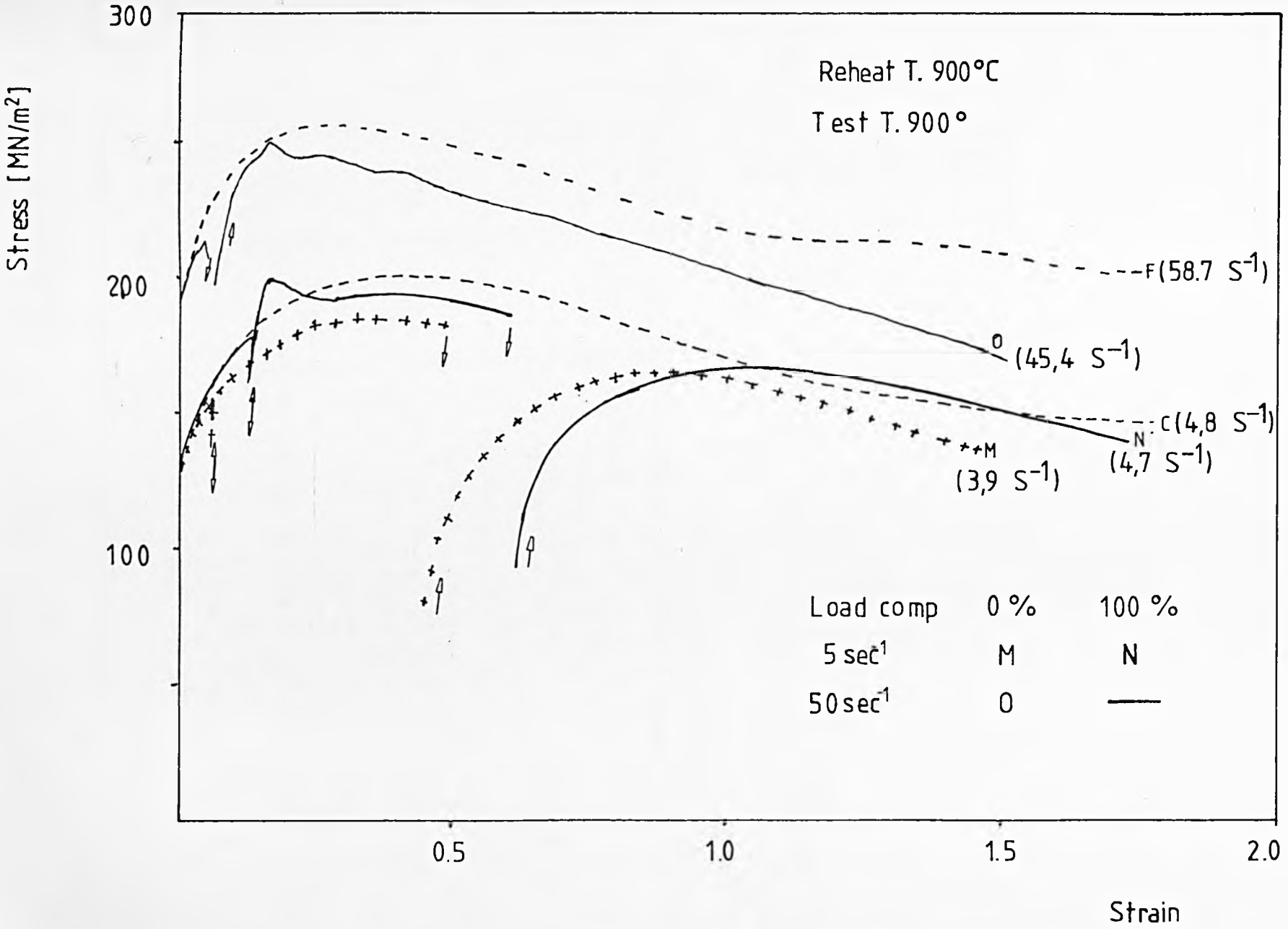
300
200
100
Stress [MN/m²]
Reheat T. 900°C
Test T. 900°
F (58.7 S⁻¹)
O (45,4 S⁻¹)
C (4,8 S⁻¹)
N (4,7 S⁻¹)
M (3,9 S⁻¹)
Load comp 0 % 100 %
5 sec⁻¹ M N
50 sec⁻¹ O
0.5
1.0
1.5
2.0
Strain

FIGURE 74: Double deformation tests on Al-1%Mg-1%Mn alloy carried out under different conditions of load cell compensation. Reheating temperature: 400°C; test temperature: 400°C; mean strain rate: 10 s^{-1}; V2 = 1.1 V1; loop gain: 10.7; time interval between deformations: 10 sec.

(a) 0% compensation (L.C.C. : 0.0)

(b) 100% compensation (L.C.C. : 5.60)

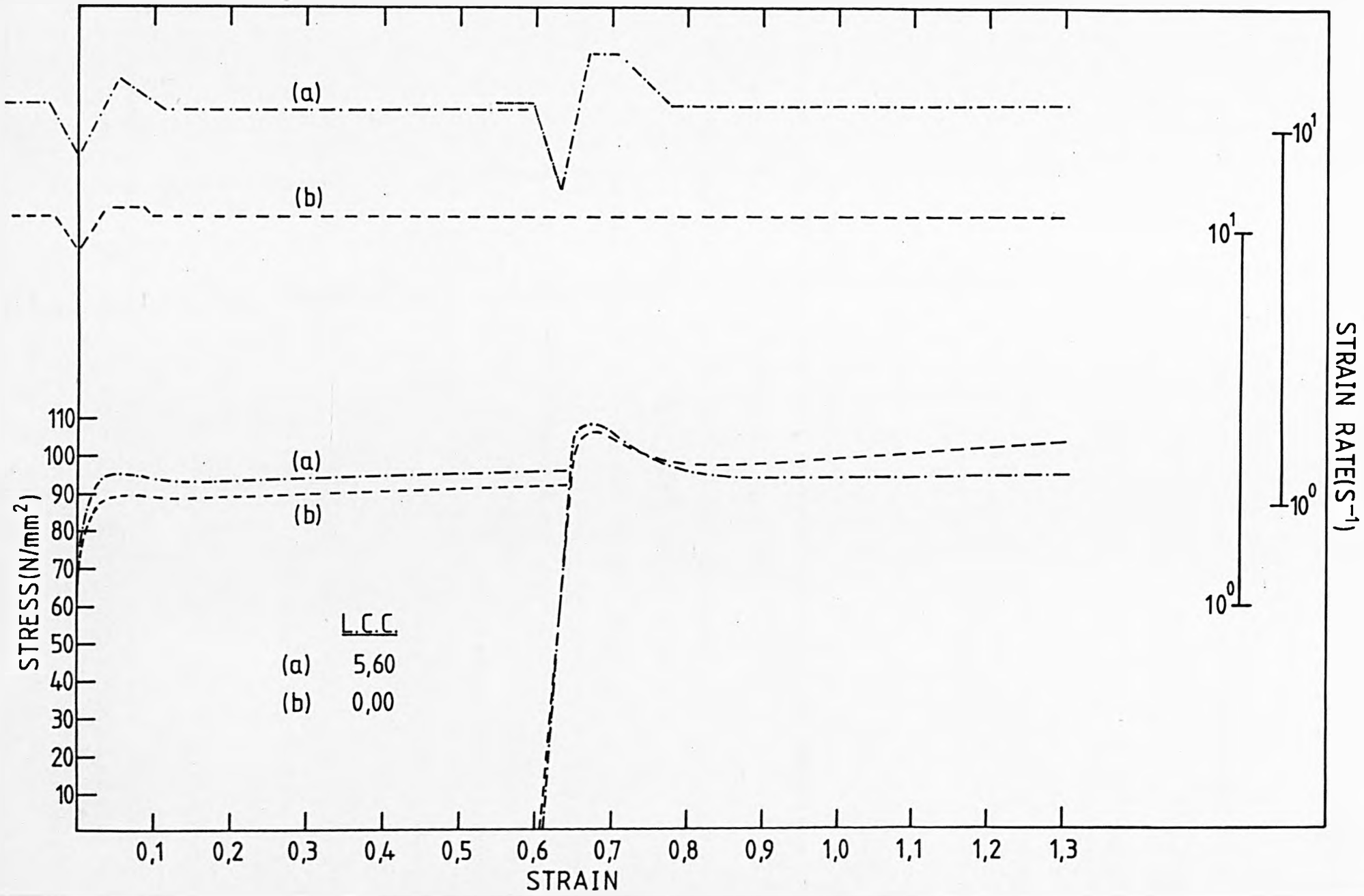
(a)
(b)
(a)
(b)
L.C.C.
(a) 5,60
(b) 0,00
STRESS(N/mm²)
110
100
90
80
70
60
50
40
30
20
10
0,1
0,2
0,3
0,4
0,5
0,6
0,7
0,8
0,9
1,0
1,1
1,2
1,3
STRAIN
10¹
10¹
10⁰
10⁰
STRAIN RATE(S⁻¹)

FIGURE 75: Double deformation tests on Al-1%Mg-1%Mn alloy carried out under different conditions of load cell compensation. Reheating temperature: 460°C; test temperature: 460°C; mean strain rate: 10 s^{-1}; V2 = 1.1 V1; loop gain: 10.7; time interval between deformations: 10 sec.

(a) 0% compensation (L.C.C. : 0.0)

(b) 100% compensation (L.C.C. : 5.60)

(c) 125% compensation (L.C.C. : 7.0)

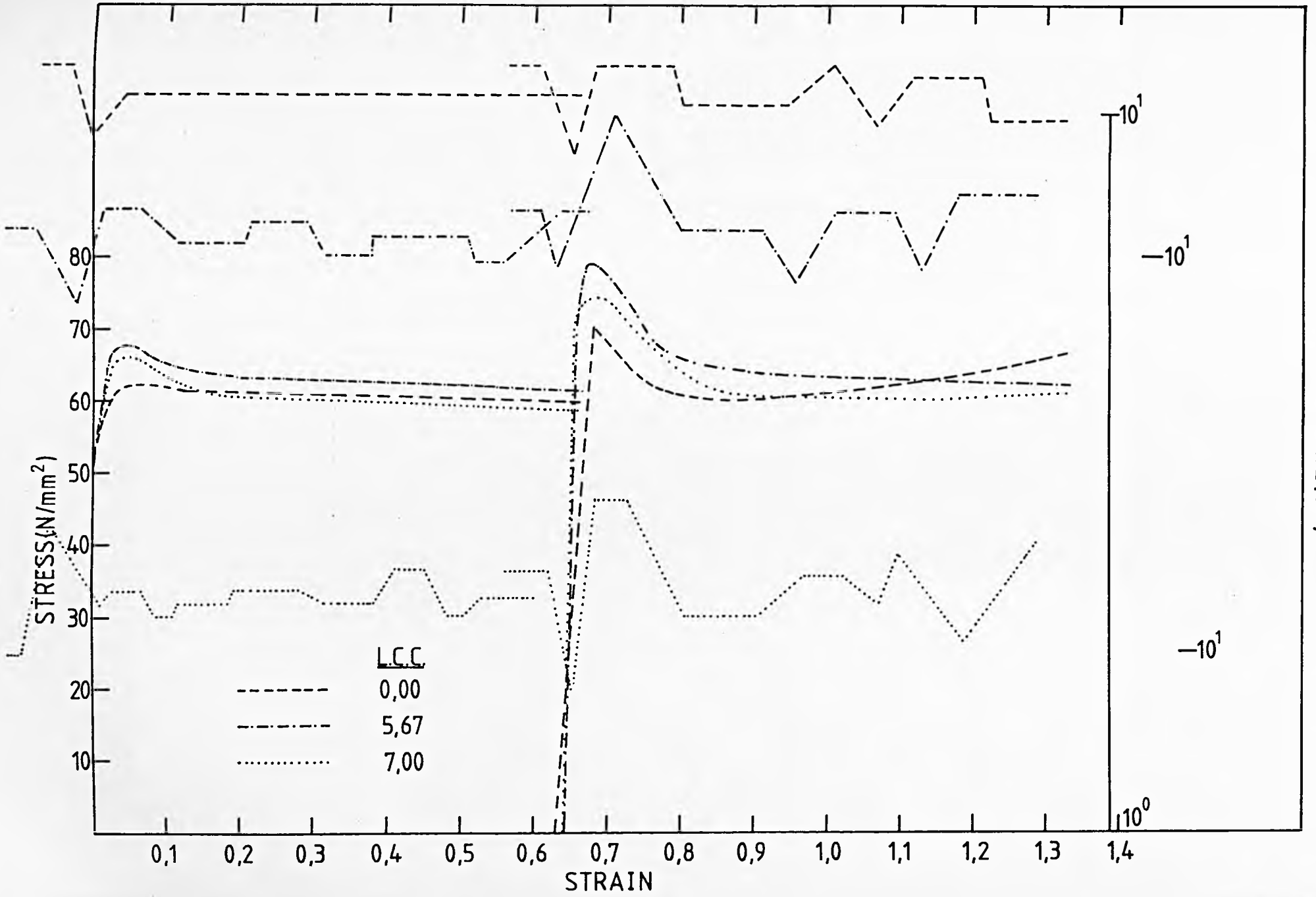
STRESS(N/mm²)
STRAIN
STRAIN RATE(S⁻¹)
L.C.C.
0,00
5,67
7,00
10
20
30
40
50
60
70
80
0,1
0,2
0,3
0,4
0,5
0,6
0,7
0,8
0,9
1,0
1,1
1,2
1,3
1,4
10¹
10¹
10¹
10⁰

FIGURE 76: Effect of tools temperature on the hardening phenomenon observed in Al-1%Mg-1%Mn alloy. Reheating temperature: 460°C; test temperature: 460°C; mean strain rate: 10 s^{-1}; V2 = 1.1 V1; loop gain: 10.7; time interval between deformations: 10 sec; load cell compensation: 5.60 (100% compensation).

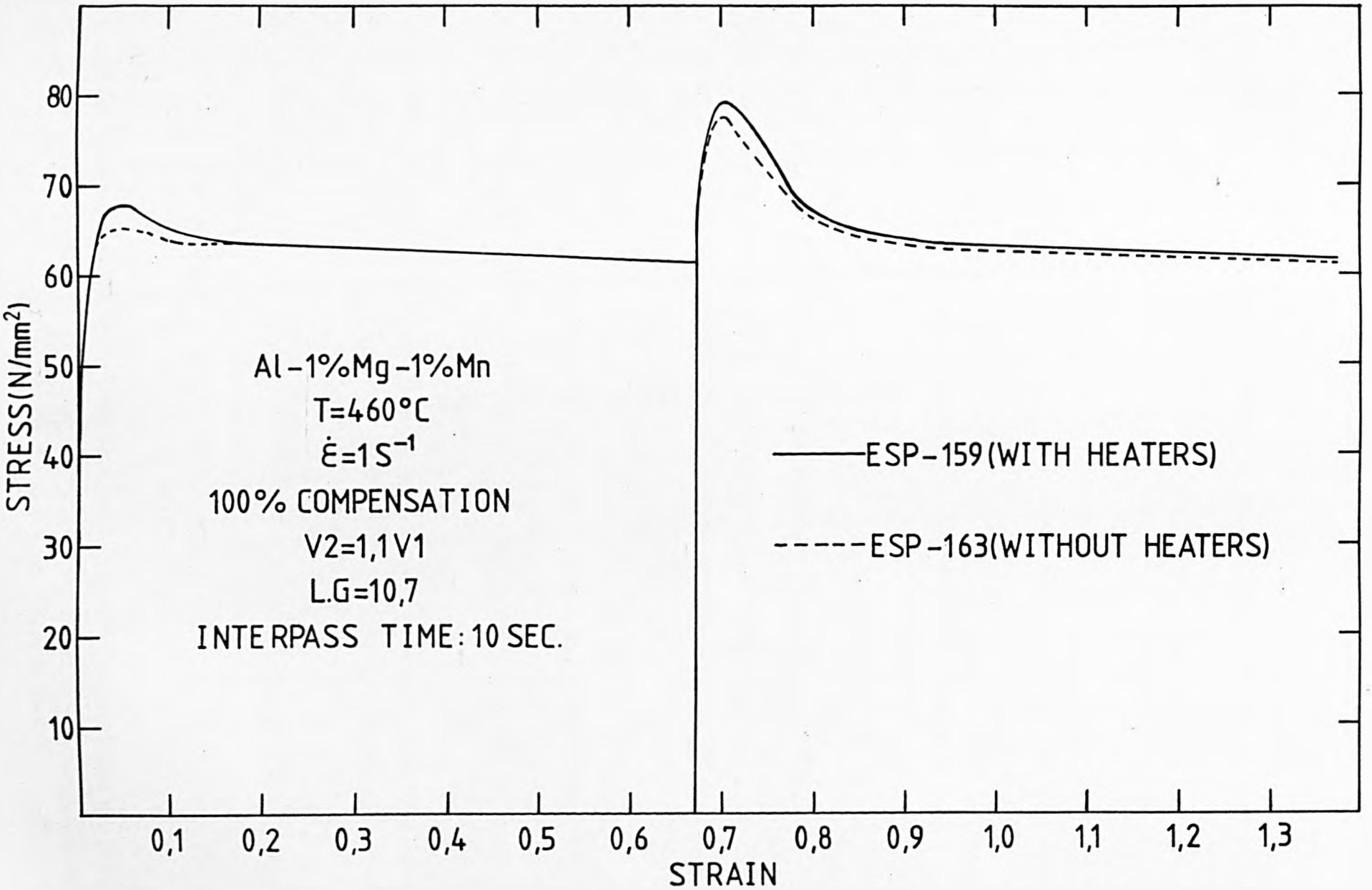
STRESS(N/mm²)
80
70
60
50
40
30
20
10
0,1
0,2
0,3
0,4
0,5
0,6
0,7
0,8
0,9
1,0
1,1
1,2
1,3
STRAIN
Al-1%Mg-1%Mn
T=460°C
Ė=1S⁻¹
100% COMPENSATION
V2=1,1V1
L.G=10,7
INTERPASS TIME: 10 SEC.
ESP-159(WITH HEATERS)
ESP-163(WITHOUT HEATERS)

FIGURE 77: Multiple deformation test on commercial-purity aluminium. Reheating temperature: 400°C; test temperature: 400°C; tools temperature: 400°C; mean strain rate: 10 s^{-1}; time intervals between deformations: 1 sec.

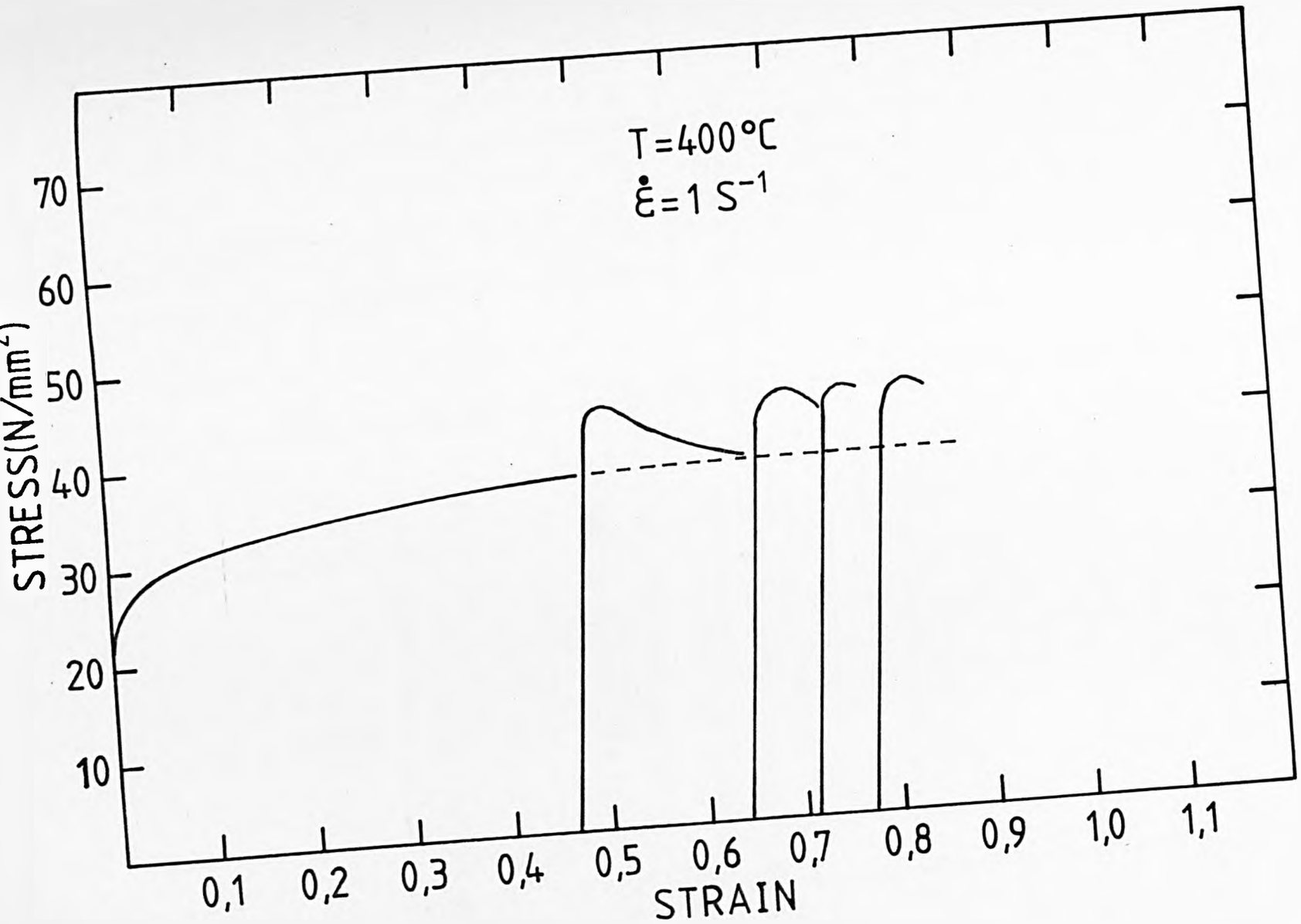
T=400°C
$\dot{\varepsilon}$=1 S^{-1}
STRESS(N/mm^2)
70
60
50
40
30
20
10
0,1
0,2
0,3
0,4
0,5
0,6
0,7
0,8
0,9
1,0
1,1
STRAIN

FIGURE 78: Multiple deformation test on commercial-purity aluminium. Reheating temperature: 400°C; test temperature: 400°C; tools temperature: 400°C; mean strain rate: 10 s^{-1}; time intervals between deformations: 1 sec.

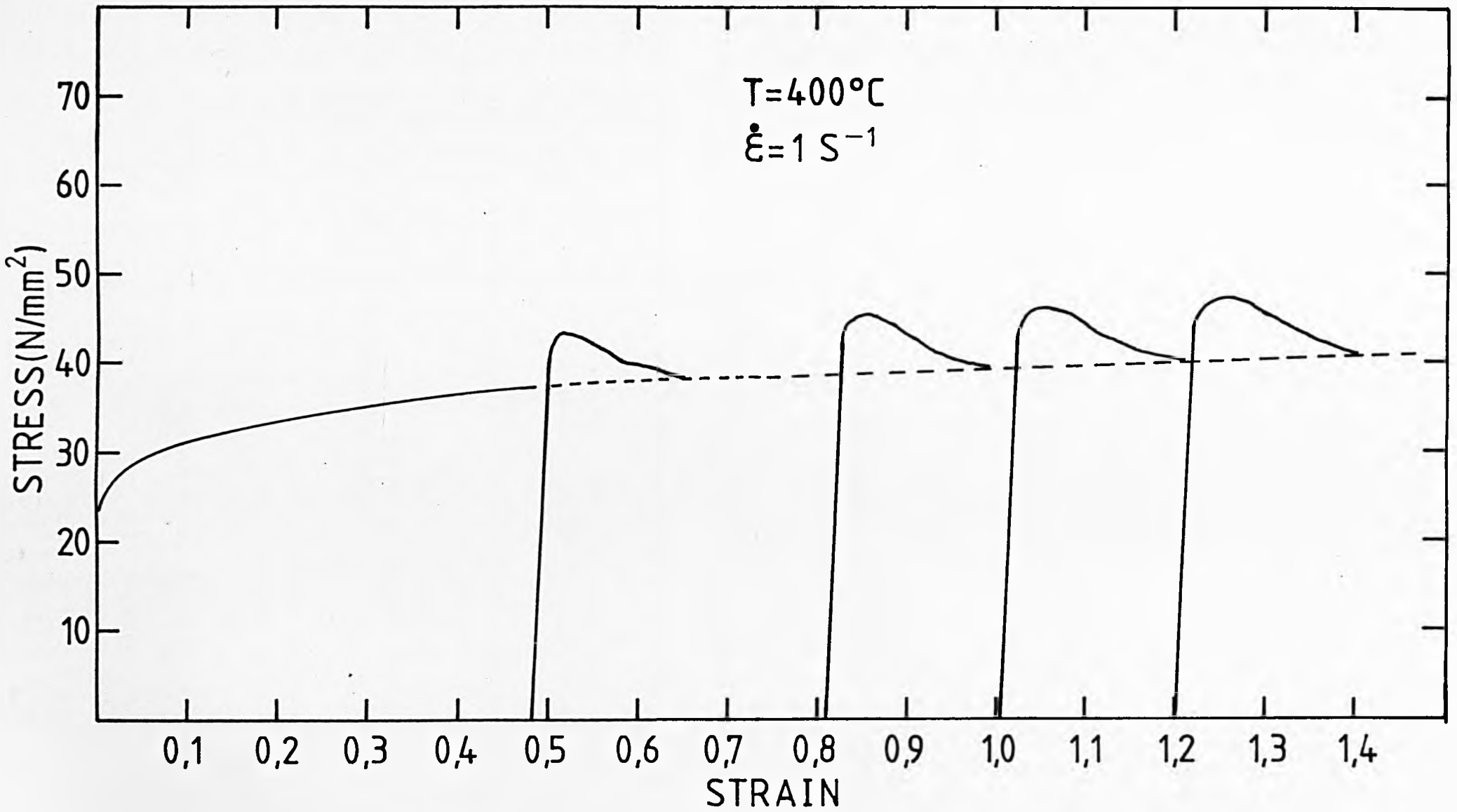
T=400°C
$\dot{\varepsilon}$=1 S^{-1}
STRESS(N/mm^2)
70
60
50
40
30
20
10
0,1
0,2
0,3
0,4
0,5
0,6
0,7
0,8
0,9
1,0
1,1
1,2
1,3
1,4
STRAIN

FIGURE 79: Multiple deformation test on Al-1%Mg-1%Mn alloy. Reheating temperature: 400°C; test temperature: 400°C; tools temperature: 400°C; mean strain rate: 10 s^{-1}; time intervals between deformations: 1 sec.

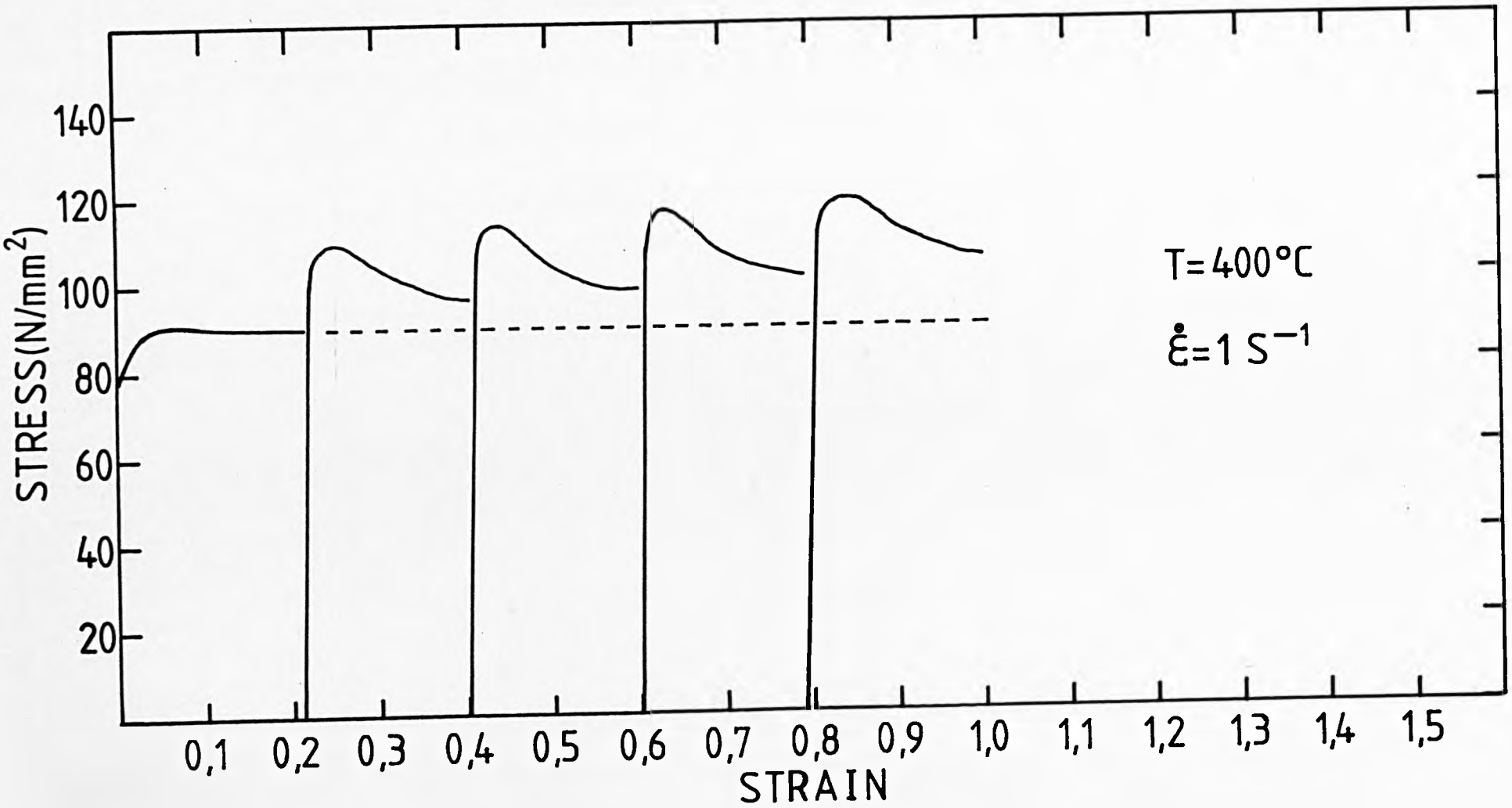
STRESS(N/mm²)
140
120
100
80
60
40
20
0,1
0,2
0,3
0,4
0,5
0,6
0,7
0,8
0,9
1,0
1,1
1,2
1,3
1,4
1,5
STRAIN
T=400°C
$\dot{\varepsilon}=1\ S^{-1}$

FIGURE 80: Mean stress-strain curve obtained for the first deformation of double deformation tests on Al-1%Mg alloy at 400°C and 1 s^{-1}. Initial grain size 90 μm.

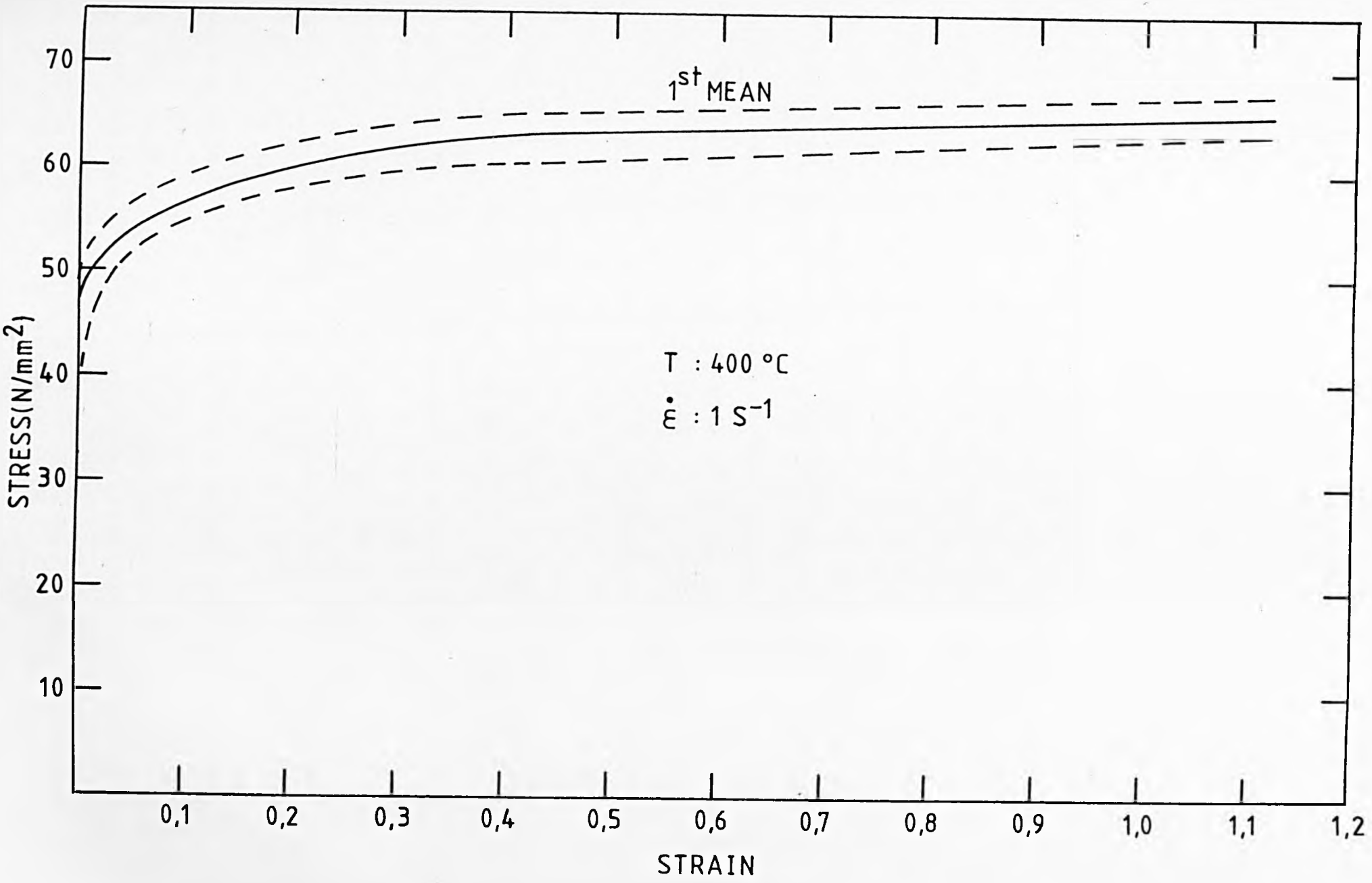
70
60
50
40
30
20
10
STRESS(N/mm2)
1st MEAN
T : 400 °C
ε̇ : 1 S-1
0,1
0,2
0,3
0,4
0,5
0,6
0,7
0,8
0,9
1,0
1,1
1,2
STRAIN

FIGURE 81: Double deformation tests on Al-1%Mg alloy with different time intervals between deformations. Test temperature: 400°C; mean strain rate: 1 s^{-1}. Initial strain applied: 0.15.

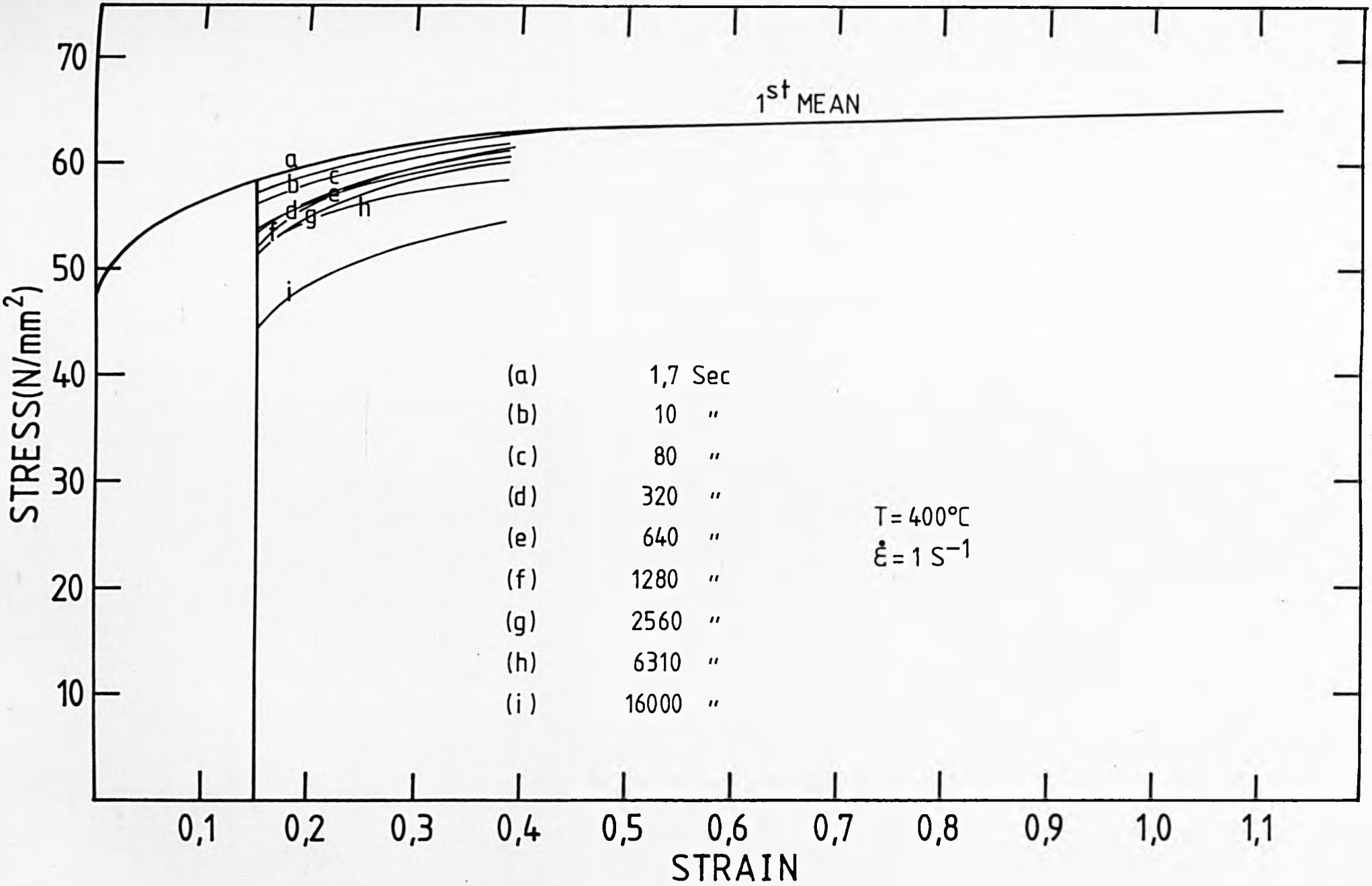
70
60
50
40
30
20
10
STRESS(N/mm²)
1st MEAN
a
b
c
d
e
f
g
h
i
(a) 1,7 Sec
(b) 10 "
(c) 80 "
(d) 320 "
(e) 640 "
(f) 1280 "
(g) 2560 "
(h) 6310 "
(i) 16000 "
T = 400°C
ε̇ = 1 S⁻¹
0,1
0,2
0,3
0,4
0,5
0,6
0,7
0,8
0,9
1,0
1,1
STRAIN

FIGURE 82: Double deformation tests on Al-1%Mg alloy with different time intervals between deformations. Test temperature: 400°C; mean strain rate: 1 s^{-1}. Initial strain applied: 0.33.

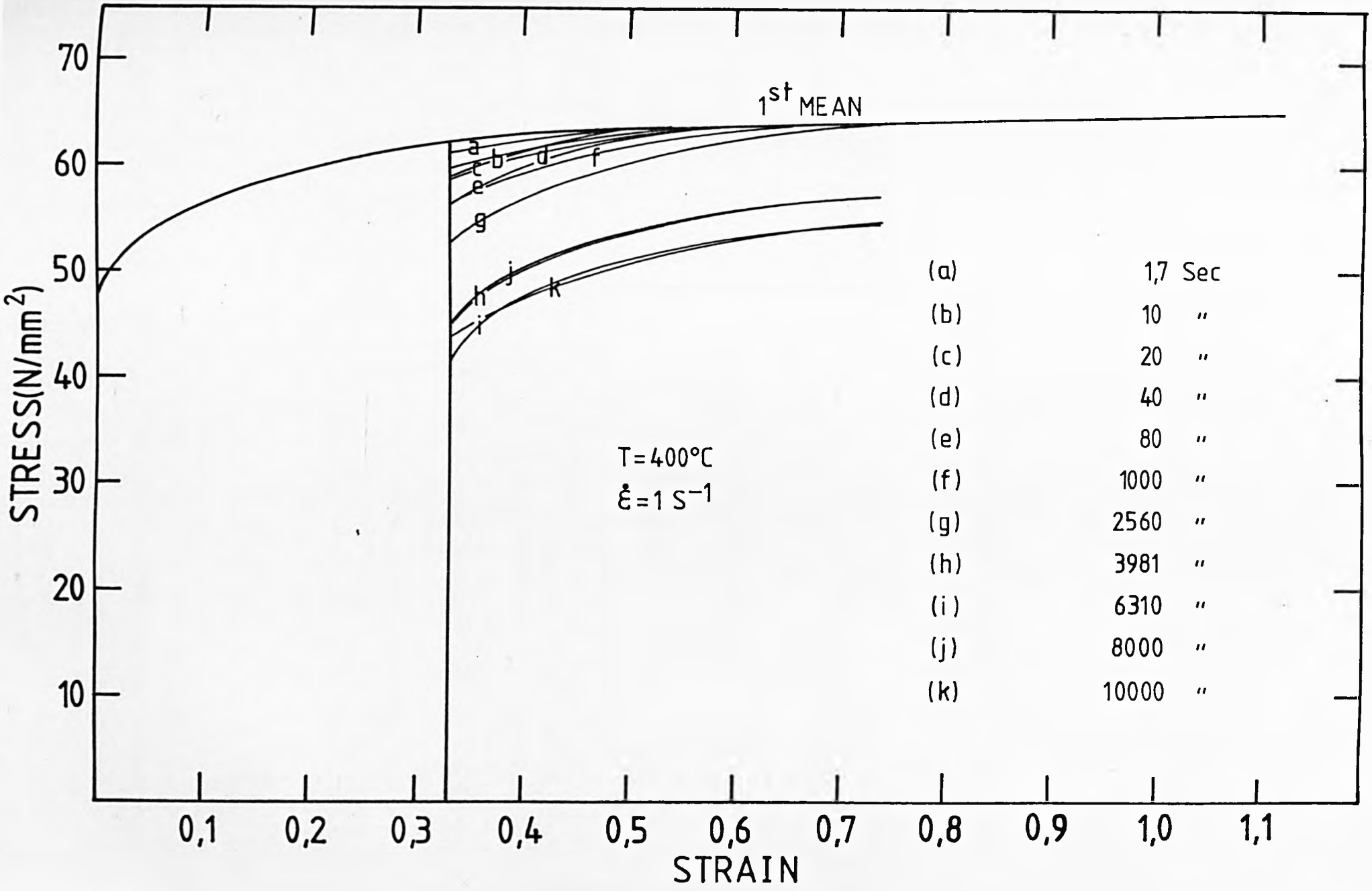
STRESS(N/mm²)
70
60
50
40
30
20
10
0,1
0,2
0,3
0,4
0,5
0,6
0,7
0,8
0,9
1,0
1,1
STRAIN
1st MEAN
a
b
c
d
e
f
g
h
i
j
k
T=400°C
ε̇=1 S⁻¹
(a) 1,7 Sec
(b) 10 "
(c) 20 "
(d) 40 "
(e) 80 "
(f) 1000 "
(g) 2560 "
(h) 3981 "
(i) 6310 "
(j) 8000 "
(k) 10000 "

FIGURE 83: Double deformation tests on Al-1%Mg alloy with different time intervals between deformations. Test temperature: 400°C; mean strain rate: 1 s^{-1}. Initial strain applied: 0.67.

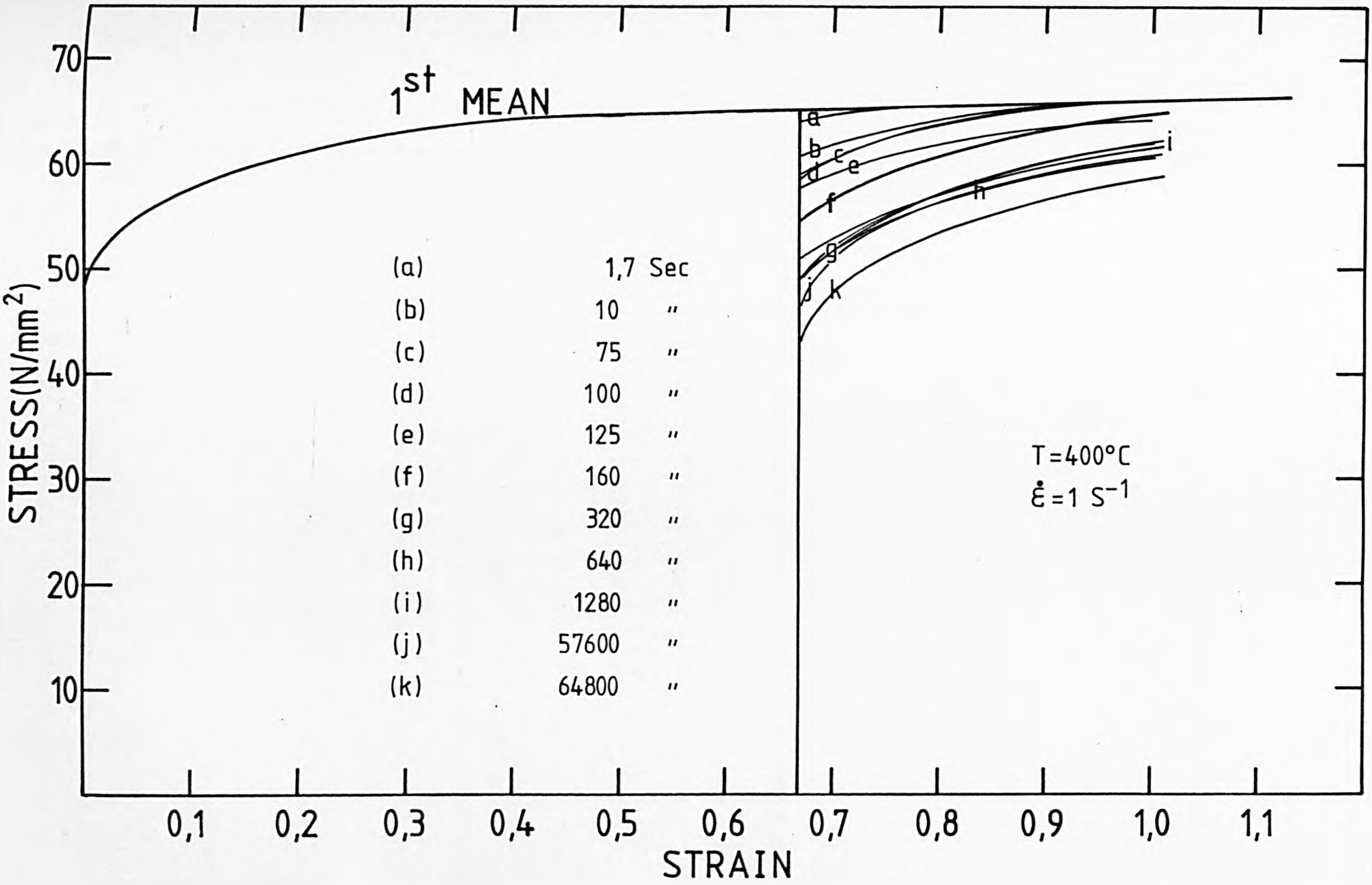
1st MEAN
STRESS(N/mm²)
STRAIN
70
60
50
40
30
20
10
0,1
0,2
0,3
0,4
0,5
0,6
0,7
0,8
0,9
1,0
1,1
(a) 1,7 Sec
(b) 10 "
(c) 75 "
(d) 100 "
(e) 125 "
(f) 160 "
(g) 320 "
(h) 640 "
(i) 1280 "
(j) 57600 "
(k) 64800 "
T=400°C
$\dot{\varepsilon}$=1 S^{-1}

FIGURE 84: Double deformation tests on Al-1%Mg alloy with different time intervals between deformations. Test temperature: 400°C; mean strain rate: 1 s^{-1}. Initial strain applied: 1.00.

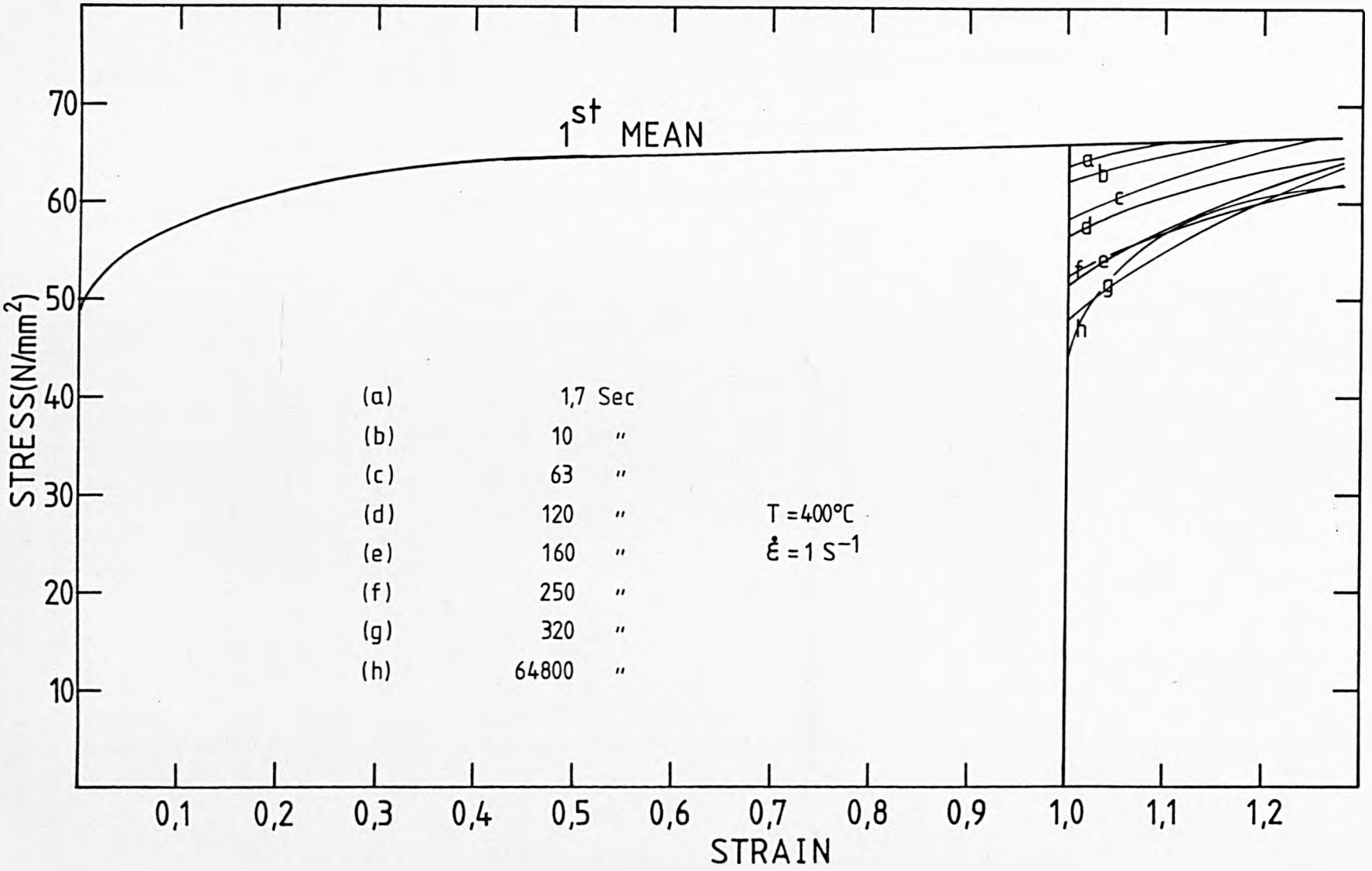
1st MEAN
STRESS(N/mm²)
STRAIN
70
60
50
40
30
20
10
0,1
0,2
0,3
0,4
0,5
0,6
0,7
0,8
0,9
1,0
1,1
1,2
a
b
c
d
e
f
g
h
(a) 1,7 Sec
(b) 10 "
(c) 63 "
(d) 120 "
(e) 160 "
(f) 250 "
(g) 320 "
(h) 64800 "
T = 400°C
$\dot{\varepsilon} = 1\ S^{-1}$

FIGURE 85: Description of the parameters involved in the definition of the restoration index R_1 (double deformation tests).

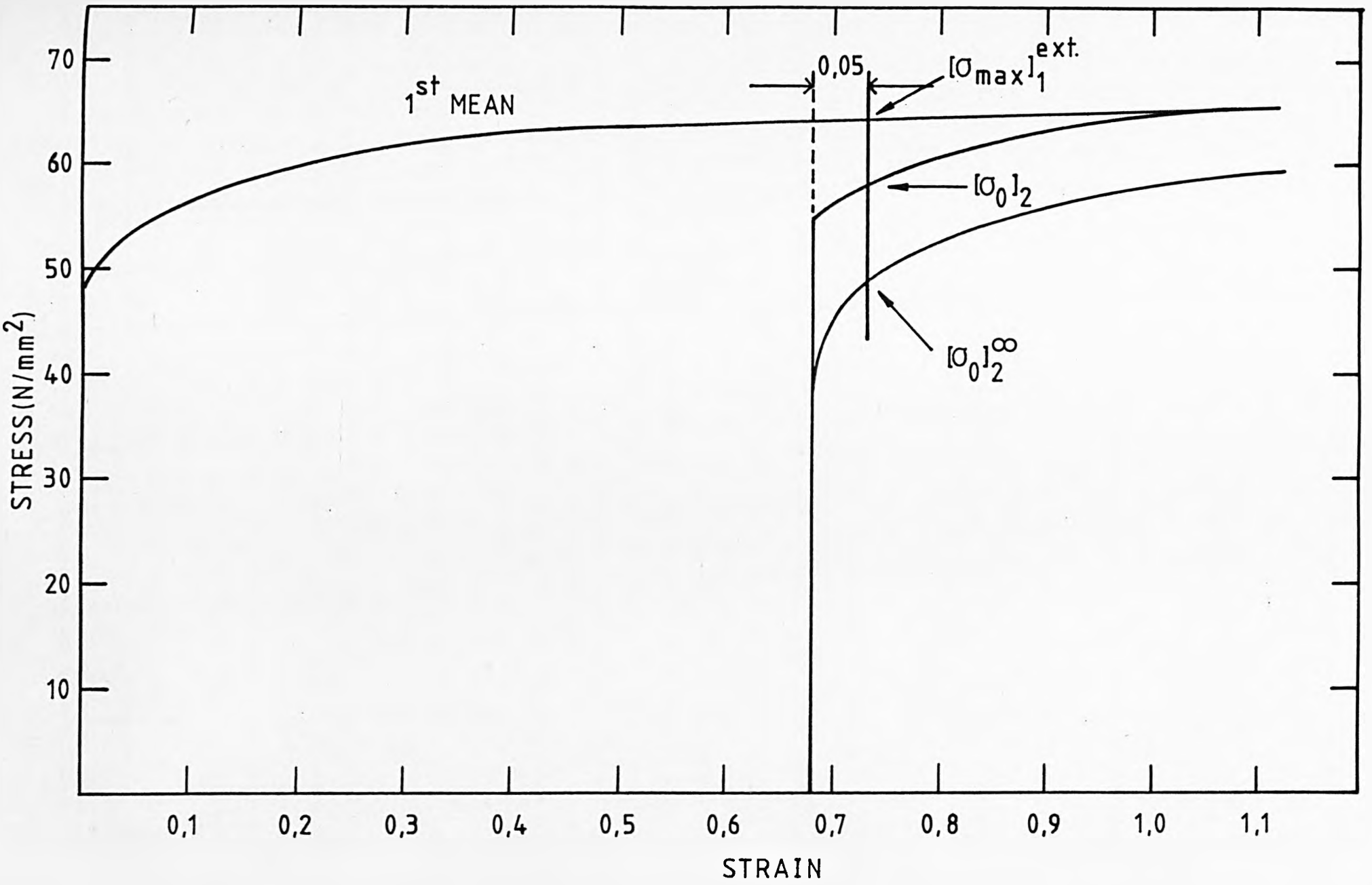
70
60
50
40
30
20
10
STRESS(N/mm2)
1st MEAN
0,05
[σmax]1ext.
[σ0]2
[σ0]2∞
0,1
0,2
0,3
0,4
0,5
0,6
0,7
0,8
0,9
1,0
1,1
STRAIN

FIGURE 86: (a) Variation of the restoration index R_1 with log [time (sec)] for Al-1%Mg alloy after deformation by different initial strains.

(b) Variation of the restoration index R_1 corrected for recovery effects with log [time (sec)].

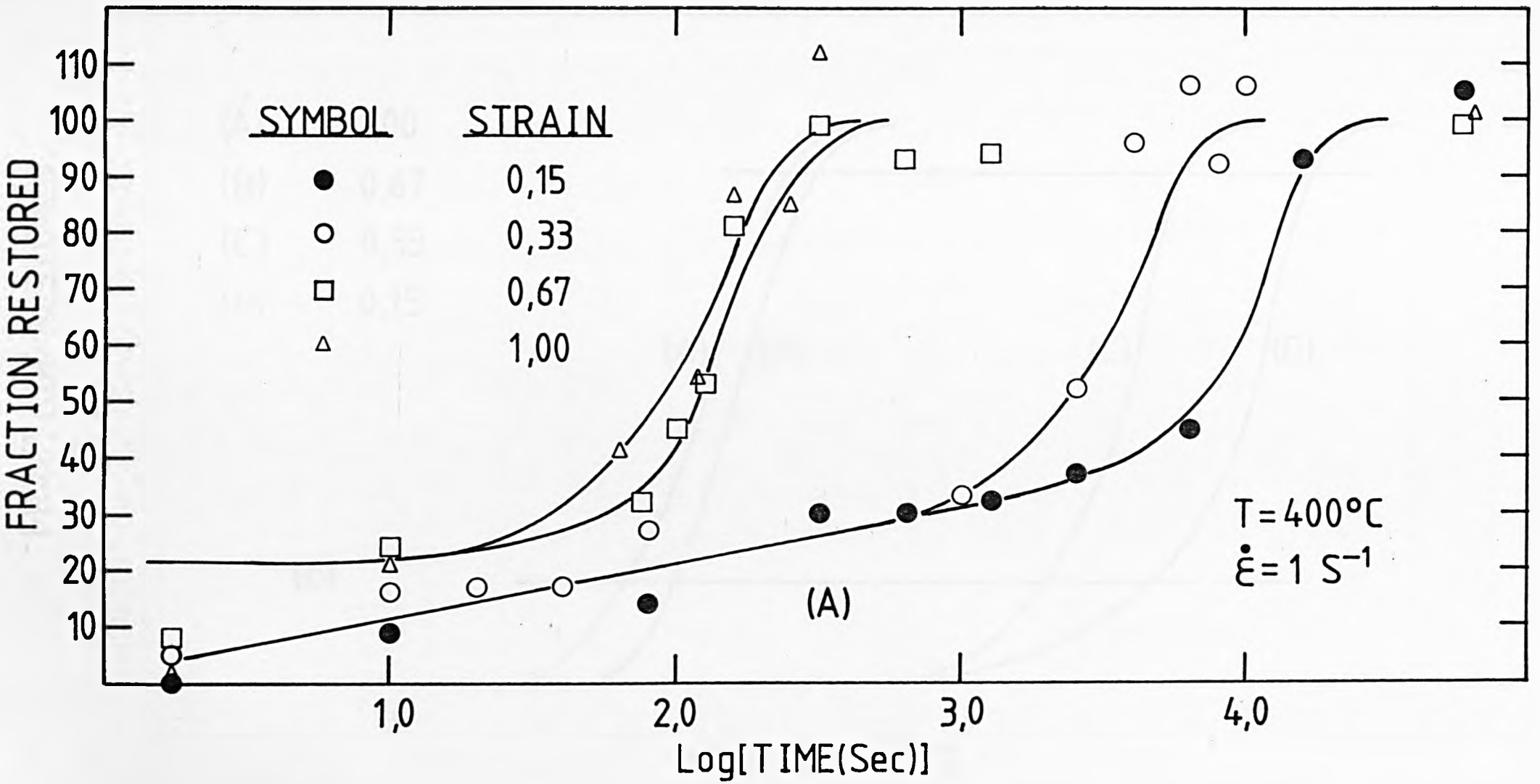
FRACTION RESTORED
110
100
90
80
70
60
50
40
30
20
10
SYMBOL
STRAIN
0,15
0,33
0,67
1,00
T = 400°C
$\dot{\varepsilon} = 1\ S^{-1}$
(A)
1,0
2,0
3,0
4,0
Log[TIME(Sec)]

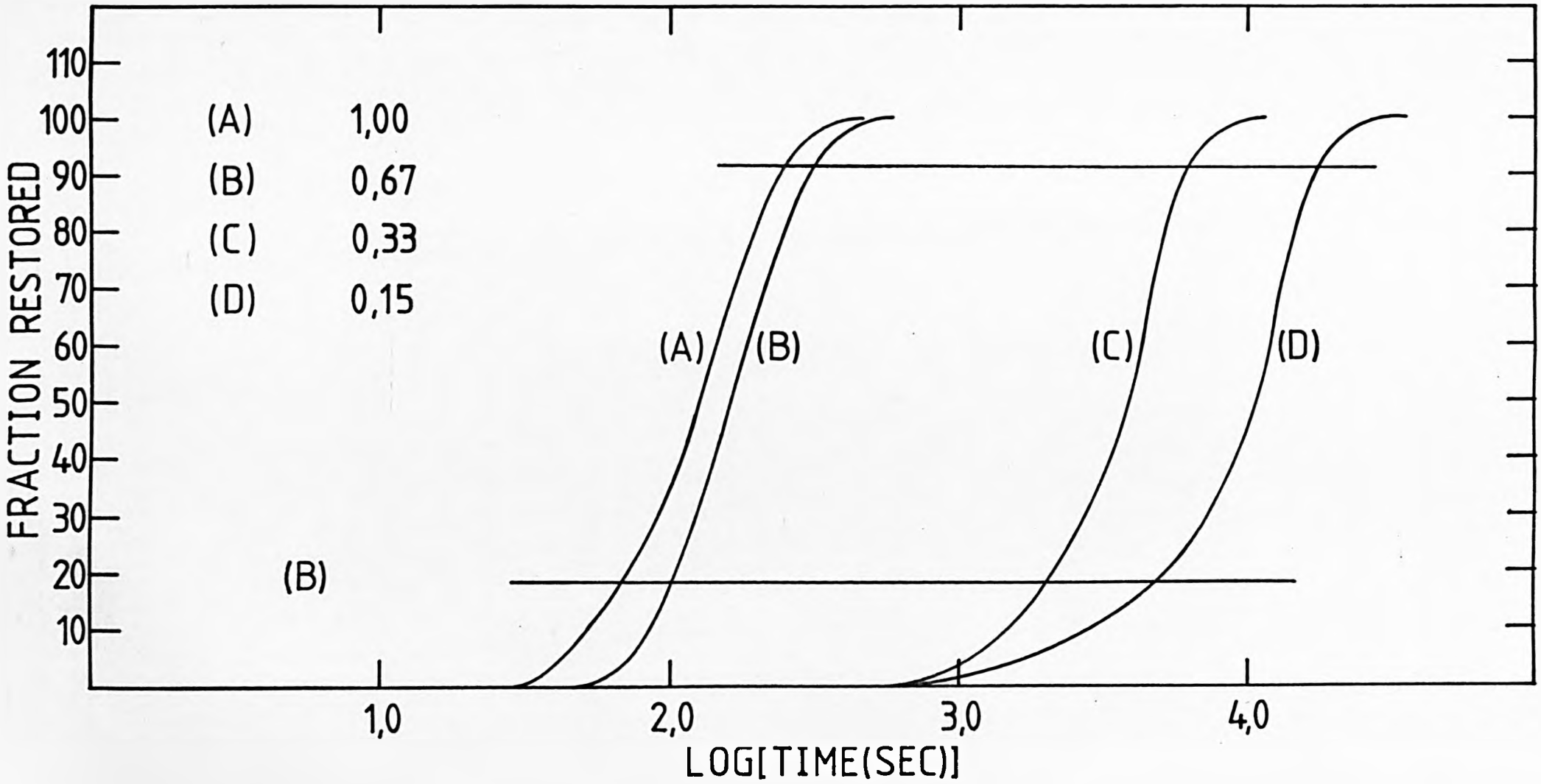
(A) 1,00
(B) 0,67
(C) 0,33
(D) 0,15
(A)
(B)
(C)
(D)
(B)
FRACTION RESTORED
110
100
90
80
70
60
50
40
30
20
10
1,0
2,0
3,0
4,0
LOG[TIME(SEC)]

FIGURE 87: Patterns of temperature distribution in the upper left quarter of the gauge section of a place strain compression specimen after deformation by different initial strains. Initial test temperature: $400^{o}C$.

(a) $\varepsilon = 0.15$, $\bar{T} = 389^{o}C$.

(b) $\varepsilon = 0.33$, $\bar{T} = 388^{o}C$.

(c) $\varepsilon = 0.67$, $\bar{T} = 384^{o}C$.

(d) $\varepsilon = 1.00$, $\bar{T} = 380^{o}C$.

(e) $\varepsilon = 1.5$, $\bar{T} = 378^{o}C$.

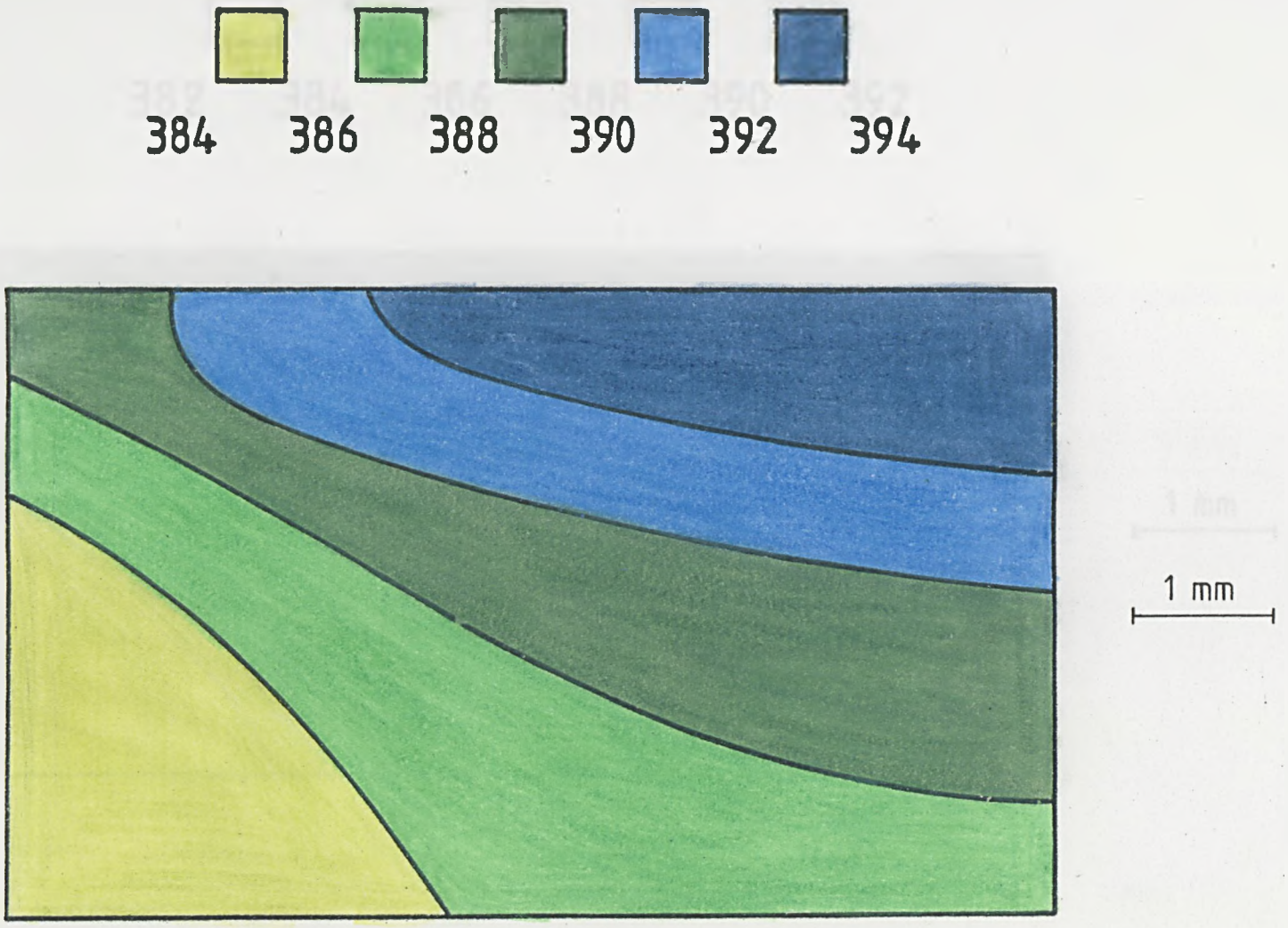

(a)

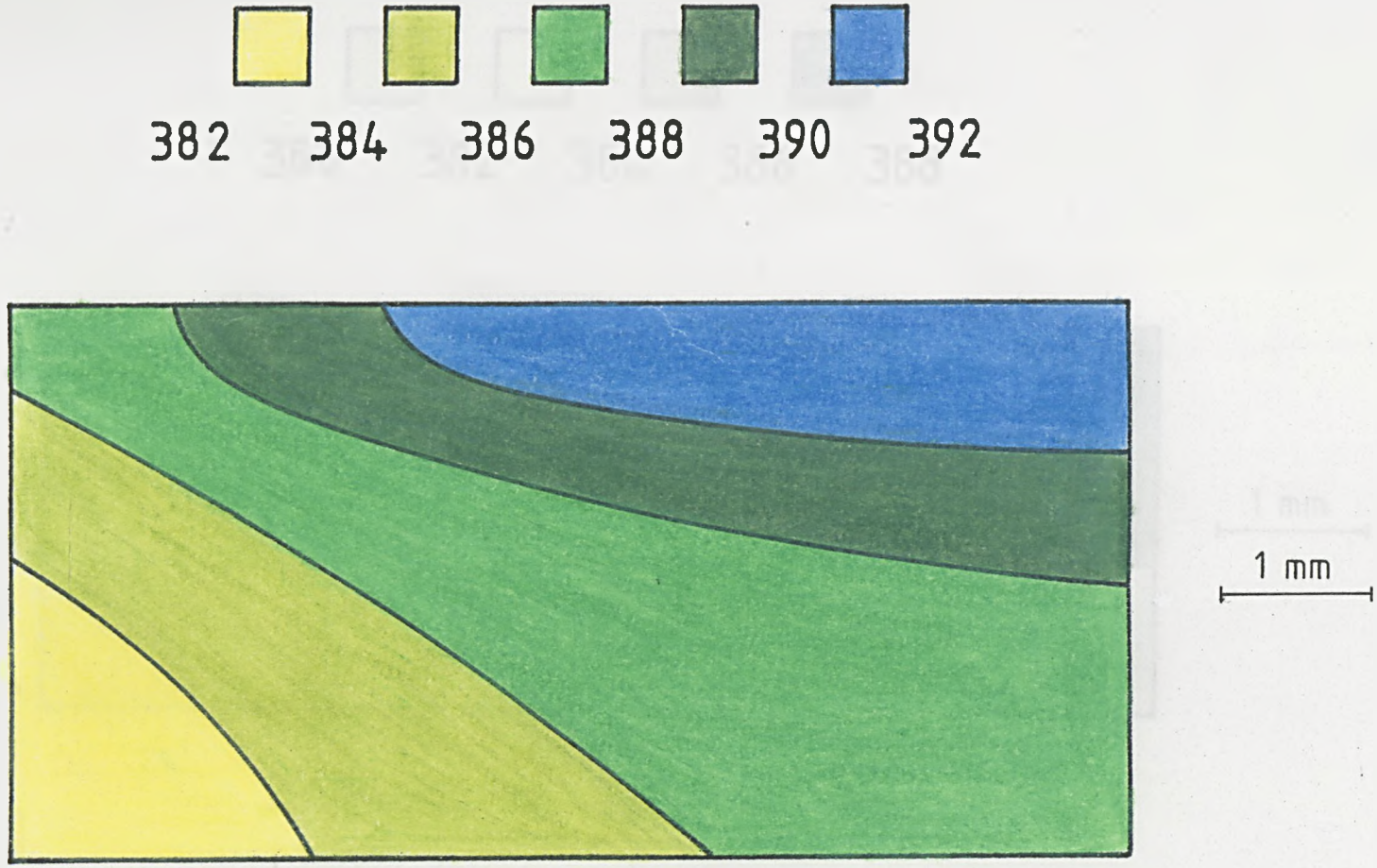

(b)

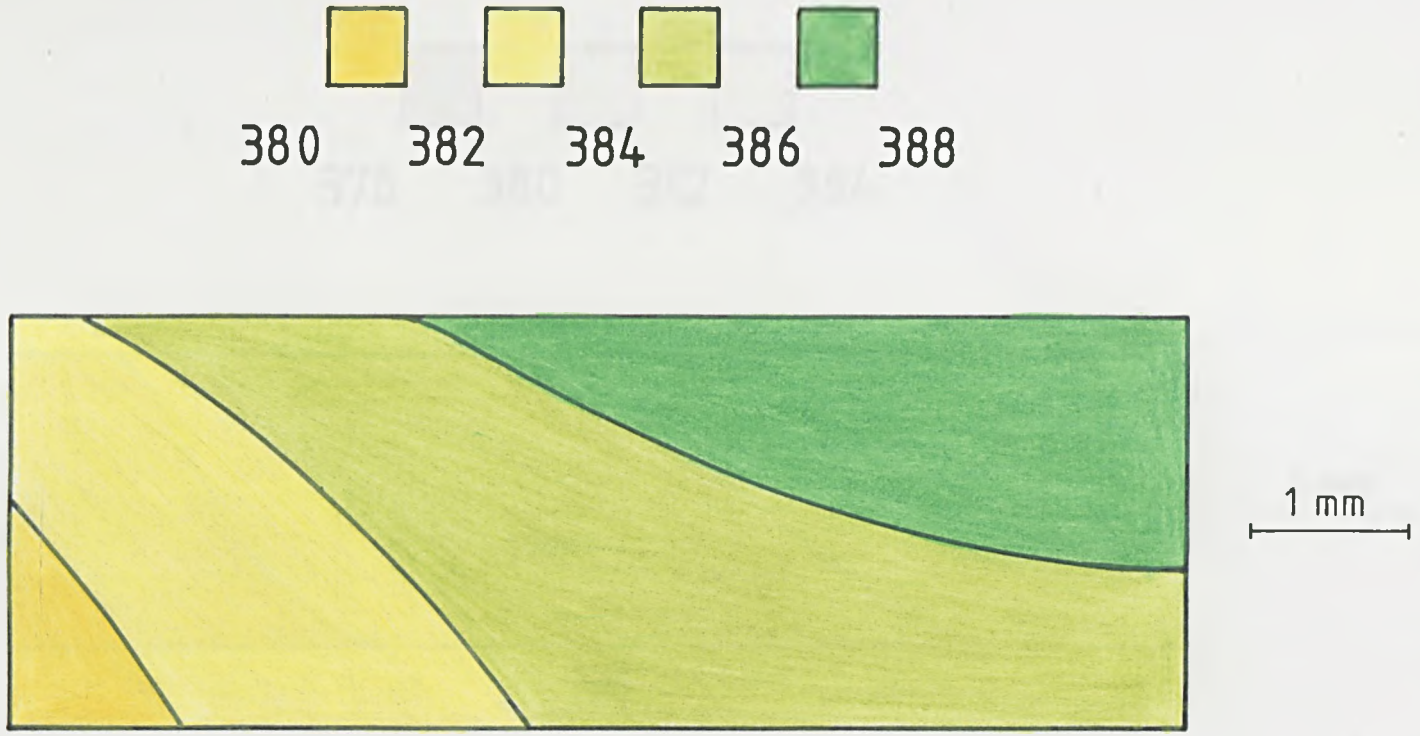

(c)

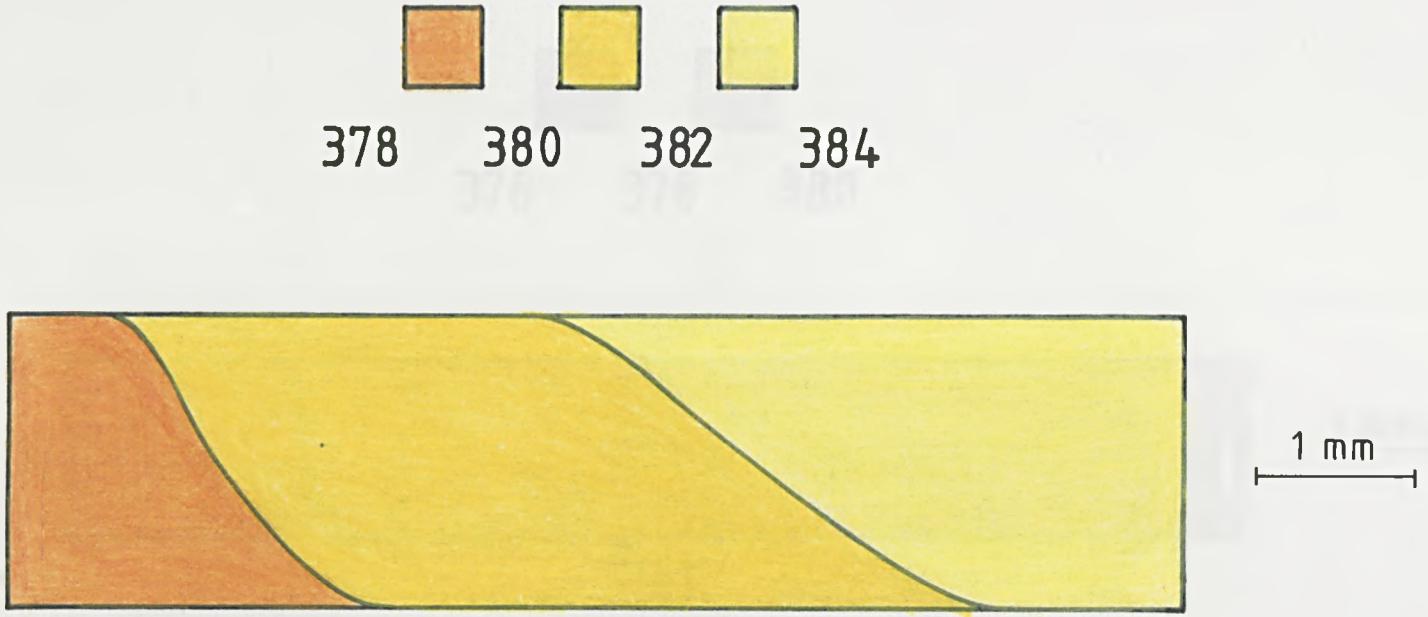

(d)

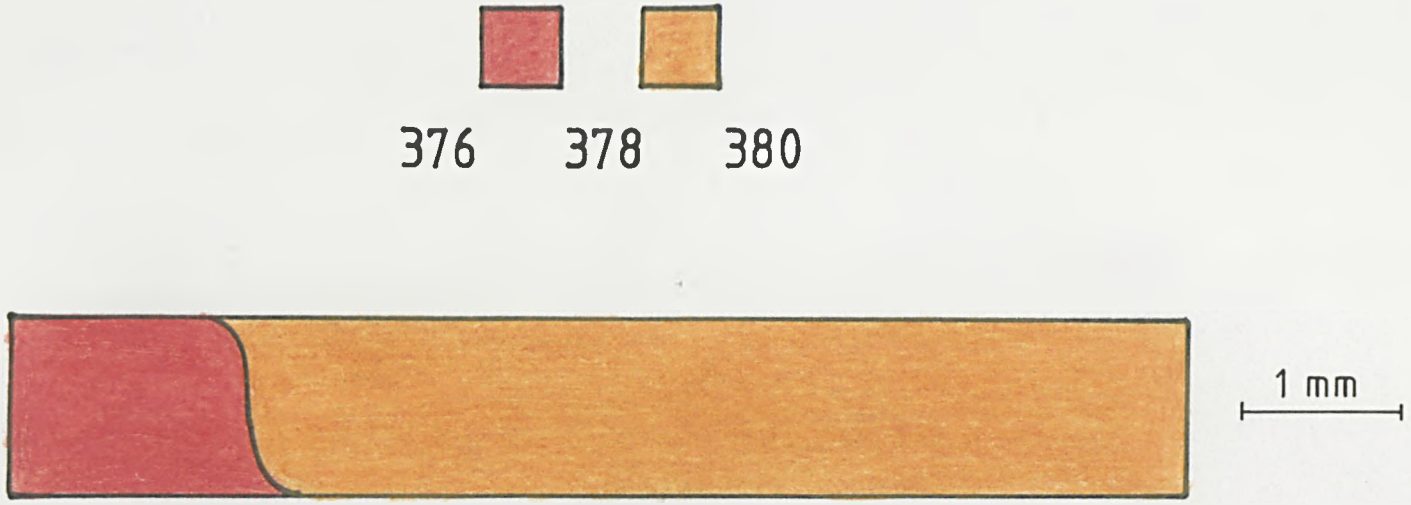

(e)

FIGURE 88: Effect of tools temperature on the restoration kinetics of Al-1%Mg alloy deformed by 0.67 strain at 400°C and 1 s^{-1}.

Initial grain size : 90 µm.

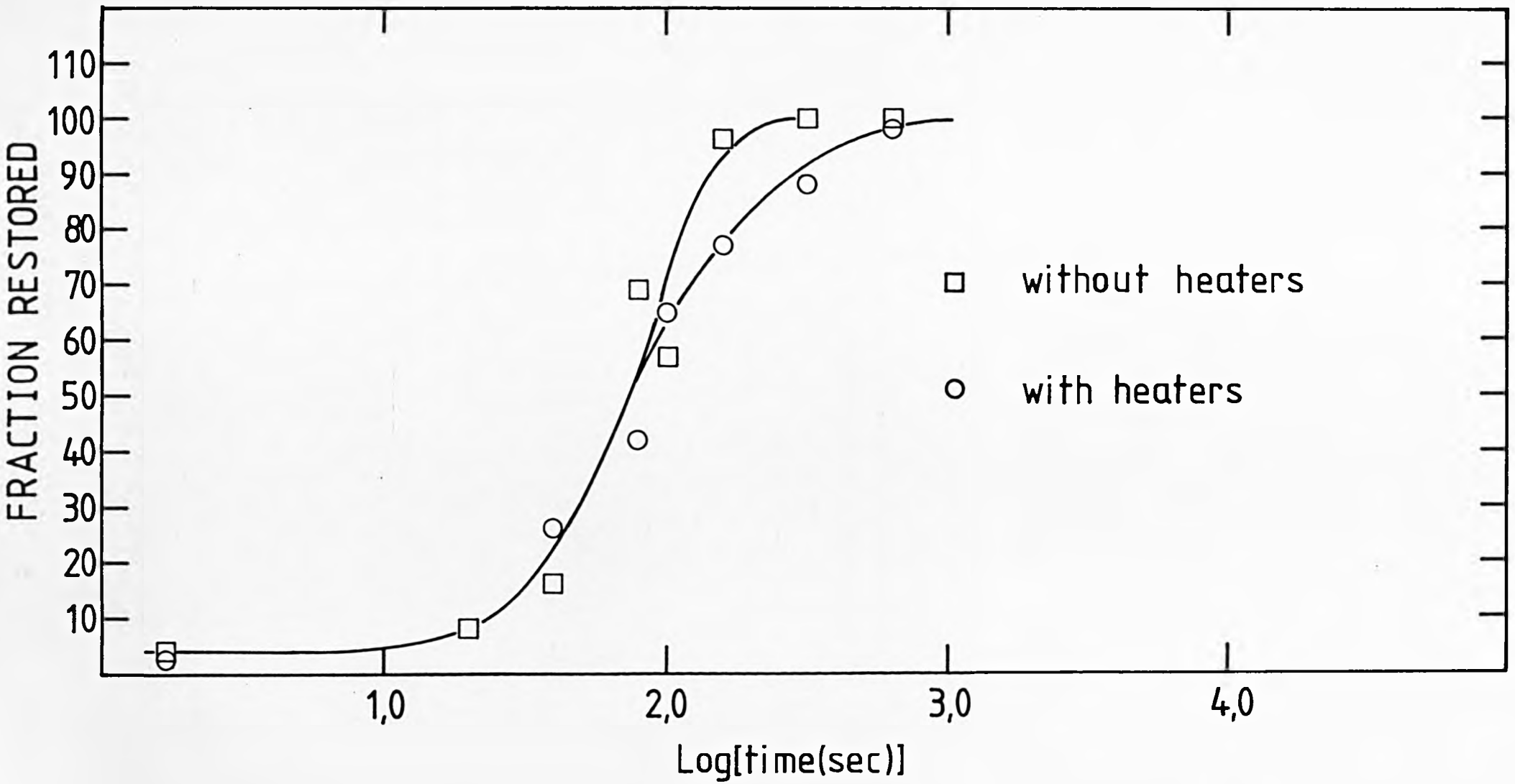
FRACTION RESTORED
110
100
90
80
70
60
50
40
30
20
10
1,0
2,0
3,0
4,0
Log[time(sec)]
without heaters
with heaters

FIGURE 89: Relation between log $t_{0.7}$ and log ε after correction for the cooling effect of the tools.

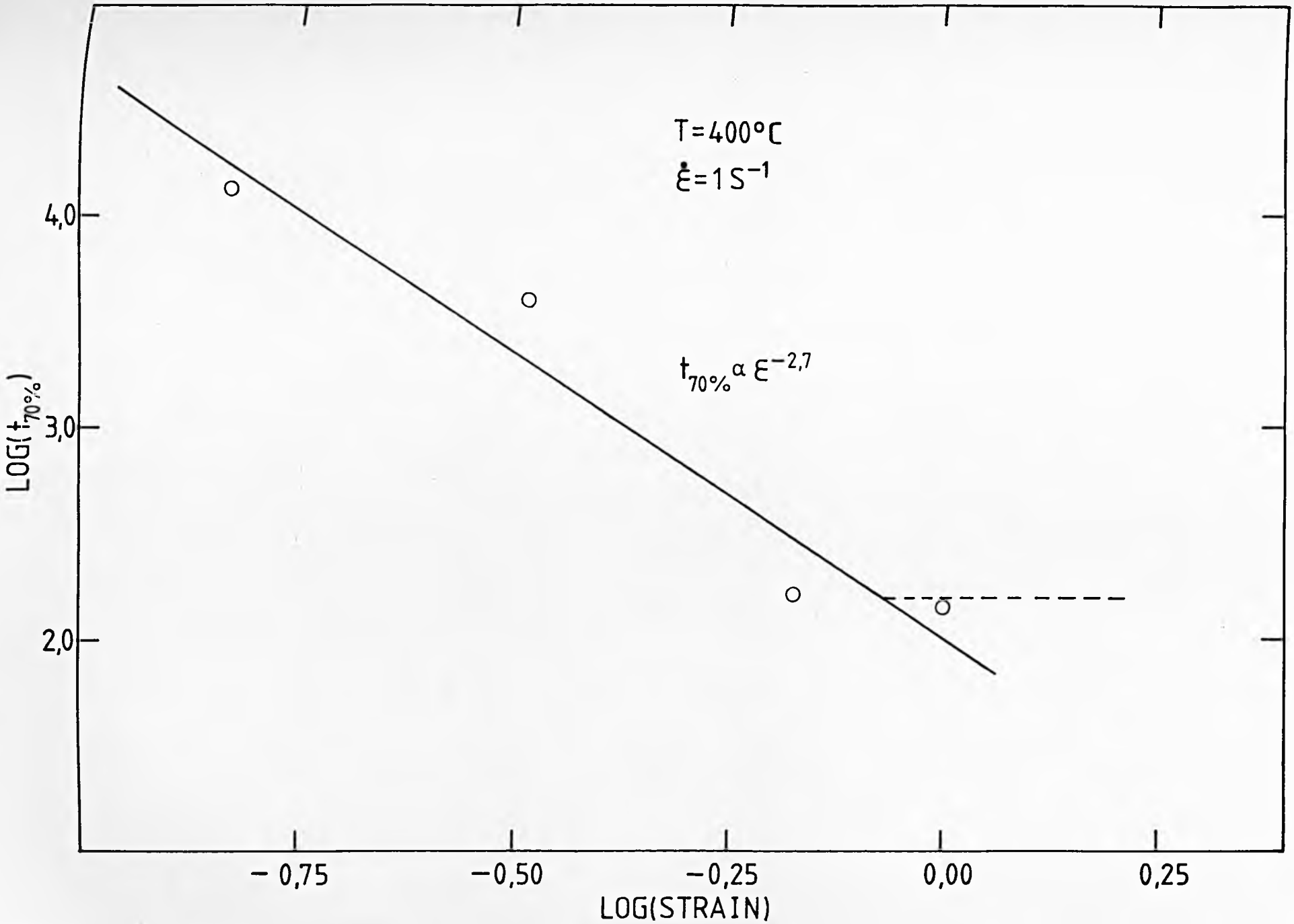
T=400°C
$\dot{\varepsilon}=1\,S^{-1}$
$t_{70\%} \alpha\, \varepsilon^{-2,7}$
LOG($t_{70\%}$)
4,0
3,0
2,0
− 0,75
−0,50
−0,25
0,00
0,25
LOG(STRAIN)

FIGURE 90: Variation of the volume fraction recrystallised with annealing time for Al-1%Mg alloy. Test temperature: 400°C Mean strain rate: 1 s^{-1}.

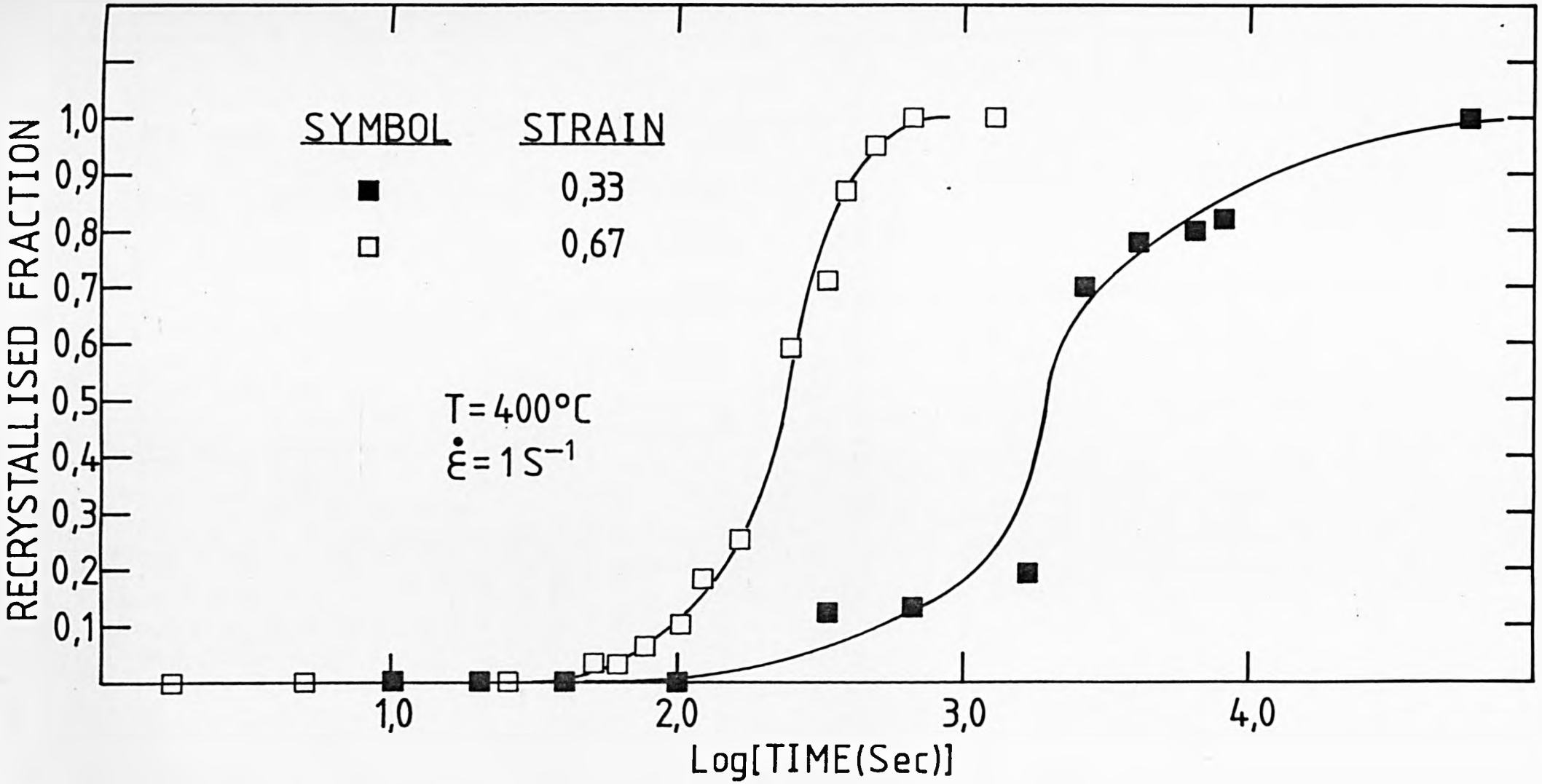
SYMBOL
STRAIN
0,33
0,67
T = 400°C
$\dot{\varepsilon} = 1\,S^{-1}$
RECRYSTALLISED FRACTION
1,0
0,9
0,8
0,7
0,6
0,5
0,4
0,3
0,2
0,1
1,0
2,0
3,0
4,0
Log[TIME(Sec)]

FIGURE 91: Avrami-type plot of the recrystallisation data of Al-1%Mg alloy.

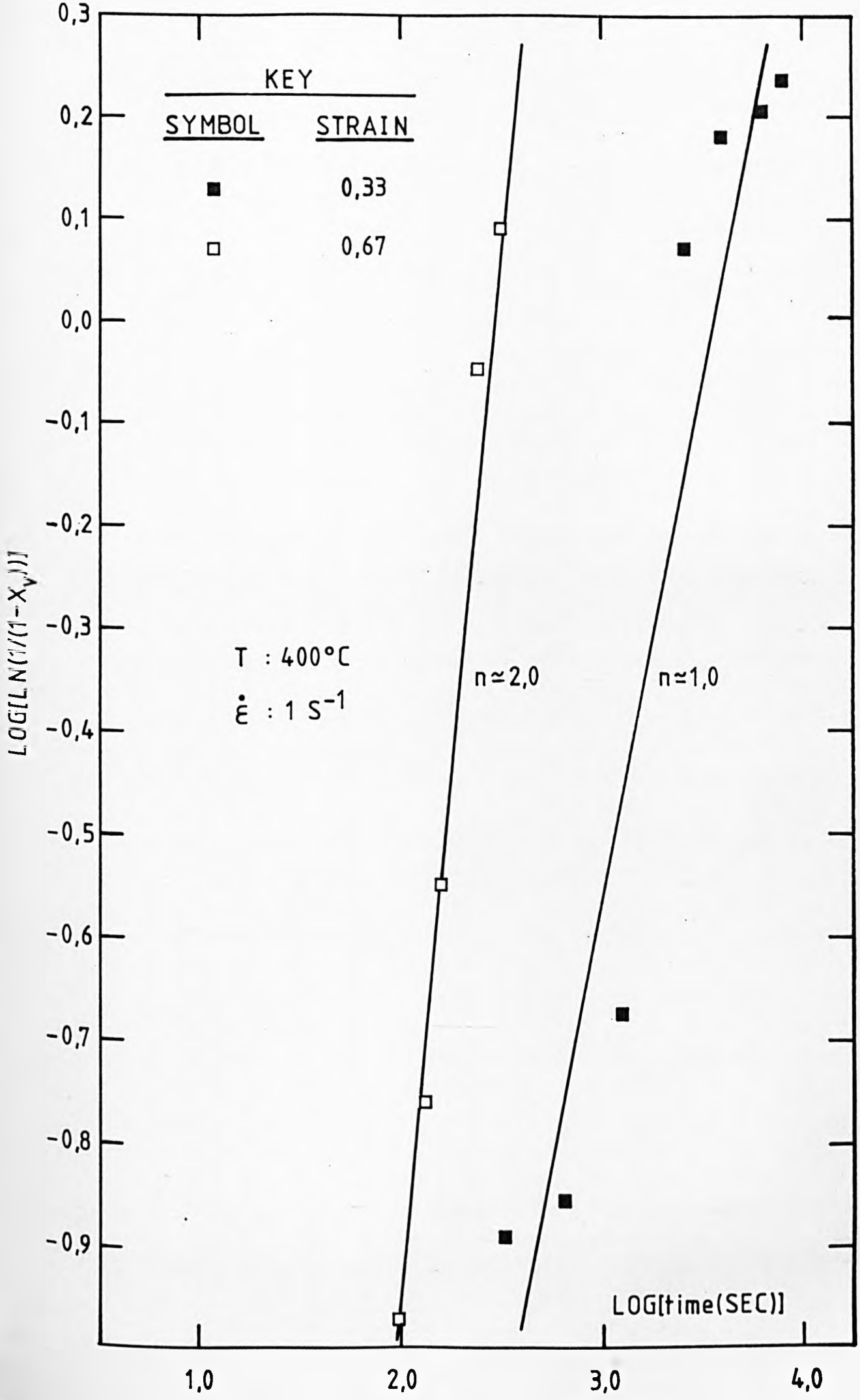
KEY
SYMBOL
STRAIN
0,33
0,67
T : 400°C
$\dot{\varepsilon}$: 1 S^{-1}
n≃2,0
n≃1,0
LOG[ln(1/(1-X_v))]
LOG[time(SEC)]
0,3
0,2
0,1
0,0
-0,1
-0,2
-0,3
-0,4
-0,5
-0,6
-0,7
-0,8
-0,9
1,0
2,0
3,0
4,0

FIGURE 92: Theoretical prediction of the variation of the volume fraction recrystallised with the parameter t/A, after deformation by different initial strains. T = 400°C, $\dot{\varepsilon} = 1\ s^{-1}$.

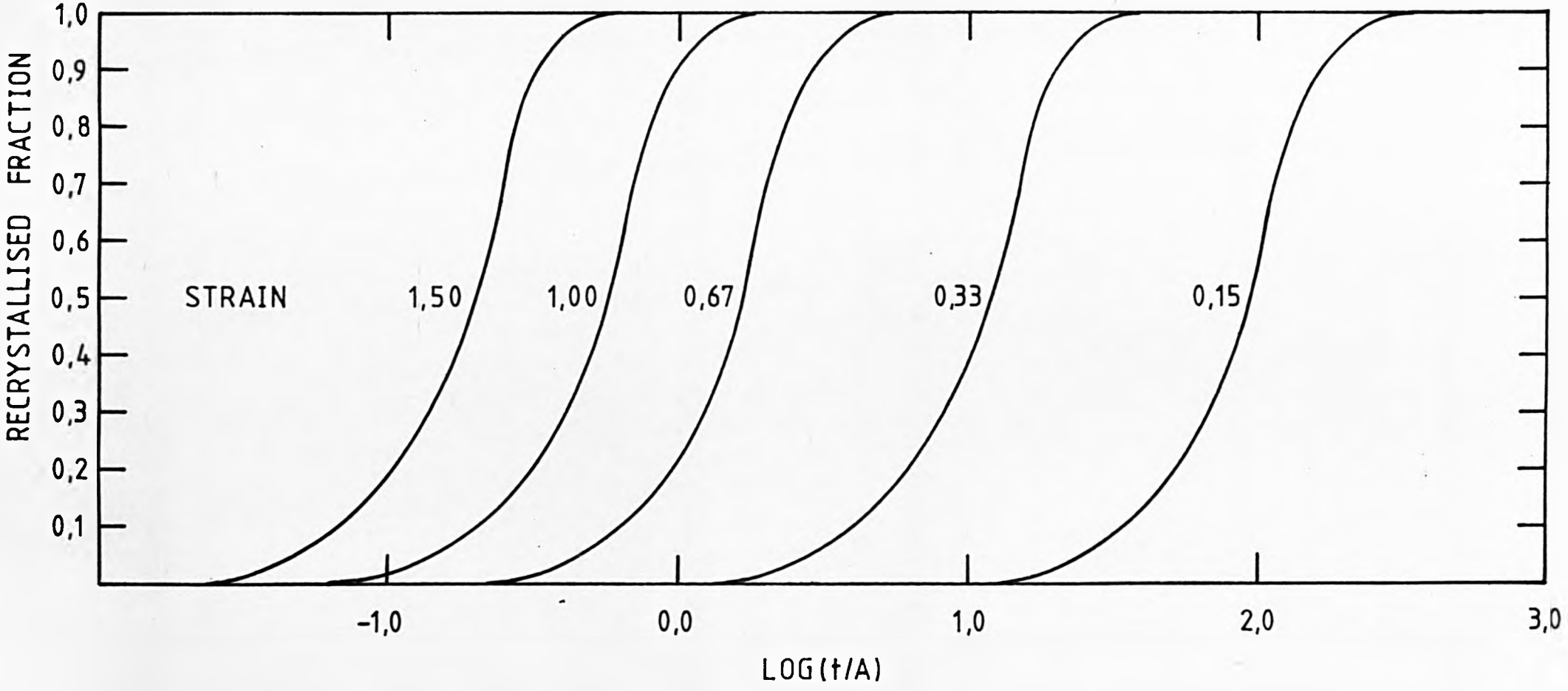
RECRYSTALLISED FRACTION
1,0
0,9
0,8
0,7
0,6
0,5
0,4
0,3
0,2
0,1
STRAIN
1,50
1,00
0,67
0,33
0,15
-1,0
0,0
1,0
2,0
3,0
LOG(t/A)

FIGURE 93: Macrographs of the gauge section of various plane strain compression specimens deformed at 400°C and 1 s^{-1}, and annealed for different intervals.

(a) ε = 0.33 and t = 2560 sec.;
(b) ε = 0.33 and t = 3981 sec.;
(c) ε = 0.67 and t = 8000 sec.;
(d) ε = 0.67 and t = 100 sec.;
(e) ε = 0.67 and t = 160 sec.;
(f) ε = 0.67 and t = 320 sec.

Mag. 7 x.

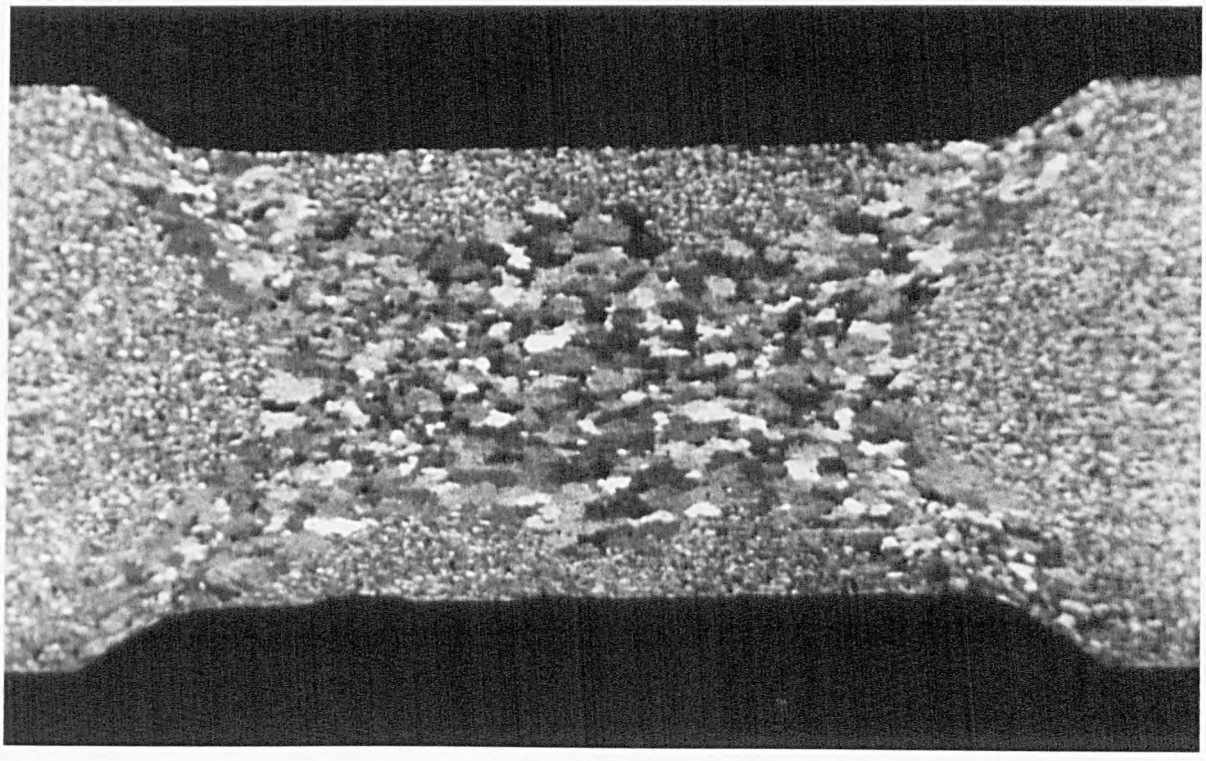

(a)

1mm

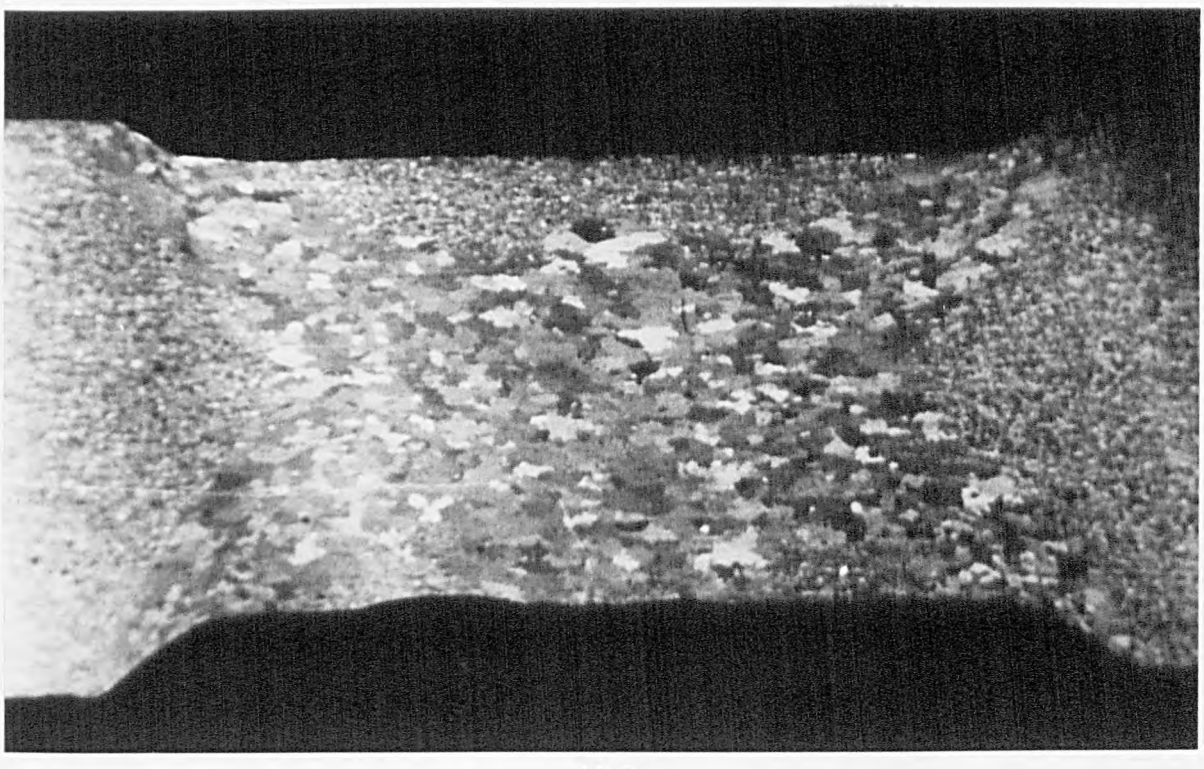

(b)

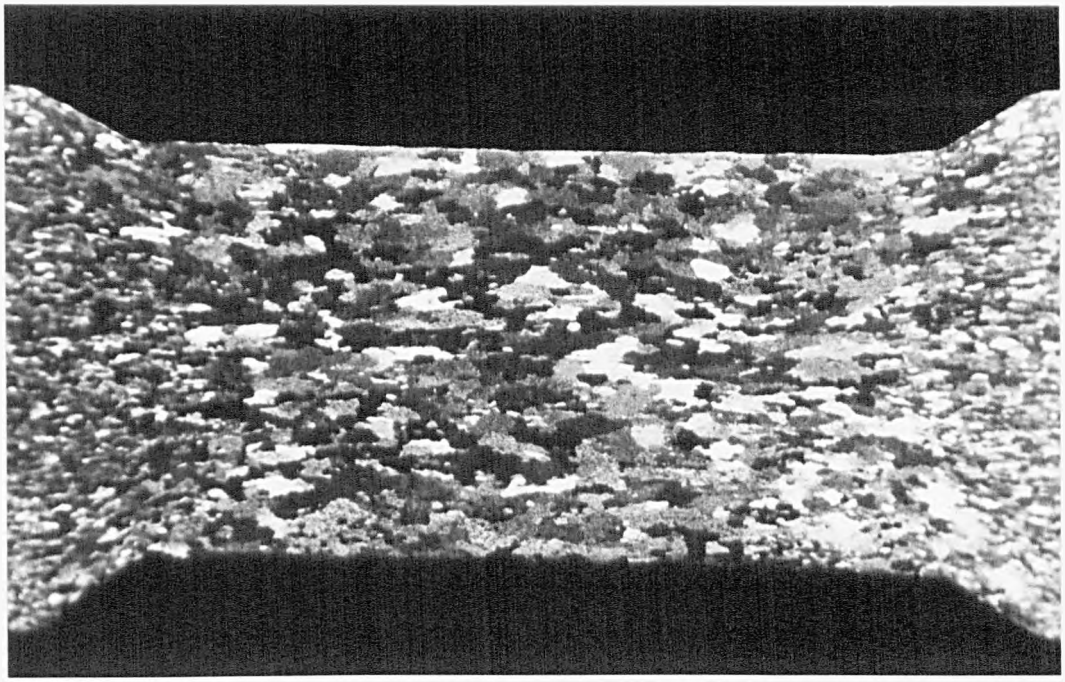

(c)

1mm

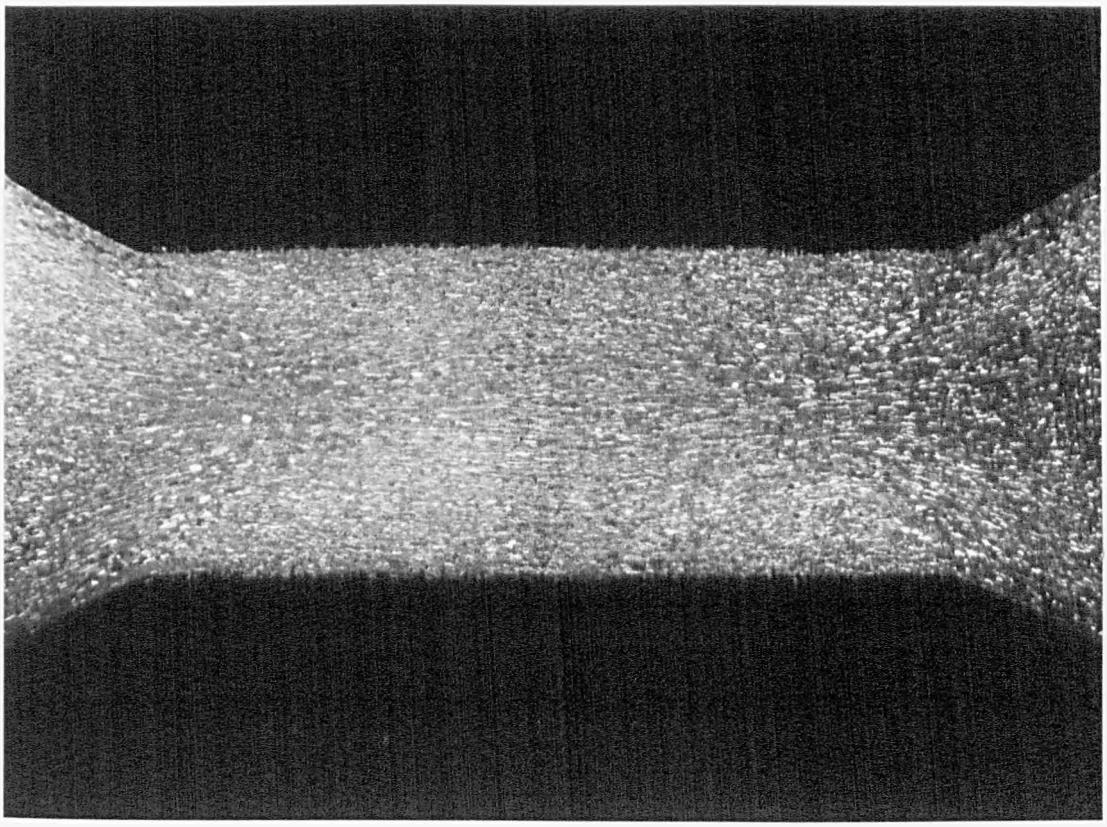

(d)

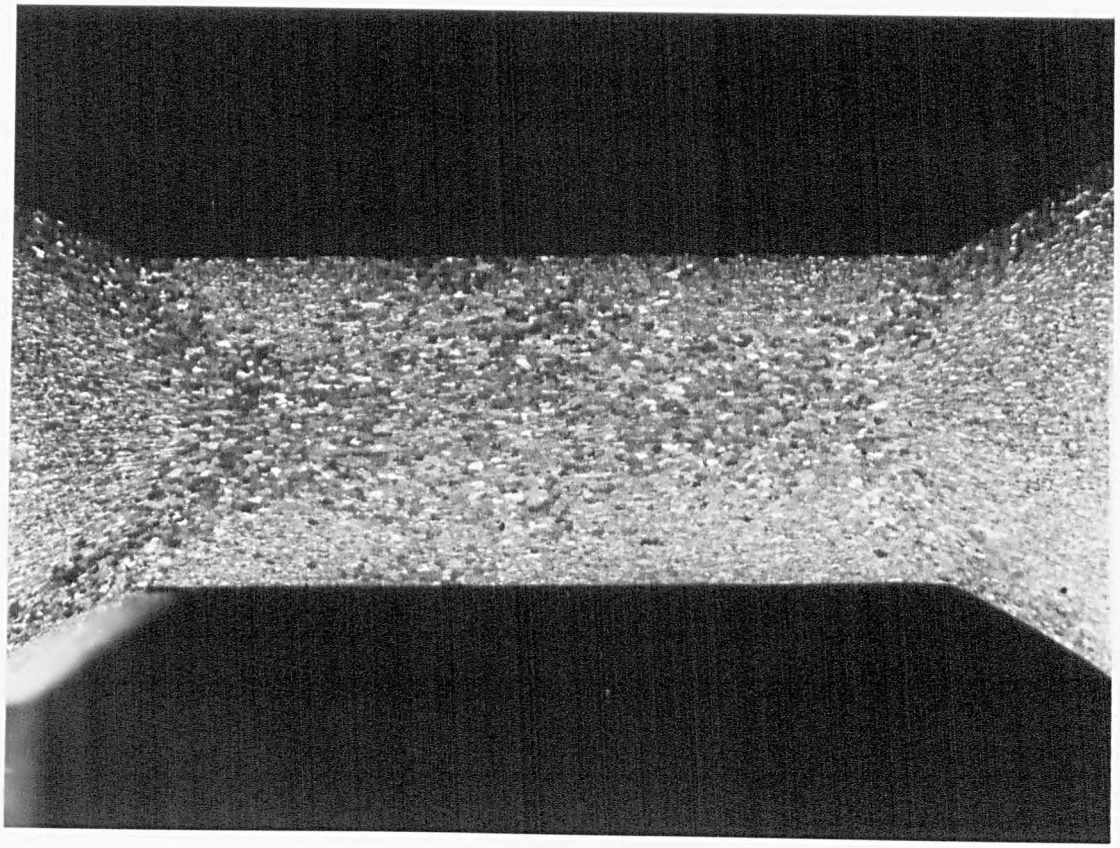

(e)

1 mm

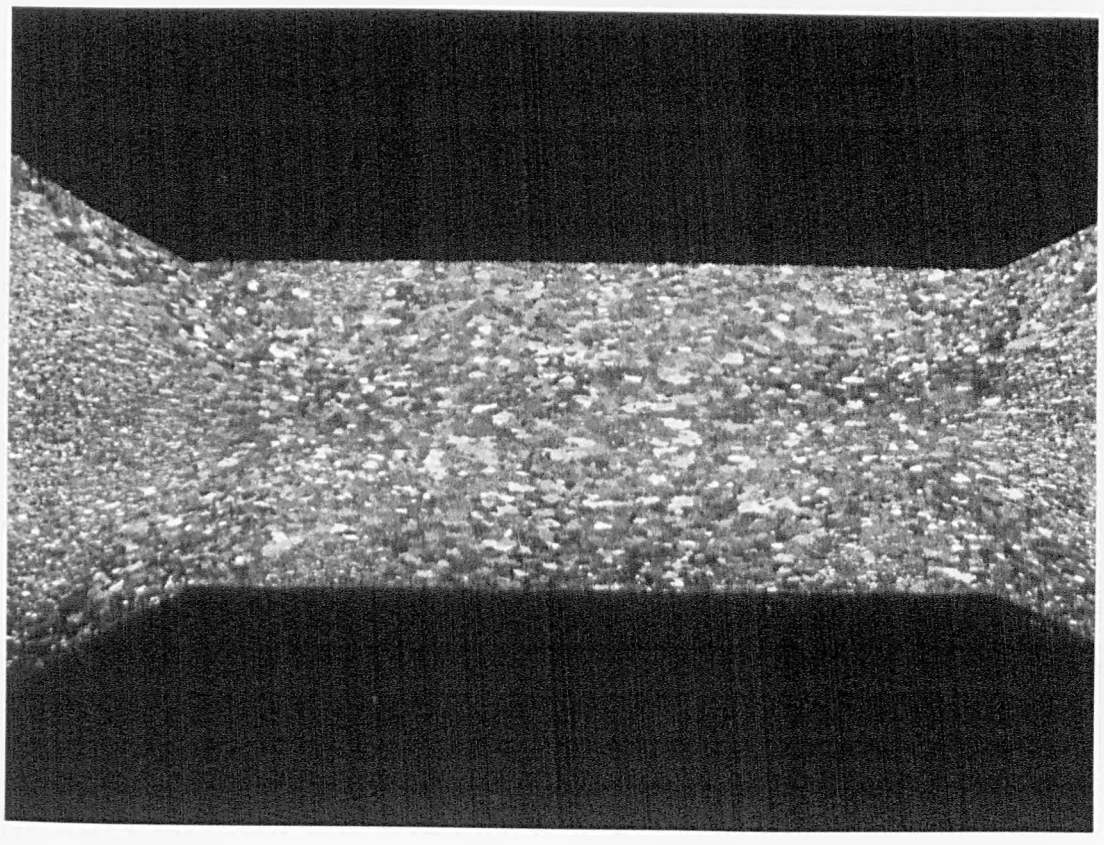

(f)

FIGURE 94: Microstructures taken at the centre of the gauge section of various plane strain compression specimens deformed at 400°C and 1 s^{-1} and annealed for different intervals.

(a) $\varepsilon = 0.33$ and t = 100 sec.;
(b) $\varepsilon = 0.33$ and t = 1280 sec.;
(c) $\varepsilon = 0.33$ and t = 2560 sec.;
(d) $\varepsilon = 0.33$ and t = 6310 sec.;
(e) Same conditions as before but taken at a transition zone between the recrystallised area and the deformed structure of a "dead zone" where recrystallisation requires the formation of new nuclei.

Mag. 100 x.

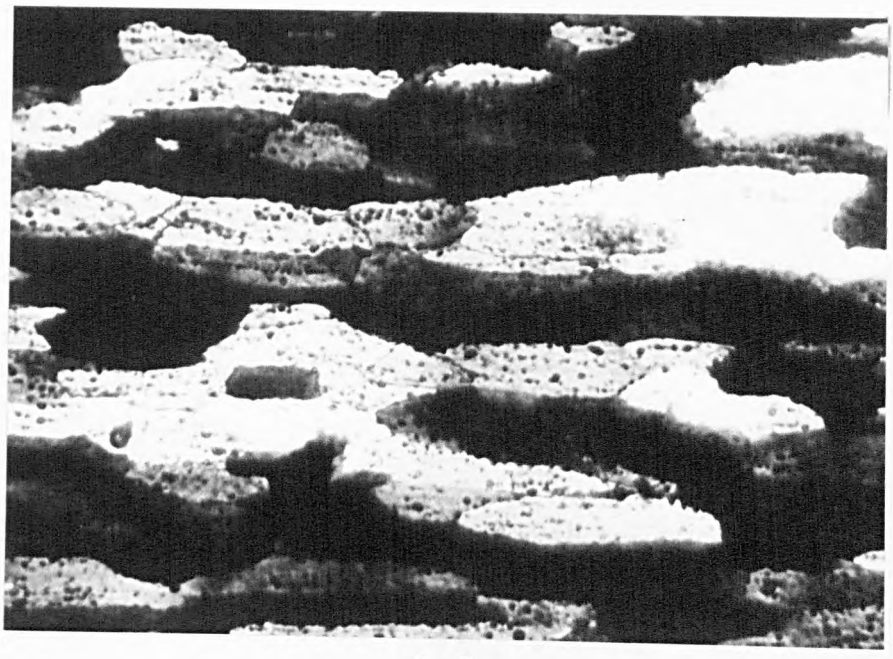

(a)

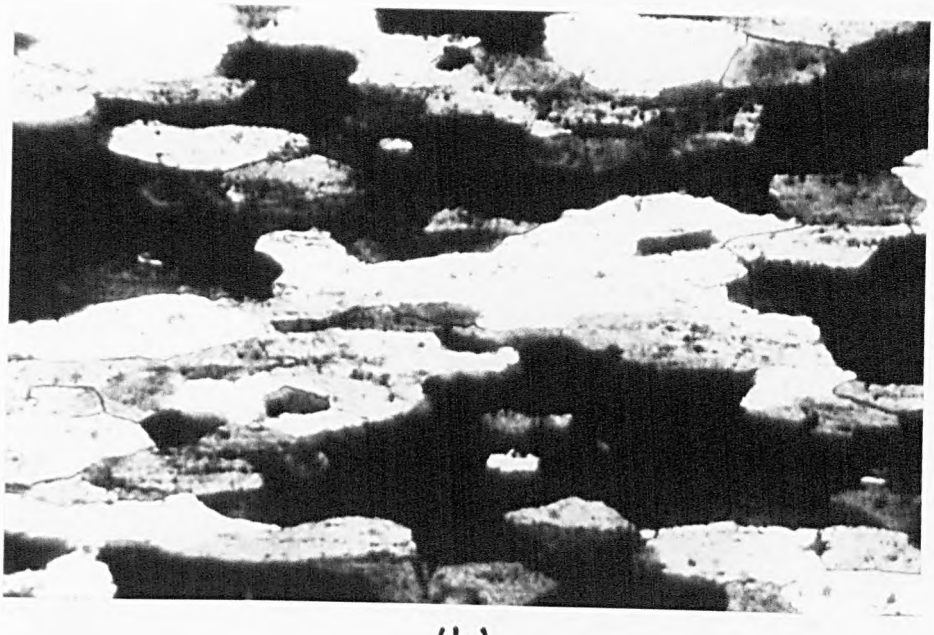

0,1 mm

(b)

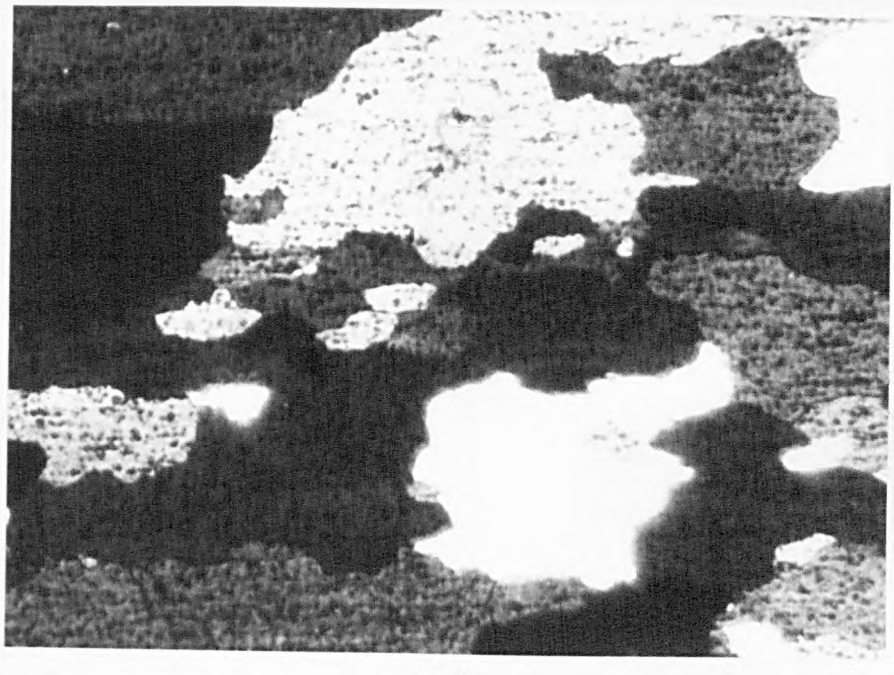

(c)

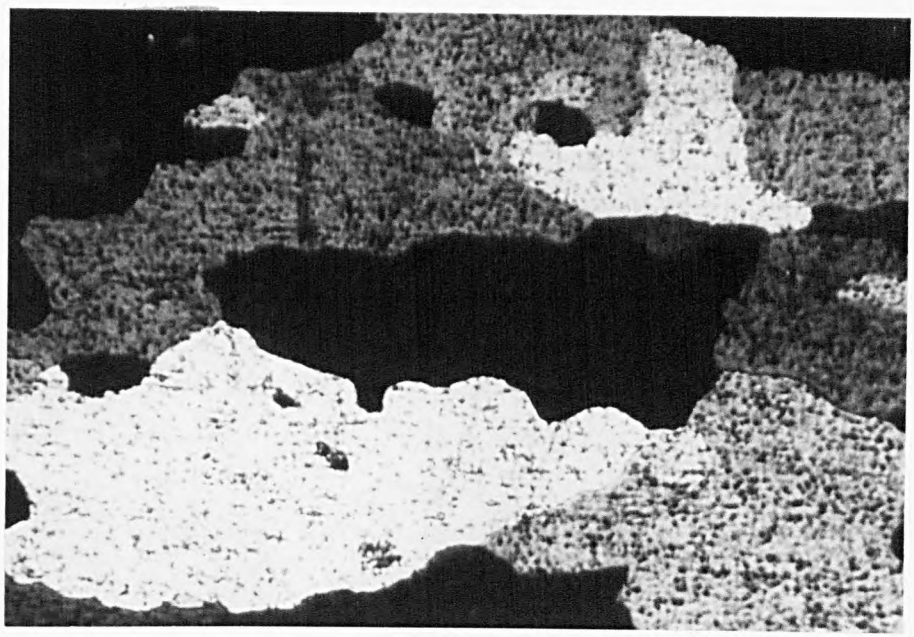

(d)

0,1mm

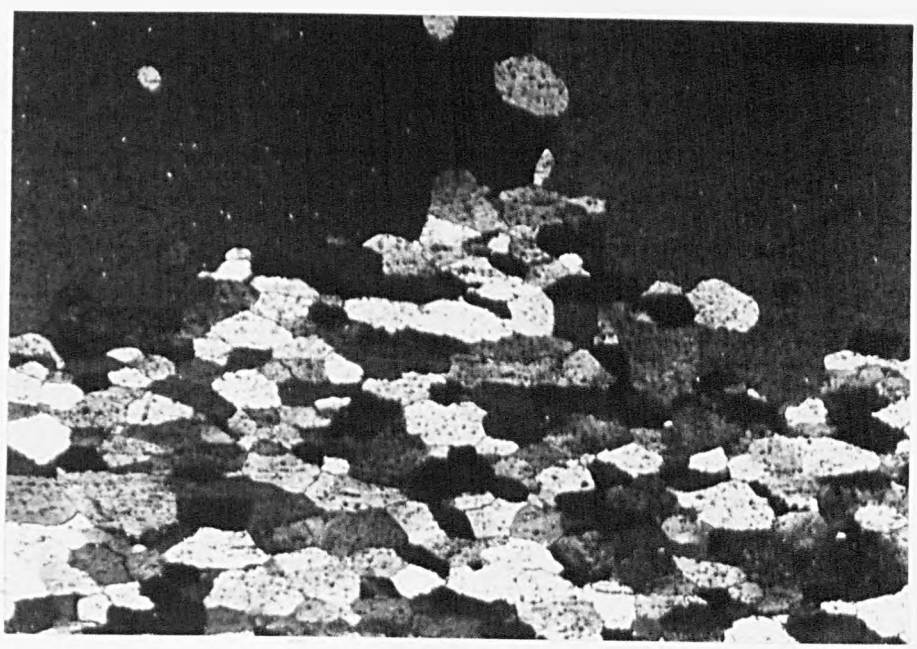

(e)

FIGURE 95: Electron micrographs of samples of a specimen deformed at 400°C and 1 s^{-1} by 0.33 strain and annealed 1000 sec.

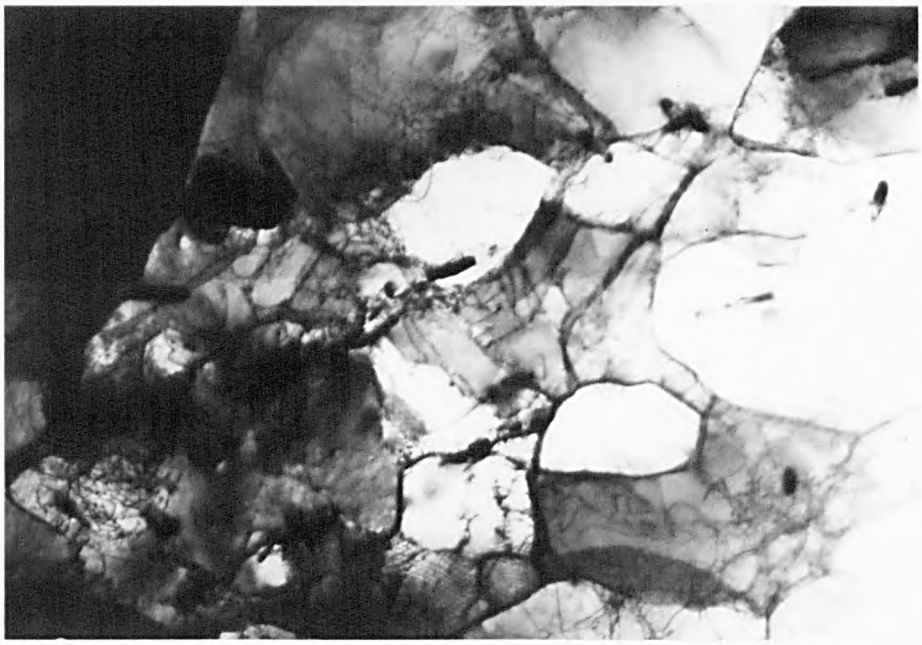

(a)

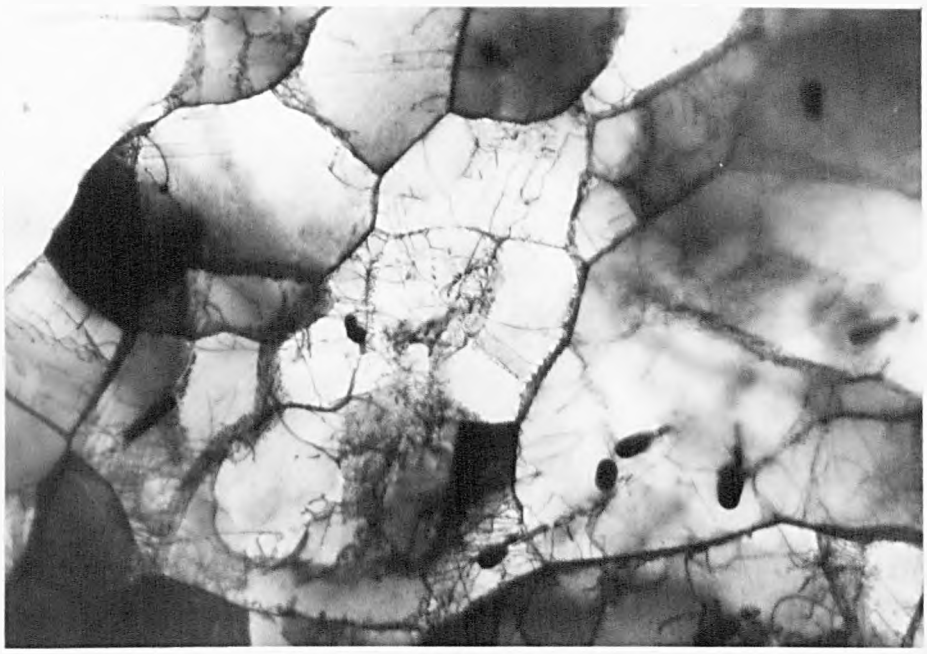

(b)

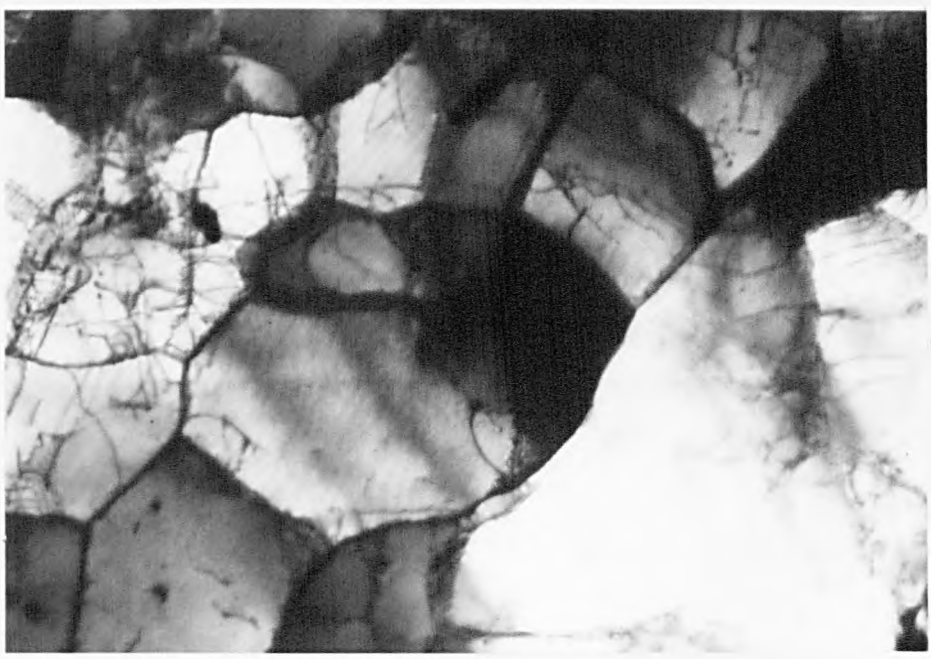

(c)

FIGURE 96: Microstructures taken at the centre of the gauge section of various plane strain compression specimens deformed by 0.67 strain at 400°C and 1 s^{-1} and annealed for different intervals.

(a) t = 80 sec;
(b) t = 100 sec;
(c) t = 160 sec;
(d) t = 320 sec.

Mag. 100 x.

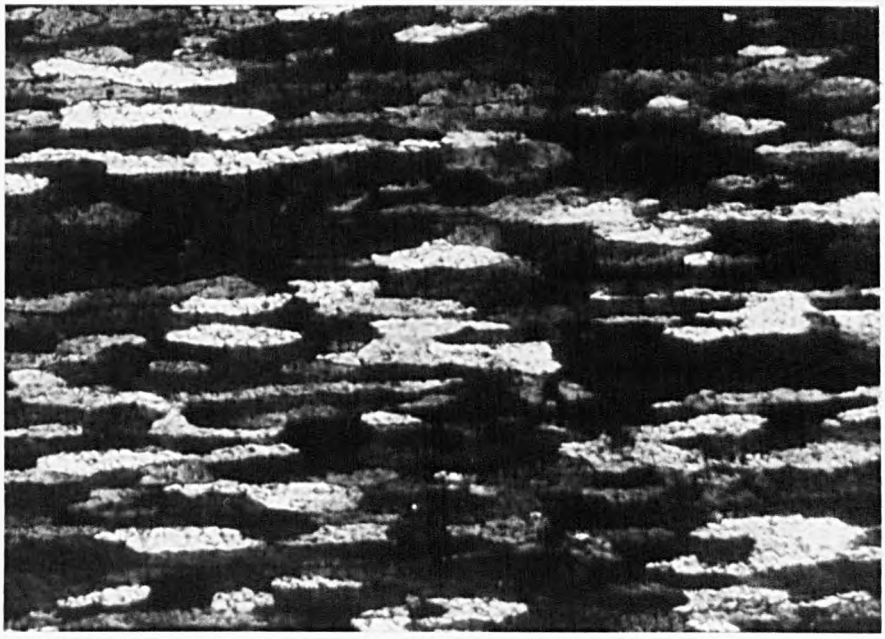

(a)

0,1mm

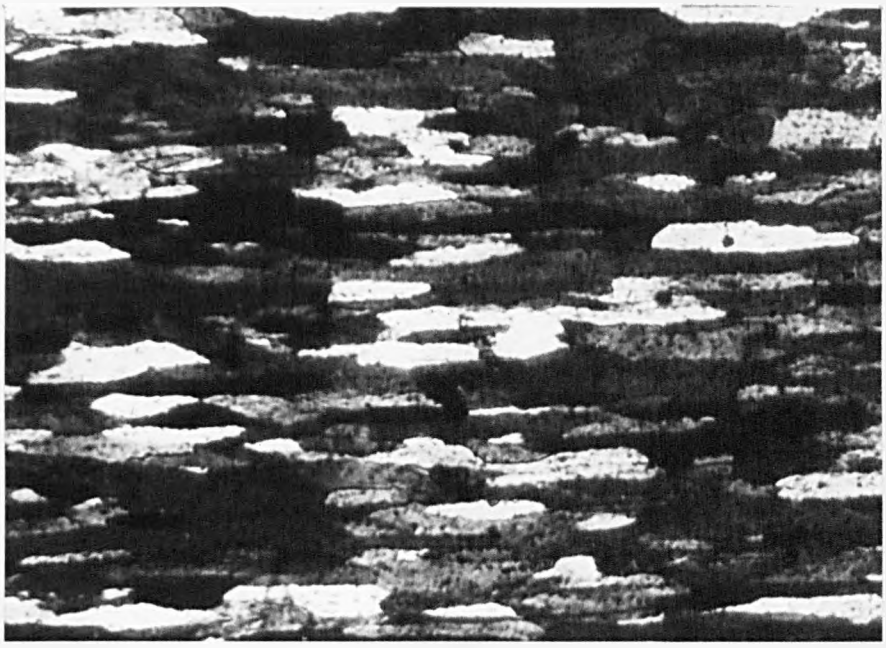

(b)

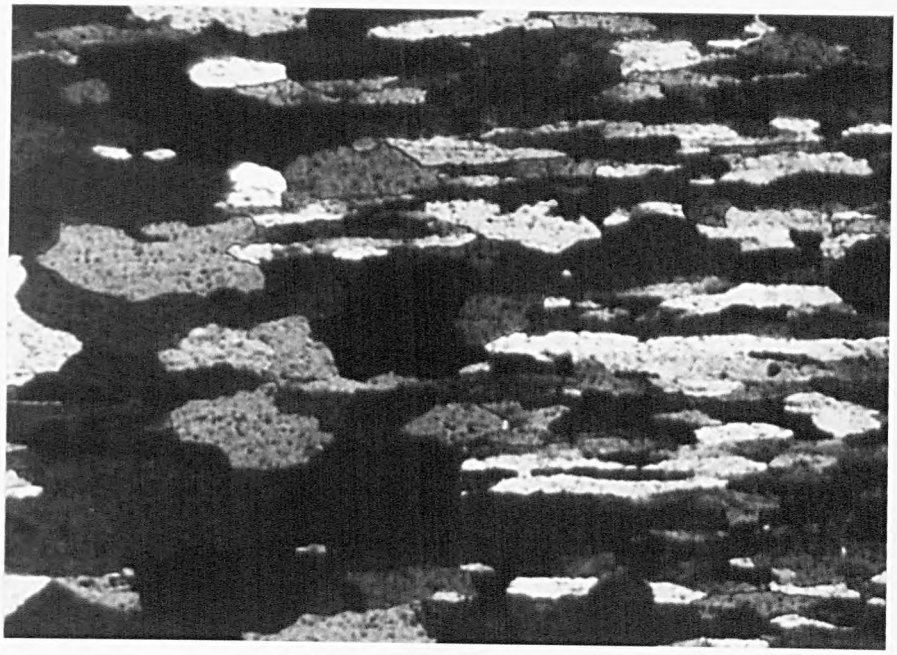

(c)

0,1 mm

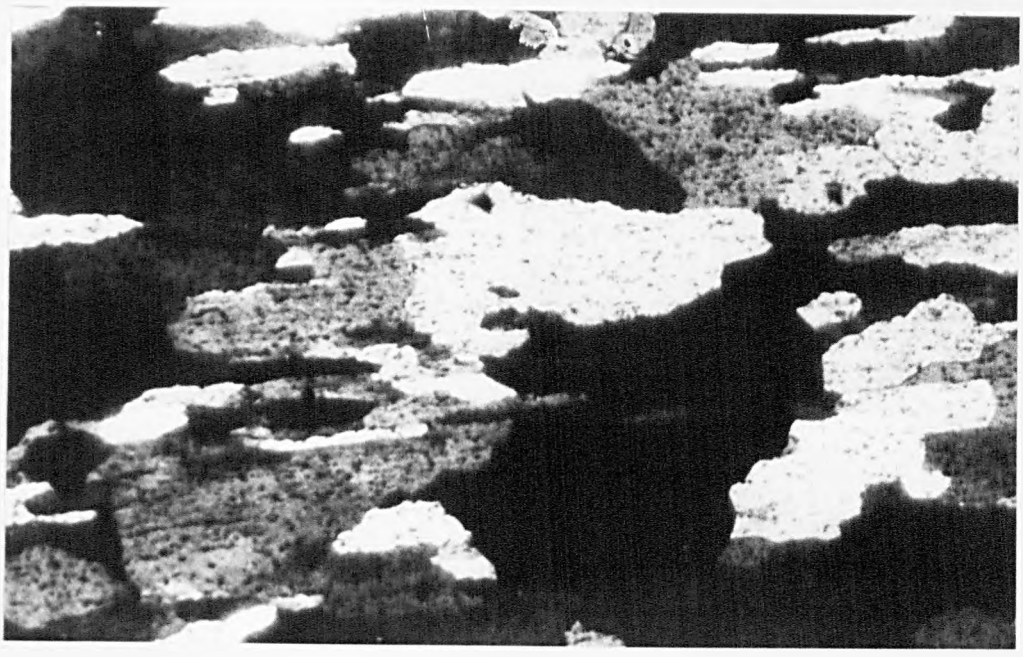

(d)

FIGURE 97: Composition of individual micrographs taken along the gauge section of various plane strain compression specimens deformed by 0.67 strain at 400°C and 1 s^{-1} and annealed for different intervals.

(a) t = 60 sec;
(b) t = 240 sec;
(c) t = 480 sec;
(d) t = 640 sec;
(e) t = 1280 sec.

Mag. ∿ 7 x.

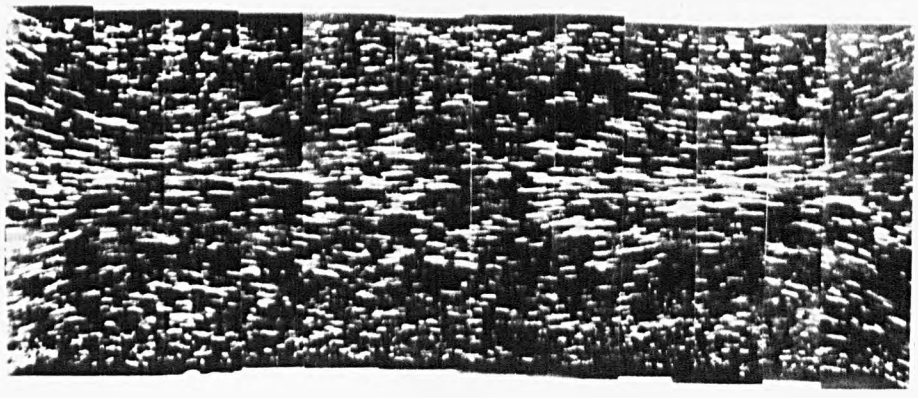

(a)

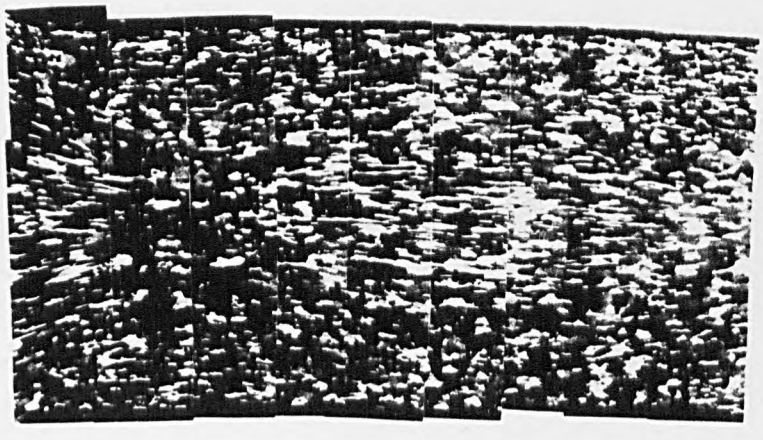

1mm

(b)

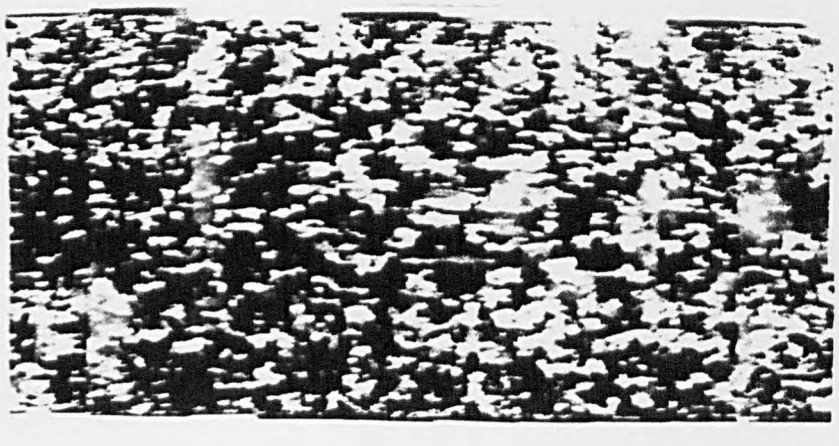

(c)

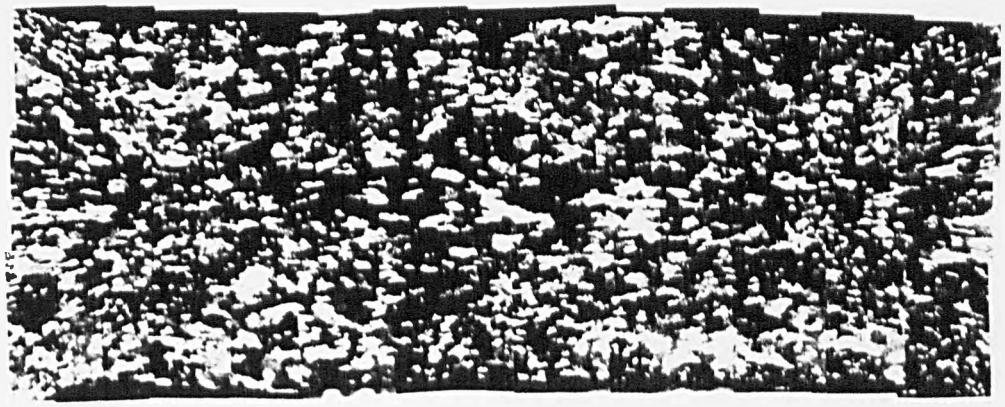

(d)

1 mm

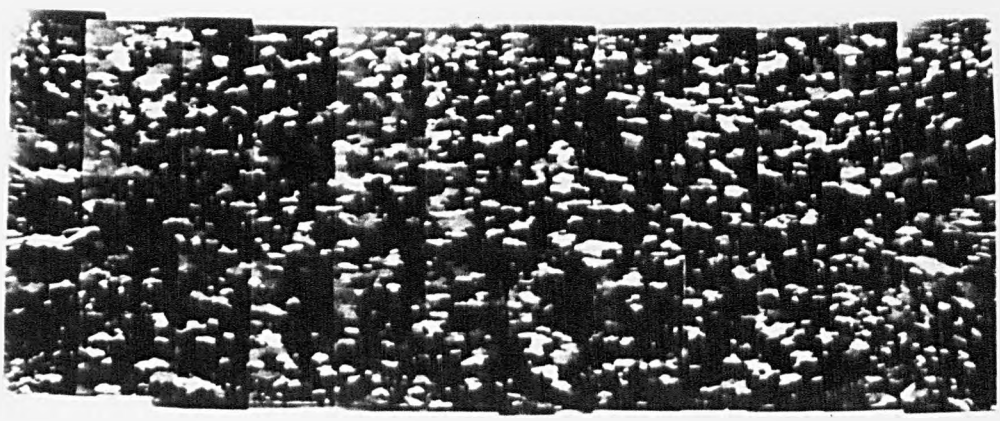

(e)

FIGURE 98: Microstructures of a specimen of Al-1%Mg-1%Mn alloy deformed by 0.67 strain at 400°C and 1 s^{-1} and annealed 300 sec. at the deformation temperature. Recrystallisation is observed to develop at the centre of the high deformation bands.

Mag. 40 x.

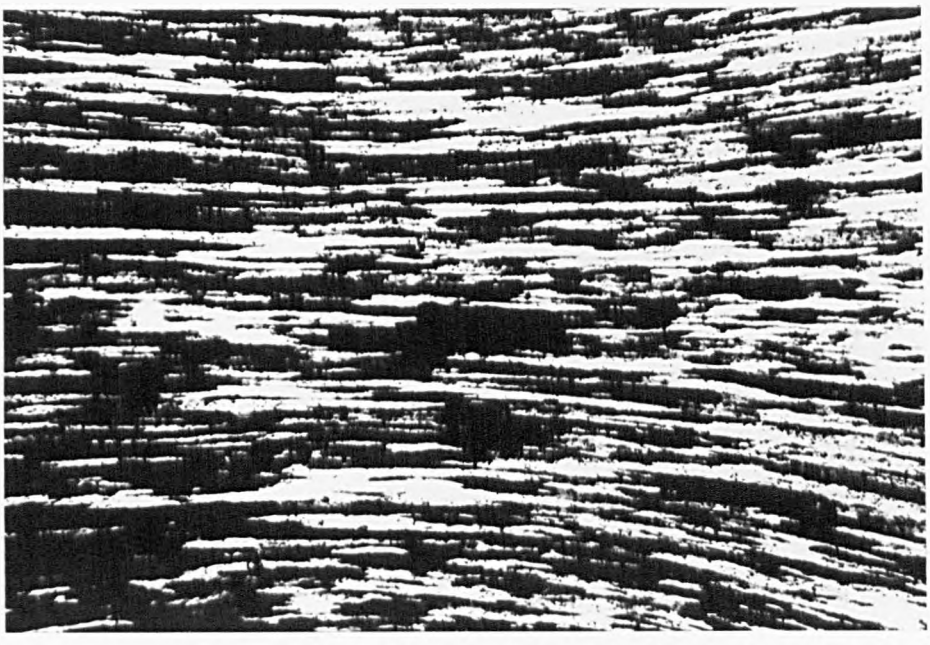

(a)

0,5 mm

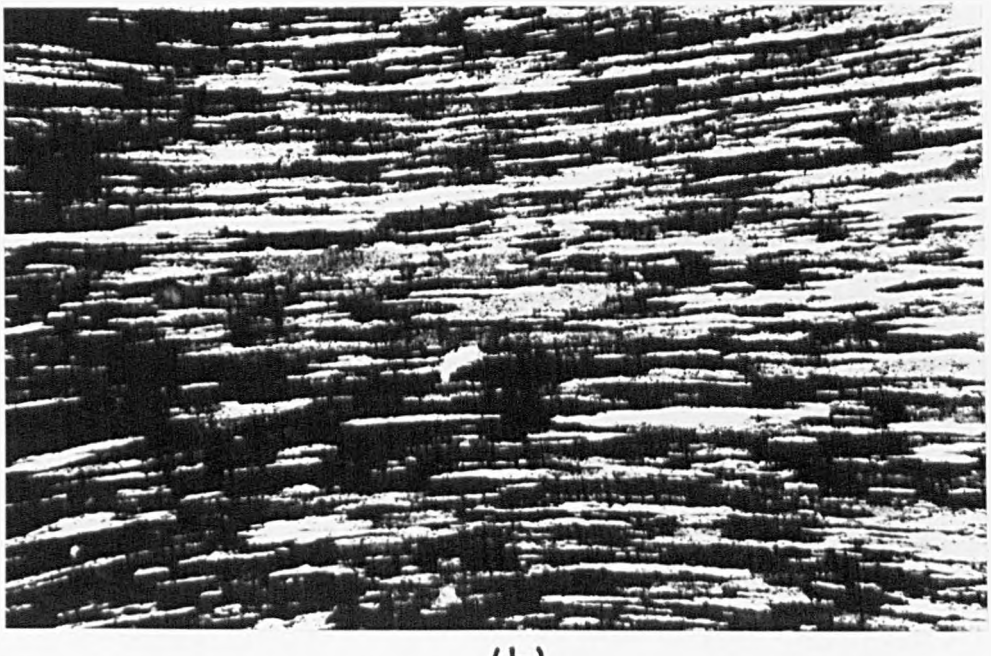

(b)

FIGURE 99: Patterns of recrystallised fraction in the upper left quarter of the gauge section of various plane strain compression specimens deformed by 0.67 strain at 400°C and 1 s^{-1} and annealed for different intervals.

(a) t = 40 sec;
(b) t = 100 sec;
(c) t = 160 sec;
(d) t = 320 sec.

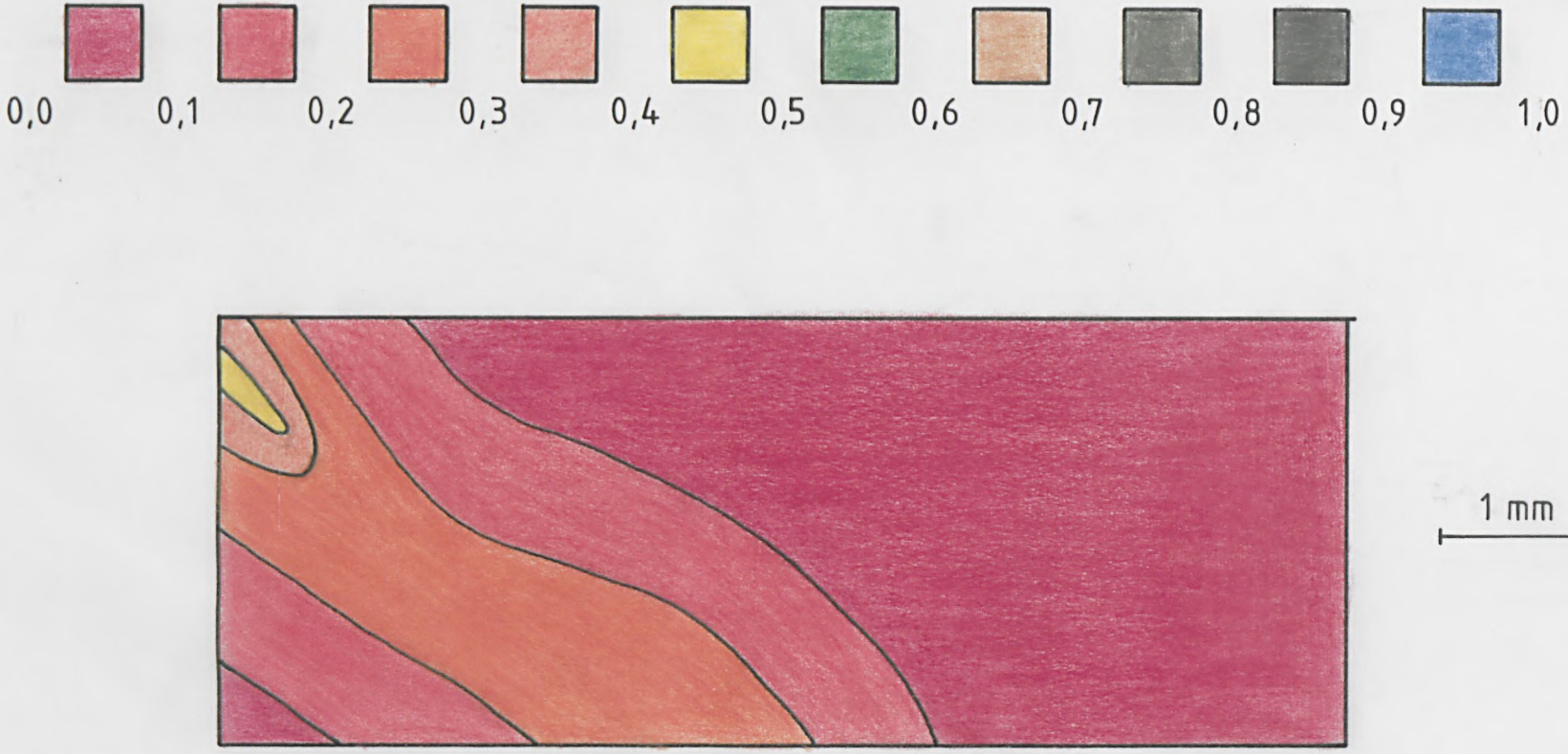

(a)

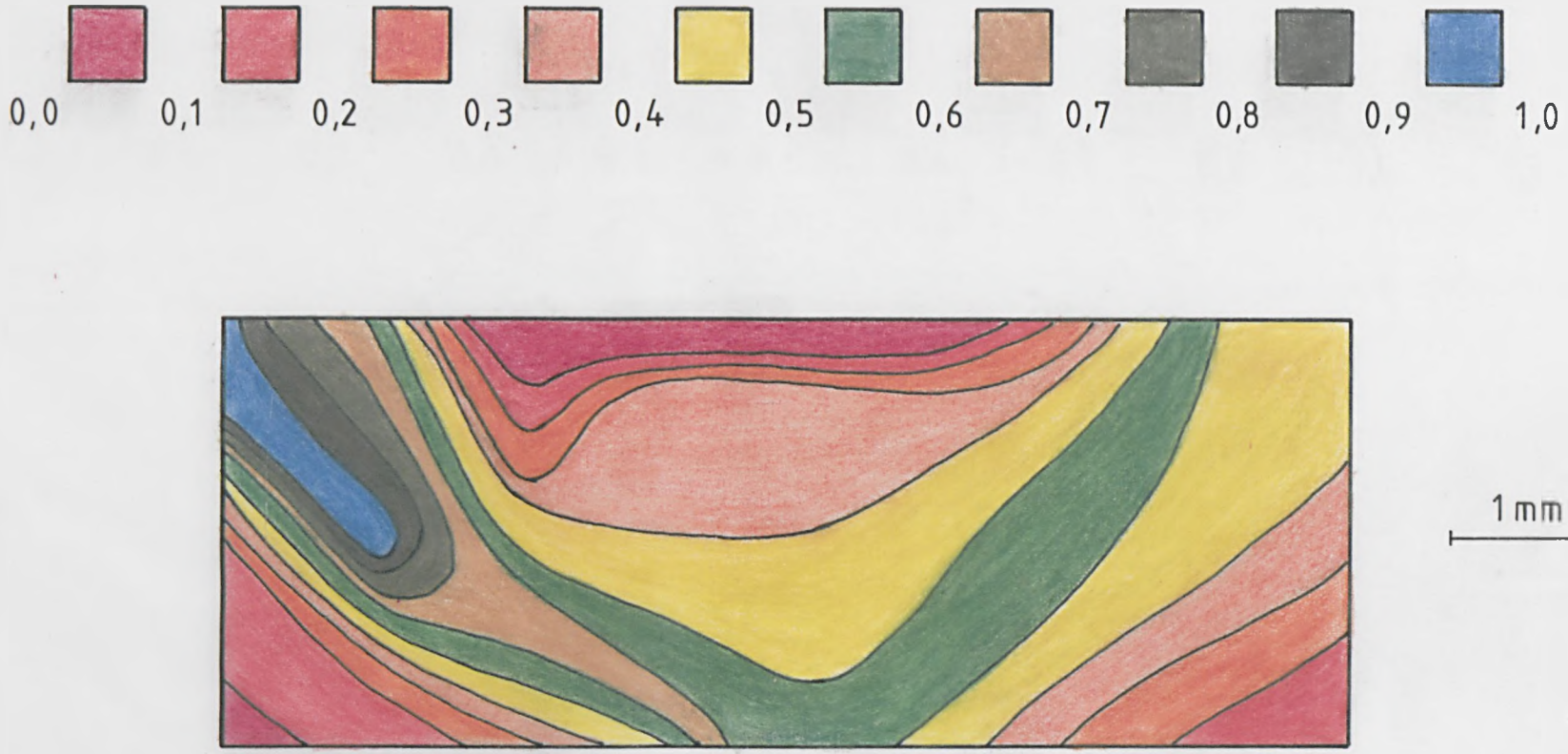

(b)

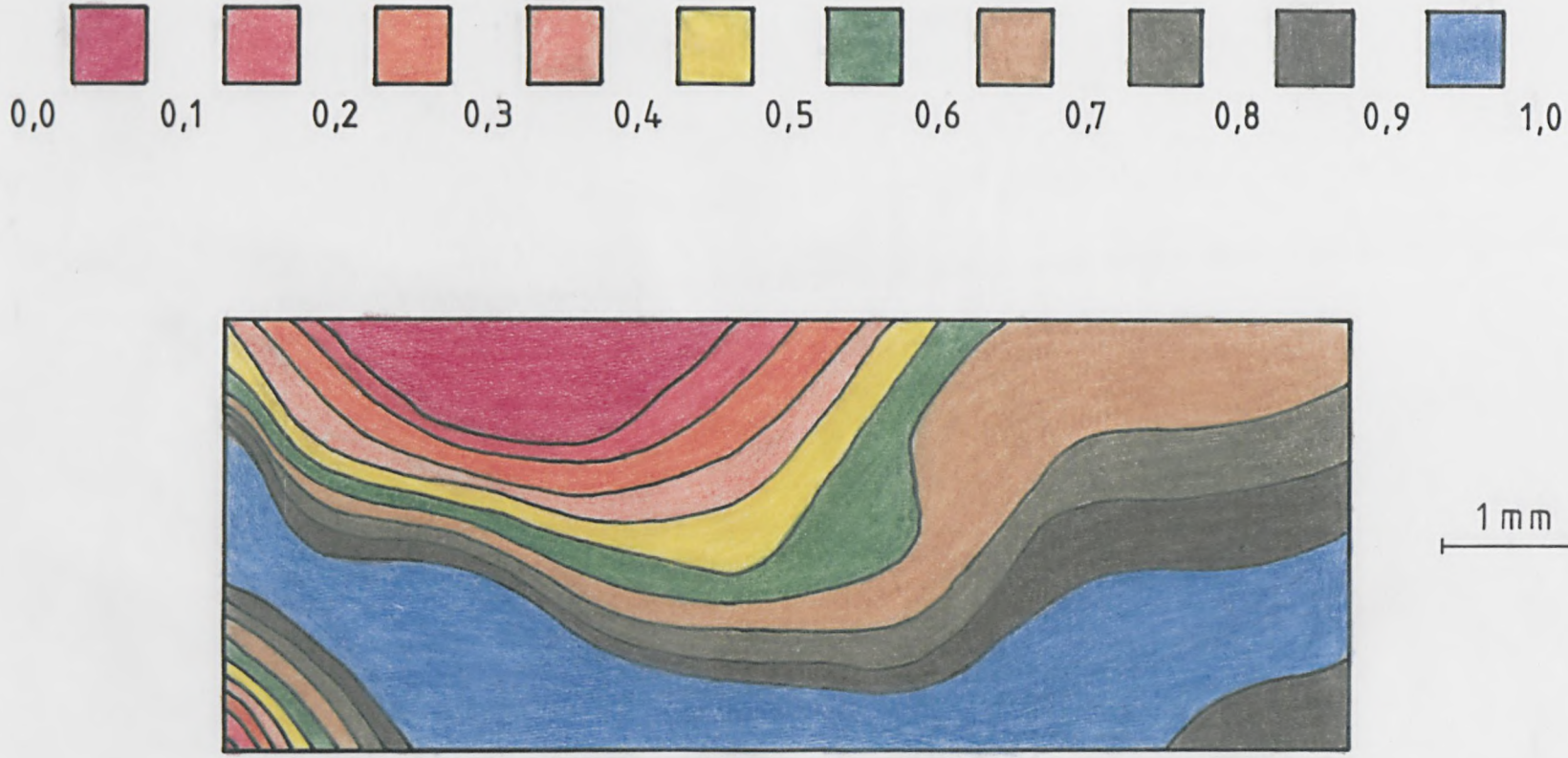

(c)

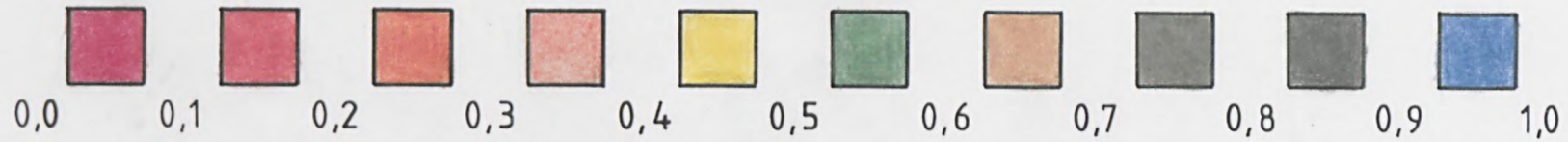

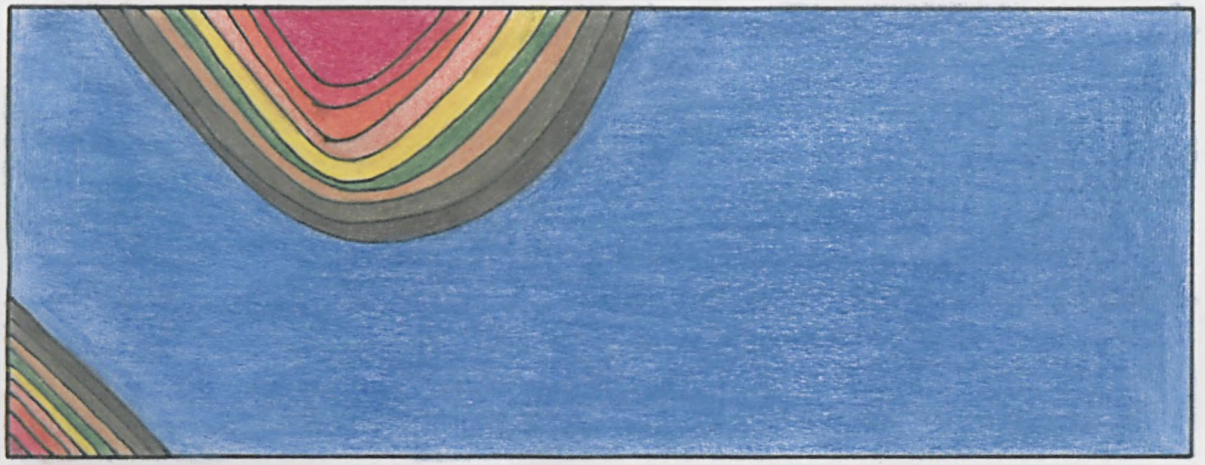

(d)

FIGURE 100: Variation of the fraction restored expressed by the restoration index R_1 and the volume fraction recrystallised for specimens of Al-1%Mg alloy deformed at 400°C and 1 s^{-1}.

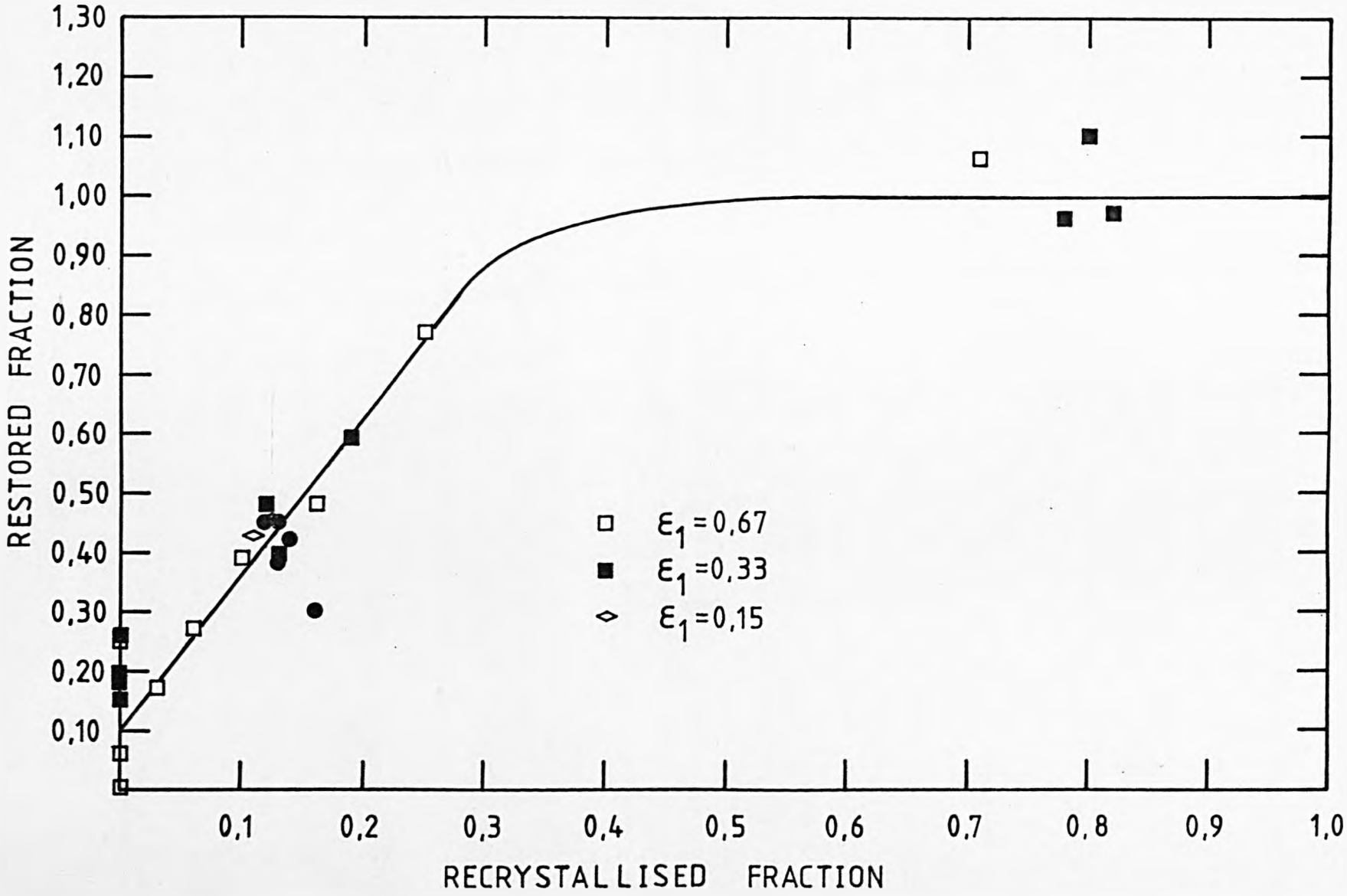
RESTORED FRACTION
1,30
1,20
1,10
1,00
0,90
0,80
0,70
0,60
0,50
0,40
0,30
0,20
0,10
0,1
0,2
0,3
0,4
0,5
0,6
0,7
0,8
0,9
1,0
RECRYSTALLISED FRACTION
ε1 = 0,67
ε1 = 0,33
ε1 = 0,15

FIGURE 101: Variation of the recrystallised grain size "d_{rex}" and the strain applied for specimens of Al-1%Mg alloy deformed at 400°C and 1 s^{-1}, with and without use of cartridge heaters into the deformation tools.

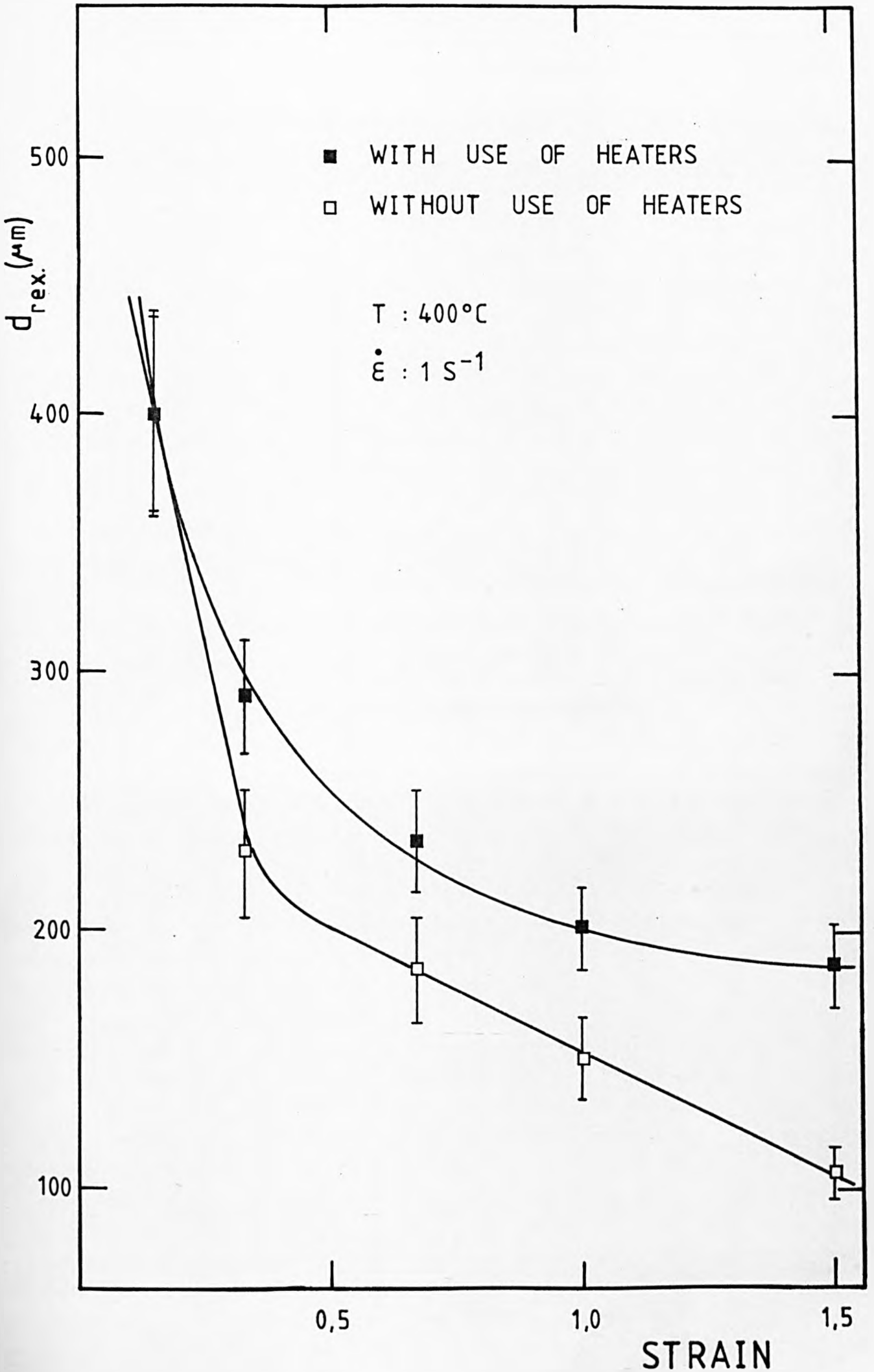
■ WITH USE OF HEATERS
□ WITHOUT USE OF HEATERS
T : 400°C
$\dot{\varepsilon}$: 1 S^{-1}
$d_{rex.}$ (µm)
500
400
300
200
100
0,5
1,0
1,5
STRAIN

FIGURE 102: Macrographs showing the distribution of the recrystallised grains along the gauge section of various plane strain compression specimens deformed at 400°C and 1 s^{-1}.

(a) ε = 0.15 (no use of heaters);
(b) ε = 0.67 (" " ");
(c) ε = 1.00 (" " ");
(d) ε = 0.33 (with use of heaters);
(e) ε = 0.67 (" " " ");
(f) ε = 1.00 (" " " ").

Mag. 7 x.

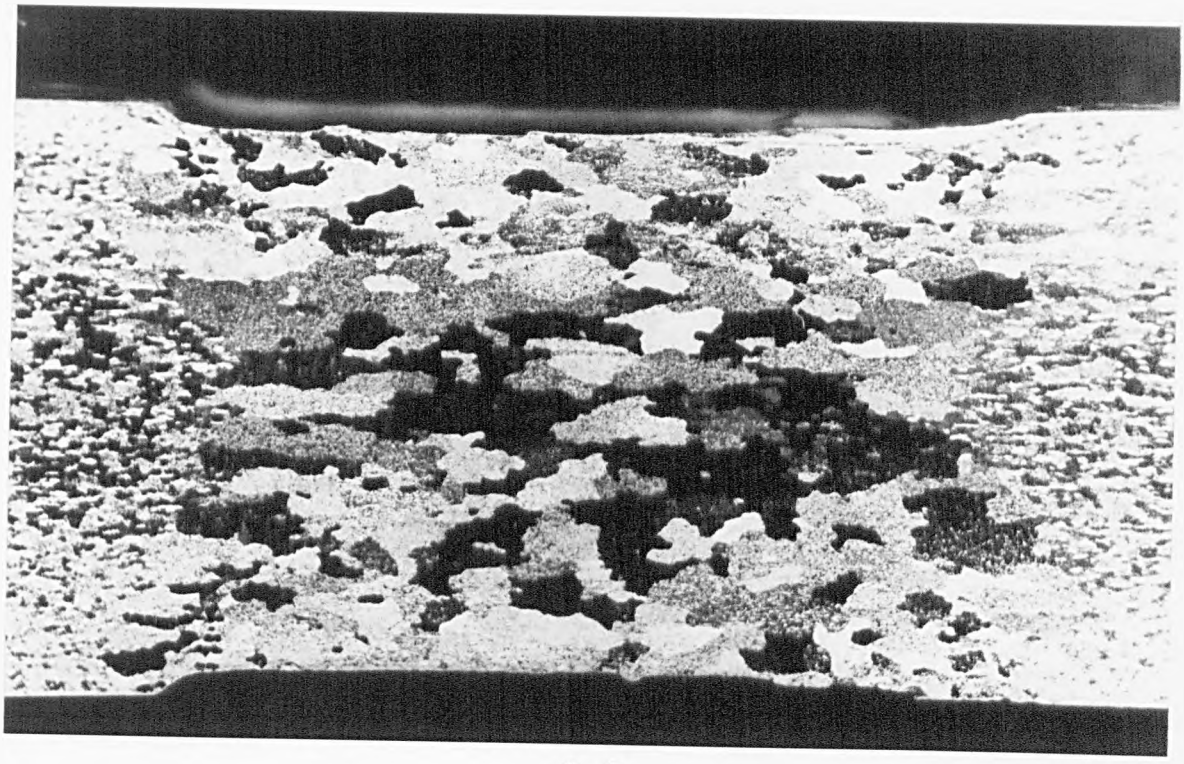

(a)

1mm

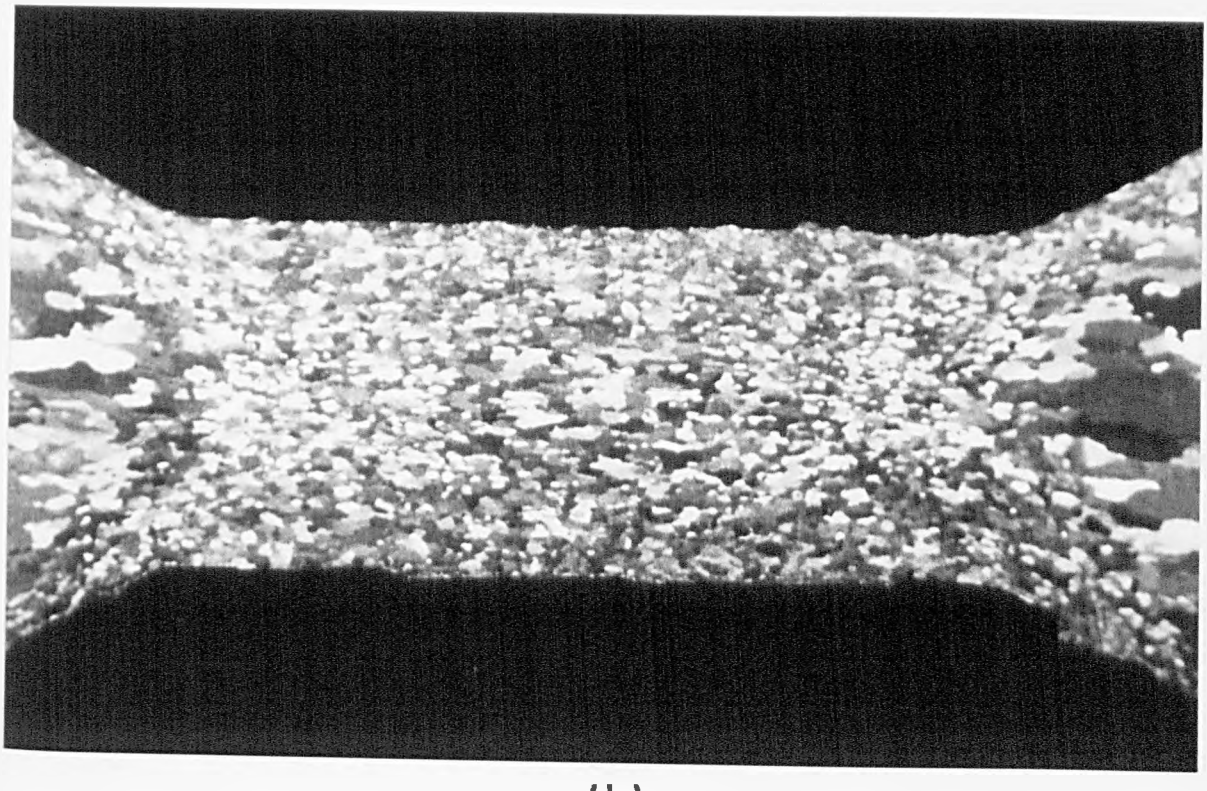

(b)

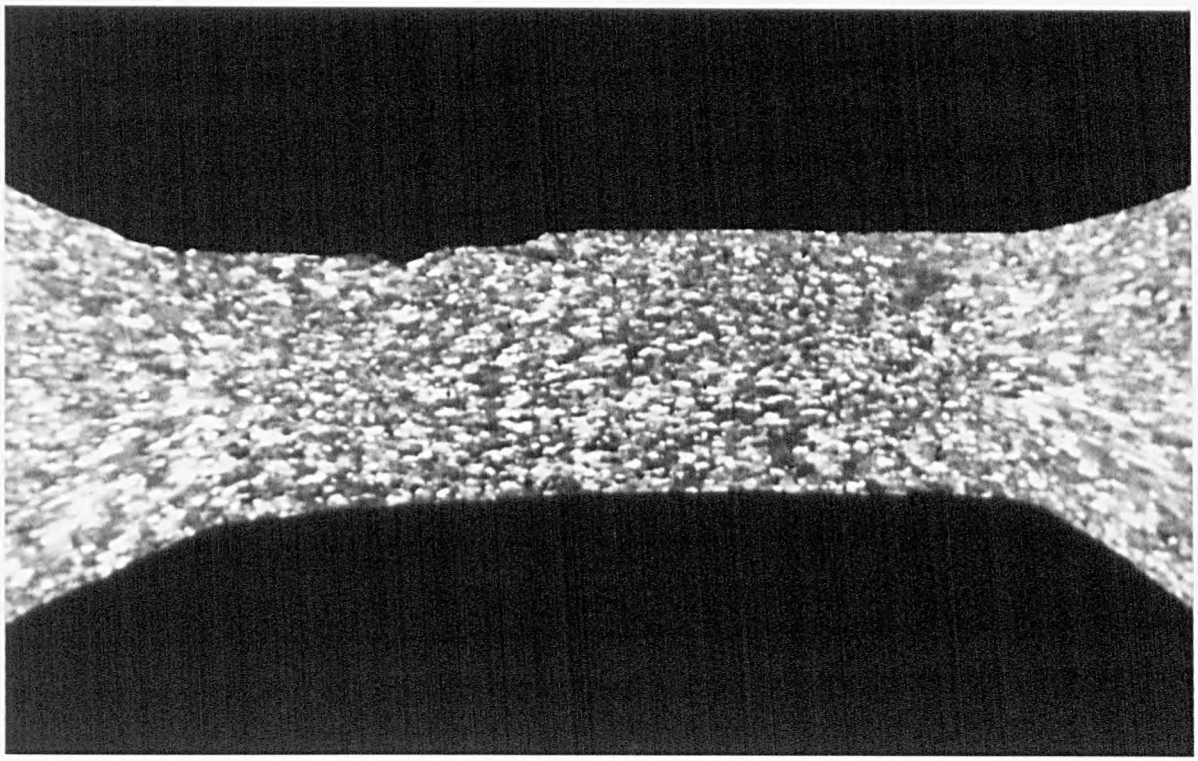

(c)

1mm

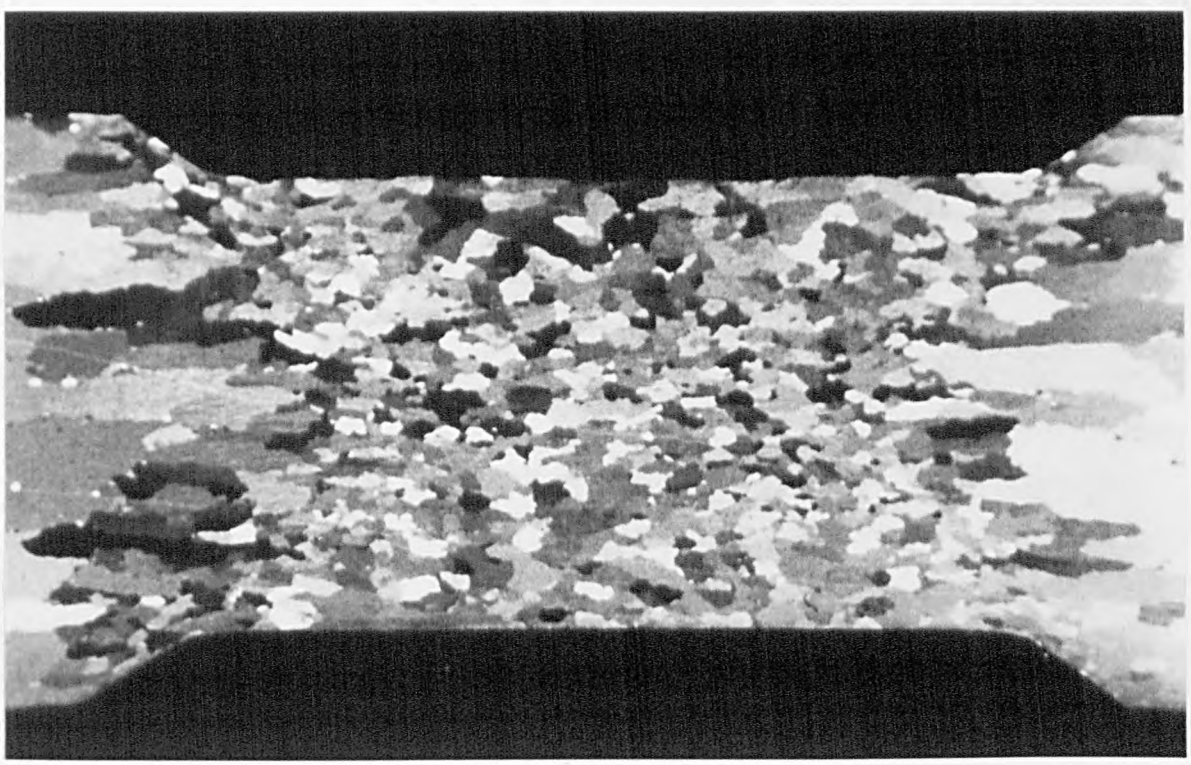

(d)

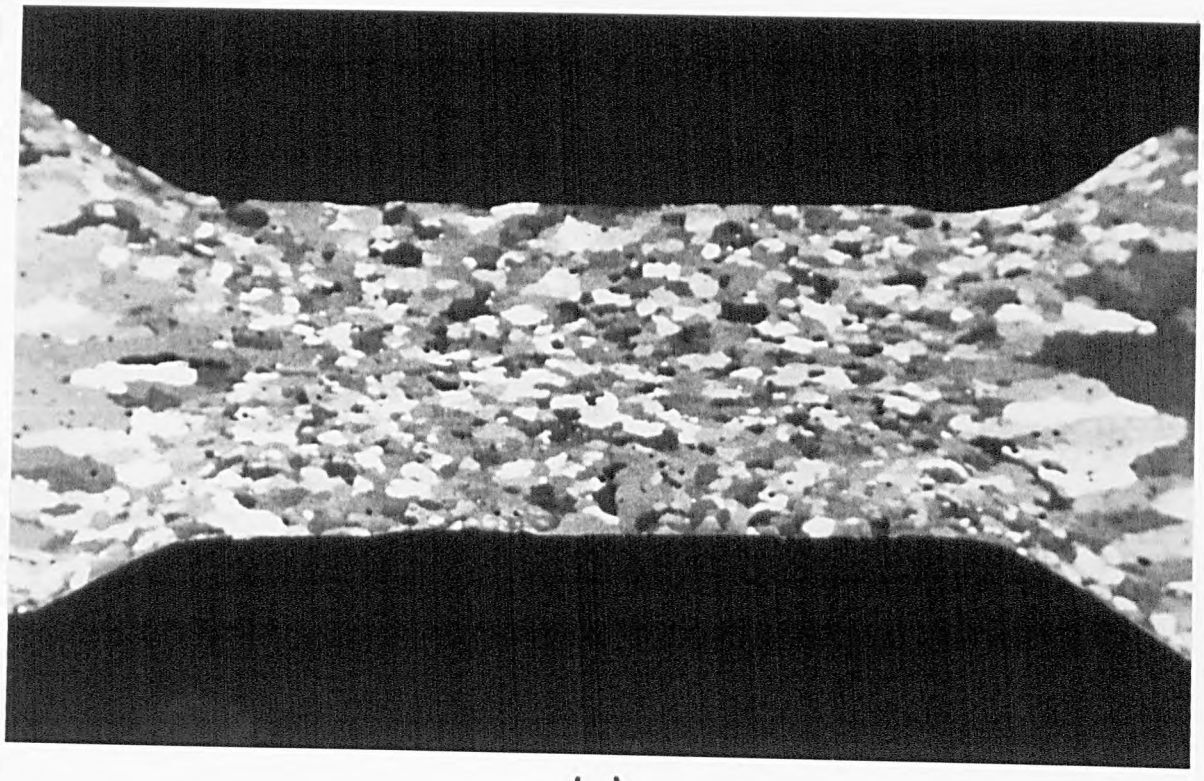

(e)

1 mm

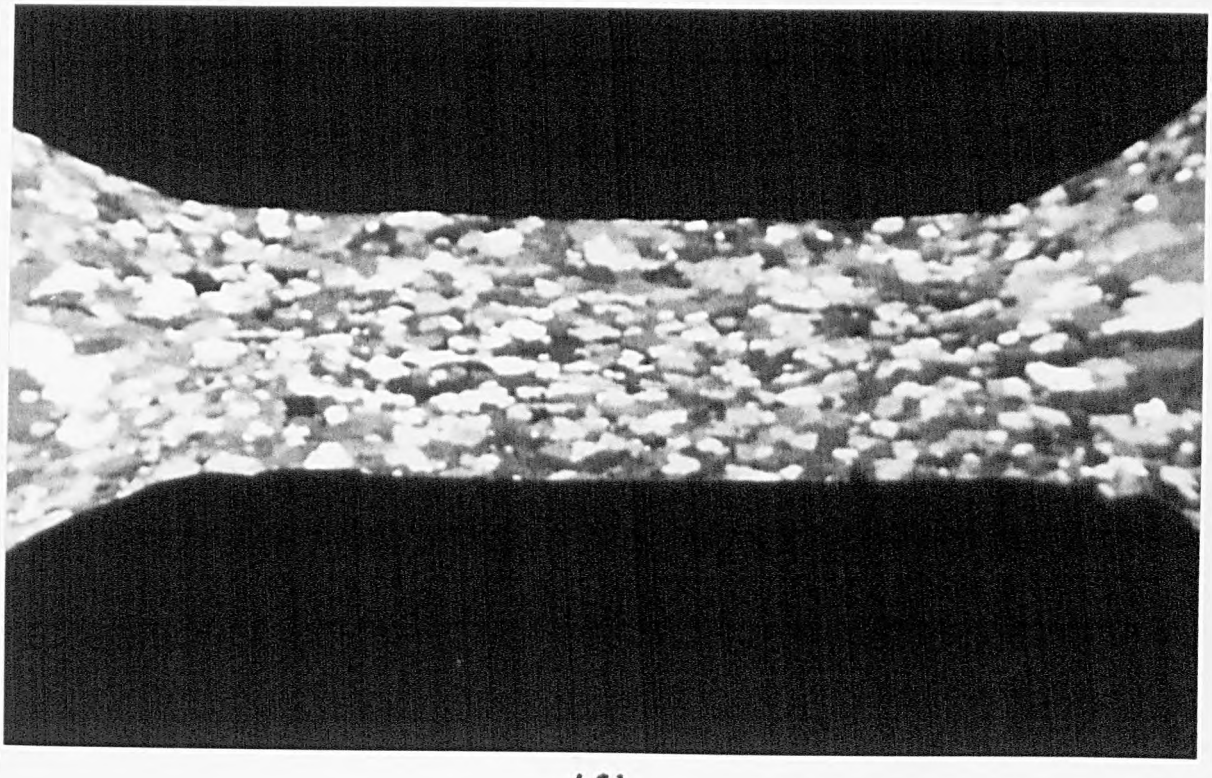

(f)

FIGURE 103: Microstructures taken at the centre of the gauge section of various plane strain compression specimens deformed at 400°C and 1 s^{-1} and fully recrystallised after annealing at the deformation temperature. No use of heaters in the deformation tools.

(a) ε = 0.33;
(b) ε = 0.67;
(c) ε = 1.00;
(d) ε = 1.50.

Mag. 100 x.

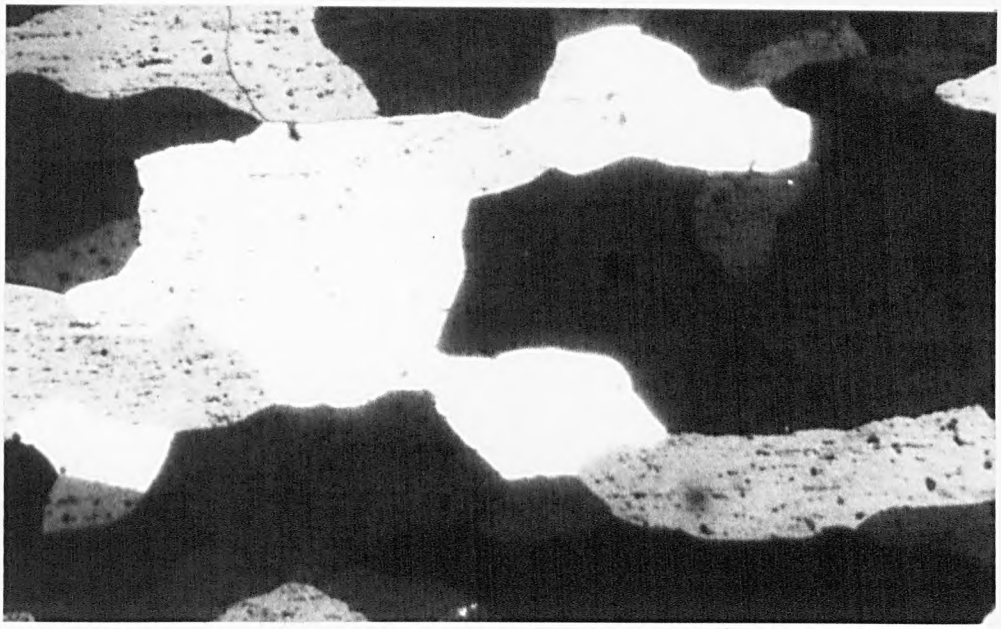

(a)

0,1 mm

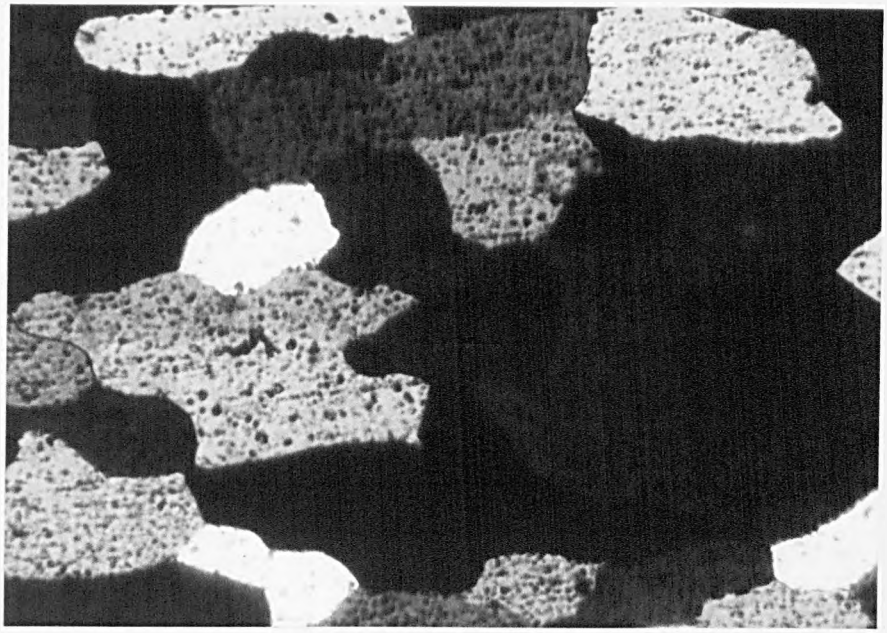

(b)

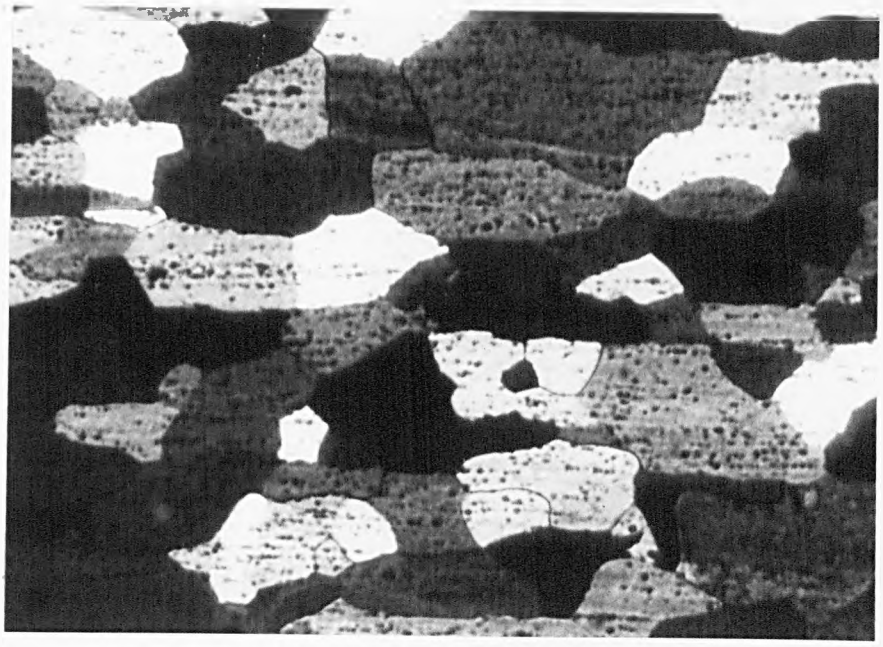

(c)

0,1 mm

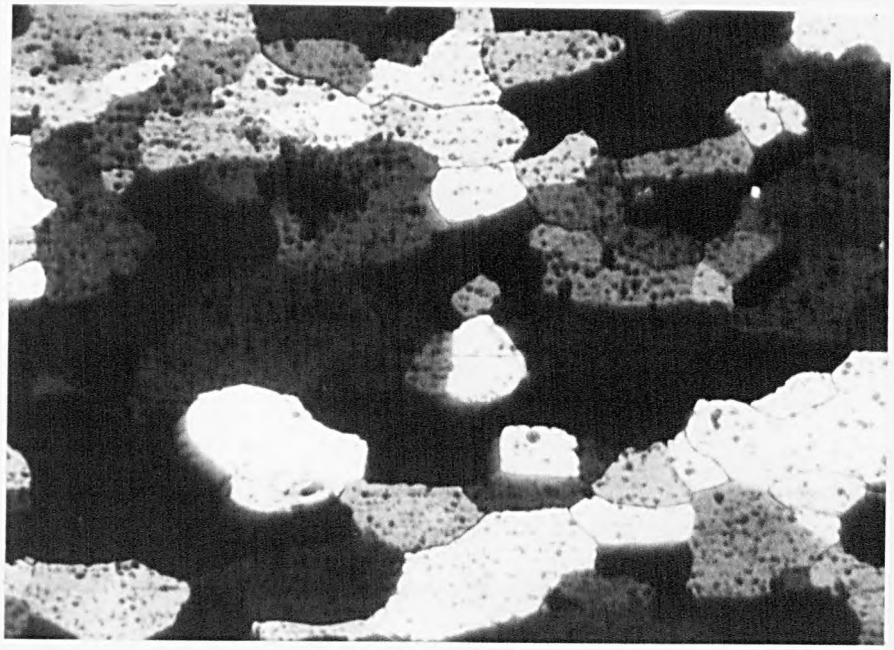

(d)

FIGURE 104: Microstructures taken at the centre of the gauge section of various plane strain compression specimens deformed at 400°C and 1 s^{-1} and fully recrystallised after annealing at the deformation temperature. Use of cartridge heaters in the deformation tools.

(a) $\varepsilon = 0.15$;
(b) $\varepsilon = 0.33$;
(c) $\varepsilon = 0.67$;
(d) $\varepsilon = 1.00$;
(e) $\varepsilon = 1.50$.

Mag. 100 x.

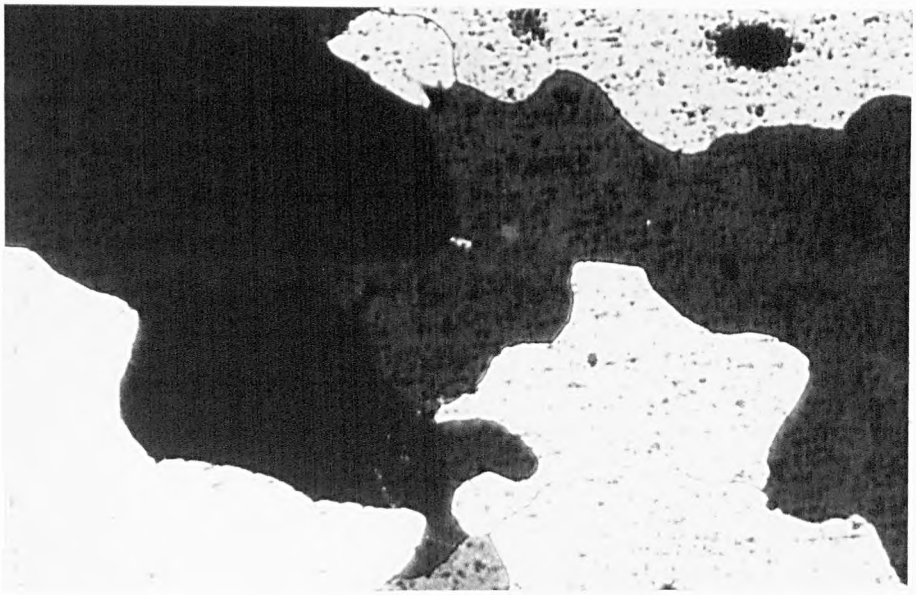

(a)

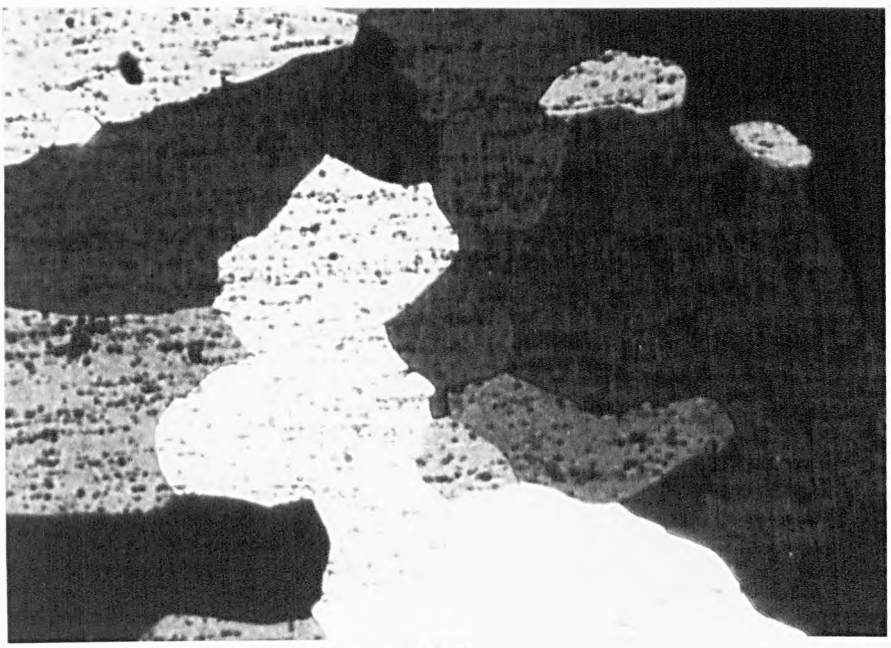

0,1 mm

(b)

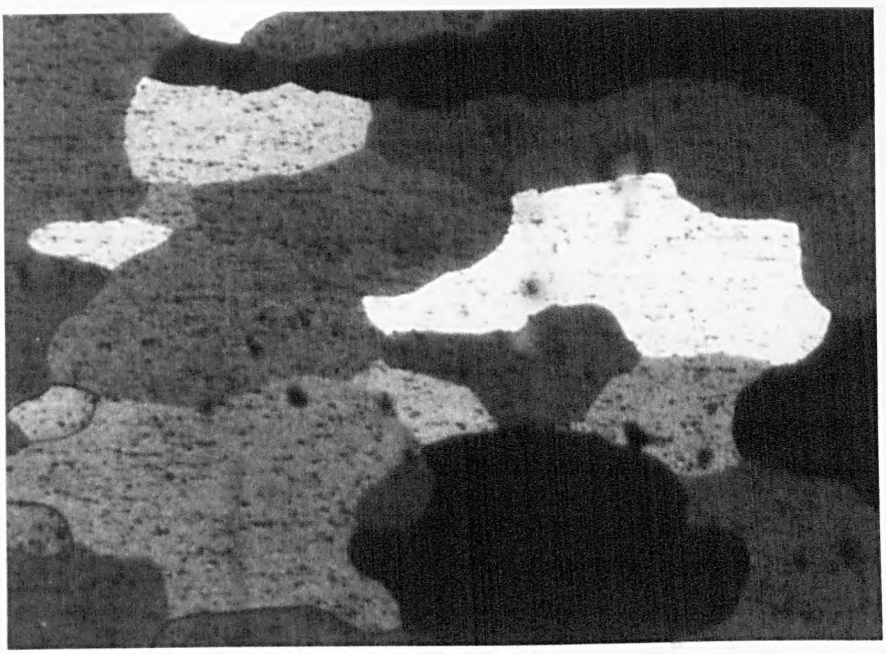

(c)

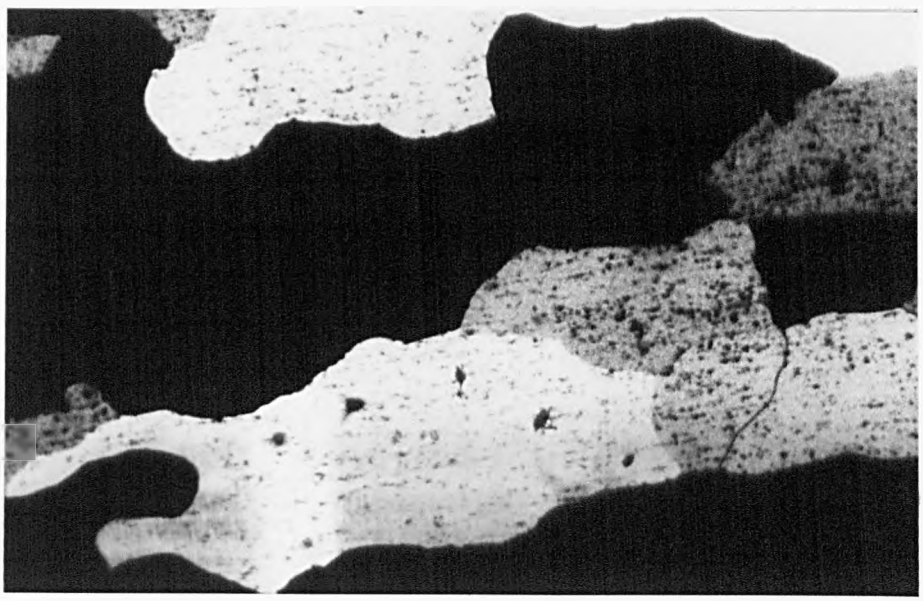

(d)

0,1 mm

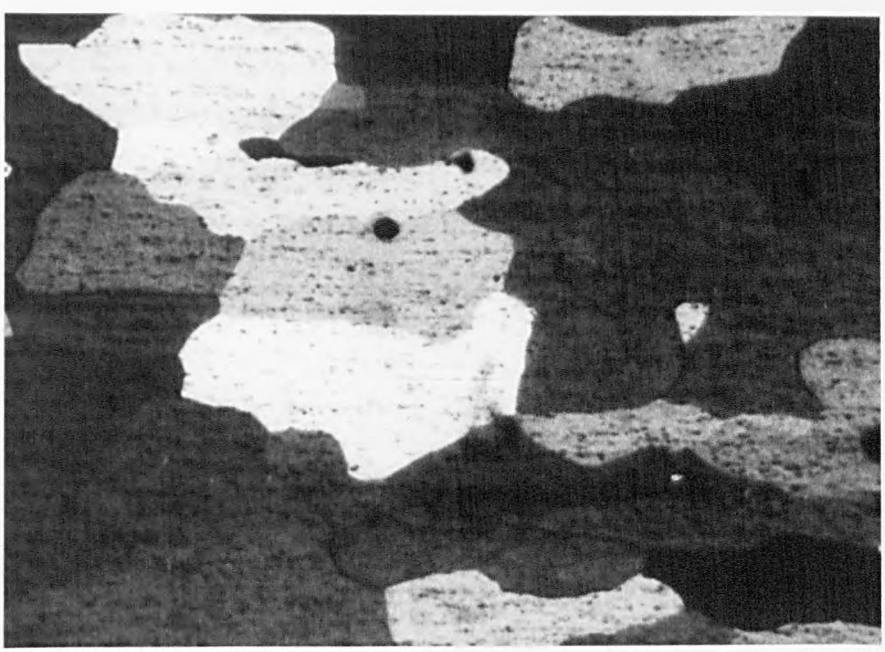

(e)

FIGURE 105: Relationship between log [d_{rex}] and log ε with and without use of cartridge heaters.

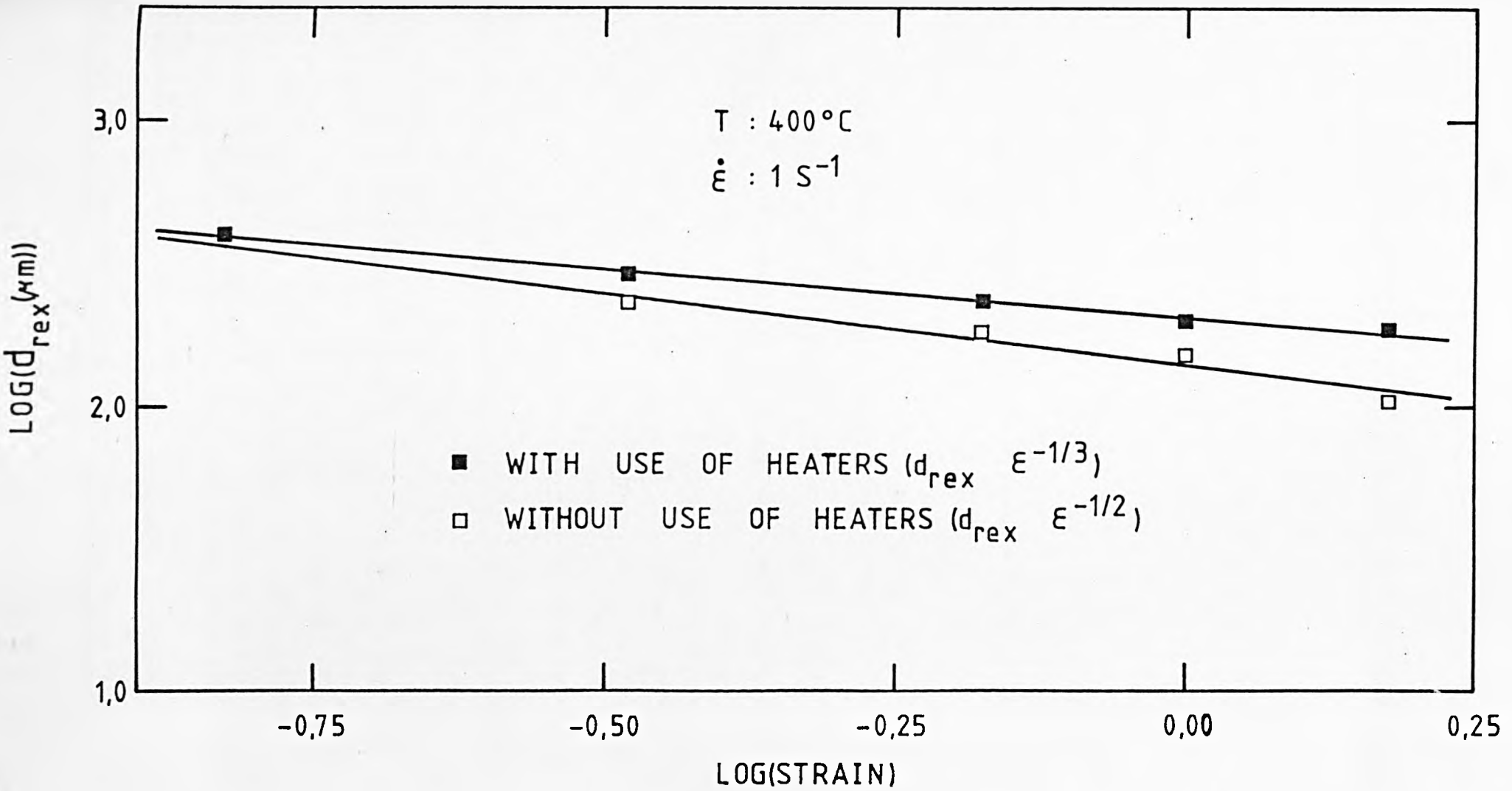
T : 400°C
$\dot{\varepsilon}$: 1 S^{-1}
WITH USE OF HEATERS (d_{rex} $\varepsilon^{-1/3}$)
WITHOUT USE OF HEATERS (d_{rex} $\varepsilon^{-1/2}$)
LOG(d_{rex}(µm))
3,0
2,0
1,0
-0,75
-0,50
-0,25
0,00
0,25
LOG(STRAIN)

FIGURE 106: Variation of the fraction restored with log [time (sec)] for Al-1%Mg alloy after deformation at different temperatures by 0.67 strain at a strain rate of 1 s^{-1}.

Initial grain size : 70 μm.

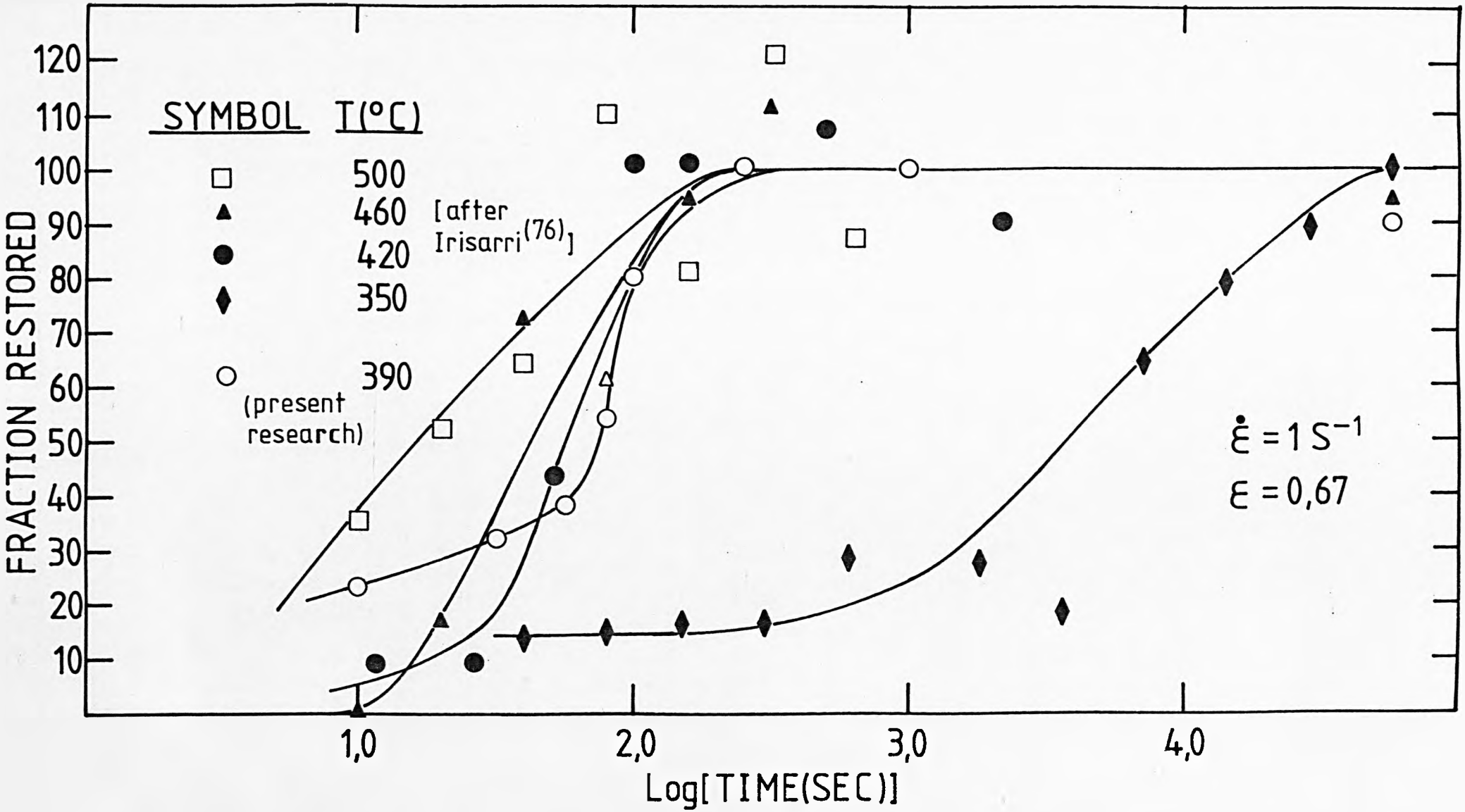
SYMBOL T(°C)
500
460
420
350
390
(present research)
[after Irisarri(76)]
$\dot{\varepsilon} = 1\,S^{-1}$
$\varepsilon = 0{,}67$
FRACTION RESTORED
120
110
100
90
80
70
60
50
40
30
20
10
1,0
2,0
3,0
4,0
Log[TIME(SEC)]

FIGURE 107: Variation of the fraction restored with log [time (sec)] for Al-1%Mg alloy after deformation at different temperatures by 0.67 strain at a strain rate of 0.1 s^{-1}.

Initial grain size : 70 μm.

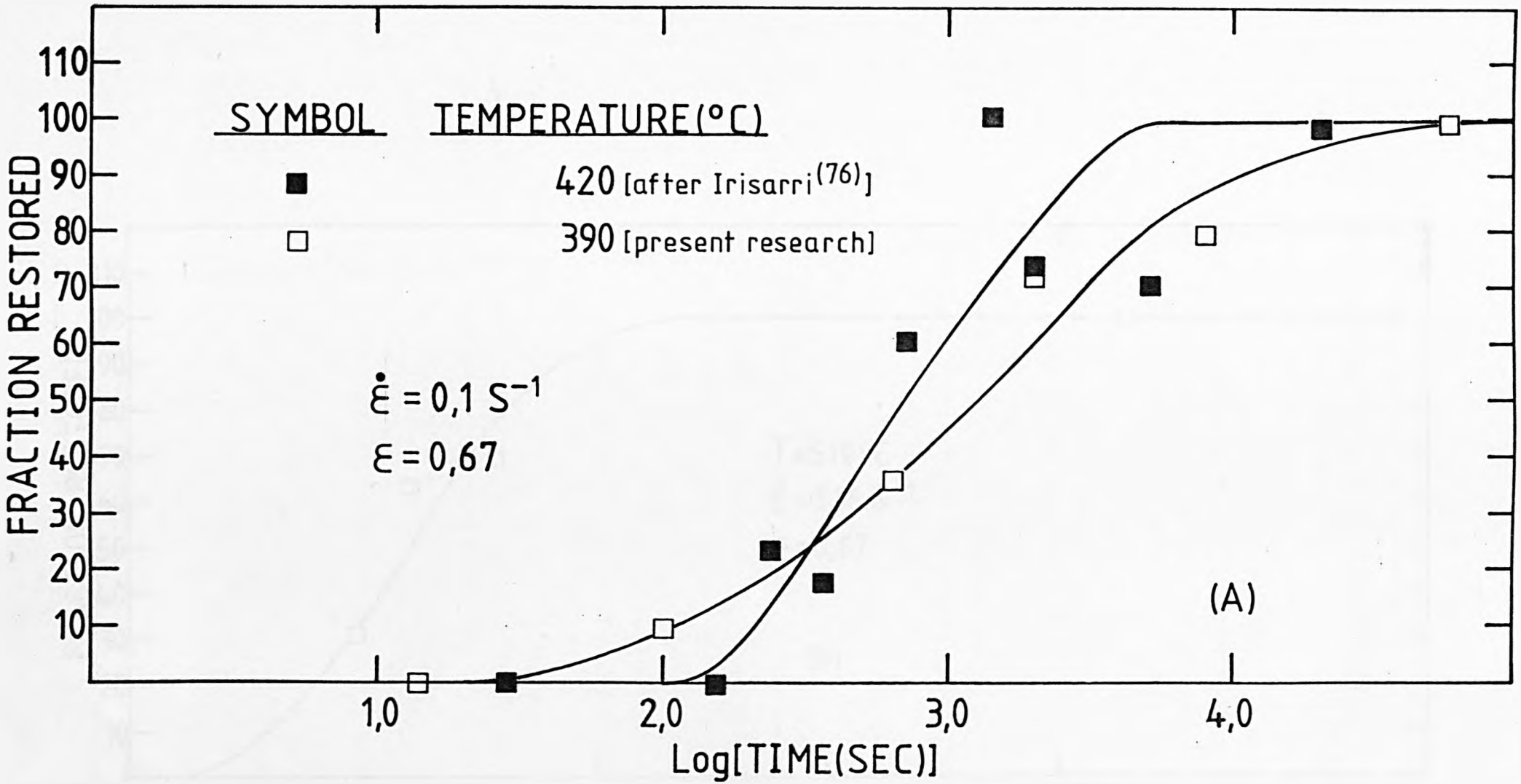
SYMBOL TEMPERATURE(°C)
420 [after Irisarri(76)]
390 [present research]
$\dot{\varepsilon} = 0,1\ S^{-1}$
$\varepsilon = 0,67$
(A)
FRACTION RESTORED
110
100
90
80
70
60
50
40
30
20
10
1,0
2,0
3,0
4,0
Log[TIME(SEC)]

FIGURE 108: Relationship between log $t_{0.5}$ and 1/T at constant strain rates. Qapp ≈ 54.8 kJ/mol.

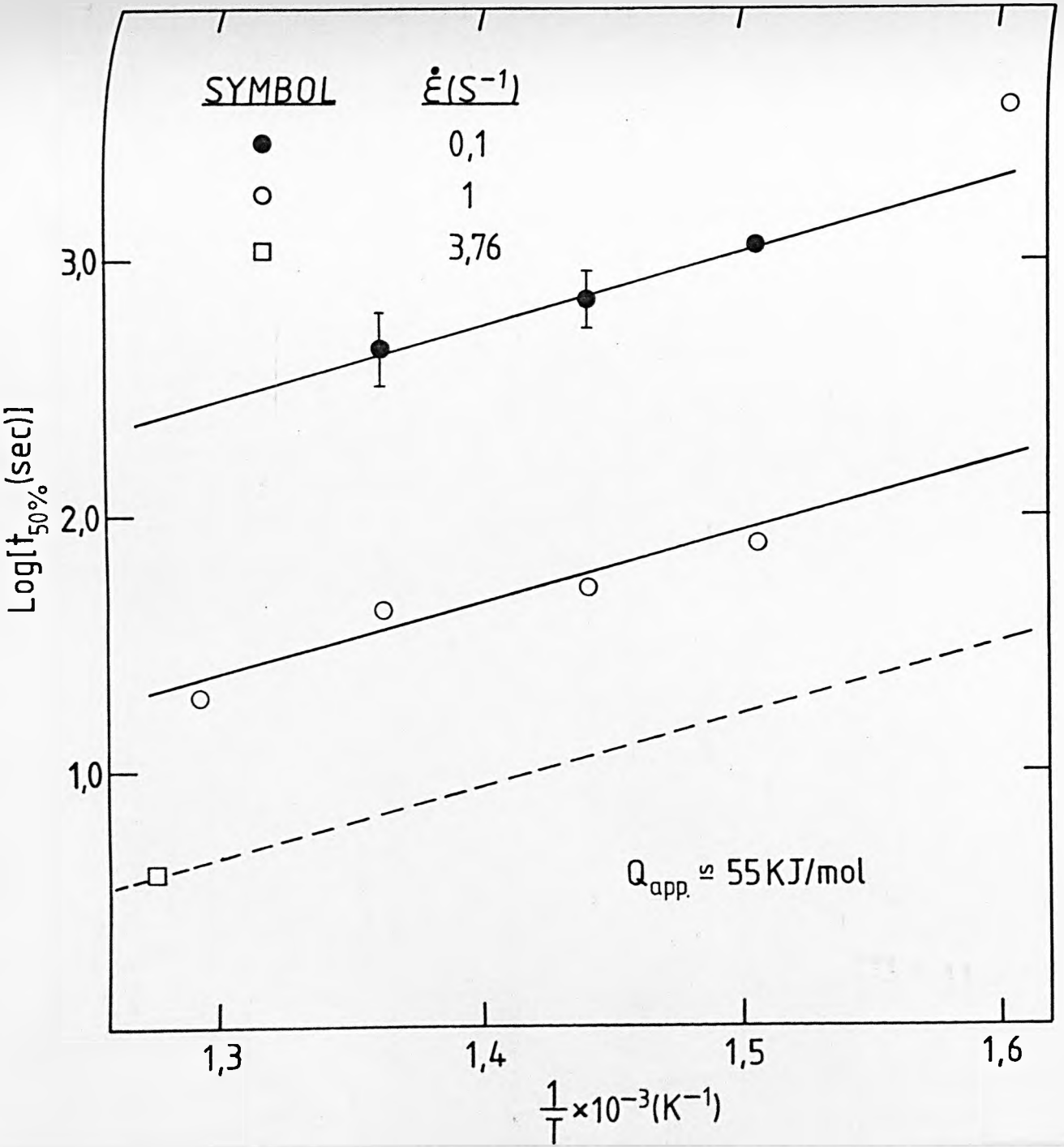
SYMBOL
$\dot{\varepsilon}(S^{-1})$
0,1
1
3,76
3,0
2,0
1,0
$Log[t_{50\%}(sec)]$
$Q_{app.} \simeq 55 KJ/mol$
1,3
1,4
1,5
1,6
$\frac{1}{T} \times 10^{-3}(K^{-1})$

FIGURE 109: Relationship between log $t_{0.5}$ and 1/T at a constant Z value of 9.716×10^{10} s^{-1}. Qrex ≃ 230 kJ/mol.

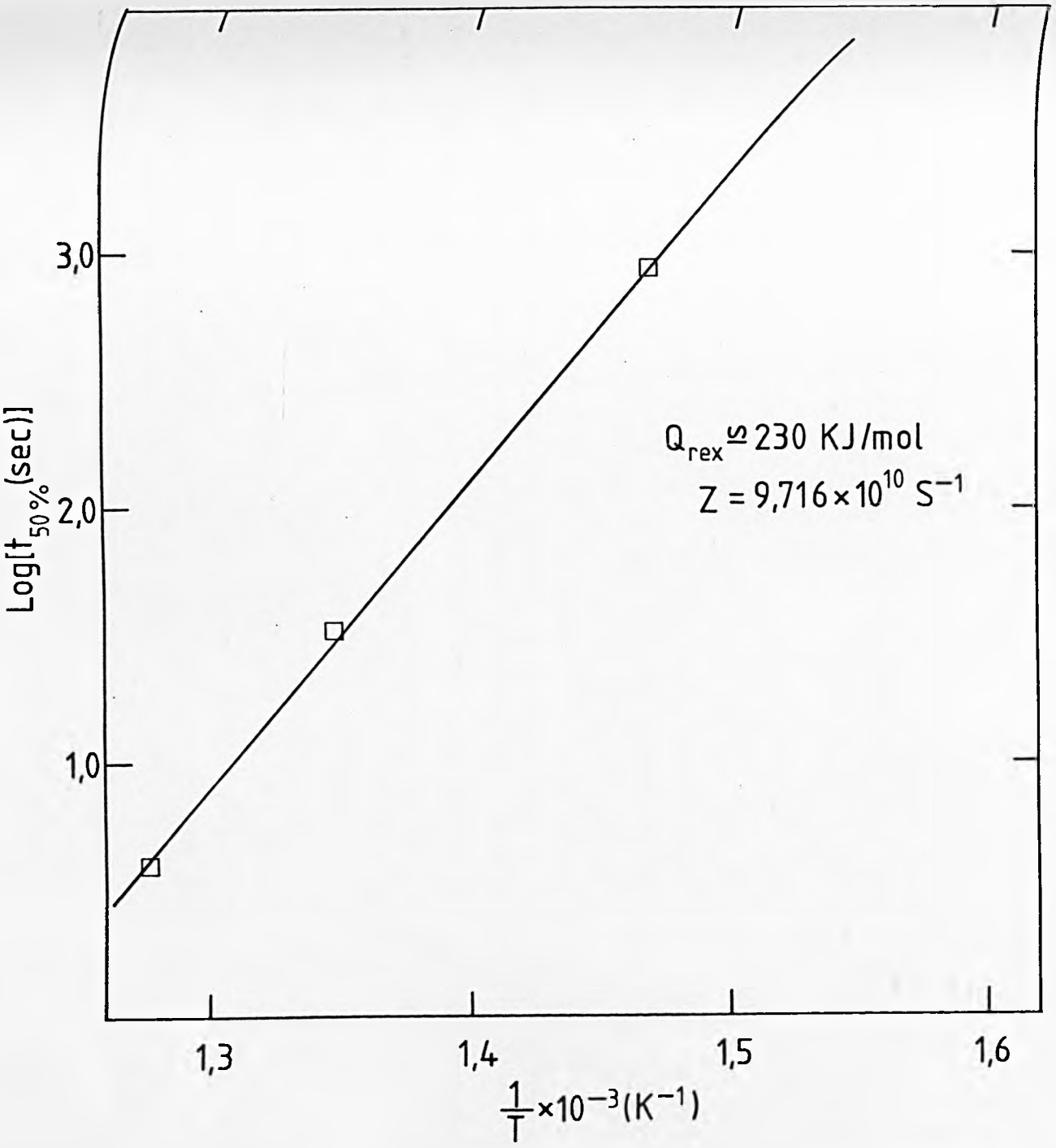
3,0
2,0
1,0
Log[t50%(sec)]
Qrex ≅ 230 KJ/mol
Z = 9,716×10^10 S^-1
1,3
1,4
1,5
1,6
1/T ×10^-3(K^-1)

FIGURE 110: Relationship between log (d_{rex}) and log Z after deformation by 0.67 strain at a strain rate 1 s^{-1}.

Initial grain size : 70 µm.

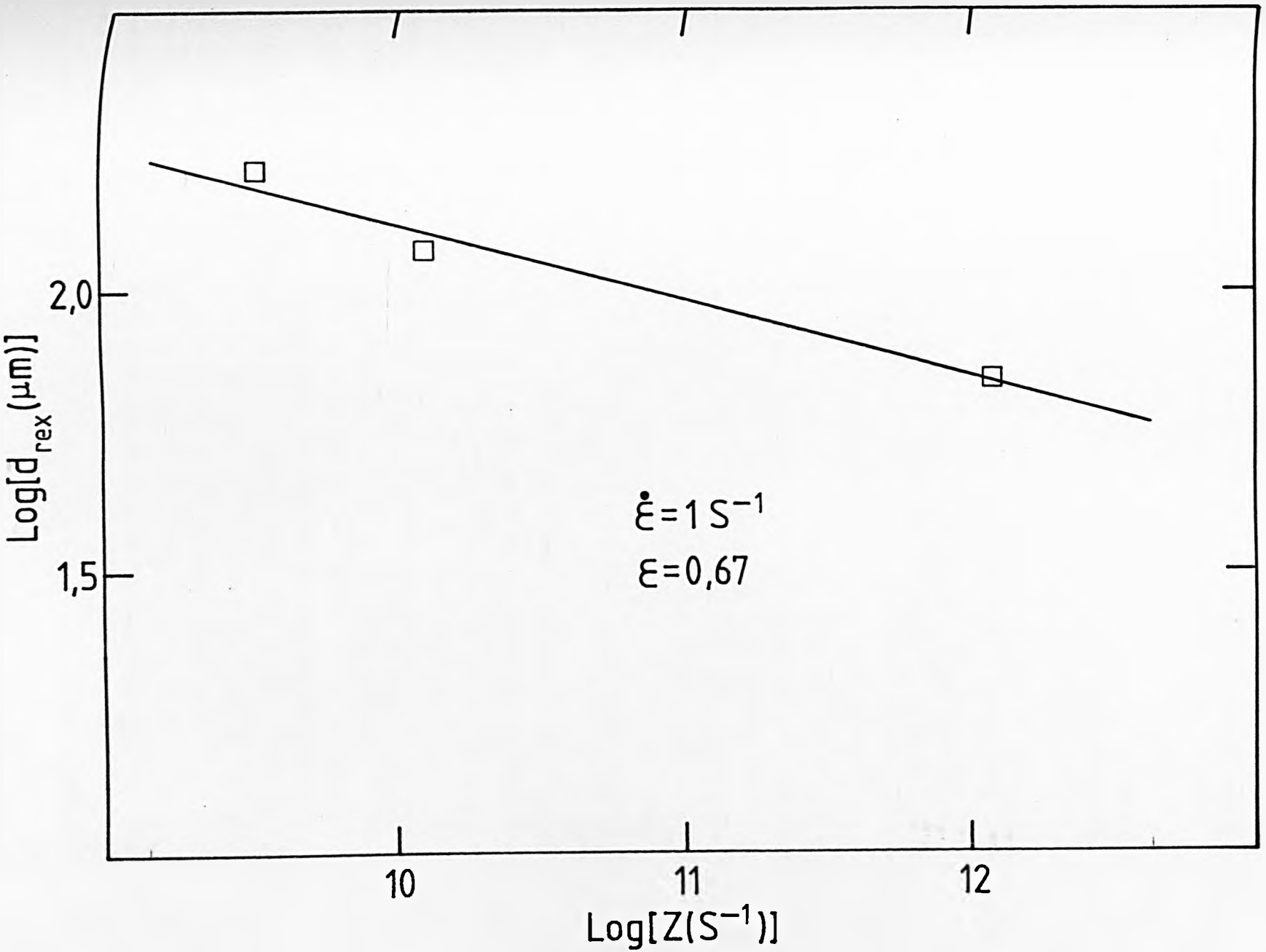
2,0
1,5
Log[d_rex(µm)]
ε̇=1 S⁻¹
ε=0,67
10
11
12
Log[Z(S⁻¹)]

FIGURE 111: Microstructures taken at the centre of the gauge section of various plane strain compression specimens deformed at different temperatures by 0.67 strain at a strain rate of 1 s^{-1} and with different initial grain sizes.

(a) T = 460°C, do = 54 µm;
(b) T = 460°C, do = 65 µm;
(c) T = 460°C, do = 91 µm;
(d) T = 460°C, do = 112 µm;
(e) T = 350°C, do = 70 µm;
(f) T = 500°C, do = 70 µm.

Mag. 100 x.

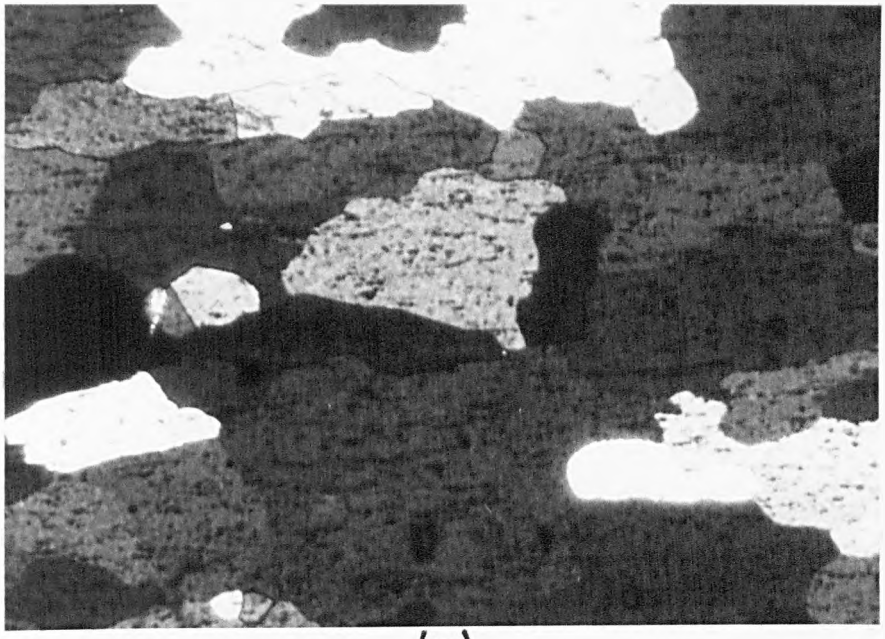

(a)

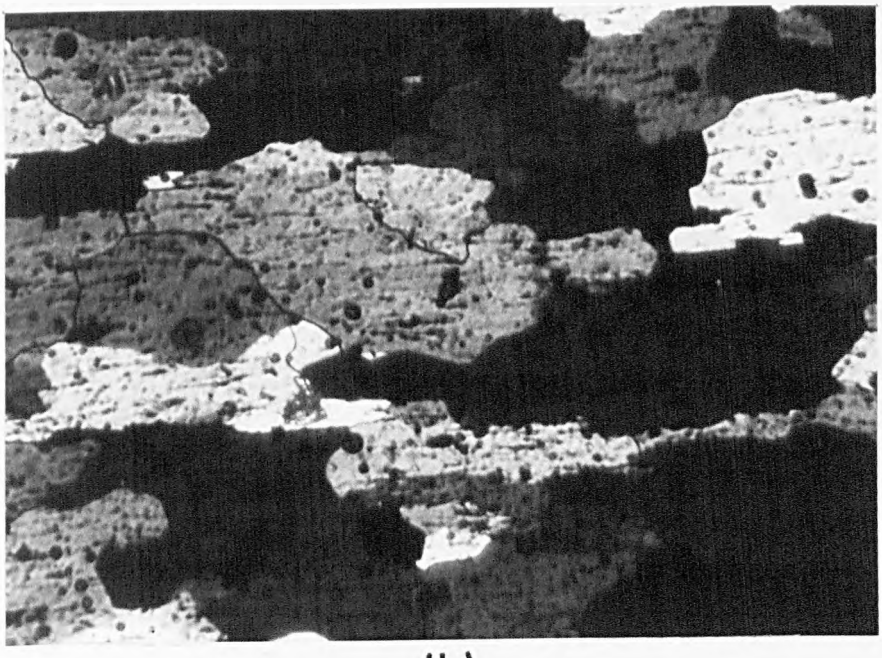

0,1 mm

(b)

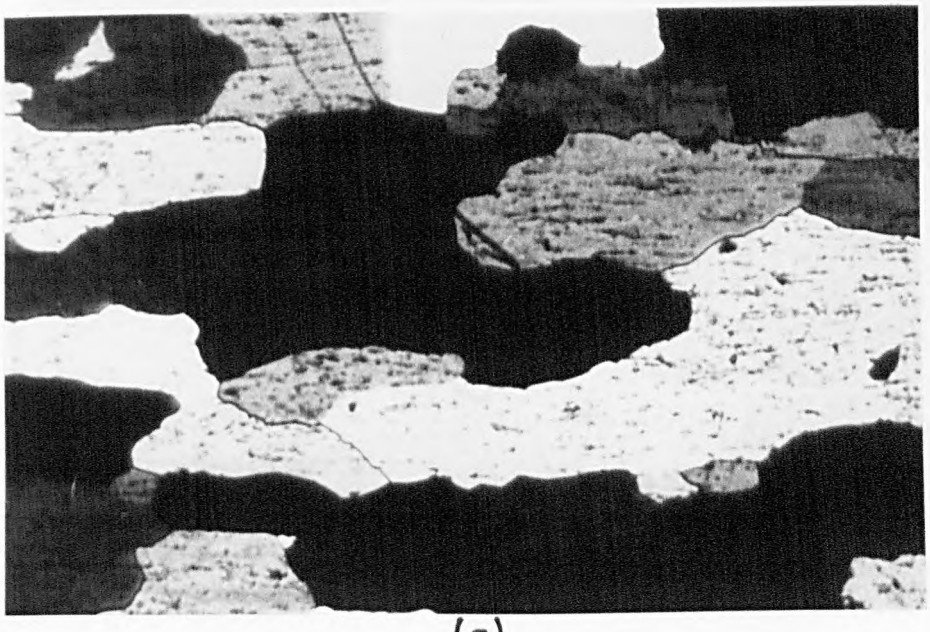

(c)

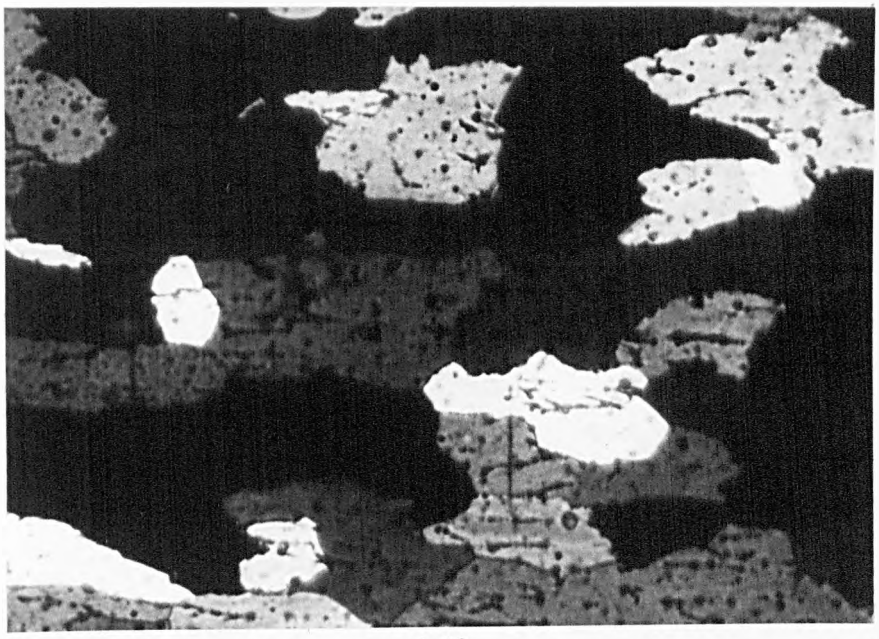

(d)

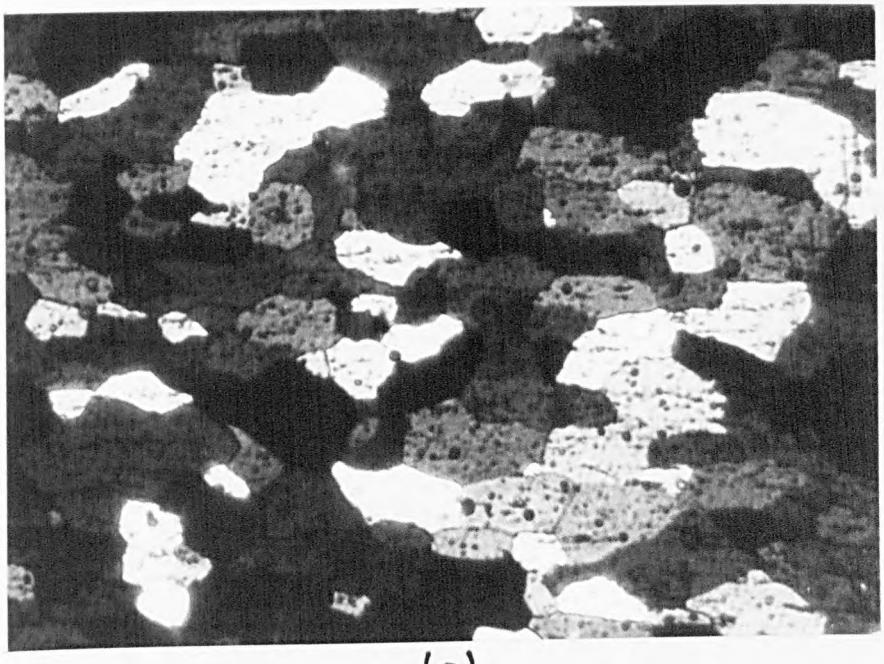

0,1 mm

(e)

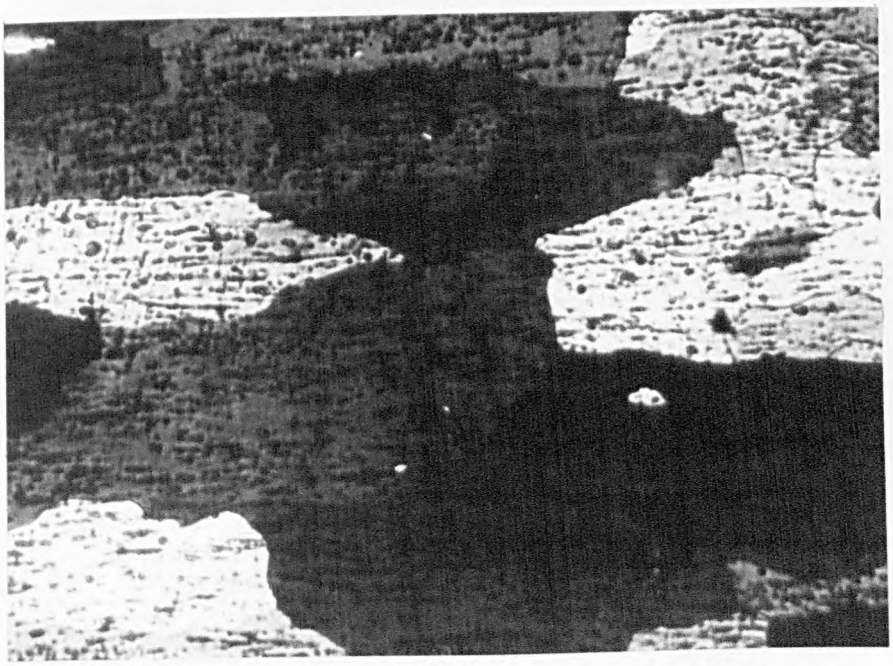

(f)

FIGURE 112: Variation of the fraction restored with log t for Al-1%Mg alloy after deformation by 0.67 strain at 460°C and a strain rate of 1 s^{-1} with specimens of different initial grain sizes.

(After Irrisari [76])

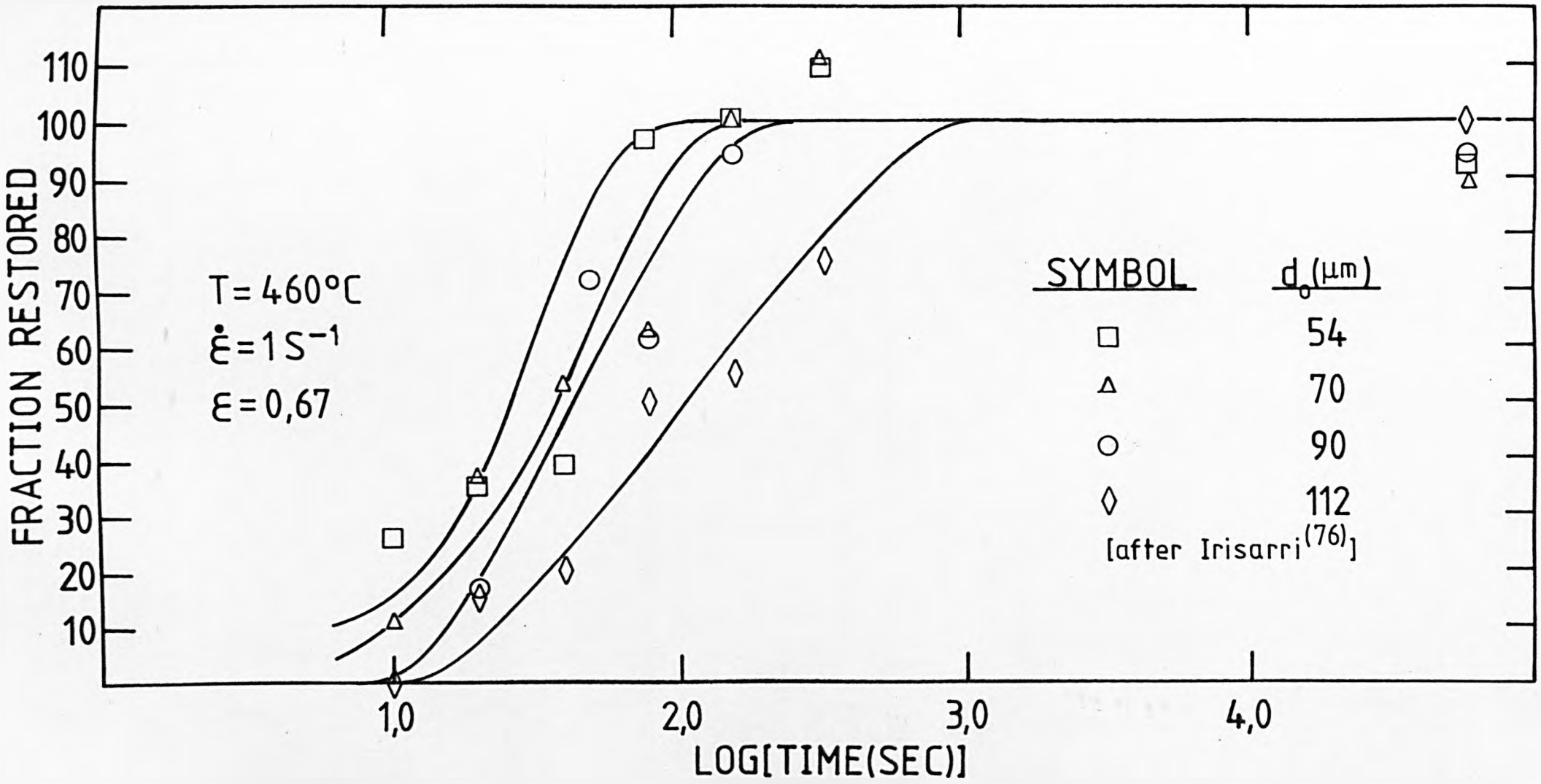
FRACTION RESTORED
110
100
90
80
70
60
50
40
30
20
10
T = 460°C
$\dot{\varepsilon} = 1\,S^{-1}$
$\varepsilon = 0{,}67$
SYMBOL
d_o (µm)
54
70
90
112
[after Irisarri(76)]
1,0
2,0
3,0
4,0
LOG[TIME(SEC)]

FIGURE 113: Relationship between log $t_{0.5}$ and log do after deformation by 0.67 strain at 460°C and a strain rate of 1 s^{-1}.

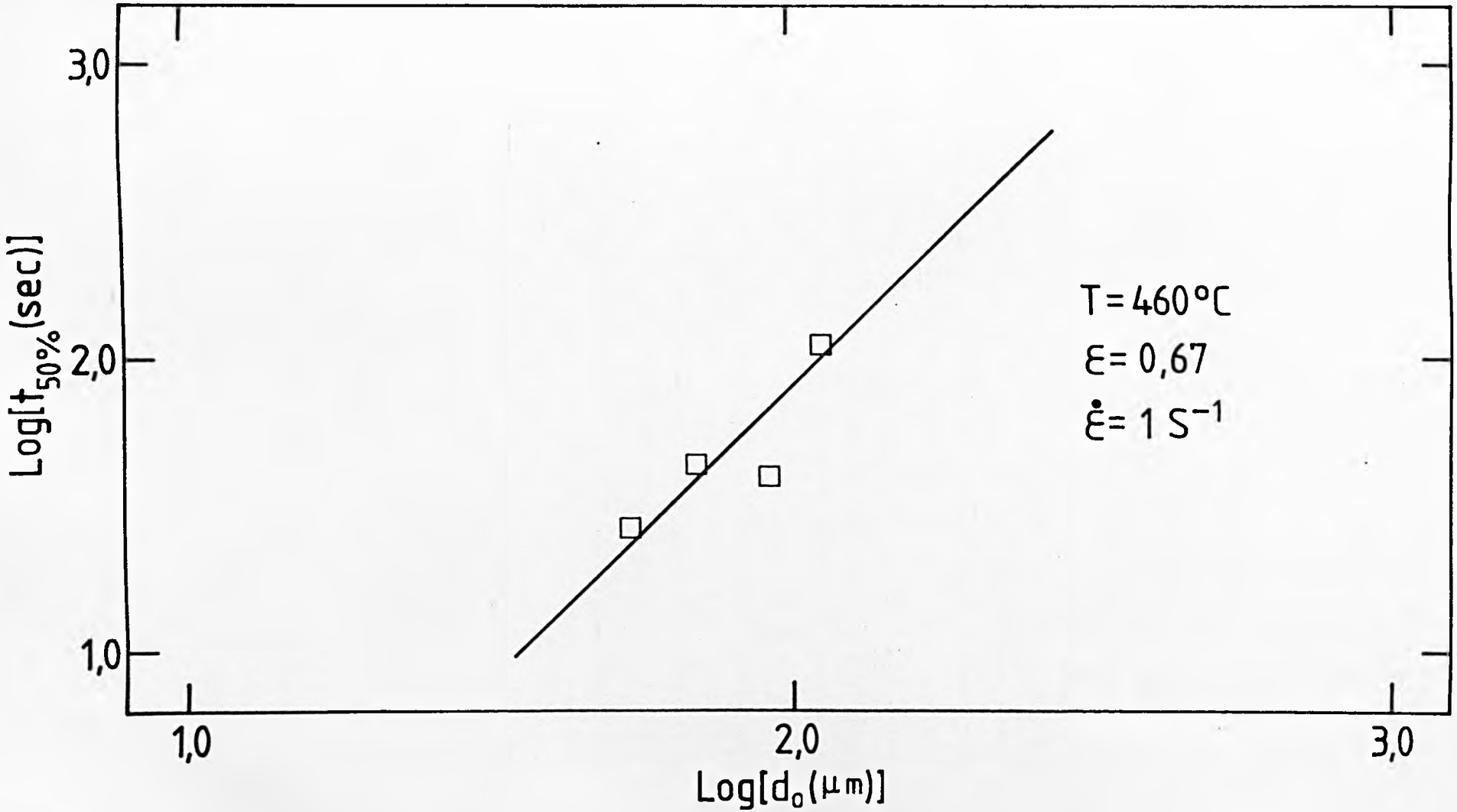
3,0
2,0
1,0
Log[$t_{50\%}$(sec)]
1,0
2,0
3,0
Log[d_o(μm)]
T = 460°C
ε = 0,67
$\dot{\varepsilon}$ = 1 S^{-1}

FIGURE 114: Relationship between log d_{rex} and log do after deformation at 460°C by a strain of 0.67 at a strain rate of 1 s^{-1}.

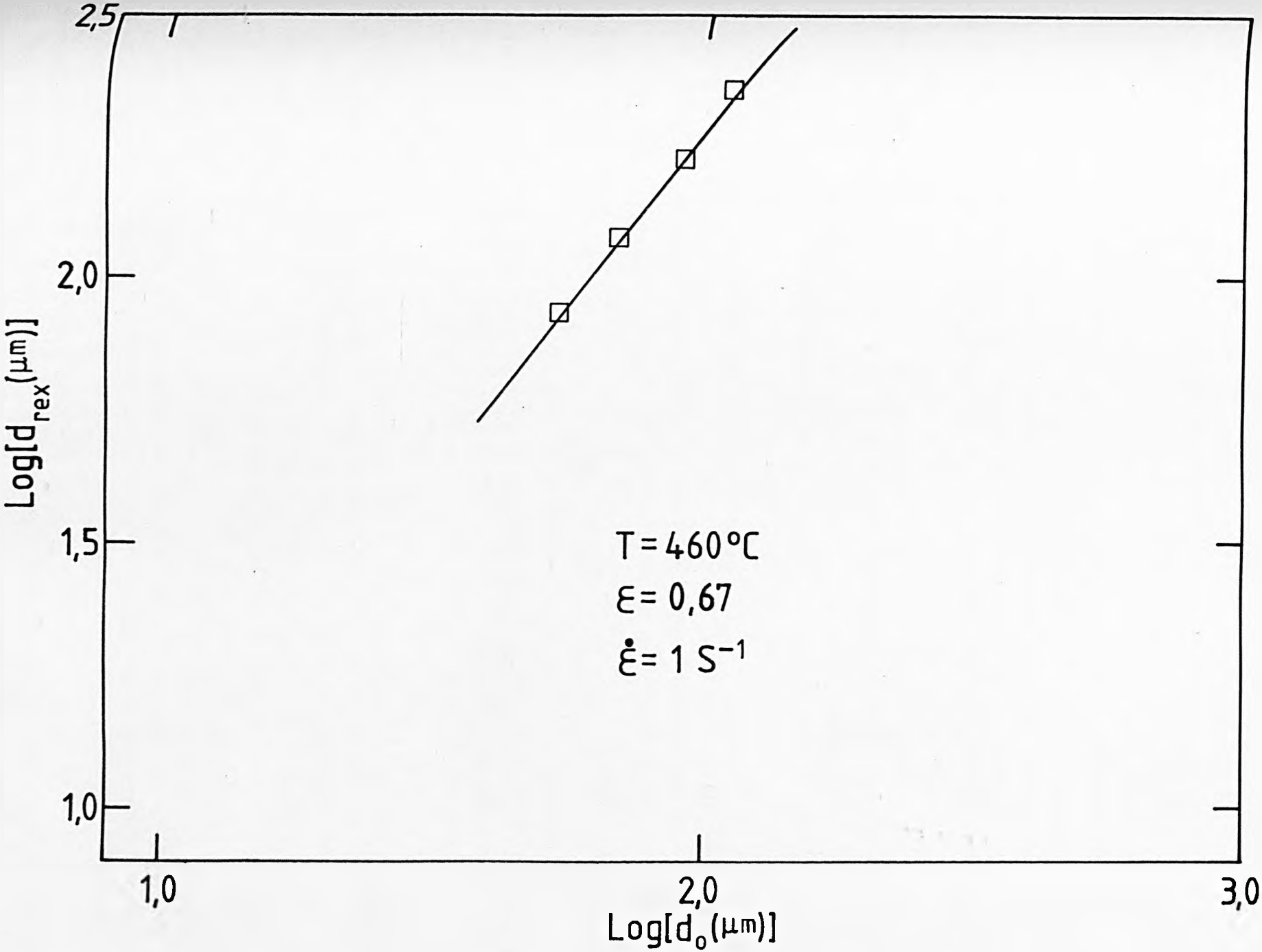
2,5
2,0
1,5
1,0
Log[d_rex(μm)]
T = 460°C
ε = 0,67
ε̇ = 1 S⁻¹
1,0
2,0
3,0
Log[d_o(μm)]

FIGURE 115: Mean stress-strain curves obtained during the second deformation of three deformation schedules after annealing times of 1.7 and 320 sec. following deformation at 400°C and a strain rate of 1 s^{-1}.

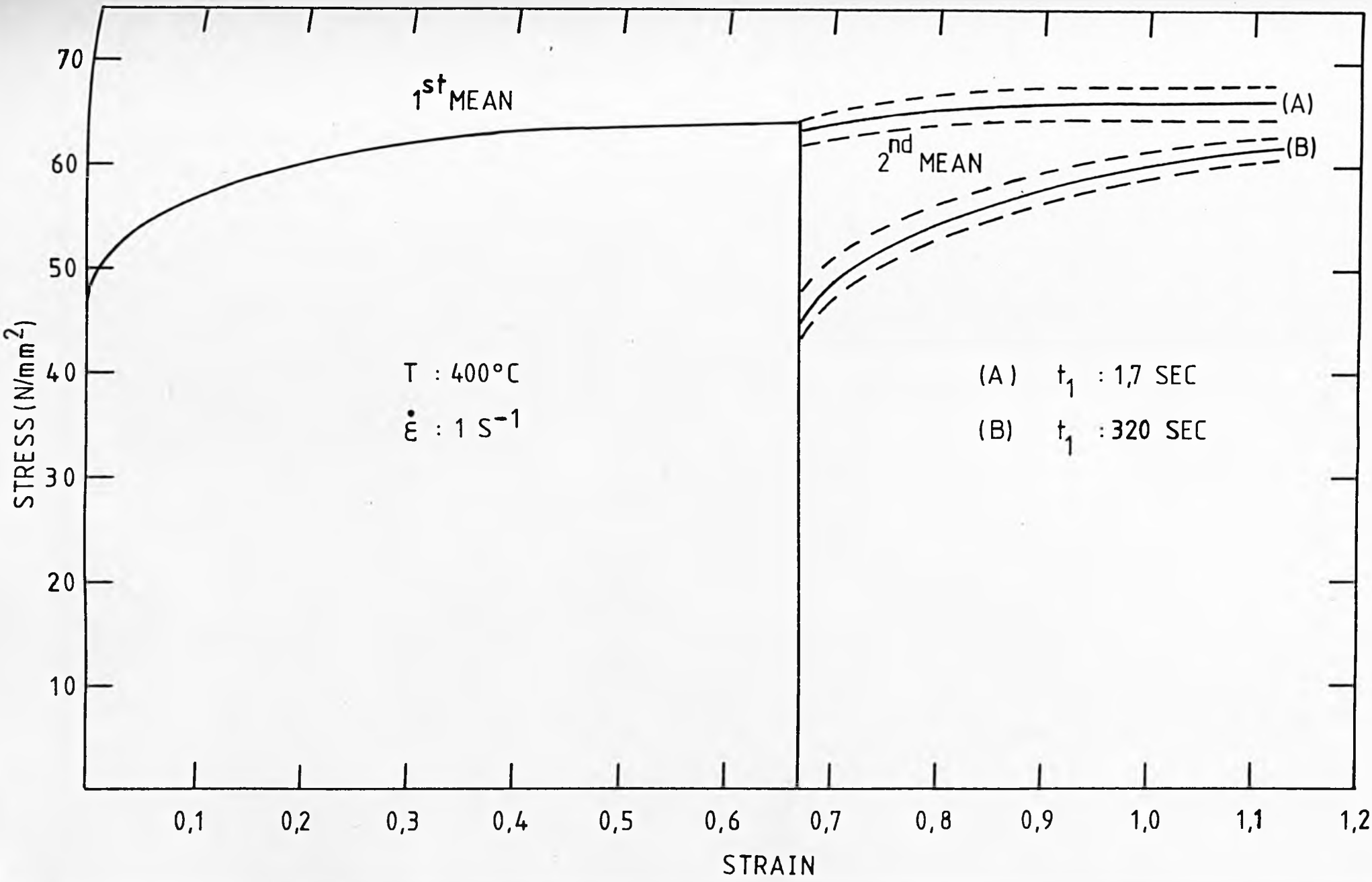
70
60
50
40
30
20
10
STRESS (N/mm²)
1st MEAN
2nd MEAN
(A)
(B)
T : 400°C
ε̇ : 1 S⁻¹
(A) t1 : 1,7 SEC
(B) t1 : 320 SEC
0,1
0,2
0,3
0,4
0,5
0,6
0,7
0,8
0,9
1,0
1,1
1,2
STRAIN

FIGURE 116: Description of the parameters involved in the definition of the restoration index in three deformation schedules R_2.

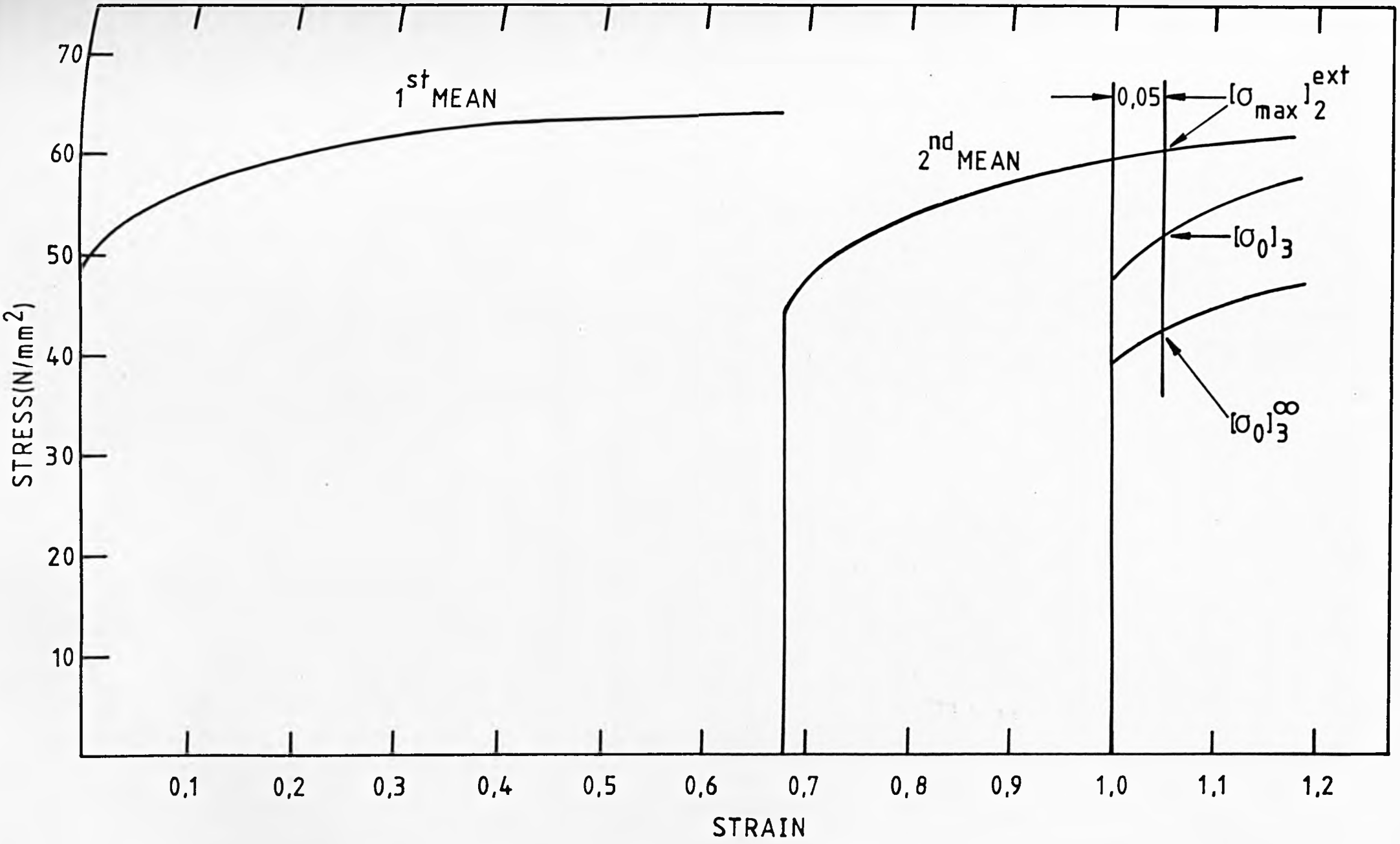
70
60
50
40
30
20
10
STRESS(N/mm2)
1st MEAN
2nd MEAN
0,05
[σmax]2ext
[σ0]3
[σ0]3∞
0,1
0,2
0,3
0,4
0,5
0,6
0,7
0,8
0,9
1,0
1,1
1,2
STRAIN

FIGURE 117: Stress-strain curves obtained in three deformation schedules with different time intervals between the second and third deformations. Temperature of deformation: 400°C; mean strain rate: 1 s^{-1}. Strain applied in the first deformation: 0.67. Strain applied in the second deformation: 0.33. Initial grain size: 90 μm.

(a) time interval between the first and second deformation t_1 : 1.7 sec.

(b) t_1 : 100 sec.

(c) t_1 : 320 sec.

(d) t_1 : 16 hrs.

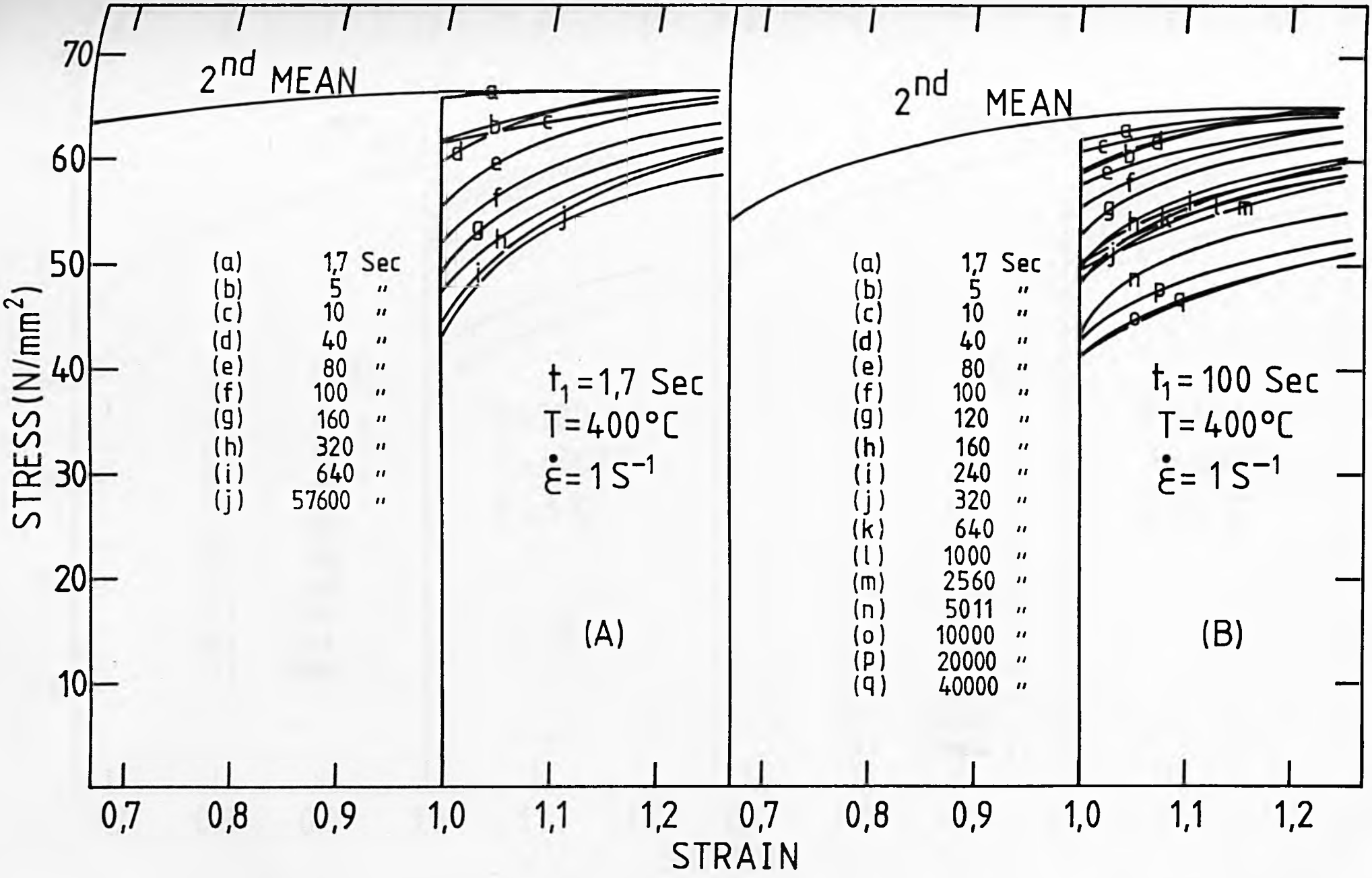
2nd MEAN
(a) 1,7 Sec
(b) 5 "
(c) 10 "
(d) 40 "
(e) 80 "
(f) 100 "
(g) 160 "
(h) 320 "
(i) 640 "
(j) 57600 "
t1 = 1,7 Sec
T = 400 °C
ε̇ = 1 S−1
(A)
2nd MEAN
(a) 1,7 Sec
(b) 5 "
(c) 10 "
(d) 40 "
(e) 80 "
(f) 100 "
(g) 120 "
(h) 160 "
(i) 240 "
(j) 320 "
(k) 640 "
(l) 1000 "
(m) 2560 "
(n) 5011 "
(o) 10000 "
(p) 20000 "
(q) 40000 "
t1 = 100 Sec
T = 400 °C
ε̇ = 1 S−1
(B)
STRESS (N/mm2)
STRAIN
70
60
50
40
30
20
10
0,7
0,8
0,9
1,0
1,1
1,2

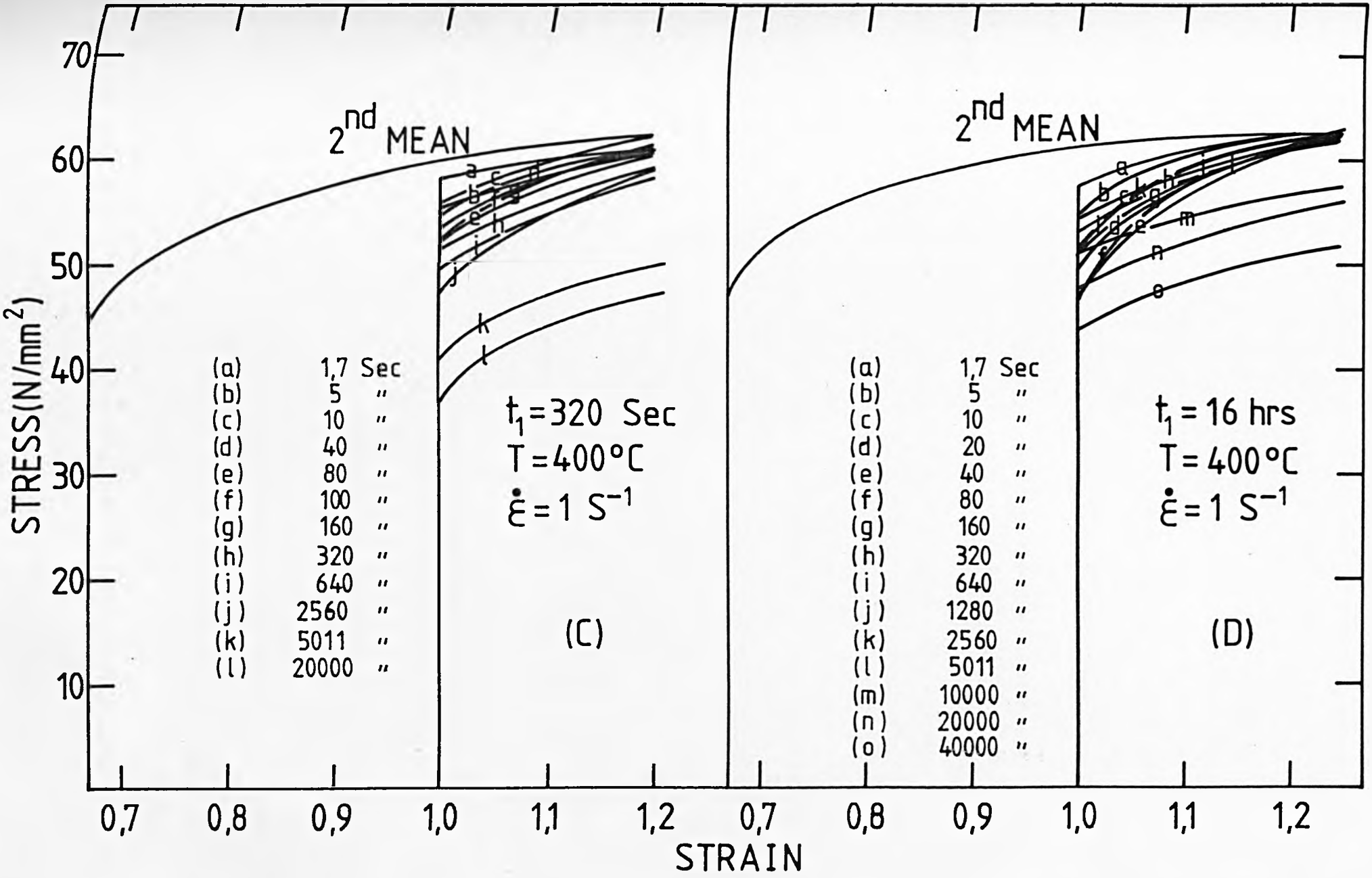
2nd MEAN
STRESS(N/mm²)
STRAIN
(a) 1,7 Sec
(b) 5 "
(c) 10 "
(d) 40 "
(e) 80 "
(f) 100 "
(g) 160 "
(h) 320 "
(i) 640 "
(j) 2560 "
(k) 5011 "
(l) 20000 "
t1=320 Sec
T=400°C
ε̇=1 S⁻¹
(C)
2nd MEAN
(a) 1,7 Sec
(b) 5 "
(c) 10 "
(d) 20 "
(e) 40 "
(f) 80 "
(g) 160 "
(h) 320 "
(i) 640 "
(j) 1280 "
(k) 2560 "
(l) 5011 "
(m) 10000 "
(n) 20000 "
(o) 40000 "
t1=16 hrs
T=400°C
ε̇=1 S⁻¹
(D)

FIGURE 118: (a) Variation of the restoration index R_2 with log [t_2 (sec)] after deformation at 400°C and a strain rate of 1 s^{-1}, and different time intervals between the first and second deformation: (A) t_1 = 1.7 sec (B) t_1 = 100 sec (C) t_1 = 320 sec and (D) t_1 = 16 hrs.

(b) Variation of the restoration index R_2 corrected for recovery effects with log [t_2 (sec)]. Deformation conditions same as above.

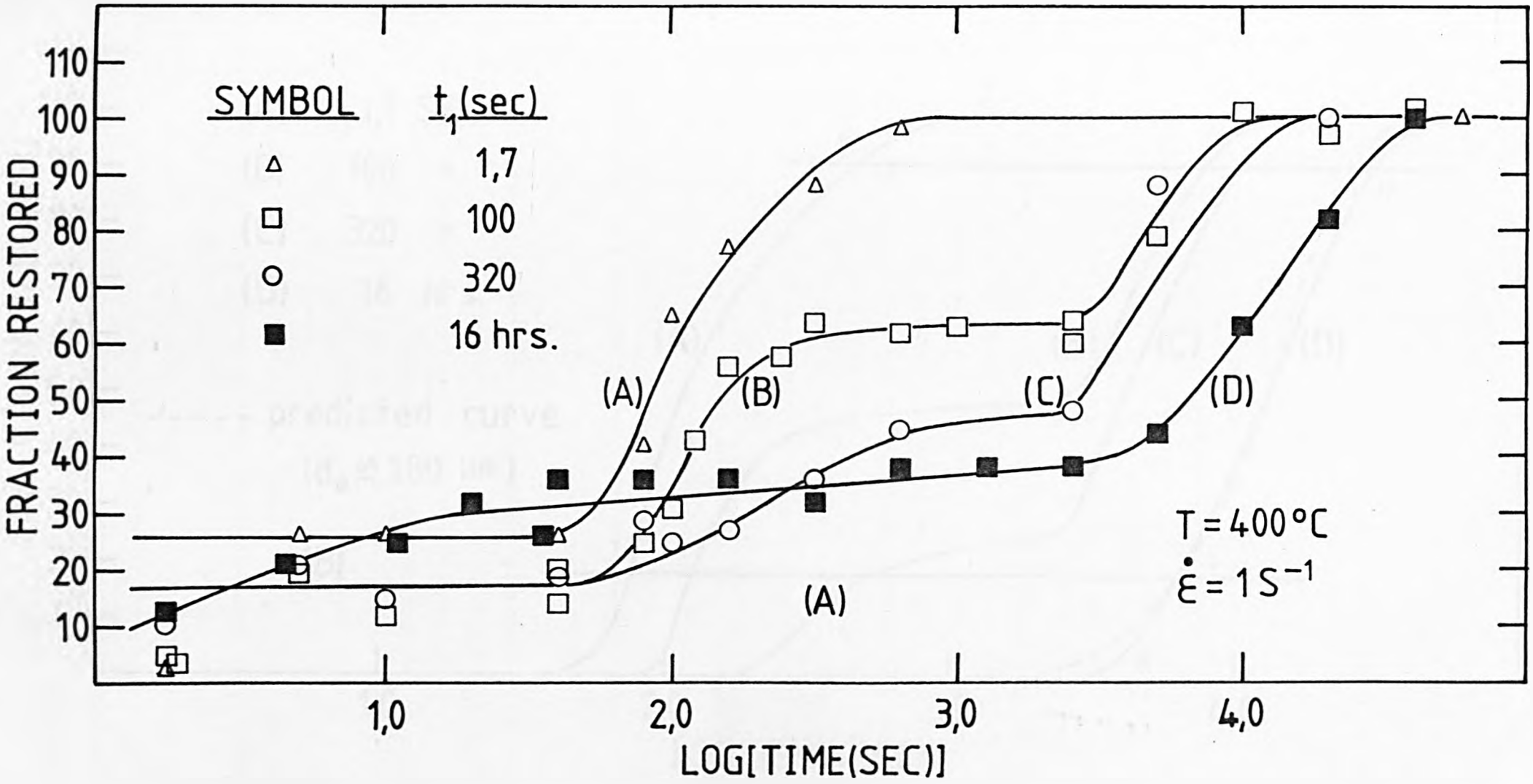
SYMBOL
t_1(sec)
1,7
100
320
16 hrs.
(A)
(B)
(C)
(D)
(A)
T = 400 °C
$\dot{\varepsilon} = 1\,S^{-1}$
FRACTION RESTORED
110
100
90
80
70
60
50
40
30
20
10
1,0
2,0
3,0
4,0
LOG[TIME(SEC)]

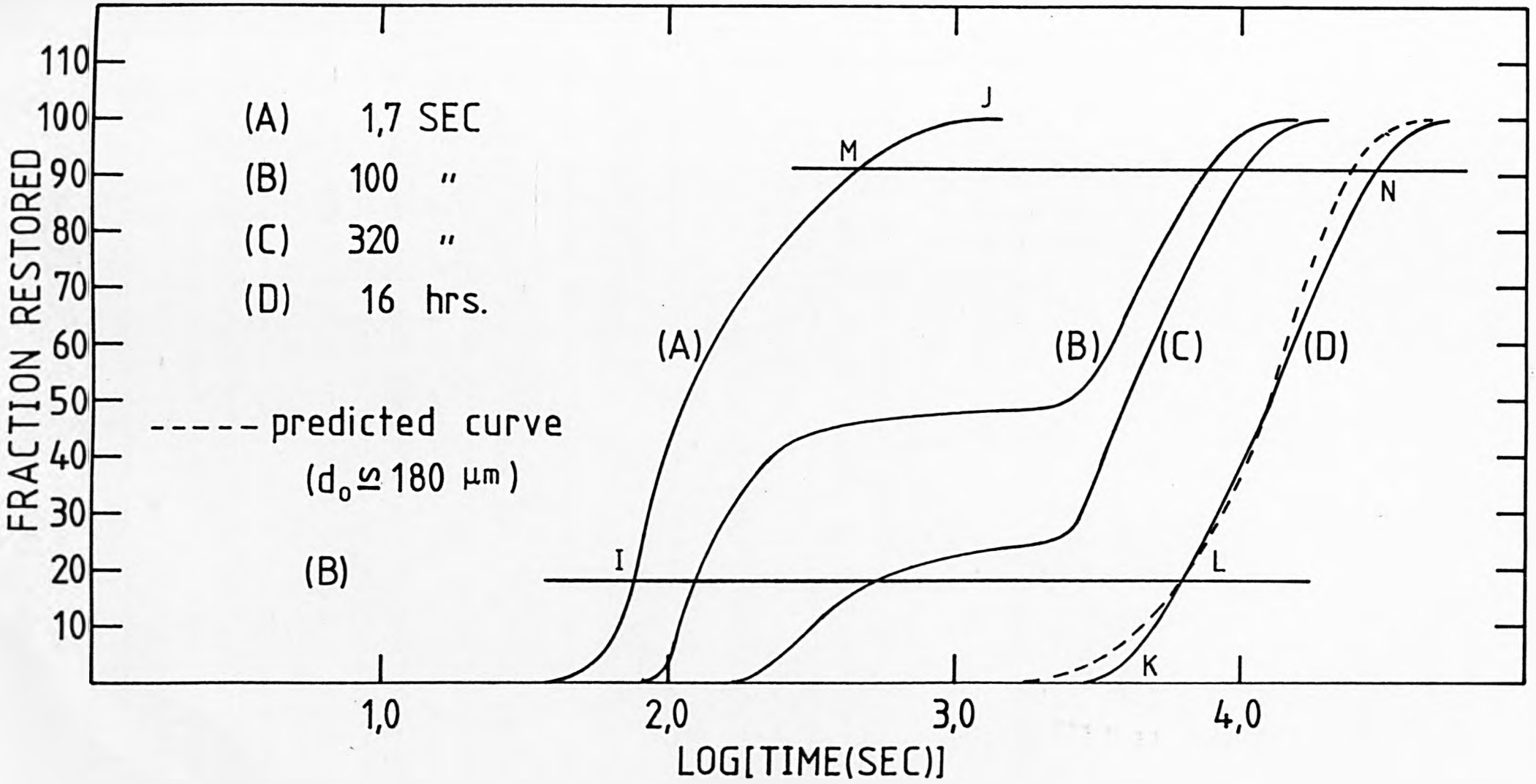
FRACTION RESTORED
110
100
90
80
70
60
50
40
30
20
10
(A) 1,7 SEC
(B) 100 "
(C) 320 "
(D) 16 hrs.
----- predicted curve
($d_o \leq 180$ µm)
(B)
(A)
(B)
(C)
(D)
I
J
K
L
M
N
1,0
2,0
3,0
4,0
LOG[TIME(SEC)]

FIGURE 119: (a) Predicted and experimental relationships between the restoration index R_2 and log $[t_2$ (sec)], assuming the model of the independent recrystallisation of fractions with different accumulated strain.

(b) Variation of the fraction restored expressed by the restoration index R_1 corrected for recovery effects and the volume fraction recrystallised for specimens of Al-1%Mg alloy deformed at 400°C and 1 s^{-1}.

(c) Theoretical predictions of the relationship between fraction restored and fraction recrystallised in three deformation schedules.

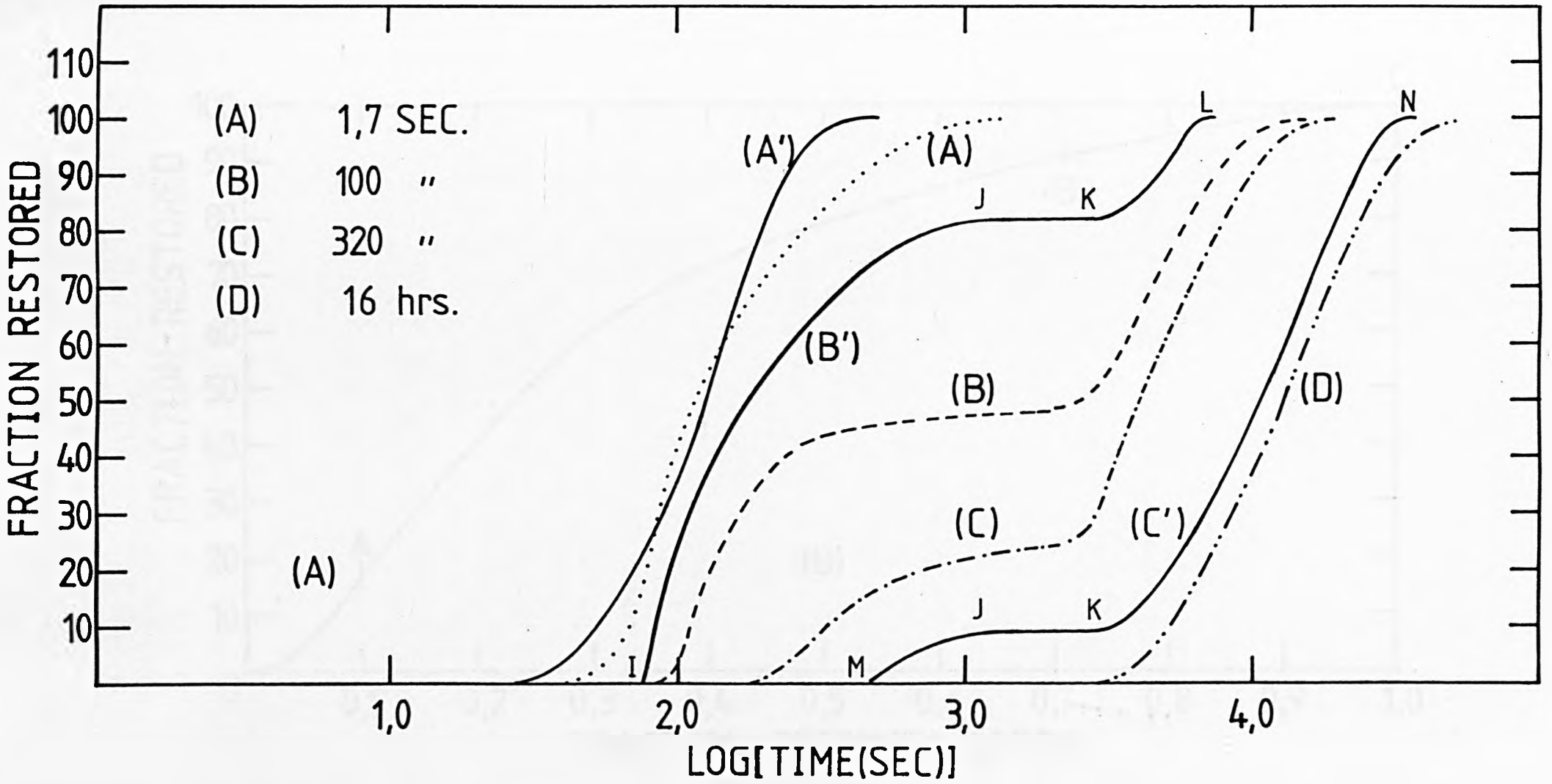
FRACTION RESTORED
110
100
90
80
70
60
50
40
30
20
10
(A) 1,7 SEC.
(B) 100 "
(C) 320 "
(D) 16 hrs.
(A')
(A)
(B')
(B)
(C)
(C')
(D)
(A)
I
J
K
L
M
N
J
K
1,0
2,0
3,0
4,0
LOG[TIME(SEC)]

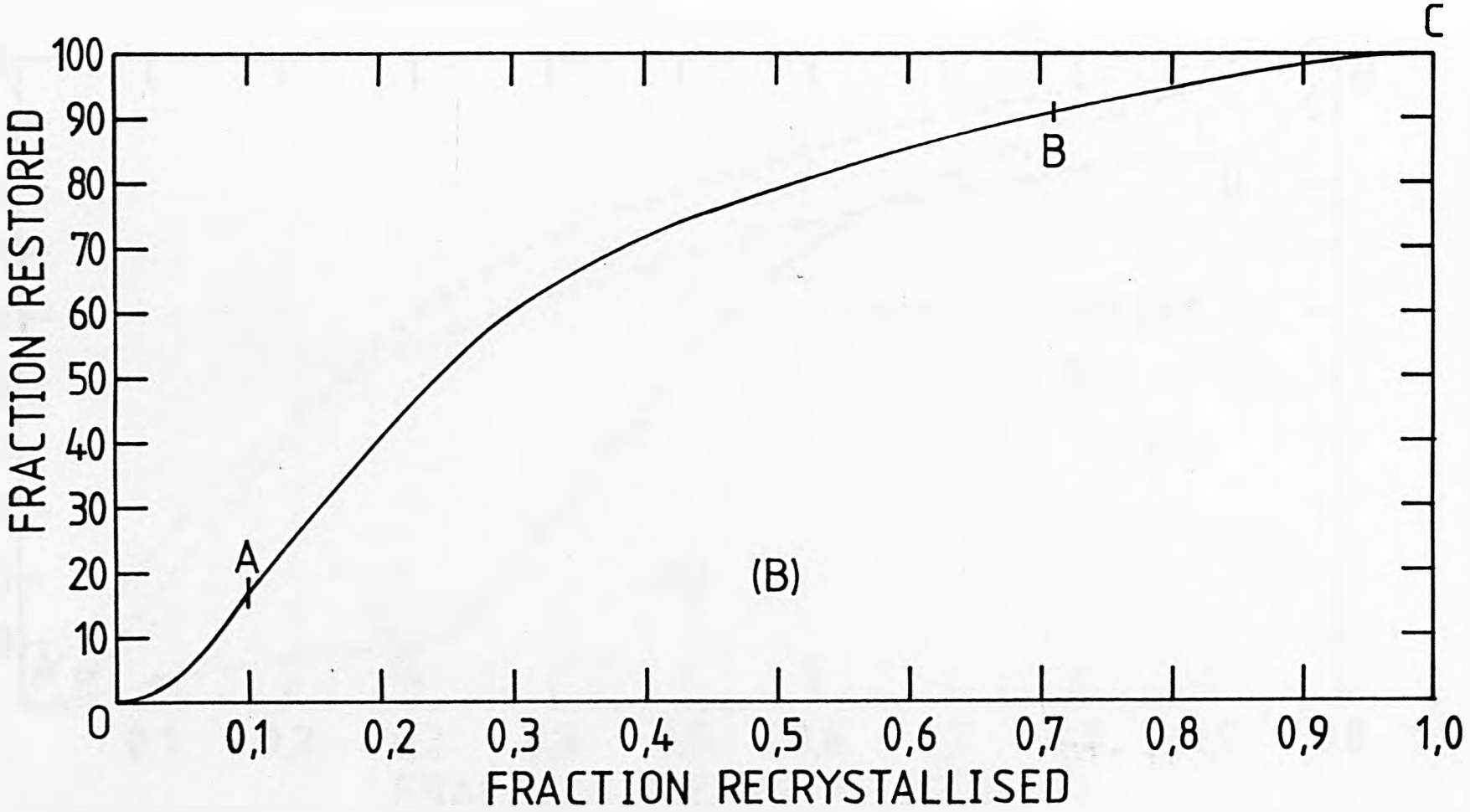
C
100
90
80
70
60
50
40
30
20
10
0
FRACTION RESTORED
B
A
(B)
0,1
0,2
0,3
0,4
0,5
0,6
0,7
0,8
0,9
1,0
FRACTION RECRYSTALLISED

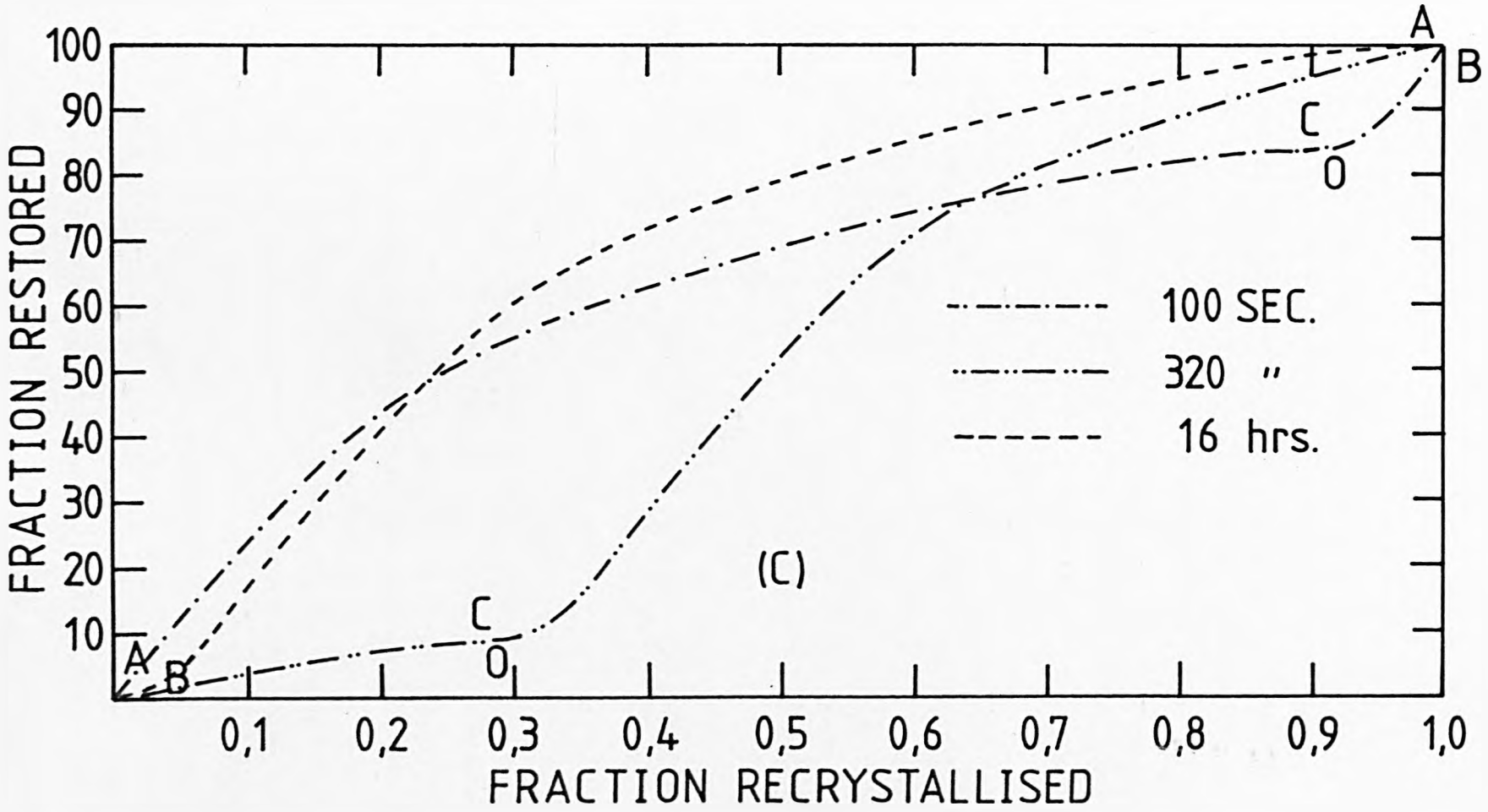
FRACTION RESTORED
100
90
80
70
60
50
40
30
20
10
A
B
C
O
100 SEC.
320 "
16 hrs.
(C)
0,1
0,2
0,3
0,4
0,5
0,6
0,7
0,8
0,9
1,0
FRACTION RECRYSTALLISED

FIGURE 120: Patterns of temperature distribution in the upper left quarter of the gauge section of a plane strain compression specimen after two deformations with different time intervals between passes.

(a) t_1 = 1.7 sec, $\bar{T}$ = 381°C.

(b) t_1 = 100 and 320 sec, $\bar{T}$ = 384°C.

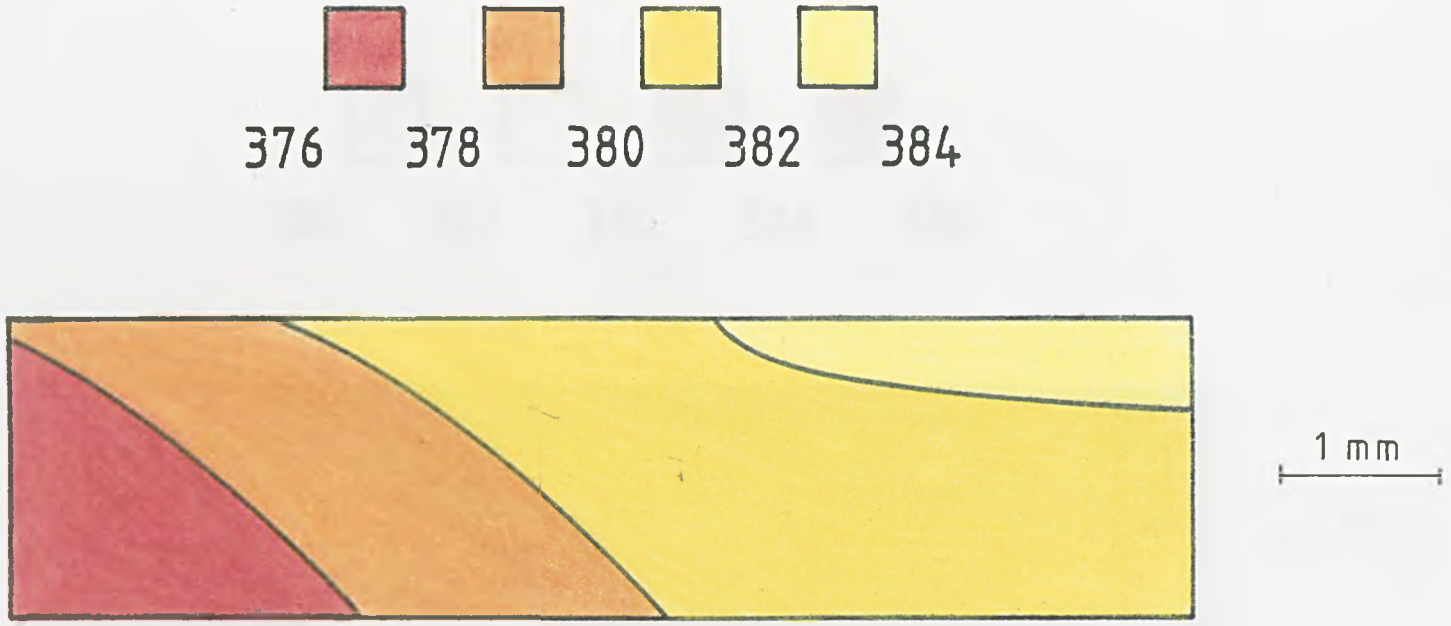

(a)

(b)

FIGURE 121: Microstructures taken at the centre of the gauge section of two plane strain compression specimens deformed at 400°C and 1 s^{-1}. Initial strain applied: 0.67. Time interval between deformations: 1.7 sec. Strain applied in the second deformation: 0.33.

(a) and (b) annealed for 105 sec. after the second deformation.

(c) structure fully recrystallised.

Mag. 100x.

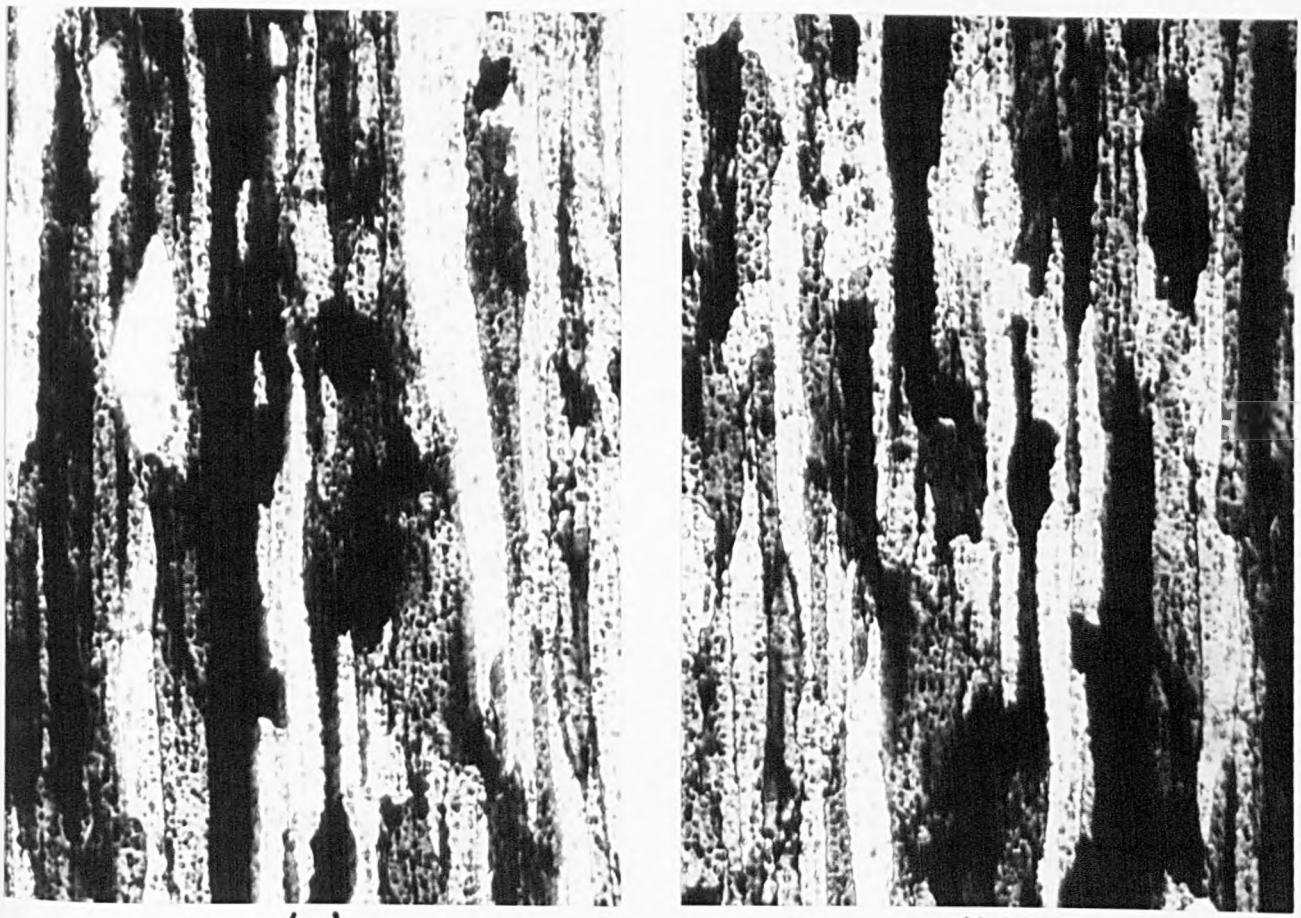
(a)
(b)
0,1 mm

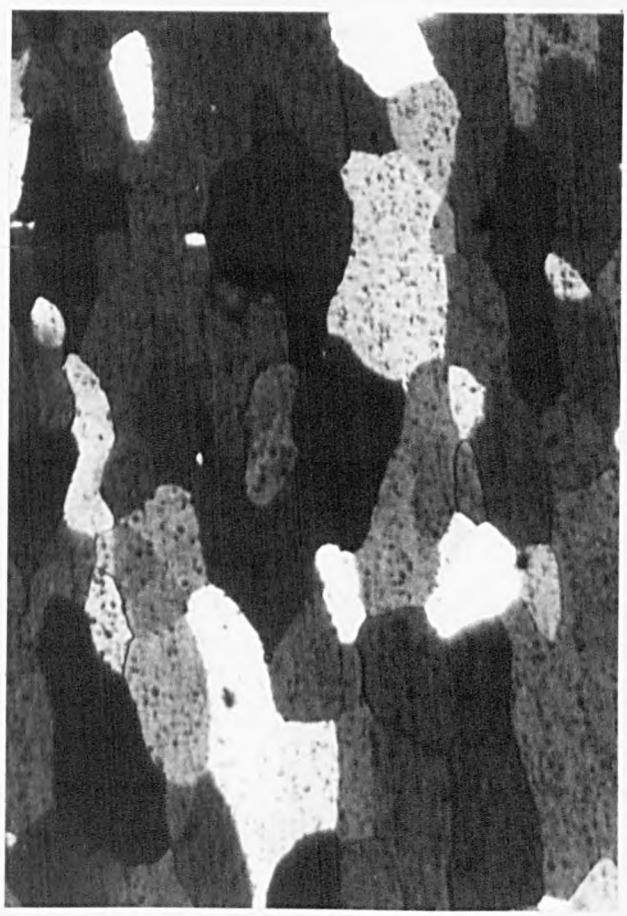
(c)

FIGURE 122: Microstructures taken at the centre of the gauge section of various plane strain compression specimens deformed at 400°C and 1 s^{-1}. Initial strain applied: 0.67. Time interval between deformations: 100 sec. Strain applied in the second deformation: 0.33.

(a) annealed for 122 sec. after the second deformation;

(b) annealed for 640 sec.;

(c) annealed for 2560 sec.;

(d) structure fully recrystallised.

Mag. 100 x.

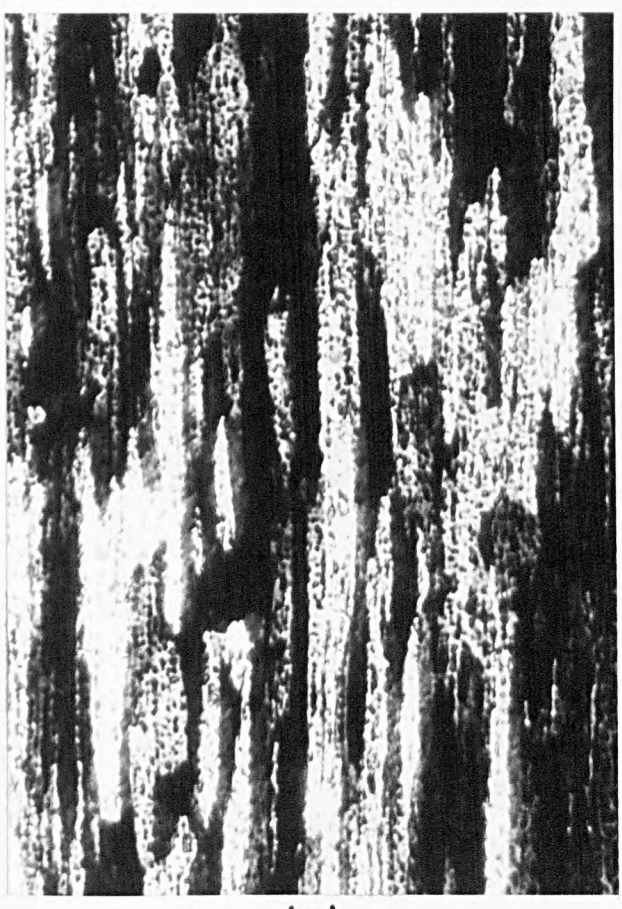

(a)

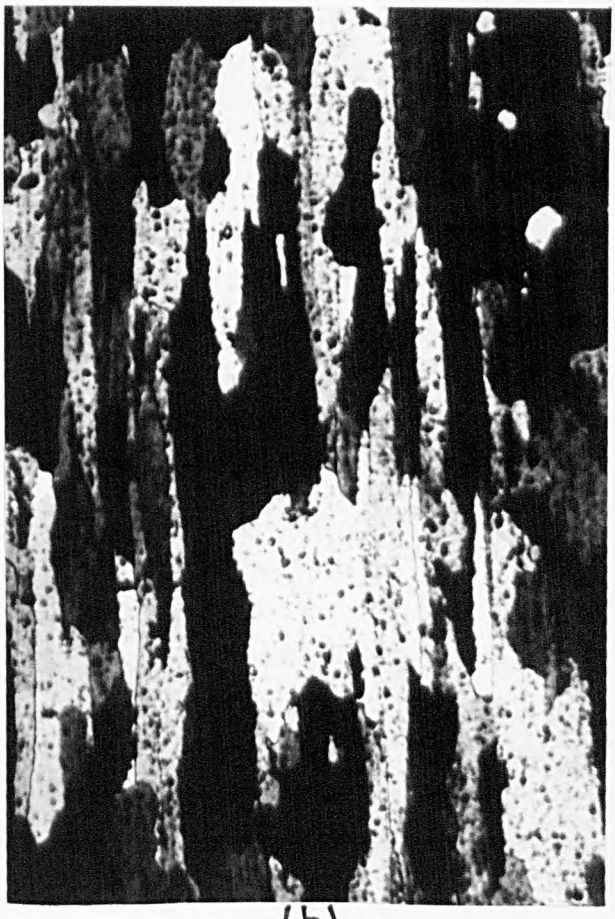

(b)

0,1 mm

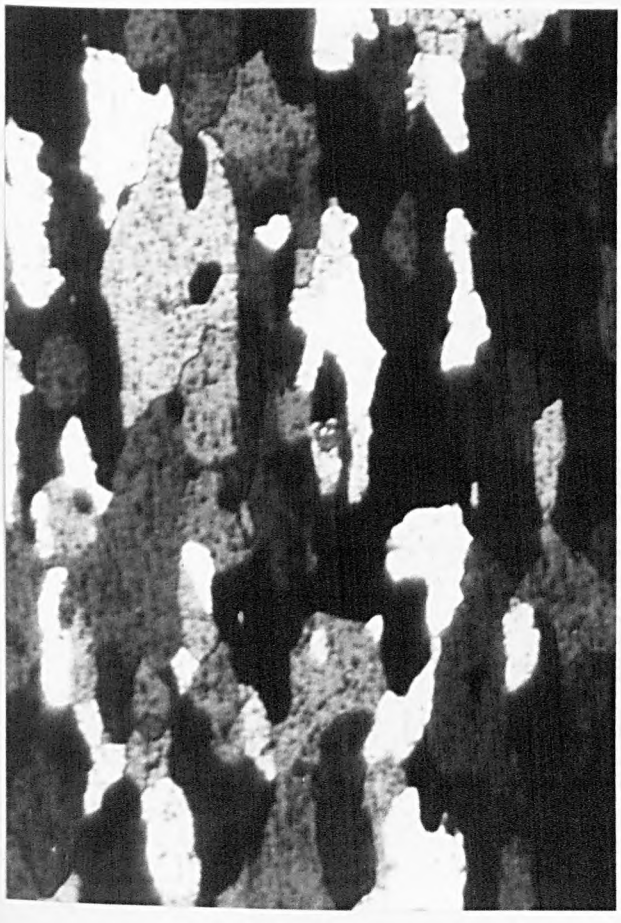

(c)

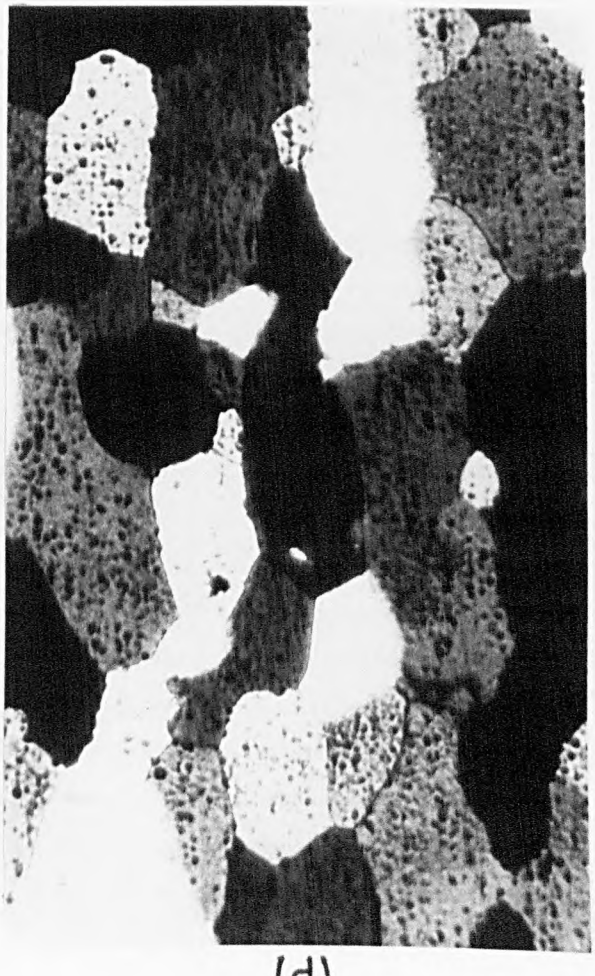

(d)

FIGURE 123: Microstructures taken at the centre of the gauge section of various plane strain compression specimens deformed at 400°C and 1 s^{-1}. Initial strain applied: 0.67. Time interval between deformations: 320 sec. Strain applied in the second deformation: 0.33.

(a) annealed for 220 sec. after the second deformation;

(b) annealed for 640 sec.;

(c) annealed for 2560 sec.;

(d) structure fully recrystallised.

Mag. 100 x.

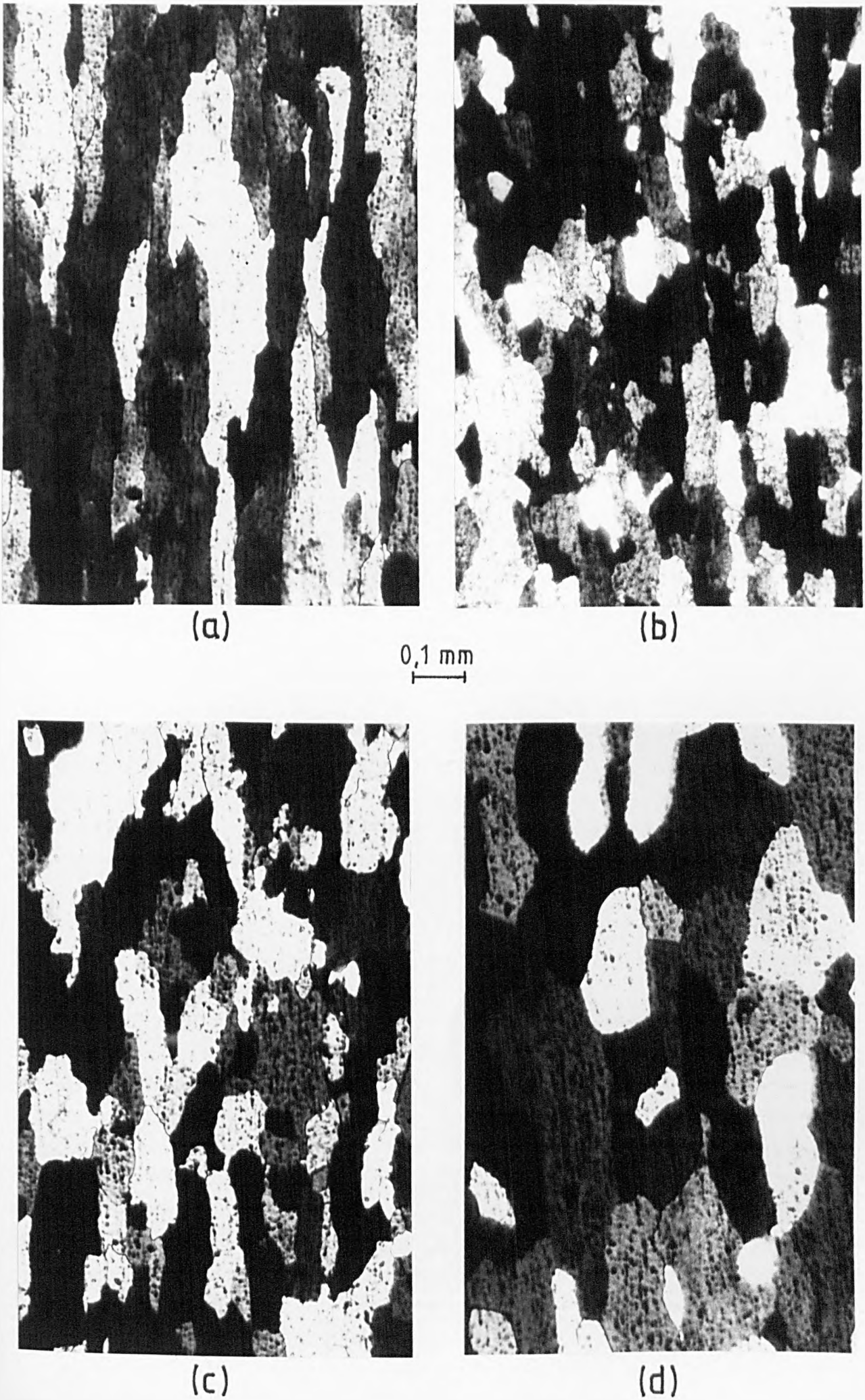
(a)
(b)
0,1 mm
(c)
(d)

FIGURE 124: Microstructures of the as-cast Al-1%Mg alloy used in rolling experiments (Experimental Schedule "A").

(a) as supplied;

(b) annealed 16 hrs. at 550°C and furnace cooled.

Mag. 100 x.

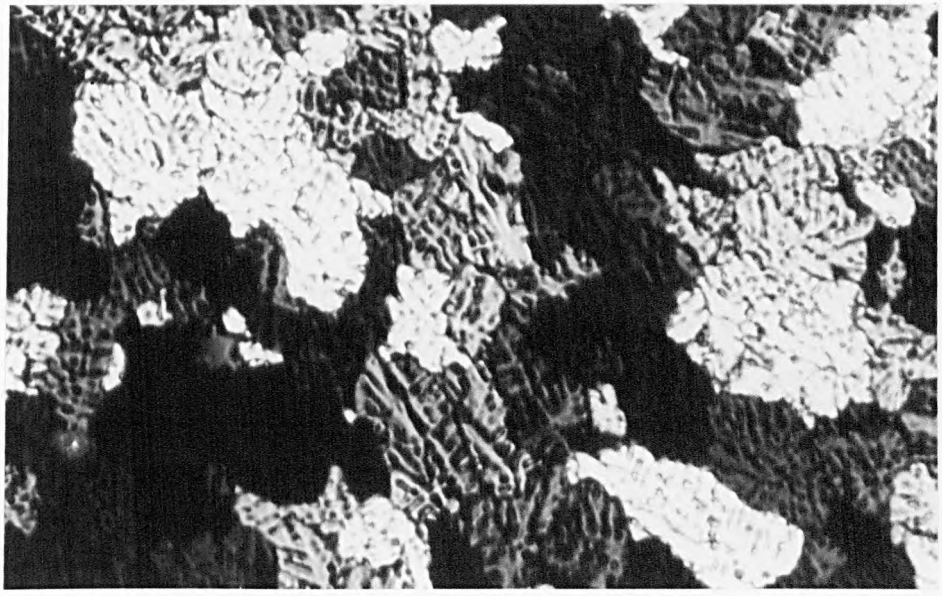

(a)

0,1 mm

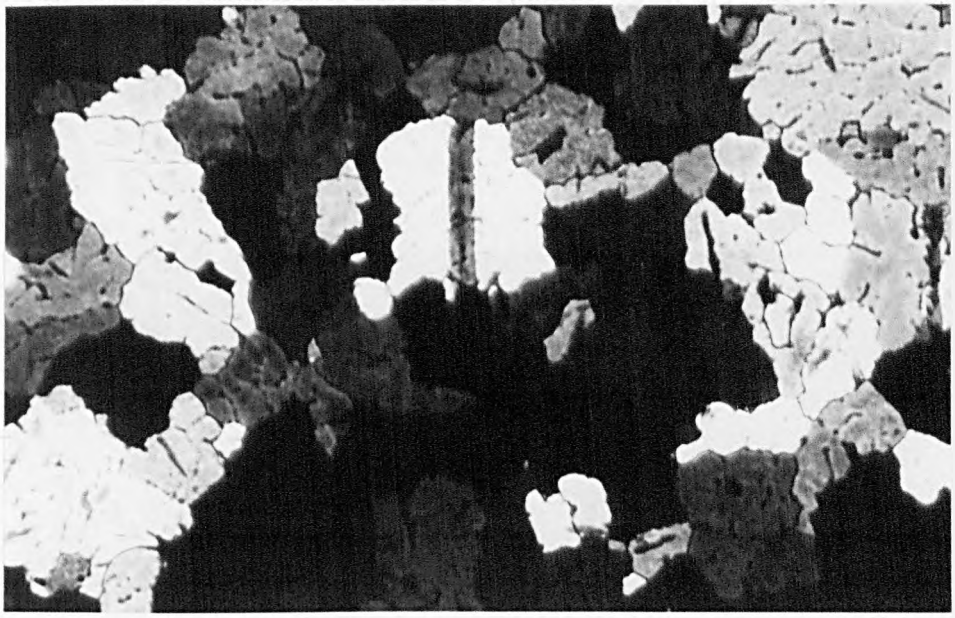

(b)

FIGURE 125: (a) Strain-time history of schedule "A" (experimental rolling of specimens of Al-1%Mg alloy).

(b) Comparison between computer predicted and experimental rolling loads for schedule "A".

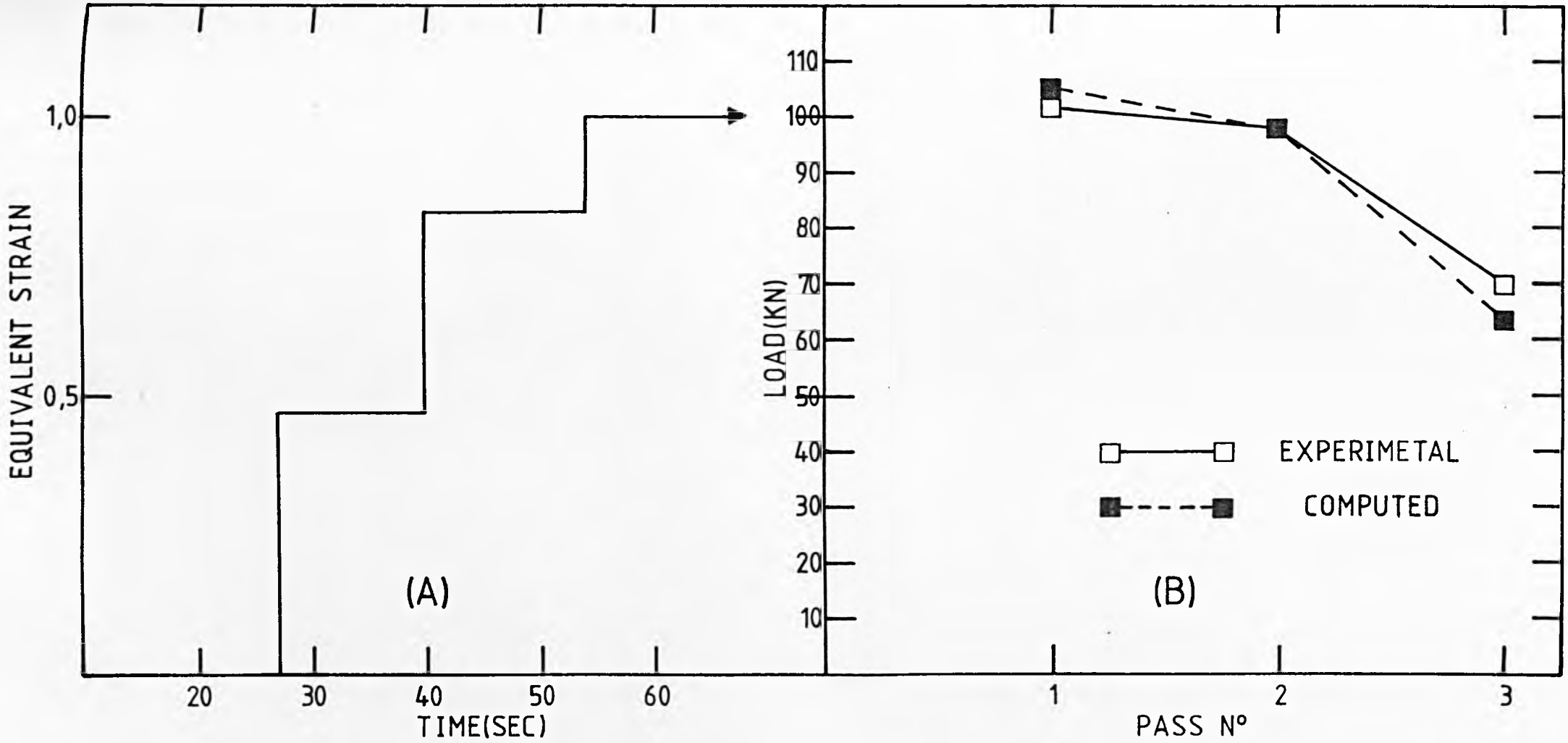
EQUIVALENT STRAIN
1,0
0,5
20
30
40
50
60
TIME(SEC)
(A)
LOAD(KN)
110
100
90
80
70
60
50
40
30
20
10
1
2
3
PASS N°
EXPERIMETAL
COMPUTED
(B)

FIGURE 126: Computer prediction of the changes in centre, mean and surface temperature during the experimental rolling of specimens of Al-1%Mg alloy (Schedule "A").

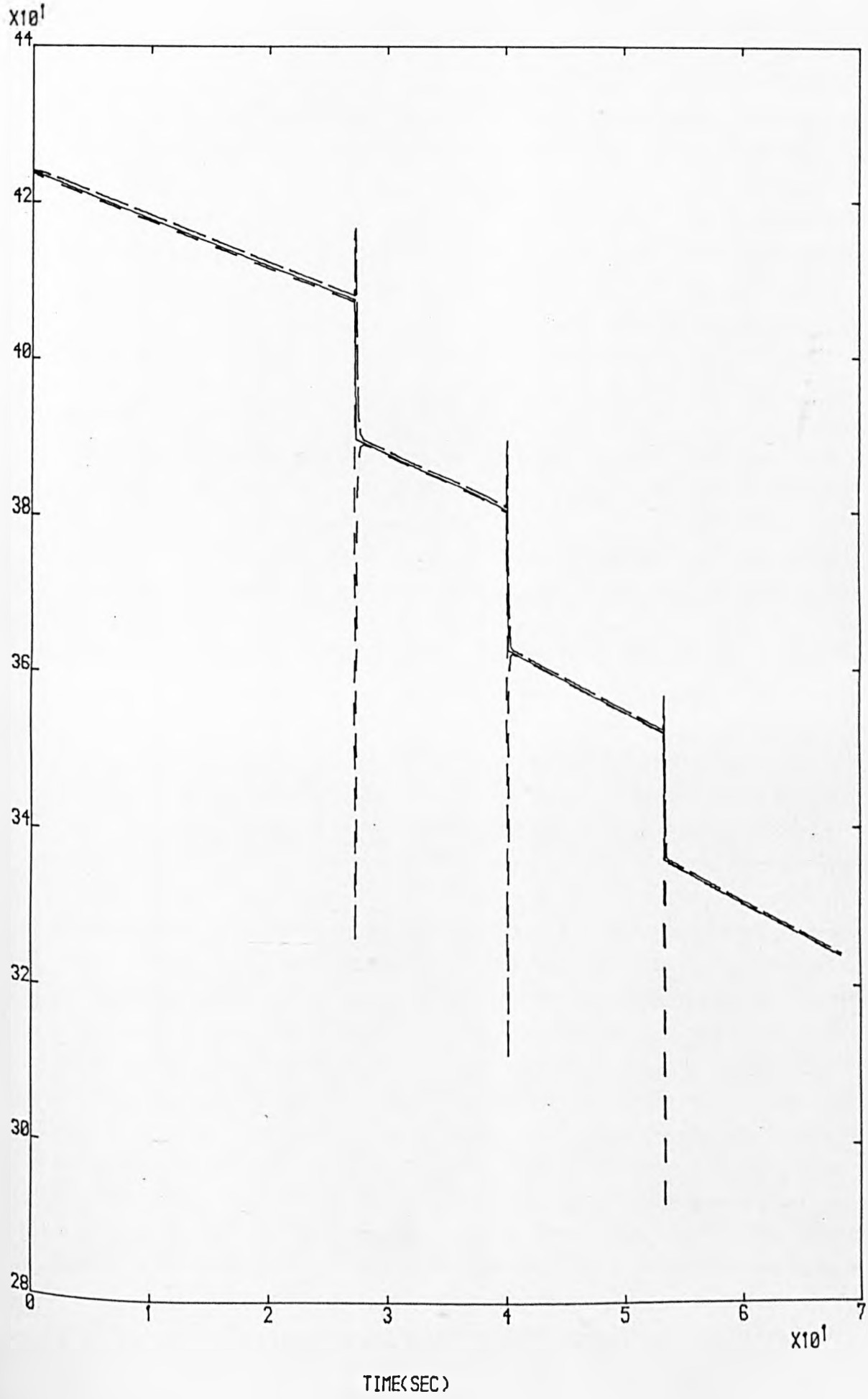
X10¹
44
42
40
38
36
34
32
30
28
0
1
2
3
4
5
6
7
X10¹
TIME(SEC)

FIGURE 127: Final microstructures observed in different rolling samples of Al-1%Mg alloy deformed according to schedule "A".

Mag. 100x.

(a)

0,1 mm

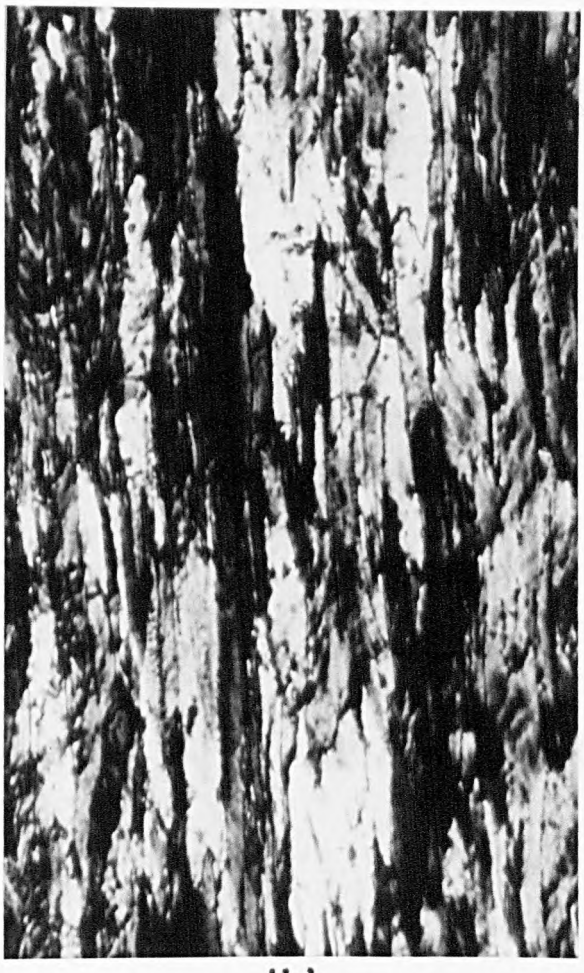

(b)

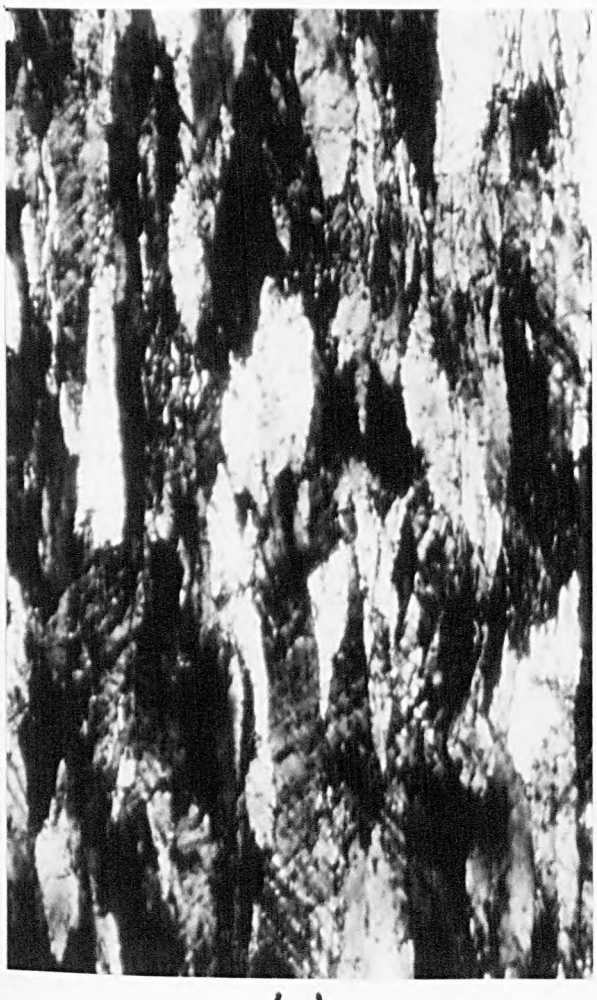

(c)

(d)

FIGURE 128: Strain-time history of the experimental rolling of specimens of commercial-purity aluminium. (Schedules B-E).

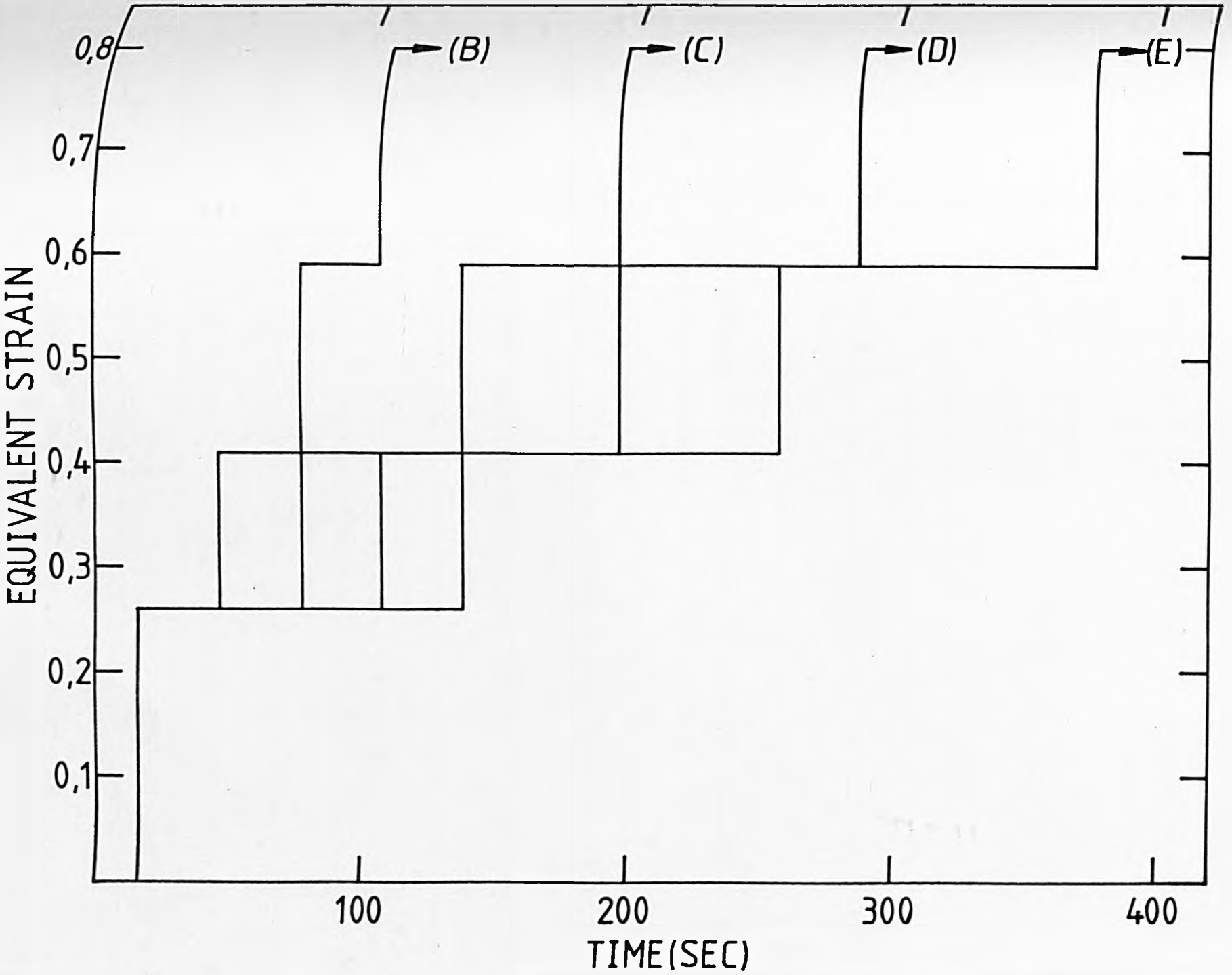
0,8
0,7
0,6
0,5
0,4
0,3
0,2
0,1
EQUIVALENT STRAIN
(B)
(C)
(D)
(E)
100
200
300
400
TIME(SEC)

FIGURE 129: Computer prediction of the changes in centre, mean and surface temperature during the experimental rolling of commercial-purity aluminium according to Schedule "B".

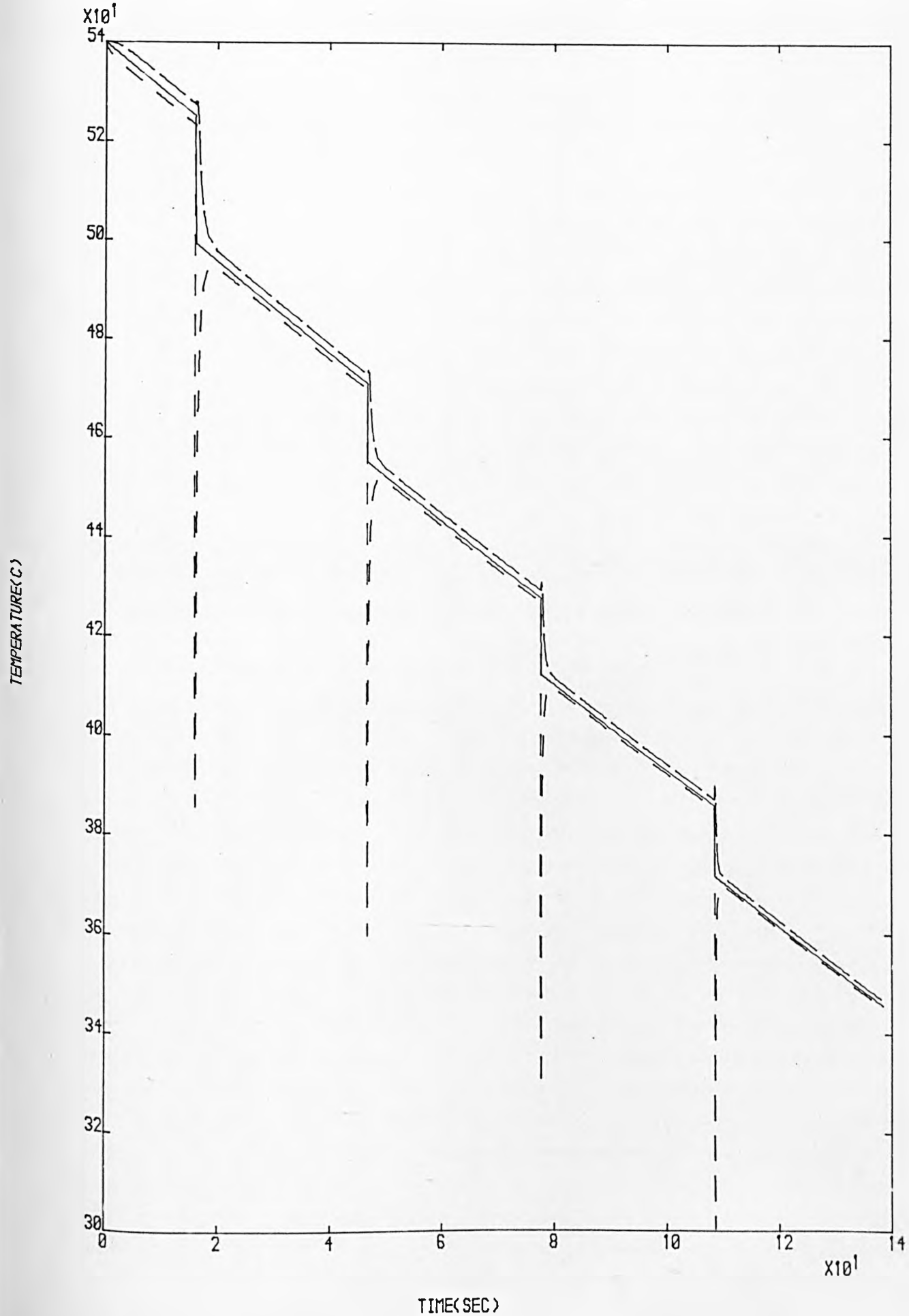
X10¹
54
52
50
48
46
44
42
40
38
36
34
32
30
0
2
4
6
8
10
12
14
X10¹
TEMPERATURE(C)
TIME(SEC)

FIGURE 130: Computer prediction of the changes in centre, mean and surface temperature during the experimental rolling of commercial-purity aluminium according to Schedule "C".

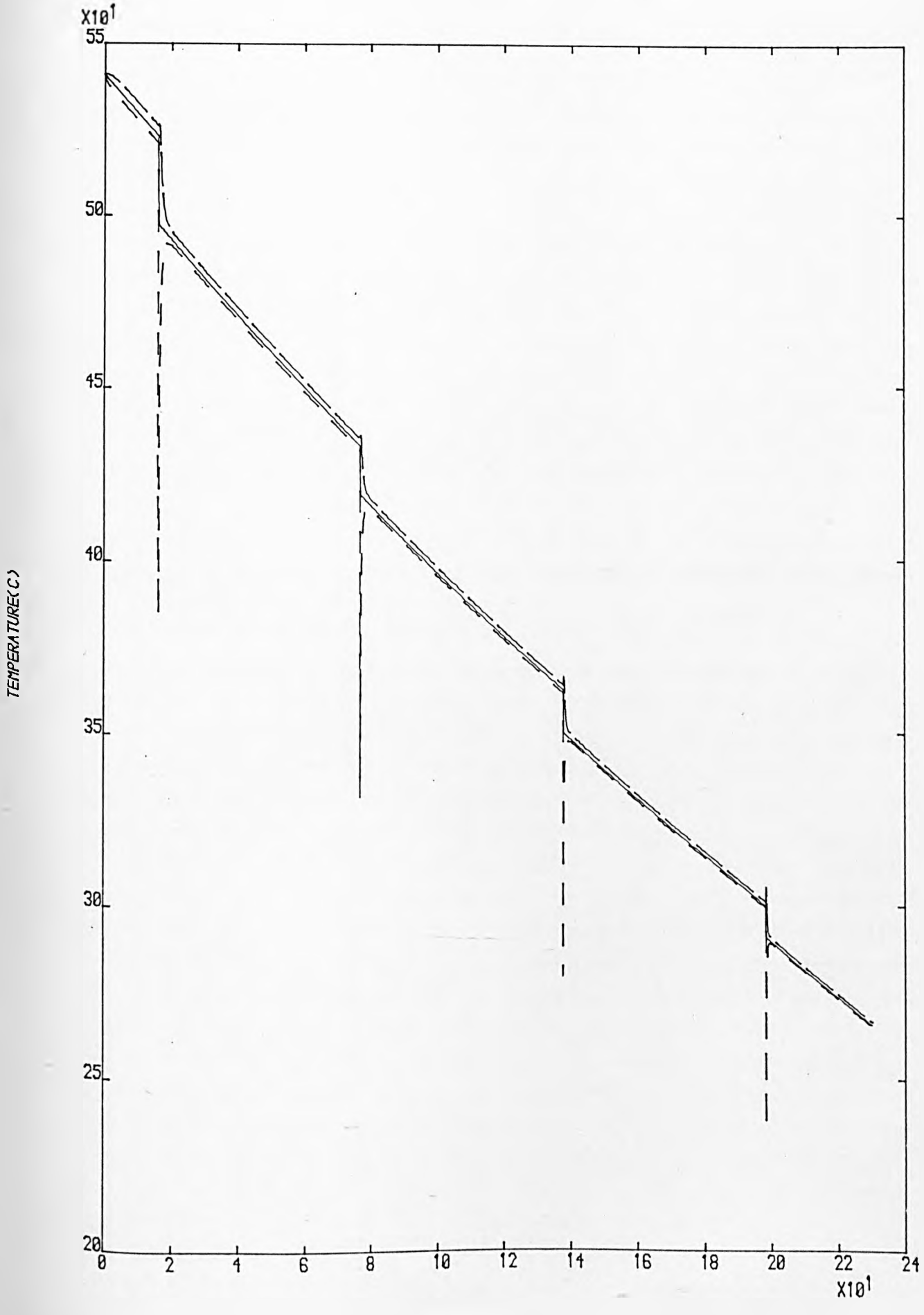
X10¹
55
50
45
40
35
30
25
20
0
2
4
6
8
10
12
14
16
18
20
22
24
X10¹
TEMPERATURE(C)
TIME(SEC)

FIGURE 131: Computer prediction of the changes in centre, mean and surface temperature during the experimental rolling of commercial-purity aluminium according to Schedule "D".

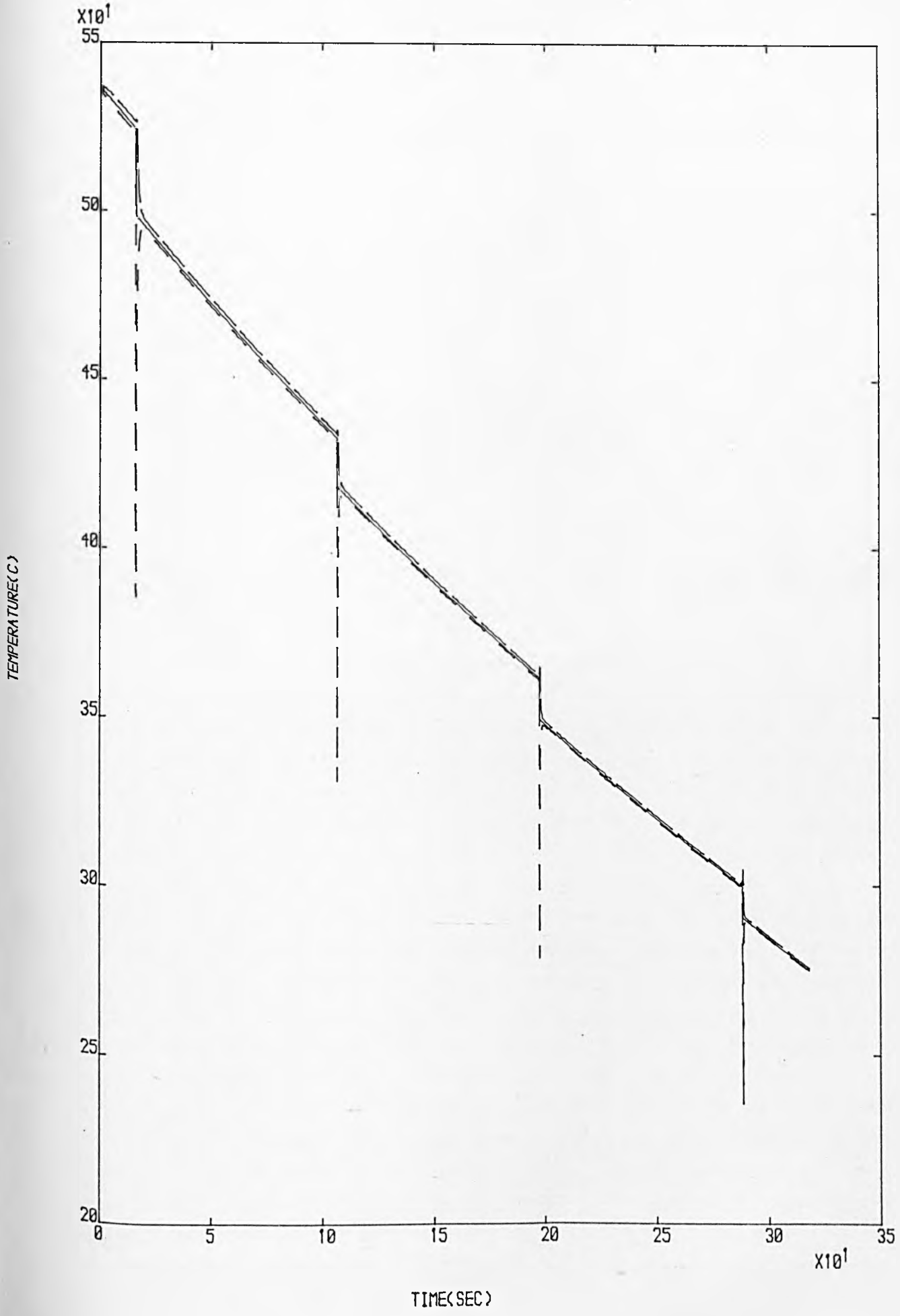
X10¹
55
50
45
40
35
30
25
20
0
5
10
15
20
25
30
35
X10¹
TEMPERATURE(C)
TIME(SEC)

FIGURE 132: Computer prediction of the changes in centre, mean and surface temperature during the experimental rolling of commercial-purity aluminium according to Schedule "E".

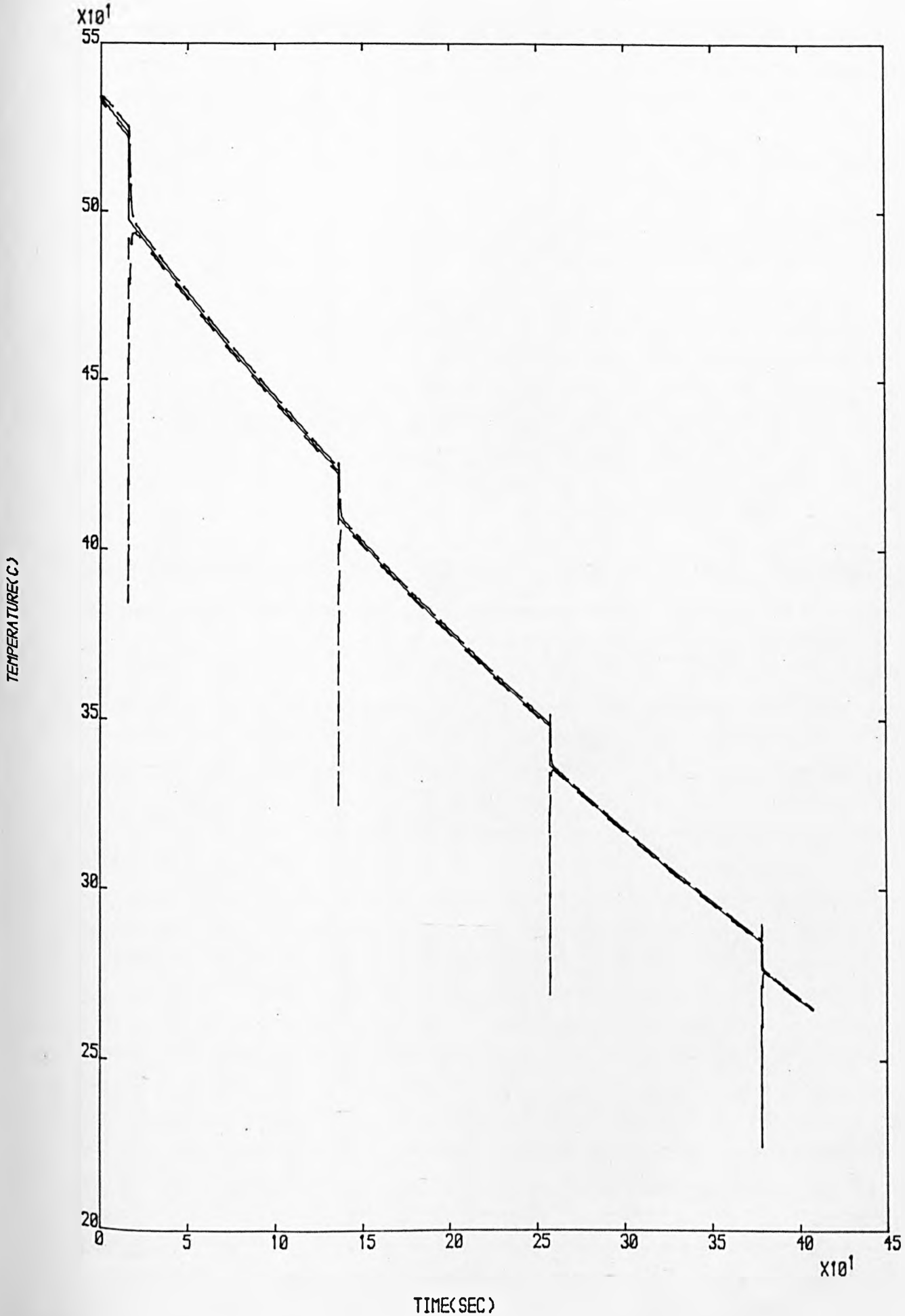
X10¹
55
50
45
40
35
30
25
20
0
5
10
15
20
25
30
35
40
45
X10¹
TEMPERATURE(C)
TIME(SEC)

FIGURE 133: Comparison between computer predicted and experimental rolling loads observed during the experimental rolling of commercial-purity aluminium: (a) Schedule "B" and (b) Schedule "C".

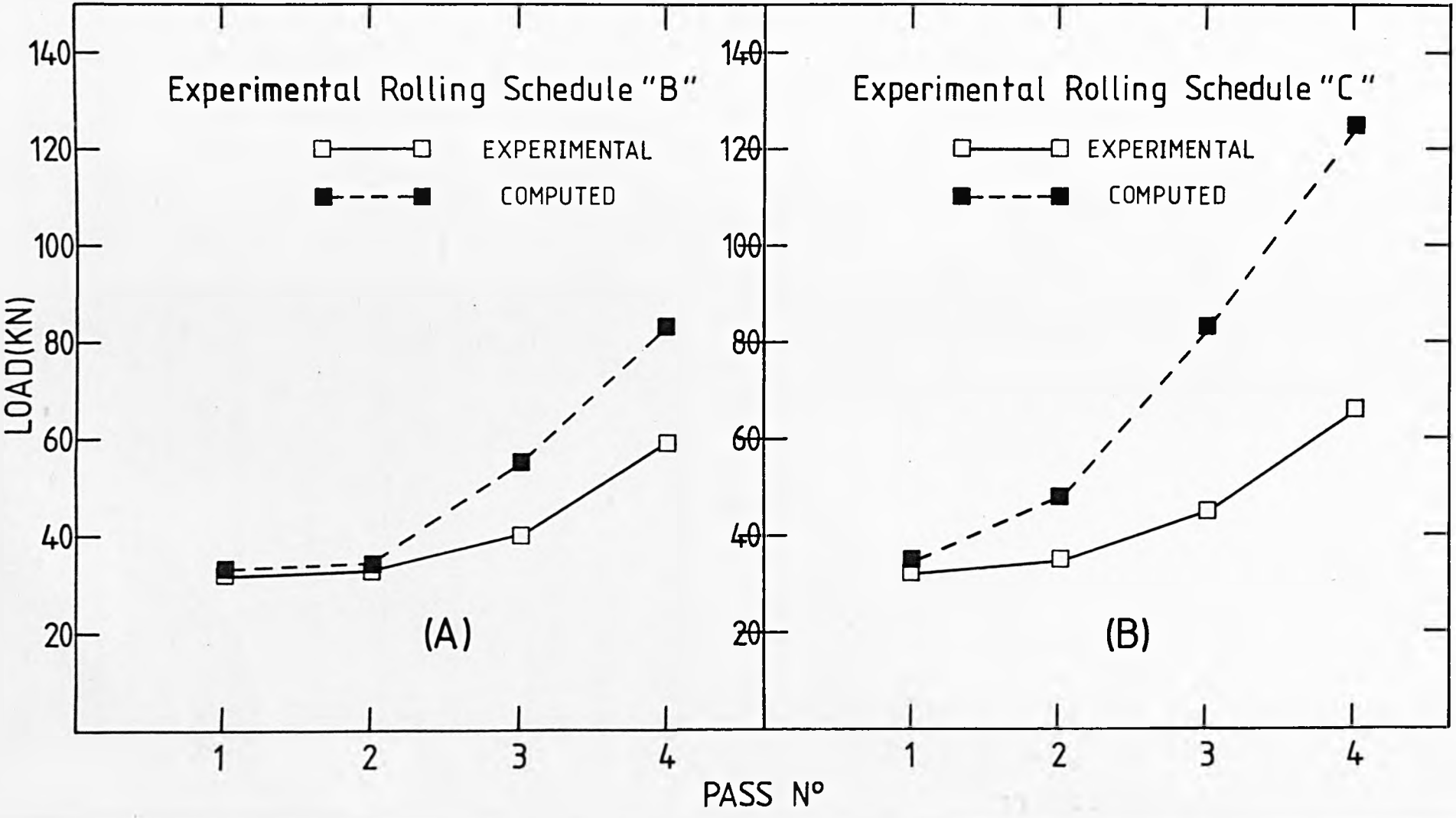
Experimental Rolling Schedule "B"
EXPERIMENTAL
COMPUTED
(A)
Experimental Rolling Schedule "C"
EXPERIMENTAL
COMPUTED
(B)
LOAD(KN)
140
120
100
80
60
40
20
1
2
3
4
PASS N°

FIGURE 134: Comparison between computer predicted and experimental rolling loads observed during the experimental rolling of commercial-purity aluminium: (a) Schedule "D" and (b) Schedule "E".

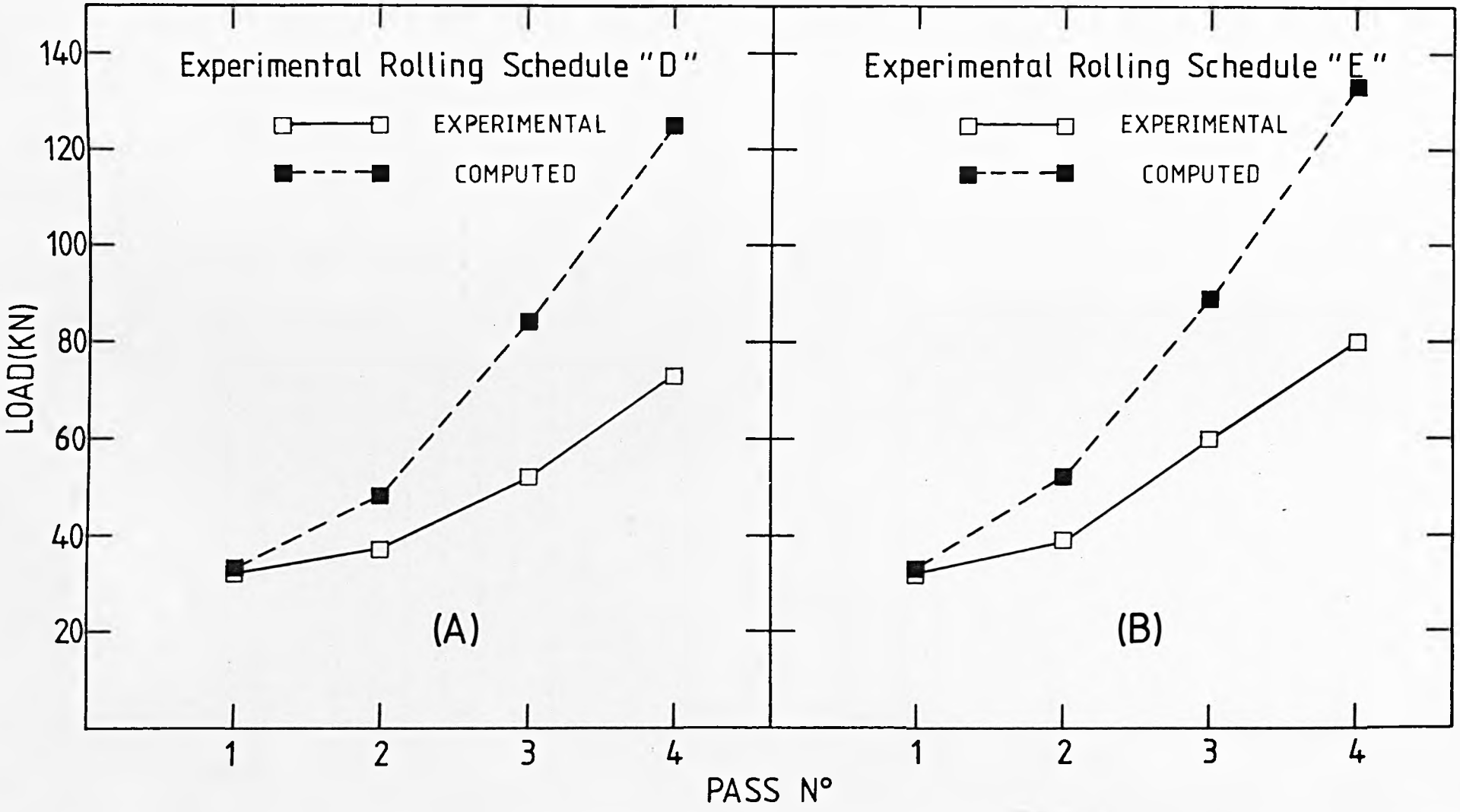
Experimental Rolling Schedule "D"
EXPERIMENTAL
COMPUTED
(A)
Experimental Rolling Schedule "E"
EXPERIMENTAL
COMPUTED
(B)
LOAD(KN)
140
120
100
80
60
40
20
1
2
3
4
1
2
3
4
PASS N°

FIGURE 135: Strain-time history of a typical industrial hot rolling operation on Al-1%Mg alloy (Industrial Schedule No.1).

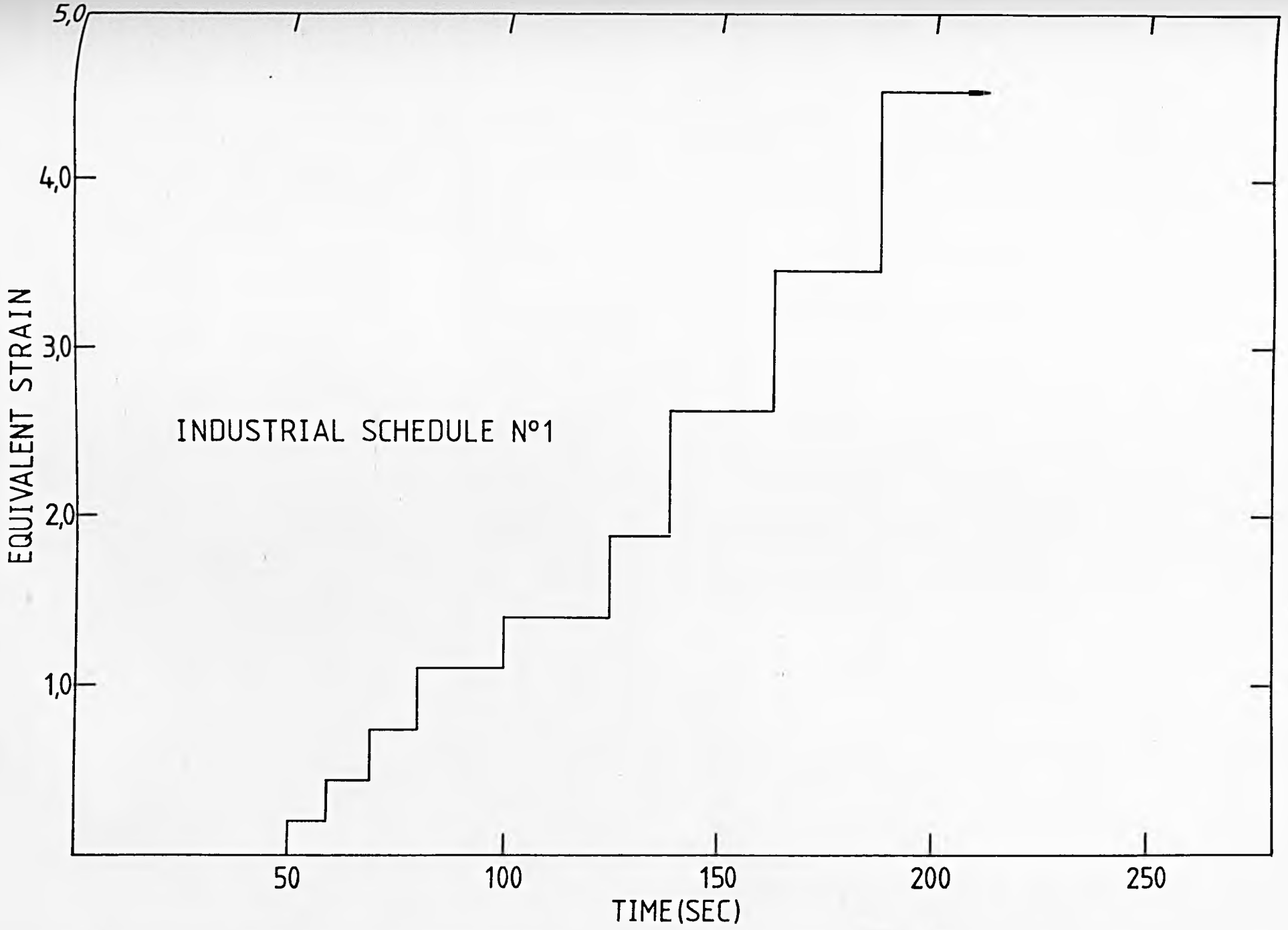
5,0
4,0
3,0
2,0
1,0
EQUIVALENT STRAIN
INDUSTRIAL SCHEDULE N°1
50
100
150
200
250
TIME (SEC)

FIGURE 136: Computer prediction of the changes in centre, mean and surface temperature during a typical industrial hot rolling operation on Al-1%Mg alloy (Industrial Schedule No.1).

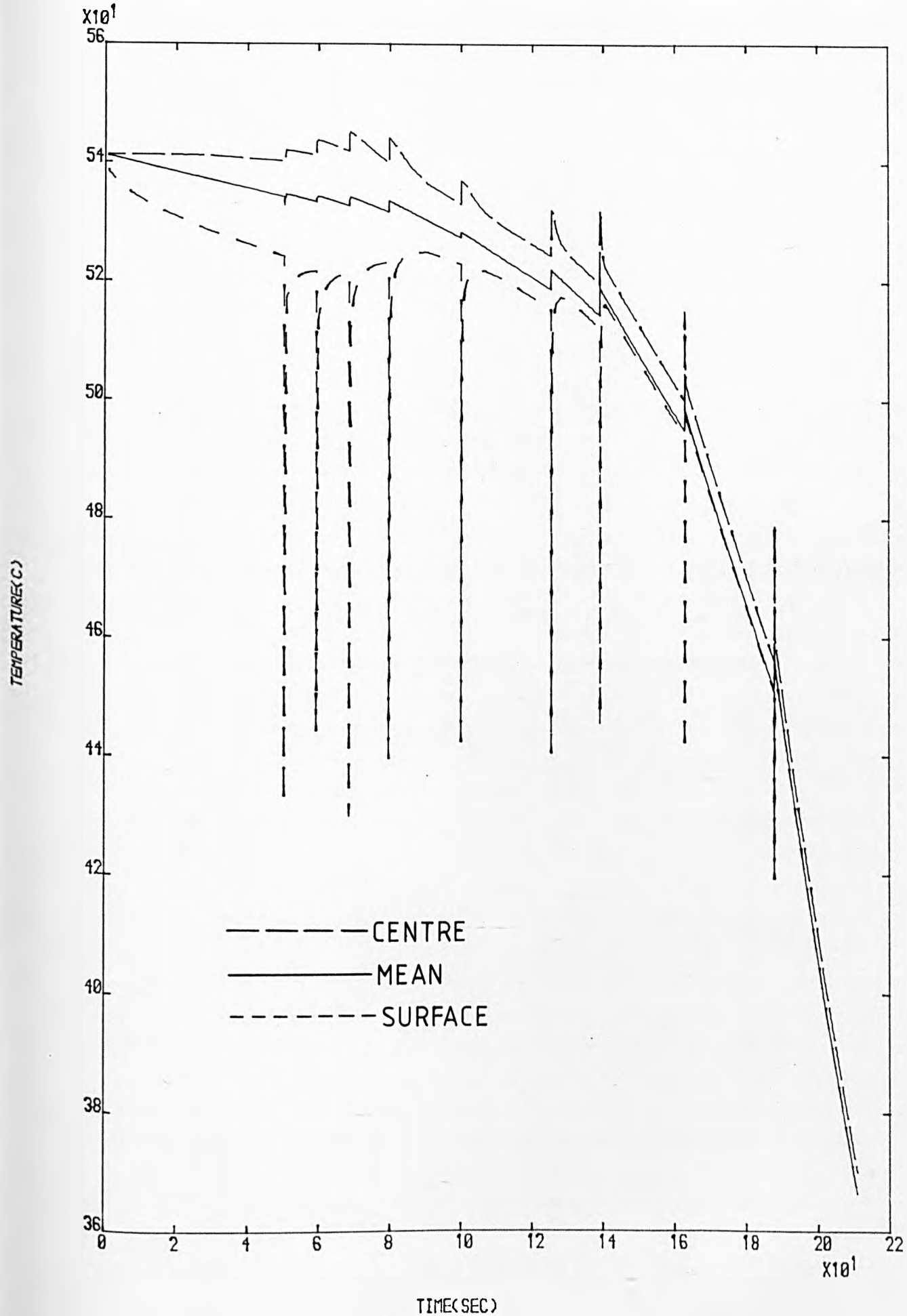
X10¹
56
54
52
50
48
46
44
42
40
38
36
TEMPERATURE(C)
0
2
4
6
8
10
12
14
16
18
20
22
X10¹
TIME(SEC)
CENTRE
MEAN
SURFACE

FIGURE 137: Computer prediction of the microstructural evolution expressed in terms of the recrystallised fraction, corresponding to the Industrial Schedule No.1.

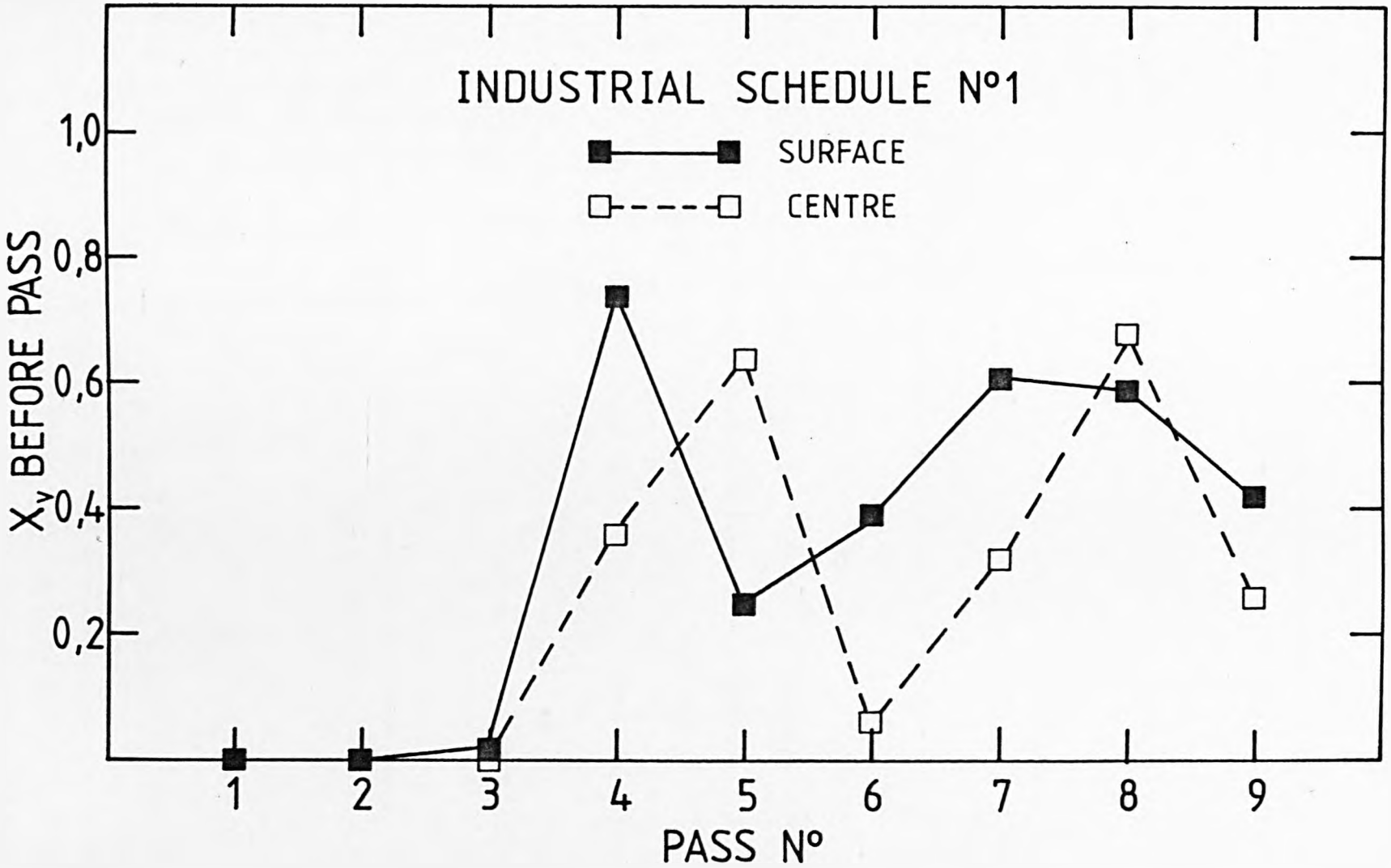
INDUSTRIAL SCHEDULE N°1
SURFACE
CENTRE
1,0
0,8
0,6
0,4
0,2
X_v BEFORE PASS
1
2
3
4
5
6
7
8
9
PASS N°

FIGURE 138: Comparison between computer predicted and experimental rolling loads observed during the industrial hot rolling of Al-1%Mg alloy. (Industrial Schedule No.1).

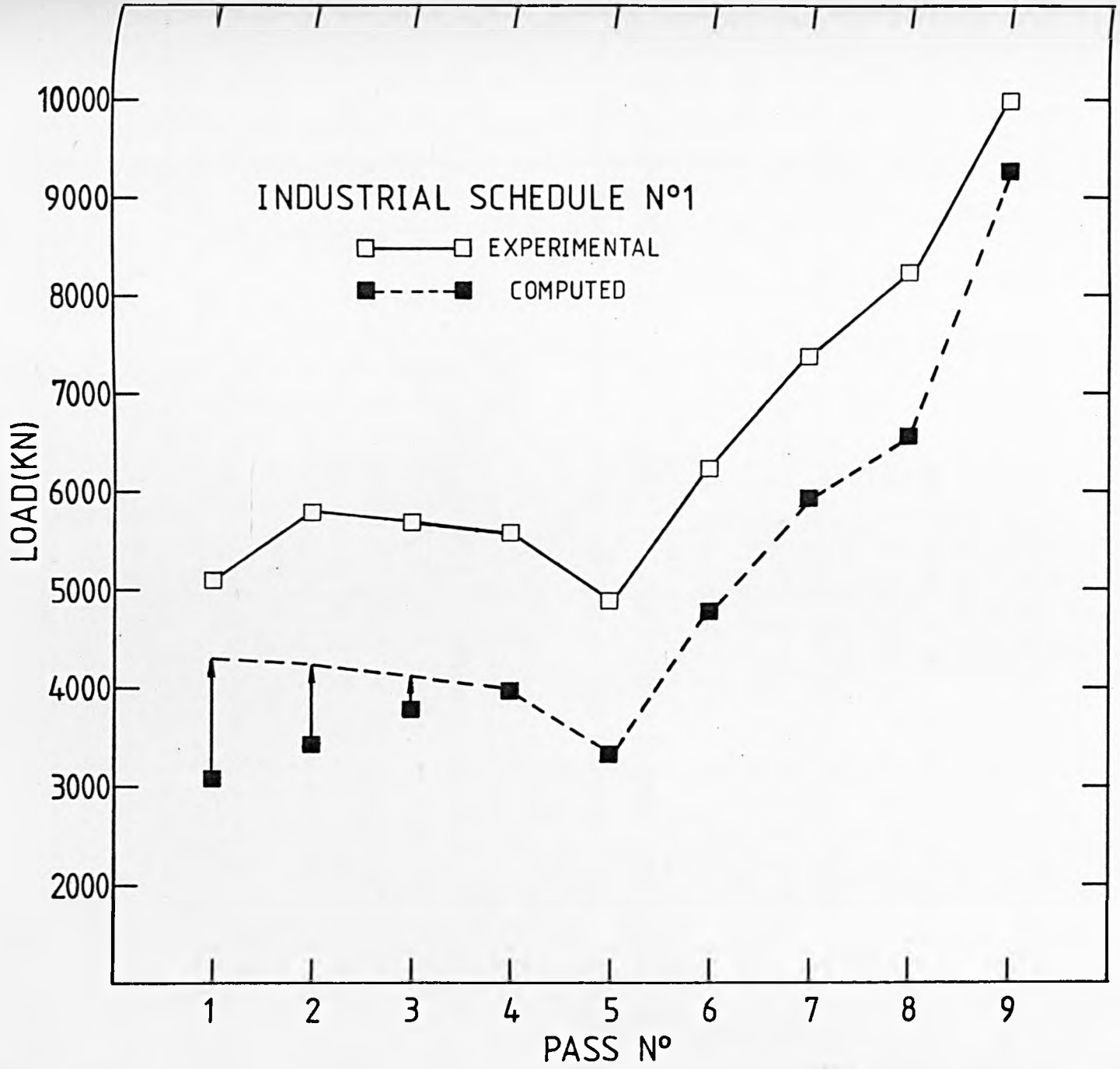
INDUSTRIAL SCHEDULE N°1
EXPERIMENTAL
COMPUTED
LOAD(KN)
10000
9000
8000
7000
6000
5000
4000
3000
2000
1
2
3
4
5
6
7
8
9
PASS N°

FIGURE 139: Section of a deformation zone in strip rolling showing the direct and shear stresses acting on a rigid triangular zone.

(After Green and Wallace [174].

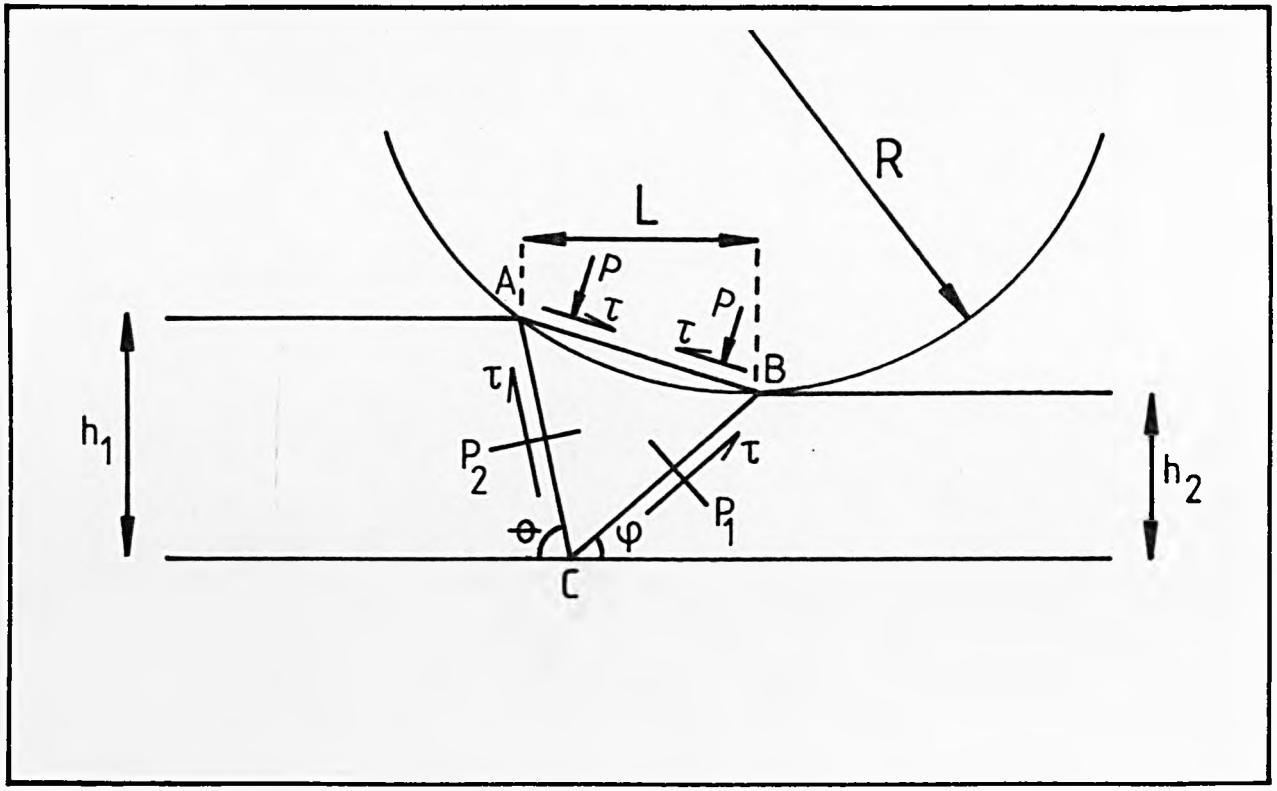
R
L
A
P
τ
τ
P
B
τ
h1
P2
τ
θ
φ
P1
h2
C

FIGURE 140: Strain-time history of a typical industrial hot rolling operation on Al-1%Mg alloy (Industrial Rolling No.2).

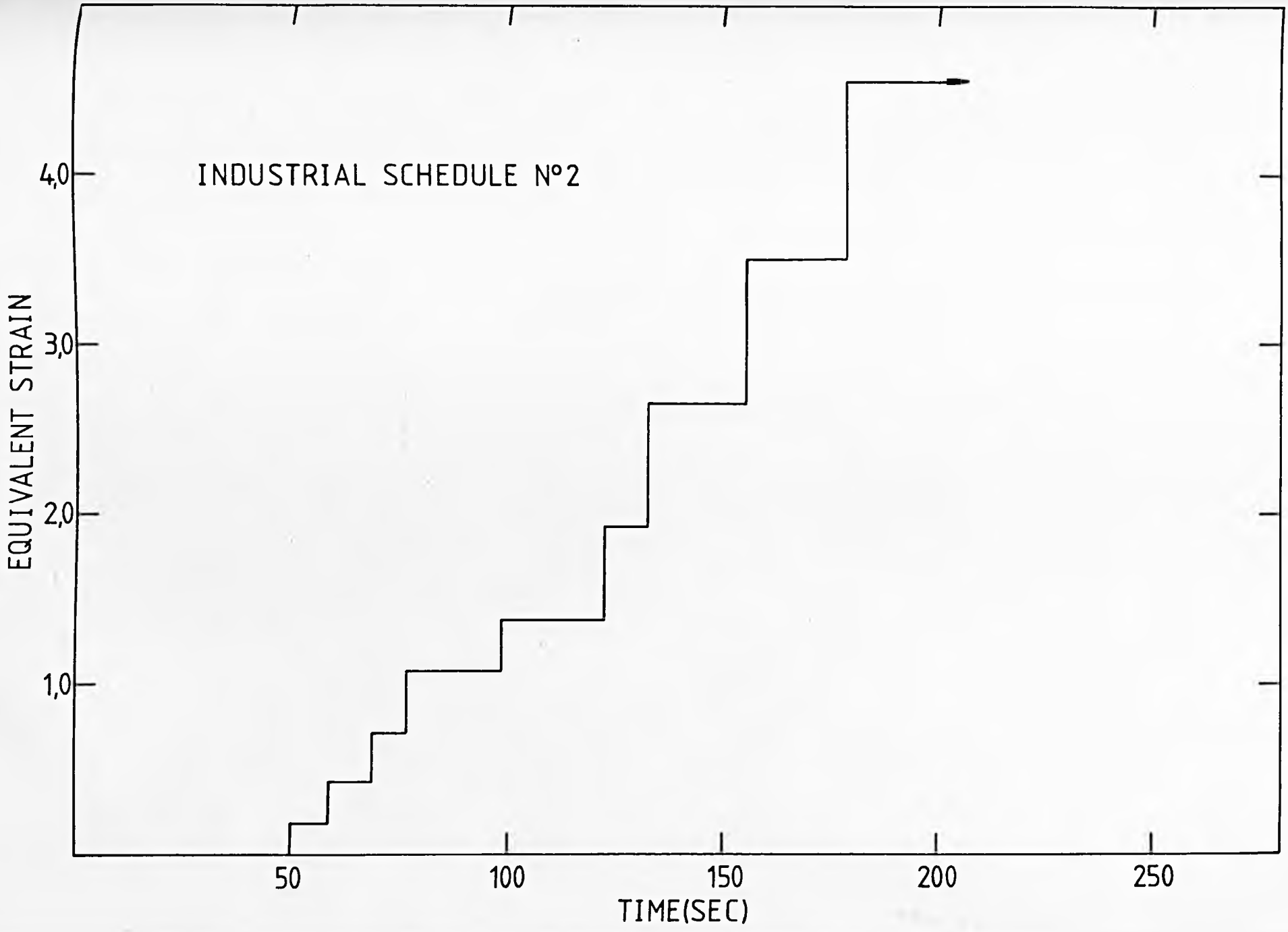
INDUSTRIAL SCHEDULE N°2
EQUIVALENT STRAIN
4,0
3,0
2,0
1,0
50
100
150
200
250
TIME(SEC)

FIGURE 141: Computer prediction of the changes in centre, mean and surface temperature during a typical industrial hot rolling operation on Al-1%Mg alloy. (Industrial Schedule No.2).

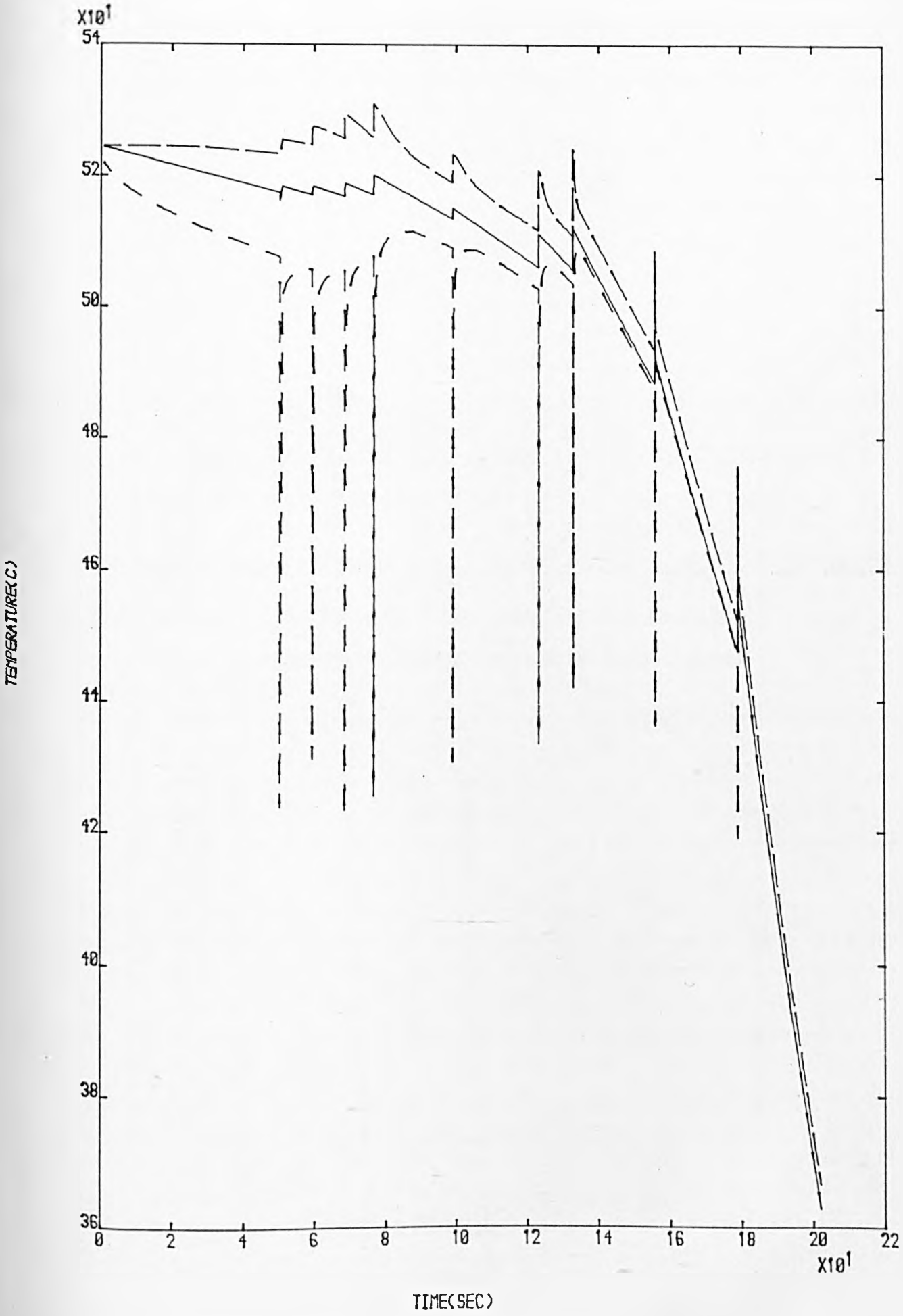
X10¹
54
52
50
48
46
44
42
40
38
36
TEMPERATURE(C)
0
2
4
6
8
10
12
14
16
18
20
22
X10¹
TIME(SEC)

FIGURE 142: Computer prediction of the microstructural evolution expressed in terms of the recrystallised fraction corresponding to the industrial schedule No.2.

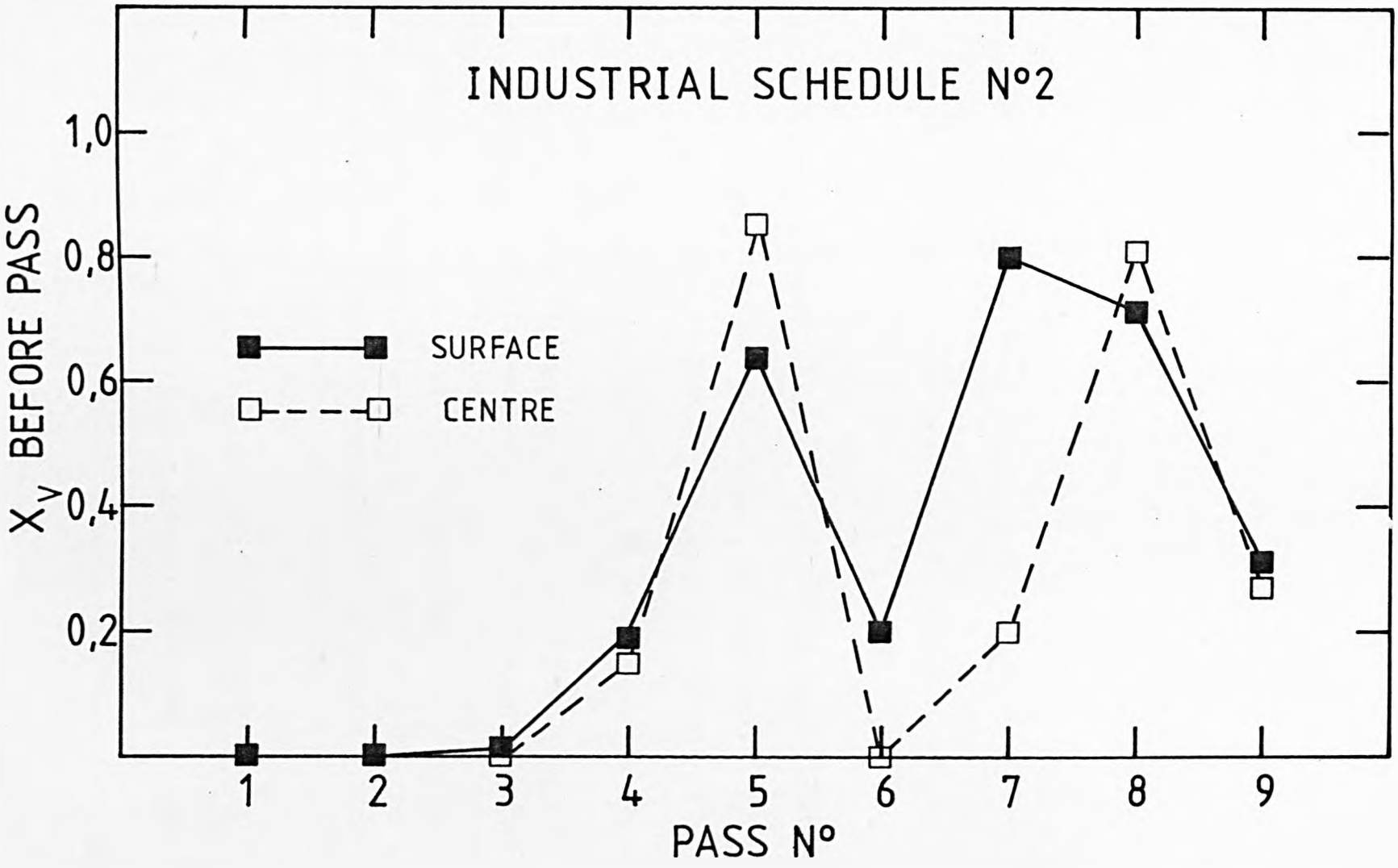
INDUSTRIAL SCHEDULE N°2
1,0
0,8
0,6
0,4
0,2
X_v BEFORE PASS
SURFACE
CENTRE
1
2
3
4
5
6
7
8
9
PASS N°

FIGURE 143: Comparison between computer predicted and experimental rolling loads observed during the industrial hot rolling of Al-1%Mg alloy. (Industrial Schedule No.2).

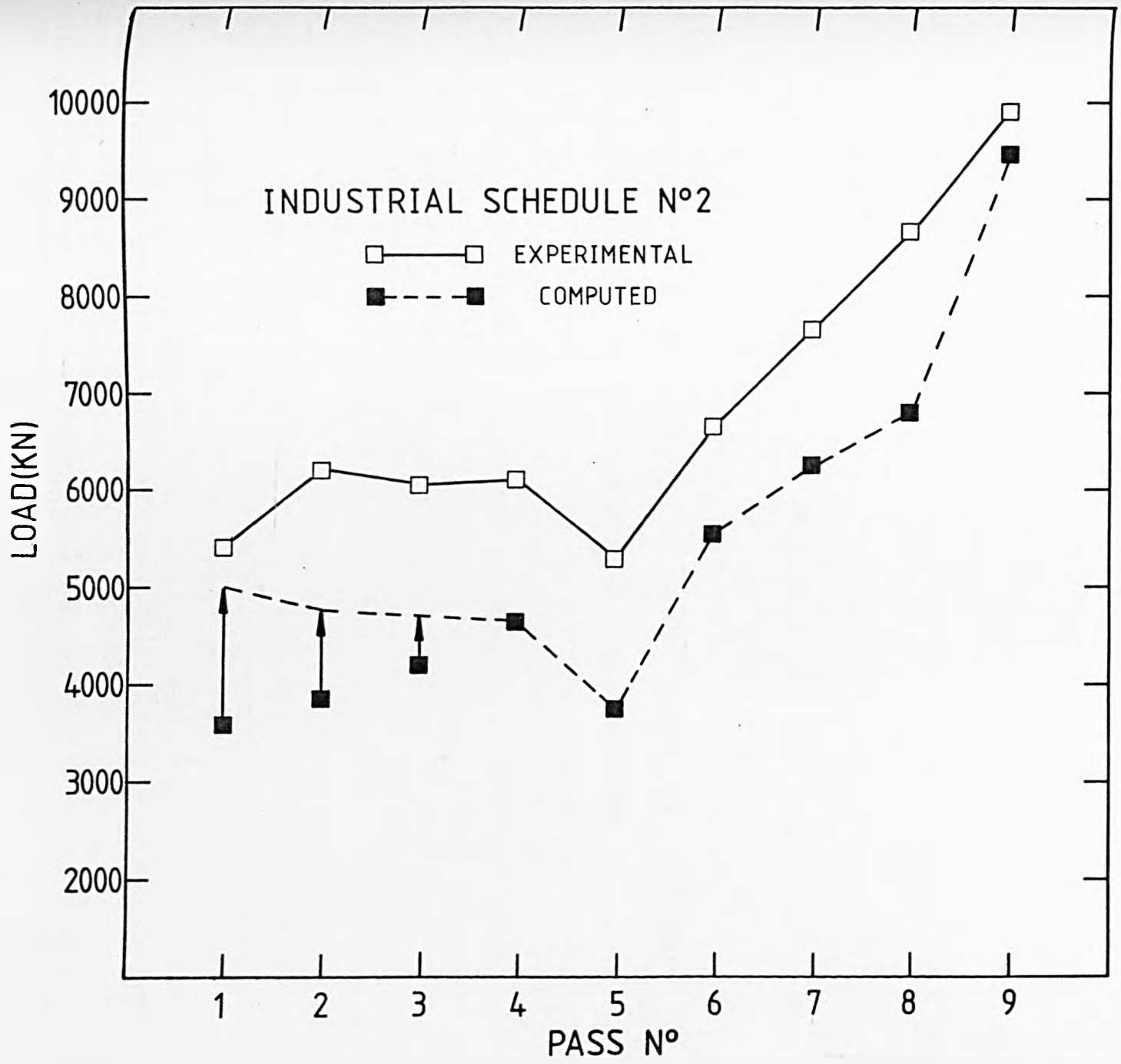
INDUSTRIAL SCHEDULE N°2
EXPERIMENTAL
COMPUTED
LOAD(KN)
10000
9000
8000
7000
6000
5000
4000
3000
2000
1
2
3
4
5
6
7
8
9
PASS N°

FIGURE 144: Strain-time history of a typical industrial hot rolling operation on commercial-purity aluminium (Industrial Schedule No.3).

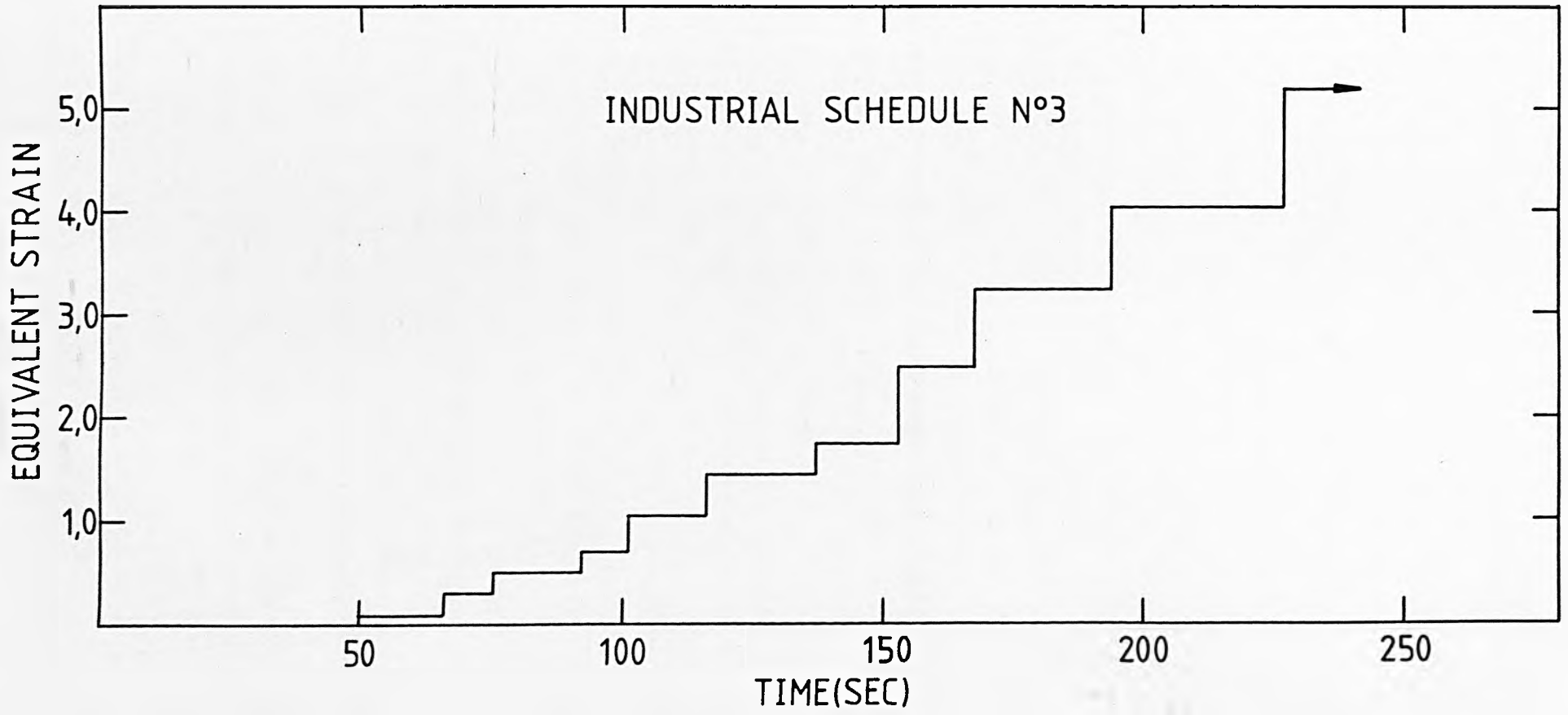
INDUSTRIAL SCHEDULE N°3
EQUIVALENT STRAIN
5,0
4,0
3,0
2,0
1,0
50
100
150
200
250
TIME(SEC)

FIGURE 145: Computer prediction of the changes in centre, mean and surface temperature during a typical industrial hot rolling operation on commercial-purity aluminium. (Industrial Schedule No.3).

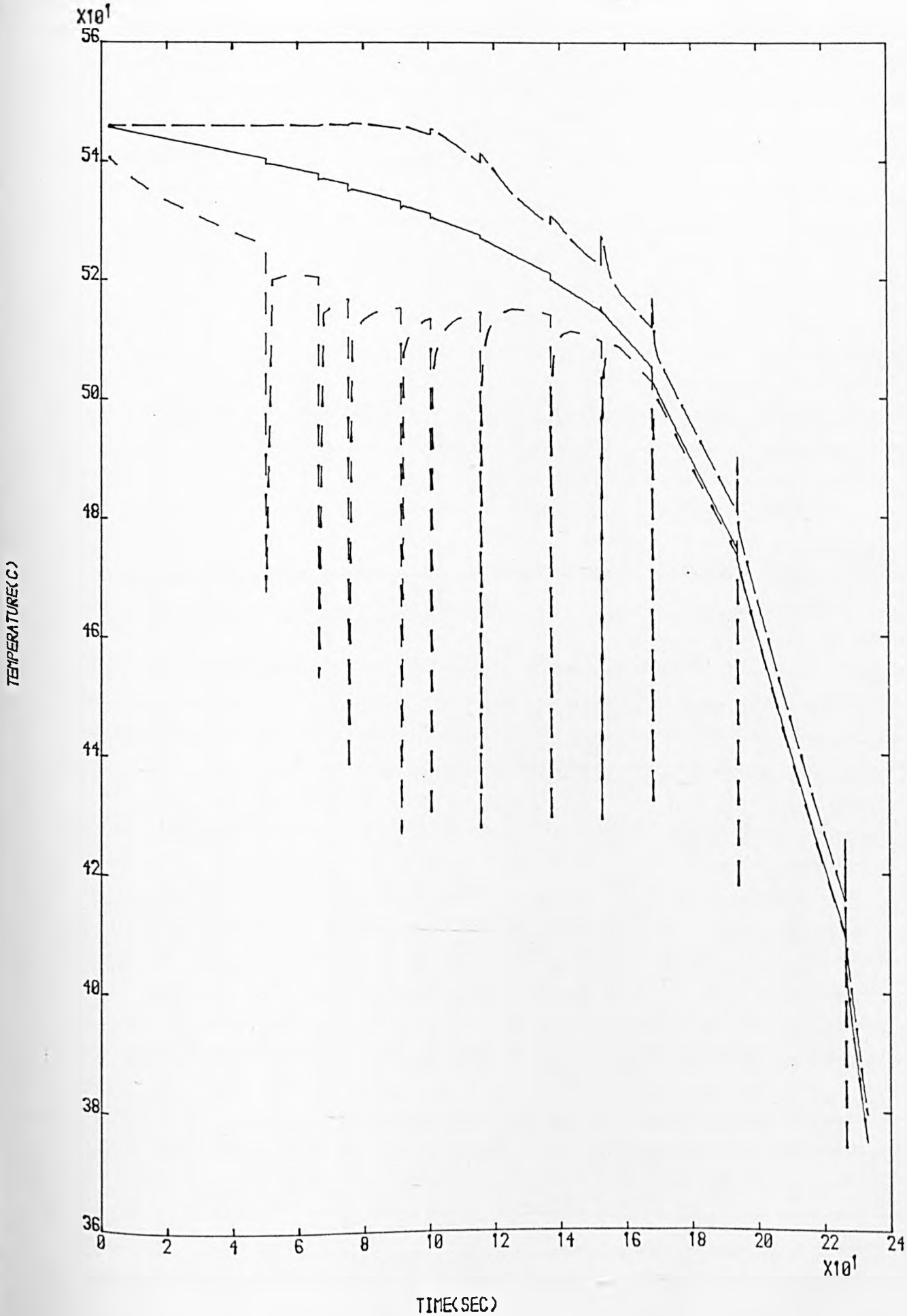
X10¹
56
54
52
50
48
46
44
42
40
38
36
TEMPERATURE(C)
0
2
4
6
8
10
12
14
16
18
20
22
24
X10¹
TIME(SEC)

FIGURE 146: Computer prediction of the microstructural evolution expressed in terms of the recrystallised fraction, corresponding to the Industrial Schedule No.3.

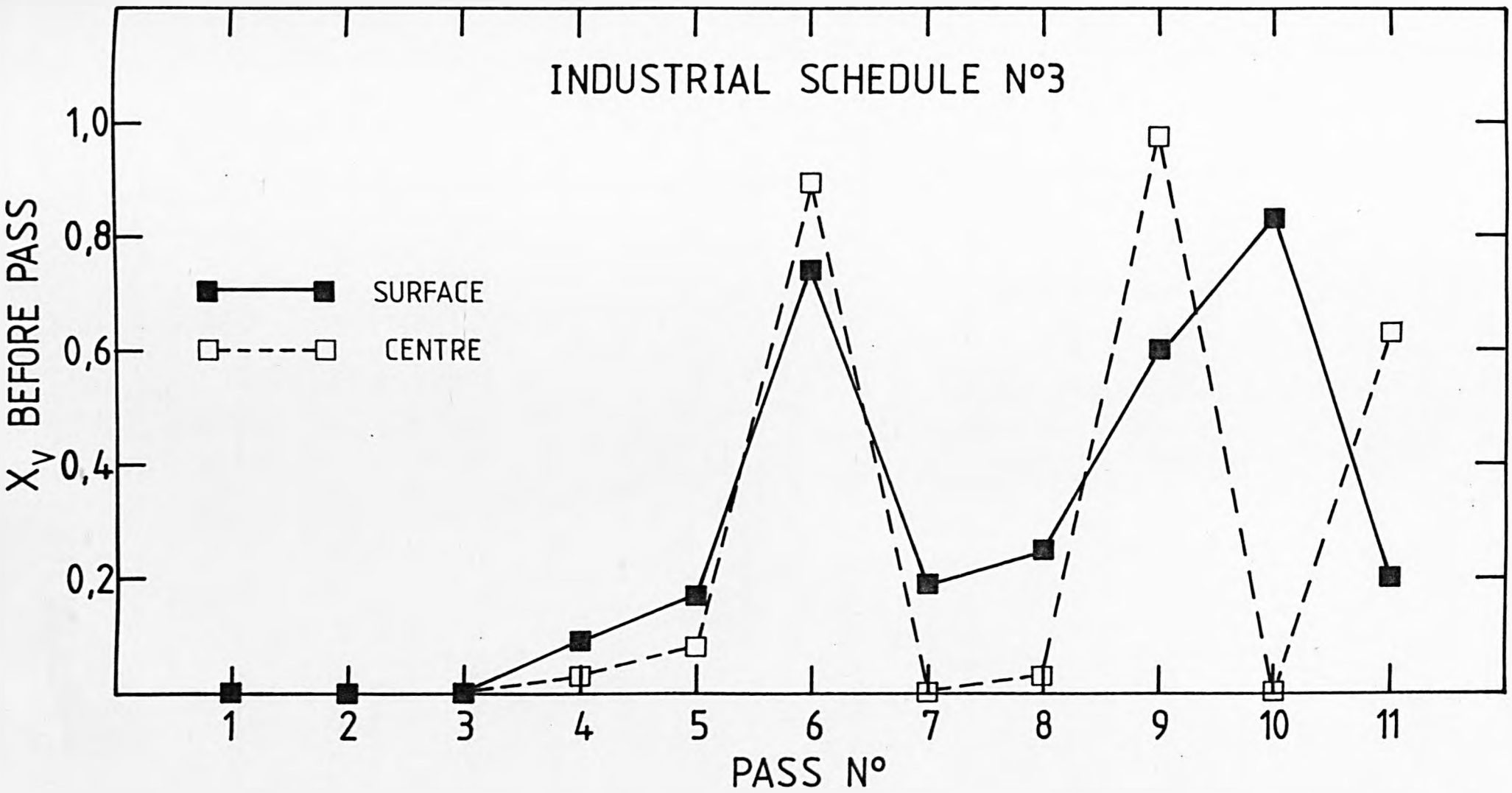
INDUSTRIAL SCHEDULE N°3
1,0
0,8
0,6
0,4
0,2
X_V BEFORE PASS
SURFACE
CENTRE
1
2
3
4
5
6
7
8
9
10
11
PASS N°

FIGURE 147: Comparison between computer predicted and experimental rolling loads observed during the industrial hot rolling of commercial-purity aluminiun. (Industrial Schedule No.3)

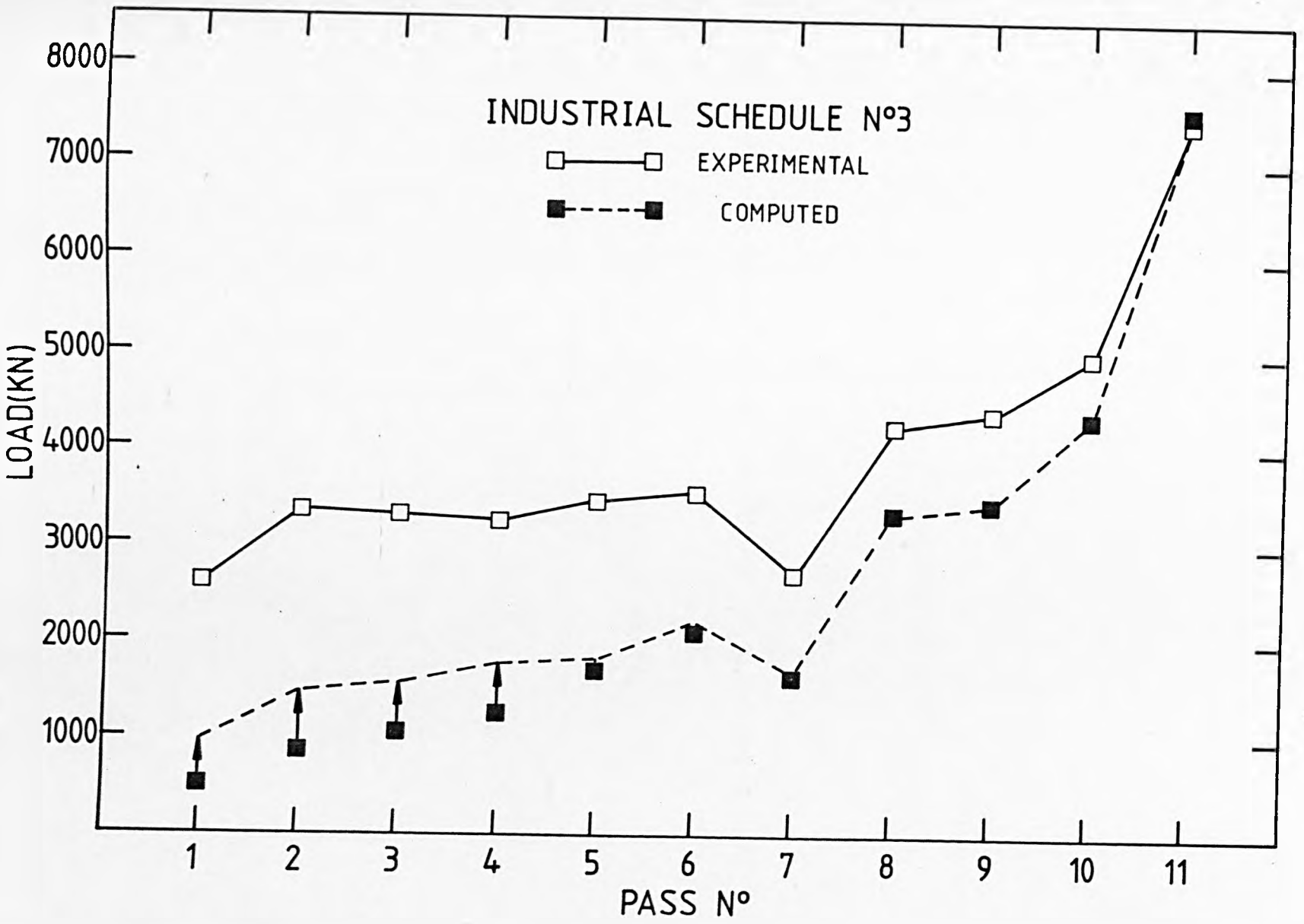
INDUSTRIAL SCHEDULE N°3
EXPERIMENTAL
COMPUTED
LOAD(KN)
8000
7000
6000
5000
4000
3000
2000
1000
1
2
3
4
5
6
7
8
9
10
11
PASS N°

FIGURE 148: Strain-time history of a typical industrial hot rolling operation on commercial-purity aluminium. (Industrial Schedule No.4).

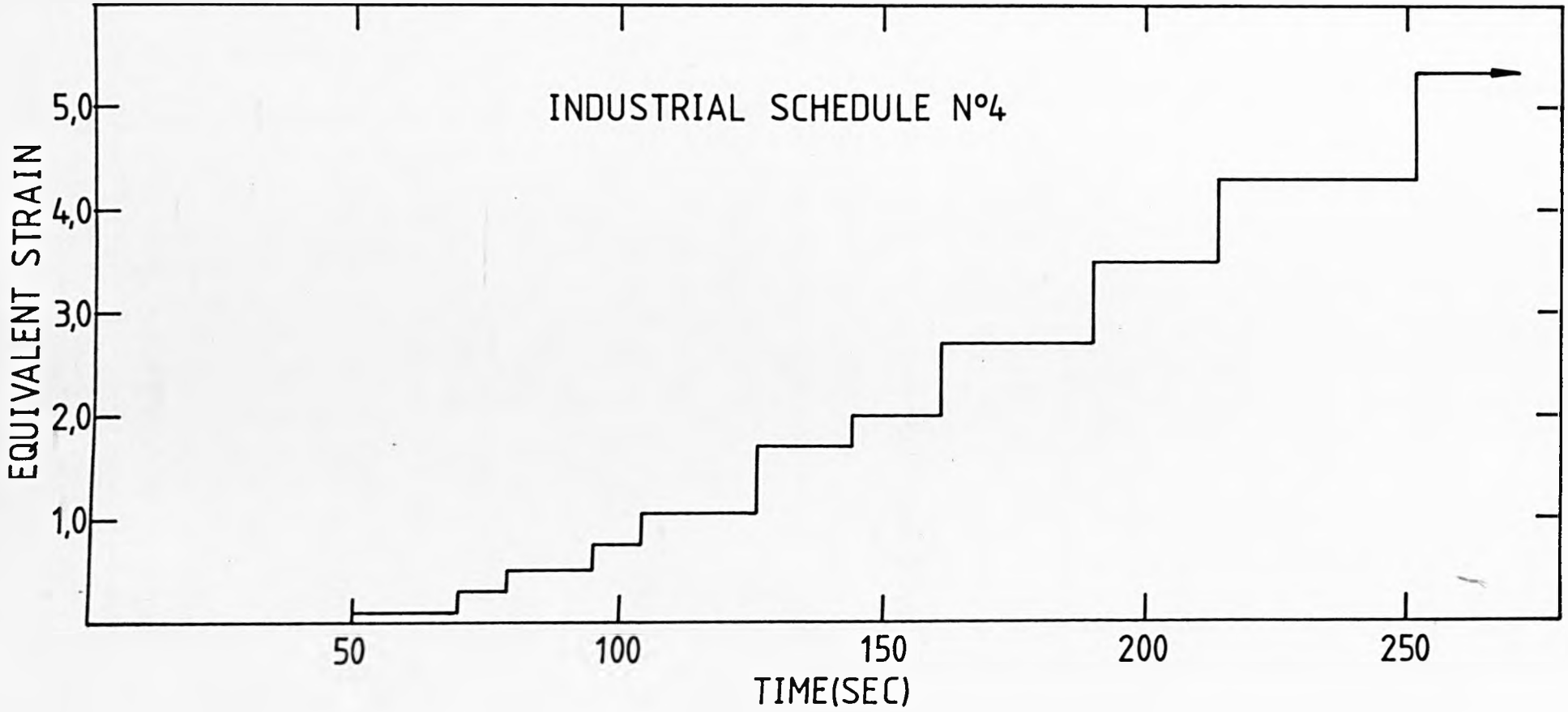
INDUSTRIAL SCHEDULE N°4
EQUIVALENT STRAIN
5,0
4,0
3,0
2,0
1,0
50
100
150
200
250
TIME(SEC)

FIGURE 149: Computer prediction of the changes in centre, mean and surface temperature during a typical industrial hot rolling operation on commercial-purity aluminium. (Industrial Schedule No.4).

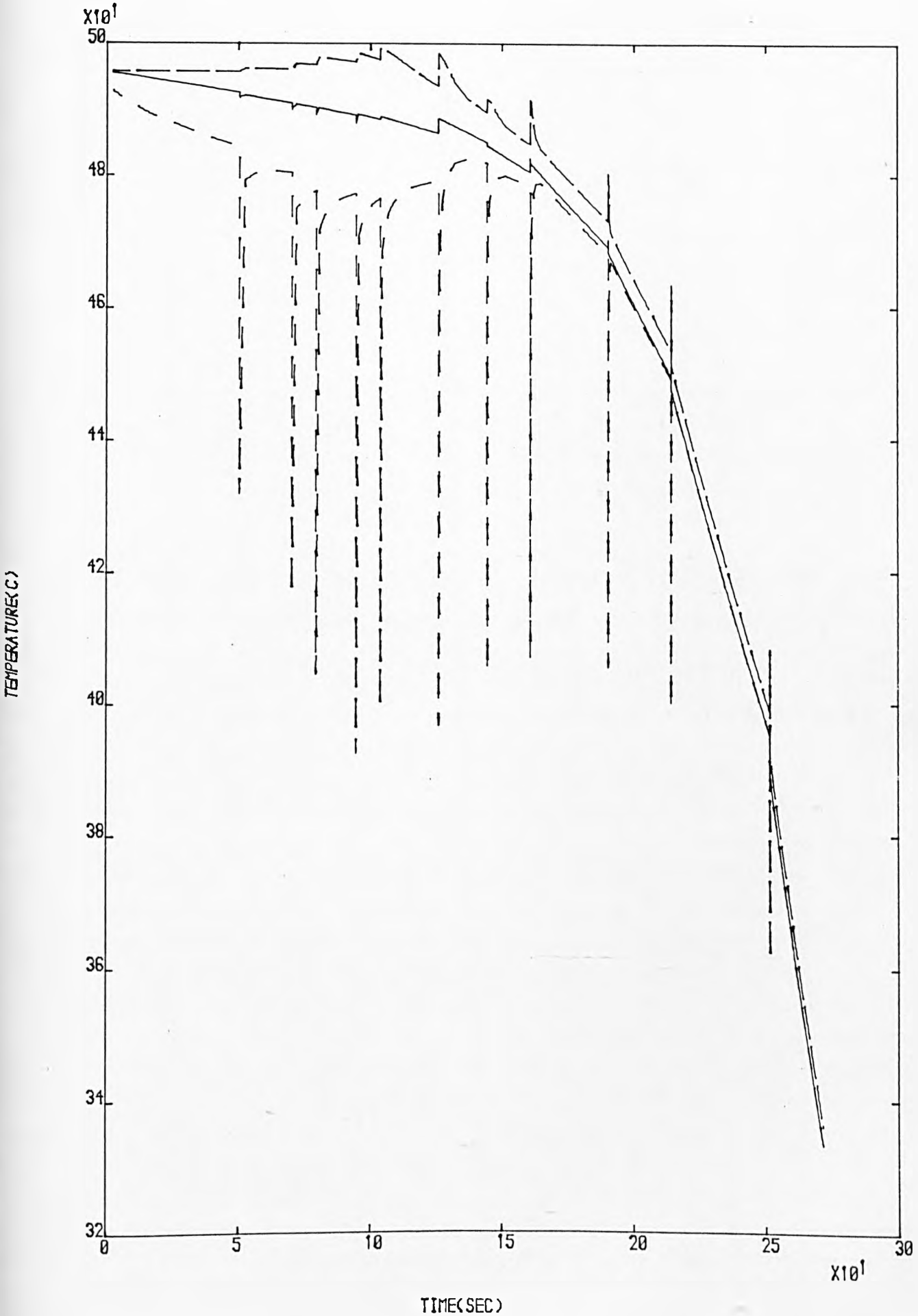
X10¹
50
48
46
44
42
40
38
36
34
32
TEMPERATURE(C)
0
5
10
15
20
25
30
X10¹
TIME(SEC)

FIGURE 150: Computer prediction of the microstructural evolution expressed in terms of the recrystallised fraction, corresponding to the Industrial Schedule No.4.

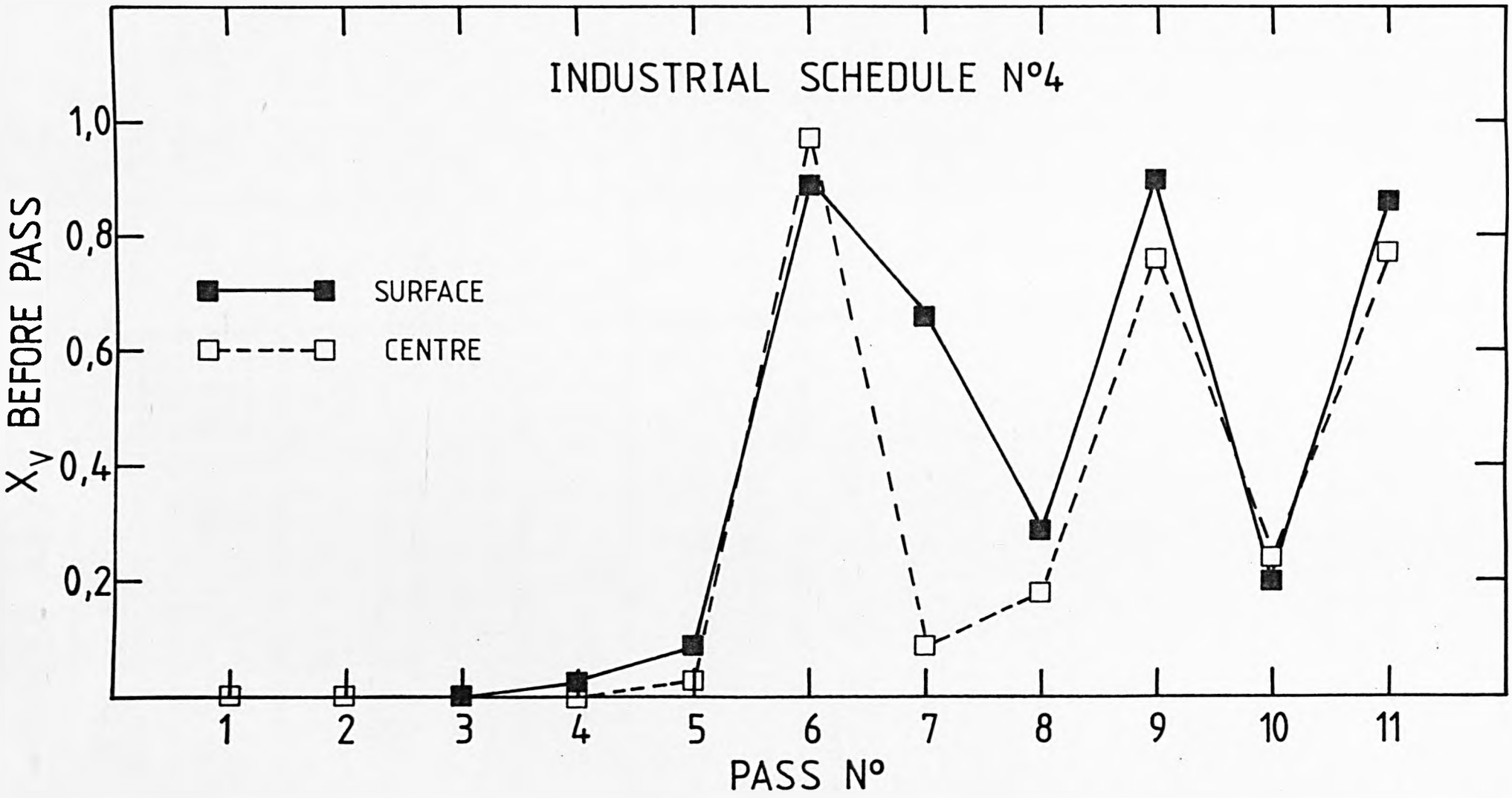
INDUSTRIAL SCHEDULE N°4
1,0
0,8
0,6
0,4
0,2
X_V BEFORE PASS
SURFACE
CENTRE
1
2
3
4
5
6
7
8
9
10
11
PASS N°

FIGURE 151: Comparison between computer predicted and experimental rolling loads observed during the industrial hot rolling of commercial-purity aluminium. (Industrial Schedule No.4).

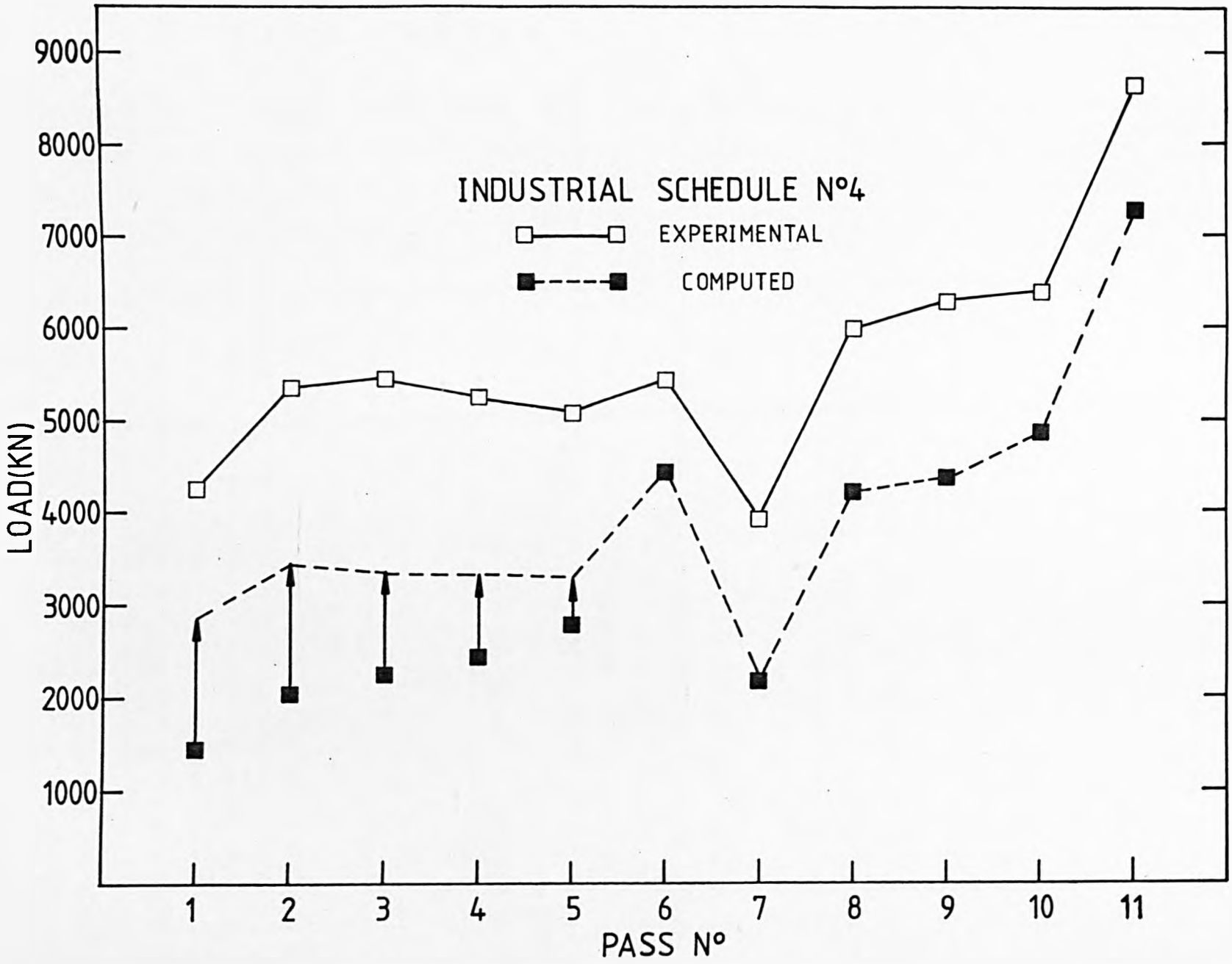
INDUSTRIAL SCHEDULE N°4
EXPERIMENTAL
COMPUTED
LOAD(KN)
9000
8000
7000
6000
5000
4000
3000
2000
1000
1
2
3
4
5
6
7
8
9
10
11
PASS N°

FIGURE 152: Strain-time histories of two typical industrial hot rolling operations on commercial-purity aluminium:

(a) Industrial Schedule No.7.

(b) Industrial Schedule No.5.

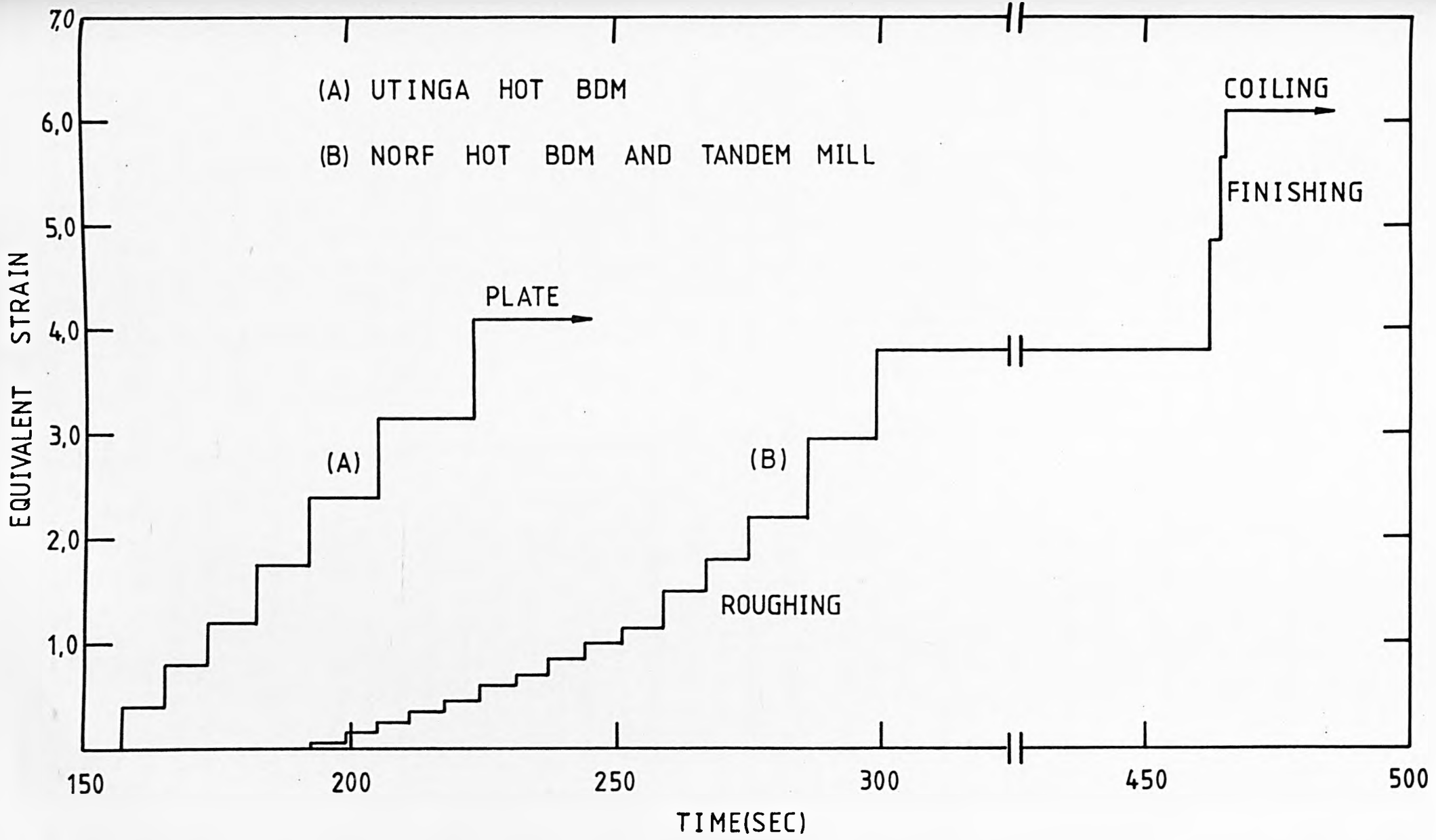
(A) UTINGA HOT BDM
(B) NORF HOT BDM AND TANDEM MILL
COILING
FINISHING
PLATE
(A)
(B)
ROUGHING
EQUIVALENT STRAIN
7,0
6,0
5,0
4,0
3,0
2,0
1,0
150
200
250
300
450
500
TIME(SEC)

FIGURE 153: Computer prediction of the changes in centre, mean and surface temperature during a typical industrial hot rolling operation on commercial-purity aluminium. (Industrial Schedule No.5).

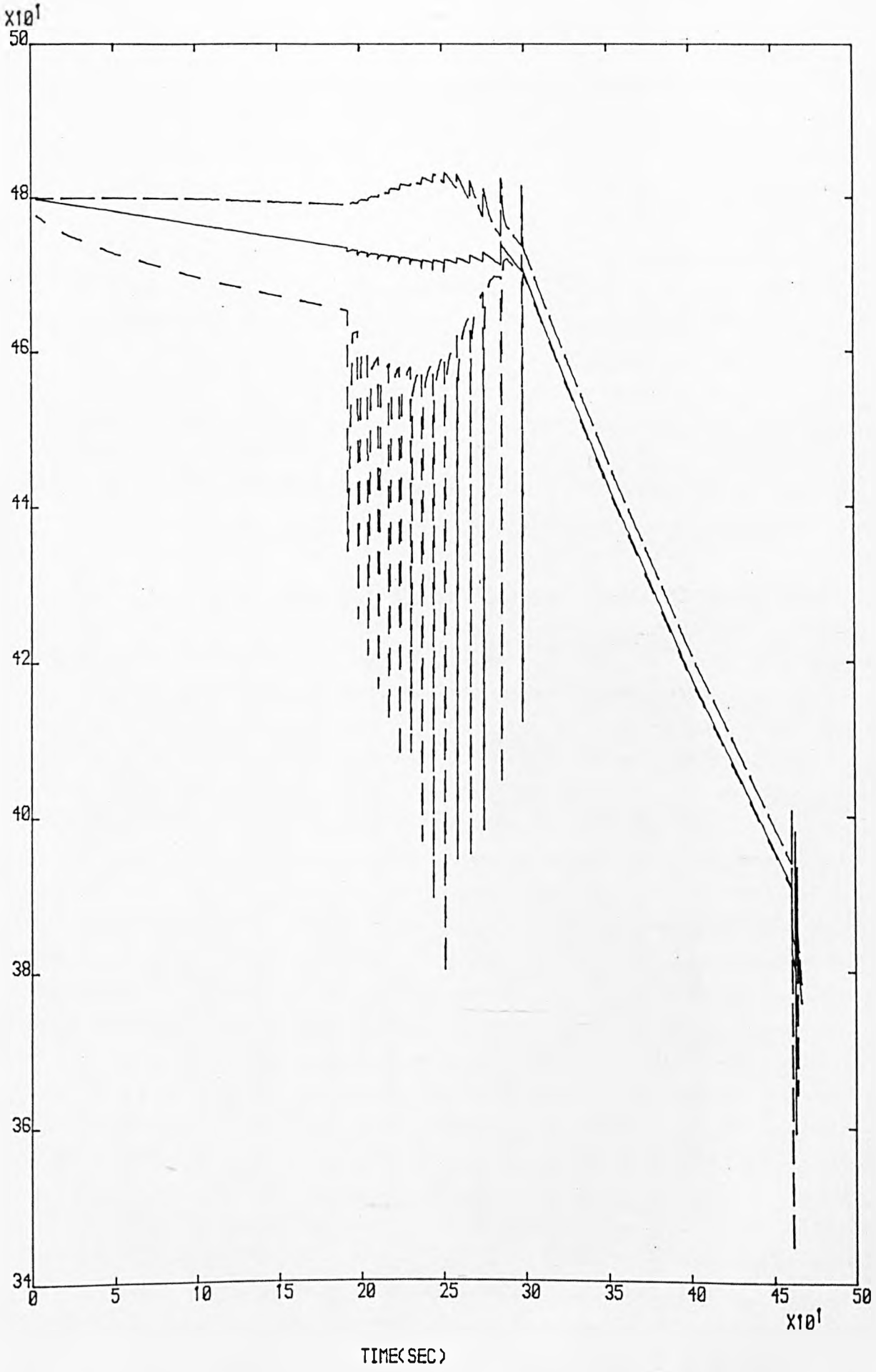
X10¹
50
48
46
44
42
40
38
36
34
0
5
10
15
20
25
30
35
40
45
50
X10¹
TEMPERATURE(C)
TIME(SEC)

FIGURE 154: Computer prediction of the microstructural evolution expressed in terms of the recrystallised fraction, corresponding to the Industrial Schedule No.5.

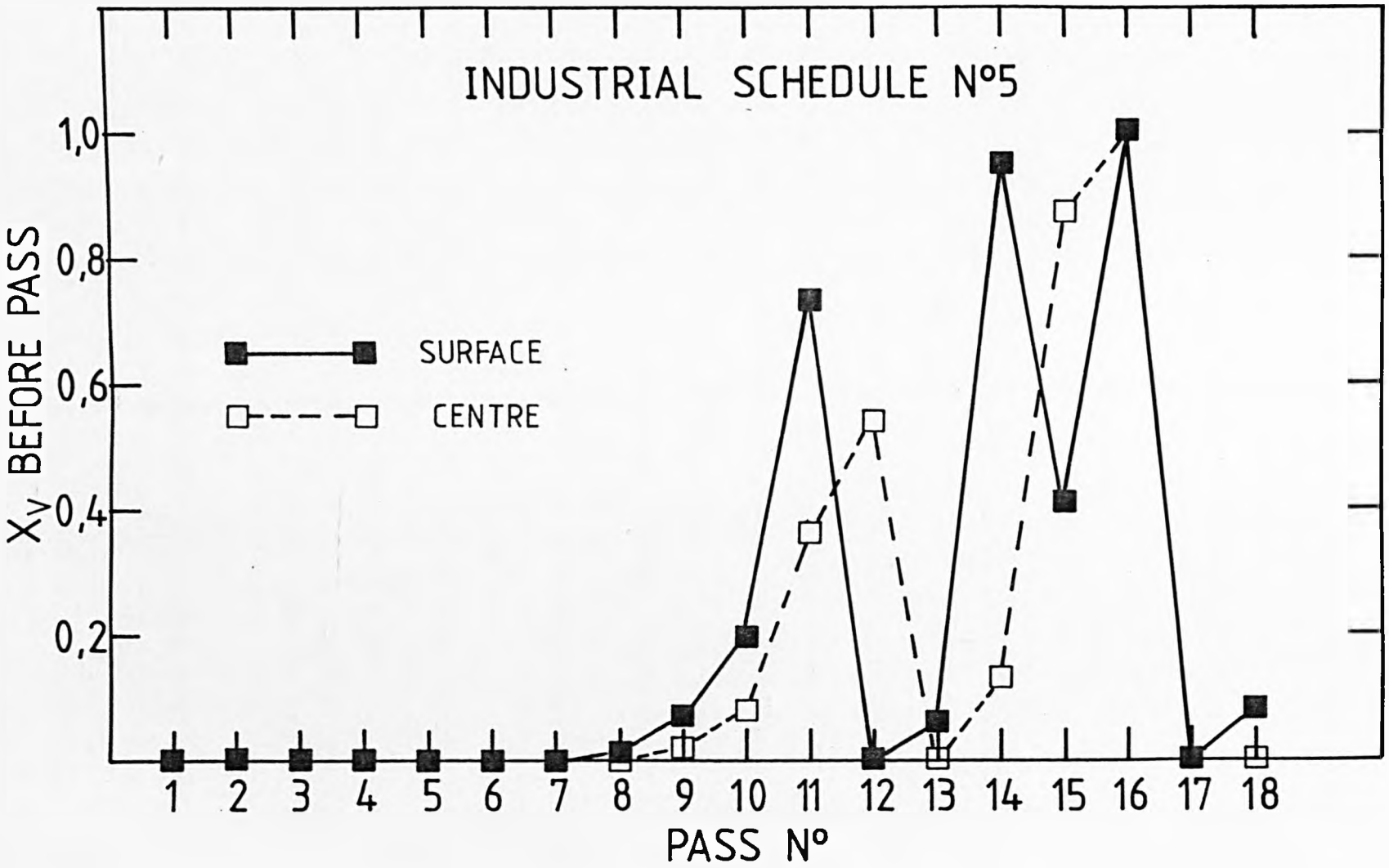
INDUSTRIAL SCHEDULE N°5
1,0
0,8
0,6
0,4
0,2
X_V BEFORE PASS
SURFACE
CENTRE
1 2 3 4 5 6 7 8 9 10 11 12 13 14 15 16 17 18
PASS N°

FIGURE 155: Comparison between computer predicted and industrial indirect assessments of rolling torques during the industrial hot rolling of commercial-purity aluminium. (Industrial Schedule No.5).

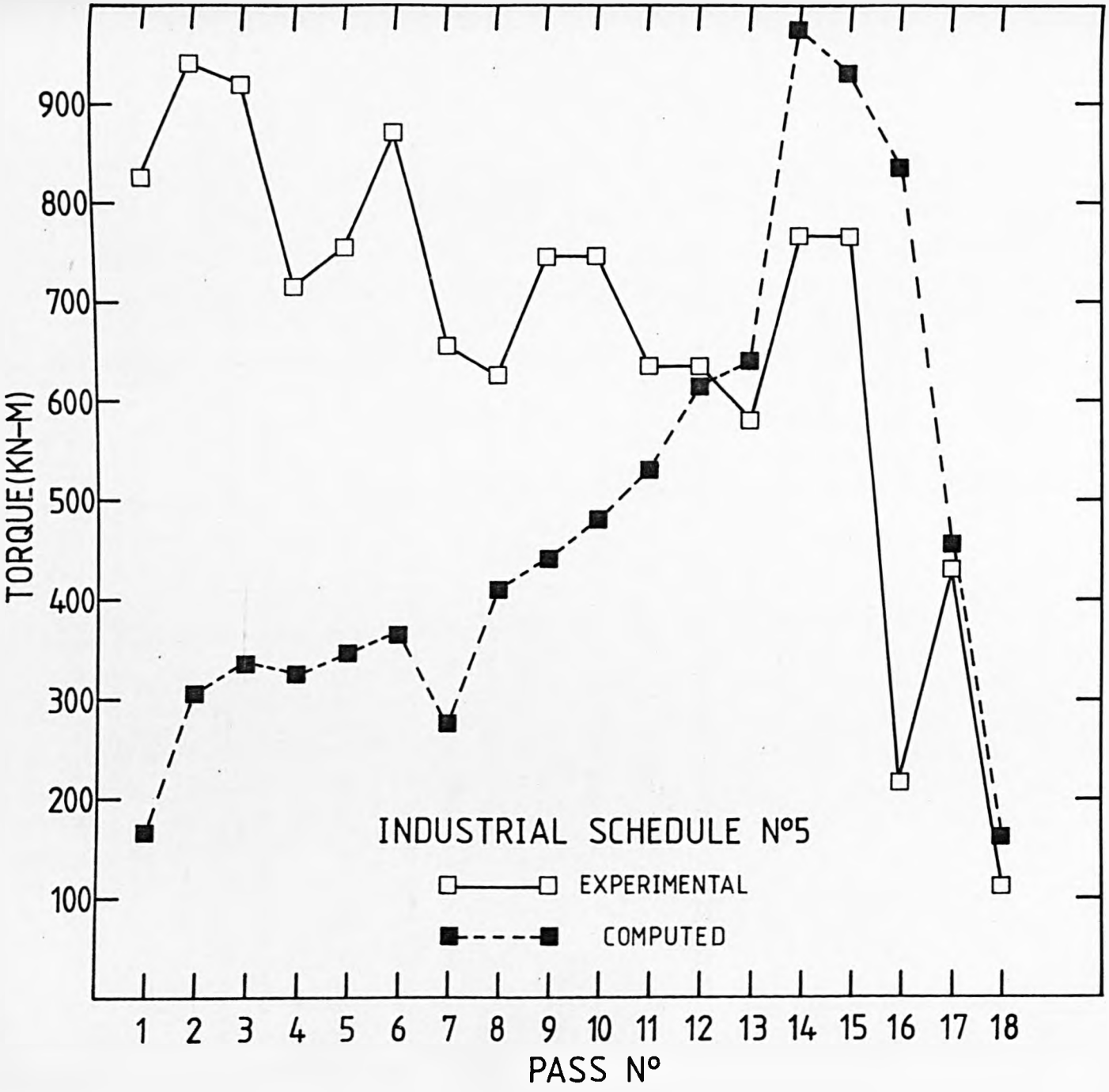
TORQUE(KN-M)
900
800
700
600
500
400
300
200
100
INDUSTRIAL SCHEDULE N°5
EXPERIMENTAL
COMPUTED
1 2 3 4 5 6 7 8 9 10 11 12 13 14 15 16 17 18
PASS N°

FIGURE 156: Strain-time history of a typical industrial hot rolling operation on commercial-purity aluminium. (Industrial Schedule No.6).

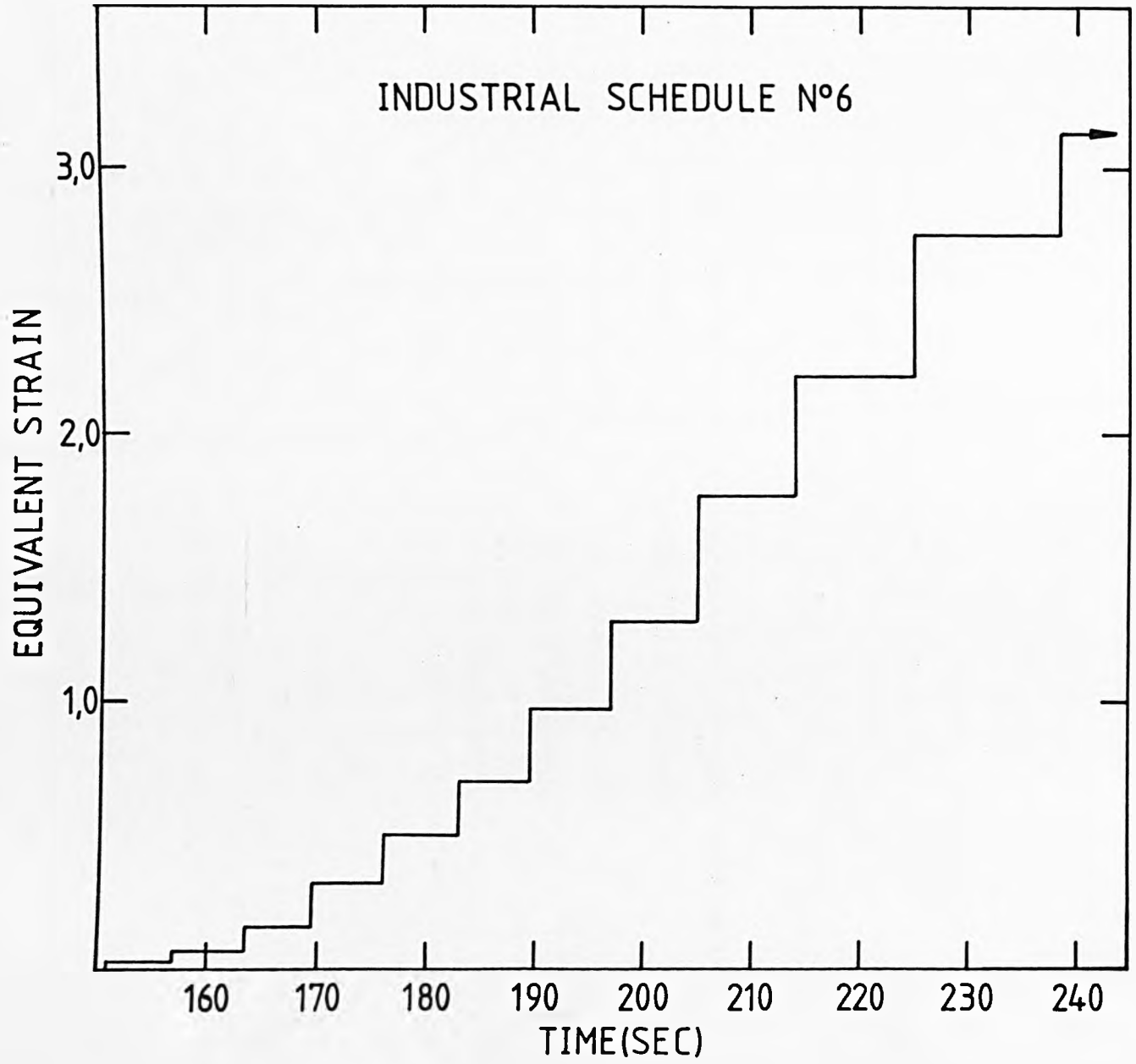
INDUSTRIAL SCHEDULE N°6
EQUIVALENT STRAIN
3,0
2,0
1,0
160
170
180
190
200
210
220
230
240
TIME(SEC)

FIGURE 157: Computer prediction of the changes in centre, mean and surface temperature during a typical industrial hot rolling operation on commercial-purity aluminium. (Industrial Schedule No.6).

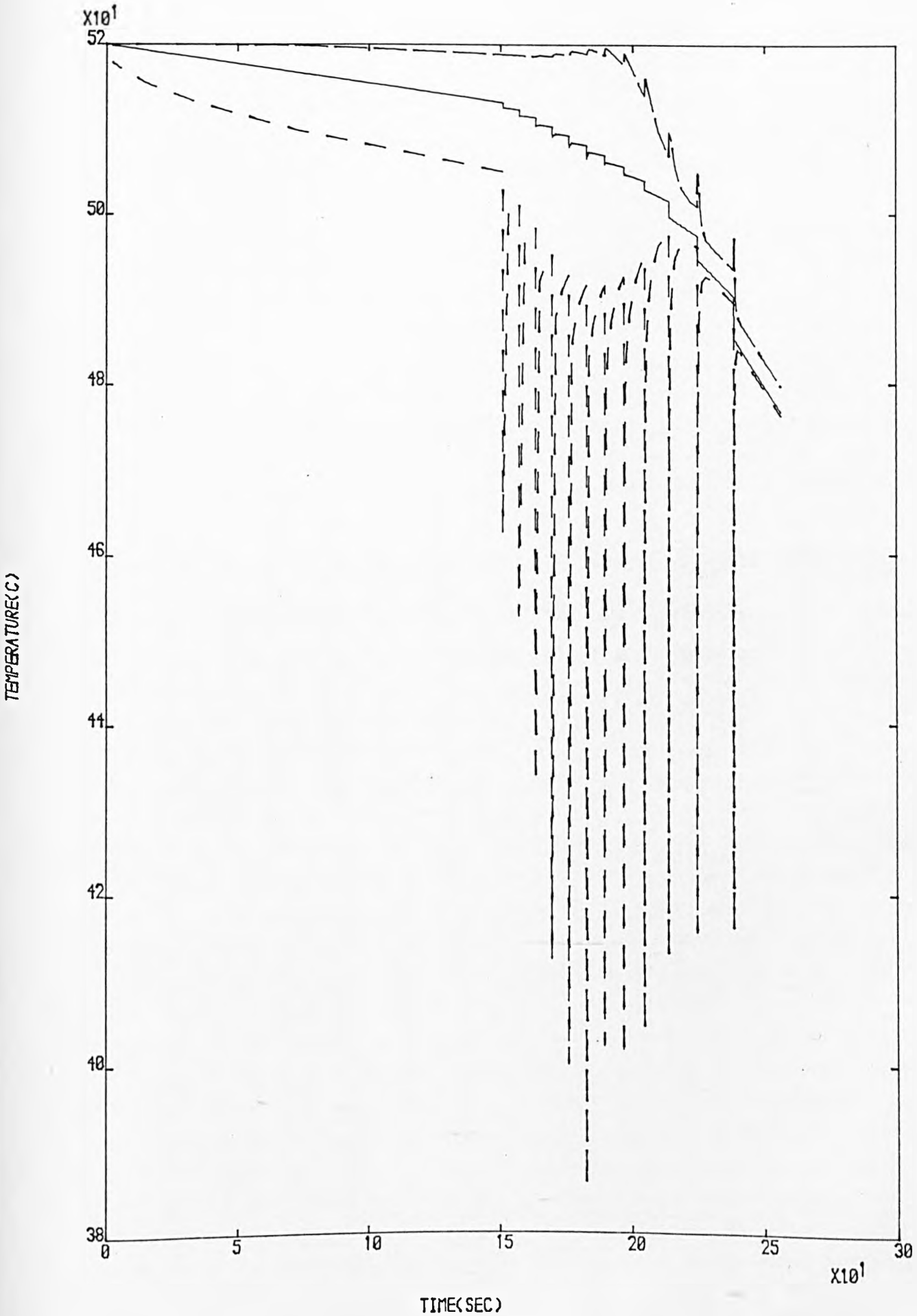
X10¹
52
50
48
46
44
42
40
38
0
5
10
15
20
25
30
X10¹
TEMPERATURE(C)
TIME(SEC)

FIGURE 158: Computer prediction of the microstructural evolution expressed in terms of the recrystallised fraction, corresponding to the Industrial Schedule No.6.

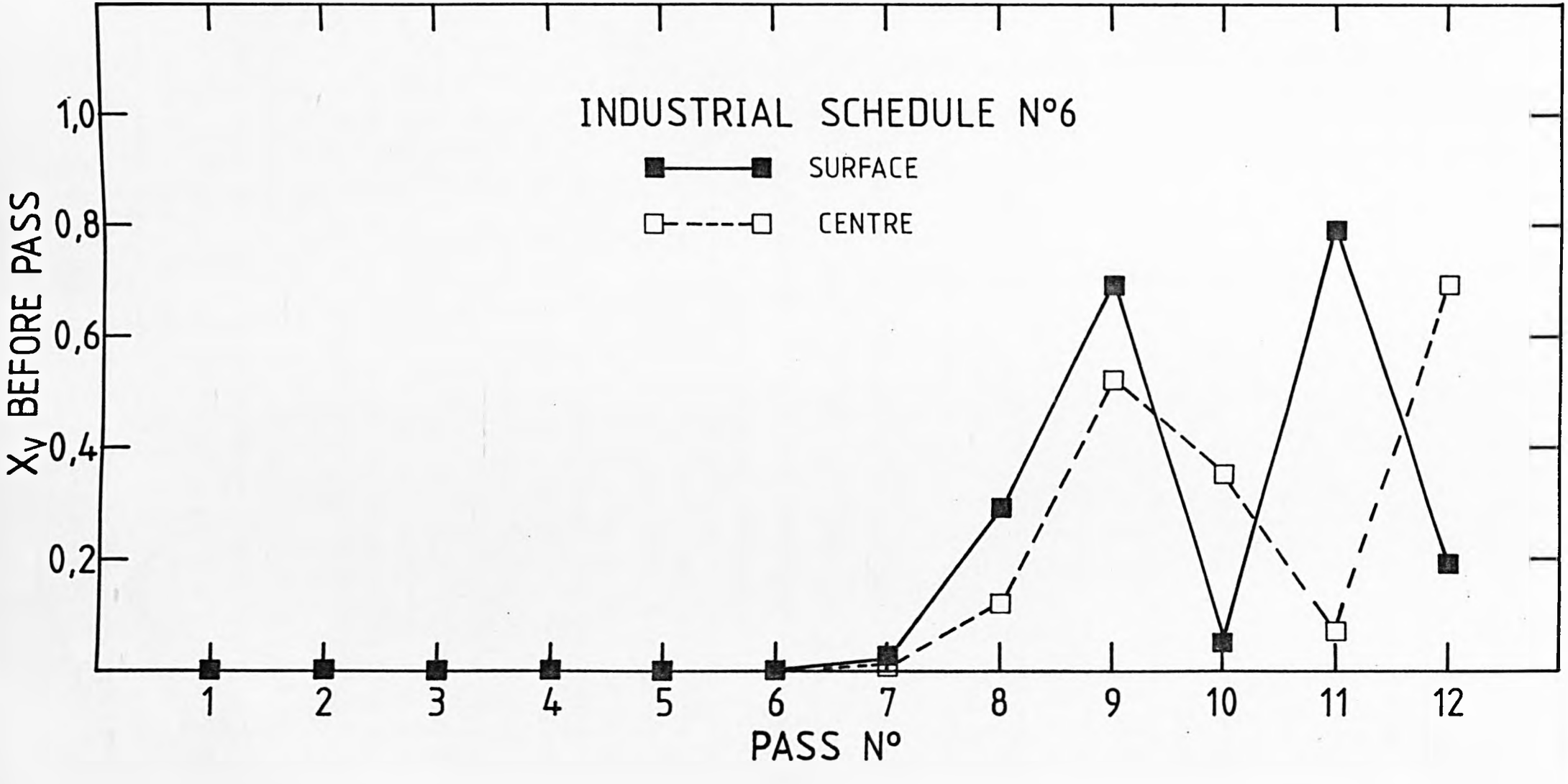
INDUSTRIAL SCHEDULE N°6
SURFACE
CENTRE
X_V BEFORE PASS
1,0
0,8
0,6
0,4
0,2
1
2
3
4
5
6
7
8
9
10
11
12
PASS N°

FIGURE 159: Comparison between computer predicted and industrial indirect assessments of rolling torques during the industrial hot rolling of commercial-purity aluminium. (Industrial Schedule No.6).

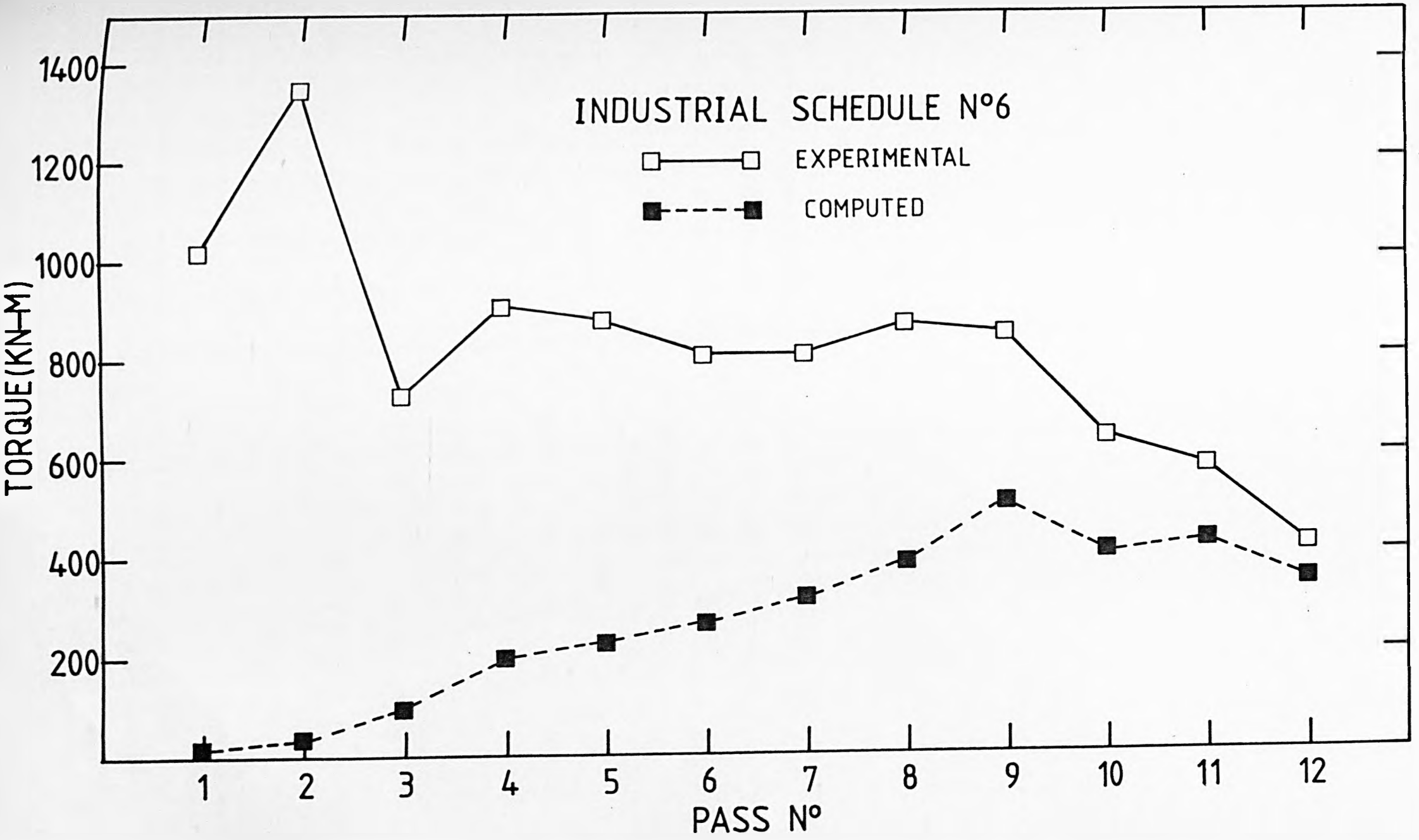
INDUSTRIAL SCHEDULE N°6
EXPERIMENTAL
COMPUTED
TORQUE(KN-M)
1400
1200
1000
800
600
400
200
1
2
3
4
5
6
7
8
9
10
11
12
PASS N°

FIGURE 160: Computer prediction of the changes in centre, mean and surface temperature during a typical industrial hot rolling operation on commercial-purity aluminium. (Industrial Schedule No.7).

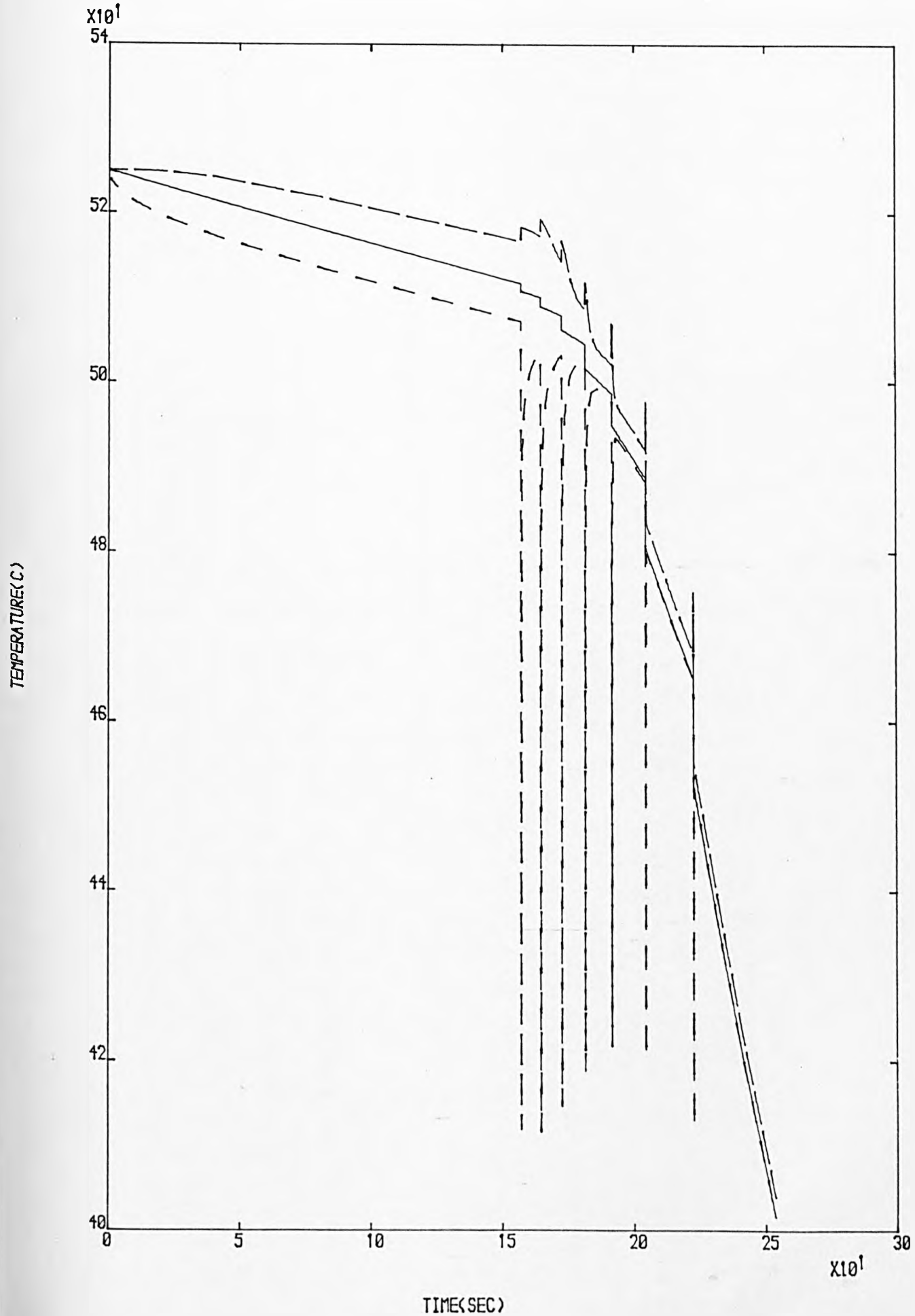
X10¹
54
52
50
48
46
44
42
40
0
5
10
15
20
25
30
X10¹
TEMPERATURE(C)
TIME(SEC)

FIGURE 161: Computer prediction of the microstructural evolution expressed in terms of the recrystallised fraction, corresponding to the Industrial Schedule No.7.

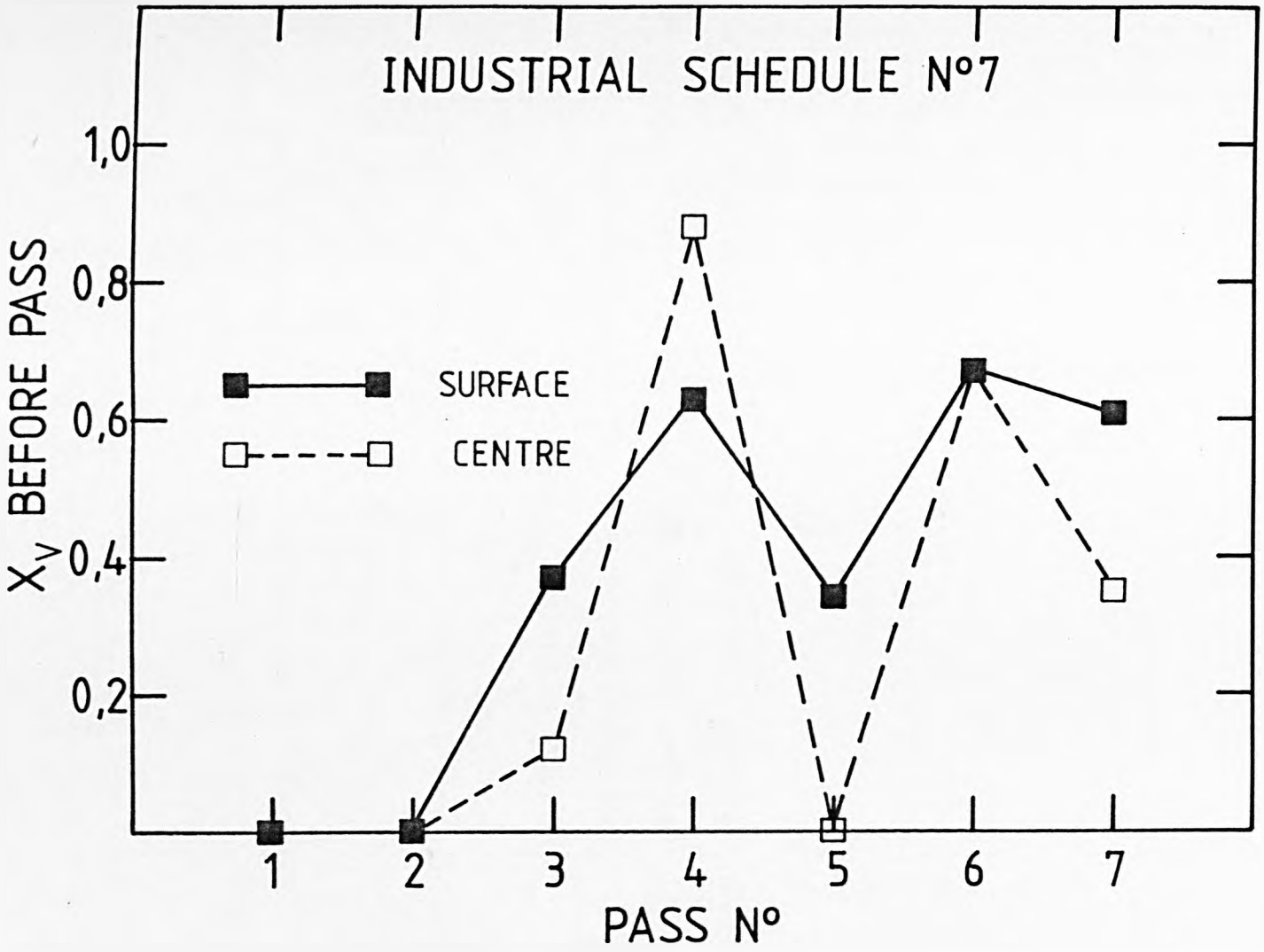
INDUSTRIAL SCHEDULE N°7
1,0
0,8
0,6
0,4
0,2
X_V BEFORE PASS
SURFACE
CENTRE
1
2
3
4
5
6
7
PASS N°

FIGURE 162: Comparison between computer predicted and industrial indirect assessments of rolling torques during the industrial hot rolling of commercial-purity aluminium. (Industrial Schedule No.7).

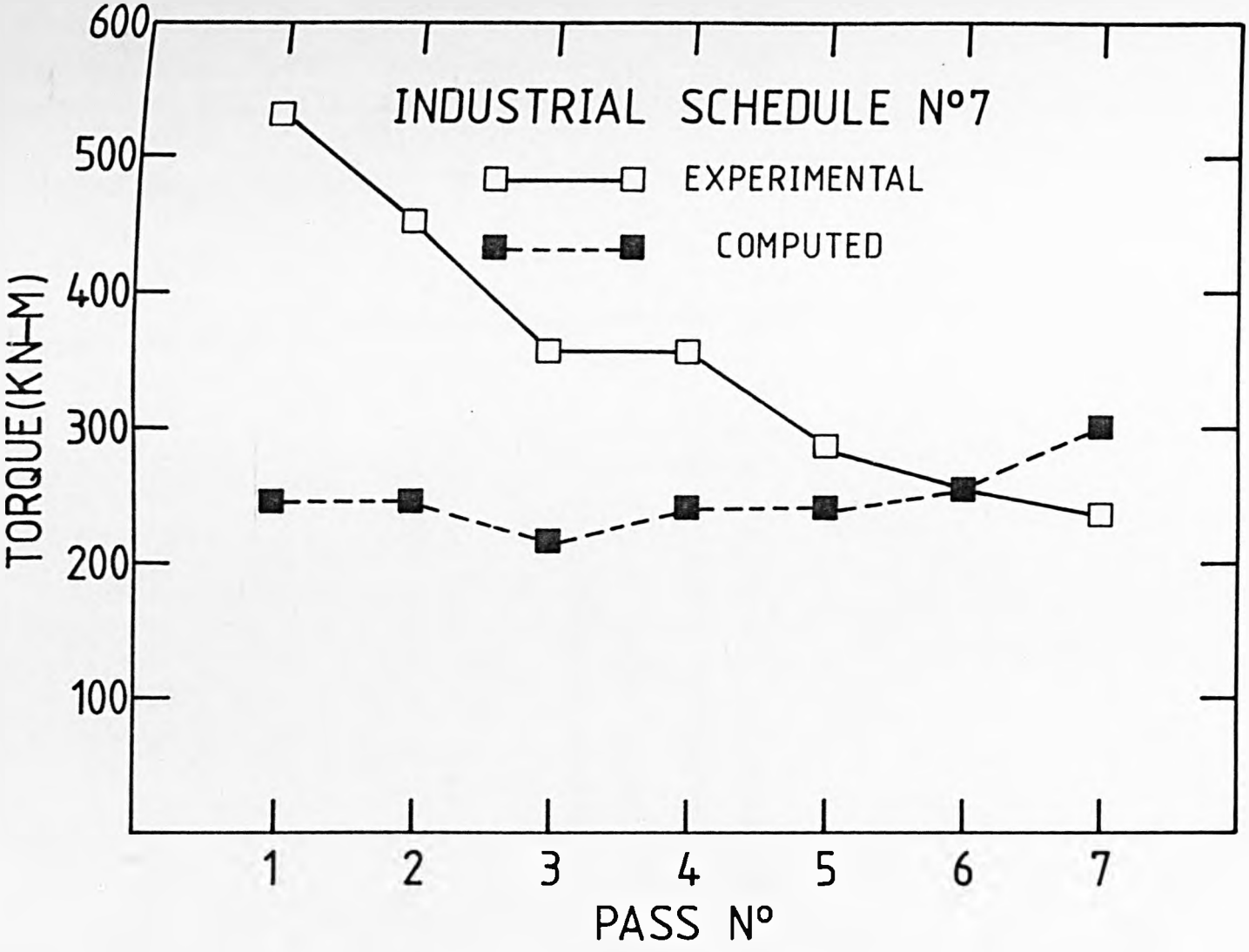
INDUSTRIAL SCHEDULE N°7
EXPERIMENTAL
COMPUTED
TORQUE(KN-M)
600
500
400
300
200
100
1
2
3
4
5
6
7
PASS N°

FIGURE 163: Variation of the surface heat transfer coefficient "H" with surface temperature "Ts" during heating up of a standard plane strain compression 10.51 mm thick. Test furnace temperature: 495°C.

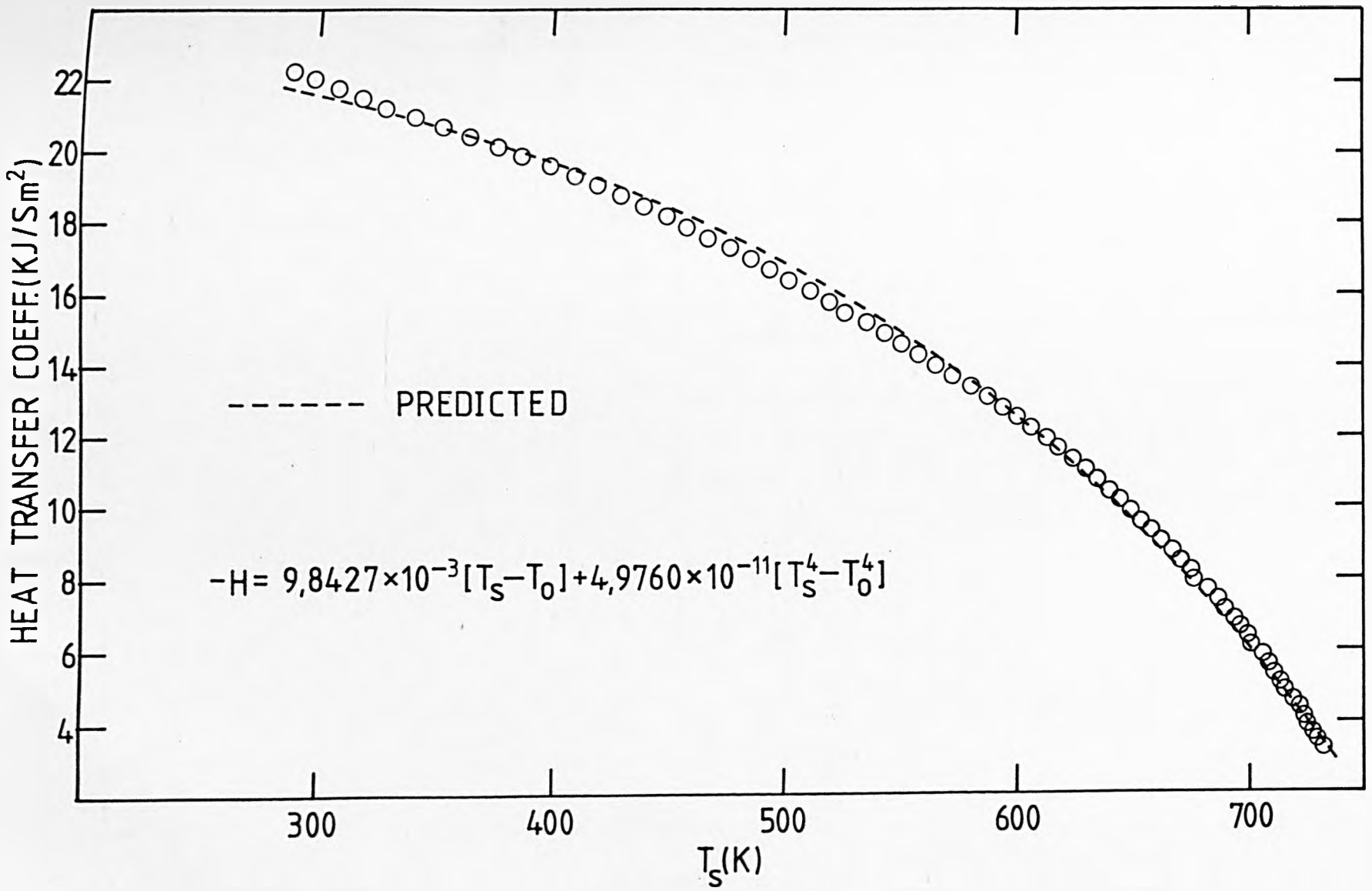
HEAT TRANSFER COEFF.(KJ/Sm²)
22
20
18
16
14
12
10
8
6
4
300
400
500
600
700
T_S(K)
------ PREDICTED
-H= 9,8427×10⁻³[T_S−T_0]+4,9760×10⁻¹¹[T_S⁴−T_0⁴]

FIGURE 164: Variation of the centre temperature "T_o" of a plane strain compression specimen 10.51 mm thick with time, during heating in the test furnace at 495°C.

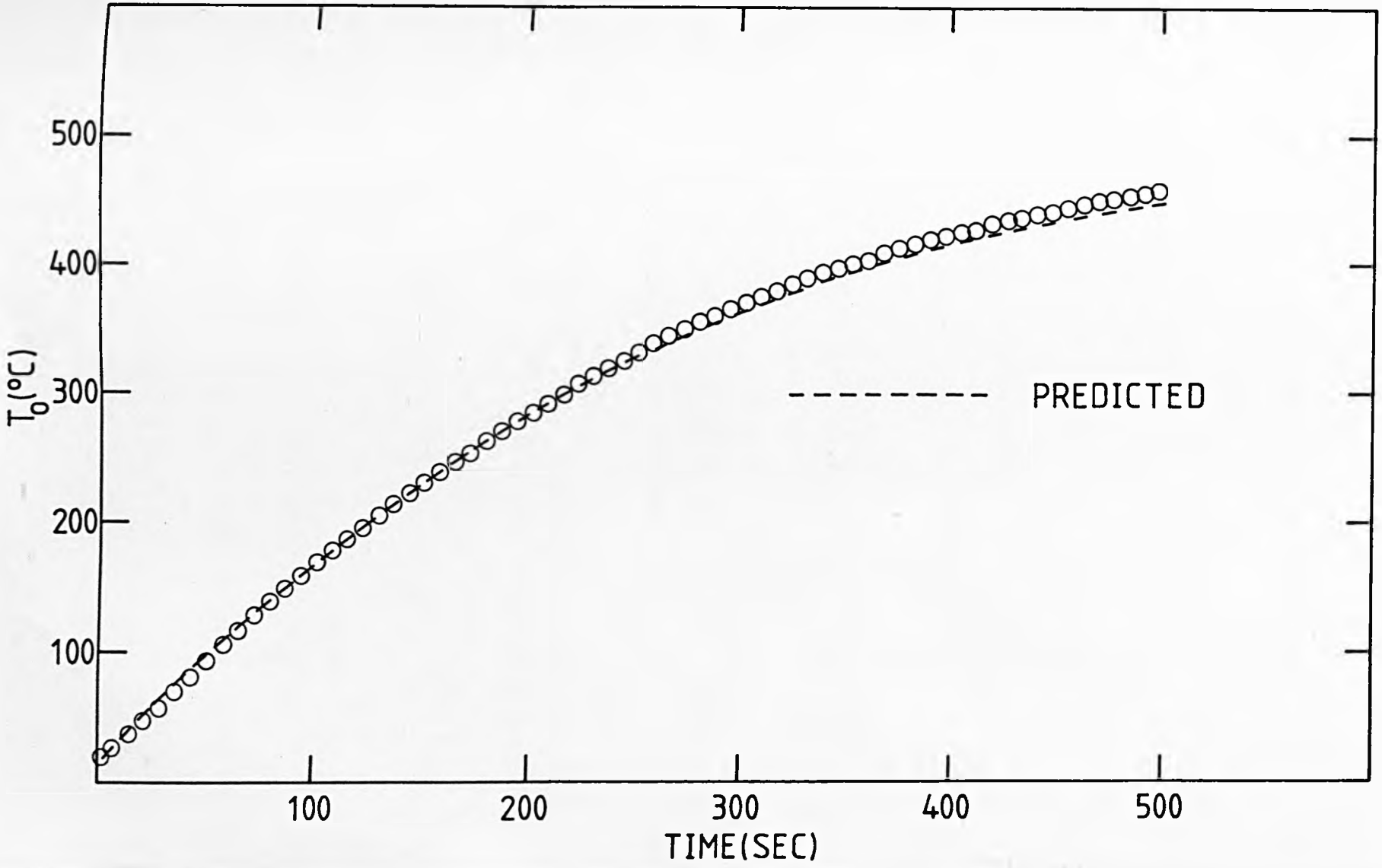
500
400
300
200
100
T_o(°C)
PREDICTED
100
200
300
400
500
TIME(SEC)

FIGURE 165: Variation of the centre temperature "T_o" of,

(a) a plane strain compression, non-lubricated specimen 10.51 mm thick with time, during air cooling on the arms of the specimen handling carriage;

(b) a plane strain compression, lubricated specimen 10.51 mm thick cooled down under similar conditions.

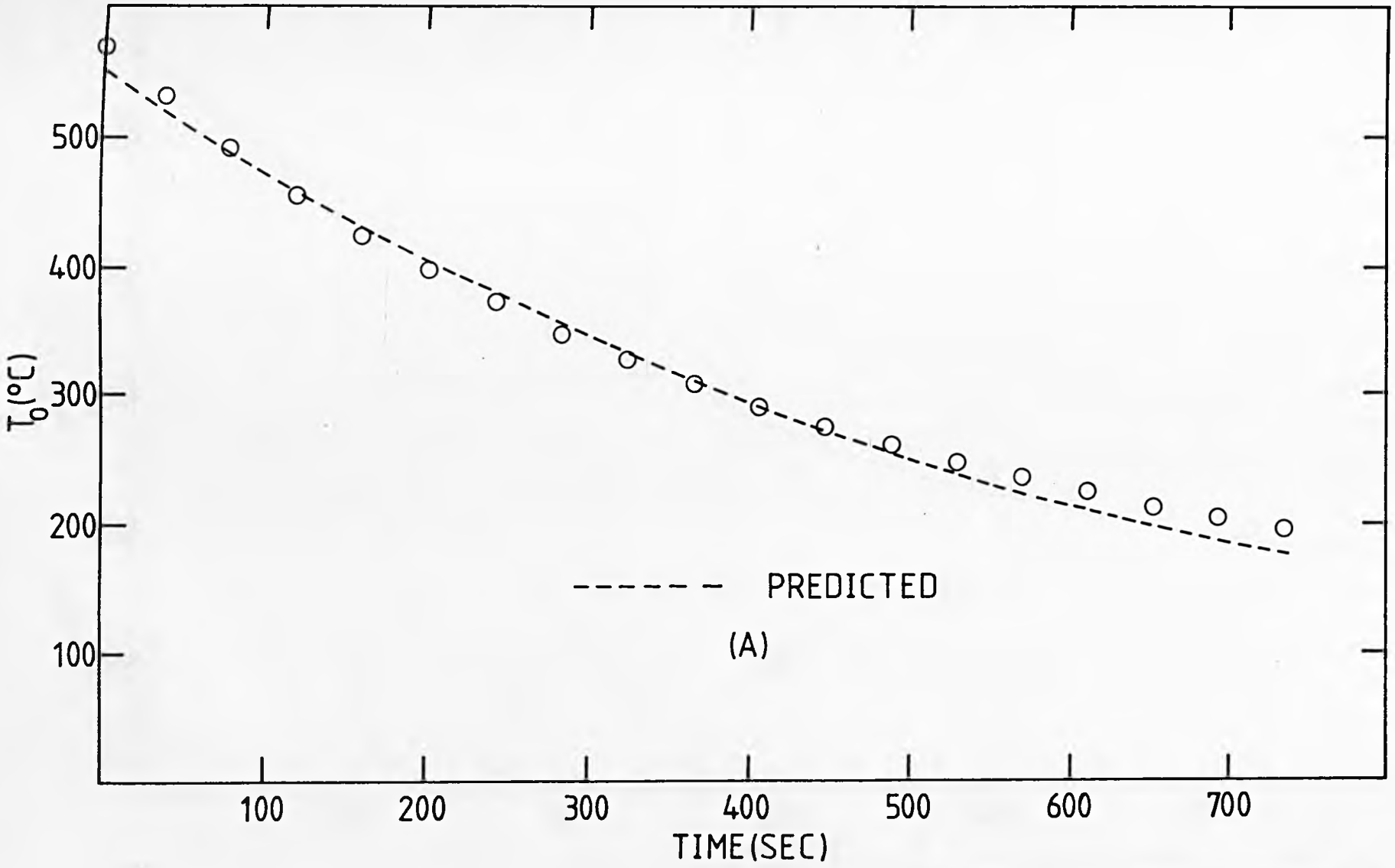
500
400
300
200
100
T_0(°C)
PREDICTED
(A)
100
200
300
400
500
600
700
TIME(SEC)

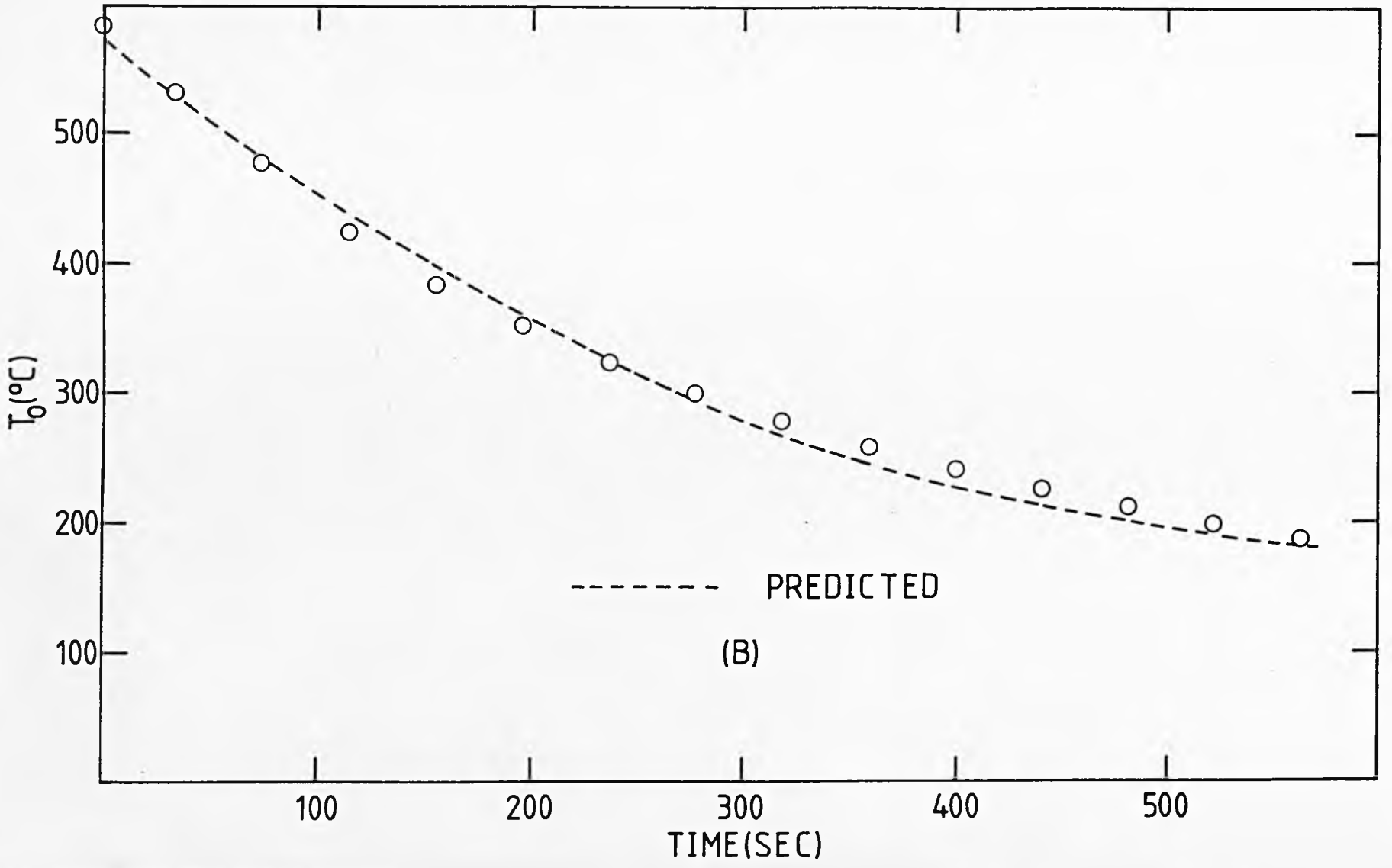
500
400
300
200
100
T_0(°C)
PREDICTED
(B)
100
200
300
400
500
TIME(SEC)